Regularization in Tidal Analysis and the Application of the Local Response Model in Moving Window Analysis

Zur Erlangung des akademischen Grades eines
DOKTORS DER NATURWISSENSCHAFTEN (Dr. rer. nat.)
von der KIT-Fakultät für Physik des
Karlsruher Instituts für Technologie (KIT)

genehmigte

DISSERTATION

von

M. Sc. Adam Jakub Ciesielski
aus Krakau (Polen)

Tag der mündlichen Prüfung:	07.07.2023
Referent:	Prof. Dr. Andreas Rietbrock
Korreferent:	Prof. Dr. Jacques Hinderer (Universität Straßburg)

Whenever people agree with me
I always feel I must be wrong.

Oscar Wilde

Abstract

The already 100 years old harmonic analysis of tides is based on the assumption of separable and non-separable contributions. The resolution discrepancy, known as the *Rayleigh criterion* in tidal analysis, is strictly related to the duration of the analyzed time series. Although convenient and the most common way for harmonic separation, it does not take into account the actual resolution limited by the signal-to-noise ratio of the data and the capabilities of modern computers and methods. A priori *wave groups* based on separable constituents had to be composed of harmonics close to the main harmonic within a predefined frequency range. It was necessary since otherwise the problem results in an ill-conditioned system of linear equations, which must be solved in order to find the tidal parameters. Even more sophisticated wave grouping schemes are based on the time series length, so the information about the actual resolution provided by the data is lost.

In addition, worldwide changes in tide patterns over the past 150 years have been noticed, but many of them still lack a clear explanation. In the analysis of gravity records, temporal variations of tidal parameters have been known for over 30 years. Data from superconducting gravimeters (SG) with unprecedented accuracy show systematic variations of tidal parameters. This is confirmed for all tidal wave groups at 19 different SG stations around the globe. The amplitude of variations usually is greater than the standard deviation by a factor of 2 (minimum) to 32 (maximum). One possible reason for temporal variations of tidal parameters is the limited frequency resolution combined with an improper ratio of harmonics in one group, unequally influenced by the ocean loading. The analysis model only considers the body response to tidal forces, while the data contains the ocean response (through loading) as well the other signal contributions which present additional variation of tidal parameters with frequency. This is expected to result in the modulation of the estimates since harmonics within a wave group have a distinct response to tidal forces (loading).

In this thesis I present an alternative approach to classical harmonic tidal analysis, which constrains the solution to be close to a reference model. This regularization stabilizes the linear regression, hence allowing for the inference of model parameters for each tidal harmonic. Overcoming the need to create a priori groups of harmonics, it enables individual treatment of all tidal harmonics. In this way, bias by a priori model parameterization is avoided or significantly reduced, while ill-conditioning does not pollute the solution with over-fitting. The inversion is done iteratively by adjusting the reference model to reduce the data misfit. The

frequency dependence of the solution is thus data-driven. I find models for the various spherical degrees independently, which is an important aspect because the ocean loading significantly differs for each degree. The procedure allows for narrow-band variations of the tidal admittance. The significance and estimate of each parameter of concern can be tested. I demonstrate the relationship between harmonic amplitude and resolution. The impact of the regularization is carefully discussed and considered. I test the method, named `RATA` (Regularization Approach to Tidal Analysis), to determine a local response model from 11.5 years of data recorded by the superconducting gravimeter SG056 at Black Forest Observatory (BFO, Schiltach). As a result, I distinguish 61 significant groups of harmonics for the local tidal response model, with no clear evidence that more groups are resolvable. Some of them highly violate the Rayleigh criterion. A few harmonics that are usually separated according to the Rayleigh criterion are not proven significant. The results are tested against outcomes for the instrument's second sensor and verified with the unconstrained inversion that uses resolved wave groups. The residual time series is smaller when compared to previous models, with no indication of over-fitting. After a successful application of this method for BFO, analyses for 5 European stations and 8 stations outside Europe are performed. The analysis of European stations confirms the consistency of the method, as well as its ability to achieve super resolution. However, the obvious consistent differences in phases and amplitudes are most likely caused by the distance to the ocean. I discover that the differences between close-frequency large-amplitude harmonics are comparable, or even smaller, than mid-amplitude distant frequency tides. The investigation of additional stations reveals significant disparities between the observed tidal response and the Earth body model assumptions. The stations located on different continents do not show similarities in their estimates. In addition, I find out that the resolution strongly depends on the quality of the data and less on the duration of the time series if it is already sufficiently long (e.g. 7 years). This is supported by the comparative analysis of only half of the data from two stations. Hence, the `RATA` method might be used to identify the significant contributions without a priori wave grouping assumption. In this way, the resolution power of the harmonic analysis is exploited to a much larger extent, and the risk of over-fitting is strongly reduced by considerations in the regularization method.

Until recently, it was impossible to assess the loading effects directly. While the situation has recently improved with the publications of detailed ocean tide models, I simply approximate the effect of the time-invariant ocean loading and radiation tides in the data by the local response models. An incorrect ratio of harmonics in a wave group may create a spurious periodic 'beat' in the synthetic tidal time series, which may easily lead to false conclusions about its reasons. The hypothesis that some of the temporal variations of tidal parameters found in previous studies were caused by inappropriate body tide models in combination with a priori wave grouping is tested. The local response model is used in a non-regularized, unconstrained moving window

analysis of 12 wave groups composed from summed harmonics. It was found that the periodic variations of groups $\mathbf{M}_2$, $\mathbf{K}_1$, $\boldsymbol{\mu}_2$, $\mathbf{N}_2$, $\mathbf{L}_2$, and $\mathbf{S}_2$ are reduced by up to a factor of 9 compared to earlier studies. Some long-period variations previously seen in the $\mathbf{M}_1$, $\mathbf{O}_1$, $\mathbf{Q}_1$, and $\mathbf{J}_1$ groups are captured as well. This was confirmed for almost all the stations, excluding Syowa, which, however, seems to not provide data of the necessary quality. The previously neglected influence of radiation tides, degree 3 tides, and significant satellite constituents were the main causes of apparent modulations in previous studies. Additional tests proved that tidal groups are well defined, so the cross-talk between parameters does not appear significant, resulting in no trade-off between estimates. The method may be used to validate how strongly given parameter contributes to the modulation.

I conclude that the vast majority of the temporal variations of tidal parameters found in previous studies were caused by inappropriate body tide models not taking effects like ocean loading or radiation into account, in combination with a priori wave grouping. I demonstrate that the application of a local model with correct adjustments explains most of the significant periodic temporal variations. Hence, a proper investigation of the remaining temporal variations to study instrument stability or time-varying contributions of ocean loading is more applicable.

Zusammenfassung

Die bereits 100 Jahre alte harmonische Gezeitenanalyse basiert auf dem Ansatz trennbarer und nicht trennbarer harmonischer Signalanteile. Die begrenzte Frequenzauflösung, die in der Gezeitenanalyse mit dem „Rayleigh-Kriterium“ beschrieben wird, hängt streng von der Dauer der analysierten Zeitreihe ab. Obwohl dies bequem und die gebräuchlichste Methode zur harmonischen Trennung ist, berücksichtigt es doch nicht die tatsächliche Auflösung, die erst durch das Signal-Rausch-Verhältnis der Daten bestimmt wird. Darüber hinaus sind die Leistungsfähigkeit moderner Computer und Methoden den früheren nummerischen Verfahren überlegen. A priori mussten früher *Wellengruppen* gebilded werden, die aus den Harmonischen nahe der Haupthармonischen innerhalb eines vordefinierten Frequenzintervalls bestehen. Dies war notwendig, da das Problem sonst zu einer schlecht konditionierten Gleichungssystem führt, das gelöst werden muss, um die Gezeitenparameter zu berechnen. Noch ausgefeiltere Wellengruppenschemata hängen hauptsächlich von der Länge der Zeitreihe ab, sodass die Informationen über die tatsächliche Auflösung, die die Daten liefern, verloren geht.

Darüber hinaus wurden in den letzten 150 Jahren weltweite Veränderungen der Gezeitenmuster beobachtet, für die es jedoch für viele noch immer keine eindeutige Erklärung gibt. Bei der Analyse von Schwersignalen sind zeitliche Variationen von Gezeitenparametern seit über 30 Jahren bekannt. Daten von supraleitenden Gravimetern (**SG**), die eine bisher nicht dagewesene Genauigkeit bieten, zeigen systematische zeitliche Variationen von Gezeitenparameter. Dies zeige ich für verschiedene Wellengruppen an 19 verschiedenen SG-Stationen rund um die Erde. Die Amplitude der Variationen ist normalerweise um den Faktor 2 (Minimum) bis 32 (Maximum) größer als die Standardabweichung. Einer der möglichen Gründe für zeitliche Variationen von Gezeitenparametern ist die Bildung von Wellengruppen in Kombination mit einem falschen Verhältnis der Amplituden von Harmonischen im Analysemodell (Body-Tide-Model) welches die Signale der Ozeanaulast nicht berüchsichtigt. Dies führt, zu unterschiedlichen Schwebungen im Analysesignal und im Messsignal. In der Folge treten periodische Variationen der Regressionsparameter auf.

Ich stelle eine Alternative zur klassischen harmonischen Gezeitenanalyse vor, die eine Lösung in der Nähe eines Referenz-Modells sucht. Diese Regularisierung stabilisiert die lineare Regression, so Modellparametern für jede einzelne Gezeitenharmonische bestimmt weden können. Dadurch entfällt die Notwendigkeit, a priori Gruppen von Harmonischen zu bilden. Alle Gezeitenharmonischen werden einzeln behandelt. Auf diese Weise wird eine Verzerrung durch

die *a priori* Modellparametrisierung vermieden oder erheblich reduziert. Gleichzeitig wird eine Überanpassung der Daten vermieden, die zu Störungen im Modell führen würde. Die Lösung des Inversionsproblems erfolgt iterativ durch Justage des Referenzmodells, wobei das Signalresiduum schrittweise reduziert wird. Die Frequenzauflösung der Lösung ist somit durch die tatsächlichen Messdaten bestimmt. Ich finde unabhängig voneinander Modelle für die verschiedenen sphärischen Grade, was ein wichtiger Aspekt ist, da die Ozeanauflast für verschiedene Grade unterschiedlich ist. Das Verfahren ermöglicht schmalbandige Variationen der Gezeitenadmittanz. Die Signifikanz und Schätzung jedes einzelnen Parameters kann getestet werden. Ich demonstriere den Zusammenhang zwischen der harmonischen Amplitude und der Auflösung. Die Auswirkungen der Regularisierung werden sorgfältig diskutiert und berücksichtigt. Ich verwende die Methode, die ich `RATA` nenne (*Regularization Approach to Tidal Analysis*), um ein lokales Modell aus 11,5 Jahren Daten zu bestimmen, die vom supraleitenden Gravimeter SG056 am Geowissenschaftlichen Gemeinschaftsobservatorium Schiltach (**BFO**, Black Forest Observatory) aufgezeichnet wurden. Als Ergebnis habe ich 61 signifikante Gruppen von Harmonischen für das lokale Gezeitenmodell unterschieden, ohne eindeutige Hinweise darauf, dass weitere Gruppen auflösbar wären. Einige von ihnen verstoßen stark gegen das Rayleigh-Kriterium. Einige Harmonische, die normalerweise nach dem Rayleigh-Kriterium getrennt wüerden, haben sich als nicht signifikant erwiesen. Die Ergebnisse wurden mit den Ergebnissen für den zweiten Sensor des Instruments verglichen und mit der ungedämpften Inversion verifiziert, die nur die auflösbaren Wellengruppen verwendet. Das Schwerresiduum ist im Vergleich zu früheren Modellen kleiner, ohne Anzeichen einer Überanpassung. Nach erfolgreicher Anwendung dieser Methode für BFO wende ich die Analyse für 5 weiter europäische Stationen und 8 Stationen außerhalb Europas an. Die Analyse europäischer Stationen bestätigt die Konsistenz der Methode sowie die Verfügbarkeit der Superauflösung. Die offensichtlichen konsistenten Unterschiede in Phasen und Amplituden sind jedoch höchstwahrscheinlich auf die Entfernung zum Ozean zurückzuführen. Ich habe herausgefunden, dass die Unterschiede zwischen Harmonischen mit geringe Frequenzabstand und großer Amplitude ähnlich oder sogar kleiner sind als bei Gezeiten mit großem Frequenzabstand und mittlerer Amplitude. Die Untersuchung anderer Stationen ergab große Unterschiede zwischen der beobachteten Gezeitenreaktion und der Vorhersage aus eiinem Erdmodells. Die Stationen auf verschiedenen Kontinenten weisen in ihren Schätzungen keine Ähnlichkeiten auf. Darüber hinaus habe ich herausgefunden, dass die Auflösung stark von der Qualität der Daten abhängt und weniger von der Dauer der Zeitreihen, sofern diese bereits ausreichend lang sind (7 jahre). Dies wurde durch den Vergleich mit der Analyse von nur der Hälfte der Zeitrehe von zwei Stationen gestützt. Daher kann die `RATA` Methode verwendet werden, um die signifikanten Beiträge ohne a priori Annahme einer Wellengruppierung zu identifizieren. Auf diese Weise wird das Auflösungsvermögen der harmonischen Analyse viel stärker ausgenutzt und durch die Regularisierung das Risiko einer Überanpassung stark reduziert.

Bis vor kurzem war es unmöglich, der Ozeanauflast direkt abzuschätzen. Während sich die Situation kürzlich durch die Veröffentlichung detaillierter detaillierter Ozeanzeitenmodelle verbessert hat, die durch Ozeanauflast verursacht werden, verbessert hat, beschreibe ich die Wirkung der zeitinvarianten Ozeanauflast und der Strahlungsgezeiten durch die lokalen Modelle. Ein falsches Verhältnis zwischen Harmonischen in einer Wellengruppe kann zu einer falschen Schwebung in der synthetischen Zeitreihe führen, die leicht zu falschen Schlussfolgerungen bezüglich der Ursachen führen kann. Die Hypothese, dass einige der in früheren Studien gefundenen zeitlichen Variationen der Gezeitenparameter durch ungeeignete Modelle der "Body-Tides" in Kombination mit einer a priori Wellengruppierung verursacht wurden, wird getestet. Das lokalen Gezeitenmodell wird in einer nicht regularieserten "Moving-Window-Analyse" mit 12 Wellengruppen als Analysemodell verwendet. Es wird festgestellt, dass periodische Variationen der Gruppen $\mathbf{M}_2$, $\mathbf{K}_1$, $\boldsymbol{\mu}_2$, $\mathbf{N}_2$, $\mathbf{L}_2$ und $\mathbf{S}_2$ um bis zu einen Faktor 9 im Vergleich zu früheren Studien reduziert werden. Einige langperiodische Variationen, die zuvor in den Gruppen $\mathbf{M}_1$, $\mathbf{O}_1$, $\mathbf{Q}_1$ und $\mathbf{J}_1$ beobachtet wurden, werden ebenfalls erfasst. Dies wurde bei fast allen Stationen bestätigt, mit Ausnahme von Syowa, die jedoch offenbar keine Daten in der erforderlichen Qualität liefert. Der bisher vernachlässigte Einfluss von Strahlungsgezeiten, Gezeiten des Grades 3 und bedeutenden Seitenlinien der Harmonischen sind die Haupturssachen für scheinbare Modulationen in früheren Studien. Zusätzliche Tests haben gezeigt, dass die Frequenzbänder der aufgelösten Wellen gut definiert sind, so dass die Wechselwirkung zwischen den Parametern nicht signifikant erscheint. Mit der Methode kann ich validieren, wie stark welche Parameter eine Modulation verursachen. Dies liegt den Schluss nahe, dass die überwiegende Mehrheit der in früheren Studien festgestellten zeitlichen Schwankungen der Gezeitenparameter durch ungeeignete Analysenmodelle verursacht wurden, die Effekte wie Ozeanauflast oder Strahlungsgezeiten (Atmosphäre) in Kombination mit einer a priori Wellengruppierung nicht berücksichtigten. Ich zeige, dass die Anwendung der lokalen Modelle durch korrekte Anpassungen die meisten signifikanten, zeitlich periodischen Variationen erklärt. Daher ist eine Untersuchung der verbleibenden zeitlichen Schwankungen beispielweise zur Untersuchung der Instrumentenstabilität zeitlich variierender Beiträge der Ozeanauflast sinnvoller.

Contents

1. Introduction

1.1. The Analysis of Earth Tides

Tidal forces are a result of the external gravitational attraction on an extended body. They are not uniform within the body because they depend on the distance to the gravity-generating object. On Earth, the primary sources of tidal forces are the Moon and the Sun. Due to their relative motion with respect to rotating Earth, these forces cause variations in the gravity field, which induce motions of the Earth body known as *Earth tides*. Compared to ocean tides, which are influenced by complex effects such as turbulent flow and water basins, Earth tides are much easier to model. The goal of analyzing Earth tides is to establish linear admittance between the observed data and the tidal forcing, hence describing the properties of the Earth. Doodson (1921) introduced the concept of decomposing the synthetic tidal potential signal into a sum of sinusoidal *tidal harmonics* at different frequencies which became the most common approach to tidal analysis. The *tidal parameters*, which are called the *admittance*, are determined using linear regression.

Tidal analysis offers a significant advantage over other methods for studying Earth properties because of the accuracy and precision of the predicted forcing. Due to the extraordinarily well developed celestial mechanics applied to tides, expected frequencies and amplitudes are known exactly. The application of Earth tides to describe Earth's structure covers study area different from seismology because significant tidal frequencies are below 6 cpd (0.069 mHz). However, most of the signal energy is concentrated along narrow frequency bands, posing a limit on frequencies for such investigations. Seismology is therefore more relevant for studying the Earth's interior, but as Brush (1996) pointed out, Jeffreys (1926) used tides to show that the average rigidity of the Earth's mantle was much greater than that of the Earth's core, implying that the core must be fluid. Calvo (2015) made an attempt to detect Free-Inner-Core-Nutation from tidal gravity data. Furthermore, corrections for gravity or deformation due to tides must be applied in various fields. Watson et al. (2006) took Earth response models into account for precise geodetic measurements and Haldar (2013) demonstrated its application to the gravity subsurface exploration surveys. Elkhoury et al. (2006) used the Earth tides response of water well levels to detect changes in permeability resulting from earthquakes. Moreover, if the rate of stress change from the Earth tides exceeds the specific level, tidal triggering of earthquakes would be expected. Yan et al. (2023); Scholz et al. (2019); Wilcock (2009) identify a possible

link between tides and earthquakes which however was not confirmed by other studies. Investigating 13,042 earthquakes in California, Vidale et al. (1998) have not found any evidence for tidal triggering. Similarly, Westerhaus and Zschau (2001) show no indication that 1999 Earthquake could be predicted in Anatolia from tidal observations. While Emter (1997) discusses a correlation between volcanic eruptions and tides, the investigations on this particular topic are rare.

Apart from Earth, tides are fundamental in studying the interior properties of other planets and their satellites, especially if there is no seismic activity. Yoder et al. (2003) determined fluid core size of Mars and later Pou et al. (2022) compared interior structure models of Mars to the recent measurements of the tidal parameters to estimate the possible core radius. Van Hoolst and Jacobs (2003) derived Mercury's response to the tidal forcing for a set of its interior structure models.

1.2. The Resolution Problem

The harmonic analysis of tides began with Darwin (1907) classification of tidal potential in terms of Keplerian frequencies and corresponding amplitudes, where he identified the most significant ones. Later, Doodson (1921) improved the method by contributing more harmonics with their coefficients based on the lunar theory of Brown and Hedrick (1920) and introduced the concept of integer numbers defining the harmonic frequencies. Further Schureman (1924) prepared the manual for tidal analysis which was based on that concept. Since then *tidal catalogs*, tidal harmonics decomposed from astronomical ephemeris applied to celestial mechanics, are used for the computation of the tide-generating potential instead of direct calculation from celestial mechanics. The recent tidal catalogs, as presented by Kudryavtsev (2008); Wenzel (1996) contain thousands of contributions. The vast majority of them are so small, that they could not be measured using the most modern and precise gravimeters, considering noise and achievable instrumental accuracy.

Due to the limited resolution of analysis methods that did not allow to distinguish all possible contributions from each harmonic back then, Venedikov (1961) introduced a concept of *wave groups* composed of harmonics close to the main harmonic within a predefined frequency range. Wave grouping takes advantage of the assumption of a smooth admittance function, *credo of smoothness*, named after Munk and Cartwright (1966) application to the response analysis method. It does not allow for sharp resonance peaks, so by grouping weak lines and allowing for the presence of noise, greater precision and fewer tidal constants are required. Venedikov (1961) also implemented a preliminary version of least-squares (**LS**) method in tidal analysis, which was further improved by Chojnicki (1973) and implemented by Schüller (1976) who investigated the use of taper windows in LS spectral analysis of tides. LS method of wave groups is still

widely used in the analysis of Earth tides (Wenzel, 1996, 1997a; Venedikov et al., 2005; Tamura and Agnew, 2008; Schüller, 2015, 2020). The main reason for wave groups in the tidal analysis nowadays is the otherwise ill-conditioned matrix in the LS problem. The condition number of the matrix becomes large and the corresponding model parameters are prone to noise in the data. Their values can change for a small variation in the measured signal, hence all the estimated tidal parameters are irrelevant. This is already a problem if too many groups are being investigated, causing a trade-off because wave grouping should always occur at the maximum possible resolution. Schüller (2015) emphasised that if the grouping is too optimistically chosen, the normal equations cannot be solved. All of the recent approaches seek model parameters for a priori defined groups (sums) of harmonics. With all the available implementations, it is impossible to handle all tidal harmonics listed in catalogs such as those by Hartmann and Wenzel (1995) individually.

The composition of wave groups in the analysis is based on the assumed separable and non-separable contributions. Applied limits on the obtainable frequency resolution are usually based on the *Rayleigh criterion*, which depends on the duration of the time series: for a given time series of length T, the difference Δf between separable frequencies of constituents satisfy $\Delta f > T^{-1}$. It was named by Godin (1970, 1972) after the similarity to the problem in Optics in his analytical investigations of its consequences for spectral analysis of tides. The first indication of the relationship between the length of observation and the distinguishable harmonics was given by Doodson (1921), who recommends that all the harmonics with frequency difference corresponding to periods larger than recorded time series should be treated as one *constituent*, giving no reason. This resolution discrepancy suggestion became a "common practice" in tidal analysis. Afterwards, Foreman and Henry (1989) modified the criterion by adding a Rayleigh constant R: $\Delta f \cdot T > R$. It is mentioned to be commonly set to 1, but the authors did not discuss the reasoning for that choice. Wenzel (1997c) links the fundamental frequency $\Delta f = T^{-1}$ in Rayleigh criterion with the frequency resolution of the discrete Fourier transform.

Although convenient and the most common way for harmonic separation, Munk and Hasselmann (1964) pointed out that the Rayleigh criterion does not take into account the actual resolution limited by the signal-to-noise ratio of the data. Ducarme and Schüller (2018) argue that there is a significant difference between truly resolvable constituents by LS method and Rayleigh criterion. The number of studies questioning this discrepancy method is recently increasing. Munk and Hasselmann (1964) suggested modifying the Rayleigh criterion according to the signal-to-noise (S/N) ratio, and Wenzel (1997b) indicated that one should not strictly follow the criterion. Schüller (2015); Ducarme and Schüller (2018) proposed various grouping schemes, supporting them with tests on synthetic data. Recently, Ciesielski and Forbriger (2020, 2021) demonstrated the relationship between the harmonic amplitude with frequency and resolution.

Foreman and Henry (1989) emphasised, that if the amplification factor or phase from any other large-amplitude harmonic in the group is significantly different from the expectation, the grouping parametrization might lead to an inaccurate (biased) estimate of tidal parameters. This is the major problem since *credo of smoothness* is not valid if tidal parameters do not smoothly vary with frequency, what Merriam (1995) demonstrated in the case of non-linear effects and Meurers et al. (2016) pointed out for tides within a wave group having different response to ocean loading.

1.3. Temporal Variations of Tidal Parameters

Haigh et al. (2020) summarized that worldwide changes in the tide patterns over the past 150 years have been noticed, but many of them still lack clear explanation. The amplitudes of tides at different locations are experiencing noticeable variations as a result of non-astronomical factors, although the response of the Earth's body to tidal forces is unlikely to shift within months or years. Over long geological time scales, the changes are influenced by tectonic processes. However, over shorter geological time scales, the changing distribution of waters and glaciers with air pressure fluctuations are the primary driving factor.

The analysis of Earth tides requires relatively long time series data to accurately estimate admittance factors. Therefore, in order to investigate temporal changes, tidal recordings of a duration of several years should be split into significantly shorter, overlapping windows. This is a principle of the moving window analysis (MWA) approach introduced by Schüller (1976). Westerhaus and Zschau (2001) applied this method to various types of data, including tilt records for monitoring temporal variations of elastic properties at the North-Anatolian-Fault Zone. Calvo et al. (2014) studied gravity records for testing the stability of gravimeter gain while Meurers (2004); Sato et al. (2006) sought for temporal variations of Earth's admittance. A similar monitoring procedure was carried by Beaumont and Berger (1974); Mukai and Fujimori (2001); Omura et al. (2001).

In gravity records analysis, Dittfeld (1991) was the first who demonstrated temporal variations of tidal parameters in Potsdam. Later, using early data from the first superconducting gravimeters (**SG**s), Meurers (2004) found an annual variation of the gravimetric factor for $\mathbf{M}_2$ - primary lunar semi-diurnal tide - strongly affected by ocean response. Similar observations were reported by Jahr (2015). Meurers et al. (2016) extended the investigation for $\mathbf{M}_2$ variations to several other European SG stations. Systematic variations of tidal parameters for the SG056 at BFO Schiltach with different periodicity are reported by Schroth (2013) for different tidal wave groups. Schroth et al. (2018) present a detailed catalog with temporal variations seen in 19 SG stations around the globe in moving window analyses for 12 wave groups.

Model errors in the air pressure correction were initially proposed to be a reason. However, the annual variation and the additional variation with 8.85 years period were identified. Ocean loading is suggested as a possible cause, along with numerical artefacts in the analysis, unstable calibration and improper preprocessing of the data. Merriam (1995) reported the modulation of *satellite harmonics* of $\mathbf{M}_2$ in tidal analysis residuals, which are equivalent to an annual cycle of $\mathbf{M}_2$ admittance in an analysis of data from the SG at Cantley. He suspected their origin in large amplitude ocean loading in the Bay of Fundy. Due to the common pattern of variations, the effects of instrumental origin are ruled out. Possible causes are shortcomings of the body tide model used in the analysis, a time-dependent response of the entire Earth including ocean loading, and cross-talk between analysis parameters. Schroth (2020) investigated loading contributions from the oceans and the atmosphere as well as non-tidal radiation-driven signals as a source of temporal variations. The affected groups contain harmonics of significant amplitude and frequency distance 8.85 years, as well as variations with the same period. This strongly points to the direction of an inappropriate ratio of tidal admittance. `Eterna 3.40`, as used by Schroth et al. (2018), assumes the fixed ratio between the admittance of tides given by the Wahr-Dehant-Zschau body tide model (Wahr, 1981a; Zschau and Wang, 1985; Dehant, 1987; Dehant et al., 1999). Schroth (2020) demonstrated how the incorrect frequency dependence of the model causes apparent beats (amplitude modulation). An incorrect ratio would create a spurious time variation in the synthetic tidal time series.

The causes and consequences of changes in tides are needed for better understanding of the nature of the Earth complex system, including effects of climate change. The temporal variations might also indicate systematic biases in the analysis method, mistakes in data preprocessing or previously unnoticed instrument deficiencies, and they should be resolved first.

1.4. Geophysical Inversion for Tidal Analysis

If we assume noise-free data, the problem of tidal analysis can be reduced to solving an algebraic set of equations. This is possible because tidal frequencies are precisely known from tidal catalogs and LS properties, in contrast to Fourier spectral analysis decomposing signal into harmonics with frequencies that are a multiple of a fundamental frequency. Thus, as long as the necessary algebraic conditions are met, the problem has an exact correct solution regardless of the length of the time series, as pointed out by Munk and Hasselmann (1964). In reality, however, there exist sources of noise influencing the resolution, so Munk and Hasselmann (1964) proposed a modified Rayleigh resolution criterion $\Delta f \cdot T > (S/N)^{-\frac{1}{2}}$. They demonstrated that a meaningful estimates of harmonics being separated in frequency by a reciprocal of 1 month could be obtained from a 3-day synthetic record contaminated with white noise.

One may not only modify the Rayleigh criterion for grouping by signal-to-noise ratio. The concept of a priori groups can be abandoned completely, which allows us to overcome the current resolution limitations in tidal analysis and infer more information from the data. In this approach, each tidal harmonic present in the catalog receives its own set of tidal parameters that are free to vary. We thus can search for harmonics that show a different dependence on frequency and spherical degree than assumed in the a priori body tide model. The resulting ill-conditioned matrix is stabilized by *Tikhonov regularization* (Tikhonov and Arsenin, 1977), also known as a *ridge regression*, in the LS objective function, which is a well-established concept in geophysics (Aster et al., 2005). The increase of variance of tidal parameters due to freedom given to each tidal harmonic is then weighted against the response model parametrization. The less significant contributions that are more prone to noise are more affected by regularization. Various approaches to regularization minimize the parameters sum, deviation from the theoretical model, deviations in the function of frequency (smoothing), etc. In this application we minimize the distance to the reference model and the errors between estimates and observations at the same time. By not grouping harmonics prior to the LS fit we allow the data to indicate if the model is inappropriate for significant harmonics that contribute to the signal.

1.5. Hypotheses

Regularization enables the estimation of a fine-resolved, data-driven, local time-invariant model without the need for a priori grouping or the Rayleigh criterion. This approach balances high resolution and problem over-determination, avoiding over-fitting while inferring essential information. I hence suggest that the forcing amplitude of harmonics may be a more relevant grouping criterion than solely considering frequency closeness of harmonics. I expect that even closely spaced harmonics that have large amplitude are better constraint and can be resolved, as opposite to the rather small amplitude tides but distant in frequency. Moreover, I expect that the S/N ratio is more important criterion for tidal resolution than only the length of the recorded time series.

Although tidal parameters across the globe should theoretically be the same for all stations if normalized by latitude-dependent body tide response, the differences in the estimates point to the ocean loading, radiation tides, instrumental and data properties, and different recording times. I expect that the regularization approach allows to find the reasonable detailed models and their (otherwise hidden) harmonic properties caused by mentioned effects. The investigation of double-sphere instruments, and European stations could provide the minimum error or proxy on the method.

I propose that the vast majority of systematic temporal variations (modulations) are a consequence of an improper ratio in a priori body tide model between significant harmonics

composing one wave group in MWA. The application of the local response model that contains the information about the actual frequency response of tides in the group a priori model should exhibit much smaller time variations of tidal parameters in comparison to MWA that uses the Wahr-Dehant-Zschau elastic body tide model only. Similar procedure should explain the temporal variations in other stations placed at different continents. This would demonstrate that the local model captures apparent variations in tidal parameters in MWA groups presented in previous studies (Meurers et al., 2016; Schroth et al., 2018).

1.6. Overview of the Content

The thesis is divided into eight chapters:

- Chapter 2 covers the theory of Earth Tides need for the thesis. It explains the tidal harmonic decomposition and tidal catalogs with reasons for different frequencies, degrees and orders. The body tide is discussed, together with non-tidal effects that influence the measurements.

- Chapter 3 introduces the method of harmonic tidal analysis of gravity records. It describes the new approaches: regularization for local response model and modified MWA for investigation of temporal changes. It discusses the differences to other available software. The general problem of resolution of tidal harmonics and error propagation is discussed in details.

- Chapter 4 lists the observatories and instruments that were used for the analysis. Preprocessing, handling of gaps and filtering is discussed there.

- Chapter 5 demonstrates the use of the regularization method, named `RATA`, on 11.5 years of the gravity data from the SG lower sensor at the Black Forest Observatory (SG 056 G1). It summarizes the estimated model and resolved tides, showing the significant contributions. Error propagation is discussed. The estimated data-driven model with a fine resolution moderately violates Rayleigh criterion. Some of the groups that would be considered as separate groups are not proven to be significant. Tides of different degrees are treated separately.

- Chapter 6 shows how the local model may be used to correct the ratios between tidal harmonics in the same group to decrease the systematic temporal variations. The results are supported by corresponding histograms and spectral analysis of the MWA. I find that periodic variations of groups $\mathbf{M}_1$, $\mathbf{K}_1$, $\boldsymbol{\mu}_2$, $\mathbf{N}_2$, $\mathbf{L}_2$, and $\mathbf{S}_2$ are reduced by up to a factor of 7 compared to earlier studies. Some variations previously seen in the $\mathbf{M}_2$ group are captured as well.

- Chapter 7 shows the local response models obtained with `RATA` method for 15 instruments, in Europe and the other continents. The display method takes into account the amplitudes of signals. The analysis of two double sphere instruments gives the possible values of minimal errors. The estimates of the resolved close-frequency harmonics are compared for European stations. The differences and common features for tidal parameters at particular stations are discussed.

- Chapter 8 demonstrates the application and power of the use of the local response models in MWA for all the investigated stations. This section proves that the vast majority of systematic variations may be explained by the improper ratio of harmonics within the group. Even long-period beats for tides that did not appear to show systematic variations decreased. For some stations the clear modulation is not present after the application of the adjustment.

- Chapter 9 Summarises the work presented in the thesis. It covers possible implications and discusses future prospects.

Appendix A contains a glossary of the specific terms used and introduced in this work. Appendix B display detailed response models in tables and plots. Appendices C-E contain the complete diagrams of the moving window analyses, corresponding histograms and spectra for all the stations. Finally, Appendix F is a compilation of temporal variations of air pressure coefficient and data misfit in MWA.

2. Theory of Tides

Tidal forces are a result of the gravitational attraction of an external body on an extended body. These forces are not uniform within the body because they depend on the distance to the gravity-generating object. In a simple two-body system, both bodies orbit around a common center of mass. In the case of the Earth and the Moon, this barycenter is always inside the Earth but far from its center, changing its position inside the Earth with the Moon's orbital motion. The relative movement alters the resulting tidal forces at given position with time. As Earth is not rigid but anelastic, the solid Earth body deforms due to such changes. Hence, tides are used to study the rheological properties of Earth.

2.1. The Tidal Potential

Although our main interest lies in tidal forces, it is more convenient to describe them with the tidal potential. In a two-body system, Fig. 2.1, the total gravitational potential

$$V_{tot} = \frac{GM}{R} \frac{1}{\sqrt{1+(a/R)^2 - 2(a/R)\cos\alpha}} \tag{2.1}$$

is generated by an external body of mass M at a distance R from an observer's position O on an extended body of radius a. The angle between the direction from the center of the extended body to the observer and the direction from the center of the extended body to the external body is α. Using Legendre polynomials, the gravitational potential

$$V_{tot} = \frac{GM}{R} \sum_{n=0}^{\infty} \left(\frac{a}{R}\right)^n P_n(\cos\alpha). \tag{2.2}$$

from which the tidal forcing is derived has a more practical form, since the gradients are considered. For $n = 0$ the corresponding term in eq. (2.2) is constant in space, so its gradient is zero; the term for $n = 1$ has a constant gradient, which can be subtracted from the tidal field. Hence, only higher terms are discussed. The resulting potential

$$V = \frac{GM}{R(t)} \sum_{n=2}^{\infty} \left(\frac{a}{R(t)}\right)^n P_n[(\cos\alpha(t))] \tag{2.3}$$

is time-dependent since bodies orbit around each other and the relative position changes with time.

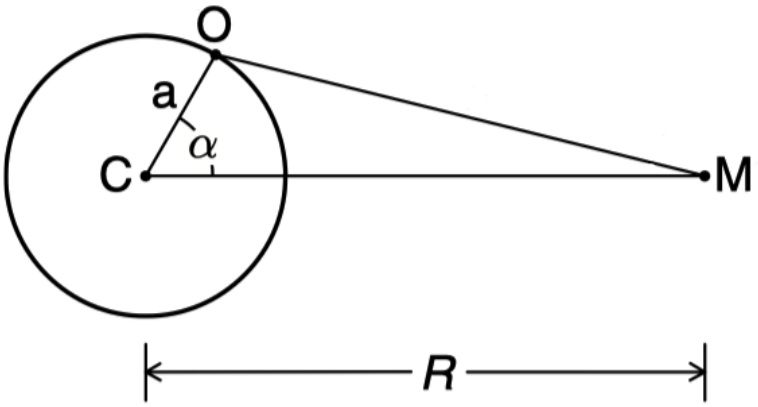

Figure 2.1.: The geometry of the two body tidal forcing problem, for details see the main text. The graphic is a modified figure from Agnew (2009).

body	relative tide amplitude
Moon	2.18
Sun	1.00
Venus	0.000113
Jupiter	0.0000131
Mars	0.0000023
Mercury	0.0000007
Saturn	0.0000005

Table 2.1.: The evaluation of the the term GM/R for different celestial bodies in the Solar System, for mean value of R as seen from the Earth. Values are normalised such that they are expressed as a fraction of $GM_\odot/R_\odot$ ($\odot$ is the Sun symbol).

By evaluating the term GM/R for specific objects in the Solar System, we determine the relative maximum tidal forces on the Earth (Table 2.1). This explains the relatively greater influence of the dominant tides on Earth originating from the Moon and the Sun, while the contributions from other sources may be comparatively negligible. The most significant other planet tide, Venusian, is likely undetectable ($< 1\text{nm/s}^2$) with available gravimeters (Agnew, 2009). A small part of the tidal forcing field whose contribution is omitted in this development is caused by the flattening of the Earth (Wilhelm, 1995). While at the very high precision it was considered by Wenzel (1996); Roosbeek (1996), Wilhelm (1995); Dahlen (1993) have shown that its influence is negligible.

The size-distance ratio (a/R) is always less than 1, so terms in the tidal potential rapidly decrease with increasing n. For the Earth and Moon system, $a/R \approx 1/60$, and the higher powers are $(a/R)^2 \approx 1/3,600$ and $(a/R)^3 \approx 1/216,000$, with the importance of the latter being disputable. In the case of the Sun, the term $(a/R)^2 \approx 1/23,000$ dominates over the higher terms. These integers n are known as tidal degrees, related to the degrees of spherical harmonics. We usually refer to them as *degree n tides*. Let us consider the observation point O at colatitude θ

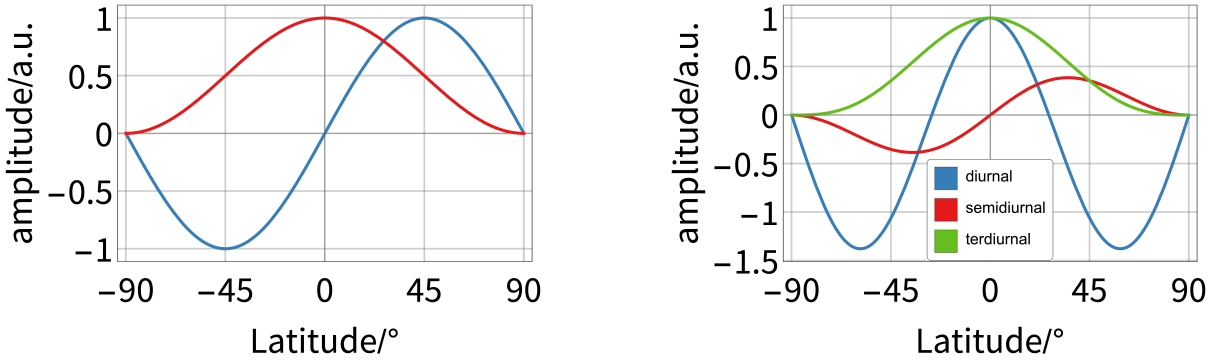

Figure 2.2.: Tidal potential for different degrees and orders, as it varies with latitude. Degree 2 tides are shown on the left, degree 3 on the right diagram. The equations as taken from Bartels (1985) do not consider constant amplitude of the particular tide.

and east longitude φ, and the moving sub-body point of the Moon at colatitude $\theta'(t)$ and east longitude $\phi'(t)$. By applying the addition theorem for fully normalized spherical harmonics, and considering observation point as time-invariant, we get

$$V = \frac{GM}{R(t)} \sum_{n=2}^{\infty} \left(\frac{a}{R(t)} \right)^n \frac{4\pi}{2n+1} \sum_{m=-n}^{n} Y^*_{nm}(\theta'(t), \phi'(t)) Y_{nm}(\theta, \phi) \tag{2.4}$$

which clearly demonstrates the relation between tidal degrees and degrees of spherical harmonics. The time dependence of the tidal potential comes from time variations in R, θ', and ϕ'. The variable ϕ' varies approximately daily as the Earth rotates. The distance and the colatitude also change, but at much slower rate and within smaller range. For a fixed time but with varying θ and ϕ, the coordinates of a particular place of observation, $Y_{nm}(\theta, \phi)$ in eq. (2.4), describe the geographical distribution of the tidal potential V on the Earth. Each degree term n in the sum in eq. (2.4) contains $2n+1$ components of different order m. Harmonic order 0 corresponds to zonal potential distribution, $m = \pm n$ to sectorial, and tesseral elsewhere. With varying θ, the tesseral tidal potential with colatitude varies as $\sin 2\theta$ and is largest at mid-latitudes, vanishing at the equator and the poles. The sectorial part varies as $\sin^2 \theta$, so it is largest at the equator and vanishes at the poles. The zonal tide varies as $3\cos^2 \theta - 1$, so it is large at the pole and (with reversed sign) at the equator (Melchior, 1978; Bartels, 1985; Agnew, 2009).

Due to Earth's daily rotation, these orders cause tidal potential to vary with frequencies around $0, 1, 2, \ldots, n$ times per day, a consequence of the harmonic development ($0 \leq |m| \leq n$). For the degree 2 tides there are long period, diurnal and semi-diurnal tides, corresponding to the consequence of zonal, tesseral and sectorial spherical harmonics, respectively. The tides at the side closer to the Moon are stronger than on the opposite what is physically described by degree 3 tides. Figure 2.2 demonstrates how potential of tides degree 2 and 3 vary with latitude (i.e. $90° - \theta$, since θ is colatitude).

2.2. Tidal Harmonics

If the orbits of the Earth and the Moon were perfectly circular and Earth rotation axis was perpendicular to the co-aligned orbits, the tidal potential would vary only based on frequencies corresponding to the relative position of the observer to the external body. Due to the constant motion rate, these frequencies would come from Earth's rotation (1 day), relative lunar revolution (1 month, Moon) and Earth's revolution (1 year, Sun). However, this is a simplification that does not reflect reality. The orbit is elliptical, inclined to each other by certain angles, and perturbed by precession. The frequencies of these periodic phenomena contributing to the tidal potential can be defined with parameters that describe the Keplerian orbits.

At the heart of this phenomenon lies the most significant frequency, Earth's rotation rate Ω. It is related to the **sidereal day**, the time required for the Earth to rotate once relative to the background of the stars (typically the First Point of Aries, the vernal equinox), on Earth approximately 86164 seconds. Sidereal day leads to the parameter ϑ, **sidereal time**, which is the angle from the observer's meridian to the great cycle that passes through vernal equinox. In addition to this, we must also consider the revolution of the Moon around the Earth. The Moon completes one full revolution in approximately 29 days, which is known as tropical month. This gives rise to a parameter of the **mean lunar longitude**, denoted by s. However, it is important to note that the lunar orbit is not a perfect circle, but rather an ellipse, with a **perigee that precesses**. This precession has a period of approximately 8.847 years, denoted by p. Furthermore, the Earth itself orbits around the Sun with a frequency of 1 cycle per (tropical) year, which we describe using the **mean solar longitude**, denoted by h. The plane of the Moon's orbit is inclined to the plane of the Earth's orbit around the Sun (ecliptic) at a mean angle of approximately 5.145°. This orbital plane also exhibits **nodal precession** (caused by the torque exerted by the Sun's gravity on the angular momentum of the Earth-Moon system), so the point where nodes countersect the celestial equator changes its position. This revolution period of the mean nodes is approximately 18.613 years, denoted by N'. Finally, we must also consider the **precession of the perihelion** of the Earth's orbit, so the change of the Sun position during the closest Earth's pass-by as seen on the stellar frame. Denoted by p_s or sometimes p_1, it occurs over a much longer period of almost 21,000 years and is distinct from the precession of the Earth's rotation axis, which occurs over a period of approximately 26,000 years and does not directly influence tides on Earth as such. The mean longitudes angles s, h, p, N', p_s (Bartels, 1985; Simon et al., 1994) slowly increase eastwards in time. They are described as polynomial functions of time in Julian centuries (Bartels, 1985; Tamura, 1987; Simon et al., 1994). Frequencies as summarised in Table 2.2 provide an essential framework for understanding the complexities of tidal potential. Sidereal time $\vartheta = \tau + s = t + h$, where τ and t

symbol	period	name	argument and cause
ϑ	23 hours 56 min 4 sec	sidereal day	sidereal time
			Earth's rotation around its axis
			with respect to the fixed stars
s	27.322 days	tropical month	the mean longitude of the Moon
			Moon's revolution around Earth
h	365.2422 days	tropical year	the mean longitude of the Sun
			Earth's revolution around Sun
p	8.847 years	-	the longitude of the lunar perigee
			orbital (apsidal) precession
			of the Moons perigee
N'	18.613 years	-	the negative longitude of the lunar
			ascending node; nodal precession
			of the plane of the Moon's orbit
p_s	20942 years	-	the longitude of the perihelion
			orbital precession of the perihelium

Table 2.2.: Mean times and longitudes affecting the tidal potential on Earth. Days are given in solar days (1 day = 24 hr), years refer to tropical years (1 year = 365.2422 days). Sidereal year is the time it takes Earth to complete one full orbit around the Sun as measured with respect to the fixed stars, so it is about 20 minutes longer than tropical year, which is full orbital cycle with respect to the Sun.

are mean lunar (89428 s) and solar (86400 s) day, respectively. In practical discussions of tidal frequencies and the tidal potential, mean lunar time τ is rather used instead of ϑ.

A detailed table and complete discussion of these frequencies can be found in (Table 1 from Bartels, 1957). We will demonstrate the origin of the *satellite harmonics* at close frequencies, and how the frequencies mix up. Assuming constant Ω, extensive algebraic transformations for the spherical triangles (Bartels, 1985; Melchior, 1978; Godin, 1972) lead to the potential expression for degree 2 diurnal tides (n=2, m=1)

$$V_{21} = K_2 \frac{6\pi}{5} \sin\epsilon [\cos\epsilon \sin\Omega t + \frac{1}{2}(1+\cos\epsilon)\sin(\Omega - 2\beta)t + \frac{1}{2}(1-\cos\epsilon)\sin(\Omega + 2\beta)t], \qquad (2.5)$$

given an external body moving at a constant speed β with its orbital plane inclined at an angle ϵ. We put constant terms to K_2, known as the Doodson constant. Three distinct frequencies can be identified in eq. (2.5). The decomposition involves three time-variant angles with frequencies Ω, $\Omega + 2\beta$, and $\Omega - 2\beta$, while β may correspond to any frequency listed in Table 2.2. In the hypothetical case of no rotation ($\Omega = 0$), the first term would vanish, leaving only two long-period harmonics at frequencies $\pm 2\beta$. Notably, if the Earth's equatorial plane is aligned with the body's orbit (inclination angle $\epsilon = 0$), there would be no diurnal tides. Other degrees and orders produce various harmonics with different amplitudes. For instance, a semi-diurnal degree 2 tide ($n = 2$, $m = 2$) can be expressed in a similar fashion:

$$V_{22} = K_2 \frac{24\pi}{5}[(1-\cos^2\epsilon)\cos 2\Omega t + \frac{1}{2}(1+\cos\epsilon)^2\cos(2\Omega - 2\beta)t + \frac{1}{2}(1-\cos\epsilon)^2\cos(2\Omega+2\beta)t]. \quad (2.6)$$

For a small inclination angle, the third term becomes negligible. In the case of an inclination angle of zero degrees ($\epsilon = 0$), only the central term contributes to the tidal potential, resulting in semi-diurnal harmonics.

Due to Earth's rotation at a significantly higher rate of Ω than all the other frequencies, the majority of tides are diurnal, semidiurnal, and so on, constituting *tidal species*. The main lines appear at frequencies corresponding to multiplication of lunar days and solar days. It should be noted that the angles ϵ and β are time-varying due to the complex astronomical properties of the system. Frequencies listed in Table 2.2, apart from their long-period effects, show significant modulation of the tidal frequencies from mixed oscillations. As a result, the number of tidal harmonics is greater than what would be predicted by the relatively simple equations like (2.5) for each degree and order of spherical harmonic. We may use the analogy to spectral analysis, that the broad lines are split into a fine structure, and combine in specific ways. Such is the mean anomaly, which represents the distance of the mean Moon from mean perigee, denoted as $s-p$ and is associated with the mean anomalistic month of 27.555 days. Higher orders, such as $2(s-p)$, $3(s-p)$, and so on, must also be considered. The mean draconic month is expressed as $s+N'$, while the mean synodic month is denoted as $s-h$. The synodic month is the average period of the Moon's orbit with respect to the line joining the Sun and Earth, which corresponds to the cycle of lunar phases. The draconic (nodical) month, on the other hand, is the average interval between two successive transits of the Moon through the same node, by nodal precession being shorter than a sidereal month. Argument $2(s-h)$ is caused by variation, the moon being alternately pulled away and accelerated towards the Earth and $s-2h+p$ by eviction, the largest inequality produced by the Sun in the monthly revolution of the Moon. Noticeably, $2(s-h) = (s-2h+p)+(s-p)$. All these perturbations have significant effects on tidal forcing, being reason for some major tides.

The interpretation of the tidal potential through the introduction of complex factors is elaborated upon by Agnew (2009). Bartels (1985); Melchior (1978) discuss the frequencies and amplitudes of major tides, providing astronomical derivations of the contributing terms, and previous works of Doodson (1921); Brown and Hedrick (1920) contain the essential astronomical theory for tides on Earth. These works were a major advances of the early attempts of writing tidal potential in terms of astronomical variables first carried by Laplace and later extended by Darwin (1907).

2.3. The Tidal Potential Catalogs

The formula (2.4) can be rearranged in to establish the relationship between the tidal potential and the ephemeris predicted by celestial mechanics, allowing for the harmonic expansion. Through some calculus (Bartels, 1957; Cartwright and Tayler, 1971; Tamura, 1987; Agnew, 2009), the potential can be expressed as follows:

$$V = \frac{GM}{a}\Re\left(\sum_{n=2}^{\infty}\sum_{m=0}^{n} T_{nm}^{*}(t)Y_{nm}(\theta,\varphi)\right) \tag{2.7}$$

Here, $R(t)$ is included in the time-variant complex coefficient $T_{nm}^{*}(t)$, which we express as a sum of sinusoidal functions:

$$T_{nm}^{*}(t) = \sum_{l=1}^{L} A_l e^{i(2\pi f_l t + \phi_l)} \tag{2.8}$$

where A_l, f_l and ϕ_l are the real-valued harmonic amplitude, frequency and phase, respectively. The practical advantage of a table of harmonic amplitudes and frequencies over decoupling the tidal potential from celestial mechanics is that once produced, it is valid over a long time for any tidal phenomenon. Additionally, such an expansion implicitly puts the description into the frequency domain, simplifying spectral analysis.

The positions of the Sun and the Moon relative to the Earth are determined by their coordinates in relation to the ecliptic and their distances, whose fundamental periods were discussed earlier. Therefore, we can express the astronomical argument ϕ_l and parameterize the frequency f_l and phase ϕ_l:

$$\begin{aligned} \phi_l &= \sum_{r=1}^{6} k_r(l)\phi_r = k_1\tau + k_2 s + k_3 h + k_4 p + k_5 N' + k_6 p_s \\ 2\pi f_l &= \sum_{r=1}^{6} k_r(l)(2\pi f_r) = k_1\dot{\tau} + k_2\dot{s} + k_3\dot{h} + k_4\dot{p} + k_5\dot{N}' + k_6\dot{p}_s \end{aligned} \tag{2.9}$$

to express the exponent argument as a sum of fundamental frequencies (f_r) and phases (ϕ_r)

$$2\pi f_l t + \phi_l = \sum_{r=1}^{6} k_r(l)(2\pi f_r t + \phi_r). \tag{2.10}$$

The integer variables k_i are Doodson arguments corresponding to the fundamental tidal periods discussed earlier in the text. Each *tidal harmonic* (tidal wave) is uniquely identified by its set of Doodson arguments. Clusters of tidal waves with a common set of first few Doodson arguments are designated according to the convention introduced by Doodson (1921) and later adopted by Munk and Cartwright (1966). Tidal waves that differ in the Doodson argument k_1 are considered separate *tidal species*. If they share k_1 and k_2, they form an individual *tidal*

group, while the common set (k_1, k_2, k_3) defines a *tidal constituent*. For the amplitudes T^*_{nm} in eq. (2.8), we may introduce the time-varying coefficients $S_{nm}(t)$ and $C_{nm}(t)$ for real and imaginary counterparts of T^*_{nm}: $C_{nm}(t)\cos(2\pi f_l t + \phi_l)$ and $S_{nm}(t)\sin(2\pi f_l t + \phi_l)$.

Tidal catalogs comprise a collection of coefficients $S_{nm}(t)$ and $C_{nm}(t)$ for all significant tidal frequencies expressed in terms of Doodson numbers. In early catalogs Doodson (1921); Cartwright and Edden (1973) these coefficients were time-independent, but further development on the astronomical ephemerides (Tamura, 1987; Simon et al., 1994) induced additional term. It is a common practice that odd sums of the degree and order, $m+n$, correspond to sine contributions, while even sums correspond to cosine. These coefficients are determined by analyzing long time series computed from ephemerides that span many years, typically from 1900 Jan 1 to 2199 Dec 30. The Fourier spectrum of the time series is expressed as closely as possible to the form given by eq. (2.8), with the set of $(k_1, \ldots, k_6)$ adjusted for each frequency. To ensure that the Doodson numbers are positive, it is conventionally required that each (except first) argument k_i is larger by 5, such that argument 0 is expressed as 5. For example, the Doodson number 155.555 corresponds to the set (1, 0, 0, 0, 0, 0).

The original tidal potential catalog by Doodson (1921) included 378 harmonics computed from analytical ephemerides using algebraic methods. Subsequent improvements to the catalog were made using numerical Fourier analysis, such as the work by Cartwright and Tayler (1971). The tidal potential catalogs have been continuously revisited due to more precise ephemerides available, such as those provided by JPL (Jet Propulsion Laboratory), which include time-dependent coefficients (Tamura et al., 1991), the implementation of other planets and effects (Hartmann and Wenzel, 1995), or including even more additional terms (Kudryavtsev, 2004). A comprehensive review on this topic is presented in Agnew (2009, pages 170-172) and technical details can be found in Doodson (1921); Bartels (1985); Cartwright and Tayler (1971); Godin (1972). In the discussion we neglected latitude-dependent geodetic coefficients and handling other effects which are present in the tidal potential development. Fig. 2.3 presents amplitudes of tidal harmonics of different degrees.

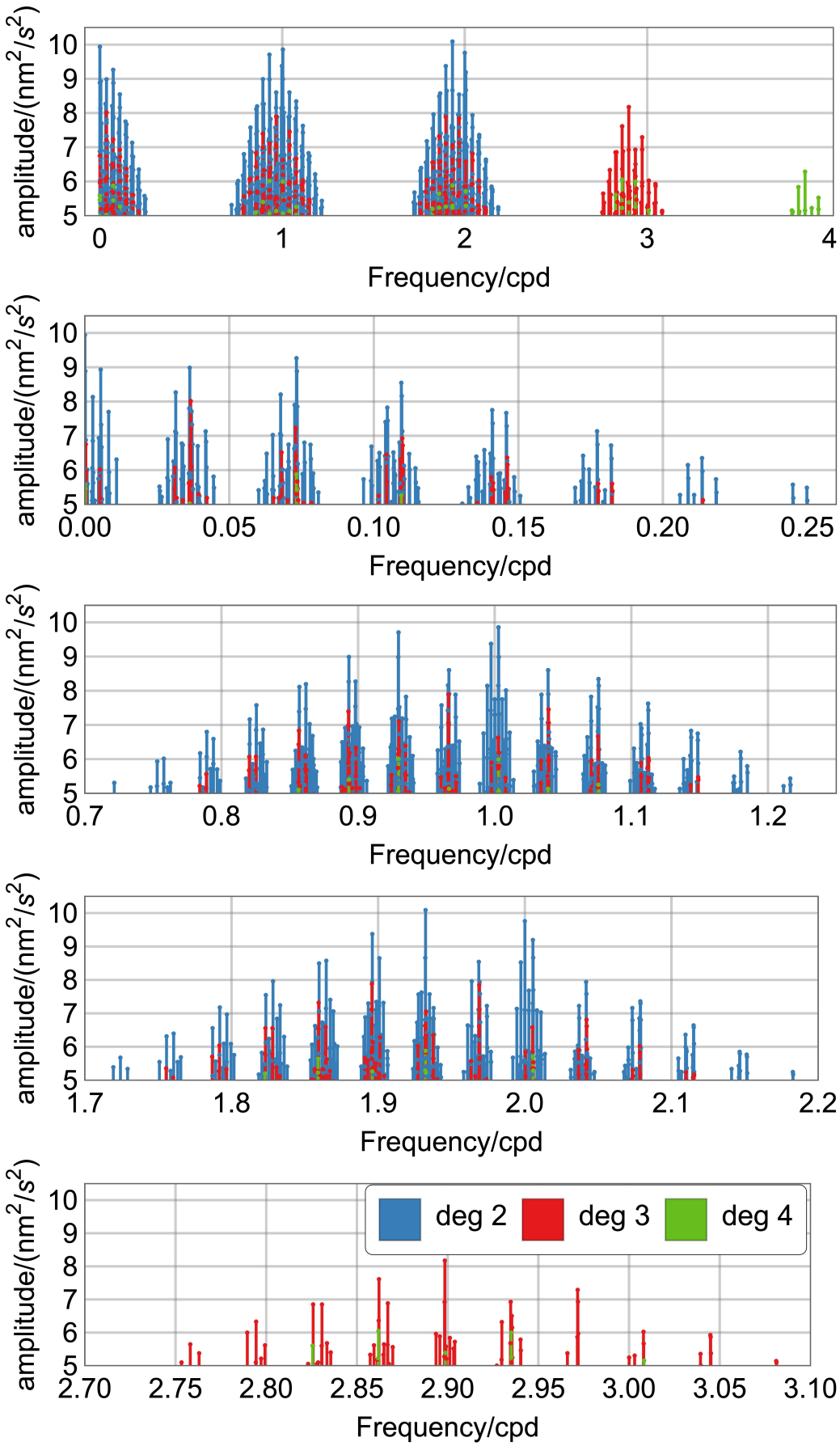

Figure 2.3.: The spectrum of the tidal potential, the amplitudes are computed from the amplitude coefficients in the Tamura (1987) catalog, $\sqrt{C_{nm}^2 + S_{nm}^2}$. Different colors represent different degrees.

2.4. Names of Harmonic Constituents

The first tidal harmonic names were introduced by Darwin (1907). Godin (1970); Melchior (1978) discuss the naming convention for more harmonics, following Doodson (1921). Doodson numbers uniquely define the frequencies of harmonics. The table provided by Bartels (1985) summarizes significant tidal waves with their frequencies, Doodson numbers, and synthesis of the argument. While Doodson (1921) and Darwin (1907) established the names up to Bartels (1957), due to the improved accuracy of instruments and increased length of recordings, more harmonics have been discussed, leading to various *ad hoc* names for the harmonics needed for analysis results (Melchior et al., 1996; Calvo, 2015; Krásná et al., 2013; Ducarme, 2012; Ducarme and Schüller, 2018; Ciesielski et al., 2023). This can cause confusion, so the authors of analyses must provide names of harmonics with their frequencies. Therefore, the most unique way to describe a particular harmonic is to provide its Doodson number together with its name when discussing the results. The increased importance of naming tides of different degree (Ray, 2020; Sulzbach et al., 2022) requires proper names for the degree 3 tides.

Tables 2.3 - 2.5 summarize the naming conventions provided by some authors. They also specify the naming convention I used for the work in this thesis. To distinguish tidal parameters for different degree, I append * and + to names of degree 3 and 4, respectively. Where I had to introduce additional groups, I took a Darwin name from Bartels (1985). In other cases, I had to introduce new names.

The important problem I want to emphasise is that increased resolution of the analysis and models, combined with the improved accuracy and precision of the instruments demands a standard, concise and accurate scheme for the naming of tidal harmonics.

Table 2.3.: Names of diurnal degree 2 tides used by different authors (Bartels, 1957; Melchior et al., 1996; Calvo, 2015, as BAR, MEL, CAL, respectively). The first column is the naming and the fundamental, finest reference grouping scheme used in this work (CIE). Column N indicates numbers of harmonics associated to the group in a frequency range (Min freq, Max freq). The largest amplitude of the harmonic at given Doodson number is in the column Lead amp, while the sum amplitude of all harmonics is in the column G. amp. Amplitudes are given in $\log\left(\frac{V\cdot 10^{10}}{\mathrm{nm^2\,s^{-2}}}\right)$. Symbol ‡ indicates that the harmonic was recognized, but not used as a separate significant tide in this thesis.

CIE	MEL	CAL	BAR	Doodson	N	Min freq	Max freq	Lead amp	G. amp
ζ_1		1158		115.855	26	0.721500	0.823399	7.165	7.572
SGQ_1	SGQ_1	SGQ_1		117.655	15	0.824605	0.833112	7.578	7.774
		$2Q_{1x}$		125.745					
$2Q_1$	$2Q_1$	$2Q_1$	$\mathbf{2Q_1}$	125.755	16	0.851182	0.859690	8.113	8.218
		SGM_{1x}		127.545					
σ_1	Sig_1	SGM_1	σ_1	127.555	6	0.860896	0.862575	8.195	8.277
SGX_1				128.554	10	0.864238	0.870023	7.023	7.33
QW_1		Q_{1x}	⋯	135.645	12	0.887327	0.893097	8.267	8.323
Q_1	Q_1	Q_1	$\mathbf{Q_1}$	135.655	11	0.893244	0.896129	8.992	9.001
ρ_1	RO_1	RO_1	ρ_1	137.455	3	0.897807	0.898101	8.27	8.347
ROX_1				137.655	11	0.898573	0.906315	7.031	7.456
OW_1				144.556	10	0.921941	0.927417	7.246	7.628
OV_1		O_{1x}	...	145.545	4	0.928623	0.929389	8.985	8.999
O_1	O_1	O_1	$\mathbf{O_1}$	145.555	2	0.929536	0.929683	9.71	9.71
OX_1		$2NO_1$		145.755	4	0.930008	0.930487	7.519	7.597
TW_1				146.554	7	0.931964	0.932892	7.191	7.286
τ_1	Tau_1	TAU_1	τ_1	147.555	14	0.934245	0.9404871	7.825	7.976
LKW_1		NTAU		153.655	6	0.958086	0.960970	7.578	7.692
		LK_{1x}		155.445					
LK_1	LK_1	LK_1	⋯	155.455	9	0.962942	0.965827	8.161	8.251
M_1	NO_1	NO_1	$\mathbf{M_1}$	155.655	4	0.966137	0.966446	8.605	8.618
MN_1		NO_{1x}		155.665	2	0.966593	0.966740	7.908	7.92
χ_1	Chi_1	CHI_1	χ_1	157.455	14	0.968565	0.974188	7.887	8.033
π_1	Pi_1	PI_1	π_1	162.556	7	0.989049	0.995143	8.144	8.167
		P_{1x}		163.545					
P_1	P_1	P_1	$\mathbf{P_1}$	163.555	7	0.996968	0.998028	9.377	9.384
S_1	S_1	S_1	$\mathbf{S_1}$	164.556	4	0.999853	1.000147	7.751	7.893
KW_1		K_{1x-}		165.545	4	1.001825	1.002591	8.154	8.162
K_1	K_1	K_1	$\mathbf{K_1}$	165.555	2	1.002738	1.002738	9.858	9.858
κ_1		K_{1x+}	⋯	165.565	1	1.002885	1.002885	8.99	8.99
KX_1				165.575	3	1.003032	1.003651	7.322	7.329
ψ_1	Psi_1	PSI_1	ψ_1	166.554	4	1.005329	1.005623	7.751	7.767
φ_1	Phi_1	PHI_1	φ_1	167.555	11	1.007595	1.013689	8.011	8.083
ϑ_1	TET_1	TET_1	ϑ_1	173.655	12	1.028550	1.034467	7.887	8.012
J_1	J_1	J_1	$\mathbf{J_1}$	175.455	7	1.036292	1.039030	8.605	8.624
ι_1		J_{1x}		175.465	12	1.039177	1.044800	7.903	8.002
SO_1	SO_1	SO_1	$\mathbf{SO_1}$	183.555	13	1.064841	1.072583	7.825	7.956
JO_1		$2J_1$		185.355	7	1.072892	1.075468	7.519	7.628
OO_1	OO_1	OO_1	$\mathbf{OO_1}$	185.555	9	1.075940	1.080944	8.343	8.597
‡ OOX_1		OO_{1x}	⋯	185.565					
OOZ_1				193.455	13	1.099161	1.107669	7.025	7.499
V_1	Nu_1	NU_1	v_1	195.455	43	1.109494	1.216397	7.625	8.049
		NU_{1x}		195.465					

Table 2.4.: Names of semidiurnal degree 2 tides used by different authors (Bartels, 1957; Melchior et al., 1996; Calvo, 2015, as BAR, MEL, CAL, respectively). The first column is the naming and the fundamental, finest reference grouping scheme used in this work (CIE). Column N indicates numbers of harmonics associated to the group in a frequency range (Min freq, Max freq). The largest amplitude of the harmonic at given Doodson number is in the column Lead amp, while the sum amplitude of all harmonics is in the column G. amp. Amplitudes are given in $\log\left(\frac{V \cdot 10^{10}}{\mathrm{nm^2\,s^{-2}}}\right)$. Symbol ‡ indicates that the harmonic was recognized, but not used as a separate significant tide in this thesis.

CIE	MEL	CAL	BAR	Doodson	N	Min freq	Max freq	Lead amp	G. amp
$3N_2$	$3N_2$	$3N_2$	$\mathbf{3N}_2$	225.855	26	1.719381	1.823399	7.547	7.889
ϵ_2	Eps_2	EPS_2	ϵ_2	227.655	15	1.825518	1.837969	7.96	8.103
$2N_2$	$2N_2$	$2N_2$	$\mathbf{2N}_2$	235.755	13	1.853920	1.862428	8.495	8.54
μ_2	Mu_2	MU_2	μ_2	237.555	6	1.863634	1.865313	8.577	8.594
MIX_2				238.554	10	1.866666	1.872142	7.406	7.625
NW_2				244.656	8	1.888387	1.893554	7.299	7.497
‡ NV_2		N_{2x}		245.645					
N_2	N_2	N_2	$\mathbf{N}_2$	245.655	9	1.894922	1.896748	9.374	9.392
NIW_2				246.654	6	1.897954	1.898720	7.344	7.608
ν_2	Nu_2	NU_2	ν_2	247.455	7	1.900545	1.901752	8.652	8.673
NIX_2				248.454	7	1.903267	1.906462	7.317	7.367
γ_2		GAM_2	γ_2	253.755	7	1.923766	1.927417	7.569	7.663
α_2		ALF_2	α_2	254.556	4	1.929389	1.930154	7.628	7.659
ω_2		M_{2x}	$\cdots$	255.545	3	1.931361	1.932127	8.664	8.67
M_2	M_2	M_2	$\mathbf{M}_2$	255.555	7	1.932274	1.933187	10.09	10.09
β_2		BET_2	β_2	256.554	7	1.934393	1.935321	7.573	7.594
δ_2		DEL_2	δ_2	257.555	12	1.936983	1.942753	7.161	7.527
λ_2	Lam_2	LAM_2	λ_2	263.655	6	1.958233	1.963708	7.959	8.001
L_2	L_2	L_2	$\mathbf{L}_2$	265.455	9	1.965827	1.968875	8.543	8.565
KNO_2	KNO_2	KNO_2	$\cdots$	265.655	2	1.969037	1.969184	7.941	7.949
LX_2				265.665	2	1.969331	1.969478	7.586	7.643
LZ_2				267.455	11	1.971303	1.976926	7.223	7.464
$2T_2$			$\mathbf{2T}_2$	271.557	4	1.991787	1.996575	7.134	7.163
T_2	T_2	T_2	$\mathbf{T}_2$	272.556	4	1.997115	1.998287	8.526	8.528
S_2	S_2	S_2	$\mathbf{S}_2$	273.555	5	1.999706	2.000766	9.759	9.76
R_2	R_2	R_2	$\mathbf{R}_2$	274.554	5	2.002591	2.003032	7.682	7.788
K_2	K_2	K_2	$\mathbf{K}_2$	275.555	4	2.004710	2.005476	9.194	9.199
KX_2		K_{2x}	$\cdots$	275.565	1	2.005623	2.005629	8.668	8.668
KY_2				275.575	1	2.005770	2.005770	7.704	7.704
KZ_2				276.554	3	2.008214	2.008508	7.09	7.111
KA_2				277.555	7	2.010333	2.013689	7.027	7.139
ζ_2		ZET_2	ζ_2	283.655	11	2.031288	2.037205	7.223	7.46
η_2	Eta_2	ETA_2	$\eta 2$	285.455	7	2.039030	2.041767	7.941	7.957
ETX_2		ETA_x		285.465	10	2.041915	2.047390	7.581	7.653
$2S_2$	$2S_2$	$2S_2$		293.555	9	2.067579	2.073496	7.161	7.373
$2K_2$	$2K_2$	$2K_2$	$\cdots$	295.555	33	2.075940	2.182843	7.359	7.908

Table 2.5.: Names of degree 3 and 4 tides used by different authors (Bartels, 1957; Melchior et al., 1996; Calvo, 2015, as BAR, MEL, CAL, respectively). The first column is the naming and the fundamental, finest reference grouping scheme used in this work. Column N indicates numbers of harmonics associated to the group in a frequency range (Min freq, Max freq). The largest amplitude of the harmonic at given Doodson number is in the column Lead amp, while the sum amplitude of all harmonics is in the column G. amp. Amplitudes are given in $\log\left(\frac{V\cdot 10^{10}}{\mathrm{nm^2\,s^{-2}}}\right)$. Amplitudes in $\log(\frac{V\cdot 10^{10}}{\mathrm{nm^2\,s^{-2}}})$.

CIE	MEL	CAL	BAR	Doodson	N	Min freq	Max freq	Lead amp.	G. amp
$2Q_1$*				125.655	17	0.784060	0.866976	6.835	7.216
Q_1*	$3MK_1$	$3MK_1$		135.555	5	0.888078	0.892935	7.397	7.554
QX_1*				135.755	4	0.893406	0.895672	6.186	6.32
ρ_1*				137.555	3	0.898263	0.901148	6.33	6.414
O_1*				145.655	14	0.924222	0.937440	7.105	7.349
LK_1*				155.545	4	0.960514	0.965990	7.062	7.091
M_1*	M_1	M_1		155.555	3	0.966137	0.966431	7.892	7.946
χ_1*				157.555	8	0.966756	0.997719	5.503	6.273
K_1*				165.455	7	1.002281	1.008051	6.628	6.903
J_1*	$3MO_1$	$3MO_1$		175.555	26	1.033716	1.149127	7.454	7.753
$3N_2$*				225.755	8	1.755363	1.823089	6.557	6.818
ϵ_2*				227.555	4	1.827799	1.832803	6.559	6.663
$2N_2$*	$3MJ_2$	$3MJ_2$		235.655	8	1.854524	1.862119	7.319	7.404
μ_2*		$3MK_x$		237.455	5	1.864091	1.869714	6.591	6.722
N_2*	$3MK_2$	$3MK_2$	⋯	245.555	7	1.890816	1.896439	7.881	7.964
ν_2*				247.555	5	1.898411	1.903886	6.284	6.422
ω_2*				255.455	4	1.926960	1.931964	6.633	6.8
M_2*				255.655	9	1.932436	1.940178	7.059	7.241
L_2*	$3MO_2$	$3MO_2$	⋯	265.555	4	1.963252	1.968875	7.846	7.874
KNO_2*		$3MO_x$		265.565	4	1.969022	1.973732	7.121	7.142
		$3MQ_2$		273.655					
K_2*		$3KM_2$		275.455	8	1.997262	2.005932	6.582	6.798
η_2*				285.555	18	2.036601	2.115426	6.81	7.2
MN_3*	MN_3	MN_3	⋯	345.655	29	2.753244	2.869713	7.613	7.871
		M_{3x}		355.545					
M_3*	M_3	M_3	$\mathbf{M_3}$	355.555	11	2.892640	2.903886	8.175	8.21
ML_3*	ML_3	ML_3		365.455	11	2.927107	2.940325	6.928	7.233
MK_3*	MK_3	MK_3		375.555	17	2.965990	3.081254	7.29	7.536
O_1+				145.555	26	0.856186	2.041767	6.013	6.813
MN_3+				345.555	14	2.789226	3.008361	6.056	6.586
		N_4		435.755					
M_4+		M_4		455.555	10	3.791964	3.937897	6.284	6.59
		K_4		475.565					

2.5. Earth Tides

If a gravimeter was placed on a rigid, oceanless Earth with no atmosphere, it would only measure the acceleration change at the specific location due to the Earth's rotation and motion of a celestial body. Assuming no other movements, such as seismic waves caused by plate tectonics, due to relative apparent motion of an external body, the measured acceleration would be only the vertical gravity change. A tiltmeter would detect the horizontal acceleration even on a rigid Earth, while a strainmeter would not detect any deflection. In reality, Earth is rather elliptical than spherical and its rheology is complex, involving various elastic and anelastic properties, which permit a deformation of the Earth's body when tidal forces are applied. The resulting redistribution of the Earth's masses produces a corresponding change in the gravitational field of the Earth as well as the displacement of the station in the undisturbed gravity field. Due to this deformation, the gravitational potential at the station varies (see Wang, 1997; Baker, 1984). At the surface of the Earth, the response in the direction of the gravity vector can be defined by the Love numbers (Love, 1911) including effects of ellipticity and rotation. We focus on numbers h describing the apparent gravity change due to radial displacement in the undisturbed gravity field and k, the change in gravitational potential due to mass displacement in the Earth. From the equations of motion for a rotating, elliptical, self gravitating elastic Earth (Wahr, 1981a), terms involving spherical harmonics of various degree to the tidal potential enter the solution due to the loss of symmetry. In the spherically symmetric non-rotating model, Love numbers only depend on the degree n of the spherical harmonic. Their values result from the elastic properties and the density of the Earth as calculated for specific Earth models, such as PREM (Preliminary Reference Earth Model; Dziewonski and Anderson, 1981). For a spherical Earth and the second degree, the Love numbers are $h_2 = 0.6032$ and $k_2 = 0.2980$ (Agnew, 2009).

The global effect on tidal gravity changes is characterized by the so-called theoretical body tides (Ducarme, 2012), which are described by an *amplitude factor* also known as the *gravimetric factor*, that represents the expected reaction of the solid Earth to tidal forces. The theoretical signal amplitudes A_l^{ini} on a theoretical Earth lead to theoretical gravimetric factor values $\delta_l^{\text{ini}} = A_l^{\text{ini}}/A_l$ (Wenzel, 1996; Agnew, 2009) in relation to rigid earth tides of amplitude A_l (Godin, 1972; Baker, 1984, see details in Chapter 3 of this thesis). To find how much gravity is amplified due to the elasticity of the Earth, we can use an expression for this gravimetric factor for a specific degree:

$$\delta_n = 1 + \frac{2h_n}{n} - \frac{n+1}{n}k_n \tag{2.11}$$

Theoretical values for gravimetric factors of different degrees for simple Earth models are $\delta_2 \approx 1.16$, $\delta_3 \approx 1.07$, and $\delta_4 \approx 1.03$ (Dehant, 1987; Baker, 1984).

The imperfect elasticity of the Earth (finite quality factor Q) modifies real Love numbers to complex. After deformation, the Earth's body returns to its previous shape, but not immediately

after the force causing the deformation has been removed. This is a reason for the delay of the measured signal relative to the applied forcing, expressed as phase, which Earth models assume to be 0°. Earth models have to be adjusted slightly to be appropriate for tidal frequencies due to dispersion caused by anelasticity (Dahlen and Tromp, 1998; Agnew, 2009) which varies between tidal bands. The Earth's body deformation caused by the tidal forcing is defined as the *body tide*.

2.6. NDFW and Earth's Rotation

At the core-mantle boundary (CMB) the solid silicate mantle meets the liquid metallic core, which is restrained by pressure forces (Souriau, 2007). Since the core is not bound to the mantle, it can rotate independently of the Earth's outer layers, allowing for a different rotation axis and rate of the mantle and outer core. The CMB has a small ellipticity, which results in a restoring force on the CMB and a damped wobble of the Earth's rotation axis (Zürn, 1997). Due to the small ellipticity of the CMB, the frequency of this rotational free oscillation falls into the diurnal tidal band, causing a resonant response in the degree 2 Love numbers near 1 cycle/day (Dehant et al., 1999; Rogister, 2001). This is known as the Nearly Diurnal Free Wobble (NDFW, terrestrial frame) or the Free Core Nutation (FCN, celestial frame) and practically affects all diurnal harmonics degree 2 (Dehant, 1987; Zürn, 1997). The frequency dependent diurnal gravimetric factor degree 2 is typically expressed in relation to O_1, the lunar main harmonic very little affected by the resonance:

$$\delta_l^{NDFW} = \delta_l - r\frac{f_l - f_{O_1}}{f_{\mathrm{NDFW}} - f_l} \tag{2.12}$$

where r is the resonance factor. The early NDFW models were introduced by Jeffreys and Vincente (1957); Molodenskii (1961), but the modern approach for these theories was described by Wahr (1981a,b); Dehant (1987). Diurnal tides also cause changes in the direction of the Earth's spin axis (the astronomical precessions and nutations), which are affected by NDFW. The tidal harmonic ψ_1 closest to the resonance is very weak in gravity (Zürn, 1997; Agnew, 2009) but large in the nutations, therefore the resonance properties can be better defined from the VLBI observations (Krásná et al., 2013). Hence, some of the best data on it come from astronomy. However, Earth tides are essential as an alternative analysis method to validate the VLBI results, as studied by Rosat et al. (2009); Amoruso and Crescentini (2020).

The combination of improved theoretical development and observations has led to the important result, which is that the period of the NDFW is significantly smaller from the originally predicted value. The difference in period implies that the ellipticity of the CMB is increased from a hydrostatic value by about 5%, the equivalent of $380-500$ m difference in radius (Math-

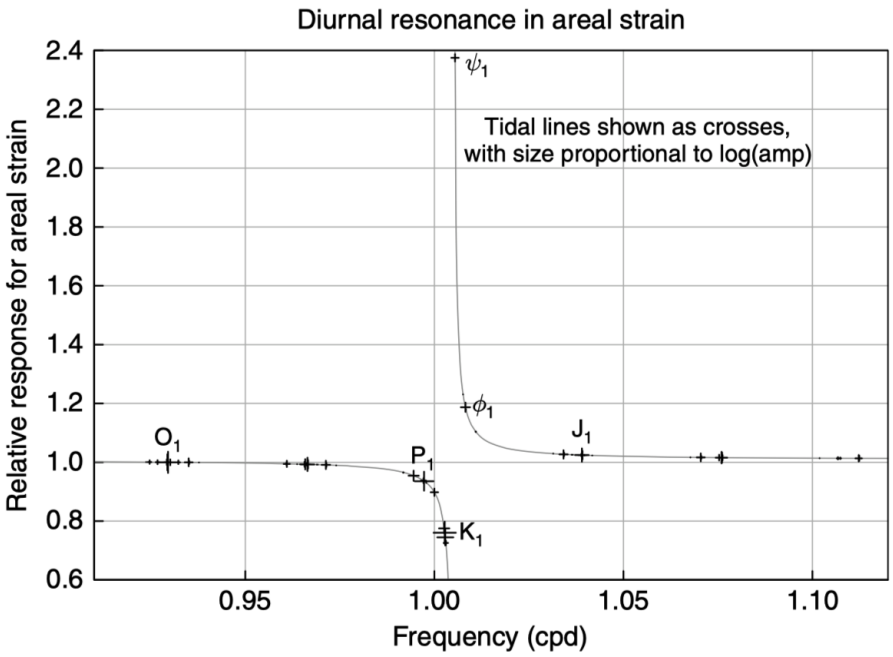

Figure 2.4.: NDFW tidal response, for the combination of Love numbers that gives the areal strain, normalized to 1 for the O_1 tide. The crosses show the locations of tidal harmonics, with size of symbol proportional to the logarithm of the amplitude of the harmonic (from Agnew, 2009).

ews et al., 2002). This difference is not detectable using seismic waves because of their long wavelengths at the CMB (Agnew, 2009).

The axis of rotation of the Earth changes its geographical coordinates over time due to various factors, such as NDFW, precession, heterogeneity, figure, tidal pull, etc. This change in coordinates induces changes in centrifugal force and effectively interferes with the gravitational potential, causing polar motion to have the same effects as the attraction of external bodies, resulting in so-called pole tide. The rotation rate of the Earth, which is the most important term in eqs. (2.5)-(2.6), also changes with time, and in addition to small temporal variations, its period gradually increases. In last thousand of years this rate is estimated to be $\approx$ 2ms in one hundredth years (Stephenson et al., 2016). The reason for the trend is tidal dissipation, which has already caused the Moon to always be oriented with the same side towards the Earth. The standard day in SI that is used in all computations is a solar day, which contains 24 hr = 86400 second. While the NDFW significantly affects tidal response, the changes induced by pole tides are rather small on estimated tidal parameters in diurnal or semi-diurnal band.

In addition to the trend, the length of day (LOD) is also subject to fluctuations on a shorter timescale (Stephenson et al., 2016) ranging from days to years, due to internal torques that arise from relative movements and mass redistribution of Earth's core, mantle, crust, oceans, atmosphere, and cryosphere. To keep the total angular momentum constant, a change of the

angular momentum in one region must necessarily be balanced by angular momentum changes in the other regions, which modifies the angular speed of the mantle. All contributions that affect the length of day must be taken into account in order to compute the correct value of tidal potential, i.e. the position of the observer with respect to the tide-generating objects. The corrections are provided on yearly basis by IERS (Bouzard and Gambis, 2009) together with leap seconds adjustments, to ensure that the time recorded by the instrument agrees with the time counted in Modified Julian Days, used in astronomy.

2.7. Tidal Models of Earth

The calculation of body tides is based on spherically layered Earth models derived from seismology. Early works by (Takeuchi, 1950; Molodenskii, 1957; Jeffreys, 1957; Wang, 1997) provided theoretical values of tidal gravity records for different assumptions of Earth interior properties. Recent models are based on equations of motion for a rotating, elliptical, self-gravitating elastic Earth, solved by Wahr (1981a). Later improvements adjusted spheroidal displacement fields that become toroidal deformations for specific degrees and orders Dehant et al. (1999).

Some recent models introduce inelasticity in the Earth'a interior, such as hydrostatic, inelastic WDZe (Wahr, 1981a; Dehant, 1987; Zschau and Wang, 1985) and non-hydrostatic, inelastic DDWnh (Dehant et al., 1999). The elastic DDWh (Dehant et al., 1999) model assumes hydrostatic equilibrium inside the Earth, while DDWnh does not consider flattening at the CMB. Hence, the theoretical gravimetric factors from the computed models provide that the Earth amplitude response, gravimetric factor δ^{ini}, is different for different degrees of the potential. As soon as the ellipticity or rotation is included, the Love numbers describing the response to tidal forces become latitude-dependent. The spherical symmetry is broken to axial symmetry. For instance, WDZe assumes a latitude dependency of tides degree 2 and tides that degree equal order ($n = m$). Although all models assume elastic and inelastic properties in Earth rheology, none of the applications of these models in tidal analysis imply a phase shift in the body tide Earth signal.

Accounting for the tidal potential varying with latitude, and between degrees and orders, the response of a spherical, non-rotating Earth to tidal forces is uniform at each point of the globe, as described by Love numbers. Large-scale heterogeneities in Earth structure, such as geological faults or subduction zones, have been shown to have only small effects on the body tide displacement (Beaumont and Berger, 1974; Zürn et al., 1976; Wang, 1997). Local anomalies in density do not affect tidal response more by 0.3% (Baker, 1984).

Recent models agree with latest observations at the level of a few tenths of a percent. For degree 2, different body tide models have been evaluated using tidal gravity observations with superconducting gravimeters data. The WDZe and MATH (Matthews, 2001) models agree with

the observations corrected for ocean tides loading at the level of 10^{-3} (Baker and Bos, 2003; Ducarme and Sun, 2001; Ducarme et al., 2007). An extensive comparison has been performed for the third degree (Melchior, 1978; Ducarme, 2012), showing consistency with the models. The tidal model commonly applied in Earth tidal analysis software is WDZe (Wenzel, 1996), and recently also DDWh or DDWnh (Ducarme, 2012; Schüller, 2020).

2.8. Loading

The oceans and the atmosphere have a tidal response that affects the solid earth tidal response, altering the apparent gravimetric factors and phases. Due to the different material properties and distribution of ocean water, atmospheric air masses and the solid Earth, their response is not uniform around the globe, hence affecting the apparent response at different locations. None of the available Earth body tide models takes this into account.

The Earth's daily rotation and solar irradiation changes cause mixed effects on tidal records. Ground and air temperature as well as pressure vary. Ground-temperature changes cause their thermoelastic deformations (Berger, 1975) and additional mass loads to the Earth cause deformations and changes in gravity by direct Newtonian attraction. Hence 'atmospheric tides' (Chapman and Lindzen, 1970), known as 'radiation tides' are observed. Some of their signals are consistent with tidal harmonics in a systematic way, significantly affecting amplification factors and phases of tidal harmonics. However, a vast part of the signal is not harmonic. It might be phase and amplitude modulated, varying in time due to the chaotic nature of weather physics. Some signals are not exactly at the given tidal frequency. Tides that are most affected by radiation and atmosphere are S_1, S_2, R_2 and T_2. The influence of radiation tide is so strong that their gravimetric factors and phases cannot describe Earth's property, because for two harmonics with the same frequency it is impossible to tell how much each part contributes (Agnew, 2009). These tides strongly mix up the estimate of the admittance for the coarser grouping, despite their relatively small catalog amplitude (Schroth, 2020; Ciesielski et al., 2023). Even if there is no tidal harmonic at particular frequency, air pressure manifests itself at specific frequencies in tidal recordings (Ducarme and Schüller, 2018; Ray et al., 2023; Ducarme, 2023).

The estimation of pure body tides is impossible on Earth since ocean tides crucially interfere with the Earth response for broad spectra of tidal frequencies and observations Ducarme (2012). This is the largest systematic influence on gravity tides. In principle, there are various approaches to minimize the loading effects in analysis. The estimation of the tidal loading vector, which takes into account the direct attraction of the water masses, the flexion of the ground, and the associated change of potential, is generally evaluated by performing a convolution integral between the ocean tide models and the load Green's function (Munk and Cartwright, 1966;

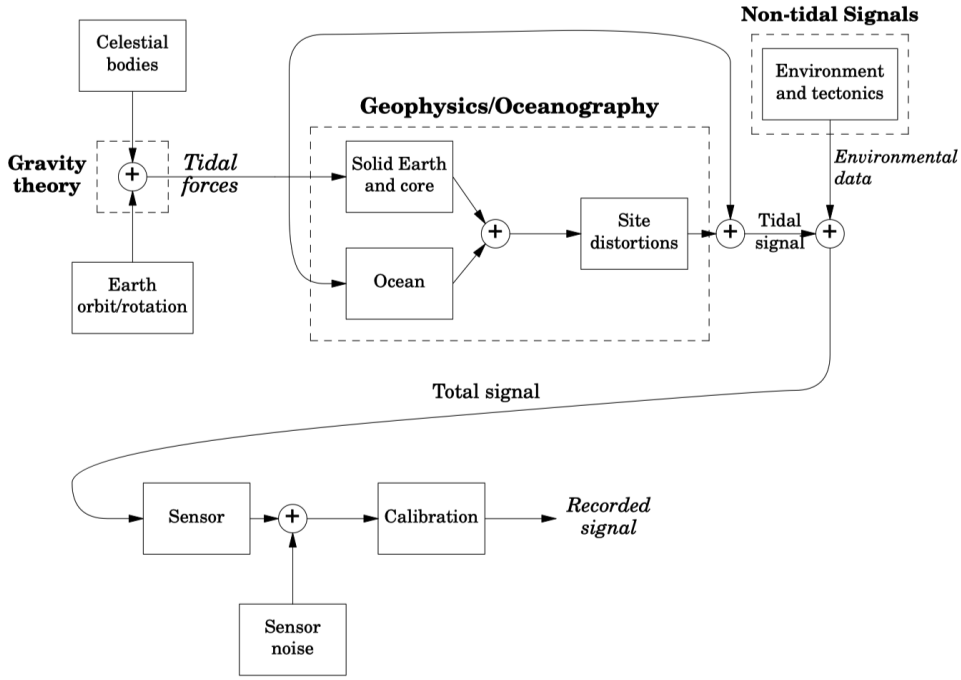

Figure 2.5.: Tidal flowchart. Entries in italics represent things we know (or think we know) to very high accuracy; entries in boldface (over the dashed boxes) represent things we can learn about using tidal data (from Agnew, 2005).

Farrell, 1972; Francis and Dehant, 1987; Foreman, 2004; Schroth, 2020). Its precision depends on the quality of the ocean tides models.

2.9. Combined Effects

From the major tides, O_1, K_1, M_2, S_2, only O_1 is known to not be significantly affected by additional processes. The response of K_1 strongly depends on the NDFW; all tides, but specially M_2 and S_2 are influenced by oceans and radiation. Hence, it is common to discuss O_1 tide, or ratios like M_2/O_1 in the results of tidal analysis (Melchior, 1978), like Calvo (2015) does.

In this thesis we do not study the effects of radiation tides or ocean tides on body tides, as Schroth (2020); Ducarme (2012); Sulzbach et al. (2022) do. Instead, we investigate local responses that include all physical contributions (e.g. ocean tides, radiation tides) that influence the local response as measured by gravity sensors. Hence, we are aware of these effects and they are included in the local response model. The conceptual flowchart Fig. 2.5 visualises all the effects contributing to the tidal signal and analysis.

3. Method

This chapter is a part of the manuscript submitted and accepted to be published as peer-reviewed article in the Journal of Geodesy. Most paragraphs are taken literally from Ciesielski et al. (2023).

3.1. Tidal Analysis

The analysis of terrestrial tides is a special case of the study of time series that involves advancements in applied mathematics, digital signal processing and numerical computing. The problem of Earth tide analysis can be simplified to finding the transfer function, or complex admittance, of a linear system (Munk and Cartwright, 1966; Chojnicki, 1973; Wenzel, 1997c). The results of tidal analysis are used for predicting future tides as well as distinguishing different causes contributing to tidal measurements.

The most common approach to finding the tidal response is the LS fit of the set of harmonic signals computed from tidal catalog to the observed signal. Although we follow this approach, we incorporate significant modifications. Therefore, the LS fit of the synthetic tidal signal is not only fitted to the observation, but is also simultaneously constrained by other assumptions. The new approach is applicable to any tidal observation, whether it be gravity, strain, tilt or surface displacement. The following theory uses symbols that are appropriate for analysis of tidal gravity. For a given tidal wave with an index l, the amplitude factor δ_l is defined as the ratio of the observed amplitude A^{obs} with respect to the theoretical rigid Earth tide of amplitude A, i.e., $\delta_l = A_l^{obs}/A$ (Godin, 1972; Baker, 1984). The complex admittance of the measurements referred $g^{\mathrm{rig}}(t)$, is expressed by a pair of tidal parameters: the *gravimetric factor* $\delta(f)$ and the *gravimetric phase* $\Phi(f)$ (also known as *phase lead*), both functions of frequency f. We use δ_l and Φ_l for these tidal parameters for tidal harmonic $g_l^{\mathrm{rig}}(t)$ at frequency f_l.

Tidal Signals

Based on a tidal catalog giving amplitude and phase for a harmonic development, we compute the gravity signal for a rigid oceanless Earth.

With a tidal catalog of L harmonics, the rigid Earth tide at a given location is

$$g^{\mathrm{rig}}(t) = \sum_{l=1}^{L} g_l^{\mathrm{rig}}(t) = \sum_{l=1}^{L} A_l \cos(2\pi f_l\, t + \phi_l)$$

with harmonic frequency f_l. The amplitude A_l and the phase ϕ_l are computed from the information given in the tidal catalog based on the station's location on the Earth's surface. For simplicity in the description we neglect the slight time dependence (e. g. Bartels, 1957; Cartwright and Tayler, 1971; Tamura, 1987; Hartmann and Wenzel, 1995) of amplitude $A_l(t)$ and the exact astronomical arguments (e. g. Simon et al., 1994; Tamura, 1987), which results in a non-linear time scale in the cos-function. The essential point is that $g_l^{\mathrm{rig}}(t)$ can be computed precisely for each given point in time.

The synthetic tidal gravity signal for a given model

$$g^{\mathrm{syn}}(t) = \sum_{l=1}^{L} g_l^{\mathrm{syn}}(t) = \sum_{l=1}^{L} \delta_l A_l \cos(2\pi f_l t + \phi_l + \Phi_l)$$

accounts for the admittance of the solid Earth by the tidal parameters δ_l and Φ_l. To express the tidal analysis problem with linear parameters, we rewrite the synthetic signal as

$$g_l^{\mathrm{syn}}(t) = X_l C_l^{\mathrm{rig}}(t) + Y_l S_l^{\mathrm{rig}}(t) \tag{3.1}$$

with the rigid Earth tide signal

$$C_l^{\mathrm{rig}}(t) = A_l \cos(2\pi f_l t + \phi_l) \tag{3.2}$$

and its quadrature

$$S_l^{\mathrm{rig}}(t) = A_l \sin(2\pi f_l t + \phi_l). \tag{3.3}$$

We use symbols similar to those used by Wenzel (1997c). The 'tidal model' is specified by the linear parameters

$$X_l = \delta_l \cos(\Phi_l) \quad \text{and} \quad Y_l = -\delta_l \sin(\Phi_l). \tag{3.4}$$

The conventional model parameters then are gravimetric factor

$$\delta_l = \sqrt{X_l^2 + Y_l^2} \quad \text{and phase} \quad \Phi_l = -\arctan\frac{Y_l}{X_l}. \tag{3.5}$$

The Objective Function

To set up the inverse problem, we express the signals by the time series samples

$$\begin{cases} g_k = g(t_k), \\ p_k = p(t_k), \\ C_{kl}^{\mathrm{rig}} = C_l^{\mathrm{rig}}(t_k), \\ S_{kl}^{\mathrm{rig}} = S_l^{\mathrm{rig}}(t_k). \end{cases} \tag{3.6}$$

where $k = 1 \ldots K$; $p(t)$ is a recording of local air pressure and $g(t)$ is recorded gravity. All of these signals are filtered and tapered prior to the analysis in a consistent way. We compute the synthetic tides for an a priori (initial) body tide model with parameters X_l^{ini} and Y_l^{ini}. Quantities X and Y are real and imaginary parts of the complex admittance to which the adjustment factors x_l and y_l are applied. The final model parameters then are

$$X_l^{\mathrm{fin}} = x_l\, X_l^{\mathrm{ini}} - y_l\, Y_l^{\mathrm{ini}} \tag{3.7a}$$

and

$$Y_l^{\mathrm{fin}} = y_l\, X_l^{\mathrm{ini}} + x_l\, Y_l^{\mathrm{ini}}. \tag{3.7b}$$

In this study factors x_l and y_l initially are set $x_l = 1$ and $y_l = 0$. Hence, the factors X_l and Y_l mostly vary smoothly with frequency f_l, but the initial model also captures other frequency dependence, notably the resonance caused by the free core nutation (FCN) in the diurnal band. The structure of eq. (3.7) is such that the adjustment factors can introduce an additional phase shift

$$\Delta\Phi_l = -\arctan\frac{y_l}{x_l} \tag{3.8}$$

even in the case where Y_l^{ini} is zero. In that sense the initial parameters define an initial synthetic tidal signal

$$C_{kl}^{\mathrm{ini}} = X_l^{\mathrm{ini}}\, C_{kl}^{\mathrm{rig}} + Y_l^{\mathrm{ini}}\, S_{kl}^{\mathrm{rig}} \tag{3.9a}$$

and its quadrature

$$S_{kl}^{\mathrm{ini}} = X_l^{\mathrm{ini}}\, S_{kl}^{\mathrm{rig}} - Y_l^{\mathrm{ini}}\, C_{kl}^{\mathrm{rig}}. \tag{3.9b}$$

The synthetic tidal gravity signal in eq. (3.1) thus is

$$g^{\mathrm{syn}}(t_k) = \sum_{l=1}^{L} x_l\, C_{kl}^{\mathrm{ini}} + y_l\, S_{kl}^{\mathrm{ini}}. \tag{3.10}$$

Tidal parameters are found using the data misfit:

$$E(x_l, y_l, r) = \frac{1}{K\,\sigma^2} \sum_{k=1}^{K} \Big(g_k - r\,R^{\mathrm{ini}}\,p_k - \sum_{l=1}^{L} (x_l\,C_{kl}^{\mathrm{ini}} + y_l\,S_{kl}^{\mathrm{ini}}) \Big)^2 \tag{3.11}$$

which has to be minimized:

$$E(x_l, y_l, r) \to \min \tag{3.12}$$

Here R^{ini} is an a priori admittance to air pressure and r is the adjustment factor to this. Due to the large number of tidal harmonics, with the vast majority having small amplitude and close frequencies, the condition number of the problem would be clearly too large to obtain meaningful results. The conventional approaches (Wenzel, 1997b,c) remove this instability by summing harmonics closely spaced in frequency, a so-called wave-group:

$$E(x_j, y_j, r) = \frac{1}{K\,\sigma^2} \sum_{k=1}^{K} \Big(g_k - r\,R^{\mathrm{ini}}\,p_k - \sum_{j=1}^{J} (x_j \sum_{l=J_j}^{J_{j+1}-1} C_{kl}^{\mathrm{ini}} + y_j \sum_{l=J_j}^{J_{j+1}-1} S_{kl}^{\mathrm{ini}}) \Big)^2 \tag{3.13}$$

In the sum above, index j sums over J groups ($J_1 = 1$ and $J_{J+1} - 1 = L$). Wave grouping is a kind of model parameterization where tidal harmonics are organized in frequency bands (Venedikov, 1961; Chojnicki, 1973). Harmonics within the same frequency band are scaled by a common factor. The objective function is then

$$E(x_j, y_j, r) \to \min \tag{3.14}$$

Individual harmonics can not be distinguished in the signal.

3.2. The Regularization Approach

The Regularization Constraint

Unlike conventional approaches we add a model constraint to the objective function. The parameters are constrained to be close to reference values, deviating from the reference only if justified by a significant decrease of data misfit. This removes the instability created by trying to determine parameters for tidal harmonics closely spaced in frequency or having a very small amplitude

$$E(x_l, y_l, r) = \frac{1}{K\,\sigma^2} \sum_{k=1}^{K} \Big(g_k - r\,R^{\mathrm{ini}} p_k - \sum_{l=1}^{L} (x_l\,C_{kl}^{\mathrm{ini}} + y_l\,S_{kl}^{\mathrm{ini}}) \Big)^2 + \\ + \frac{\alpha^2}{2L+1} \left\{ \left(r - r^{\mathrm{ref}} \right)^2 + \sum_{l=1}^{L} \left[\left(x_l - x_l^{\mathrm{ref}} \right)^2 + \left(y_l - y_l^{\mathrm{ref}} \right)^2 \right] \right\}. \tag{3.15}$$

The second term (in curly braces) of eq. (3.15) expresses a model constraint. When minimizing

$$E(x_l, y_l, r) \to \min \tag{3.16}$$

with respect to x_l, y_l, and r, model parameters that are close to their reference values x_l^{ref}, y_l^{ref}, and r^{ref}, respectively, will be preferred. Model parameters will only deviate from the reference if the data misfit expressed in the first term of eq. (3.15) is significantly reduced. The solution of the optimization problem seeks a compromise between minimizing the data misfit on the one hand and keeping model parameters within range of the reference values on the other hand. The trade-off parameter α adjusts the emphasis on one criterion over the other. Wave grouping is not needed.

The σ should specify the expected rms-amplitude of the noise level in the data in units of data which makes the expression dimensionless. A normalized data misfit near unity indicates that the fit is successful with respect to the noise level. A significantly smaller value would indicate over-fitting of the data.

Finding the Minimum

The parameters x_l, y_l, and r which minimize the objective function in eq. (3.15) are the solution of a system of linear equations, which is found by searching the stationary point with

$$\frac{\partial E}{\partial x_l} = \frac{\partial E}{\partial y_l} = \frac{\partial E}{\partial r} \stackrel{!}{=} 0 \quad \forall \quad l = 1 \ldots L \tag{3.17}$$

as is common for least-squares problems. To set up the system of linear equations, we collect the regressors in the so-called 'forward operator' matrix $\boldsymbol{G}$ with

$$G_{kl} = C_{kl}^{\mathrm{ini}} \text{ for } l = 1 \ldots L, \tag{3.18a}$$

$$G_{k(L+l)} = S_{kl}^{\mathrm{ini}} \text{ for } l = 1 \ldots L, \text{ and} \tag{3.18b}$$

$$G_{k(2L+1)} = R^{\mathrm{ini}} p_k. \tag{3.18c}$$

Model adjustment factors are collected in parameter vector $\vec{m}$ with

$$m_l = x_l \text{ for } l = 1 \dots L, \tag{3.19a}$$

$$m_{(L+l)} = y_l \text{ for } l = 1 \dots L, \text{ and} \tag{3.19b}$$

$$m_{(2L+1)} = r. \tag{3.19c}$$

We let R^{ini} have units of $1\,\text{nm}\,\text{s}^{-2}\,\text{hPa}^{-1}$ so that all columns in $\boldsymbol{G}$ have units of $1\,\text{nm}\,\text{s}^{-2}$ and all m_l $(l = 1 \dots 2L+1)$ are dimensionless. The signal vector of synthetic gravity then is

$$\vec{g}^{\text{syn}} = \boldsymbol{G}\,\vec{m}. \tag{3.20}$$

and

$$E(\vec{m}) = {s_d}^2 \left(\vec{g} - \boldsymbol{G}\left(\delta\vec{m} + \vec{m}^{\text{ref}}\right)\right)^2 + \alpha^2\,{s_m}^2\,(\delta\vec{m})^2, \tag{3.21}$$

where the elements g_k of vector $\vec{g}$ are the samples of observed gravity and $\delta\vec{m} = \vec{m} - \vec{m}^{\text{ref}}$ is the update of the adjustment factors (model parameters) with respect to their reference values. We abbreviate the scaling factors

$$s_d = \frac{1}{\sigma\sqrt{K}} \quad \text{and} \quad s_m = \frac{1}{\sqrt{2L+1}}. \tag{3.22}$$

By substituting

$$\vec{a} = s_m\,\delta\vec{m}, \tag{3.23}$$

$$\boldsymbol{A} = \frac{s_d}{s_m}\boldsymbol{G}, \text{ and} \tag{3.24}$$

$$\vec{d} = s_d\left(\vec{g} - \boldsymbol{G}\vec{m}^{\text{ref}}\right) \tag{3.25}$$

we find the system of linear equations

$$\left(\boldsymbol{A}^T\boldsymbol{A} + \alpha^2\mathbf{1}\right)\vec{a} = \boldsymbol{A}^T\,\vec{d}. \tag{3.26}$$

Its solution $\vec{a}$ satisfies the least-squares condition in eq. (3.17). We find the solution by computing the singular value decomposition of the matrix

$$\boldsymbol{A} = \boldsymbol{U}\boldsymbol{\Lambda}\boldsymbol{V}^T, \tag{3.27}$$

where $\boldsymbol{U}$ and $\boldsymbol{V}$ are the orthonormal matrices of eigenvectors in data space and model space, respectively and where

$$\boldsymbol{\Lambda} = \text{diag}(\lambda_j) \tag{3.28}$$

is the diagonal matrix of singular values, of which $L \leq (2L+1)$ are non-zero with $\lambda_j > 0$. The factorization has to be computed only once to find the solution

$$\vec{a} = \boldsymbol{V} \left(\frac{\eta_j}{\lambda_j} \right) \boldsymbol{\Lambda}^{-1} \boldsymbol{U}^T \vec{d} \tag{3.29}$$

for any value α, which controls the filter factors

$$\eta_j = \frac{1}{1 + \frac{\alpha^2}{\lambda_j^2}}. \tag{3.30}$$

From this solution the vector of model parameter adjustment factors is obtained by

$$\vec{m} = \vec{m}^{\text{ref}} + \sqrt{2L+1}\, \vec{a}. \tag{3.31}$$

If $\alpha = 0$, all $\eta_j = 1$, hence $\vec{a} = \boldsymbol{V} \boldsymbol{\Lambda}^{-1} \boldsymbol{U}^T \vec{d}$ in eq. (3.29).

Singular Value Decomposition and Amplitudes

There are numerous methods for solving LS problems, including cases where regularization terms are added to the objective function. Some obvious choices include Cholesky decomposition, QR-factorization and Singular Value Decomposition (**SVD**). Usually, SVD is not commonly used, even though it does not require square, positive definite matrices, because any rectangular matrix $\mathbf{A}$ in the equation $\mathbf{A}\vec{x} = \vec{b}$ can be used to solve the equation $\mathbf{A}^T\mathbf{A}\vec{x} = \mathbf{A}^T\vec{b}$. Then matrix $\mathbf{A}^T\mathbf{A}$ fulfils the necessary requirements. `Eterna 3.40` uses Cholesky decomposition to solve the system of equations. However, SVD is the most numerically stable and accurate (see Chapter 3.5 for details). While SVD is computationally expensive, modern libraries have increased the efficiency of the algorithm. Additionally, when solutions need to be found for various α, the preconditioning, as derived in eq. (3.29), makes SVD superior for regularization approach among other methods. While SVD has to be computed only once for given inverse problem, providing results for various range of trade-off parameter α. The conventional approaches would have to compute the solution for each α separately. One run of the inversion program, depending of the time series length currently takes 2 hours on average. If we wanted to explore the whole spectrum of α it would take about a week, assuming the same performance. Furthermore, the decomposition itself allows for the investigation of the resolution in terms of data resolution matrix, model resolution matrix, and spectra of singular values.

Previous investigations of the singular value decomposition of the forcing operator in tidal analysis (Ciesielski and Forbriger, 2019, 2020) suggest that the model resolution matrix is rather diagonal for the main, large amplitude harmonics. From the orthonormal matrix $\mathbf{V}$, related to the model resolution matrix, we can find a correlation between model space and singular value

space. This is if the corresponding elements of matrix **V** are close to 1, which is the case for harmonics of larger amplitude or distant in frequency. The analysis suggests an interpretation of a direct relationship between SVs and forcing, clearly for large tides, especially in longer time series. This is not surprising since that signals composing the forward operator are almost purely harmonic and the immediate neighbours of large amplitude harmonics typically have small amplitude. As a result, there is a strong relation between singular values and rms-amplitude of tidal harmonics forcing signal, which we can visualise on Fig. 3.1. This observation is essential, because in fact signals corresponding to large singular values are these significantly contributing to the signal, so their estimates are stable and not prone to noise (Aster et al., 2005). When investigating shorter time series, it is noticeable that algebraic conditions change, resulting in smaller resolution (Ciesielski and Forbriger, 2020). Therefore, it is reasonable to resolve tidal contributions mainly based on their amplitudes (or SVD) and then adjust the resolution by taking their frequency distances into account.

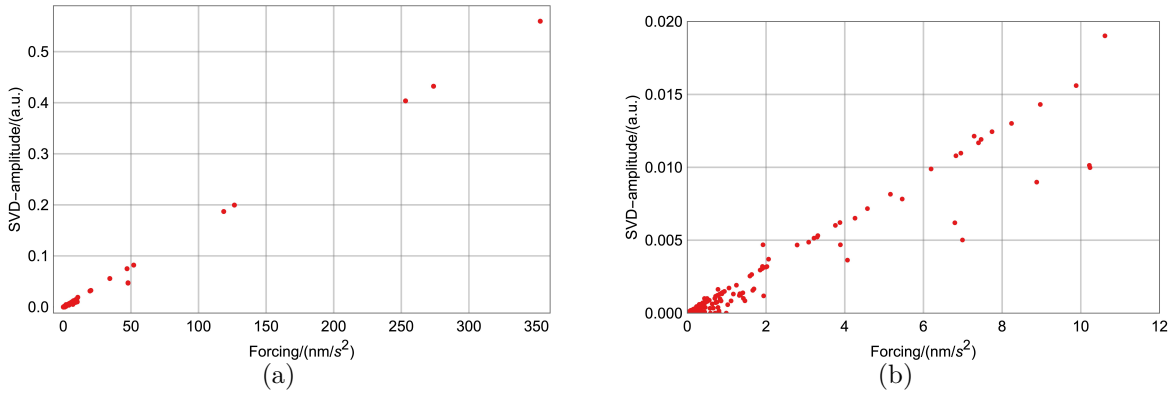

Figure 3.1.: Apparent relation of singular values to RMS forcing amplitude of tides at the BFO. The analysis for the whole investigated time series (11.5 y). Fig. 3.1a displays the relation for the all tides. Fig. 3.1b shows the relation for the harmonics with forcing amplitude less than 12 $\mathrm{nm\,s^{-2}}$.

In addition, `Eterna 3.40` Wenzel (1996) and its successors (Schüller, 2015) report the condition number as a criterion for numerical stability regarding the resolution. It is not surprising, since the condition number measures how much the output value of the solution can change for a small change in the input data. In SVD, the condition number is the ratio between the largest and the smallest singular values. Hence we can directly relate the resolvable harmonics to their singular values and constrain the rest to the reference values.

The Resolution

Chap. 1 introduces the Rayleigh resolution criterion (Doodson, 1921; Godin, 1970, 1972), which is commonly used to identify resolvable harmonics. The criterion is based on the direct relation between the length of time series and the minimum frequency distance between tidal harmonics that may be treated separately (Godin, 1972; Wenzel, 1997b). It draws an analogy to optics,

where two spectral lines may be considered as just resolved when they are separated by the distance of two elementary frequency bands. However, the analogy to optics is not fully proper since Fourier spectral analysis has different properties than LS spectral analysis. In tidal analysis, frequencies are exactly known, and the focus is on amplitudes at given frequencies rather than finding frequencies and amplitudes. This has huge consequences for actual resolution (Munk and Hasselmann, 1964; Ducarme and Schüller, 2018; Ciesielski and Forbriger, 2020). The resolution of LS is affected only by noise, or possible linear-dependence of the regressors. Some broadband noise affects the results of tidal parameters, which was shown by Schüller (1976), who suggests use of tapers.

In conventional tidal analysis the wave grouping is based on Rayleigh criterion and the residual spectra are inspected with Fourier analysis to ensure no over-fitting. Munk and Hasselmann (1964) suggested adjusting the Rayleigh criterion for different noise levels, while Ducarme and Schüller (2018) propose different grouping schemes that could serve as more appropriate approach balancing the trade-off between the wave-grouping-biased resolution loss and over-fitting.

In the regularization, the frequency resolution does not directly depend on the length of time series. As significant, we consider only harmonics whose amplitudes are at least of the estimated RMS-noise level and we inspect singular value spectra for confirmation. We observe a deviation of the significant estimates from the (improper) reference model for reasonable values of α, which expresses the trade-off between reference model bias and data variance. As a result, the apparent resolution might be rather coarse in some groups and stunningly fine in others, allowing for super-resolution exploration. Moreover, achieving hyper-resolution (fundamental frequency p_s) in a few years records may be hypothetically possible, but tidal harmonics with that frequency difference have small amplitudes, so in reality the noise level does not allow for it.

Reference Groups and Iterations

In the eq. (3.15) we minimize an objective function that involves the difference between the estimated model and the reference model, which is also the initial a priori body tide model. However, generally we might prefer to obtain a solution that minimizes some other measure of the estimated model. For example, in tidal analysis we could use the second derivative of $|\vec{m}|$, which reflects a preference for a "smooth" model, in line with the assumption of a smooth response function. In this work, we focus on the zeroth-order Tikhonov regularization, the simplest regularization method, which minimizes the term $|\Delta_{\mathrm{m}}|$. Nevertheless, applying higher orders of regularization could be a further improvement of the method.

The parameters of large-amplitude harmonics are the first to depart from their values, while the parameters of their small-amplitude neighbours stay at the reference values or account for noise in the data. Therefore, the response function would not be smooth at all but have many

"jumps" at harmonics of large amplitude. We would not accept a tidal model if the parameters of minor harmonics differ from their immediate large-amplitude neighbours. Although the amplitudes of these harmonics are not significant, the wrong sum of signals from even 1100 harmonics of various - from small to moderate - amplitudes can affect the estimated function. Due to their small amplitude a difference to the admittance with respect to their neighbours they are not likely to be resolved since they are prone to noise. Moreover, there is no physical reason to allow these harmonics to let their parameter estimates depart from those in proximity, except at resonances, or if data strongly supports this. This is in agreement with the 'credo of smoothness' (Munk and Cartwright, 1966). Therefore, we adjust the values for the reference model in a finite frequency band to the new parameters assumed by the large-amplitude harmonics. We do this by defining *reference groups*, which are groups of harmonics that share the same values of reference model parameters x_l^{ref} and y_l^{ref}. No grouping in the sense of summation takes place, and the number of free parameters remains constant throughout the whole procedure. Such parametrization still allows parameters (adjustment factors) x_l and y_l of any harmonic to deviate if further distance to the reference model should be justified by the data in the following analysis. Hence more significant harmonics could be inferred, and the resolution ability is not lost.

In the subsequent iteration we solve the regression problem with a constraint to this updated reference model. When the parameters of the reference model are appropriate to express the observed signal, the parameters of the harmonics will align with the reference values. This is unique and makes the method superior in terms of the resolution because the incorrect assumption of reference groups may be immediately noticed. Non-significant harmonics rather follow the updated reference model, while the significant harmonics tend to differ from the reference model if it does not reflect their true values. Therefore, the resolution and significant harmonics might be easily verified. Where the large amplitude harmonics keep further departing from the new reference level, the reference model gets updated once again. If the parameters of two significant harmonics within one reference group depart in opposite directions, we split the reference group into two or more subgroups, to account for the conflicting constraints imposed by the observed signal. This way we iteratively approach a detailed model of tidal admittance, where adjusting reference groups based on constraints imposed by the data is part of the procedure. Moreover, reference groups are not defined solely along frequency. We separate harmonics of degree 2, three, and four into different reference groups. The frequency bandwidths of the reference groups for degree 3 and four is much larger than for degree 2. The data does not call for a stronger frequency dependence for admittance of degree 3 and four.

In summary, we manually design a tidal model based on the solution of the model constraint regression. In each iteration we use this model as a reference constrain and test, whether the

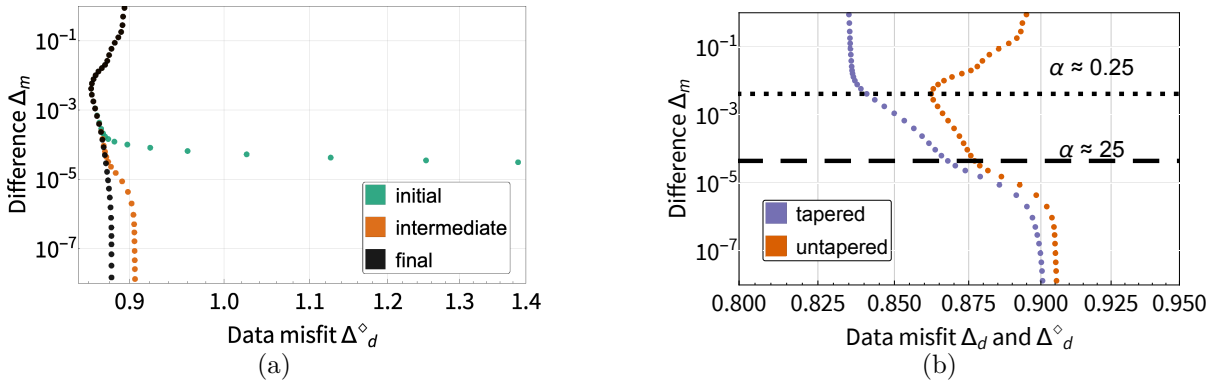

Figure 3.2.: Misfit curves in the regularization approach to tidal analysis, from the analysis of 11.5 years of data at the Black Forest Observatory. Left: Data misfit $\Delta^{\diamond}_{\mathrm{d}}(\alpha)$ is computed for the untapered data by eq. (3.34). Distance $\Delta_{\mathrm{m}}(\alpha)$ to the reference model is computed by eq. (3.32). Both are a function of α. The curves for three stages in the iterative procedure are displayed: initial reference model (green), first iteration (orange), final model (black). Right: First iteration, two curves. Data misfit $\Delta^{\diamond}_{\mathrm{d}}(\alpha)$ is computed for the untapered data by eq. (3.34), data misfit $\Delta_{\mathrm{d}}(\alpha)$ is computed for the tapered data by eq. (3.33) and properly scaled to account for signal loss due to taper window. Distance $\Delta_{\mathrm{m}}(\alpha)$ to the reference model is computed by eq. (3.32). All are functions of α. The misfit curve for tapered (purple), and untapered (orange) data misfit are displayed. The dashed line shows the Δ_{m} level of the first trade-off point at $\alpha \approx 25$ and the dotted line represents the Δ_{m} of the second trade-off point at $\alpha \approx 0.25$.

optimized tidal parameters stay with the value of the model. If not, we update the model accordingly and enter the next iteration.

Finding the Optimal Parameter by Misfit Curve

The solution in eq. (3.31) to the optimization problem in eq. (3.16) not only depends on the recorded gravity $\vec{g}$ and air pressure $\vec{p}$. It is deliberately controlled by the choice of the reference model $\vec{m}^{\mathrm{ref}}$ and the trade-off parameter α, in particular. We commonly choose the value of α by trial and error from a set of solutions computed for different values.

For large α the improvement of the model will be small. At the opposite end, for small α the data will be overfitted by using unreasonable model parameters. This effect can be expressed by the trade-off between distance to the reference model

$$\Delta_{\mathrm{m}}(\alpha) = \frac{|\vec{m}(\alpha) - \vec{m}^{\mathrm{ref}}|}{\sqrt{2L+1}} \tag{3.32}$$

and data misfit

$$\Delta_{\mathrm{d}}(\alpha) = \frac{|\vec{g} - \boldsymbol{G}\vec{m}(\alpha)|}{\sqrt{K}\,\sigma}. \tag{3.33}$$

Because of the minimization condition in eq. (3.16), $\Delta_\mathrm{d}(\alpha)$ necessarily decreases monotonically with decreasing α while $\Delta_\mathrm{m}(\alpha)$ increases. While $\Delta_\mathrm{d}(\alpha)$ decreases with decreasing α the misfit

$$\Delta_\mathrm{d}^\diamond(\alpha) = \frac{|\vec{g}^\diamond - \boldsymbol{G}^\diamond \vec{m}(\alpha)|}{\sqrt{K}\,\sigma^\diamond} \tag{3.34}$$

of the untapared data $\vec{g}^\diamond$ and $\boldsymbol{G}^\diamond \vec{m}(\alpha)$ can behave in a different way. Quantity $\sigma^\diamond$ in eq. (3.34) is the expected rms noise level in the (untapered) data, while σ in eq. (3.33) and used in eq. (3.15) accounts for the taper loss.

To search for the optimum, we chart $\Delta_\mathrm{m}(\alpha)$ against $\Delta_\mathrm{d}^\diamond(\alpha)$ as shown in Figure 3.2. Generally, at large α the model parameters are tied to the reference values $\vec{m}^\mathrm{ref}$, $\Delta_\mathrm{m}(\alpha)$ approaches zero and $\Delta_\mathrm{d}^\diamond(\alpha)$ saturates (Figure 3.2b). With decreasing α an increase in $\Delta_\mathrm{m}(\alpha)$ indicates that model parameters are adjusted in order to reduce data misfit. There is typically a range of α where $\Delta_\mathrm{d}^\diamond(\alpha)$ significantly decreases with moderate increase in $\Delta_\mathrm{m}(\alpha)$. Eventually $\Delta_\mathrm{d}^\diamond(\alpha)$ approaches 1, the rms level of residuals equals that of the expected estimated noise. With further decreasing α the value of $\Delta_\mathrm{m}(\alpha)$ monotonically increases, while there appears a threshold above which $\Delta_\mathrm{d}^\diamond(\alpha)$ starts to increase again, which indicates that the procedure increasingly fits noise in the tapered data (overfitting). Values of α below this threshold (trade-off point at $\Delta_\mathrm{m} \approx 0.01$ in Figure 3.2a) must be avoided. Usually values of α will be chosen larger than this threshold. In the cases displayed in Figure 3.2a the optimal value is chosen at the first trade-off point, ($\Delta_\mathrm{m} \approx 10^{-4}$, $\Delta_\mathrm{d}^\diamond \approx 0.88$) because a strong scatter of model parameters is observed for smaller values of α as discussed below for Figure 3.3. Figure 3.2b compares the curve for $\Delta_\mathrm{d}^\diamond(\alpha)$ with that for $\Delta_\mathrm{d}(\alpha)$, which clearly indicates overfitting for $\alpha < 0.25$. While the model becomes more appropriate for the tapered data, it becomes less and less appropriate for the untapered data.

In addition to the misfit curves, we investigate the amplitude spectrum of $\vec{g}^\diamond - \boldsymbol{G}^\diamond \vec{m}(\alpha)$, which should indicate that a decrease of $\Delta_\mathrm{d}^\diamond(\alpha)$ is due to a reduced amplitude of remainders of tidal harmonics in the residual time series. Likewise we investigate the actual model parameter update $\vec{m}(\alpha) - \vec{m}^\mathrm{ref}$. Figure 3.3 gives an example, how unrealistic scatter of model parameters develops, if α is taken too small. The considerations will be further discussed below along with the development of the local response model.

Termination of the Iteration

At each iteration we investigate the misfit curve, the departure of model parameters from the reference as α decreases, and the Fourier amplitude spectrum of the data residual. As we proceed, the necessary updates of the reference model become smaller, and the first trade-off point of the misfit curve becomes weaker and finally almost vanishes as shown in Figure 3.2. In the first iterations we clearly see signals at tidal frequencies vanishing from the residual. As the iterative procedure progresses the reduction in data misfit becomes smaller, as seen in Figure 3.2,

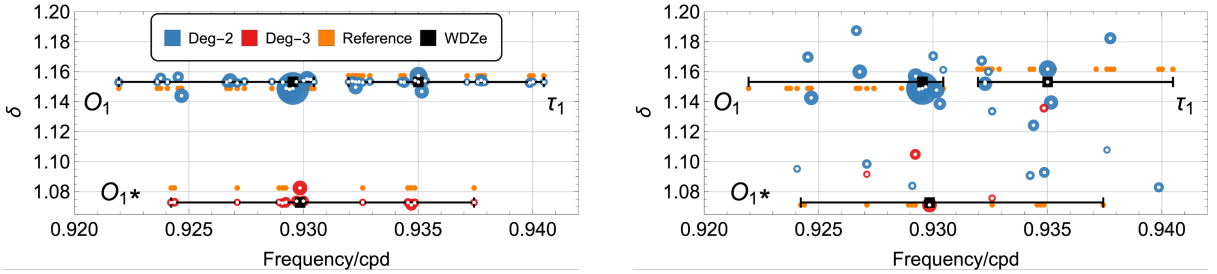

Figure 3.3.: Gravimetric factors for the harmonics in the groups O_1 and τ_1. The circles refer to: the degree-2 parameter estimate (blue), the degree-3 parameter estimate (red), the actual new reference model (small orange; left) and the hypothetical new reference model (small orange; right) for the next iteration. The diameter of circles corresponds to the logarithm of the harmonic forcing amplitude. Because some of the minor-amplitude harmonics are obscured by larger dots, each of the harmonics is indicated by a white dot overlayed to the larger blue ones. The level of black lines corresponds to the initial reference WDZe model, at the given frequency range of the proposed reference groups. Black squares show the frequency of the harmonic with the largest amplitude. Left: parameter estimates for the first trade-off point of the misfit curve at $\alpha \approx 25$ and $\Delta_m \approx 10^{-4}$ (see Figure 3.2). Right: parameter estimates for the second trade-off point at $\alpha \approx 0.25$ and $\Delta_m \approx 0.01$. For some harmonics, the gravimetric factors are off-scale in the right diagram.

while some narrow-band signals remain, which apparently are not of tidal origin. We terminate the iteration when no significant reduction in data misfit is achieved and the model parameters have converged to a local reference model.

`RATA` Method Summary

The steps described in this chapter were visualised and some technical specifications were provided. The concept of the iterative procedure is presented in the Fig. 3.4.

Unconstrained Analysis and Wave-Grouping

In cases where we aim to find the optimal parameters based on the recorded gravity only without further constraint, we set $\alpha = 0$ and resort to a wave-grouping approach. This is the case in the standard moving window tidal analysis (Calvo et al., 2014; Meurers et al., 2016; Schroth et al., 2018). However, we then compose wave-groups by summing over columns of matrices $\boldsymbol{C}^{\mathrm{ini}}$ and $\boldsymbol{S}^{\mathrm{ini}}$ (their matrix elements are C^{ini}_{kl} and S^{ini}_{kl}, respectively) in eqs. (3.9a) and (3.9b), thus reducing the number of columns, as in eq. (3.13). The solution nevertheless is computed with the above given expressions and singular value decomposition and instead single harmonic signal the parameter is given to the a priori summed wave group. The column index l in that approach (in particular for the derived factors x_l and y_l) is then replaced by index j which specifies the wave-group of tidal harmonics.

Columns contributing to the same wave-group are not necessarily adjacent to each other. In particular we may choose all columns for tidal harmonics of degree 2 to go into one group and those of degree 3 to go into a different group within a given frequency interval. This is the

case in the the error propagation analysis, in which the groups from the final stationary local model has been used in unconstraint analysis.

We also use an unconstrained approach in the framework of a moving window analysis and use a rather conventional definition of wave-groups there. However, before the a priori wave grouping, the final stationary local model (parameters X_l^{ini} and Y_l^{ini}) is used as initial model in eq. (3.9), instead of WDZe.

3.3. Implementation

The Rigid Earth Tide Signal

Although any tidal catalog in the form published with `Eterna 3.40` (Wenzel, 1997a) could be used for this method, we decided to use the tidal catalog compiled by Tamura (1987). This catalog lists $L = 1200$ harmonics and is sufficiently accurate to capture all tidal signals resolvable in the recorded data. Using this catalog speeds up the computation of the singular value decomposition in comparison to using the 12,935 harmonics listed in the catalog compiled by Hartmann and Wenzel (1995). The latter not only provides more degrees and terms for Moon and Sun than Tamura (1987), but it also includes Earth-flattening effects and the influence of other planets. From the reasons discussed in Chapter 2 we conclude they are negligible for the purpose of this study. Based on the tidal catalog we compute the 'rigid Earth tides' time series further adjusted to body tidal response by applying WDZe -model with a modified version of `predict` from the `Eterna 3.40`-package (Wenzel, 1997a), `predict rigid`. The program is modified such that it outputs all C_{kl}^{rig} and its quadrature S_{kl}^{rig} in eq. (3.6) and not just their sum.

The Initial Tidal Parameters

As the initial model X_l^{ini} and Y_l^{ini}, defined in eqs. (3.1) and (3.9), we frequently use the theoretical body tide model for given location as implemented in `Eterna 3.40` (Wenzel, 1997a), 'WDZe'. Though the theory behind it is viscoelastic, `Eterna 3.40` neglects the phase, thus $Y_l^{\mathrm{WDZe}} = 0$. We use the updated FCN (free core nutation) period derived by Krásná et al. (2013) from VLBI, which is consistent with the theory for a non-hydrostatic inelastic Earth as presented by Dehant et al. (1999). This updates the original value used in `Eterna 3.40`, taken from Wahr (1981a, his table 1).

Throughout the entire procedure we set $\sigma = 1\,\mathrm{nm\,s^{-2}}$, which corresponds to $\sigma^{\diamond} \approx 1.4\,\mathrm{nm\,s^{-2}}$ in the case of a cosine taper function. We use the WDZe-model for X_l^{ini} and Y_l^{ini} ($l = 1 \ldots L$) and $R^{\mathrm{ini}} = 1\,\mathrm{nm\,s^{-2}\,hPa^{-1}}$ as the a priori model to setup $\boldsymbol{G}$ in eq. (3.18). All parameter adjustments will be expressed with respect to this model. For the initial iteration we set the reference parameters to $x_l^{\mathrm{ref}} = 1$, $y_l^{\mathrm{ref}} = 0$ ($l = 1 \ldots L$) and $r^{\mathrm{ref}} = -3.5$.

Where body tide parameters (gravimetric factor and phase) for a station specific model are available in form of the local response model, we use specific values for X_l^{ini} and Y_l^{ini}, as derived by a previous tidal analysis for the respective station. As will be demonstrated, this can have significant consequences in a moving window analysis.

`RATA` Software

The program used to solve the inverse problem in the sense of eqs. (3.27) to (3.31) is newly implemented in `C++`. We call it `RATA` (Regularization Approach to Tidal Analysis). Essential tasks of linear algebra are handled by the `Eigen`-library provided by Guennebaud et al. (2010). The calculations were performed on a supercomputer, but in principle, for a small number of harmonics or short time series, it may run on a PC.

A filter is applied to all time series consistently. The synthetic time series sequence as well as observations are convolved with the same zero-phase finite-impulse-response (FIR) band-pass or high-pass filter. While in `Eterna 3.40` the synthetic tidal signals C_l^{ini}, and S_l^{ini} are only scaled by the filter gain corresponding to the frequency, we apply the full FIR filter.

`RATA` offers means to run a moving window analysis. For a longer time series, the regressors $\vec{p}$, $\boldsymbol{C}^{\text{ini}}$, and $\boldsymbol{S}^{\text{ini}}$ as defined in eq. (3.6) need to be computed only once. The program then subdivides all long time series into shorter, overlapping segments and computes the inversion result for each segment separately. Such analysis of different time windows (MWA, see Chapter 3.4 for details) may be done regardless of the regularization. In this work if unconstrained analysis is discussed, it implicitly assumes a priori wave grouping.

Prior to the actual tidal analysis for the respective data segment, the program applies a taper window function to all time series consistently. Tapering in tidal analysis is a subject of controversy. In a regression problem where data can be completely represented by a set of harmonic functions with known frequency and phase, there is no risk of spectral leakage and tapering is dispensable. Tapering, however, helps to reduce spectral leakage in the recorded data from signals that are not present in the regressors (Schüller, 1976). As in `Eterna 3.40` we apply a cosine window taper to the time series. We consider this a compromise between loss of signal energy and mitigation of spectral leakage (Harris, 1978; Schüller, 1976).

3.4. Error Propagation and Model Validation

It is reasonable that parameter estimates are given with associated confidence intervals, values that describe the intervals for which the true parameter value is within these two limits. Unfortunately, this often takes white noise assumption, which is generally not true in many geophysical processes. Non-linear effects are one example. In addition, defining confidence intervals for regularized solutions is not a simple task, hence, other methods for results validation

are often use. Quite often, the problem of uncertainty of estimates is as complicated as finding estimates. We summarise the problem in this section.

Confidence Intervals for A Priori Groups

The covariance matrix in least-squares solution is (Aster et al., 2005):

$$\mathbf{cov} = (\mathbf{A}^T\mathbf{A})^{-1} \tag{3.35}$$

Assuming problem is not ill-posed with $\alpha = 0$ and a-priori grouping, using SVD:

$$\mathbf{A}^{-1} = \mathbf{V}\mathbf{\Lambda}^{-1}\mathbf{U}^T \tag{3.36}$$

Hence,

$$\mathbf{A}^{-1}(\mathbf{A}^{-1})^T = \mathbf{V}\mathbf{\Lambda}^{-1}\mathbf{U}^T\mathbf{U}\mathbf{\Lambda}^{-1}\mathbf{V}^T \tag{3.37}$$

Thus,

$$(\mathbf{A}^T\mathbf{A})^{-1} = \mathbf{V}\mathbf{\Lambda}^{-2}\mathbf{V}^T \tag{3.38}$$

So finally:

$$\mathbf{cov} = \mathbf{V}\mathbf{\Lambda}^{-2}\mathbf{V}^T \tag{3.39}$$

We define degrees of freedom $v = K - (2L+1)$. If we define covariance matrix as in (3.39), the variances and covariances of parameter estimates in our normalisation should have form:

$$\begin{cases} \sigma_x^2 = \frac{t^2_{0.975,\infty}}{v} \cdot \Delta_{\mathrm{d}}^{\diamond 2} \cdot \mathrm{cov}(x,x) \\ \\ \sigma_{xy} = \frac{t_{0.975,\infty}}{\sqrt{v \cdot N}} \Delta_{\mathrm{d}}^{\diamond} \cdot \mathrm{cov}(x,y) \end{cases} \tag{3.40}$$

We define $\mathrm{cov}(x,y)$ as the covariance matrix element corresponding to parameters x and y. To get confidence intervals for variances we use value from two-sided Student's t-distribution corresponding to 95% confidence intervals and > 120 degrees of freedom, i.e. $t_{0.975,\infty} = 1.960$.

In `Eterna 3.40` $t = 1$ but investigation of residual spectra gives additional weights to tidal estimates, that should handle the false assumption of the white spectra of the noise. Moreover, **cov** is not computed explicitly as in definition (3.35), but is a leftover term in triangular matrix of Cholesky decomposition. Thus there might be additional scaling factor in function of K applied to $\mathrm{cov}(x,x)$ and $\mathrm{cov}(x,y)$ in comparison.

The formula for uncertainty (standard deviation) of variable that is a function of observable is as following:

$$\sigma(f(x,y)) = \sqrt{\sigma_x^2 \left(\frac{\partial f}{\partial x}\right)^2 + \sigma_y^2 \left(\frac{\partial f}{\partial y}\right)^2 + 2\sigma_{xy} \frac{\partial f}{\partial x} \frac{\partial f}{\partial y}} \tag{3.41}$$

we obtain their standard deviations:

$$\begin{cases} \sigma(\delta_j) = \delta_j^{-1} \sqrt{\sigma_{X_j}^2 X_j^2 + \sigma_{Y_j}^2 Y_j^2 + 2\sigma_{X_j Y_j} X_j Y_j} \\ \\ \sigma(\Phi_j) = \delta_j^{-2} \sqrt{\sigma_{X_j}^2 Y_j^2 + \sigma_{Y_j}^2 X_j^2 - 2\sigma_{X_j Y_j} X_j Y_j} \end{cases} \tag{3.42}$$

If δ is scaled by δ^{ini}, theoretical body response, the standard deviation $\sigma(\delta)$ is also scaled with this factor.

Moving Window Tidal Analysis

In statistics, the jackknife resampling technique is used to test a model using different portions of the data, making it a cross-validation method. This method can be used to estimate the bias or variance of an estimator calculated over the entire sample. The MWA is also a jackknifing technique that is applied to verify the estimated tidal parameters, their variance, trends, analysis method correctness, and instrument stability. To ensure proper comparison, it is important that all the windows investigated using this method have the same length, due to statistical and numerical reasons.

We expect that the local models partly capture the time-invariant signal modulation (beat) that is reported by Calvo (2015); Schroth et al. (2018). To investigate the remaining components in the apparent admittance of the Earth (including oceans and atmosphere) we run a moving window analysis (MWA) like Schroth et al. (2018) do. We subdivide the total time series into segments of 90 days length, which overlap such that the moving window progresses in intervals of 1 day. The full length time series are prepared in advance by decimation and filtering the recordings as well as C_{kl}^{rig} and S_{kl}^{rig} as defined in eq. (3.6). With the parameters of the given local response model (parameters X_l^{ini} and Y_l^{ini}) we compute the samples (index k) of the initial synthetic tidal signals of all harmonics (index l)

$$C_{kl}^{\mathrm{ini}} = X_l^{\mathrm{ini}} C_{kl}^{\mathrm{rig}} + Y_l^{\mathrm{ini}} S_{kl}^{\mathrm{rig}} \tag{3.43a}$$

and its quadrature

$$S_{kl}^{\mathrm{ini}} = X_l^{\mathrm{ini}} S_{kl}^{\mathrm{rig}} - Y_l^{\mathrm{ini}} C_{kl}^{\mathrm{rig}}, \tag{3.43b}$$

as defined in eq. (3.9). C_{kl}^{ini} and S_{kl}^{ini} are the elements of matrices $\boldsymbol{C}^{\mathrm{ini}}$ and $\boldsymbol{S}^{\mathrm{ini}}$, respectively.

In order to compute results which are directly comparable to those presented by Schroth et al. (2018), we use a priori grouping and dismiss regularization by setting $\alpha = 0$. We take the sum over the synthetic signals for all harmonics within each wave group in matrices $\boldsymbol{C}^{\mathrm{ini}}$ and $\boldsymbol{S}^{\mathrm{ini}}$. The matrices $\bar{\boldsymbol{C}}^{\mathrm{ini}}$ and $\bar{\boldsymbol{S}}^{\mathrm{ini}}$, which result from this summation, contain only 12 columns each. The wave groups are defined in Table 6.1.

Within each time window of the MWA we compute factors x_j and y_j with respect to the elements $\bar{C}_{kj}^{\mathrm{ini}}$ and $\bar{S}_{kj}^{\mathrm{ini}}$ of matrices $\bar{\boldsymbol{C}}^{\mathrm{ini}}$ and $\bar{\boldsymbol{S}}^{\mathrm{ini}}$, respectively, by minimizing the objective function in eq. (3.15) without model constraint, i. e. $\alpha = 0$. Thus, we obtain time depending tidal parameters with a value of gravimetric factor

$$\delta_j^{\mathrm{MWA}} = \sqrt{{X_j^{\mathrm{MWA}}}^2 + {Y_j^{\mathrm{MWA}}}^2} \tag{3.44a}$$

and phase

$$\Phi_j^{\mathrm{MWA}} = -\arctan \frac{Y_j^{\mathrm{MWA}}}{X_j^{\mathrm{MWA}}}, \tag{3.44b}$$

where

$$X_j^{\mathrm{MWA}} = x_j\, X_j^{\mathrm{ini}} - y_j\, Y_j^{\mathrm{ini}} \tag{3.45a}$$

and

$$Y_j^{\mathrm{MWA}} = y_j\, X_j^{\mathrm{ini}} + x_j\, Y_j^{\mathrm{ini}}. \tag{3.45b}$$

The index j specifies the wave group, not the time window.

We run the very same analysis a second time, but with the WDZe-model as a reference. In eqs. (3.43) to (3.45) is replaced by WDZe then. The comparison of the obtained MWA time series for δ_l and Φ_l shows in how far the local response model appropriately adjusts the beating in the tidal signal. Due to various effects not included in WDZe the grouping may cause the bias in the results. Moreover, latitude-dependent gravimetric factors differs for different stations, making direct comparison difficult. We mitigate this problem by the transition to the variations with respect to the local response model for given station. In that way, are amplitude factor:

$$\tilde{\delta}_j^{\mathrm{MWA}} = \frac{\delta_j^{\mathrm{MWA(WDZe)}}}{\delta_j^{\mathrm{MWA(ini)}}} \tag{3.46a}$$

variation should oscillate around 1, and phase

$$\tilde{\Phi}_j^{\mathrm{MWA}} = -\Phi_j^{\mathrm{MWA(WDZe)}} - \Phi_j^{\mathrm{MWA(ini)}} \tag{3.46b}$$

around 0. In these formulas, superscript $^{\mathrm{ini}}$ indicates the local response model for the given station and $^{\mathrm{WDZe}}$ the local WDZe body tide model.

Confidence Intervals for Regularization

The regularization introduces bias to the objective function, hence it decreases the variance of the parameters. Simplifying, the condition number of the problem is inversely proportional to α (Aster et al., 2005). Thus increasing α will decrease the sensitivity of the solution to perturbations in the data. Other way round, increasing α also increases the error in the solution due to regularization bias and decreases resolution. Not knowing how appropriate is the regularization term, and also what is the nature of the noise in the measured signal, the task to find some measure of accuracy of regularized solutions is not easy. Some methods for error estimation are provided by Aster et al. (2005). The way for finding some boundaries on the error propagation could be achieved by investigation of the resolution matrices and some 'spike tests'. There are authors who suggest to use $\boldsymbol{A}^{-g}$ expressed by:

$$\vec{a} = \left(\boldsymbol{A}^T\boldsymbol{A} + \alpha^2\mathbf{1}\right)^{-1}\boldsymbol{A}^T\vec{d} = \boldsymbol{A}^{-g}\vec{d} \tag{3.47}$$

to form a model covariance matrix:

$$\mathbf{cov} = \boldsymbol{A}^{-g}(\boldsymbol{A}^{-g})^T \tag{3.48}$$

due to the complexity of the problem of confidence intervals in the regularization approach, we will not discuss them in any of the mentioned ways which are applied to regularized problems. As a kind of proxy, we occasionally use results from the unconstrained inversion or those estimated with MWA

3.5. The Comparison Between Eterna 3.40 and Unconstrained RATA

We tested the new software to confirm whether for simplified, identical inverse problems, the estimates are the same as those resulting with established software, like Eterna 3.40. It turned out, that even if RATA would use the same setup, the same catalog, for the same data decimated in the same way, with no regularization ($\alpha = 0$) and the same wave groups, still, there are some differences that have minor, but noticeable impact on the estimates. These effects should not significantly interfere with the results of tidal analysis.

The Taper Misconception

`Eterna 3.40` allows user to apply taper prior to the analysis. Even though it is called the 'Hann window', in fact, `Eterna 3.40` applies the cosine window, which is a square root of the Hann window (Harris, 1978). The difference arises from the Cholesky decomposition, as `Eterna 3.40` squares the matrix of the forward operator in order for the matrix to be squared and positive-defined. The squared elements are multiplied by the Hann window, $w[x] = \sin^2(\frac{\pi x}{N})$ and the square of the expected noise level. Thus, the effective taper window is a square root of the Hann window, which is a sine/cosine window, $w[x] = \sin(\frac{\pi x}{N})$. This means, that `Eterna 3.40` allows user to choose between a boxcar/rectangular window (effectively no taper) and a cosine window. In `RATA` users can apply any of three windows, be it rectangular, cosine or Hann.

To avoid confusion, we want to emphasise that the cosine taper window we use is the same cosine window as would be used in `Eterna 3.40` which is given a wrong name there.

Numerical Methods

`Eterna 3.40` solves normal equations by squaring the forward operator matrix and applying optimized algorithm for Cholesky decomposition (Press et al., 1992). On the other hand, `RATA` uses SVD to find the estimates, even if there is no regularization ($\alpha = 0$). In principle Cholesky decomposition should be faster, so is `Eterna 3.40`, but the differences are rather not significant since the problem for wave groups is solved in minutes or seconds. It is known that Cholesky decomposition is less numerically accurate and stable because the condition number of the squared matrix is also squared. SVD operates directly on a forward operator $\mathbf{A}$, in contrast to Cholesky decomposition, which computes $\mathbf{A}^T\mathbf{A}$. It works on sums of squared double precision numbers, so computation result is sensitive to numeric round-off, especially for less significant contributions. Hence, it squares the condition number and the numerical precision for small contributions is lost. The test on 12 wave groups and the usual MWA length of 90 days using BFO data showed that the maximum differences in the estimates of parameters by applying two different kinds of decomposition are at the maximum level of 0.00015 for the lowest-amplitude group, $\mathbf{OO}_1$, and 0.00002 for $\mathbf{M}_3$* and $\mathbf{L}_2$ (X_j^{MWA}). The synthetic signal g^{syn} differs by RMS-amplitude about 0.001 $\mathrm{nm\,s^{-2}}$. If one year is investigated, the differences are at least twice smaller. The precision that `Eterna 3.40` provides for the estimates is at the level of 0.0001. If SVD was performed exactly on the same data input that `Eterna 3.40` would use for Cholesky decomposition, numerical differences were practically 0. The main conclusion is, that there are practically no significant differences between these two methods, especially when compared to confidence intervals. However, differences exist, and less significant groups with small amplitudes are prone to numerical errors in `Eterna 3.40`, especially if the grouping was chosen too optimistically for the time series, which is too short.

Time Lag

Each instrument records the time of an event with a time lag, which is a difference between the time as recorded by the instrument's clock and the actual time as measured by an astronomical clock. This difference is usually provided by hourly sampled files in standard format, as read by `Eterna 3.40` and added to astronomical phases each time the routine is called. When `RATA` computes tidal forcing, it uses `predict rigid`, which requires the calibration-lag file for the time lag. This file is created from level-1 calibration files or level-2 data hourly sampled data files.

The Phase of Astronomical Arguments

To update the astronomical arguments in the corresponding cosine function in each iteration, the time variable in eq. (3.1) is used. `Eterna 3.40` updates the phases depending on the length of the time series, typically every midnight, month, or year, but `predict rigid` updates the phase every time the function is called (i.e. for every computed instance) to increase accuracy and correctness. The resulting differences of synthetic signal are not significant, at the level of 10^{-9} nm s^{-2}, but above numerical zero $\sim 10^{-14}$.

A Filter Response

The synthetic time series sequence and observations are convolved with the same zero-phase finite-impulse-response (FIR) band-pass or high-pass filter. `Eterna 3.40`, assumes tidal harmonics to be a harmonic signal, so the signal C^{ini}, and S^{ini} is only scaled by the filter gain corresponding to the frequency. In `RATA`, we apply the full FIR filter to avoid residuals that result from irregularities in the time scale, such as leap-seconds, changes in the length of day, and rotation axis (polar tide), which are updated daily. The leap second causes a filter response, which can result in a difference in amplitude of about 0.0015 nm s^{-2} and shape and length of filter sequence if two filtered synthetic time series are compared.

The constant irregularity, or trend, is a linear change in the tidal harmonic signal (coefficients $S_{nm}(t)$ and $C_{nm}(t)$). The differences in filtered harmonic signal between two methods are at the level 10^{-12} nm s^{-2} for minor harmonics to 10^{-6} nm s^{-2} for K_1, so the total difference for the synthetic signal should be below 10^{-3}nm s^{-2}. The amplitudes slightly increase over time, and the values were compared for 1 year of data.

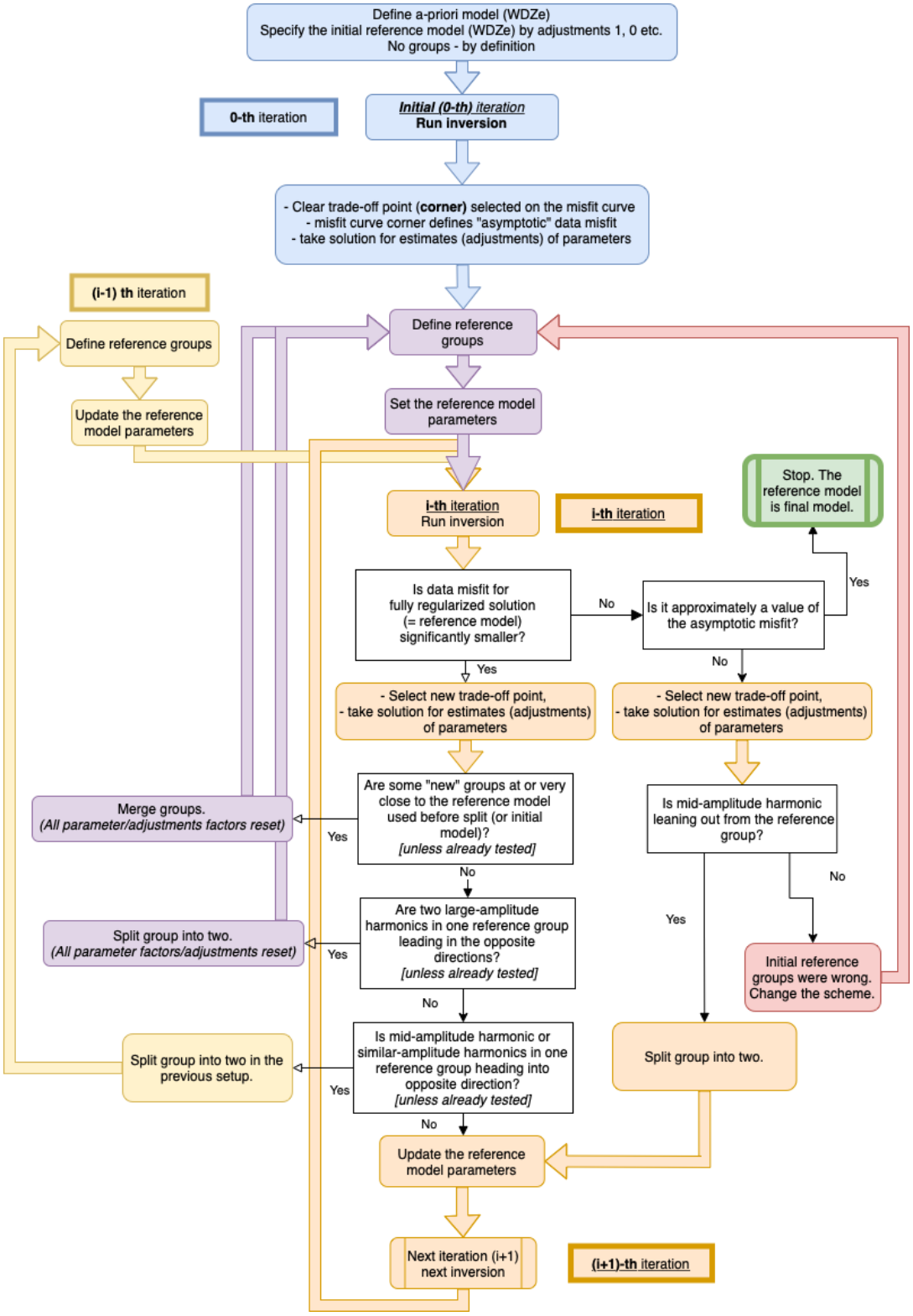

Figure 3.4.: Flowchart illustrating the `RATA` iteration procedure. Blue color represents the initial setup, that has to be performed only once within the workflow. White boxes are 'decision branches'. Items in orange are linear iterative paths. If the purple points are met, the parameters have to be reset to initial adjustments, but the reference group are modified only a little. Yellow track indicates, that the last setup has to be altered. Red color is a clear information, that there was something wrong with our analysis. Green box is the end of the procedure. If we alter the grouping scheme, or reset the parameters, we keep information about the decisions (reference grouping, parameter update, etc.) that were made prior to that point.

4. Data and Processing

4.1. Data Source and Stations

I use level-2 data with a 60 s sampling interval, correction code 32 for SG sensors and locally recorded air pressure as provided in the IGETS data base (International Geodynamics and Earth Tide Service, 2017; Voigt et al., 2016) in Global Geodynamics Project (GGP). The data were pre-processed by EOST (Boy, 2019). Only the analysed data from Syowa are with correction code 22, pre-processed at ICET (International Center for Earth Tides). Figures 4.1a - 4.1b provide a comprehensive overview of the locations of the stations and corresponding time series lengths. The length of the time series corresponds to the available 1-minute sampled level-2 data in the IGETS database. If data in 1-minute samples are available for a longer period of time but the data correction code 32 is only provided for a shorter time, the available data length corresponds to the latter, hence it might be shorter than other already pre-processed records available there. Additionally, data from different instruments at the same stations are considered separate measurements in the comparison.

As seen from figures 4.1a - 4.1b, there are not many observatories that could provide the best quality data with no possible disturbances or their time series are yet too short. While the information on location in most cases is only an indicator of possible issues, if there is another station in a similar region of the world with more promising data available, it has been chosen for this work, as shown in Fig. 4.2a. Few stations in Europe have been chosen mainly to serve as a sanity check for the method, such that similar results should be obtained: Schiltach, Strasbourg, Moxa, Bad Homburg, as shown in Fig. 4.2b. The station in Strasbourg was chosen as the closest to BFO in Schiltach, even though the instruments are near the big city and there are indications that they might have some issues. Bad Homburg is in the centre of the small town. The instrument in Moxa is placed in the tunnel, far from towns and cities, similar to instruments in BFO. Membach has been chosen since its data is of very good quality, and interestingly, it should be perturbed by the effects of ocean loading. I am interested in determining to which extent this could be "captured" or explained by the local time-invariant response model. Similarly, Sutherland, Cantley, Canberra and Tigo-Concepcion lay at the coast, or very close to the coast, hence the various ocean loading signals are present there. For example, Merriam (1995) found non-linear tides at the Bay of Fundy (Cantley) using the response method. I use data from Sutherland even though the big astronomical facility is placed there (SAO), whose moving

domes of optical telescopes might affect gravity observations. A similar problem faces Canberra but the facility is much smaller. Cantley has only one small remote-sensing dish antenna. Tigo Concepcion is placed on the outskirts of the city. Since outside Europe and Japan there is no big choice of observatories, one cannot be too picky. Djougou is the Central African station close to the equator and relatively far from the ocean, hence it is interesting. The proximity of the small city should not disturb the measurements too much. Only one Japanese station has been chosen for Asia to represent the region. The Japanese station Kamioka is next to the Super-Kamiokande neutrino detector. However, it is the only Asian station with data error code 32 and sufficiently long recording time. Estimates for main degree 3 tides from the selected stations except Schiltach, Djougou, Kamioka and Tigo Concepcion could be somehow compared with Ducarme (2012). Nevertheless, some of the stations selected for analysis could not meet some criteria for location, but they were analysed for particular reasons that were already mentioned.

Some other European stations, like Onsala, Mëtsahovi, Yebes, Wettzell or Medicina could provide interesting results. I do not analyse these stations not because all these instruments are located at the radio astronomical observatories, but mainly because I already have a sufficient selection of Central European stations with long records for this analysis. The only two continental stations, Boulder and Wuhan are not considered in the analysis. The instrument in Wuhan is placed in the famous big city, and the data from both stations seem to have a significantly larger S/N ratio from the rest.

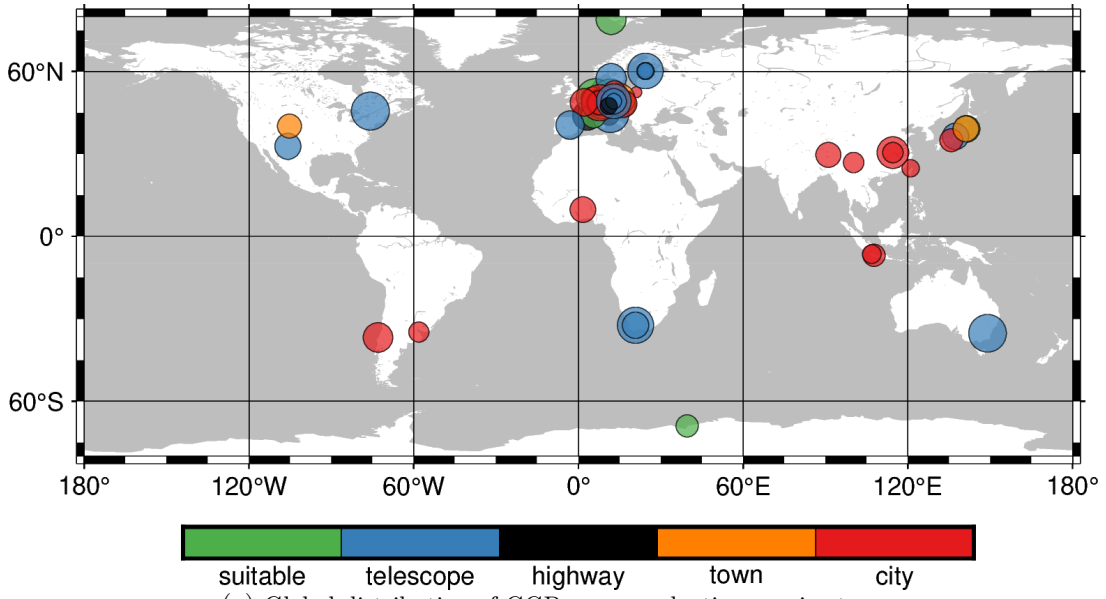

(a) Global distribution of GGP superconducting gravimeters.

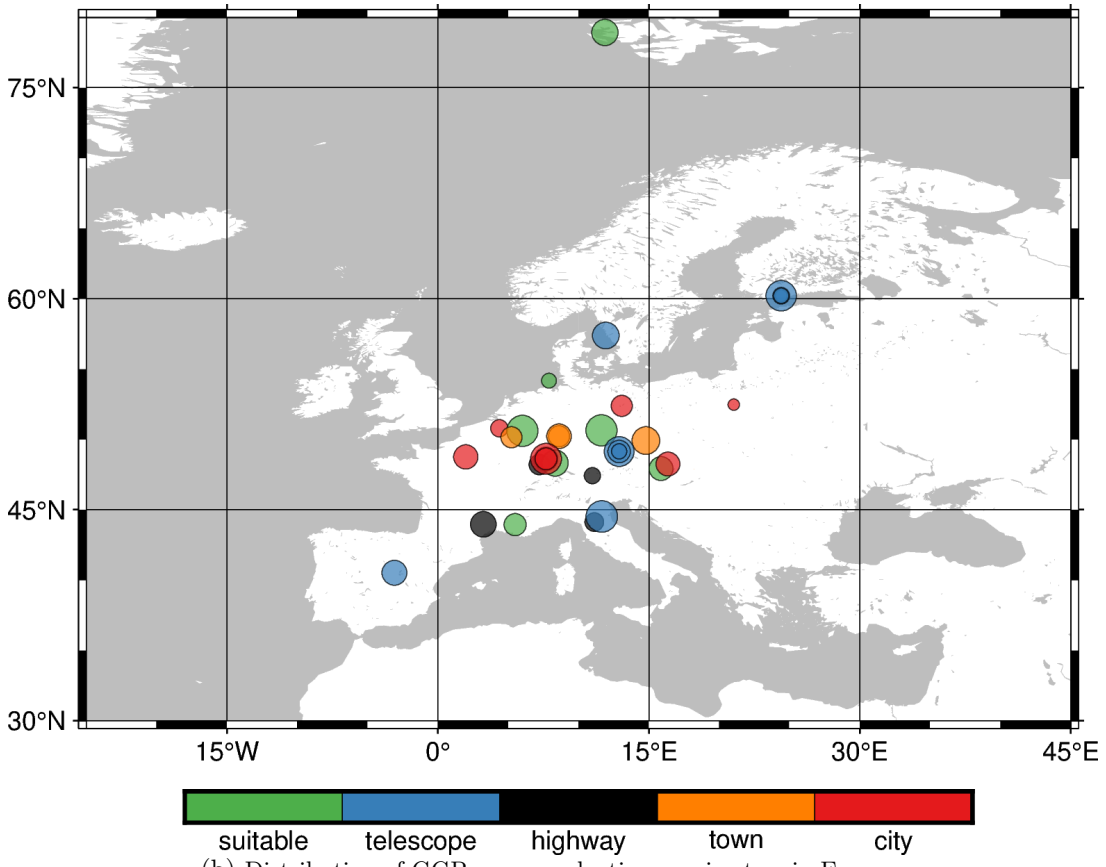

(b) Distribution of GGP superconducting gravimeters in Europe.

Figure 4.1.: Comparison of the location of the station indicating the main feature in the proximity of the instrument that could potentially interfere with the measurements. The radius of the circle indicates the length of the available data for one instrument, taken to the power of 0.3 for display purposes. Some stations could provide data for different instruments at the same location which do not necessarily overlap, but they are treated separately in the comparison. The station at Zugspitze is actually placed next to the cable car, but it is assigned to the category "highway".

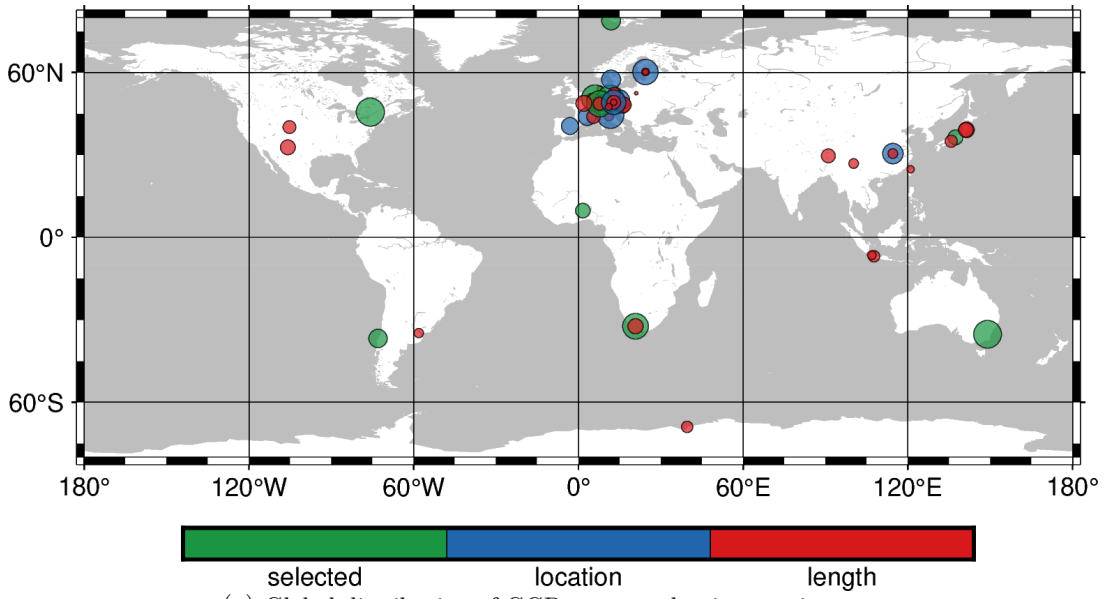

(a) Global distribution of GGP superconducting gravimeters.

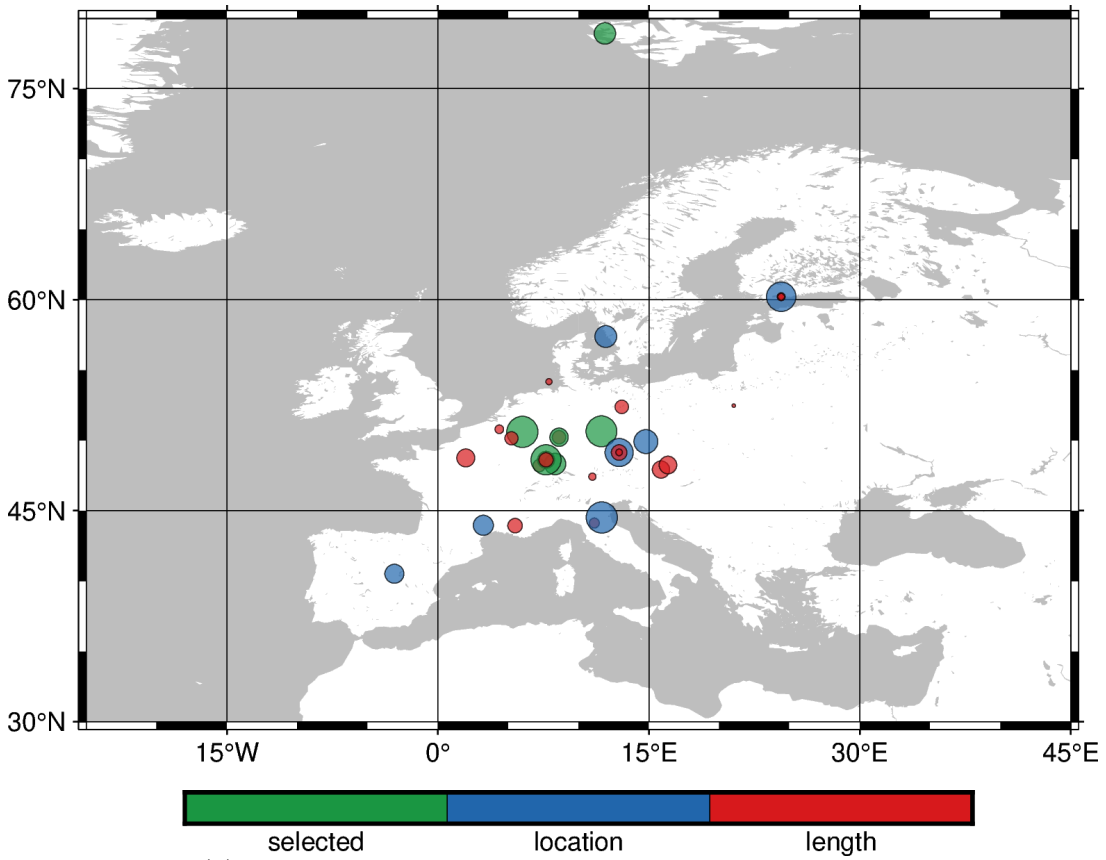

(b) Distribution of GGP superconducting gravimeters in Europe.

Figure 4.2.: Comparison of the location of the station indicating the reason for which the station was not used for the study. The radius of the circle indicates the length of the available data, taken to the power of 0.65 to emphasise the difference between the available time series length.

4.2. Analyzed Data and Gaps

The data pre-processing steps involve scaling the acceleration units and removing steps, and flagging gaps and transient signals (earthquakes, glitches) exceeding a threshold in the signal's time derivative. The flagged time windows are replaced by synthetic tides or data from the MERRA-2 model for gravity and air pressure, respectively. The consequences of the approach are discussed in Boy et al. (2020). The gap-filled version of the data was used to develop the BFO local response model from 2009-10-01 to 2021-03-31 (i.e. 11.5 years). The flagged time windows were carefully checked, and no synthetic data above the usual noise level was found in the residuals of the analyses. For the other observatories, gaps longer than 1 day were discarded, and for shorter gaps, the synthetic tidal signal was used. Local air pressure was used to correct for the impact of mass fluctuations in the atmosphere, and loading of the global atmosphere was not needed in the diurnal and semi-diurnal period band.

Time periods of analysed data and analysed record length in 15-minute samples for selected stations are given in Table 4.1. For Sutherland and Cantley the available record length is about twice longer than used for the analysis, but after initial local model estimation and a consequent moving window analysis, only the periods with the "best-quality" data were reconsidered.

Code	Place	Instrument	Start	End	Length	Years	Blocks
BH	Bad Homburg	GWR SG044	2007-02	2017-03	334296	9.534	15
CB	Canberra	GWR C031	1997-07	2021-12	790580	22.547	46
CA	Cantley	GWR T012	1997-07	2012-12*	458798	13.093	22
DJ	Djagou	GWR o060	2010-07	2018-11	241800	6.896	27
KA	Kamioka	GWR T016	2004-10	2013-7	273913	7.817	25
MB	Membach	GWR C021	1998-06	2021-03	754746	21.525	34
MO	Moxa	CD034L	2000-01	2022-06	700924	19.990	39
		CD034U			664600	18.954	41
NY	Ny-Ålesund	GWR C039	1999-09	2012-06	259581	7.403	70
BF*	Schiltach	GWR SG-056L	2009-10	2021-03	402169	11.470	1*
		GWR SG-056U			402169	11.470	1*
ST	Strasbourg	GWR C026	1997-02	2018-11	669579	19.096	45
SU	Sutherland	GWR D037L	2010-01*	2022-06	219626	7.123	12
SY	Syowa	GWR T016-TT70	1997-07	2003-01	145800	4.160	13
TC	Tigo Concepcion	GWR RT038	2002-12	2015-04	336216	9.589	24

Table 4.1.: The list of analysed instruments with corresponding stations location and periods of available data in IGETS database at the time of analysis. Length indicates the number of 15-minute samples after gap elimination, decimation and filtering. In the column "Blocks" the number of blocks with gap-free data or containing gaps shorter than 24 hours being filled with synthetic tides. Analysis for BFO Schiltach used all the available data with filled gaps with careful analysis of residuals afterwards. Instruments at Schiltach, Moxa and Sutherland are double-sphere devices. For Sutherland, the lower sphere was used. Star next to date indicate, that more data were available, but I did not make use for them to estimate the local response model.

I use local air pressure to at least partly correct for the impact of mass fluctuations in the atmosphere as suggested by Warburton and Goodkind (1977); Merriam (1992); Crossley et al. (1995). The consideration of loading of the global atmosphere (Klügel and Wziontek, 2009; Atmacs service, 2022; Boy et al., 2002, 2009; EOST, 2022) is not needed in the diurnal and semi-diurnal period band.

4.3. Instrumental Lag

The instrumental lag correction is crucial for estimating tidal parameters accurately. The calibration file (.cal) or hourly sampled data files (correction code h2) are used to obtain the necessary information. The precise GPS position of each observatory was provided in the most recent level-1 data file, and `predict rigid` was used to compute the most accurate synthetic body tide, WDZe-scaled rigid earth tidal forcing.

4.4. Decimation and Filtering

In tidal analysis, the data is decimated to a sampling interval of 15 minutes after applying the finite impulse response (FIR) low-pass filter `n20s5m02`, which is provided together with `Eterna 3.40` (Wenzel, 1996, 1997a). The filter's gain is less than 10^{-7} in the stop band and deviates less than 10^{-7} from one at frequencies of 4 cpd and smaller. The choice of decimation filters is important in tidal analysis as variations at the level of 10^3 of the gravimetric factor are sought. The filter of our choice affects tidal frequencies below $2 \cdot 10^{-5}$ and rejects frequencies above Nyquist rate at the similar level. Before tidal analysis, the `n10m10m2` FIR high-pass filter is applied consistently to observations and regressors, with a corner frequency of 0.48 cpd. The analyzed frequency band ranges from 0.48 cpd, capturing tidal constituents from the diurnal, semi-diurnal, and ter-diurnal band as well as higher frequencies. Drift signals originating from the instrument or meteorology are not accounted for as they are removed by the high-pass filter.

5. The Time-Invariant Local Response Model BF21

This chapter is a part of the manuscript submitted and accepted to be published as peer-reviewed article in the Journal of Geodesy. Most paragraphs are taken literally from Ciesielski et al. (2023).

5.1. Introduction

We apply a new harmonic tidal analysis method, which constrains the solution to be near a reference model, described in Chapter 3. We determine a local response model from 11.5 years of data recorded by the superconducting gravimeter SG056 at Black Forest Observatory (BFO, Schiltach). We demonstrate how the procedure of the `RATA` method with regularization stabilizes the linear regression, allowing us to infer model parameters for each tidal harmonic. This overcomes the need to create a priori groups of summed harmonics and allows to explore super-resolution of tides discussed by Munk and Hasselmann (1964). We handle the trade-off between the over-fitting due to the too narrow grouping and bias from too coarse grouping by using regularization instead of a priori grouping. We demonstrate the application of iterative inversion procedure with adjusting the reference model to reduce the data misfit. The frequency dependence of the solution is thus data-driven. Our procedure allows narrow-band variations of the tidal admittance and to explore the significant contributions to the signal. We find models for the different spherical degrees independently. We discuss the residuals and the improvement in tidal synthetic data if BF21 model is used and error propagation (confidence intervals) of the method.

5.2. Iterative Procedure

Initial Parameters

We explore the misfit curve with 51 logarithmically spaced samples for values of $\alpha = 10^{-5} \dots 10^{5}$. The misfit curve for this initial reference is displayed in Figure 3.2 by green dots. For large values of α (bottom-right side of the plot) the distance to the reference model vanishes and the data misfit approaches the value $\Delta_{\mathrm{d}}^{\diamond} \approx 13$ (outside the plot range) as obtained for the WDZe-model. By gradually reducing α, the model parameters start to depart from the reference. Distance to the reference model $\Delta_{\mathrm{m}}(\alpha)$ increases but $\Delta_{\mathrm{d}}^{\diamond}(\alpha)$ decreases. We meet the first trade-off point at $\Delta_{\mathrm{m}}(25) \approx 2 \times 10^{-4}$. Figure 3.3 (left panel) displays the parameters for O_1 and τ_1 at this

trade-off point. The parameters for harmonics of small amplitudes still stick at the reference values (orange), while the parameters of harmonics of large amplitude start to deviate from the reference.

Further decreasing α certainly decreases data misfit to the second trade-off point, in Figure 3.2 at $\Delta_{\mathrm{m}}(0.25) \approx 0.01$. Beyond this value the misfit computed for the untapered data $\Delta_{\mathrm{d}}^{\circ}(\alpha)$ increases again, despite the misfit of the tapered data $\Delta_{\mathrm{d}}(\alpha)$ in the objective function in eq. (3.21) necessarily further decreases, as shown in Figure 3.2b. The model hence is only more appropriate for tapered than for untapered data, which clearly indicates over-fitting. Despite finding the smallest value of data misfit at the second trade-off point, we choose the solution for the first. The reason is demonstrated in the right diagram of Figure 3.3 (right panel). At the second trade-off point the small amplitude harmonics scatter strongly, they are mainly driven by noise in the signal, with $\alpha \approx 0.25$ the regularization being too weak.

Reference Grouping

The wave groups used by Melchior et al. (1996) serve us as an initial set. They used a time series of similar duration (12 years). In the following we will specify the groups by the Darwin names of the harmonics with the largest amplitude within the reference group. A full list of the groups in the final model from the current study is given in Tables 5.1 and 5.2. Some reference groups consist of few other groups that are defined in Tables 2.3-2.5. Other than Melchior et al. (1996) we completely separate degree 3 from degree 2 tides within groups. Thus, groups defined only to infer the degree 3 tides were discarded in the scheme, and they constituted larger groups.

Figure 3.3 (left) shows that the parameters for the large-amplitude harmonics O_1, τ_1, and $O_1{}^*$ depart from the reference, while their small-amplitude neighbours stay with the reference due to the regularization. We update the degree 3 reference for the entire displayed frequency band to $O_1{}^*$ uniformly. O_1 and τ_1 depart in opposite direction. For this reason we split the frequency range into two reference groups, O_1 at the lower frequencies and τ_1 at the higher frequencies, each of them being adjusted to a new reference value, which is uniform within the reference group. Opposite departure of significant-amplitude parameters from a uniform reference level always indicates, that the data calls for the reference group to be split in two or more subgroups. In a few cases we subsequently join (merge) reference groups, if the new parameter updates indicate that all harmonics in the larger frequency range could well go with the same parameter value. This was applied to degree 2 tides L_2 and KNO_2 to constitute L_2. All degree 4 harmonics form one single reference group from the very beginning. Most degree 3 tides were joined into larger reference groups since due to their small amplitudes the grouping scheme was too fine and most small tides were not significant. Tables 5.1 and 5.2 specify the groups in the final reference model. The group symbols used in the following text refer to these tables. Where a reference group spans a larger frequency band, we use parentheses like (γ_2,

$\mathbf{M}_2$, δ_2), which refers to the entire $\mathbf{M}_2$-group in Table 5 presented by Melchior et al. (1996). The symbol $\mathbf{M}_2$ in bold font in this parenthesis indicates the largest amplitude harmonic in the group, the harmonic which usually drives the update of the reference level. The symbol $\mathbf{M}_2$ in bold font but outside parenthesis indicates, that we discuss a priori summed wave group (not harmonic nor reference group). We needed 5 iterations (i.e. inversion runs) including the initial iteration to obtain (and confirm) the final model.

Groups Treated Specifically

From the very beginning, we split tidal group (γ_2, $\mathbf{M}_2$, δ_2) into three: (γ_2, $\boldsymbol{\alpha}_2$), (ω_2, $\mathbf{M}_2$) and ($\boldsymbol{\beta}_2$, δ_2) in order to capture the annual modulation discussed by Schroth et al. (2018). As the iteration of the model update proceeds, it turns out that the data calls for different levels of all groups from γ_2 to δ_2. Therefore, we decided to split two M_2 satellites from their previous groups: γ_2 (from α_2) and δ_2 (from β_2). Moreover, we split ($\mathbf{K}_1$, κ_1) from the beginning, where κ_1 is the major amplitude nodal satellite to K_1 with Doodson number 165.565.

S_1 contains the frequency of 1 cpd at which the recording contains gravity signals driven by solar radiation rather than tidal forces (the so-called 'radiation tides'). For this reason we put 164.556 and 164.554 into the separate group S_1 and adjust the reference parameters of 164.544 and 164.566 to the average of the parameters of P_1 and K_1. The two latter harmonics have negligibly small amplitude (3% of already small S_1) and because of their frequencies they are not expected to be strongly influenced by the radiation.

In cases where the parameters of the major amplitude harmonic in a group remain at the reference value, we consider this signal not resolved by the data. In such cases we merge smaller groups to larger groups. This primarily took place for parameters of degree 3 harmonics and for degree 4 we end up with one single group M_4+ covering the entire tidal frequency band (all species). For the very same reason we initially merged (R_2, $\mathbf{K}_2$), because the parameters for R_2 remained at the level of the WDZe-model. The subsequent inversion however clearly indicated that the parameter value previously set for K_2 is not appropriate for R_2. The parameter for the latter clearly departed in direction of the WDZe-model. We then kept R_2 and K_2 separate in subsequent iterations.

In the last iteration we identified four additional groups that might be split: ζ_1 (from SGQ_1), QW_1 (from Q_1), ι_1 (from J_1) and ω_2 (from M_2). The new groups do not have established names. They are treated in special way in the sense, that after splitting these groups, we did not reset the factors to the initial values, thus this action should rather be considered as the 'final adjustment'. The reason for this is the more conservative assumption due to their medium amplitude ($2-10$ times smaller than harmonics in very close frequency vicinity, differing by fourth digit in the Doodson number, corresponding to the precessional 8.85 years period except

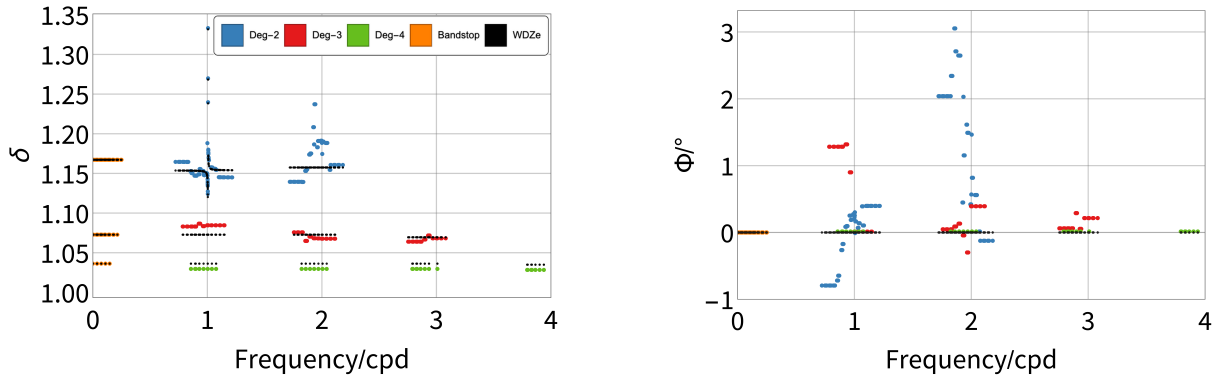

Figure 5.1.: Gravimetric factor (left) and phase (right) of the BF21-model. The dots are: initial reference model (WDZe, small black), degree 2 parameter estimate (blue), degree 3 parameter estimate (red), degree 4 parameter estimate (green). Orange dots indicate all three degrees for harmonics which are outside the passband of the high-pass filter. They are not modified by the inversion but are used in the computation of $\boldsymbol{G}$ in eq. (3.18). The phase of S_1 is almost 10° (Table 5.3) and is off-scale for this reason. The values of all other groups are within the axes-range of the diagrams. More detailed plots, showing all species separately, are in Fig. 5.4.

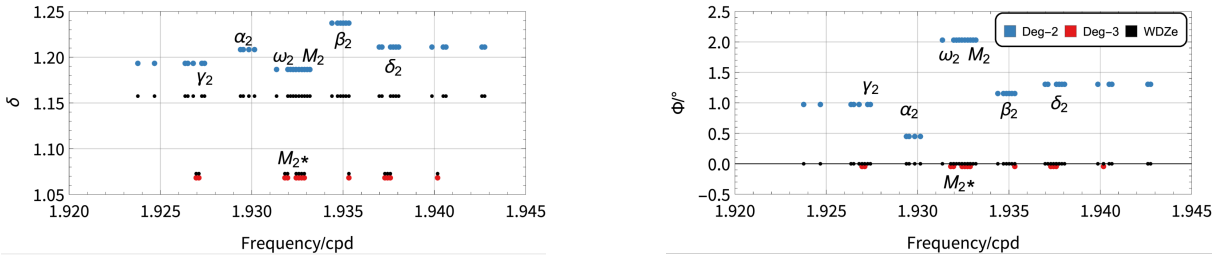

Figure 5.2.: Gravimetric factor (left) and phase (right) of the BF21-model in M_2 tidal group. The dots are: initial reference WDZe-model model (small black), degree 2 parameter estimate (blue), degree 3 parameter estimate (red).

ζ_1). These harmonics could potentially have their estimates affected by noise, and showed 'unclear deviations' from the reference in the previous iterations.

5.3. The Final Model BF21

The final tidal model, which we call BF21, is specified by the numerical values of its parameters in Tables 5.3 and 5.4. A graphical display is shown in Figs. 5.1, 5.2, and 5.3. The dots in the diagrams are displayed for each of the 1200 harmonics in the Tamura (1987) catalog. The factors x_l and y_l are adjusted to be uniform within each of the reference groups specified in Tables 5.1 and 5.2. Gravimetric factor and phase are computed by eq. (3.5) from the final model parameters

$$X_l^{\mathrm{BF21}} = x_l\, X_l^{\mathrm{WDZe}} - y_l\, Y_l^{\mathrm{WDZe}} \tag{5.1a}$$

and

$$Y_l^{\mathrm{BF21}} = y_l\, X_l^{\mathrm{WDZe}} + x_l\, Y_l^{\mathrm{WDZe}} \tag{5.1b}$$

corresponding to eq. (3.7).

Fig. 5.1 gives an overview of the entire model in terms of gravimetric factor (left) and phase (right). The parameters of the WDZe-model are displayed by black dots for comparison. Due to the high-pass filter, no signal is available at the frequencies below 0.5 cpd. Hence the parameters there stick to the WDZe-model. In the diurnal band the very narrow FCN-resonance dominates the degree 2 response (blue dots) in gravimetric factor and correspondingly in phase. In the semidiurnal band a kind of resonant character is seen as well in the gravimetric factor and the corresponding phase lead of degree 2. The resonance is less sharp and is presumably due to the signal contributed by ocean loading. The frequency dependence of the response at degree 3 is much weaker, with no clear resonance being present. For the degree 4 response the model is uniform at all frequencies by definition of the reference groups. Neither the degree 3 nor the degree 4 parameters follow the frequency dependence of the degree 2 parameters. Further, the degree 3 and the degree 4 parameters depart largerly from the reference level in opposite direction. A common, uniform ratio between parameters of different degree obviously is not appropriate. If used, there is good reason to expect a beating pattern in the tidal signal, which would cause a periodic variation of parameters in a MWA, as discussed by Schroth et al. (2018) and Schroth (2020).

Schroth (2020) discusses the temporal variation of the parameters for the $\mathbf{M}_1$ group and the hypothesis that they are caused by ocean-loading in particular. Müller et al. (2014) investigate apparent annual modulation of the oceanic M_1-response by adjusting the satellites α_2 and β_2 in their time-invariant oceanic tidal model. Likewise we seek for a finer resolution of the model in the M_2-group and split the band from 1.923 cpd to 1.943 cpd into six groups γ_2, α_2, ω_2, M_2, β_2, and δ_2 (Table 5.3). Fig. 5.2 provides diagrams for the final model parameters focused on this frequency range. During the iterative procedure it turned out that the parameters of all four satellite groups γ_2, α_2, β_2, and δ_2 should be updated with distinct values. This pattern produces annual as well as semi-annual modulation of the signal.

The variation of the gravimetric factor with frequency (Fig. 5.1) in the diurnal band is dominated by the FCN resonance. This resonance is specified in the WDZe-model based on precise results from VLBI observations. The tidal analysis just applies an adjustment to this resonance as shown in Fig. 5.3. The strongest deviation from the WDZe-parameters appears in the gravimetric factor and phase (off-scale in Fig. 5.1 right) of S_1. This is due to non-tidal (thermal) forcing of masses in the atmosphere and the parameters do not represent the tidal response of Earth's body. For the other major-amplitude groups in the diurnal band there is

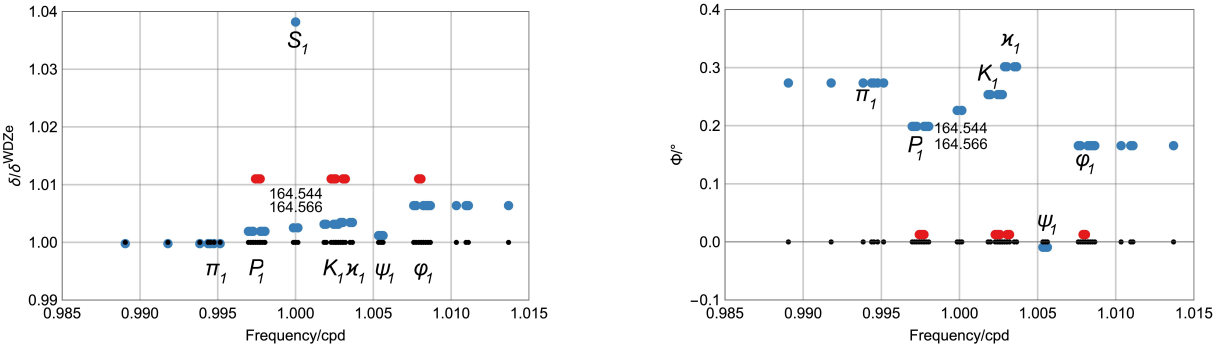

Figure 5.3.: Adjustment factors (left) and phases (right) of the BF21 model in the NDFW resonance frequency band. The dots are: initial reference WDZe model (small black), degree 2 parameter estimate (blue), degree 3 parameter estimate (red). The estimates for two low-amplitude satellite harmonics of S_1 are interpolated between P_1 and K_1.

little frequency dependence seen in the adjustment, which indicates that the FCN resonance in the WDZe-parameters is appropriate. A rather uniform factor is applied, which appears different for the degree two and the degree 3 response.

Amplitude factors for degree 3 tides were investigated by Ducarme (2012). A collection of M_1*, N_2*, L_2* and M_3* (there: $\mathbf{M_1}$, $\mathbf{3MK_2}$, $\mathbf{3MO_2}$ and $\mathbf{M_3}$) estimates for 16 SG stations is presented for comparison with different Earth models. The estimates of these harmonics in BF21 align with his results from Strasbourg, Bad Homburg and Wettzell. The detailed model of degree 3 tides for Moxa presented there is very similar to the BF21 model in terms of the observed response monotonicity. Even though most of the tidal parameters from BF21 model differ more than confidence intervals, in these Central European stations the ratio between tides of degree 2 and 3 changes in the same way along frequency, which is visible as a systematic trend. Above all these estimates, including BF21 confirm that the a priori ratio in all the studied observatories differ from the theoretical Earth models, which should cause apparent modulation in the MWA procedure.

The definition of reference groups is presented in tables 5.1 and 5.2. The final parameters of the local response model BF21 are presented in tables 5.3 and 5.4. Melchior et al. (1996) use $3MK_1$ for Q_1*, $3MO_1$ for J_1*, 3MJ2 for $2N_2$*, $3MK_2$ for N_2* and $3MO_2$ for L_2*.

5.4. Precision and Accuracy

Tables 5.3 and 5.4 list the parameters δ_1, Φ_1, x^{WDZe}, and y^{WDZe} of the final local response model BF21 for each wave group listed in Tables 5.1 and 5.2. They represent the time-invariant component in the tidal gravity signal recorded at BFO including the forcing and the response of the Earth in terms of its body, atmosphere and oceans. Parameters for different groups will represent these properties with different accuracy, because of: different amplitude of the constituents, the model being constrained by the reference, non-tidal signals in the records, and the

Table 5.1.: Definition of degree 2 reference groups in the final BF21-model. See Table 5.2 for a definition of column heads. In fact, only two harmonics form S_1 group, 164.556 and 164.554. Horizontal lines indicate boundaries of MWA-groups as specified in Table 6.1.

N	Name	Lead acc	Gr acc	Lead amp	Gr amp	Min freq	Max freq	Doodson
		$\mathrm{nm\,s^{-2}}$	$\mathrm{nm\,s^{-2}}$	$\log(\frac{V\cdot 10^{10}}{\mathrm{nm^2\,s^{-2}}})$	$\log(\frac{V\cdot 10^{10}}{\mathrm{nm^2\,s^{-2}}})$	cpd	cpd	number
26	ζ_1	0.718	1.864	7.165	7.572	0.721500	0.823399	115.855
15	SGQ_1	1.850	2.900	7.578	7.774	0.824605	0.833112	117.655
16	$2Q_1$	6.193	7.886	8.113	8.218	0.851182	0.859690	125.755
16	σ_1	7.464	10.025	8.195	8.323	0.860896	0.870023	127.555
12	QW_1	8.877	10.086	8.267	8.323	0.887327	0.893097	135.645
12	Q_1	47.060	48.130	8.992	9.001	0.893244	0.896129	135.655
15	ρ_1	8.968	12.088	8.270	8.400	0.897807	0.906315	137.455
23	O_1	253.110	306.397	9.710	9.793	0.921941	0.930449	145.555
21	τ_1	3.315	5.652	7.825	8.057	0.931964	0.940487	147.555
15	LK_1	7.288	11.440	8.161	8.357	0.958086	0.965827	155.455
7	M_1	20.271	25.075	8.605	8.698	0.966137	0.966740	155.655
14	χ_1	3.877	5.422	7.887	8.033	0.968565	0.974188	157.455
7	π_1	6.949	7.315	8.144	8.167	0.989049	0.995143	162.556
7	P_1	118.550	120.276	9.377	9.384	0.996968	0.998028	163.555
4	S_1	2.789	3.869	7.751	7.893	0.999853	1.000147	164.556
8	K_1	352.730	359.850	9.858	9.866	1.001825	1.002738	165.555
5	κ_1	47.796	48.837	8.990	9.000	1.002885	1.003651	165.565
4	ψ_1	3.081	3.193	7.751	7.767	1.005329	1.005623	166.554
11	φ_1	5.160	6.091	8.011	8.083	1.007595	1.013689	167.555
12	ϑ_1	3.762	5.019	7.887	8.012	1.028550	1.034467	173.655
8	J_1	19.610	20.479	8.605	8.624	1.036292	1.039030	175.455
12	ι_1	3.888	4.886	7.903	8.002	1.039177	1.044800	175.465
12	SO_1	3.217	4.334	7.825	7.954	1.064841	1.071083	183.555
19	OO_1	10.613	21.109	8.343	8.642	1.072583	1.080944	185.555
56	V_1	2.062	7.034	7.625	8.157	1.099161	1.216397	195.455
26	$3N_2$	0.771	1.704	7.547	7.889	1.719381	1.823399	225.855
15	ϵ_2	1.996	2.774	7.960	8.103	1.825518	1.837969	227.655
13	$2N_2$	6.824	7.565	8.495	8.540	1.853920	1.862428	235.755
16	μ_2	8.239	9.492	8.577	8.639	1.863634	1.872142	237.555
18	N_2	51.943	54.866	9.374	9.398	1.888387	1.896748	245.655
20	ν_2	9.880	11.754	8.652	8.728	1.897954	1.906462	247.455
7	γ_2	0.822	1.020	7.569	7.663	1.923766	1.927417	253.755
4	α_2	0.941	1.009	7.628	7.659	1.929389	1.930154	254.556
4	ω_2	10.216	10.367	8.664	8.670	1.931361	1.932127	255.545
9	M_2	273.830	274.069	10.092	10.092	1.932274	1.933187	255.555
7	β_2	0.829	0.870	7.573	7.594	1.934393	1.935321	256.554
12	δ_2	0.322	0.746	7.161	7.527	1.936983	1.942753	257.555
6	λ_2	2.021	2.223	7.959	8.001	1.958233	1.963708	263.655
25	L_2	7.741	11.732	8.543	8.724	1.965827	1.976926	265.455
8	T_2	7.397	7.741	8.526	8.546	1.991787	1.998287	272.556
5	S_2	126.500	126.812	9.759	9.760	1.999706	2.000766	273.555
5	R_2	1.057	1.350	7.682	7.788	2.002591	2.003032	274.554
18	K_2	34.329	46.717	9.194	9.328	2.004710	2.013689	275.555
29	η_2	1.907	3.590	7.941	8.216	2.031288	2.047390	285.455
9	$2S_2$	0.317	0.517	7.161	7.373	2.067579	2.073496	293.555
33	$2K_2$	0.501	1.776	7.359	7.908	2.075940	2.182843	295.555

Table 5.2.: Definition of degree 3 and 4 reference groups in the final BF21-model. The column heads are N: Number of harmonics in tidal catalog constituting a reference group; Lead acc: RMS of acceleration of the most significant harmonic; Gr acc: RMS of acceleration of the total signal of the group; Lead amp: Catalog tidal potential V amplitude of the most significant harmonic; Gr amp: Catalog tidal potential V amplitude of the total signal of the group; Min/Max freq: The smallest and the highest frequency in a group, respectively; Doodson: Doodson number of the most significant harmonic. Logarithms are taken to the base of 10. Horizontal lines indicate boundaries of MWA-groups as specified in Table 6.1, where commonly M_4+ constitutes one group together with 3cpd tides.

N	Name	Lead acc	Gr acc	Lead amp	Gr amp	Min freq	Max freq	Doodson
		$\mathrm{nm\,s^{-2}}$	$\mathrm{nm\,s^{-2}}$	$\log(\frac{V\cdot 10^{10}}{\mathrm{m^2\,s^{-2}}})$	$\log(\frac{V\cdot 10^{10}}{\mathrm{m^2\,s^{-2}}})$	cpd	cpd	number
29	Q_1*	1.662	3.802	7.397	7.756	0.784060	0.901148	135.555
14	O_1*	0.876	1.536	7.105	7.349	0.924222	0.937440	145.655
12	M_1*	5.460	7.101	7.892	8.006	0.960514	0.971760	155.555
36	J_1*	1.923	4.442	7.454	7.817	0.997424	1.149127	175.555
12	$3N_2$*	0.216	0.672	6.557	7.048	1.755363	1.832803	225.755
13	$2N_2$*	1.247	1.832	7.319	7.486	1.854524	1.869714	235.655
12	N_2*	4.575	5.702	7.881	7.976	1.890816	1.903886	245.555
13	M_2*	0.696	1.443	7.059	7.376	1.926960	1.940178	255.655
8	L_2*	4.261	5.387	7.846	7.948	1.963252	1.973732	265.555
26	K_2*	0.230	1.329	6.582	7.345	1.997262	2.115426	275.455
29	MN_3*	0.900	1.627	7.613	7.871	2.753244	2.869713	345.655
11	M_3*	3.299	3.573	8.175	8.210	2.892640	2.903886	355.555
11	ML_3*	0.187	0.377	6.928	7.233	2.927107	2.940325	365.455
17	MK_3*	0.427	0.752	7.290	7.536	2.965990	3.081254	375.555
24	M_4+	0.039	0.785	6.284	7.215	2.789226	3.937897	455.555

Table 5.3.: Degree 2 parameters for the BF21-model. See Table 5.4 for a definition of column heads. Estimates for S_1 are only valid for 164.556 and 164.554, see text for details.

Wave	δ_1	Φ_1	x^{WDZe}	y^{WDZe}	$\delta_2-\delta_1$	$\delta_u-\delta_1$	$2\sigma(\delta_u)$	$\Phi_2-\Phi_1$	$\Phi_u-\Phi_1$	$2\sigma(\Phi_u)$
		$/^\circ$			$/10^{-4}$	$/10^{-4}$	$/10^{-4}$	$/10^{-4\,\circ}$	$/10^{-4\,\circ}$	$/10^{-4\,\circ}$
ζ_1	1.1645	-0.7939	1.0094	0.0140	25	466	88	839	5470	4163
SGQ_1	1.1645	-0.7939	1.0094	0.0140	-26	-11	38	77	-650	1878
$2Q_1$	1.1530	-0.7189	0.9995	0.0125	12	8	12	111	-25	584
σ_1	1.1504	-0.6463	0.9972	0.0112	5	-1	10	171	-60	480
QW_1	1.1472	-0.2656	0.9946	0.0046	39	-37	22	-267	-2366	1084
Q_1	1.1472	-0.2638	0.9946	0.0046	2	-5	3	42	-183	132
ρ_1	1.1471	-0.1725	0.9946	0.0030	-5	3	8	-305	-40	401
O_1	1.1489	0.0850	0.9963	-0.0015	0	0	0	4	-1	15
τ_1	1.1556	0.0955	1.0021	-0.0017	-1	-10	15	1072	-118	767
LK_1	1.1530	0.2522	1.0003	-0.0044	0	-1	10	-19	-96	521
M_1	1.1519	0.2517	0.9993	-0.0044	1	1	4	-38	-58	191
χ_1	1.1479	0.1874	0.9960	-0.0033	-7	2	18	1241	27	921
π_1	1.1491	0.2737	0.9998	-0.0048	5	2	9	-427	17	441
P_1	1.1500	0.1989	1.0019	-0.0035	1	0	1	37	13	26
S_1	1.1882	10.8910	1.0195	-0.1962	102	250	31	-8500	3210	1465
K_1	1.1370	0.2537	1.0031	-0.0044	0	0	0	30	-1	14
κ_1	1.1360	0.3016	1.0034	-0.0053	-2	1	2	45	-16	99
ψ_1	1.2699	-0.0092	1.0012	0.0002	1	-2	22	-1121	-80	1002
φ_1	1.1763	0.1658	1.0064	-0.0029	-5	3	12	1032	-172	586
ϑ_1	1.1573	0.0692	1.0016	-0.0012	11	-1	19	1751	121	927
J_1	1.1577	0.1386	1.0021	-0.0024	1	-1	7	160	54	326
ι_1	1.1577	0.1389	1.0021	-0.0024	-15	-22	55	739	510	2748
SO_1	1.1558	0.3909	1.0010	-0.0068	-7	-1	23	-513	114	1150
OO_1	1.1545	0.1050	1.0000	-0.0018	4	3	9	360	248	461
V_1	1.1452	0.3973	0.9921	-0.0069	-16	8	44	-1876	-21	2206
$3N_2$	1.1394	2.0397	0.9838	-0.0350	-18	-112	77	-1230	6630	3923
ϵ_2	1.1392	2.3419	0.9834	-0.0402	-4	-2	31	340	379	1568
$2N_2$	1.1533	3.0533	0.9949	-0.0531	2	0	9	68	56	468
μ_2	1.1551	2.7101	0.9968	-0.0472	1	1	7	63	55	364
N_2	1.1738	2.6477	1.0130	-0.0468	1	0	1	13	20	61
ν_2	1.1751	2.6463	1.0142	-0.0469	-5	1	6	52	46	298
γ_2	1.1933	0.9732	1.0308	-0.0175	-20	-50	73	577	7659	3518
α_2	1.2083	0.4484	1.0439	-0.0082	-37	102	65	-133	1174	3065
ω_2	1.1866	2.0296	1.0245	-0.0363	-22	-24	10	521	466	465
M_2	1.1866	2.0301	1.0245	-0.0363	2	1	0	26	-4	19
β_2	1.2372	1.1532	1.0687	-0.0215	14	234	73	145	2824	3336
δ_2	1.2111	1.3043	1.0460	-0.0238	3	-343	124	567	23379	6022
λ_2	1.1830	1.6129	1.0216	-0.0288	-1	1	30	-495	166	1440
L_2	1.1909	1.4913	1.0285	-0.0268	0	0	8	116	-102	386
T_2	1.1913	0.4209	1.0291	-0.0076	12	-2	8	-306	99	405
S_2	1.1885	0.5681	1.0268	-0.0102	-2	0	0	59	21	24
R_2	1.1746	1.4646	1.0144	-0.0259	-133	28	48	-847	588	2312
K_2	1.1902	0.8176	1.0282	-0.0147	2	-1	2	100	-229	110
η_2	1.1884	0.5598	1.0267	-0.0100	-9	35	44	-796	257	2128
$2S_2$	1.1546	0.0142	0.9975	-0.0002	-12	-131	278	576	2806	13966
$2K_2$	1.1607	-0.1239	1.0028	0.0022	56	179	209	-29	-2170	10184

Table 5.4.: Degree 3 and 4 parameters for the BF21-model. The columns heads are: Wave: Name of the group as defined in Table 5.1. δ_1: gravimetric factor of the harmonic of largest amplitude. Φ_1: phase lead for the harmonic of largest amplitude in degrees. x^{WDZe}: in-phase factor with respect to the WDZe-model. y^{WDZe}: quadrature factor with respect to the WDZe-model. $\delta_2-\delta_1$, $\delta_\mathrm{u}-\delta_1$, $\Phi_2-\Phi_1$, and $\Phi_\mathrm{u}-\Phi_1$: differences between parameters from different models (see below and text). $2\sigma(\delta\mathrm{u})$, $2\sigma(\Phi\mathrm{u})$: confidence interval for a 2σ confidence level for gravimetric factor and phase, respectively. δ_1, Φ_1, x^{WDZe}, and y^{WDZe} refer to parameters of the BF21-model obtained from constrained inversion of data from sensor 1 of SG056. δ_2 and Φ_2 are gravimetric factor and phase of the BF21G2-model obtained from constrained inversion of data from sensor 2 of SG056. δ_u and Φ_u are gravimetric factor and phase of the BF21u-model obtained from unconstrained inversion of data from sensor 1 of SG056. The actual gravimetric factor and phase varies within the wave group due to the frequency dependence in particular in the diurnal band. Factors x^{WDZe} and y^{WDZe} are constant within the wave group and apply to the frequency dependent WDZe-model and are give additionally for this reason. While M_4+ is given with its δ factor, the degree 4 body response is different for different tidal species. The gravimetric factor presented in the table corresponds to M_4+ harmonic, i.e. (455.555). The factors x^{WDZe} and y^{WDZe} are identical for all degree 4 tides.

Wave	δ_1	Φ_1 / °	x^{WDZe}	y^{WDZe}	$\delta_2-\delta_1$ / 10^{-4}	$\delta_\mathrm{u}-\delta_1$ / 10^{-4}	$2\sigma(\delta_\mathrm{u})$ / 10^{-4}	$\Phi_2-\Phi_1$ / 10^{-4} °	$\Phi_\mathrm{u}-\Phi_1$ / 10^{-4} °	$2\sigma(\Phi_\mathrm{u})$ / 10^{-4} °
Q_1*	1.0831	1.2829	1.0093	-0.0226	26	-142	99	-4029	19691	5305
O_1*	1.0867	1.3182	1.0127	-0.0233	53	42	56	-2695	5596	2966
M_1*	1.0836	0.9002	1.0099	-0.0159	-9	-2	10	304	-74	542
J_1*	1.0846	0.0126	1.0110	-0.0002	-5	16	94	-85	-2295	4961
$3N_2$*	1.0758	0.0475	1.0028	-0.0008	-24	-127	221	-642	-3236	11922
$2N_2$*	1.0649	0.0888	0.9927	-0.0015	9	-22	55	-1714	41	2990
N_2*	1.0703	0.1322	0.9977	-0.0023	-2	-2	15	-543	114	823
M_2*	1.0683	-0.0438	0.9958	0.0008	-24	-45	95	920	-229	5137
L_2*	1.0681	-0.2997	0.9956	0.0052	-2	2	16	-179	-41	837
K_2*	1.0677	0.3926	0.9953	-0.0068	11	-198	177	145	10576	9695
MN_3*	1.0640	0.0621	0.9948	-0.0011	3	-3	58	159	-633	3148
M_3*	1.0667	0.2893	0.9974	-0.0050	6	0	17	-104	-2	897
ML_3*	1.0717	0.0535	1.0021	-0.0009	6	199	275	-37	4357	14418
MK_3*	1.0682	0.2150	0.9988	-0.0037	4	-20	179	-597	5586	9628
M_4+	1.0283	0.0143	0.9936	-0.0002	1	-52	106	-17	12345	5918
AIR	-3.2826	X	-3.2826	X	-338	211	23	X	X	X

time-variant component of Earth's admittance. There would be different approaches to estimate error bars, but none of them would provide an ultimate answer. Statistical considerations of error propagation, jackknife or bootstrap re-sampling, synthetic tests under the effect of added white noise, or a systematic analysis of trade-off are just a few that could be mentioned. In this section, we discuss some selected aspects of the variability seen in the model parameters, which can serve as estimates for error bars. Corresponding values of error estimates are given in Tables 5.3 and 5.4 together with the model parameters.

Exploring Constraints

Significant information on the constraints put by the gravity data on the model parameters is already obtained during the iterative procedure discussed above. Changes in model parameters are repeatedly tested against the regularization constraint. A deviation from the initial WDZe reference model will only be accepted, if the recorded data calls for it. This deviation is represented by a deviation of factors x_l^{WDZe} and y_l^{WDZe} from 1 and 0, respectively. This procedure and its consequences for the wave grouping chosen in the final model is discussed above.

Results for the Second Gravity Sensor

The difference between the analysis results for two co-located sensors may represent a lower limit for the confidence intervals. The SG056 is a dual-sphere instrument which operates two different gravity probes within the same sensor unit. Forbriger and Heck (2018) describe the essential properties of this instrument. The probe mass of the lower sensor (G1) is 17.7 g, the upper sensor (G2) in the unit uses a sphere of 4.34 g. Data recorded by the former typically appears less noisy, although it more likely saturates during stronger ground motion. The parameters for the BF21-model (Tables 5.3 and 5.4) are computed for data from sensor G1.

We additionally analyze data from sensor G2 in the very same (model-regularized, iterative) way and for the same time window as described above for the analysis of G1 data. In Tables 5.3 and 5.4 the parameters for this BF21G2-model are referred to as δ_2 and Φ_2. Because both sensors operate in the same unit they practically experience the same environmental noise source (including gravity noise from the atmosphere and hydrosphere as well as some instrumental noise sources). The inferred tidal model would be expected to be identical, though it is not. The difference $\delta_2 - \delta_1$ and $\Phi_2 - \Phi_1$ between the model parameters of both models are a measure for uncertainty and bias being produced by trade-off in the inversion as well as different instrumental noise and gap handling. The accuracy of the model parameters must not be assumed to be better than these differences, which are given in Tables 5.3 and 5.4 as well.

Unconstrained Inversion

Using the groups defined in Tables 5.1 and 5.2 for an a priori grouping, we run an unconstrained inversion for the data of sensor G1. The values for gravimetric factor δ_u and phase Φ_u for this BF21u-model together with confidence intervals at the 1σ-level are displayed in Fig. 5.4 and compared to the parameters of the BF21-model. The differences $\delta_u - \delta_1$ and $\Phi_u - \Phi_1$, for gravimetric factor and phase, respectively, are given in in Tables 5.1 and 5.2.

Error Propagation

The confidence intervals shown in Fig. 5.4 are computed by unconstrained inversion after a priori wave-grouping. These values represent error propagation based on the covariance matrix of the linear regression and the variance of the residual of the fit. They are a statistical measure of the variance if the residual is Gaussian white noise. `Eterna 3.40` outputs such values (however, with frequency-dependent weights, see Chapter 3.4 for details) as standard deviation of model parameters. Although the fit residual, as is known, deviates from Gaussian white noise, this provides a helpful estimate of confidence intervals. We list confidence intervals $2\sigma(\delta_u)$ and $2\sigma(\Phi_u)$ at the 2σ-level in Tables 5.3 and 5.4. As expected, the smaller the signal amplitude of the respective group (see Tables 5.1 and 5.2), the larger the confidence interval. Diagrams display 1σ interval, while the tables and discussion use 2σ levels. The inconsistency is intentional.

Comparison

For most of the groups the models BF21 , BF21u , BF21G2 estimates δ_1, δ_2, δ_u and Φ_1, Φ_2, Φ_u appear consistent within the 2σ intervals, in particular for those of larger amplitude like O_1, M_1, P_1, K_1, κ_1, J_1, $2N_2$, N_2, L_2, S_2, K_2, M_1*, and M_3*. For some groups the difference to the unconstrained model is not consistent within these intervals, like the ζ_1 and M_4+. The estimates for them may be questionable due to their small amplitude, anyway, and are kept close to the reference in the constrained cases.

The error propagation for S_1 indicates a precision, which obviously does not match the found discrepancy, which for the gravimetric factor is eight times the 2σ-interval for the unconstrained model and three times for the model for sensor G2. S_1 is a case, where the assumption of Gaussion white noise in the residual most likely is violated, due to the non-tidal radiation driven signals at this frequency. For ψ_1, φ_1, and ϑ_1 (all in the vicinity of the FCN resonance), the difference in gravimetric factors obtained from both sensors is within the 2σ-interval, as well as the difference for the unconstrained model. The situation for the phases is less clear.

A similar situation is seen near M_2. The error for M_2 is generally small due to the large amplitude of the signal. Nevertheless, the error propagation appears to underestimate the error intervals. For M_2 we expect a time-variant loading contribution from the oceans and the white

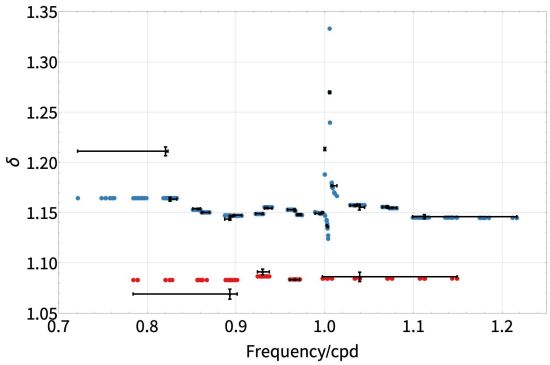

(a) Gravimetric factor of diurnal band

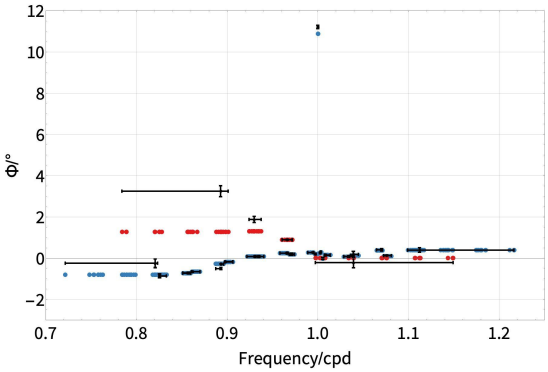

(b) Gravimetric phase of diurnal band

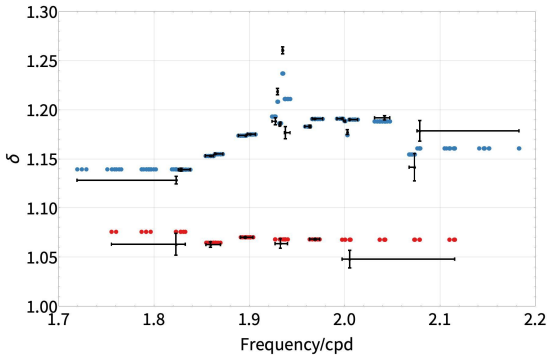

(c) Gravimetric factor of semidiurnal band

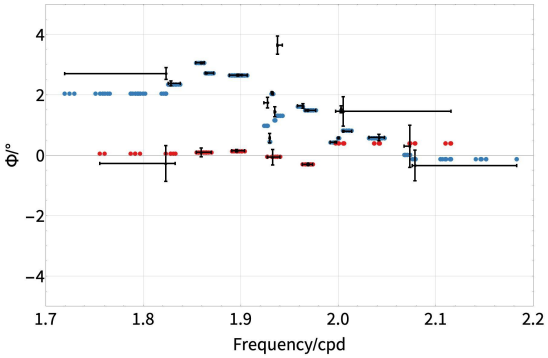

(d) Gravimetric phase of semidiurnal band

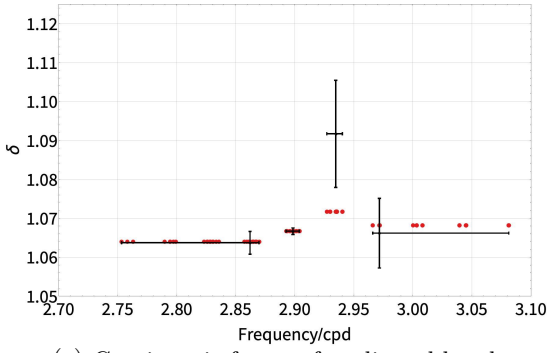

(e) Gravimetric factor of terdiurnal band

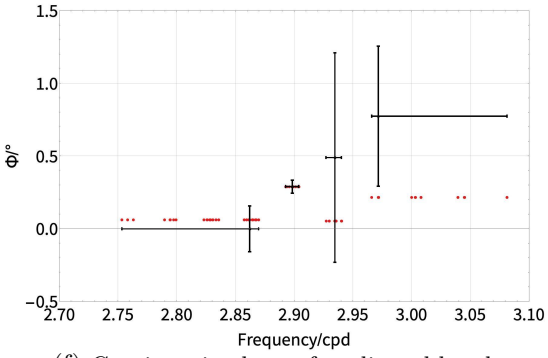

(f) Gravimetric phase of terdiurnal band

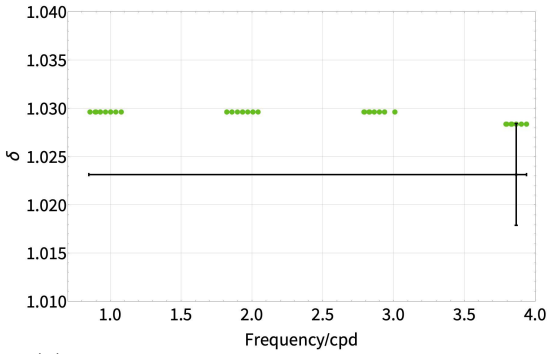

(g) Gravimetric factor of degree 4 harmonics

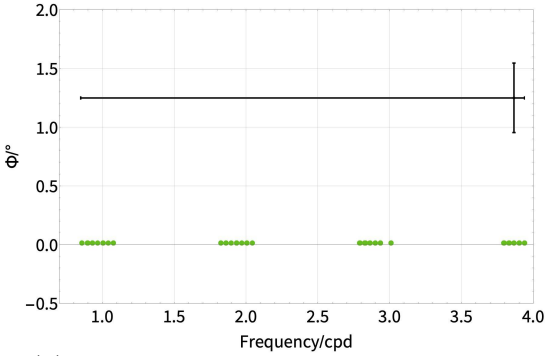

(h) Gravimetric phase of degree 4 harmonics

Figure 5.4.: Parameters for the model BF21u as obtained from unconstrained linear regression after a-priori grouping (see text). Their confidence intervals at the 1σ-level are displayed as error-bars. The horizontal bars specify the frequency interval of the respective group. They are compared with the parameters of the BF21-model as is obtained by constrained, iterative inversion (blue, red, and green dots show parameters for degree 2, 3, and 4, respectively).

Gaussian noise assumption is inappropriate. α_2, β_2, γ_2, and δ_2 are used to capture a slight time-invariant resonance-like feature seen in the semidiurnal band at M_2. They show a similar situation like discussed above for ψ_1, φ_1, and ϑ_1.

Both models BF21 and BF21G2 result from a constrained inversion. The two may show a bias in the direction of the WDZe-model, which was used as the initial reference. This may be the cause for differences between parameters of BF21 and BF21G2 being smaller than the corresponding differences between parameters of BF21 and BF21u for some waves.

5.5. The Residual Signal

In geodesy one seeks a good tidal model for predicting tides, such that they can be subtracted from the gravity signal. I used the BF21 model estimated with `RATA` and the ('standard') model provided by Black Forest Observatory, estimated with standard tidal analysis and `Eterna 3.40` in 2015. I demonstrate these two different models, and later use them to represent tides in gravity signal at the BFO, for 2 weeks of data. We clearly see that the "old" model shows coarser structure (Figs. 5.5a - 5.5b). This is clear for variation in M_2 group, and for degree 3 tides. The estimates of most degree 3 tides are rather fixed in the ratio to degree 2, since they were not resolved. Tides of degree 4 have fixed ratio to their degree 2, and, due to common frequencies, some have the same adjustment factors. Since most of tides degree 3 and 4 have rather minor amplitude, there are tides M_1* and L_2* which have large forcing amplitudes. The `Eterna 3.40` model is based on only six years of data, which by principle of a Rayleigh criterion limits its resolution compared to 11.5 years used for BF21. While I only speculate, it is highly probable that time series of just few years would provide similar resolution using `RATA` (see results for Sutherland or Kamioka in Chapter 7 and discussion there), but the estimates would differ and the error propagation might be larger.

Fig. 5.5c compares residual tidal signals from the synthetic tides subtracted from the gravity for two models, while fig. 5.5d is the corresponding spectral analysis. Clearly, the BF21 explains more signal of tidal origin. The corresponding RMS-amplitude for `Eterna 3.40` model is 1.07 $\mathrm{nm\,s^{-2}}$, while the BF21 shows this value at 0.865 $\mathrm{nm\,s^{-2}}$. The BF21 model cannot explain all the residual signal in the data, and the signal main pattern is the same, but the amplitude was significantly reduced.

In tidal analysis, the residual spectra must be carefully analysed during the process of estimation of the final model. This minimizes the risk of possible over-fitting (due to increased resolution) on the one hand and increased data misfit (due to the grouping being too coarse) on the other. For this reasons the residual spectra have to be carefully analysed. In standard tidal analysis, as done with `Eterna 3.40`, such investigations are necessary due to a priori grouping. Too coarse grouping could fix harmonics of significantly different estimates at one

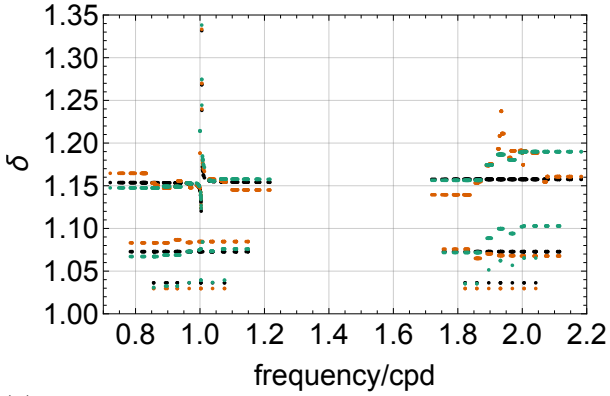

(a) Gravimetric factor of diurnal and semidiurnal tides as expressed by the two local models, estimated with `RATA` and `Eterna 3.40`. The fixed ratio between tides degree 2, 3 and 4 as implemented in `Eterna 3.40` is visible. The complex response in tidal groups $\mathbf{M}_2$ and $\mathbf{L}_2$ is not present in `Eterna 3.40` model.

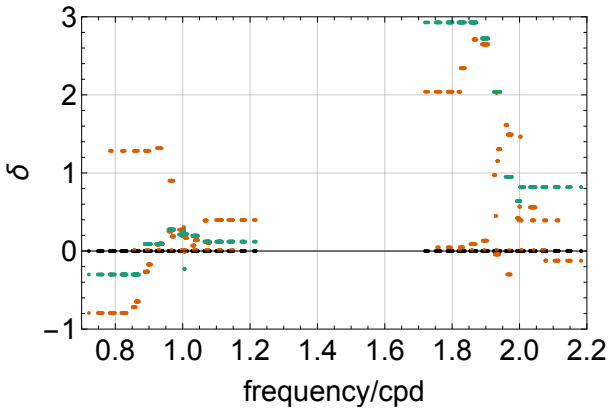

(b) Gravimetric phases of diurnal and semidiurnal tides as expressed by the two local models. The complex, detailed pattern of different phases for different tides and degrees resolved by `RATA` is noticeable and gives more insight to the phase response if compared with `Eterna 3.40`.

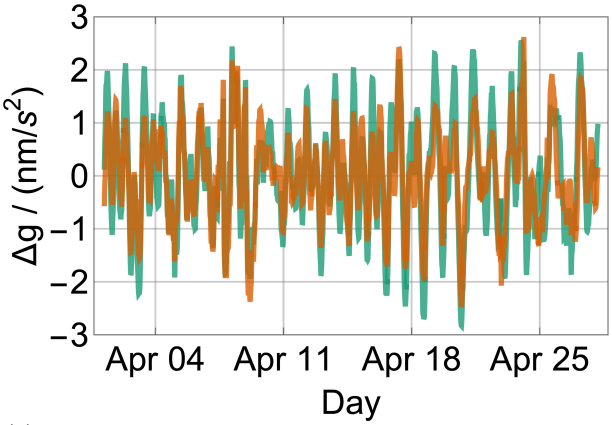

(c) Gravity residual time series after application of two models. There is a clear reduction of tidal signal with the `RATA` model

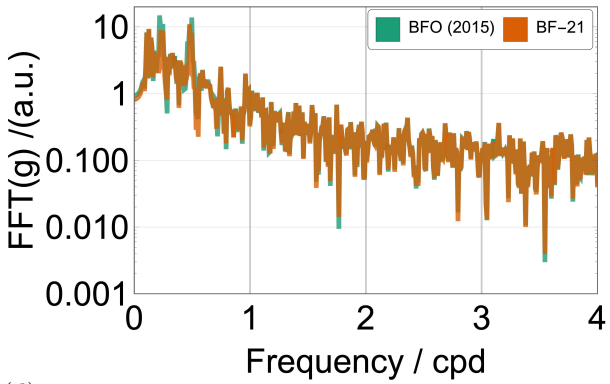

(d) Spectra of the gravity residual time series after application of two models.

Figure 5.5.: Comparison of two models used to describe the local response at the Black Forest Observatory. The former model was estimated with conventional `Eterna 3.40` approach by Eva Schroth (green). The results for the new approach, `RATA`, is presented in the chapter (BF21 model, orange).

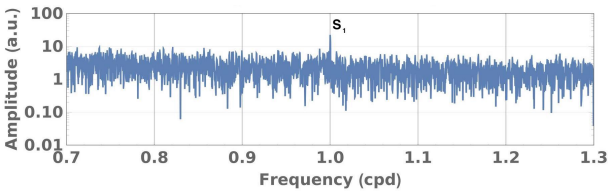

(a) Residuals at frequency range of diurnal tidal harmonics

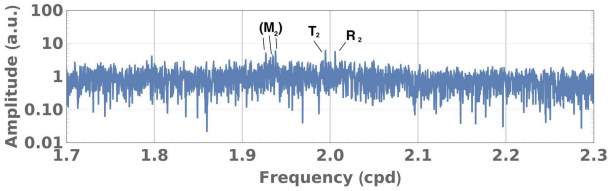

(b) Residuals at frequency range of semidiurnal tidal harmonics

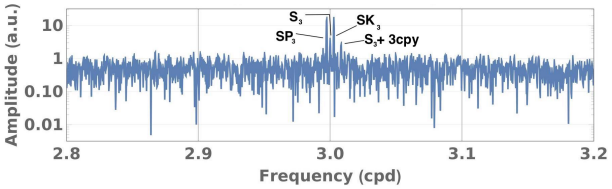

(c) Residuals at frequency range of terdiurnal tidal harmonics

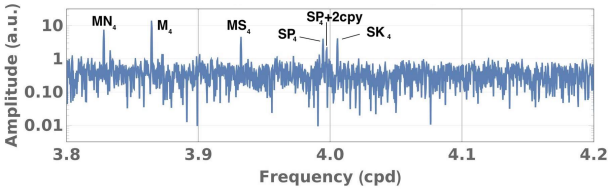

(d) Residuals at frequency range of quarterdiurnal tidal harmonics

Figure 5.6.: Residual spectra for the final BF21 model of the analysis of 11.5 years of gravity data from the lower SG sensor at the BFO. The identified lines are expected from the non-harmonic phenomena they are associated with (ocean response, radiation).

value. Since the data could not fit the synthetic signal from forward operator with common factor in the regression, the residual harmonic signal should be present. If the grouping is too coarse, or regularization of some parameters too strong, there is a risk of similar problem in `RATA` procedure. Hence, this is an essential step for validation of the final model. We carefully analysed the residuals from tidal analysis using `RATA` after the final iteration, making the BF21 model, which we present in Fig. 5.6.

We clearly identified signals of atmospheric and oceanic origin, which were expected to be seen in the residual signal. Since these signals are radiation and ocean driven, they are not exactly tidal frequencies with with various amplitudes and phases. Hence, they cannot be inferred with the local response model. There are visible peaks at every multiplication of 1 cpd, with a distinctively large feature at 7 cpd, which is already known (Ducarme, 2023) and still lacks explanation. The atmosphere modulation of S_3*, at 3 cpd−2 cpy, 3 cpd±1 cpy (SP_3*, SK_3*) and 3 cpd+3 cpy has been found, similarly to results of other stations as performed with `Eterna 3.40` by Calvo (2015) and with by Ducarme and Schüller (2018). We consequently have different modulations of ocean and atmosphere of M_4+, 3.86 cpd, at 3.86 cpd −1 cpm (MN_4+), 3.86 cpd+2 cpm (MS_4+), 4 cpd±1 cpy (we name it SP_4 and SK_4+, consequently) and 4 cpd+2 cpy which are clear in the residual spectra.

Since the BF21 was estimated with the gap-filled data with synthetics, we also inspected times for which artificial time series was used. The residuals for such windows are smooth, with no high-frequency components compared to other analysed data. Since they are not zero, they rather follow the pattern of the residual signal, we may conclude that they do not bias the result

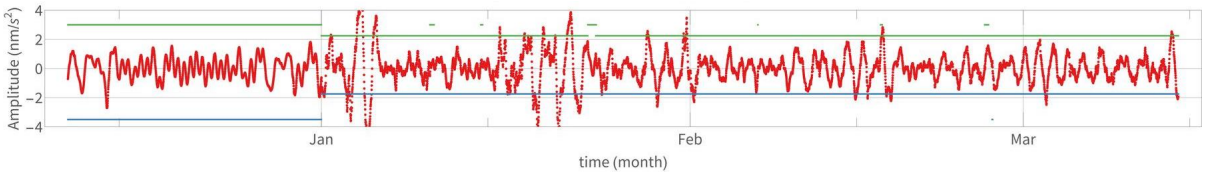

(a) Residuals at 2017/2018.

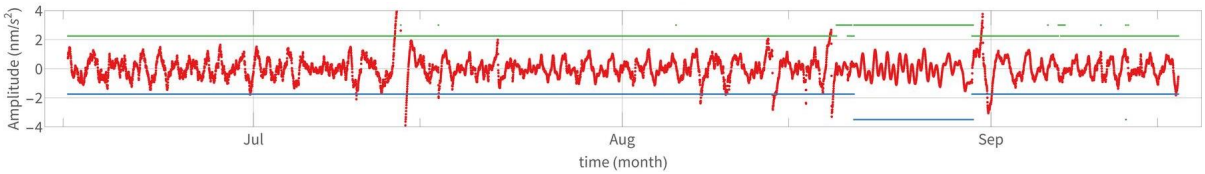

(b) Residuals in 2018.

Figure 5.7.: Residuals of the final BF21 model (red) in the analysis of 11.5 years of gravity data from the lower SG sensor at the BFO. The green line shows the data availability for gravity, the blue line for air pressure. The value of green line at 3 and blue at −3.5 indicate gap-filled data. While the residuals for these periods are smooth, indiciating less high-frequency signals, their long-frequency behaviour is similar to the residuals in non-filled data time.

(Fig. 5.7). Hence, even though some gaps were relatively long (even weeks), we obtained the meaningful paramter estimates for the station.

5.6. Summary

We implement and demonstrate a robust harmonic tidal analysis method, which uses a constraint to a reference model in order to regularize the regression problem. It is robust in the sense that parameters for each harmonic in the tidal catalog can be inferred without encountering a singularity. No a priori wave grouping is needed. The solution is found by updating the reference model, where parameters for harmonics deviate from the reference for specific harmonics. This update is done uniformly for all harmonics in a finite frequency band in order to account for the credo of smoothness. Different adjustments are only applied, where results of the linear regression problem indicate that harmonics significantly require different parameters to reduce the data misfit. In that sense grouping is applied to the reference model only, not to the parameters in the linear regression. This grouping is data driven and not applied a priori, contrary to conventional applications based on the Rayleigh criterion.

We apply this approach to 11.5 years of gravity data recorded with the superconducting gravimeter SG056 at Black Forest Observatory (BFO, Schiltach). With this analysis we demonstrate that the robust approach can exploit the super-resolution of tides as suggested by Munk and Hasselmann (1964). According to Rayleigh criterion, the fundamental frequency would be 1/11.5 cpy, and the analysis indicates the mean noise level at $\Delta_d \approx 0.88$ nms^{-2}. This tidal model captures the local response of the Earth as a whole (including oceans and atmosphere). We separate the response parameters for tides of degrees 2, 3 and 4 and demonstrate that the

optimal model differs from the ratio between degree two and three body tides as hard-coded in programs like `Eterna 3.40`. Then again we find that groups (like KNO_2) being kept separate in other studies (e. g. Melchior et al., 1996; Calvo, 2015) do not receive specific constraints from the data and should be kept together with their major neighbours (L_2 in the case of KNO_2).

The final model for sensor 1 of SG056, which we call BF21, has a very fine structure. In total we identify 46 degree 2 groups, 14 (purely) degree 3 groups and 1 degree 4 group, as given in Tables 5.1 and 5.2. This goes beyond what is possible with traditional implementations, which only allow for wave grouping being done along frequency. All parameters estimated by analysis of the 11.5 years of gravity for both spheres of SG056 are listed in Tables 5.3 and 5.4. The estimate for the air pressure (AIR) factor R^{BF21} is also displayed there.

The proposed robust approach to tidal analysis allows us to exploit the super-resolution of tides. It supports a truly data-driven wave grouping and could in principle be further developed to infer a continuous and smooth frequency-dependent model. Moreover, with this approach it is possible to deliberately test models of Earth's admittance by setting a specific reference model and testing whether the data constraint drives the parameters of specific harmonics away from the reference. The trade-off curve (Fig. 3.2), which uses the misfit for untapered data, effectively helps to avoid over-fitting. The model constraint causes a general tendency towards the reference model, which is unfavorable. For this reason, deliberate testing of parameters is an essential part of the iterative procedure.

6. Validating the Local Response Model BF21 with the MWA Technique

This chapter is a part of the manuscript submitted and accepted to be published as peer-reviewed article in the Journal of Geodesy. Most paragraphs are taken literally from Ciesielski et al. (2023).

6.1. Introduction

The separate analysis of consequential subsets of the long time series, as discussed in Chapter 1 and Chapter 3, is essential for investigations of the time-stability of the instrument, such as gain factor changes, and possible time-variance of parameters hidden in the analysis of the full records. Hence such methods are recently applied for spring and superconducting gravimeters by analysing very long gravity records.

Non-detected temporal changes of the gravimeter transfer function are basically reflected by temporal variations of tidal parameters, which, however, might be caused also by other reasons. Calvo et al. (2014); Meurers et al. (2016) demonstrated that data sets of 1-yr window exhibits temporal variations of the tidal parameters. Following Meurers et al. (2016), Schroth et al. (2018) investigated 3-month windows in the MWA approach and presented systematic temporal variations of tidal parameters for most stations in GGP project.

If MWA is carried out, tidal harmonics have to be grouped a priori, due to the short length of time series in each window. The grouping as defined by frequency ranges (indicated by reference groups) used for the MWA without regularization, but with a priori grouping as specified in Table 6.1. This approach makes an assumption of equal tidal parameters within a group. However, this is violated due to implicitly mixing constituents with response dependent on tidal degree and order. We know from Chapter 2 and Chapter 3 that theoretical models from seismology make assumptions about earth response for different degrees and apply corrections for effects of NDFW. We do not know how appropriately these models describe tidal response, what is the problem investigated by Baker and Bos (2003); Ducarme (2012). Proper estimation of these models is difficult, since tides within a group have different response to the ocean load (Sulzbach et al., 2022; Meurers et al., 2016).

Table 6.1.: Definition of a priori groups for the moving window analysis (MWA). For diurnal and semidiurnal species, some harmonics from degree 3 reference groups were split into the corresponding frequency bands of degree 2 tides, i.e. harmonics from $\mathbf{J_1}^*$ were distributed into $\mathbf{K}_1$, $\mathbf{J}_1$ and $\mathbf{OO}_1$ *MWA groups*. Degree 4 $\mathbf{M_4}+$ tide was split in similar manner into corresponding MWA wave (tidal) groups.

Reference groups	Name	Min freq / cpd	Max freq / cpd
(ζ_1, $\mathbf{Q}_1$, ρ_1)	$\mathbf{Q}_1$	0.501370	0.911390
($\mathbf{O}_1$, τ_1)	$\mathbf{O}_1$	0.911391	0.947991
(LK_1, $\mathbf{M}_1$, χ_1)	$\mathbf{M}_1$	0.947992	0.981854
(π_1, $\mathbf{K}_1$, φ_1)	$\mathbf{K}_1$	0.981855	1.023622
(ϑ_1, $\mathbf{J}_1$, ι_1)	$\mathbf{J}_1$	1.023623	1.057485
(SO_1, $\mathbf{OO}_1$, V_1)	$\mathbf{OO}_1$	1.057486	1.470243
($3\mathrm{N}_2$, $\boldsymbol{\mu}_2$)	$\boldsymbol{\mu}_2$	1.470244	1.880264
($\mathbf{N}_2$, ν_2)	$\mathbf{N}_2$	1.880265	1.914128
(γ_2, $\mathbf{M}_2$, δ_2)	$\mathbf{M}_2$	1.914129	1.950419
(λ_2, $\mathbf{L}_2$)	$\mathbf{L}_2$	1.950420	1.984282
(T_2, $\mathbf{S}_2$, $2\mathrm{K}_2$)	$\mathbf{S}_2$	1.984283	2.451943
(MN_3*, $\mathbf{M}_3$*, MK_3*)	$\mathbf{M}_3$*	2.451944	4.000000

6.2. Previous Studies

Meurers et al. (2016) suggest that temporal variations can be caused by improper calibration due to instrument instability, undetected offsets and/or spikes in the gravity data in the preprocessing or from numerical artefacts. The first two effects obviously cause temporal variations of tidal parameters, however, rather not in systematic way for all the stations. This was emphasised by Schroth et al. (2018), that variation of instrumental gain would affect the tidal parameters of all groups in the same way. What authors (Meurers et al., 2016) explain as numerical artifacts is actually the frequency resolution and improper ratio of harmonics due to the loading affecting harmonics from one group in a different way. Meurers et al. (2016) draw attention to a problem of excessively filling gaps by wrong model which should cause anomalous features at a specific site within a specific period. In our investigation (see Chapter 5.5) we have not found enough evidence that would suggest that use of the artificial data results in larger temporal variations than in other parts of data, but the problem is worth further investigation. Nevertheless, all the stations listed in Chapter 8 were investigated with the data for which only short gaps were filled with synthetics.

Moreover, Schroth et al. (2018) suspected time-dependent response of the Earth to tidal forcing, or trade-off between parameters for different wave groups in the inversion. The first problem is beyond the discussion of this thesis and leads to the study of changes in the ocean's behaviour due to a changing ocean climate or for validation of non-stationary ocean models (Schroth et al., 2018; Schroth, 2020; Haigh et al., 2020). The second one was investigated in this chapter. The grouping in MWA, as given in Table 6.1 is coarse enough that condition number

is always sufficiently small for the results to be stable. Schroth et al. (2018) also indicates the modulation possibility from the body tide model used in the analysis in the coarse grouping, where the harmonics within group have different estimates. This effect was demonstrated by Schroth (2020) on synthetic harmonics in $\mathbf{K}_1$ group. Schroth et al. (2018) give a list of potential satellites that might cause these patterns. We test the hypothesis that some of the temporal variations of tidal parameters found in previous studies were caused by inappropriate body tide models in combination with a priori wave grouping. We demonstrate that the application of local model by correct adjustments explains most of significant harmonic temporal variations. Using BF21 as an a priori model in a non-regularized moving window analysis of wave groups composed from summed harmonics, we find that periodic variations of groups $\mathbf{M}_1$, $\mathbf{K}_1$, $\boldsymbol{\mu}_2$, $\mathbf{N}_2$, $\mathbf{L}_2$, and $\mathbf{S}_2$ are reduced by up to a factor of 7 compared to earlier studies. Some variations previously seen in the $\mathbf{M}_2$ group are captured as well. We highlight the major tides that caused the modulation in these groups. Additional tests proved that tidal groups are well defined in their frequencies, so the cross-talk between parameters does not exist, resulting in no trade-off, and we can use them to validate how much which parameters cause the modulation in MWA.

6.3. Use of the A Priori Local Model

Meurers et al. (2016) claimed that it is impossible to assess the loading effects directly, because no ocean load models exist for degree 3 tidal waves. The situation recently improved when Sulzbach et al. (2022) presented the recent detailed catalog for gravimetric signatures of degree 3 tides. Alternatively, the averaged ocean response can be approximated for its time-invariant properties with the local response model, derived from the long time series. The true estimates, and hence ratios withing MWA groups differ from the theory provided by WDZe a priori body tide model. We would like to demonstrate how important is to use the proper ratio between significant harmonic satellites in a priori grouping in MWA. Not only ocean response, but also radiation has to be adjusted properly. If the ratios are not considered carefully, the resulting beating and bias may easily lead to false conclusions about reasons of temporal variations. Similar idea was already used by Foreman and Henry (1989) for shallow water harmonic analysis. In their approach, the ratios between harmonics within wave groups were deduced (corrected) based on relationships from the study of longer time series. Such adjustment took place after LS fit, in contrary to our method, where the ratios are corrected before the LS fit. The proper adjustments to the body tide comes from the local response model, eq. (3.43). We then, after the application of the local response model, consequently run MWA for short periods, and obtain common factor for each wave group. Hence, the apparent ratio between harmonics, resulting from the proper body tide and ocean response, is included in the model.

6.4. The MWA Results and Temporal Variations

Figures 6.2 - 6.4 show results of the moving window analysis for all twelve wave groups. We overlay the values for the analysis which uses the WDZe-model (in green) for comparison by the results shown by Schroth et al. (2018, in black) to demonstrate the consistency with their results. Small differences between the green and the black curves are due to the different handling of gaps in MWA and processing of the data (e.g. decimation).

For all affected parameters shown in Fig. 6.2 - 6.4 the amplitude of temporal variation is significantly reduced when running the MWA with respect to the BF21-model rather than the WDZe-model. While the results with respect to the WDZe-model have clearly periodic character, the results with respect to the BF21-model almost do not show this. For $\mathbf{K}_1$ group the annual variation was captured by the more appropriate ratio between K_1, P_1 and S_1 in the BF21-model. Some periodic variations remain, but with reduced amplitude and they are less systematic. We suppose they are caused by thermally driven signal components at the S_1 frequency.

Schroth et al. (2018, their Table 4) discuss possible causes of periodic variations in the MWA results, based on the frequency distance of major tidal contributions. For $\mathbf{K}_1$ they discuss the consequences of the group parameter being not appropriate for the signal at $\mathbf{S}_1$. For $\boldsymbol{\mu}_2$ (their $\mathbf{2N}_2$) they discuss the satellites at a distance of 1/0.56 per year (μ_2 and $2N_2$, the larger variational tide from M_2, Bartels, 1985). The parameters for these contributions are adjusted separately in the BF21-model and the semi-annual variation consequently is reduced in Figs. 6.9e and 6.9f. Similarly variations at a period of 0.56 years are expected for $\mathbf{N}_2$ (ν_2, the larger evectional tide from M_2) and for $\mathbf{L}_2$ (λ_2, the smaller evectional tide from M_2). Both are adjusted independently from the rest of the groups in the BF21-model, which reduces the semi-annual variations in Figs. 6.9g to 6.10d. The groups $\mathbf{N}_2$ and $\mathbf{L}_2$ contain significant contributions at degree 3, which appear as satellites to the main degree 2 harmonic at a distance of 1/8.8 per year (precessional p satellite harmonics, N_2* and L_2*, respectively). A modulation with the corresponding period is obvious in Figs. 6.9g to 6.10d for the parameters computed with respect to the WDZe-model. The BF21-model uses independent parameters for the degree 3 tides, adjusted to the observations. Consequently the variations with 8.8 years period are gone, in the MWA with respect to the BF21-model.

The BF21-model in the frequency bands of the MWA-groups as listed in Appendix C (Table 6.1) is in fact more detailed than what is discussed at the above paragraphs (cf. Tables 5.3 and 5.4). In how far further details contribute to the changes between the MWA-results with respect to the WDZe-model on the one hand and the BF21-model on the other hand, is not discussed here, since we focus on the main contributors.

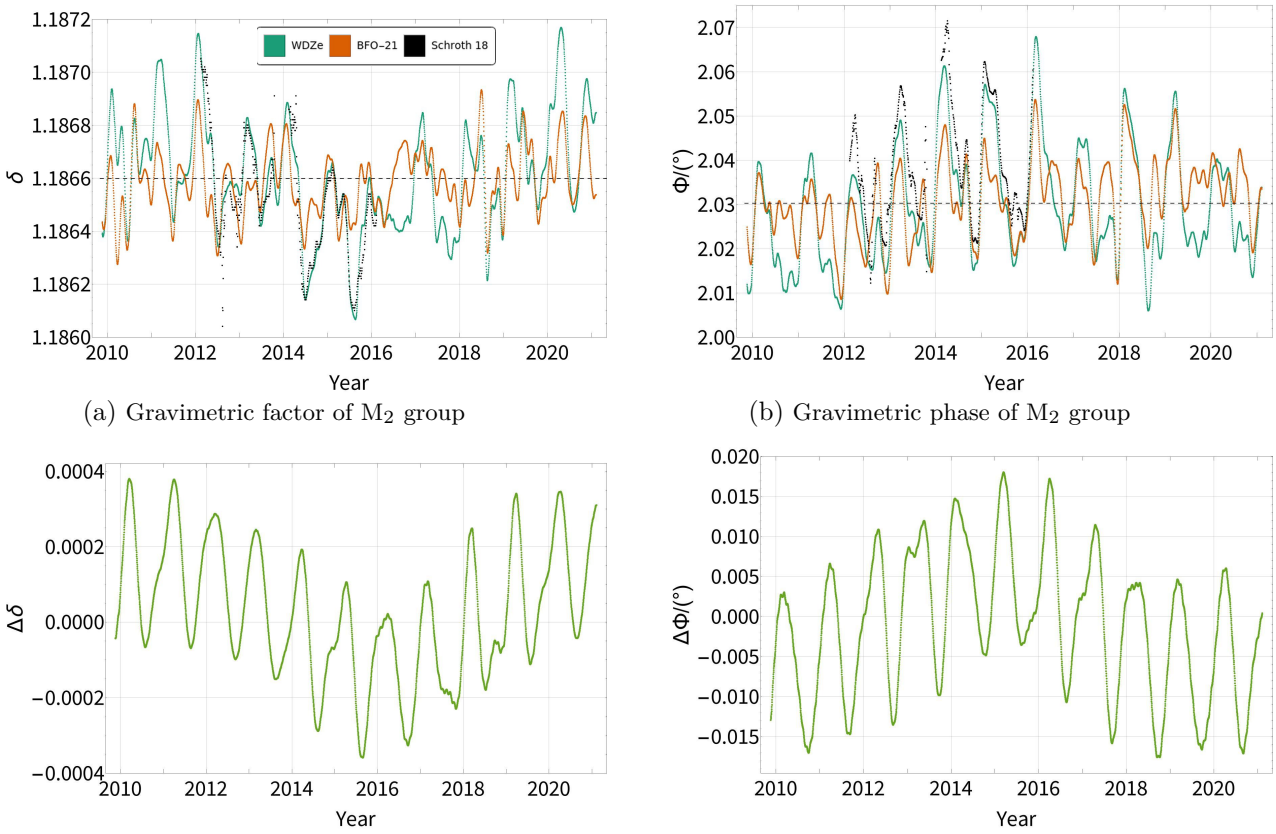

(a) Gravimetric factor of M_2 group

(b) Gravimetric phase of M_2 group

(c) Gravimetric factor differences of M_2 group

(d) Gravimetric phase differences of M_2 group

Figure 6.1.: The results of MWA for tidal group $\mathbf{M_2}$. Top: gravimetric factor (left) and phase (right). Tidal parameters correspond to the main harmonic in the group, which gives the group its name. Colors are: green: MWA with respect to the WDZe-model, orange: MWA with respect to the BF21-model, black: results by Schroth et al. (2018) for comparison. Bottom: difference between results with respect to BF21-model and with respect to WDZe-model.

For the $\mathbf{M_2}$-group (Figs. 6.1a and 6.1b) the differences between the two results is not as clear. However, the variation amplitude is clearly reduced in the MWA with respect to the BF21-model. The variations of annual periodicity are captured by the fine-grained structure presented by α_2, β_2, M_2, γ_2, and δ_2. This becomes obvious, when computing the difference between both results, as shown in Figs. 6.1c and 6.1d. Significant variations of rather random nature remain in the case of $\mathbf{M_2}$. The cause for the frequency dependence of tidal parameters within the $\mathbf{M_2}$-group should not be searched in the Earth body. It might be due to a resonance in the ocean's admittance to tidal forcing within the $\mathbf{M_2}$ frequency range, which is part of the loading signal.

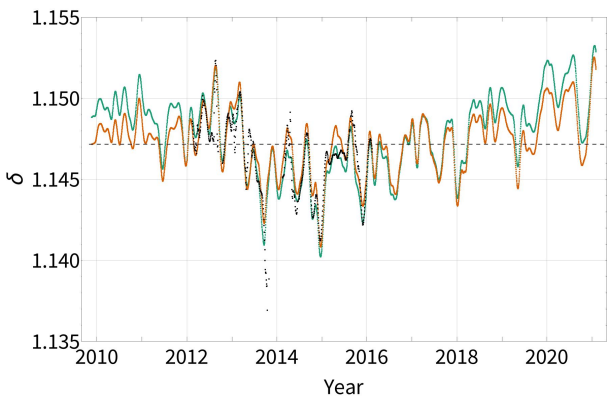

(a) Gravimetric factor of $\mathbf{Q}_1$ group

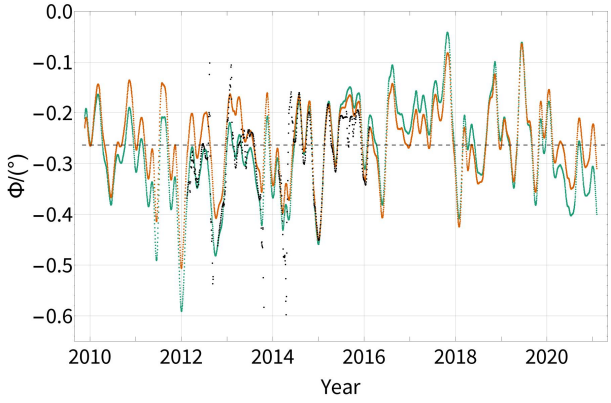

(b) Gravimetric phase of $\mathbf{Q}_1$ group

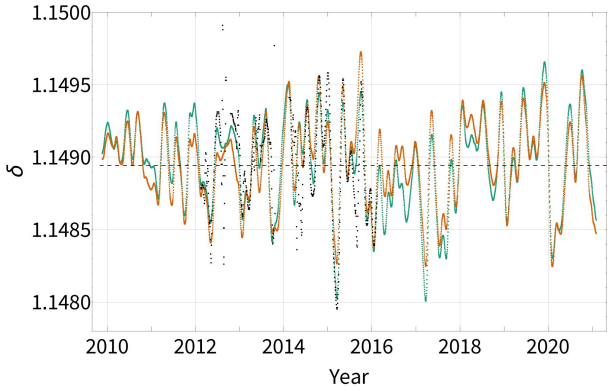

(c) Gravimetric factor of $\mathbf{O}_1$ group

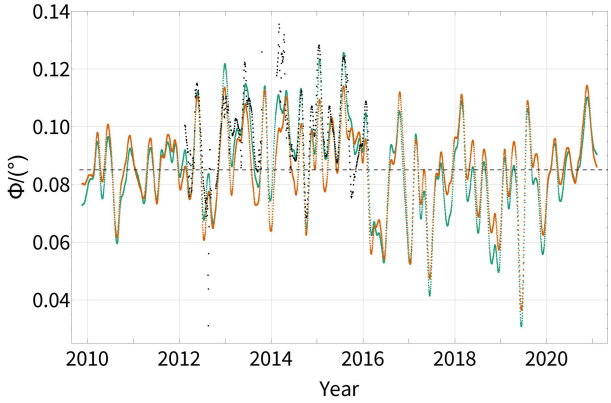

(d) Gravimetric phase of $\mathbf{O}_1$ group

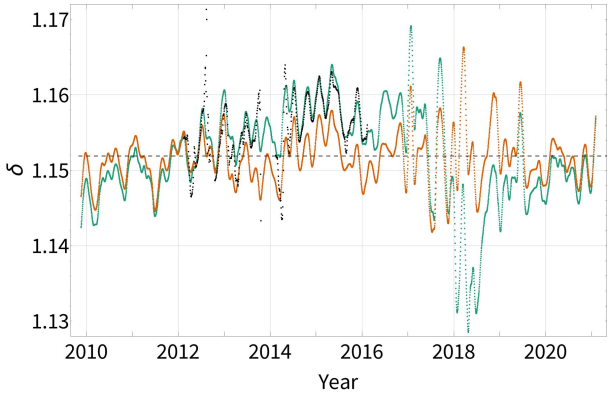

(e) Gravimetric factor of $\mathbf{M}_1$ group

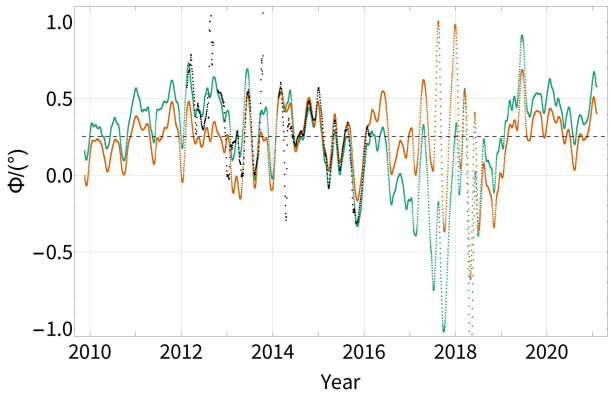

(f) Gravimetric phase of $\mathbf{M}_1$ group

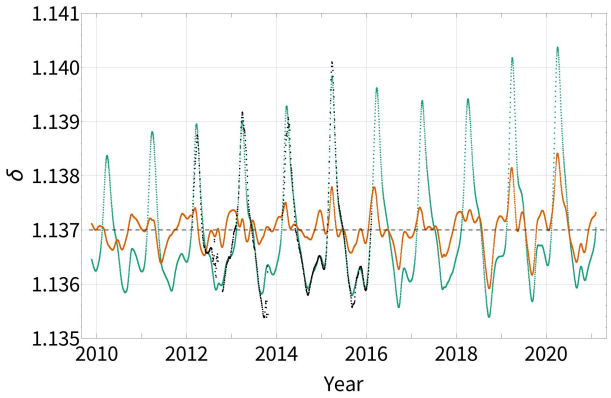

(g) Gravimetric factor of $\mathbf{K}_1$ group

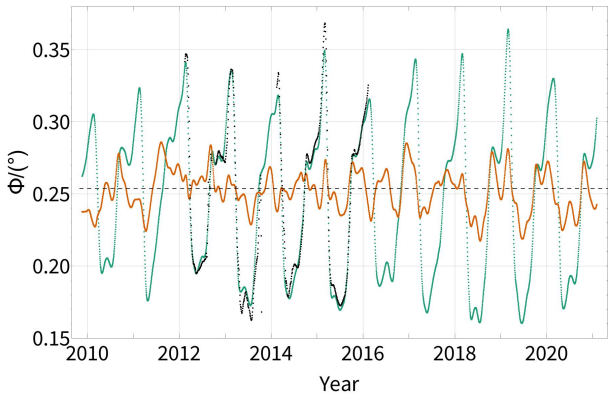

(h) Gravimetric phase of $\mathbf{K}_1$ group

Figure 6.2.: The results of MWA for tidal groups $\mathbf{Q}_1$, $\mathbf{O}_1$, $\mathbf{M}_1$ and $\mathbf{K}_1$ (top to bottom) for gravimetric factor (left) and phase (right). Colors: green: MWA with a-priori WDZe-model, orange: MWA with a-priori BF21-model, black: results by Schroth et al. (2018) for comparison.

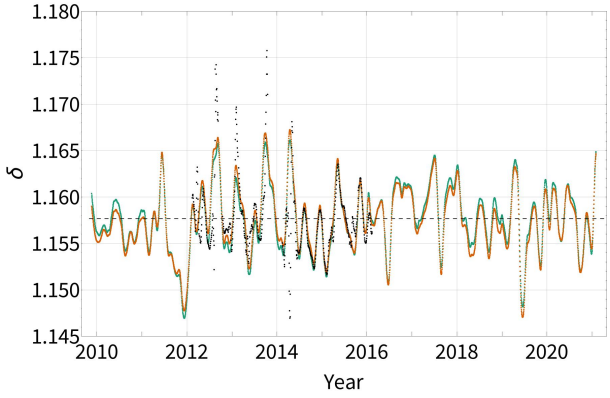

(a) Gravimetric factor of $\mathbf{J}_1$ group

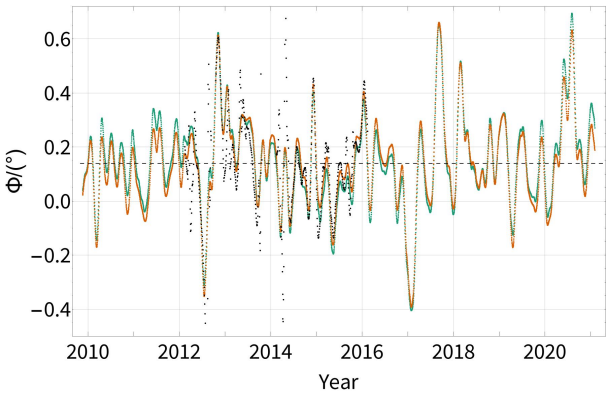

(b) Gravimetric phase of $\mathbf{J}_1$ group

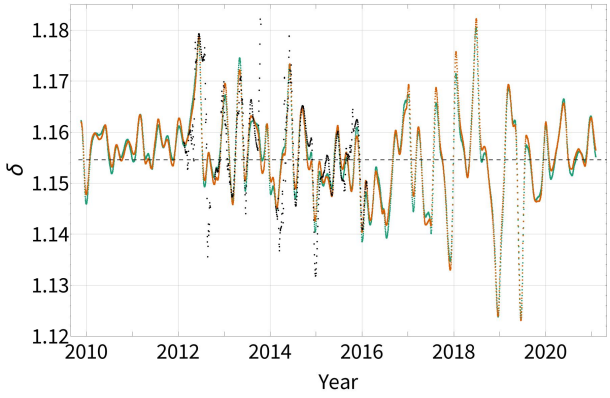

(c) Gravimetric factor of $\mathrm{O}\mathbf{O}_1$ group

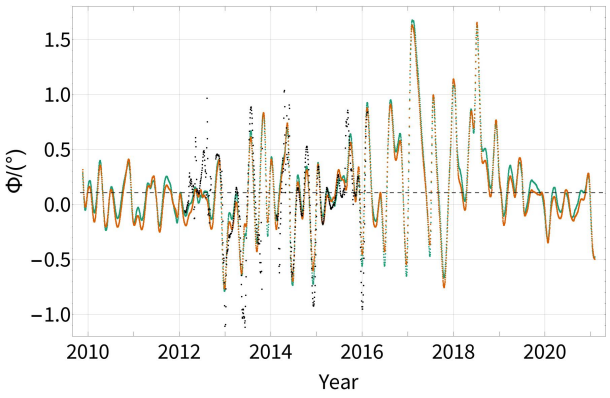

(d) Gravimetric phase of $\mathbf{OO}_1$ group

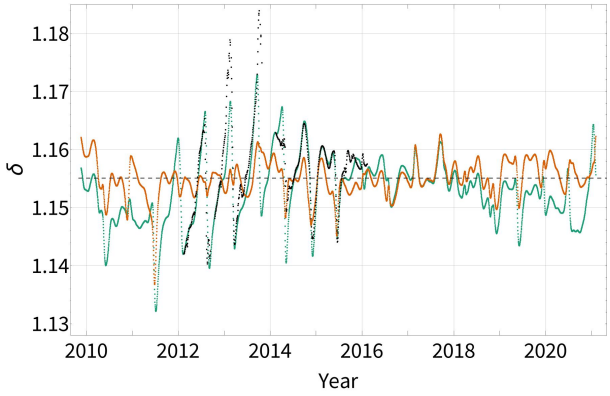

(e) Gravimetric factor of $\boldsymbol{\mu}_2$ group

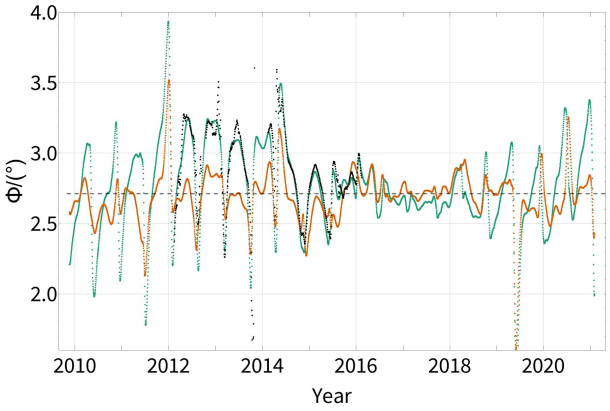

(f) Gravimetric phase of $\boldsymbol{\mu}_2$ group

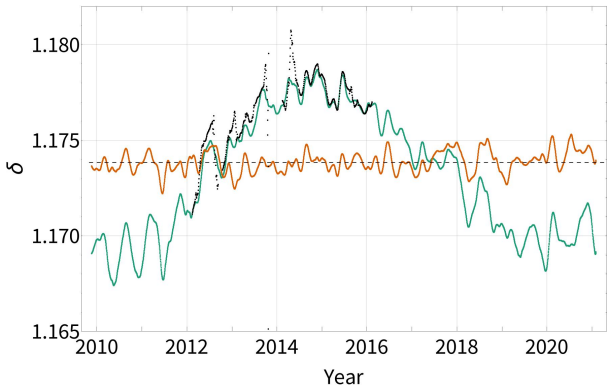

(g) Gravimetric factor of $\mathbf{N}_2$ group

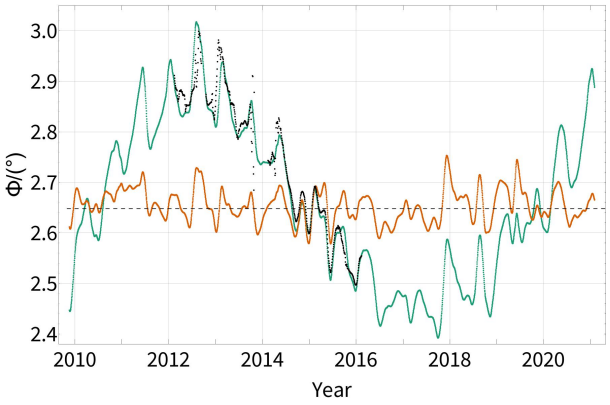

(h) Gravimetric phase of $\mathbf{N}_2$ group

Figure 6.3.: The results of MWA for tidal groups $\mathbf{J}_1$, $\mathbf{OO}_1$, $\boldsymbol{\mu}_2$ and $\mathbf{N}_2$ (top to bottom) for gravimetric factor (left) and phase (right). Colors: green: MWA with a-priori WDZe-model, orange: MWA with a-priori BF21-model, black: results by Schroth et al. (2018) for comparison.

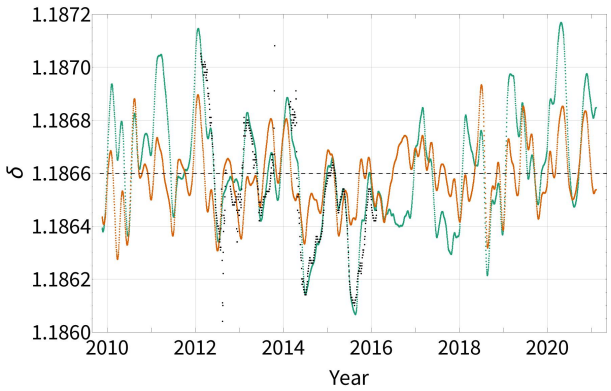

(a) Gravimetric factor of $\mathbf{M}_2$ group

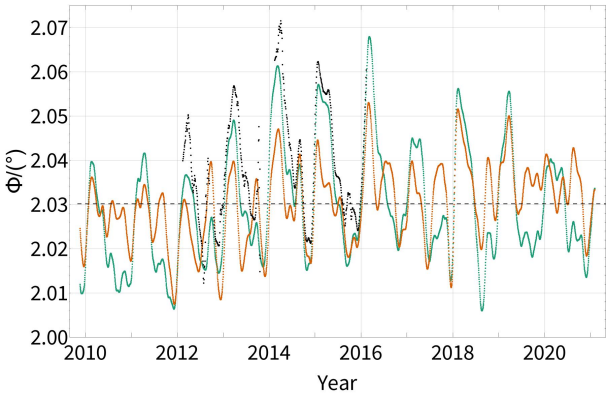

(b) Gravimetric phase of $\mathbf{M}_2$ group

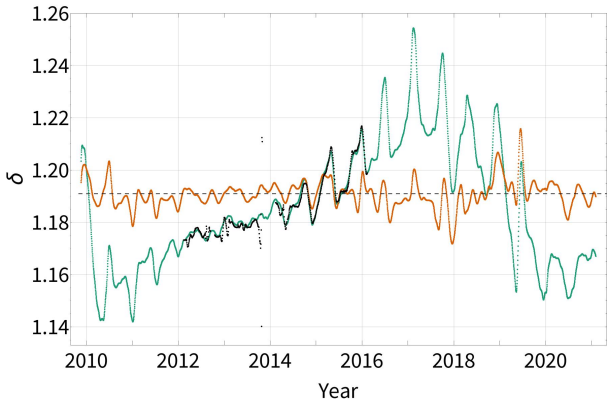

(c) Gravimetric factor of $\mathbf{L}_2$ group

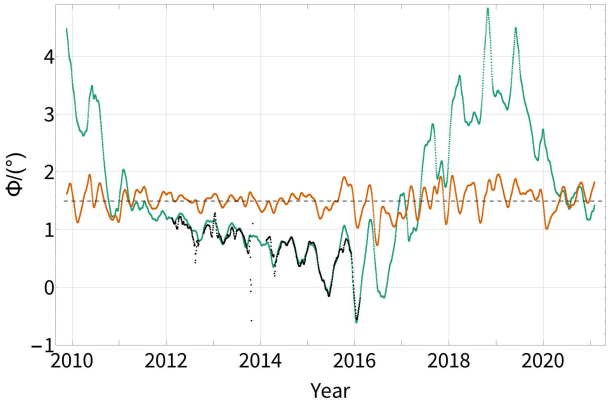

(d) Gravimetric phase of $\mathbf{L}_2$ group

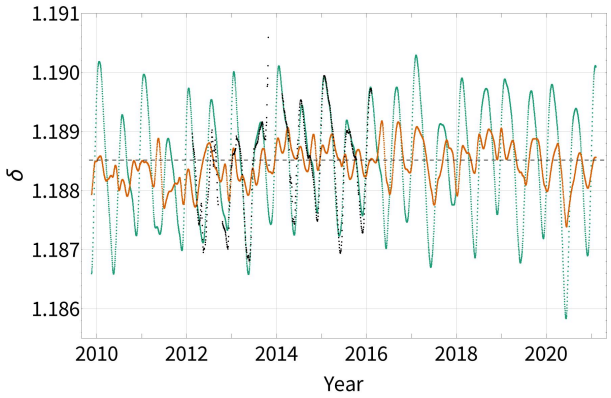

(e) Gravimetric factor of $\mathbf{S}_2$ group

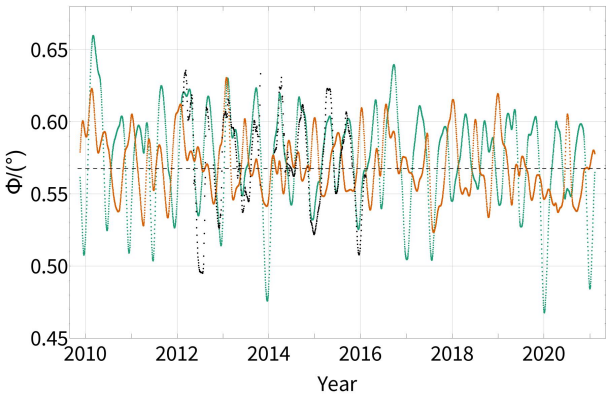

(f) Gravimetric phase of $\mathbf{S}_2$ group

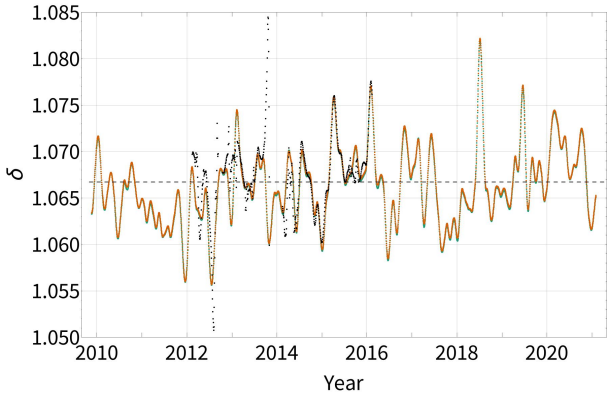

(g) Gravimetric factor of $\mathbf{M}_3$* group

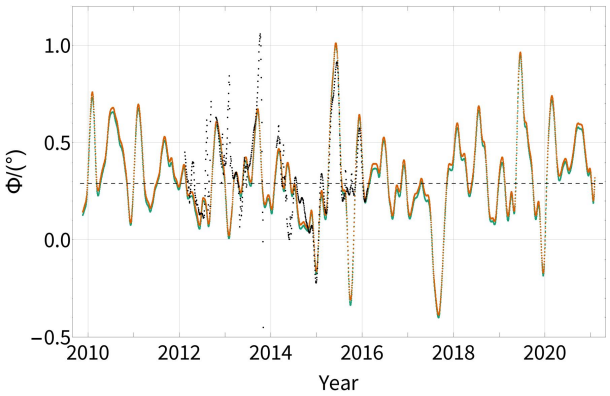

(h) Gravimetric phase of $\mathbf{M}_3$* group

Figure 6.4.: The results of MWA for tidal groups $\mathbf{M}_2$, $\mathbf{L}_2$, $\mathbf{S}_2$ and $\mathbf{M}_3$* (top to bottom) for gravimetric factor (left) and phase (right). Colors: green: MWA with a-priori WDZe-model, orange: MWA with a-priori BF21-model, black: results by Schroth et al. (2018) for comparison.

6.5. Histograms of Moving Window Analysis

We certainly expect noise in the data which would influence the estimates. For short windows in MWA the distribution of parameter estimates may reflect the actual noise. Hence, I created histograms of parameter values in moving window analysis, for two investigated a priori response models, displayed in Figs. 6.5 - 6.7. For most groups, the distribution is more reasonable, Gaussian, if the BF21 was used. The parameters with WDZe have distribution that does not meet the expectation, i.e. is rather uniform than normal, has high skewness or appears as a sum of two Gaussians. Such properties are clear in groups $\mathbf{K}_1$, $\mathbf{N}_2$ or $\mathbf{L}_2$, both factor and phase, reaching extreme values in $\mathbf{L}_2$. In fact, the small improvement in terms of narrowing the distribution is even noticeable for $\mathbf{M}_2$. This suggests that the actual noise in the data may show Gaussian nature for given frequency ranges.

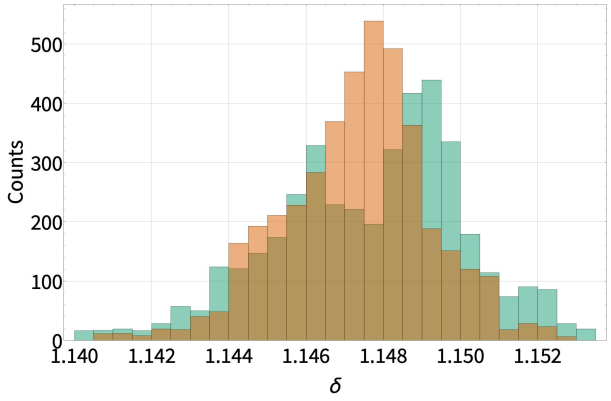

(a) Gravimetric factor of $\mathbf{Q}_1$ group

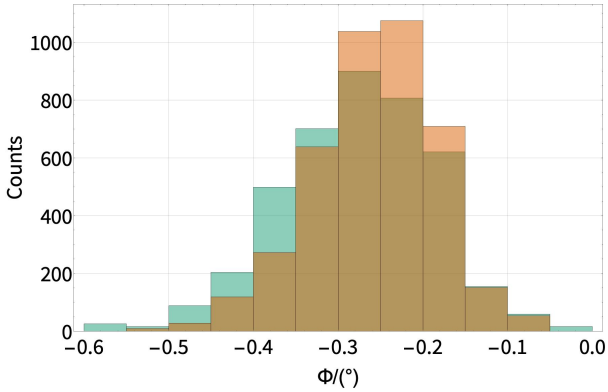

(b) Gravimetric phase of $\mathbf{Q}_1$ group

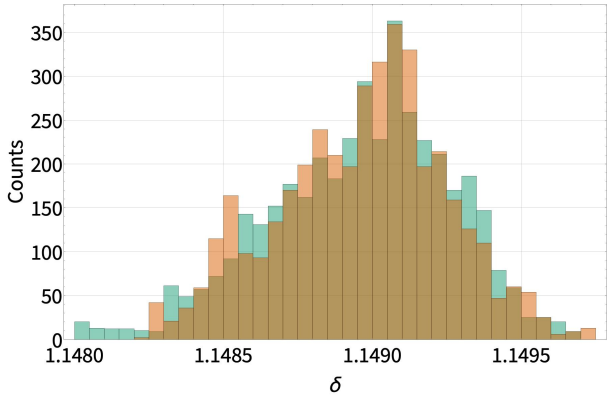

(c) Gravimetric factor of $\mathbf{O}_1$ group

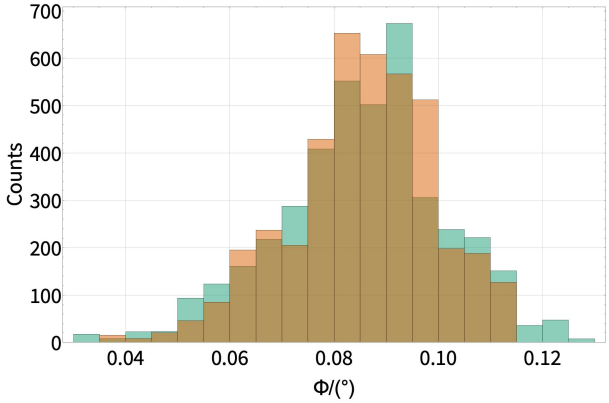

(d) Gravimetric phase of $\mathbf{O}_1$ group

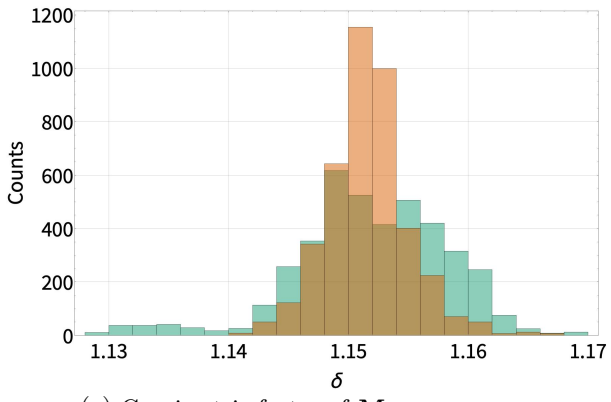

(e) Gravimetric factor of $\mathbf{M}_1$ group

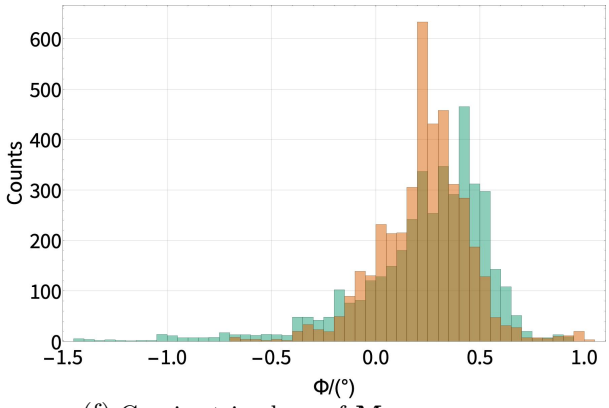

(f) Gravimetric phase of $\mathbf{M}_1$ group

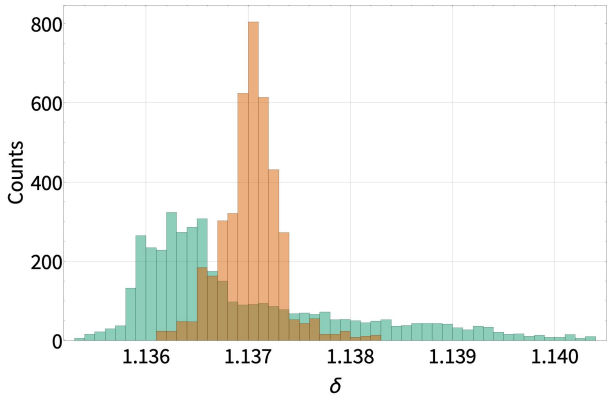

(g) Gravimetric factor of $\mathbf{K}_1$ group

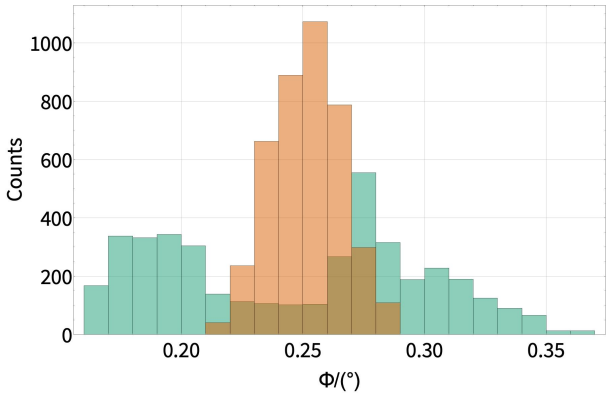

(h) Gravimetric phase of $\mathbf{K}_1$ group

Figure 6.5.: The histograms of moving window analysis for tidal groups $\mathbf{Q}_1$, $\mathbf{O}_1$, $\mathbf{M}_1$ and $\mathbf{K}_1$ (top to bottom) for gravimetric factor (left) and phase (right). Colors: green: MWA with a-priori WDZe-model, orange: MWA with a-priori BF21-model.

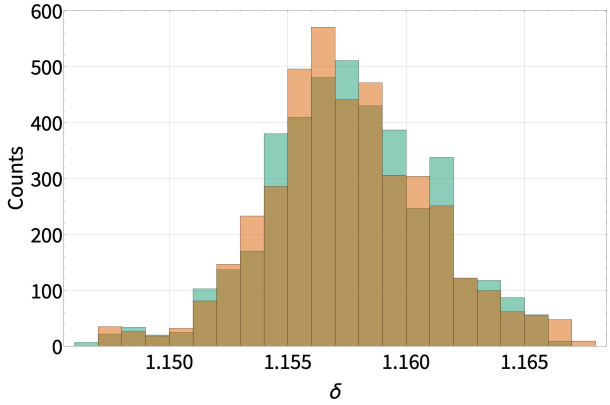

(a) Gravimetric factor of $\mathbf{J}_1$ group

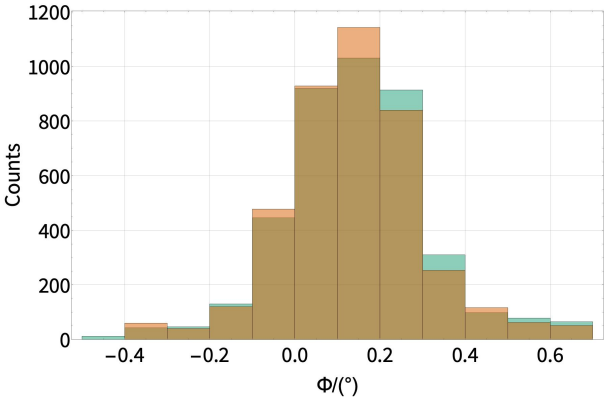

(b) Gravimetric phase of $\mathbf{J}_1$ group

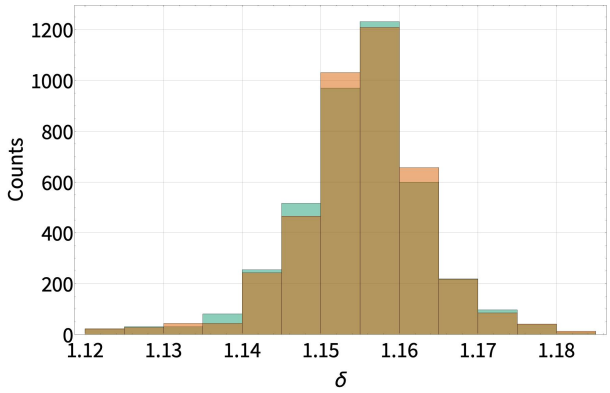

(c) Gravimetric factor of $\mathbf{OO}_1$ group

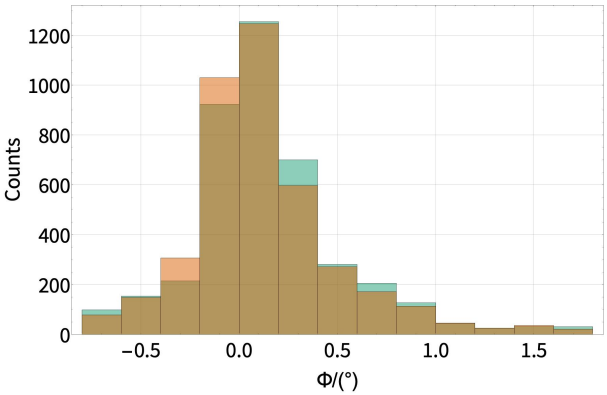

(d) Gravimetric phase of $\mathbf{OO}_1$ group

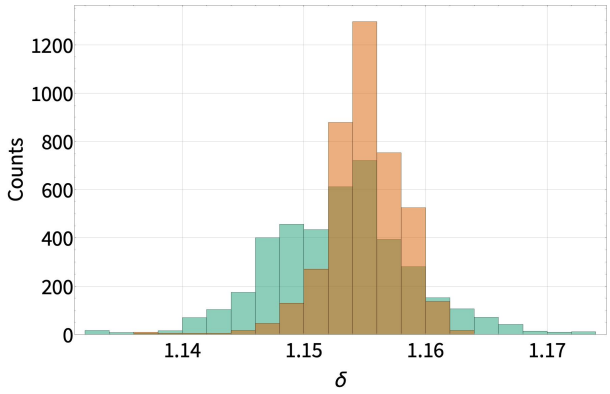

(e) Gravimetric factor of $\boldsymbol{\mu}_2$ group

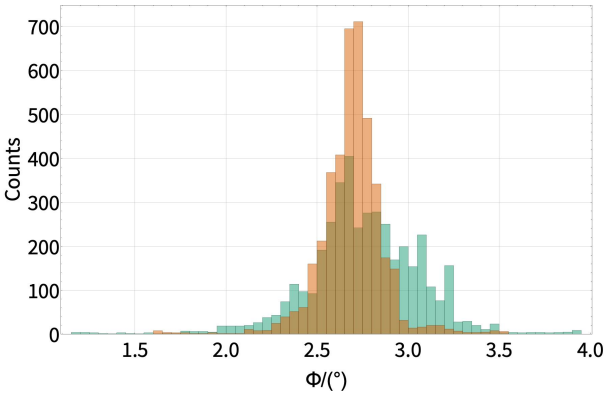

(f) Gravimetric phase of $\boldsymbol{\mu}_2$ group

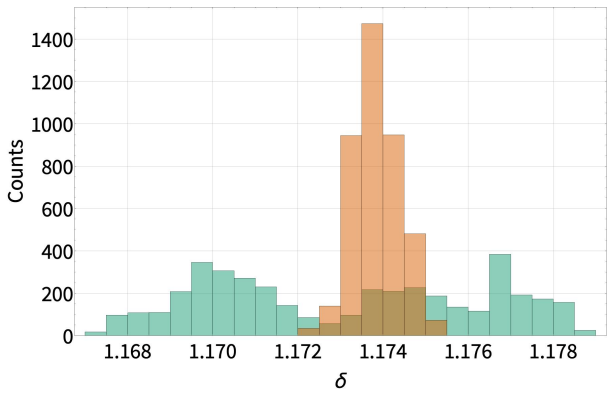

(g) Gravimetric factor of $\mathbf{N}_2$ group

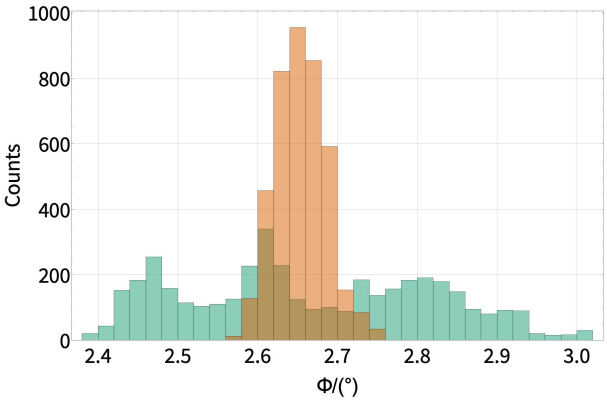

(h) Gravimetric phase of $\mathbf{N}_2$ group

Figure 6.6.: The histograms of moving window analysis for tidal groups $\mathbf{J}_1$, $\mathbf{OO}_1$, $\boldsymbol{\mu}_2$ and $\mathbf{N}_2$ (top to bottom) for gravimetric factor (left) and phase (right). Colors: green: MWA with a-priori WDZe-model, orange: MWA with a-priori BF21-model.

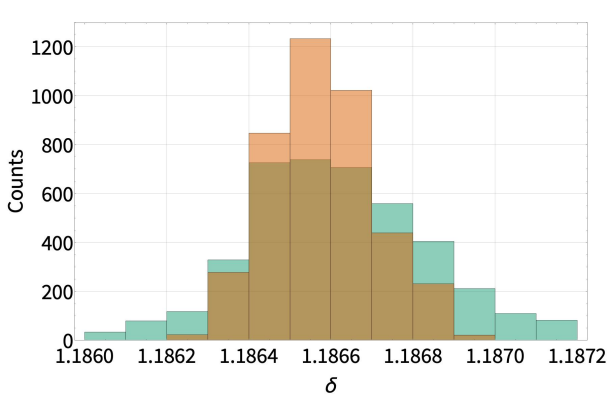

(a) Gravimetric factor of $\mathbf{M}_2$ group

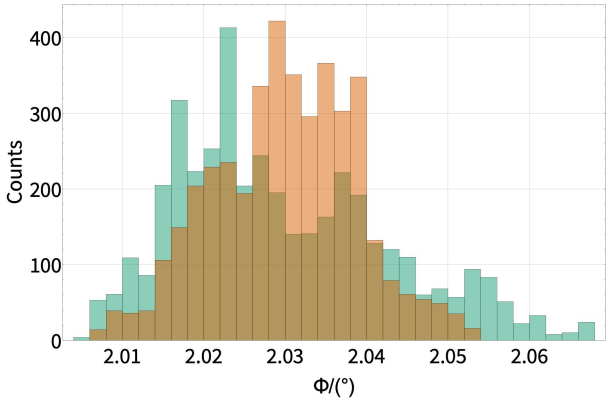

(b) Gravimetric phase of $\mathbf{M}_2$ group

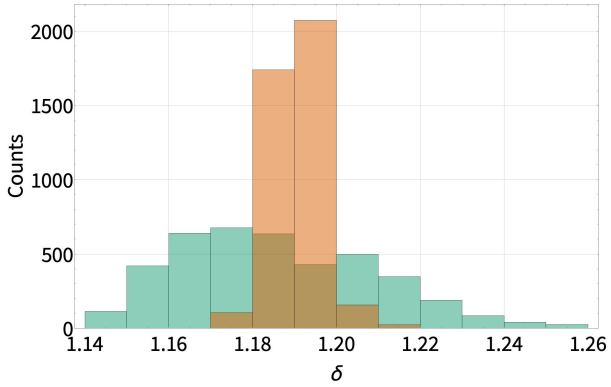

(c) Gravimetric factor of $\mathbf{L}_2$ group

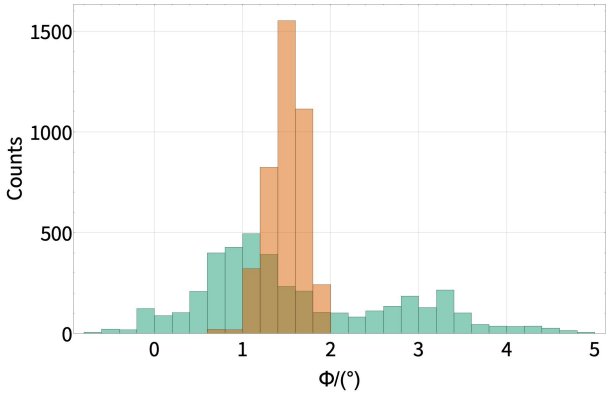

(d) Gravimetric phase of $\mathbf{L}_2$ group

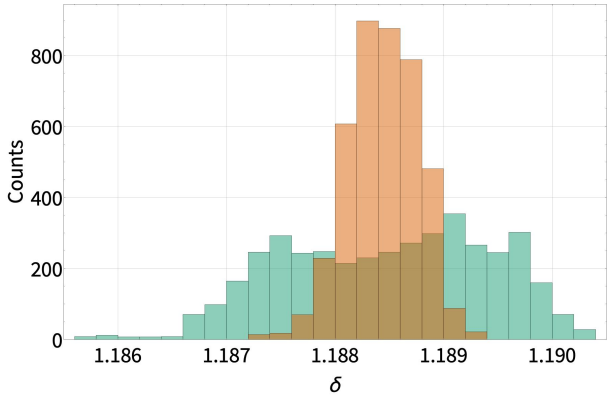

(e) Gravimetric factor of $\mathbf{S}_2$ group

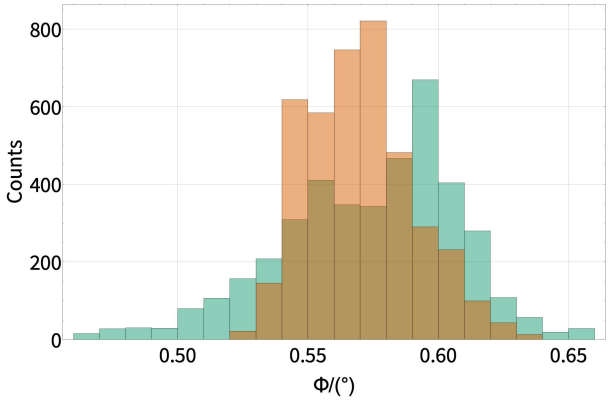

(f) Gravimetric phase of $\mathbf{S}_2$ group

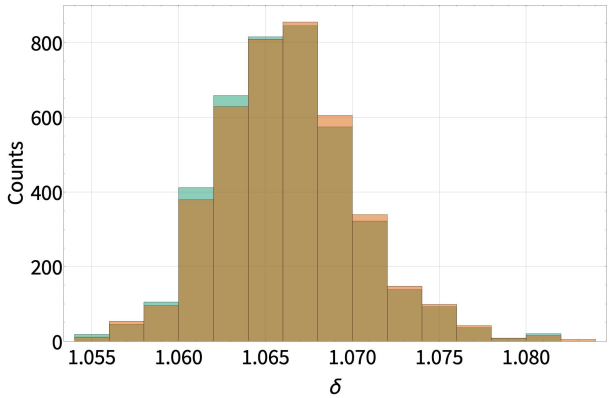

(g) Gravimetric factor of $\mathbf{M}_3$* group

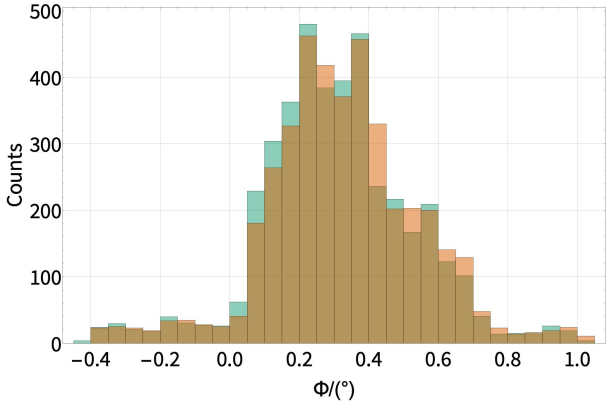

(h) Gravimetric phase of $\mathbf{M}_3$* group

Figure 6.7.: The histograms of moving window analysis for tidal groups $\mathbf{M}_2$, $\mathbf{L}_2$, $\mathbf{S}_2$ and $\mathbf{M}_3$* (top to bottom) for gravimetric factor (left) and phase (right). Colors: green: MWA with a-priori WDZe-model, orange: MWA with a-priori BF21-model.

6.6. Spectra of Moving Window Analyses

The results of MWA with WDZe a priori body tide model showed a clear modulation of harmonic signals. Therefore, I identified the frequencies and relative amplitudes of such variations with spectral analysis. The application of the local response model BF21 resulted in a decrease of such modulation, given the signal is coherent, i.e. has constant amplitude, frequency and phase. The plots with Fourier spectra of the MWA are displayed in Figs. 6.2 - 6.4. The Fourier amplitude spectra are displayed in Figs. 6.8 - 6.10. The units on the y-axis are arbitrary (a.u.). The MWA results were not tapered for the purpose of this analysis. Linear trends with constant offsets were subtracted before applying the Fourier transformation. Groups $\mathbf{K}_1$, $\boldsymbol{\mu}_2$ and $\mathbf{N}_2$ are good demonstrations of the method and the beating problem with WDZe model. Particular modulation frequencies in $\mathbf{L}_2$, $\mathbf{N}_2$ and $\mathbf{M}_2$ were significantly decreased. They are consequence of fixed ratio of degree 3 to the main degree 2 harmonic at a distance of $1/8.8 \approx 0.11$ per year ($\mathbf{L}_2$, $\mathbf{N}_2$), as well as other tides degree 2 at other frequencies.

Overtone patterns in $\mathbf{M}_1$ or $\mathbf{J}_1$ are not present if the local response model was used. Similarly, the peaks in $\mathbf{Q}_1$ and $\mathbf{O}_1$ for frequencies around 12 cpy (1/month) and 2 cpy, respectively, have smaller amplitude. In these two groups one may notice some subtle adjustments (stronger for phase) in long-period frequencies which must result from the improved degree 2 to 3 ratio at a distance of $1/8.8 \approx 0.11$ per year.

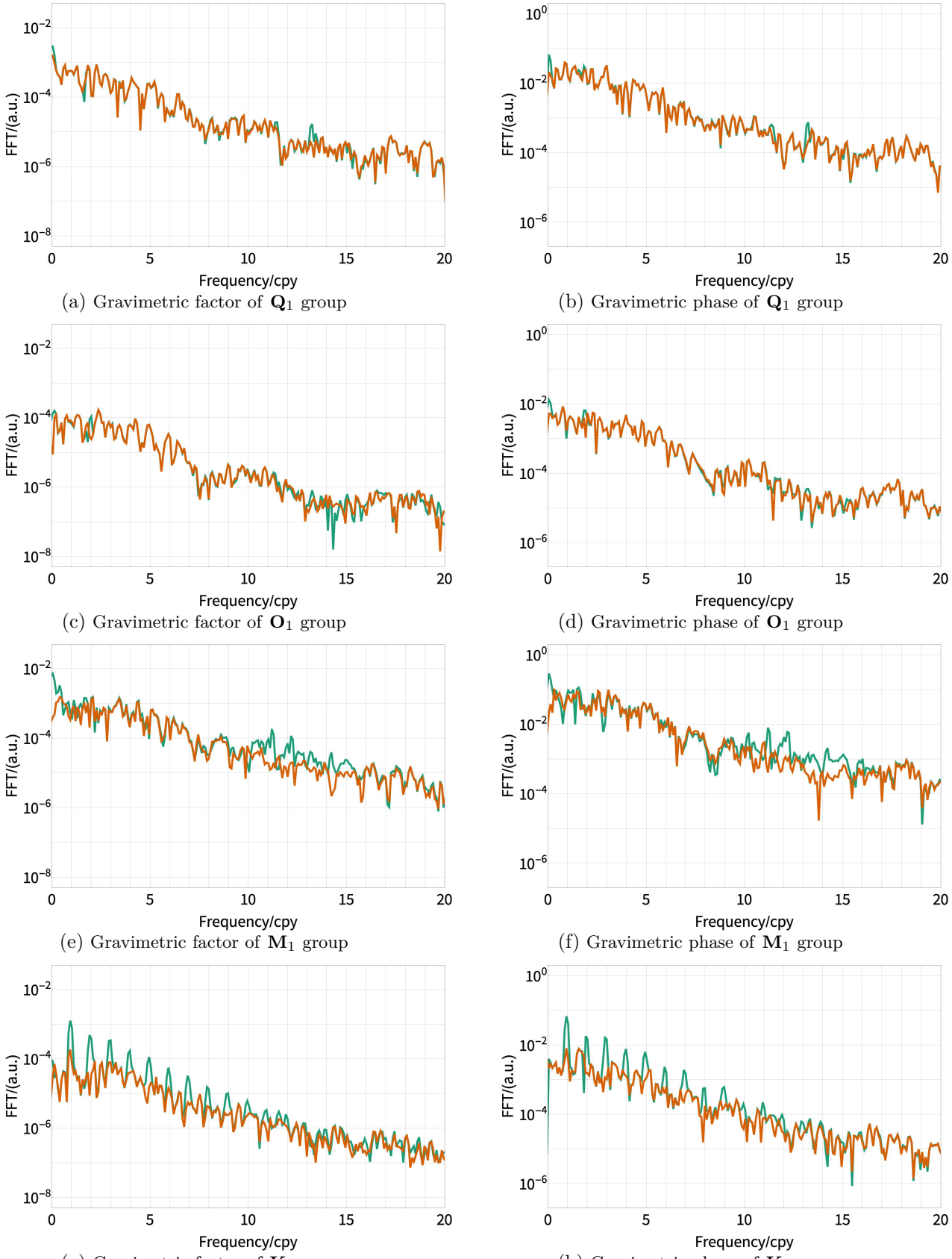

(a) Gravimetric factor of $\mathbf{Q}_1$ group

(b) Gravimetric phase of $\mathbf{Q}_1$ group

(c) Gravimetric factor of $\mathbf{O}_1$ group

(d) Gravimetric phase of $\mathbf{O}_1$ group

(e) Gravimetric factor of $\mathbf{M}_1$ group

(f) Gravimetric phase of $\mathbf{M}_1$ group

(g) Gravimetric factor of $\mathbf{K}_1$ group

(h) Gravimetric phase of $\mathbf{K}_1$ group

Figure 6.8.: The spectra of moving window analysis for tidal groups $\mathbf{Q}_1$, $\mathbf{O}_1$, $\mathbf{M}_1$ and $\mathbf{K}_1$ (top to bottom) for gravimetric factor (left) and phase (right). Colors: green: MWA with a-priori WDZe-model, orange: MWA with a-priori BF21-model.

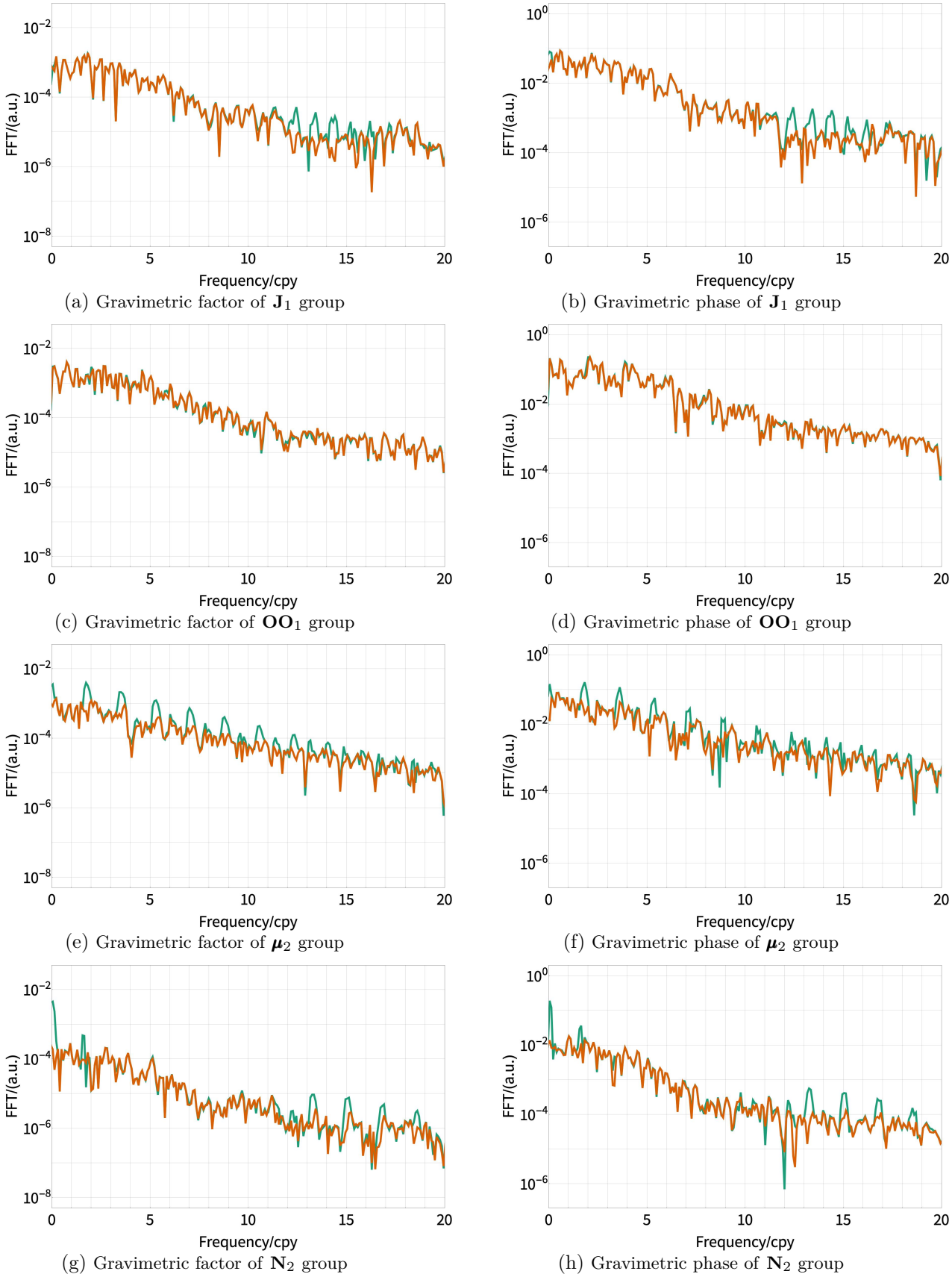

(a) Gravimetric factor of $\mathbf{J}_1$ group

(b) Gravimetric phase of $\mathbf{J}_1$ group

(c) Gravimetric factor of $\mathbf{OO}_1$ group

(d) Gravimetric phase of $\mathbf{OO}_1$ group

(e) Gravimetric factor of $\boldsymbol{\mu}_2$ group

(f) Gravimetric phase of $\boldsymbol{\mu}_2$ group

(g) Gravimetric factor of $\mathbf{N}_2$ group

(h) Gravimetric phase of $\mathbf{N}_2$ group

Figure 6.9.: The spectra of moving window analysis for tidal groups $\mathbf{J}_1$, $\mathbf{OO}_1$, $\boldsymbol{\mu}_2$ and $\mathbf{N}_2$ (top to bottom) for gravimetric factor (left) and phase (right). Colors: green: MWA with a-priori WDZe-model, orange: MWA with a-priori BF21-model.

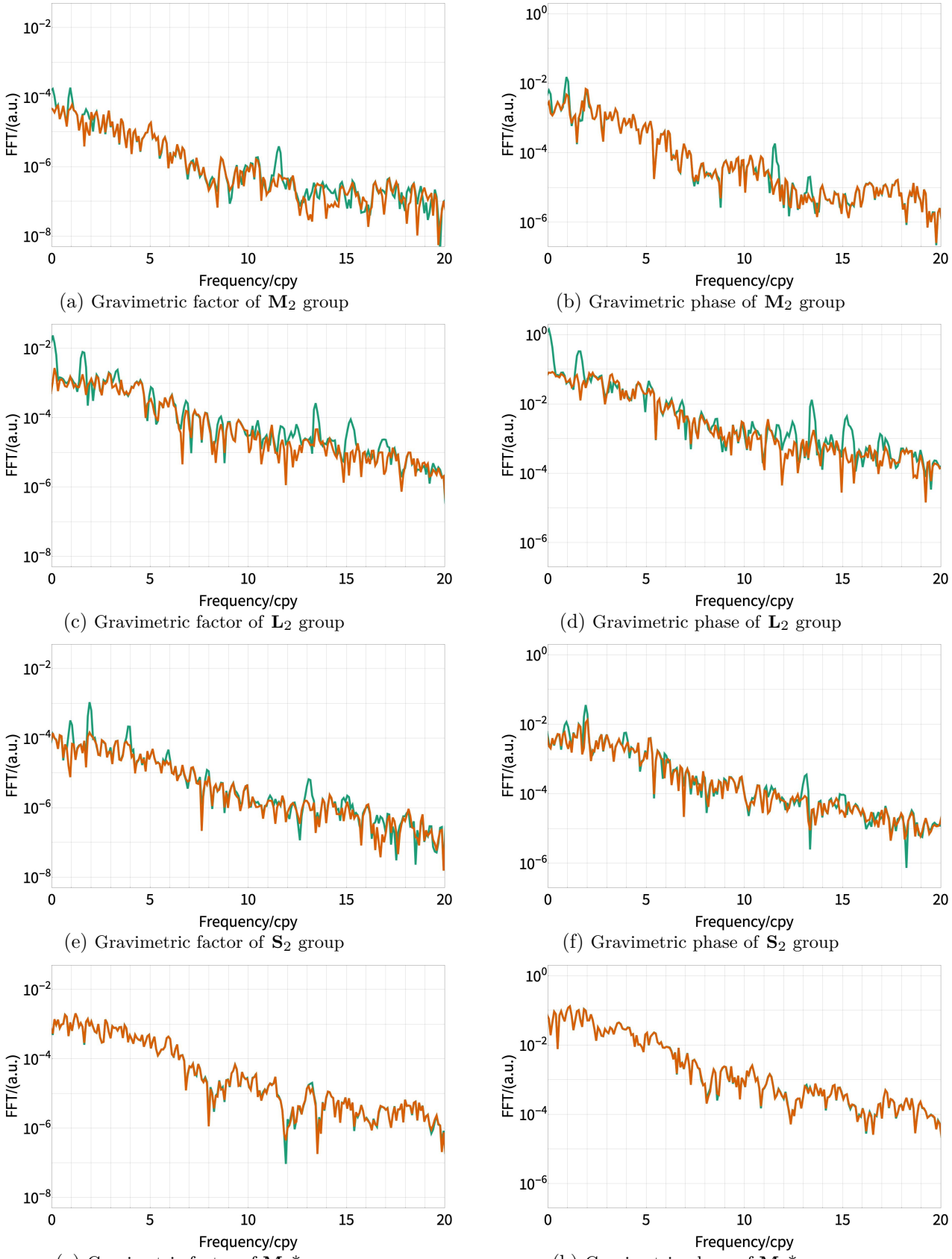

(a) Gravimetric factor of $\mathbf{M}_2$ group

(b) Gravimetric phase of $\mathbf{M}_2$ group

(c) Gravimetric factor of $\mathbf{L}_2$ group

(d) Gravimetric phase of $\mathbf{L}_2$ group

(e) Gravimetric factor of $\mathbf{S}_2$ group

(f) Gravimetric phase of $\mathbf{S}_2$ group

(g) Gravimetric factor of $\mathbf{M}_3$* group

(h) Gravimetric phase of $\mathbf{M}_3$* group

Figure 6.10.: The spectra of moving window analysis for tidal groups $\mathbf{M}_2$, $\mathbf{L}_2$, $\mathbf{S}_2$ and $\mathbf{M}_3$* (top to bottom) for gravimetric factor (left) and phase (right). Colors: green: MWA with a-priori WDZe-model, orange: MWA with a-priori BF21-model.

6.7. Parameter Trade-Off and Variation Confirmation

After application of the local response adjustments (BF21) to the a priori WDZe body tide model (eq. 3.44), I found out that the main cause of temporal variations are wrongly assumed ratio between admittances of specific tides forming a MWA group. In most cases, there is not only one ratio that differs within a group with various modulation frequencies. With our approach, we can investigate in detail which harmonic ratio is responsible for each beat in the MWA. The simple experiment for $\mathbf{K}_1$ group is demonstrated in Fig. 6.11. Different ratios between K_1, S_1 and P_1 have been used, and the temporal variations of $\mathbf{K}_1$ group has been investigated. We hence confirm, that S_1 is the main contributor to the temporal variations due to the wrong $\delta_{S_1}/\delta_{K_1}$ ratio and $\Phi_{S_1} - \Phi_{K_1}$ difference. Schroth et al. (2018) suggested that a trade-off between parameters may occur in LS solution if parameters cannot be well determined. If this was true in this grouping setup, significant modification of a priori model for one group should also affect estimates of the others. Large differences for only one group, a column in matrices $\bar{\boldsymbol{C}}^{\text{ini}}$ and $\bar{\boldsymbol{S}}^{\text{ini}}$ should then result in a signal 'leaking' to other groups, since the regressors cannot fit the signal properly. This appears to not be the case, and the groups are so well constraint that there is no difference for other groups. Only the altered group obtains modified estimates, regardless of time window. Since S_1 is radiation driven, one may expect that at least pressure regressor factor should change after such modficiations in $\mathbf{K}_1$ group. As shown in Fig. 6.11 even for this parameter it appears to be a minor effect. The other groups did not show any difference in their temporal variations for different S_1, K_1, P_1 ratios investigated here.

6.8. MWA of Air Pressure and Data Misfit

Figures 6.12 display the results of MWA for air pressure factor and data misfit. The expectation is that the variation in air pressure coefficient should not be strongly altered depending on the a priori model used. This is confirmed in the figures. The data misfit (tapered and untapered) should be in general slightly smaller with the BF21. The results matched these expectation, however, there are some (not many) instances where misfit is larger if the BF21 is used, compared to WDZe. Dashed lines provide values that are results from the analysis of the full time series. The temporal variation of the air pressure do not change significantly between applied models.

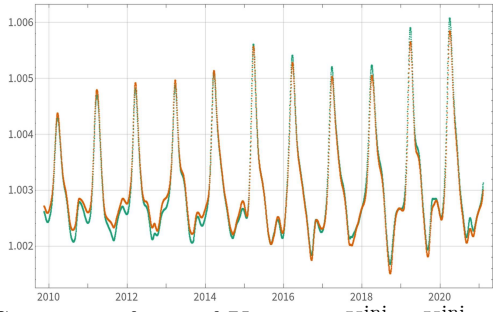

(a) Gravimetric factor of $\mathbf{K}_1$, given $X^{\text{ini}}_{S_1} = X^{\text{ini}}_{K_1} = X^{\text{ini}}_{P_1}$ in the BF21 a priori model. The change in variation is due to the improved $X^{\text{ini}}_{\kappa_1}/X^{\text{ini}}_{K_1}$ and $X^{\text{ini}}_{K_{1*}}/X^{\text{ini}}_{K_1}$.

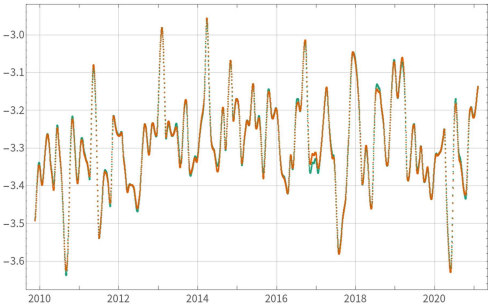

(b) Air pressure coefficient change for Fig. 6.11a case.

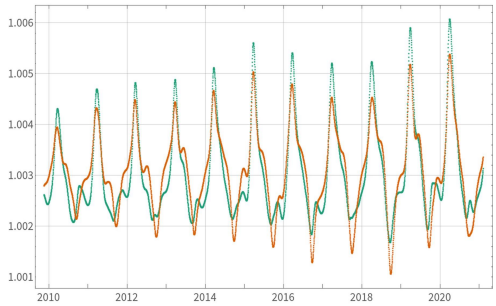

(c) Gravimetric factor of K_1, given $X^{\text{ini}}_{S_1} = X^{\text{ini}}_{K_1}$ in the BF21 a priori model. The change in variation is due to the improved $X^{\text{ini}}_{K_1}$ ratio to $X^{\text{ini}}_{\kappa_1}$, $X^{\text{ini}}_{P_1}$ and $X^{\text{ini}}_{K_{1*}}$.

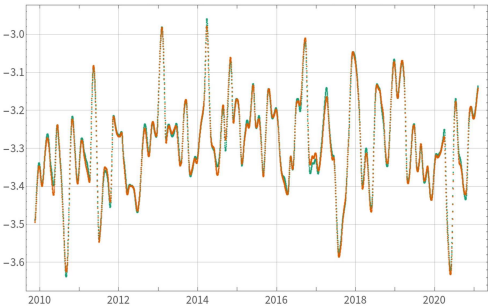

(d) Air pressure coefficient change for Fig. 6.11c case.

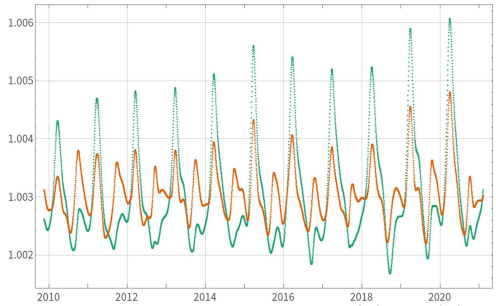

(e) Gravimetric factor of K_1, given $X^{\text{ini}}_{P_1} = X^{\text{ini}}_{K_1}$ in the BF21 a priori model. The change in variation is due to the improved $X^{\text{ini}}_{K_1}$ ratio to $X^{\text{ini}}_{\kappa_1}$, $X^{\text{ini}}_{S_1}$ and $X^{\text{ini}}_{K_{1*}}$.

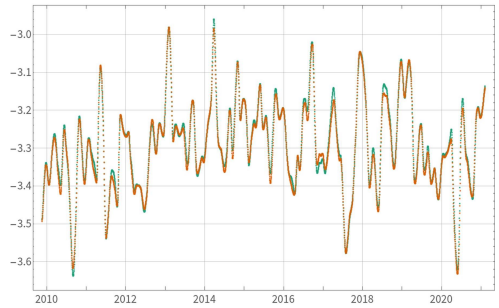

(f) Air pressure coefficient change for Fig. 6.11e case.

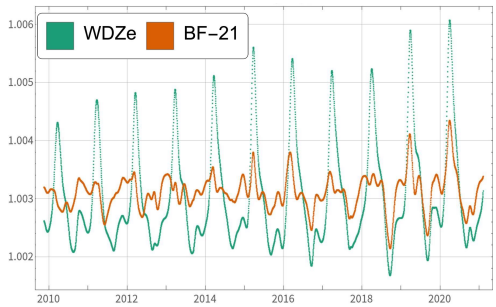

(g) Gravimetric factor of K_1, given BF21 a priori model. The main change in variation is due to the improved all ratios.

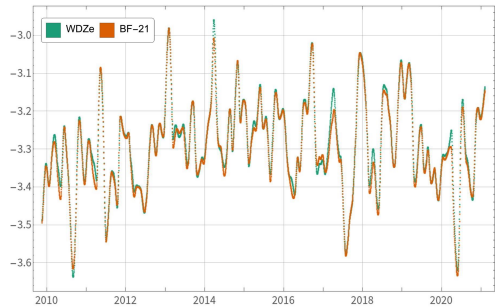

(h) Air pressure coefficient change for Fig. 6.11g case.

Figure 6.11.: The results of MWA for tidal group $\mathbf{K}_1$ air pressure factor. Some ratios in BF21-model were altered for the purpose of the test. Colors: blue-green: MWA with a-priori WDZe-model, orange: MWA with a-priori BF21-model or its variation. The significance of a proper $X^{\text{ini}}_{S_1}/X^{\text{ini}}_{K_1}$ ratio is clear. We notice lack of significant changes for air pressure factor due to the modified ratio.

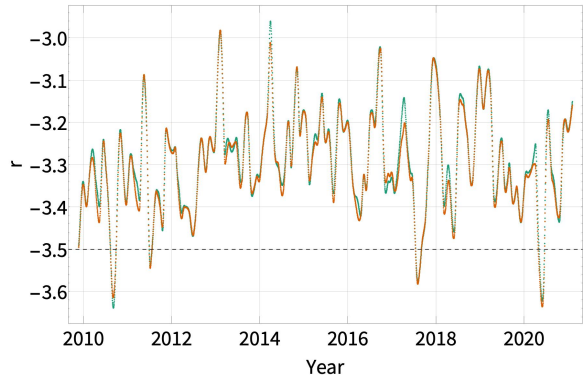

(a) Regression factor of air pressure

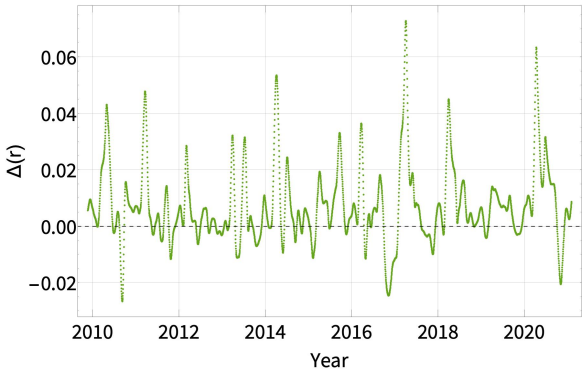

(b) Differences in air pressure regression factor.

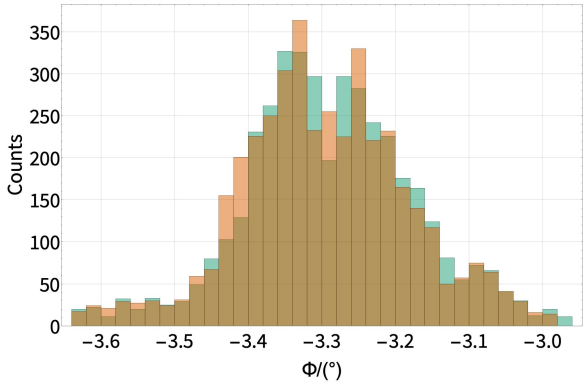

(c) Histogram of the coefficient for air pressure regression factor

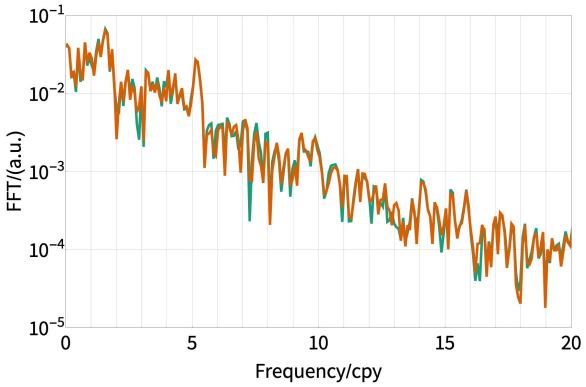

(d) Spectra of the coefficient for air pressure regression factor.

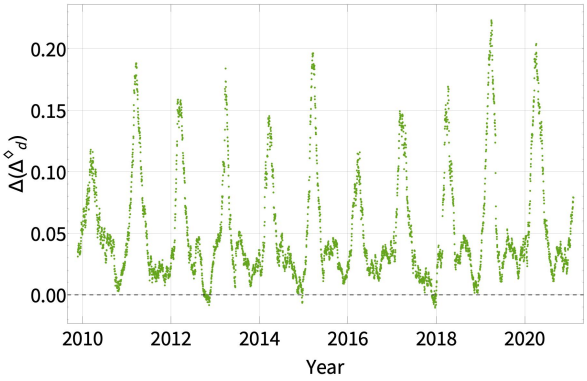

(e) Differences in data misfit of untapered signals.

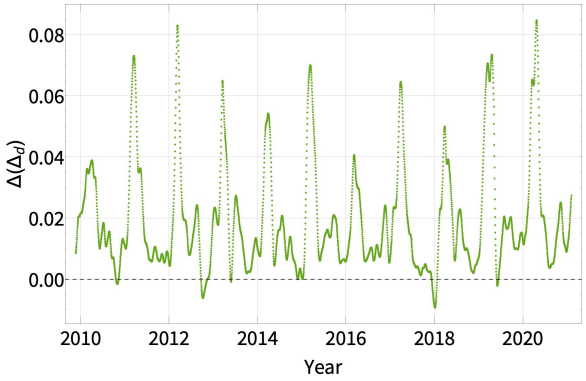

(f) Differences in data misfit of tapered signals.

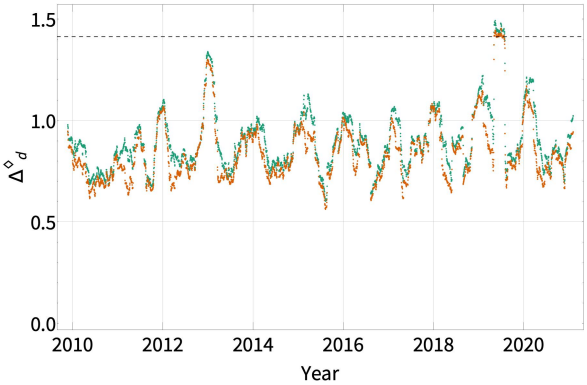

(g) Data misfit of untapered signals.

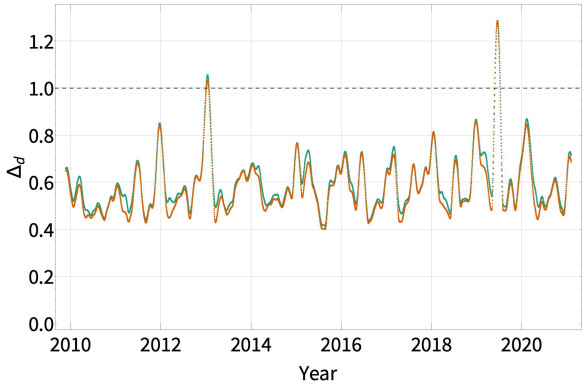

(h) Data misfit of tapered signals.

Figure 6.12.: The moving window analysis: air pressure regression factor, its spectra and distribution; data misfit tapered and untapered. Colors: blue-green: MWA with a-priori WDZe-model, orange: MWA with a-priori BF21-model, green - differences between these two, WDZe-model - BF21-model.

6.9. Time-Variant Admittance

The results from the moving window analysis indicate that the actual admittance changes with time. Hence, there exists no single true value with error bars. The results specify a corridor in which the parameters of local time-invariant model are expected to be found. In that sense the error bound in Tables 5.3 and 5.4 are consistent with the variation seen in Figs. 6.1 - 6.4. It appears that the time-invariant parameters for harmonics μ_2, N_2, L_2, and the large-amplitude satellites are derived with a high accuracy, below the level of the remaining variation seen for groups $\boldsymbol{\mu}_2$, $\mathbf{N}_2$, $\mathbf{L}_2$ containing these harmonics. Certainly, the local response model is constrained by 11.5 years of data, a time span much larger than the period of the remaining cycles seen in the MWA.

6.10. Summary

The too coarse frequency resolution in traditional, unconstrained tidal analysis was suspected to be the cause of some of the temporal variations found for tidal parameters. The results presented in the current contribution corroborate this hypothesis. We use the local response model BF21 as the a-priori body-tide model in an unconstrained moving window analysis (MWA). The MWA uses the same wave grouping as applied by Schroth et al. (2018). We demonstrate that the quasi-periodic temporal variations for some wave groups are reduced by up to a factor of seven in amplitude. We compared harmonics that were suggested by Schroth et al. (2018) for causes of variations. For groups $\mathbf{M}_1$, $\mathbf{K}_1$, $\boldsymbol{\mu}_2$, $\mathbf{N}_2$, $\mathbf{L}_2$, and $\mathbf{S}_2$ temporal variations are clearly reduced or even vanish. For $\mathbf{K}_1$ it is not only essential to keep the radiation tides (S_1) separate, but also to allow for a small adjustment of the frequency dependence within the NDFW resonance. The latter most likely is not due to the FCN model used in the a-priori body tide model being wrong, but due to unknown ocean loading effects taking place in this frequency band. Only part of the variations previously seen for $\mathbf{M}_2$ are captured by the local response model as well. This leaves room for the remaining variations of the parameters for $\mathbf{M}_2$ being caused by time varying ocean loading, as discussed by Schroth (2020). Some of the constituents (like α_2, β_2, or S_1), which are responsible for the temporal variation of larger groups, turn out to be not constant themselves. In the BF21-model they do not exactly capture the time-invariant tidal response of the Earth, but rather the specific response (in case of α_2 and β_2) or a specific non-tidal signal contribution (in case of S_1) in the analyzed time window. In our investigations we have not found any proof of significant cross-talk between estimates of tidal parameters between wave groups, if we assume improper ratio (Fig. 6.11). It points into the direction, that signal is harmonic enough and relatively close to the true values such that it only interferes with the frequencies within the group. The example of $\mathbf{K}_1$ group (Fig. 6.11) demonstrates that significant beats are caused by the wrong ratio between the main harmonic K_1 with another harmonic of large amplitude (P_1)

as well as with a harmonic with the amplitude 100 times smaller but whose estimates are far from theory (S_1). Since S_1 is radiation tide, it is not uniform between years, hence we cannot get rid of it completely in the MWA. Similarly, modulation within group $\mathbf{M}_2$ is time dependent, yet we can decrease its amplitude with estimates of harmonics like α_2 or β_2. Groups whose response is expected to be more time-invariant, like $\mathbf{L}_2$, shows the full power of the method, by reducing its unique temporal variation to variation appearing similar to the random signal. This way our analysis clearly shows that in a search for time-variant components of Earth's admittance, a detailed local reference model must be used as a basis to which adjustments are applied. Then the remaining variations can be more reliably investigated for the response changes, or identification of instrument stability or data pre-processing problems. To find this detailed model of the local response, regularization and data-driven grouping are needed. Approaches based on a priori grouping schemes, like based on the Rayleigh criterion, likely miss essential properties of the admittance function.

7. Comparison of 13 Stations Distributed on the Globe in Terms of a Local Response Model

7.1. Introduction

I applied the `RATA` regularization method to tidal analysis in order to determine the response model of other stations. The method was explained in Chapter 3 and demonstrated in Chapter 5. As discussed in Chapter 4, I focused on the longest high-quality data, which were pre-processed consistently across different stations at different continents. For verification purposes, I additionally selected a few closely located stations in Central and Western Europe. The objective is to provide detailed, data-driven tidal responses. We should not expect significant deviations from the model for stations that are in close proximity to each other except for radiation tides. Hence, the local response models for all stations located in Central Europe should be rather similar and their comparison serves as s proxy for the method. I included Membach in the study to investigate how the distance to the North Sea may affect the results. By studying stations in different parts of the world, we can derive better local response models. It is important to note that I did not apply corrections for ocean response in the same way as Schroth (2020) and Sulzbach et al. (2022), nor do I discuss global properties to discriminate between earth models, as demonstrated by Baker and Bos (2003) and Ducarme (2012). However, the estimates derived using the `RATA` method can be used for future investigations that implement ocean loading corrections. The precision achieved with superconducting gravimeters would greatly benefit from accurate cotidal oceanic maps, not only for the main constituents but also for the minor ones. Corrections for ocean loading could aid in determining common patterns around the globe in the follow-up study and help discriminate between tidal models.

Local response models are necessary for adjustments in a priori local response models used to study temporal variations. The model captures the harmonic signals at tidal frequencies contributing to the local response. By using the actual response, we can determine how much of the temporal variations are real and how significant the incorrect ratio is in other stations. I consider the MWA as a satisfactory cross-validation technique for the `RATA` method. After estimating the model, in Chapter 8, I perform the analysis with the a priori grouping to provide some proxy for standard deviations. As discussed in Chapter 5 and Chapter 3, this is just one way to estimate confidence intervals and should be considered carefully.

For the definitions of all tide names and their frequencies, please refer to Chapter 3. Tables with values and detailed plots for the response models are presented in Appendix B. A summary including the number of iterations, data misfit, and resolved groups is provided in Table 7.1.

Table 7.1.: Overview of the `RATA` method applied to all stations. For each station defined by its code and location, the length of the analyzed time series is given. 'Corner $\Delta_d^\diamond$' represents the data misfit value of the misfit corner at the initial iteration. 'Final $\Delta_d^\diamond$' is the data misfit value for the final local response model after the last iteration. The columns 'Deg-2' and 'Deg-3' provide information about the number of resolved groups. 'It.' column indicates the number of iterations required to obtain the final estimate, and the last column, 'r' is the estimated air pressure admittance factor.

Code	Location	time	Corner $\Delta_d^\diamond$	Final $\Delta_d^\diamond$	Deg-2	Deg-3	It.	r
		years	$\mathrm{nm\,s^{-2}}$	$\mathrm{nm\,s^{-2}}$				
BH	Bad Homburg	9.534	0.82	0.80	50	13	3	-3.3309
CB	Canberra	22.547	1.00	0.97	59	17	3	-3.4318
CA	Cantley	13.093	2.38	2.38	46	10	2	-3.4256
DJ	Djougou	6.896	1.20	1.10	40	12	4	-3.2236
KA	Kamioka	7.817	1.70	1.64	49	13	4	-3.0432
MB	Membach	21.525	1.14	1.13	55	14	2	-3.2836
MO	Moxa	19.990	0.90	0.84	57	14	2	-3.3343
MOu	(upper sensor)	18.954	0.90	0.89				-3.3533
NY	Ny-Ålesund	7.403	4.27	3.28	36	12	4	-4.3250
BF	Schiltach	11.470	0.90	0.88	46	14	4	-3.2826
BFu	(upper sensor)	11.470	0.99	0.97				-3.3165
ST	Strasbourg	19.096	0.96	0.94	43	9	3	-3.3904
SU	Sutherland	7.123	1.05	1.03	54	19	2	-3.1102
SY	Syowa	4.160	3.80	3.38	37	11	3	-4.0146
TC	Tigo Concepcion	9.589	1.95	1.89	37	12	3	-3.7020

7.2. The Method and the Display

I follow the method described in Chapter 5. I start with the initial WDZe analysis model and explore the solution for the misfit corner. I then inspect which harmonics deviate strongly from the initial WDZe reference model. In this method, the reference groups may contain various 'fundamental' reference groups, which are defined in Tables 2.3 to 2.5. I take into account the amplitude of forcing harmonics and the broadband RMS noise amplitude. Initially, I define rather coarse reference groups, and I modify the scheme if indications arise to alter the reference groups. Consequently, in the second iteration, I resolve many reference groups, resulting in superfine structure in some sense. In the last iteration, for some stations, I allowed 'final adjustments' to certain tides. I treat S_1 in the same manner as described in Chapter 5. Due to the large amplitudes of LK_1* and M_1*, and the resonant features exhibited by M_1* in the ocean, I decided to group χ_1* with LK_1* rather than with M_1*. However, given the small amplitude of χ_1* and the relatively small differences in the estimates, following the reference model, I

concluded that it has a minor effect on the tide to which its estimate is constrained. In most stations, group κ_1 was treated separately from the initial iteration. I specify all the interesting findings and group splits in consecutive iterations. Due to the theoretical different response of tides degree 4, order 4 from other orders, I define two degree 4 groups, MN_3+ and M_4+. Their amplitudes, however, are very small. The data supports its small deviation from the reference model, which may be nevertheless influenced by noise. Detailed information about the grouping is listed in Appendix B.

In Chapter 5 the acronym BF21 was used to specify final parameters of the local response model estimated for the Black Forest Observatory (lower sensor), δ^{BF21} and Φ^{BF21} were used for gravimetric factor and phase. In this chapter I use δ^{LRM} and Φ^{LRM} gravimetric factor and phase in local response model for a particular station that is discussed. Considering the significant differences in estimates between stations and the different theoretical body responses as described by WDZe for different stations, I display the ratio $\delta^{\mathrm{LRM}}/\delta^{\mathrm{WDZe}}$ instead of the actual estimates for local models, δ^{LRM}. This normalization emphasizes essential information on how much the ratio, as predicted by the theoretical model or in the a priori grouping for MWA, is inadequate. Thus, the focus is on the adjustment needed for the body tide model rather than the estimate values (which may slightly differ even among European stations in theory). The phase of WDZe, as implemented in `Eterna 3.40`, is set to $\Phi^{\mathrm{WDZe}} = 0$ since body tide models derived from seismology do not exhibit significant phase lags, although they assume anelasticity of the mantle (Agnew, 2009; Dehant et al., 1999). As the method heavily relies on the amplitude of the harmonics but allows minor tides to be independent (yet regularized), for the display of final models I scaled the diameter of each point (harmonic) with the theoretical forcing amplitude. Thus, emphasis is placed on the large-amplitude tides. This is essential because out of the 1200 harmonics, only a few dozen are truly important (see Chapter 3.2 for more details). Tides degree 2 and 3 undergo different 'diameter' scaling, since tides degree 3 are relatively weak but they are shown on separate diagrams. For display reasons, estimates of S_1 are usually outside the plot, however their values are stated in the text.

7.3. Double-Sphere Gravimeters

Dual-sensor superconducting gravimeters are essentially two identical sensors located within the same unit, in the same place, measuring the same gravity field simultaneously. They are subject to the same external effects, such as radiation tides, Newtonian attraction of the atmosphere, and local short disturbances. In addition, they generally should encounter the same electronic issues. Consequently, we would anticipate that the tidal estimates obtained from both instruments would be identical. However, as we observed in Chapter 5, this is not the case.

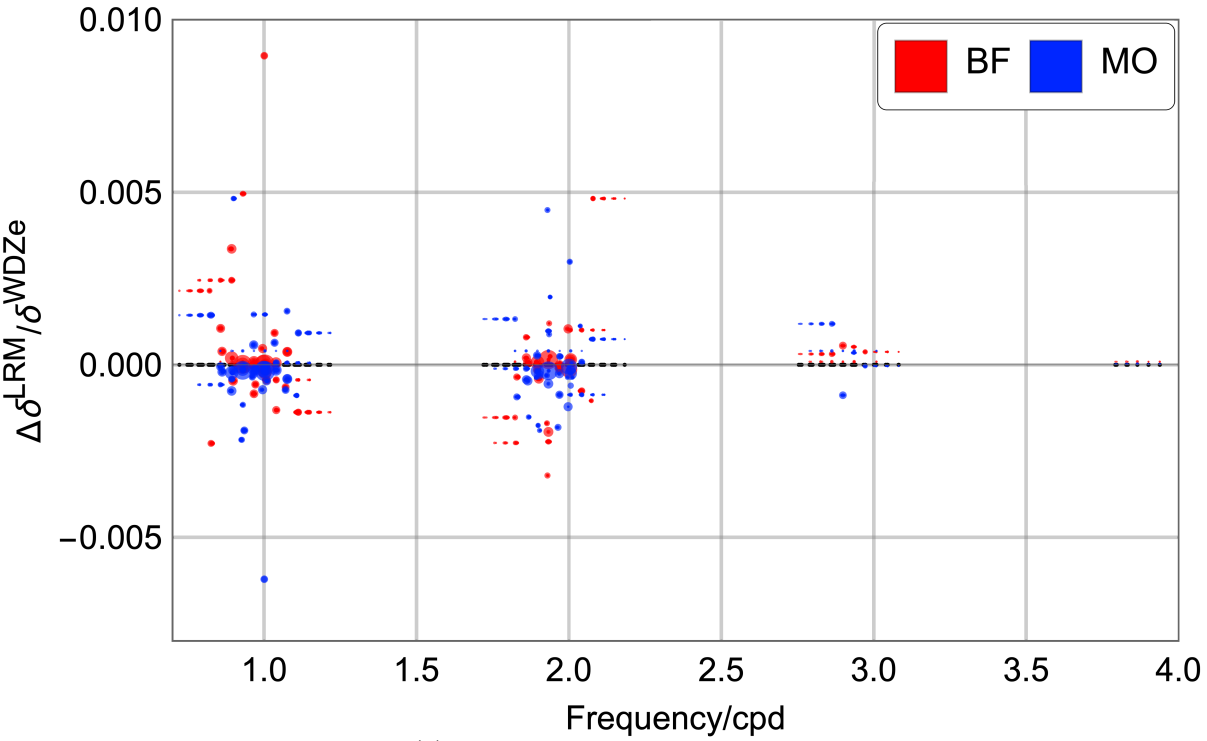

(a) Gravimetric factor differences.

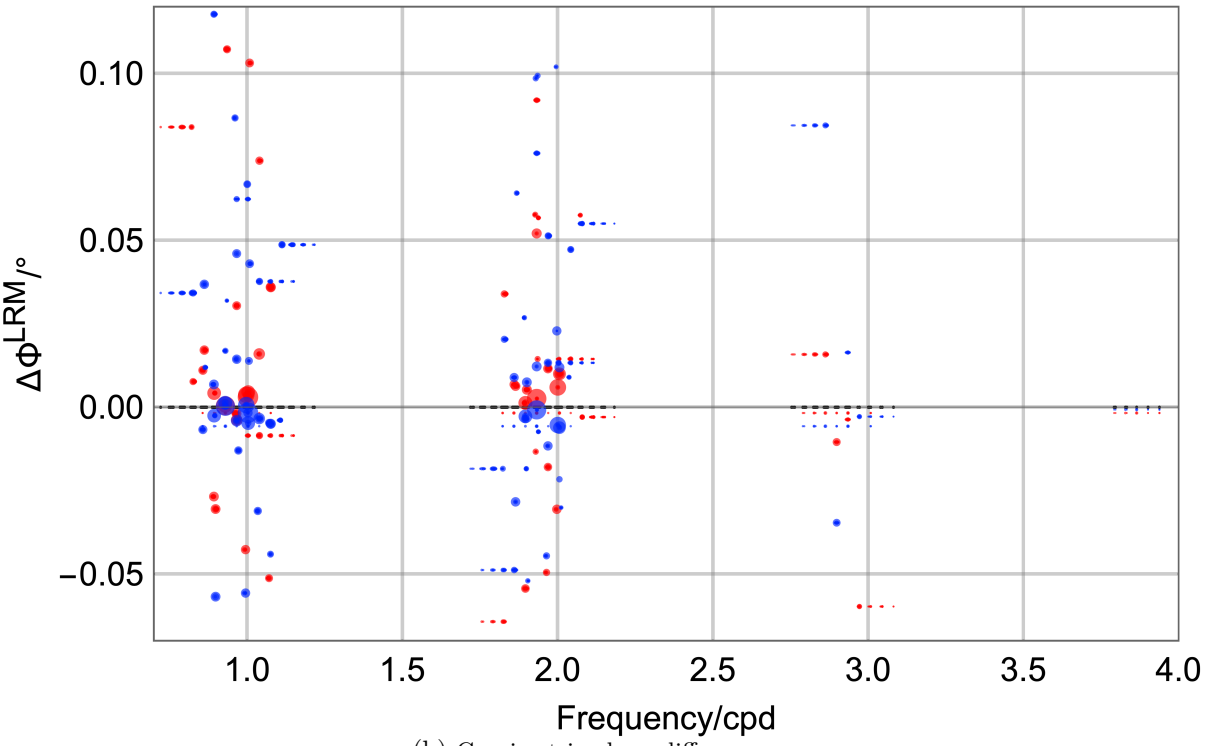

(b) Gravimetric phase differences.

Figure 7.1.: Differences between estimates for tides resulting from `RATA` for two stations with different sensors. The results represent BFO Schiltach (red) and Moxa (blue). The diameter of each point corresponds to the forcing amplitude of the harmonic. Differences are calculated as $\delta_U - \delta_L$, where U represents the upper sensor, and L the lower. Consequently, the phase difference is taken as $\Phi_U - \Phi_L$.

Therefore, the differences between the estimates provide a minimum confidence interval that must be taken into account when comparing them with other stations.

I also examine the Moxa observatory, another double-sphere instrument located in Europe. This observatory is situated far from the ocean and provides a very long gravity records. From the comparison shown in Figure 7.1, we observe that the differences between estimates are at the level of 0.001-0.005 (gravimetric factor) and 0.05-0.1 (phase). The deviations are mainly prominent at the lowest and highest frequencies of species and for S_1, which exhibit larger discrepancies. Therefore, I consider these values as the lower limit when discussing uncertainties and differences between various stations. This also has implications for the analysis of temporal variations, as we can expect variations in amplitudes at least at the level of the corresponding uncertainties for specific tides.

7.4. Resolution and Significance

I specifically selected stations with the longest available time series in order to obtain the most reliable estimates. For certain stations that had extensive records, such as Cantley and Sutherland, I made the decision to use only half of the available data while it still this provides a reasonable time series length. Obviously, one would prefer to use the full data, however, the investigation of the residuals and the MWA results revealed the problems with these data. To avoid false conclusions since we suspect the data might be unreliable, I did not include corresponding halves in the analysis leading to the local response model estimates. Some stations, like Canberra, Moxa, and Strasbourg, have time series lengths of approximately 20 years. According to the Rayleigh criterion, we should already be capable of resolving nodal harmonics using standard tidal analysis methods. However, I also examined shorter time series, such as Djougou and Ny-Ålesund, which only span 7 years, and Bad Homburg, Tigo-Concepcion, and Kamioka, all of which have less than 10 years of data. In the case of stations like Djougou or Bad Homburg, a coarse grouping approach would be preferable to avoid overfitting. Therefore, based on the Rayleigh criterion, it is expected that nodal harmonics ($\pm N'$) would not be fully resolved. Similarly, there may be doubts as to whether precessional tides ($\pm p$) should be treated separately.

In the analysis of all stations, I was able to resolve satellite harmonics that have never been treated separately for time series of that length. These contributions are significant based on their deviation from the reference model and misfit curve, regardless of the length of the time series. Examples of such resolved satellite harmonics include OV_1 (145.545) as a satellite of O_1 (145.555), κ_1 (165.545) and KW_1 (165.545) as satellites of K_1 (165.555), ω_2 as a satellite of M_2, and frequently LX_2 as a satellite of KNO_2 and L_2. In fact, for certain time series, I even allowed for further separation of harmonics, regardless of the length of the time series.

For instance, the analyzed time series for the local model of Sutherland was 7 years long, which is only half of the available time series used to verify with the MWA procedure. However, I found that the resolution did not significantly decrease with this step, and furthermore, the resolved model better explained the MWA variations (further comments are provided below and in Chapter 8). I had a similar observation for Cantley. Additionally, in Bad Homburg, during the second iteration, I treated the following tides separately: OW_1 (144.556), OV_1 (145.554), O_1 (145.555), OX_1 (145.554), LKW_1 (154.655), and LK_1 (155.455). The estimates appeared reasonable and did not deviate significantly in the frequency response function.

While some of these resolved harmonics (e.g., OW_1, OX_1) exhibit larger deviations between stations, similar-amplitude harmonics that would be resolved in conventional analysis due to their frequency distance, such as $2Q_1$, SGQ_1, V_1, and $2K_2$, show similar deviations of estimates between stations. Most of the estimates between major tides for the stations in Europe do not differ more than the satellite harmonics (Fig. 7.2). This comparison with the minimum error estimated from the two-sensor instrument provides a good indication that the results are meaningful. Thanks to the regularization, these results avoid the problem of over-fitting. Not only I may achieve smaller frequency separation, but the number of distinguished groups for a time record of a short duration far exceeds what is usually obtained with conventional approaches like `Eterna 3.40`.

Another important aspect to consider is that there are groups, especially in longer time series, that are not resolved with this method. These groups have small amplitudes and tend to closely follow the reference model, providing no evidence of their meaningfulness. I conducted frequent tests to determine the significance of the harmonic R_2. All experiments consistently showed that although tides T_2, S_2, or K_2 may be at a similar level due to the influence of the ocean, radiation has a significant effect on the estimates of R_2. In most stations, I found KNO_2 to be significant. In contrary, in some cases where harmonics technically could be resolved due to their relatively large frequency distance and long time series, I found them to be non-resolvable or not significant. Examples of such harmonics include $2T_2$, $2S_2$, and $2K_2$. Performing standard LS tidal analysis may lead to over-fitting when dealing with these small-amplitude harmonics and large condition numbers. The problem of confidence intervals for estimates is not straightforward (refer to Chapter 3.4 for more details). Another validation of the estimated parameters and resolution is the application of the response model to the MWA procedure, which will be discussed in Chapter 8.

A common characteristic of all the estimates is that the ratios described by the theory in the WDZe model are incorrect. This applies not only to the ratio between tides of degree 2 and 3 but also to the smooth, monotonous trends in the frequency response function for harmonics forming the same MWA groups, which are clearly visible.

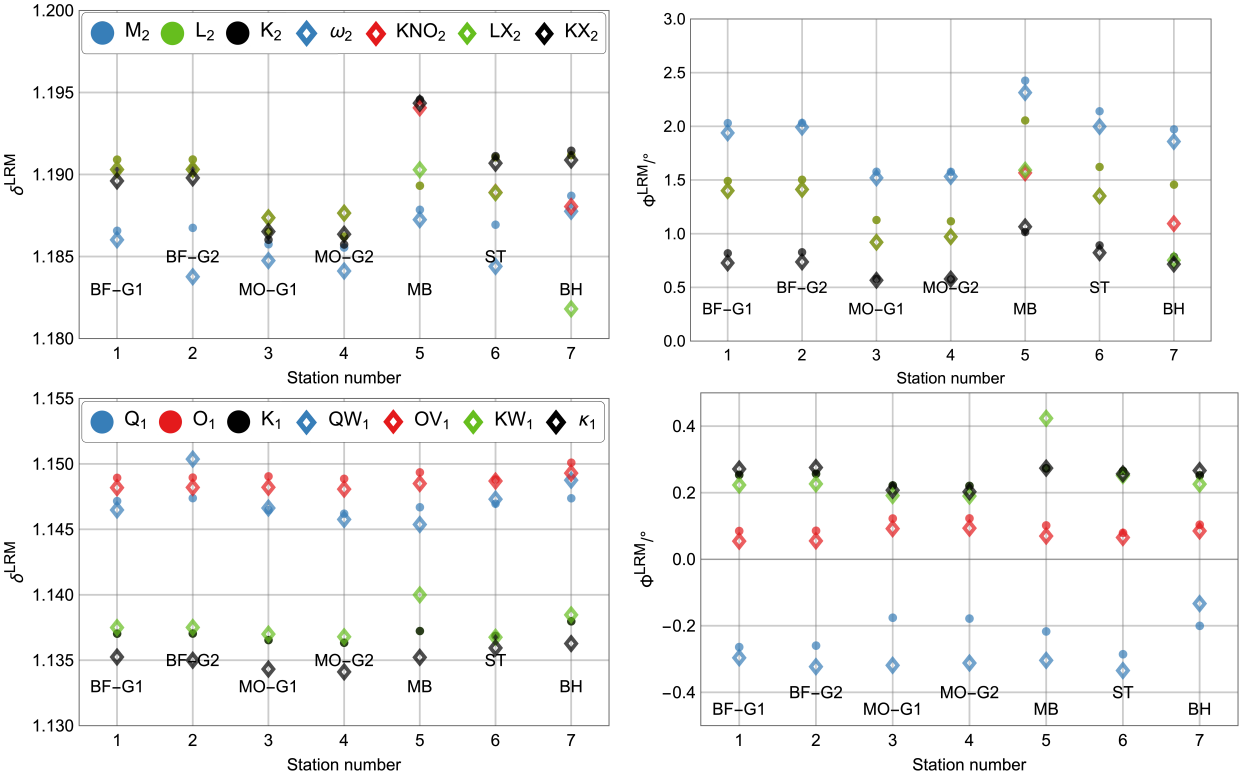

Figure 7.2.: Gravimetric factors (left) and phases (right) estimated for European stations, with `RATA` method. Top panels present estimates for semidiurnal tides, bottom panels - diurnal tides, for the main harmonics (circles) and the resolved satellites (diamonds) at different stations. Tide QW_1 is a satellite of Q_1, OV_1 of O_1, KW_1 and κ_1 are of K_1. In the semidiurnal band, ω_2 is from M_2, KNO_2 and LX_2 from L_2, KW_2 from K_2. Some of these satellite harmonics were not treated separately from their main tides in the analysis of some observatories, resulting in the same parameters. The deviations between stations for major tides appear at the similar level as those of the resolved satellite harmonics.

One conclusion is that if the time series already contains a few (or sufficient) years of data, increasing the time series length sometimes does not significantly improve the number of resolved harmonics. By adding noisier data we may rather worsen the resolution and decrease the relevance of the results. The second conclusion is that in such cases, errors propagate more due to the small amplitude of the harmonic rather than close frequency spacing. The resolution strongly depends on the noise, data quality and all kind of disturbances present in the data

7.5. European Stations

The root mean square (RMS) noise level at all European stations differs at most by 30%, ranging from 0.82 $\mathrm{nm\,s^{-2}}$ (Bad Homburg) to 1.14 $\mathrm{nm\,s^{-2}}$ (Membach). The final models were achieved in a maximum of three iterations (four in the Black Forest, but the difference between the third and fourth iterations was minor). The first iterations are usually coarser, consisting of reference groups such as ($\mathrm{LK_1}$ $\mathbf{M_1}$, $\mathrm{MN_1}$), (γ_2, $\boldsymbol{\alpha}_2$), or even ($\mathbf{M_2}$, ω_2), ($\mathbf{L_2}$, $\mathrm{LZ_2}$), and (ζ_2, $\boldsymbol{\eta}_2$, $\mathrm{2K_2}$). After

the first iteration, many of these tides were split into finer groupings, which were rarely further split during the procedure.

The amplitude-frequency response for diurnal tides (Fig. 7.3a) of degree 2 tides for all investigated stations within Europe shows clear similarities. In the diurnal band, there is a consistent need for adjustment from group Q_1 to K_1 (or κ_1). A clear trend is visible, where Q_1 appears to be overestimated and K_1 underestimated by the WDZe model. It is worth noting that τ_1 does not follow this trend and its value is similar to the one provided by theory. Another trend can be observed from K_1 to V_1, which shows a decreasing amplitude with increasing frequency. Notably, there is a steep drop in amplitude from the low-frequency neighbour harmonic SGQ_1 to Q_1. The estimate of the tide V_1 appears to be below δ^{WDZe} for all stations except Strasbourg and Membach. In Schiltach and Bad Homburg, the ratio is approximately 0.99. The estimates for the longer-period SGQ_1 are around $\delta^{\mathrm{LRM}}/\delta^{\mathrm{WDZe}} \approx 1.01$ for most stations, except Moxa and Strasbourg, which are just above δ^{WDZe}. The values of nodal tides, such as OV_1 or κ_1, do not show larger differences between stations compared to the major tides O_1 and K_1, regardless of the station and time series length. The estimates of some harmonics, like χ_1, or small-amplitude satellites LKW_1 (from LK_1) and OW_1 (from OV_1), are not consistent between stations, while the larger tides M_1, LK_1, and OV_1 have rather similar amplitudes. Similarly, tides V_1, SGQ_1, and Q_1 differ significantly between observatories. In the vicinity of the nodal diurnal frequency, the harmonics do not have exactly the same estimates, but they differ by no more than 0.002 between stations. This holds true for all harmonics except the radiation tide S_1. The values of the small resonant tide φ_1 also vary significantly between stations.

In the semidiurnal band (Fig. 7.3c) all analysed stations show the same shape of frequency response, clearly influenced by strong ocean loading and attraction. Tides ϵ_2 and $2N_2$ are $\delta^{\mathrm{LRM}}/\delta^{\mathrm{WDZe}}$ in range 0.98-0.99, with 0.98 at Membach and 0.99 in Moxa. The results for Strasbourg are less aligned with the other stations, since its estimate ϵ_2 is at 0.99 with smaller $2N_2$ being 0.98. Generally, the amplitude ratio increases with frequency for all the stations, reaching maximum for K_2 - except Moxa, where the ratio is the smallest from the stations and maximum is at L_1. We may notice that the size of "hump" in frequency response decreases with the distance to the ocean. The tide M_2 or ω_2 does not differ significantly between stations (Fig. 7.4). While some stations have the same estimates for γ_2, satellite harmonics responsible for annual modulation, α_2 and β_2, have amplitudes at very different level (Fig. 7.4), reaching even $\delta^{\mathrm{LRM}}/\delta^{\mathrm{WDZe}} \approx 1.06$ for β_1. Similarly, radiation tides T_2 and R_2 are different between stations. The response reaches similar values for the stations at higher frequencies of semidiurnal band $2K_2$, i.e. $\delta^{\mathrm{LRM}}/\delta^{\mathrm{WDZe}} \approx 1.01$ for most stations, and $\delta^{\mathrm{LRM}}/\delta^{\mathrm{WDZe}} \approx 1.02$ at Moxa. It reaches $\delta^{\mathrm{LRM}}/\delta^{\mathrm{WDZe}} \approx 1.025$ for Strasbourg. Phase differences do not differ much for all resolved tides in M_2 group between Bad Homburg and Schiltach. Similar estimates, but correspondingly shifted are seen in Membach. Moxa and Strasbourg are different in that respect. All the other resolved

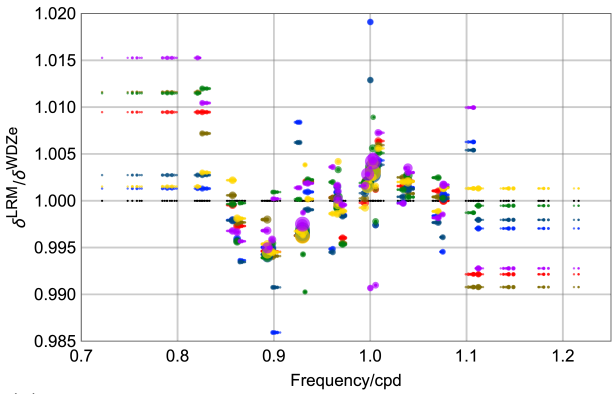

(a) Gravimetric factor of diurnal band, tides degree 2

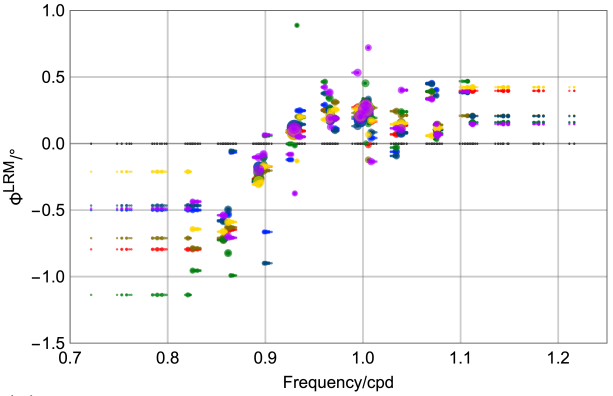

(b) Gravimetric phase of diurnal band, tides degree 2

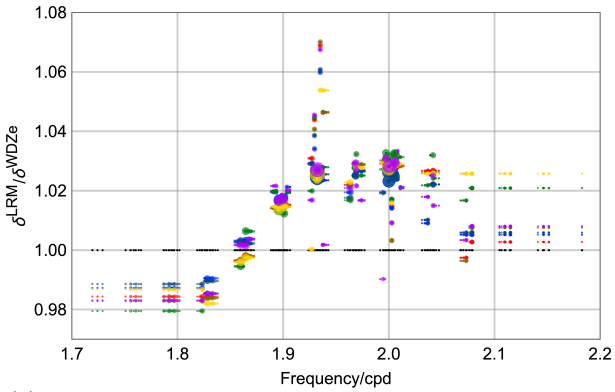

(c) Gravimetric factor of semidiurnal band, tides degree 2

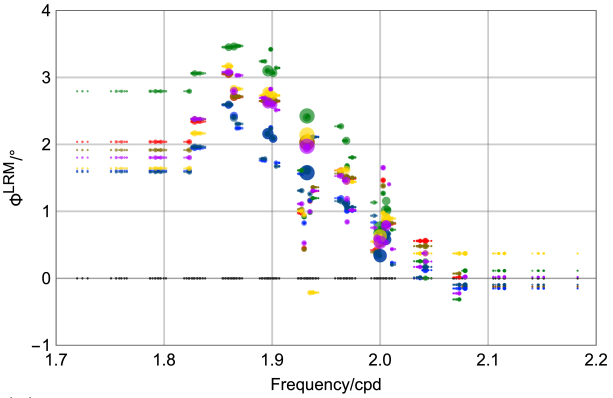

(d) Gravimetric phase of semidiurnal band, tides degree 2

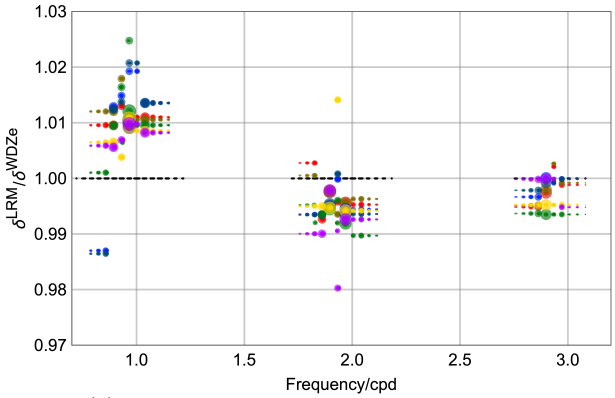

(e) Gravimetric factor of tides degree 3

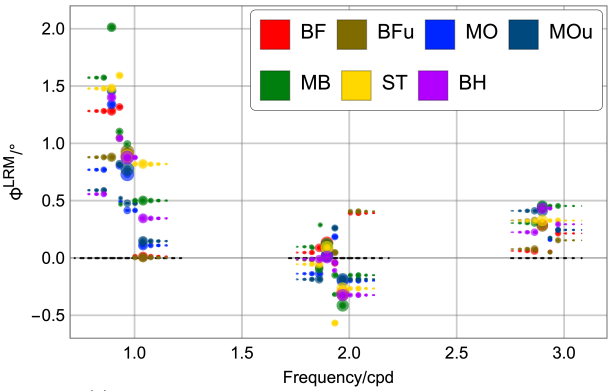

(f) Gravimetric phase of tides degree 3

Figure 7.3.: Parameters for the local response models (δ^{LRM} and Φ^{LRM}) in relation to WDZe for European stations, as obtained from `RATA` method. Diameter of the point corresponds to the forcing amplitude of the harmonic.

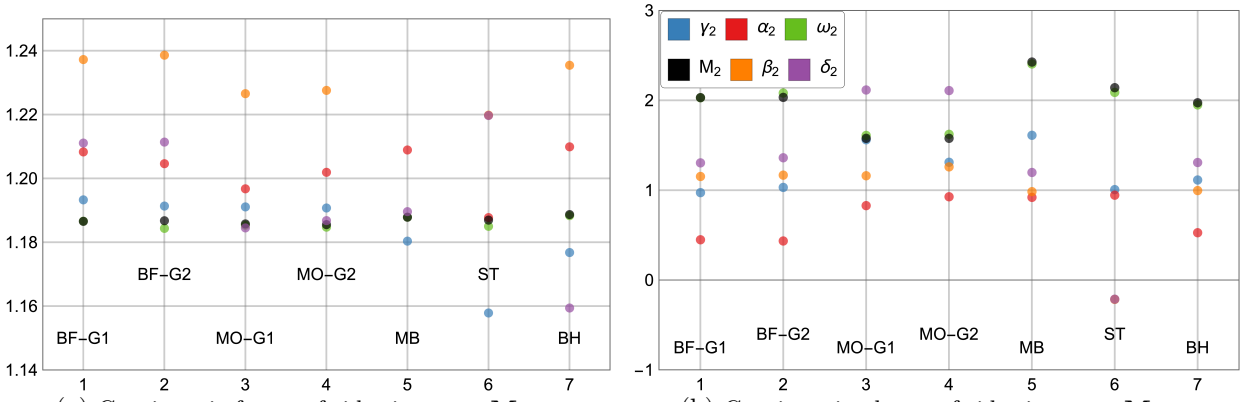

(a) Gravimetric factor of tides in group $\mathbf{M_2}$. (b) Gravimetric phases of tides in group $\mathbf{M_2}$.

Figure 7.4.: Gravimetric factors (left) and phases (right) estimated with `RATA` method for European stations. Results in $\mathbf{M_2}$ wave group at different stations. Some tides were not treated separately for some stations, hence they have the same parameters. I suppose the main differences between estimates are caused by the distance to the ocean.

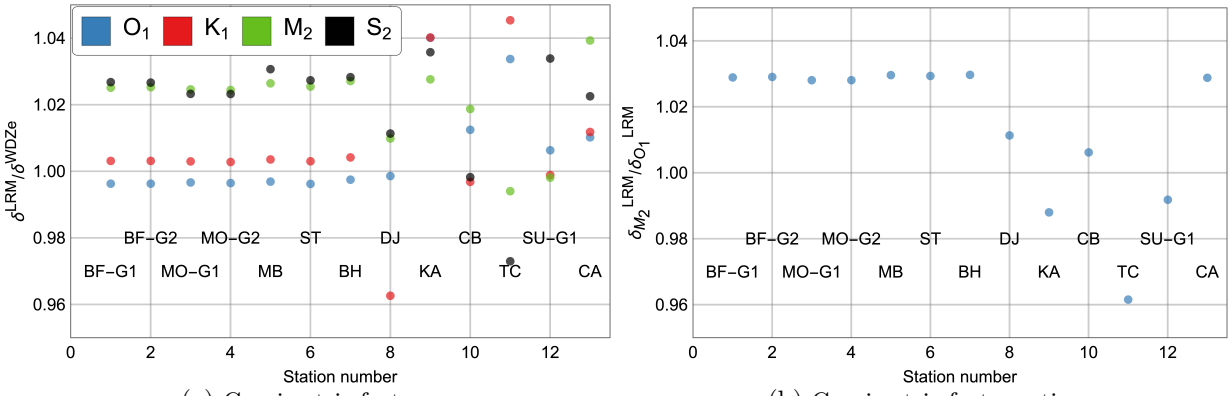

(a) Gravimetric factor (b) Gravimetric factor ratio

Figure 7.5.: Gravimetric factors of large amplitude tides in the local response models, all analysed stations.

harmonics that have small amplitudes but large frequency distance, or large amplitudes and small frequency distance, appear at reasonable values, however with visible scattering between stations, especially for the former. I conclude that this suggests the correct fine splitting with the method, and gives some estimate on the confidence intervals for particular tides.

The phase response (Fig.7.3a) in the diurnal band is almost the same for all the stations. Some minor but noticeable differences at a level of max about 0.2° are seen for major harmonics. Only some groups estimated by mid-amplitude harmonics, like SGQ_1 or ζ_1, or satellite harmonics in groups Q_1 and O_1 that have no established names clearly do not follow the trend. The semidiurnal phase (Fig.7.3d) response has a similar pattern of phases between stations. However, they appear systematically shifted between stations and coincide with the distance to the coast. This points to the clear influence of the ocean. Starting at the phase about 2° for ϵ_2, it increases to μ_2 between 2.5° and 4°. Also, some harmonics close in frequency (nodal and precessional

satellites), as well as small amplitude, have close estimates. We may notice that the phase peak, largest at μ_2, decreases with the distance to the ocean, being largest in Membach and smallest in Moxa. The phase is approximately 0° for $2K_2$, except Strasbourg. Strikingly, tides degree 3 appear at very different values, depending on the station. However, L_2* and M_1*, the two most significant tides degree 3, show very similar estimates for all stations, in factor and phase.

7.6. Middle Latitudes

As we see in Chapter 4, most stations in GGP are in the middle latitudes, mainly Europe and East Asia. I investigate at least one station on each continent. However, I discuss the two hemispheres separately.

The Northern Hemisphere

The first RMS amplitude at Cantley was computed to be 4 $\mathrm{nm\,s^{-2}}$. After selecting only the first half of the available data for analysis it decreased to 2.38 $\mathrm{nm\,s^{-2}}$, which is still a very high level compared to other stations in the region. Unfortunately, there are no other stations available for comparison in this region. Boulder was not used due to the short duration of available data, and the estimated noise level was similar. The corresponding noise level in Kamioka is reasonable, at approximately 1.7 $\mathrm{nm\,s^{-2}}$. For both stations, there were clear indications of deviations from the reference for most of the potentially significant tides. I allowed for finer resolution, especially in the diurnal band, after the first iteration. The degree 2 tides had very similar reference groups to the BF21 model, with minor differences: KNO_2, ω_2, and KW_2 were used as different reference groups. The final model in Cantley was obtained after 2 iterations. In the analysis of the half of the available data (in total approximately 19 years) I used the same reference grouping. However, the application of the local response model to the MWA method showed that large deviations were still present. The large offset-like variations of parameters indicate times when the instrument was not operating correctly, and these instances were not identified during the preprocessing. Despite the shorter time series, the resulting model generally decreased the amplitude of temporal variations. For a more detailed discussion, please refer to Chapter 8. In the case of Kamioka, due to the large differences from the theoretical values as given in the WDZe model, 4 iterations were needed to obtain an accurate model. Moxa from European stations was used for comparison purposes.

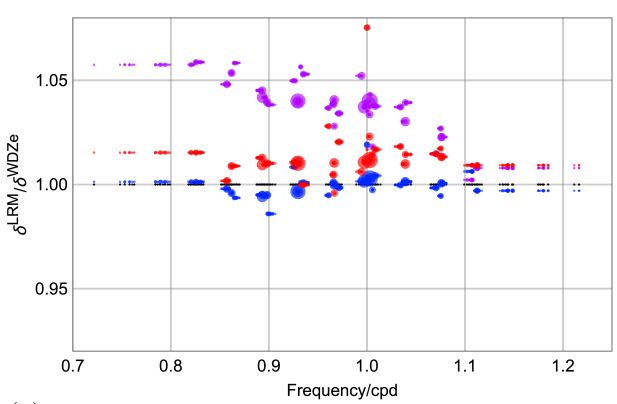

(a) Gravimetric factor of diurnal band, tides degree 2

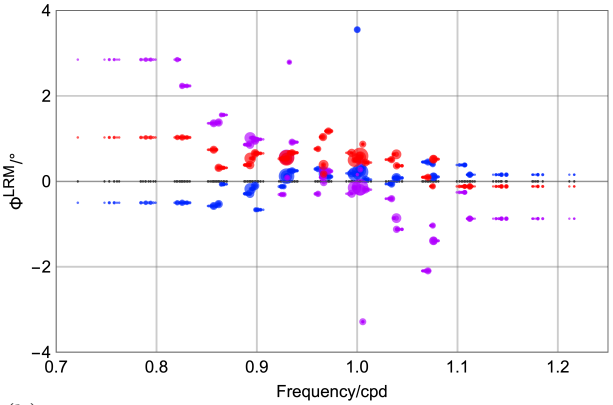

(b) Gravimetric phase of diurnal band, tides degree 2

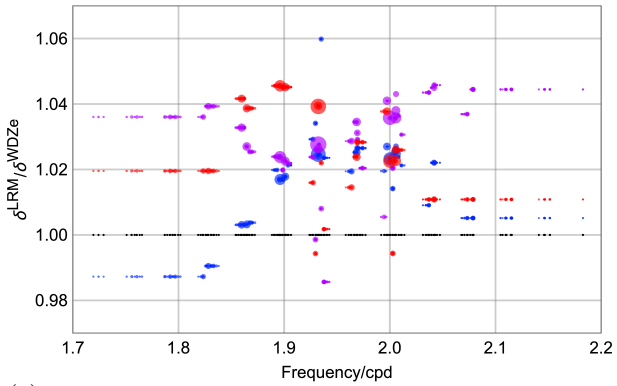

(c) Gravimetric factor of semidiurnal band, tides degree 2

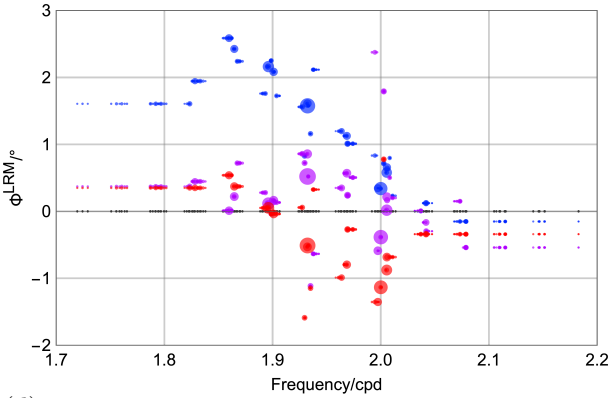

(d) Gravimetric phase of semidiurnal band, tides degree 2

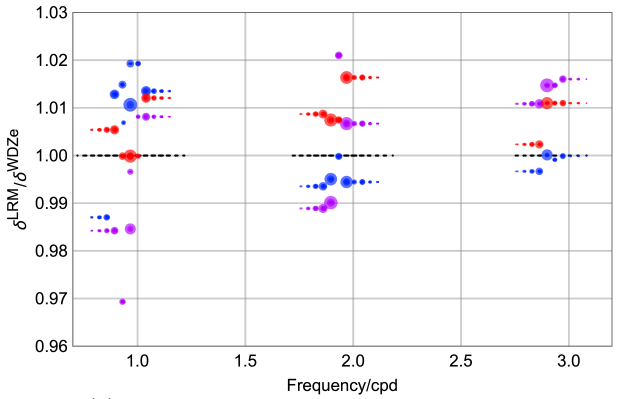

(e) Gravimetric factor of tides degree 3

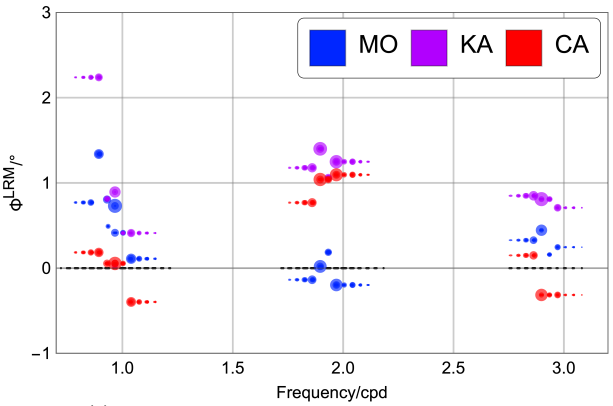

(f) Gravimetric phase of tides degree 3

Figure 7.6.: Parameters for the local response models (δ^{LRM} and Φ^{LRM}) in relation to WDZe for the Northern Hemisphere, as obtained from `RATA` method. Diameter of the point corresponds to the forcing amplitude of the harmonic. Moxa observatory is chosen to represent Europe.

Even though the three stations are at similar latitudes, there is no common pattern observed in any respect (Fig. 7.6). This applies to both the amplitude factors and phases of both degree 2 and degree 3 tides. The main reason for the different tidal response is most certainly the influence of the oceans. Cantley, being on the other side of the Atlantic Ocean compared to Moxa, is affected differently. Similarly, Kamioka, located in the North Pacific, experiences a completely different water system.

Interestingly, the degree 2 amplitude response for Kamioka starts at $\delta^{\mathrm{LRM}}/\delta^{\mathrm{WDZe}} \approx 1.06$ for SGQ_1 and reaches $\delta^{\mathrm{LRM}}/\delta^{\mathrm{WDZe}} \approx 1.01$ at V_1. Most tides are amplified by $\delta^{\mathrm{LRM}}/\delta^{\mathrm{WDZe}} \approx 1.04$. Additionally, for Kamioka, the response of semidiurnal tides is at $\delta^{\mathrm{LRM}}/\delta^{\mathrm{WDZe}} \approx 1.04$ at both frequency edges, with a negative "hump" and a minimum at 1.02 for N_2. This behavior is exactly opposite to what was observed in Europe, where the major tides were larger than the "mean value" estimated by drawing a line between the estimates of ϵ_2 and $2\mathrm{K}_2$. For Cantley, in the diurnal band, a rather constant amplification is observed for all degree 2 tides, with some scattering of parameters at frequencies around M_1 and K_1. In the semidiurnal band, there is a "hump-like" feature for tides from μ_2 to M_2 at $\delta^{\mathrm{LRM}}/\delta^{\mathrm{WDZe}} \approx 1.04$, decreasing to $\delta^{\mathrm{LRM}}/\delta^{\mathrm{WDZe}} \approx 1.02$ at S_2. No similarities are observed between stations in the degree 3 response.

Regarding the gravimetric phase, for semidiurnal tides both Cantley and Europe show a decreasing trend from N_2 to K_2 - in Europe from the phase at a level of 2.5° to -0.5° and from 0.5° to -1° in Cantley. However, this does not seem to be the case in Kamioka, which shows a variety of phase values within a range from 1° to -1°. The phase response in the degree 2 diurnal band is different for each station, but there are some similarities in the sense, that values for the main tides do not scatter much. Cantley exhibits a rather constant value of 0.5° for tides from Q_1 to OO_1, with an exception for scattering around M_1. The values are somehow similar to Europe, which are rather close to 0.25°, only starting from slightly negative values for low frequencies. In Kamioka, a decrease in phase with frequency is observed, ranging from 3° in ζ_1 to -1.5° in V_1. Additionally, in Kamioka, a striking S_1 radiation tide at 1.28 (outside the plot) is observed, and the phase is shifted by more than 30°. In Cantley, phase of S_1 is almost 6° (also outside the plot). Degree 3 phases show no similarities between stations at all, only the decreasing trend of diurnal tides seems to be common, but at different values. In Kamioka, phases of degree 3 tides are positive across each species.

The Southern Hemisphere

South from equator, I investigated three stations located at very similar latitudes but at large distances from each other, similar to the stations in the Northern Hemisphere. However, each of these stations is affected by different oceans. Tigo is primarily influenced by the Southern Pacific Ocean and to some extent by the South Atlantic Ocean. Sutherland, being an inland station, is surrounded by the Southern Atlantic Ocean and the Southern Indian Ocean. Canberra is

primarily located on the coast of the South Pacific Ocean, but we can expect some influence from the Indian Ocean as well. All three stations are affected by the Antarctic (Southern) Ocean.

Canberra and Sutherland show noise levels of approximately 1 $\mathrm{nm\,s^{-2}}$, while Tigo has a noise level twice as high. The final estimates for Sutherland were obtained after 2 iterations, while for the other stations - 3 iterations. Similarly to the approach in the Northern Hemisphere, I initially used a coarse grouping for the primary investigation, and then performed a very fine group split in the reference for the first iteration. Only a few reference groups were further split. I kept a relatively coarse grouping for semidiurnal tides in the first iteration, which I then further split into a finer structure in the second iteration for Sutherland and Canberra, but not for Tigo.

In terms of amplitude response, we can observe distinct patterns for each station. The only similarity we can notice is between Sutherland and Moxa, where in the diurnal band they appear as symmetrically reflected around 1 cpd (Fig. 7.7a). However, Sutherland's amplitudes are generally lower compared to the theoretical response. If we consider the decreasing trend for diurnal frequencies in Kamioka, a similar pattern is observed in Canberra, but with amplitudes decreasing to approximately $\delta^{\mathrm{LRM}}/\delta^{\mathrm{WDZe}} \approx 0.98$. In the semidiurnal band (Fig. 7.7c), Tigo and Canberra start with relatively high amplitudes of $\delta^{\mathrm{LRM}}/\delta^{\mathrm{WDZe}} > 1.07$ for $3\mathrm{N}_2$, while Kamioka exhibits a steep decrease to as low as 0.94 for $2\mathrm{K}_2$. The key point here is that the true amplitude estimates differ significantly within the a priori groups used in MWA compared to the theory provided by WDZe, indicating strong beating potential.

Regarding the phase response (Fig.7.7b and Fig.7.7d), it is significantly different from what we observed in the Northern Hemisphere. However, for the semidiurnal tides, except for the modulation harmonics of M_2, Tigo-Conception and Canberra show similar phase estimates, except for group S_2. This is in contrast to Sutherland, where the phase appears shifted by 5° from the other two stations and exhibits an opposite character. Even significant tides within the same groups show different phases, indicating the potential for beating. Interestingly, the phases for diurnal tides in Canberra do not vary much within the groups, which on one hand might explain the lack of systematic variations in some of the MWA groups. On the other hand, even small differences in tides with large amplitudes, as well as incorrect $\mathrm{S}_1/\mathrm{K}_1$ ratios, can result in beating. Tides of degree 3 (Fig. 7.7f) exhibit completely different patterns compared to what we observe in the Northern Hemisphere, and there is no uniform behavior. Tide Q_1* is amplified by a large factor $\delta^{\mathrm{LRM}}/\delta^{\mathrm{WDZe}} \approx 1.15$, outside the plot. Nevertheless, it is clear that the assumption of a fixed ratio between tides of degree 2 and 3 is far from reality. The estimates for S_1 obviously deviate from the a priori body tide model. Gravimetric factors are $\delta^{\mathrm{LRM}}/\delta^{\mathrm{WDZe}} = 1.1137$ in Canberra and surprising $\delta^{\mathrm{LRM}}/\delta^{\mathrm{WDZe}} = 0.8888$ in Tigo. Also, phases are $\Phi^{\mathrm{LRM}} \approx -17°$ for Tigo and Canberra, and $\Phi^{\mathrm{LRM}} \approx -30°$ for Sutherland.

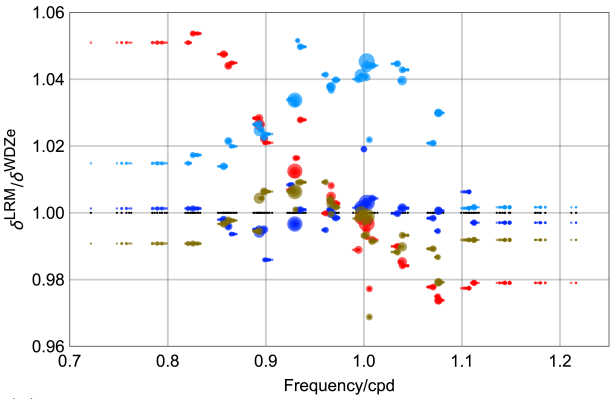

(a) Gravimetric factor of diurnal band, tides degree 2

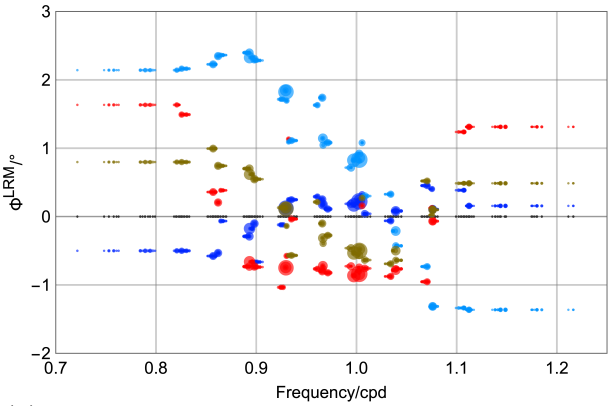

(b) Gravimetric phase of diurnal band, tides degree 2

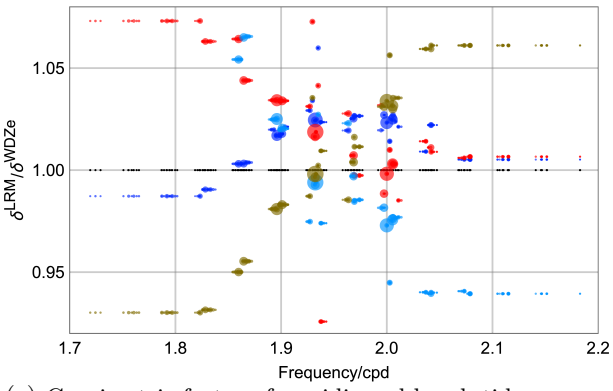

(c) Gravimetric factor of semidiurnal band, tides degree 2

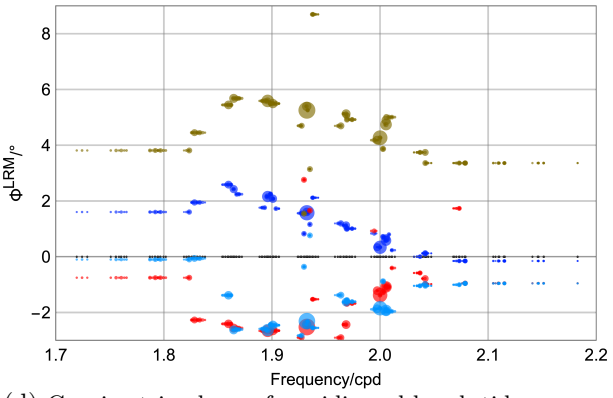

(d) Gravimetric phase of semidiurnal band, tides degree 2

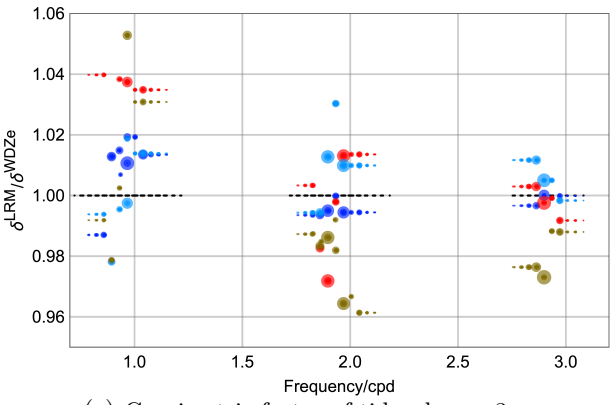

(e) Gravimetric factor of tides degree 3

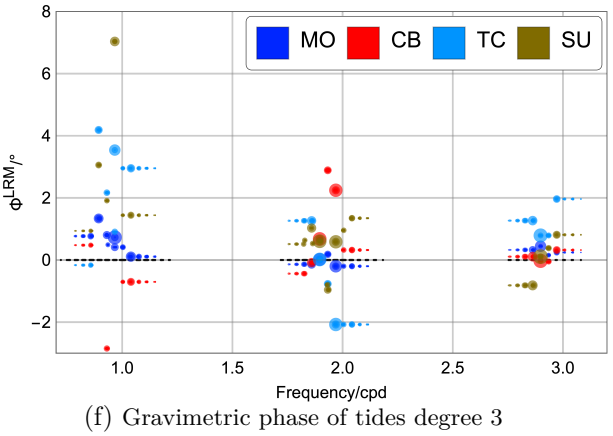

(f) Gravimetric phase of tides degree 3

Figure 7.7.: Parameters for the local response models (δ^{LRM} and Φ^{LRM}) in relation to WDZe for the Southern Hemisphere, as obtained from `RATA` method. Diameter of the point corresponds to the forcing amplitude of the harmonic. Results from Moxa for comparison.

7.7. Subtropical: Djougou

This is the only station between Tropics of Cancer and Capricorn which I analyzed. It is observed that at these latitudes, diurnal tides of degree 2 have relatively smaller amplitudes compared to mid-latitudes, as do degree 3 semidiurnal tides (see Fig. 2.2). In contrast, semidiurnal degree 2 tides are expected to have larger amplitudes. The station exhibits a reasonable signal-to-noise ratio, with a noise level RMS amplitude of approximately 1.2 $\mathrm{nm\,s^{-2}}$. The final model was obtained after 4 iterations.

Contrary to the previous stations at mid-latitudes, I found it necessary to perform a finer split of reference groups in the semidiurnal tides. However, the groups in the diurnal band were kept relatively coarse, for example, all degree 2 tides in the $\mathbf{OO}_1$ MWA group were kept together. I did not modify this scheme in subsequent iterations. Additionally, I decided to split tides $\mathrm{LK1}_1$, OV_1, and κ_1 from their main harmonics in the group, namely M_1, O_1, and K_1. These decisions contradict what the Rayleigh criterion would suggest, considering the data length of less than 7 years. It is possible to compare the obtained fine structure with the response model for BFO estimated using the conventional approach for a similar length of time series (Fig. 5.5).

I found an extreme value for the radiation tide S_1 with a ratio of $\delta^{\mathrm{LRM}}/\delta^{\mathrm{WDZe}} \approx 2$ and a phase shift of approximately 50°, and it is likely a major factor contributing to the beating observed in MWA. While the instrument is placed in a hut in the savanna, due to the geographical conditions, it is possible that the radiation tide might be determined more accurately than in stations at mid-latitudes where weather conditions change frequently.

In terms of diurnal tides of degree 3 (Fig.7.8e - Fig.7.8f), they were underestimated with ratios ranging from $\delta^{\mathrm{LRM}}/\delta^{\mathrm{WDZe}} \approx 1.03$ to 1.05, except for LK_1* which had a ratio of approximately 0.965. As expected from theory, semidiurnal degree 3 tides are relatively small, which is why the grouping was kept coarse. Degree 2 tides exhibit a rapid decrease in response with frequency (Fig. 7.8a), ranging from 1.02 for SGQ_1 to 0.96 for J_1. On the other hand, semidiurnal degree 2 tides show an increase in response with frequency, somewhat similar to the European stations. Degree 3 tides exhibit a variety of responses, ranging from 0.96 for M_2* to 1.015 for L_2*.

Looking at the phase response (Fig. 7.8b - 7.8f), a simplified impression is that tides of degree 3 are the inverse estimates of tides of degree 2. Both exhibit trends, and the shape of the phase response indicates the incorrectness of the assumed ratio. Notably, the phase estimates in L_2 are roughly the same, which explains the relatively small beating in MWA. Similarly, the phase in LK_1* and M_1* exhibits significantly different estimates. The estimates in the $\mathbf{M}_2$ MWA group do not deviate as much as in other stations, indicating that although the annual modulation is present, it is not as pronounced.

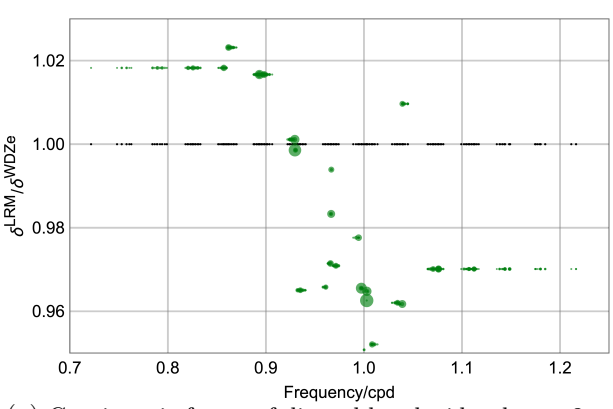

(a) Gravimetric factor of diurnal band, tides degree 2

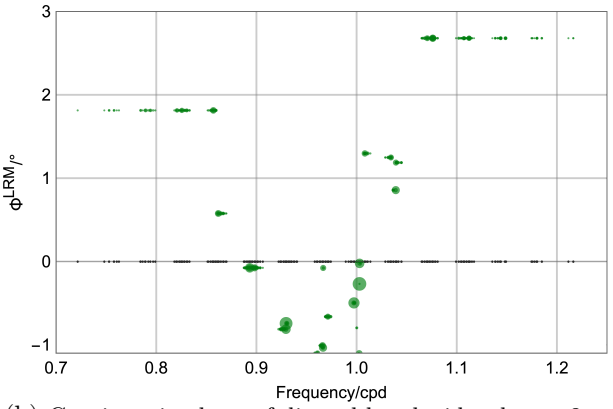

(b) Gravimetric phase of diurnal band, tides degree 2

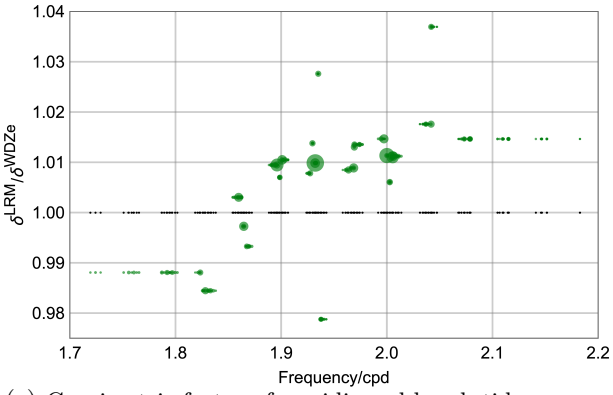

(c) Gravimetric factor of semidiurnal band, tides degree 2

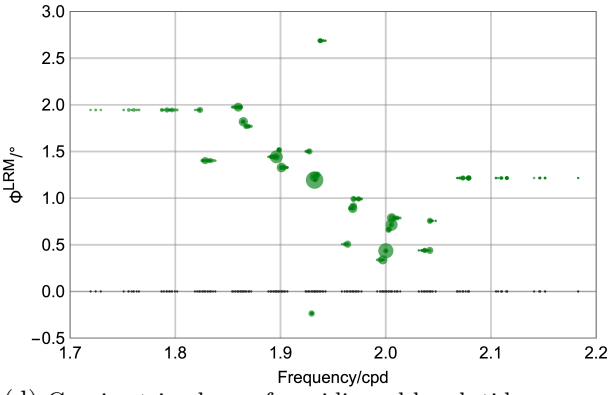

(d) Gravimetric phase of semidiurnal band, tides degree 2

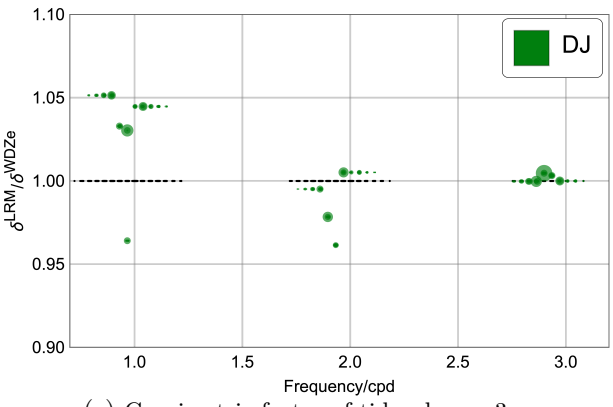

(e) Gravimetric factor of tides degree 3

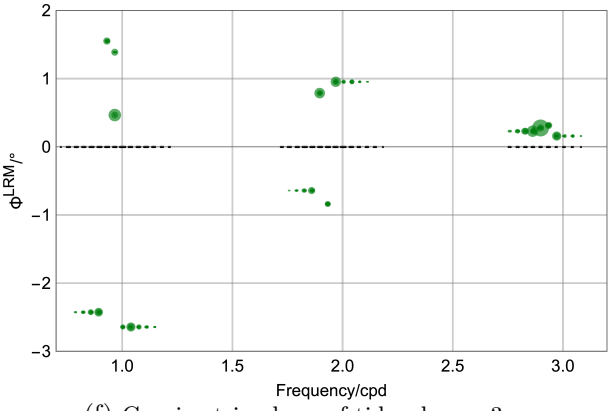

(f) Gravimetric phase of tides degree 3

Figure 7.8.: Parameters for the local response models (δ^{LRM} and Φ^{LRM}) in relation to WDZe for Djougou, as obtained from `RATA` method. Diameter of the point corresponds to the forcing amplitude of the harmonic.

7.8. Subpolar: Ny-Ålesund and Syowa

The station at Ny-Ålesund, located close to the Arctic in the Svalbard archipelago in the North Sea, exhibits interesting results in MWA, particularly in the semidiurnal band where temporal variations of unusual magnitude are observed. Degree 2 tides generally do not have large amplitudes there. Diurnal degree 3 tides, in particular, are expected to be the largest among all degree 3 species. Based on this knowledge and supported by the data, I applied a coarse grouping approach for degree 3 semidiurnal and terdiurnal tides. The resolution of reference groups in degree 2 semidiurnal tides was also kept rather coarse compared to other stations I analyzed.

An important aspect is that the reference groups were primarily based on the amplitude of the harmonics. As a result, I separated κ_1 from K_1, OV_1 from O_1, and ω_2 from M_2. However, I did not separate π_1 from P_1, $2S_2$ from K_2, nor λ_2 from L_2. The iterative procedure required four iterations to obtain the final model for the station at Ny-Ålesund.

Analyzing the local response model for the station at Ny-Ålesund, we observe significant differences in the ratio of semidiurnal degree 2 to degree 3 tides (Fig. 7.9). While most degree 2 tides have amplitudes in the range of $\delta^{\mathrm{LRM}}/\delta^{\mathrm{WDZe}} \approx 0.4 - 0.9$, degree 3 tides have amplitudes greater than 1. Extreme value was estimated for Q_1*, $\delta^{\mathrm{LRM}}/\delta^{\mathrm{WDZe}} \approx 1.22$. Similarly, the phase of degree 2 tides varies from $-80°$ to $80°$ between harmonics, while degree 3 tides have phase estimates around $-10°$ to $0°$. This behavior can be attributed to the specific effect of the surrounding ocean at these latitudes. The incorrect assumption of the response within groups with such deviations certainly causes modulations in MWA.

In the diurnal band, degree 2 tides at Ny-Ålesund exhibit some similarities in the overall pattern when compared to European stations, although the differences are much larger. However, they do not deviate as much as in the case of semidiurnal tides. The ratio between degree 2 and degree 3 tides is different from 1. Notably, the estimate for S_1 has a scaled amplitude of 0.6 and a phase of approximately $-10°$. The behavior of radiation tides in this region is not clear, given the different seasonality than in Europe. Due to the deviations from the assumed ratios in the WDZe model, the improved local response model should lead to a decrease in the amplitude of diurnal tides to some extent and result in significantly reduced temporal variations in the semidiurnal band.

Moving on to the final station in the global coverage, Syowa, it has an RMS-amplitude of noise at 3.8 $\mathrm{nm\,s^{-2}}$. The reference grouping scheme for this station also appeared to be rather coarse. It is important to note that except for the δ estimates in the diurnal band, the results for Syowa appear to be very chaotic and unreasonable in terms of estimates. The local response model (Fig. 7.10) did not significantly change the temporal variations in MWA, as discussed in

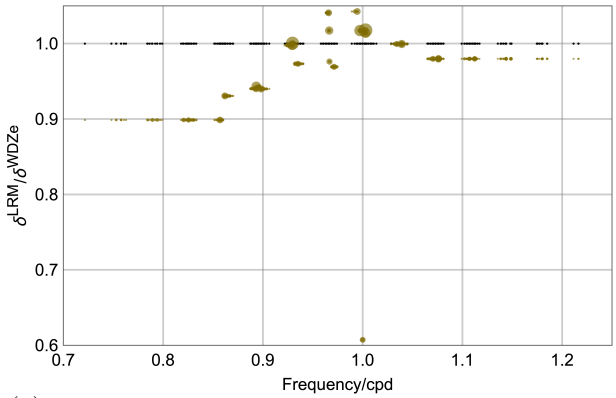

(a) Gravimetric factor of diurnal band, tides degree 2

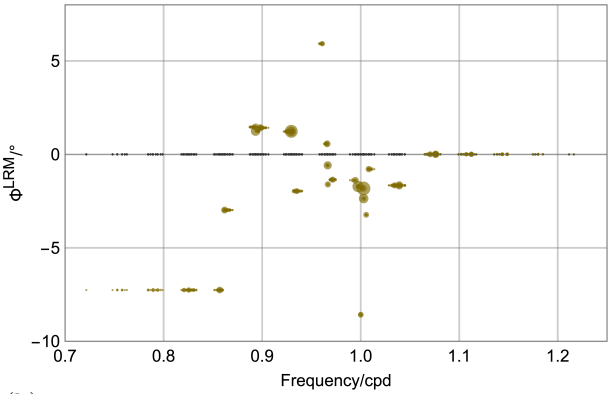

(b) Gravimetric phase of diurnal band, tides degree 2

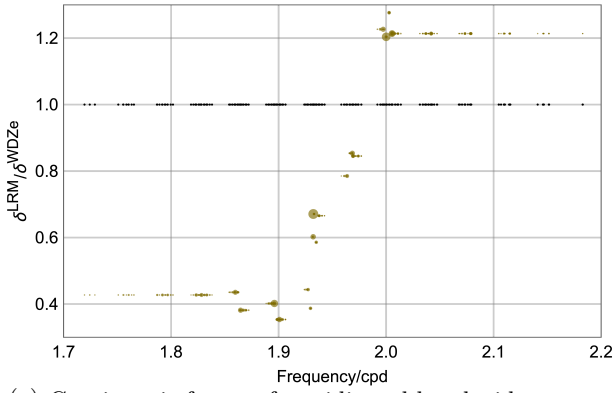

(c) Gravimetric factor of semidiurnal band, tides degree 2

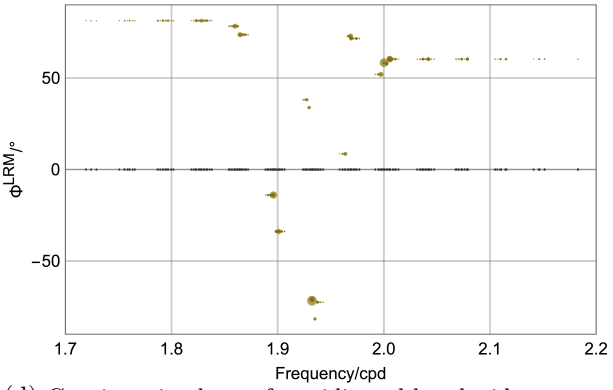

(d) Gravimetric phase of semidiurnal band, tides degree 2

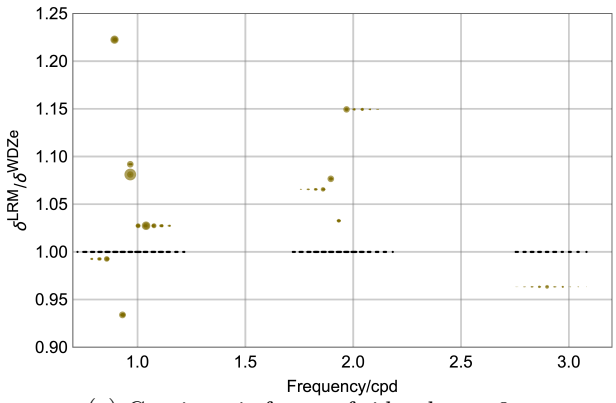

(e) Gravimetric factor of tides degree 3

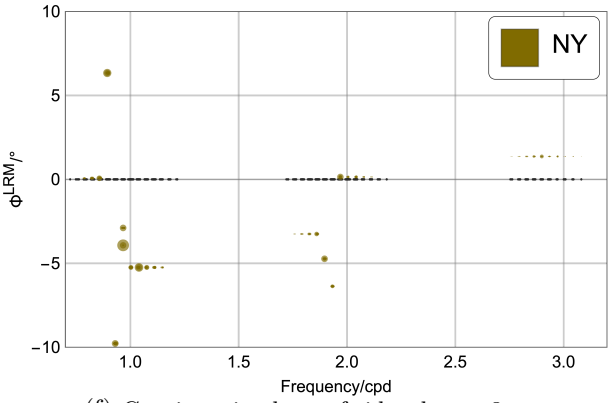

(f) Gravimetric phase of tides degree 3

Figure 7.9.: Parameters for the local response models (δ^{LRM} and Φ^{LRM}) in relation to WDZe for Ny-Ålesund, as obtained from `RATA` method. Diameter of the point corresponds to the forcing amplitude of the harmonic.

Chapter 8. Therefore, I do not further discuss the estimates for this station, as the results are likely strongly affected by noise of various origins.

7.9. Summary

The `RATA` method allows for much finer resolution than is typically obtained with the `Eterna 3.40` method, using the Rayleigh criterion as a general rule for group definition. The regularization stabilizes the possible noise-influenced over-fitting for minor contributions. The ability to inspect all harmonics with a regularization constraint gives a possibility for proper exploration of estimates for tidal harmonics. Apparently, large-amplitude satellites separated from the main harmonic by nodal or precessional frequency of 8.8 or 18.6 years can be resolved even in few years length gravity time series. Effectively, these harmonics usually are not much different in phases and amplitudes due to the smooth response. Seasonal modulation in the $\mathbf{M}_2$ group due to different estimates of its annual satellites is apparent and varies between stations. I suspect the exact values of estimates for α_2, β_2, γ_2, and δ_2 may also depend on time, but it has not been tested yet. Tides of degree 3 are also treated separately, and major ones were resolved. Not all harmonics that would satisfy the criterion in conventional wave grouping analysis may be resolved according to the `RATA` approach. The main criterion that affects the resolution is the noise.

The estimated amplitude response significantly differs from the theoretical WDZe model. In addition, for stations within all MWA groups, not only degree 2 and 3 tides but also the degree 2 tides themselves have a ratio different than expected. This is particularly significant for harmonics of large amplitude. Therefore, I would expect that beating in temporal variations is much smaller if the local models are used for all stations. This mainly applies to tides that contain satellite harmonics with large amplitude and different estimates, such as $\mathbf{M}_1$, $\mathbf{K}_1$, $\mathbf{S}_2$, $\mathbf{N}_2$, and $\mathbf{L}_2$. I would expect reduced amplitudes of variations for other groups as well. For Djougou and Kamioka, I expect a large reduction of temporal variations due to the deviations of S_1 from theoretical values. Similarly, although the data from Ny-Ålesund lack systematic consistency compared with other stations and show huge variations, we see some reasonable patterns in the semidiurnal tides, which have larger amplitudes there. The unclear estimates for Syowa will be tested to determine if some temporal variations could be explained by an improved ratio.

Interestingly, the harmonic Q_1*, commonly known as 3MK1, which is a significant degree 3 tide (135.555), has unexpectedly different estimates in Canberra and Ny-Ålesund compared to all the stations investigated so far. Their significantly larger amplitude of δ^{LRM} would be 1.23 for Canberra, even larger than the estimated degree 2 tides (1.15-1.21). The reason for this is unclear, but some local ocean resonances might be a potential cause. We see that degree 3 tides

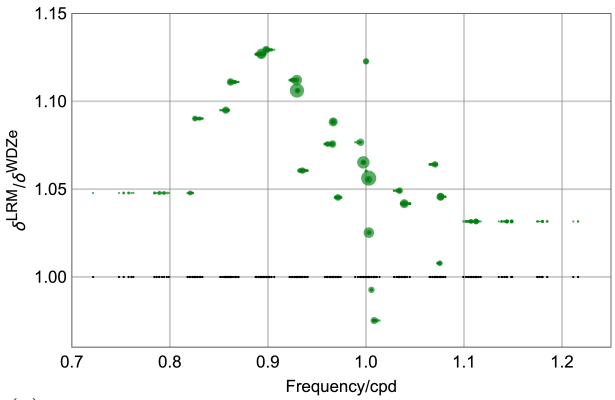

(a) Gravimetric factor of diurnal band, tides degree 2

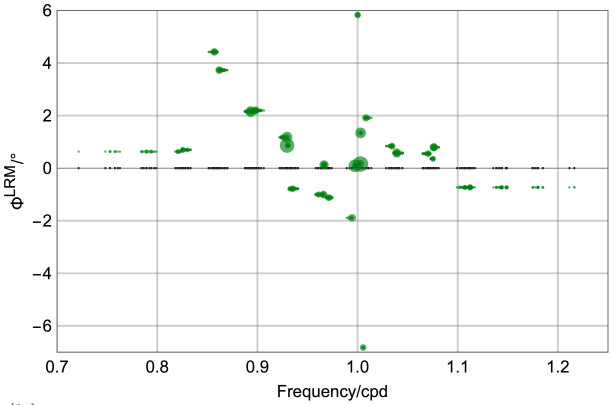

(b) Gravimetric phase of diurnal band, tides degree 2

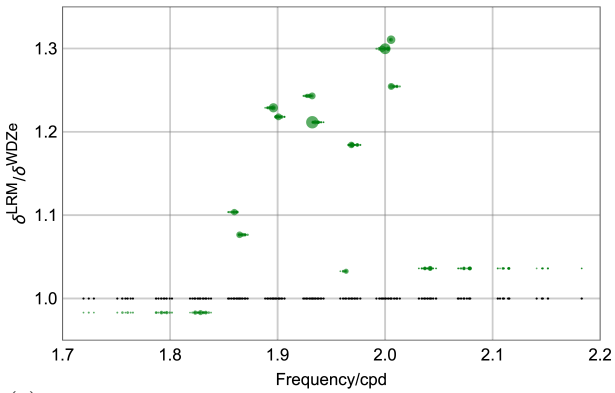

(c) Gravimetric factor of semidiurnal band, tides degree 2

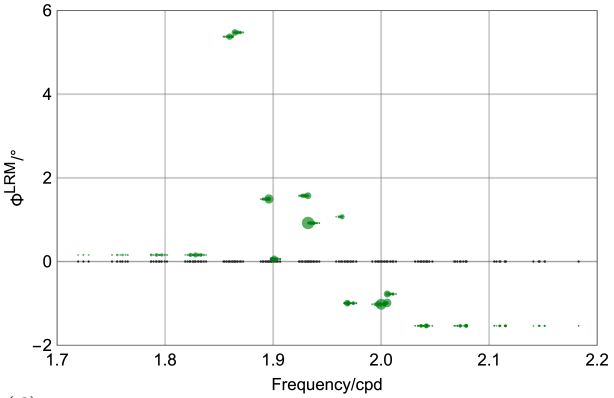

(d) Gravimetric phase of semidiurnal band, tides degree 2

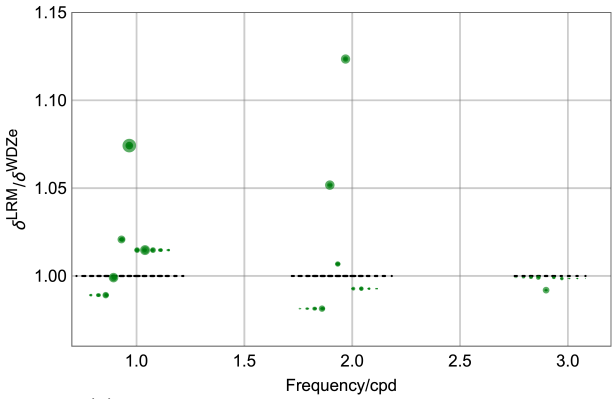

(e) Gravimetric factor of tides degree 3

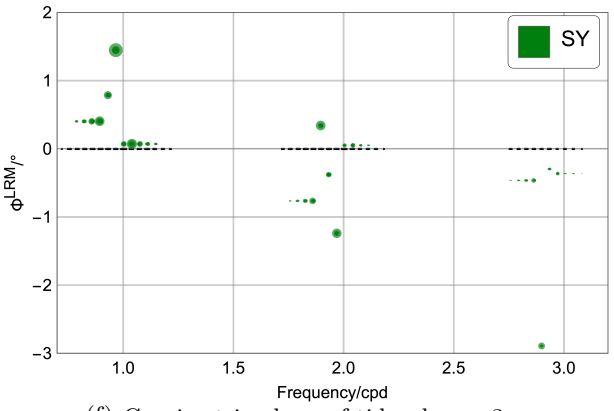

(f) Gravimetric phase of tides degree 3

Figure 7.10.: Parameters for the local response models (δ^{LRM} and Φ^{LRM}) in relation to WDZe for Syowa, as obtained from `RATA` method. Diameter of the point corresponds to the forcing amplitude of the harmonic.

experience less ocean loading than degree 2, which agrees with the results obtained by Ducarme (2012).

8. Temporal Variations Across the Globe

I will prove that the majority of temporal variations previously found at various stations in Europe and in other continents, as presented by Schroth et al. (2018), can be explained by an improper local response model used for a priori grouping. The method demonstrated in Chapter 6 is applied to the local response models developed in Chapter 7. Temporal variations for groups in which long-period temporal changes, not as clearly noticeable by eye, can also decrease. This is caused by the improved ratio of tides degree 2 to 3, or small adjustment of satellite harmonics at the close frequency. I identify the primary causes of large-amplitude temporal variations. The remaining temporal variations are subject to discussion. Certainly, there are physical causes of modulation, and they become clear if the systemic errors caused by local models are removed. The actual modulation within $\mathbf{M}_2$ group is an example. The detailed analysis for each station, including histograms and spectral analysis, are presented in Appendices C - E.

8.1. Method

The first analysis of 3-month windows was presented by Meurers et al. (2016) for some European stations. They were further extended by Schroth et al. (2018), who provided comprehensive moving window analyses on most stations in the GGP project with sufficient data to investigate temporal variations. Schroth et al. (2018) indicate that tidal parameters of $\mathbf{O}_1$ as well as $\mathbf{J}_1$, $\mathbf{OO}_1$, and $\mathbf{M}_3$* show no clear periodicity. I demonstrate the application of the method as described in Chapter 6 for other stations. This not only explains a vast part of temporal variations but also validates the estimates for local response models. Compared to the principle of the analysis that Schroth et al. (2018) or Meurers et al. (2016) performed, I only modify the a priori body tide model. The adjustments express the correct ratio between harmonic amplitudes and offsets between their phases prior to grouping. No additional model for the influence of oceans has been used, contrary to Schroth (2020). However, the local model response already captures some averaged, time-invariant ocean properties. To take into account the time-varying solar tides, an air pressure record has been used. I also investigate the periodicity of all parameters by means of the Fourier Transform (Appendix E).

The selected stations are listed in Chapter 4. Due to the different characters of variations depending on the locations, I separately discuss the moving window analyses of European sta-

tions from those outside Europe. European stations were selected to visualize a similar pattern of temporal variations and how the local a priori model alters this. This should prove the consistency of the method. The other stations placed in different continents for this reason are discussed separately since the variations differ. However, it gives a complete overview of temporal variations and proves the method to be reasonable regardless of their location. Additionally, the stations at Cantley, Ny-Ålesund, and Syowa show temporal variations that have a much larger amplitude than others, even when the local response model has been used. Therefore, these three remaining stations are discussed separately.

The collection of results provides proof that an improper model used before grouping is responsible for systematic temporal variations and beating patterns in the MWA technique. Removing these effects by using a proper local model, like the one derived with `RATA`, we can better study the true physical variations, resulting from the ocean loading contribution. The other deviations might be instrument-related, such as an incorrect gain factors, data preprocessing or instrumental instability.

8.2. The Display

Each estimated factor is a physical quantity. Hence, the mean values would correspond to the value of the tidal parameter for the main harmonic in the group, already including the amplification due to the Earth body response, local effects, and ocean response. Gravimetric factors and phases are rather displayed on separate plots. This is how Schroth et al. (2018); Meurers et al. (2016); Calvo et al. (2014) show their results, and I used this approach in Chapter 6. However, since the estimates are different for different harmonics and places, they are usually hard to compare if displayed together. Calvo (2015); Meurers et al. (2016); Schroth (2020) noticed that problem with the common display of results for all stations in one plot. Therefore, I display them in a different way to jointly demonstrate temporal variations from multiple stations.

The purpose of the response a priori model is to account for the different ratio between factors within the group. Therefore, the initial rigid tide is algebraically multiplied by the local response model (or body tide). The more reasonable this model is, the closer the estimates in least squares (LS) are to 1 and 0 for factor and phase, respectively. Therefore, to investigate temporal variations for different groups and places, I do not transform estimates to give them true physical values of gravimetric factor and phase by adjusting them with the local response model, as in eqs. (3.44) - (3.45). The meaning of the results is therefore how much the estimates temporarily vary in “normalized” units. In the analysis I apply the local response model as estimated and presented in Chapter 7 to the estimates inferred with the WDZe, a priori body tide model as in eq. (3.46). This accounts for the mean or expected value of the estimates and shows how much bias is introduced for different stations by using incorrect ratios. I do not

display standard deviations in MWA because they are relatively small and would complicate the interpretation of the joint display from multiple observatories.

8.3. European Pattern of Temporal Variations

Common Temporal Variations

First, I discuss MWA results for 5 Central European stations with 7 sensors (see Chapter 4). The first investigation uses the WDZe a priori analysis model only, but the estimates are "normalized" as in eq. (3.46) by the corresponding values from the local response model for the largest tide in the group (see Chapter 7 and Appendix B).

The common character of temporal variations of signals as presented in Figures 8.1 - 8.2 is easily recognizable. This is in contradiction to the statement of Meurers et al. (2016), who claimed that there is no significant correlation between the temporal variation of admittance. Even though the stations cover different time spans, in the joint plot, one is not able to clearly distinguish the segments coming from distinct observatories. The long-period (p and N') and short-period (h) characters of tidal parameters (for given groups) in the MWA results are similar and visible regardless of the station and time span. This observation might be easily missed by confusing display that does not take into account local response adjustment and presents the actual values of tidal parameters.

Systematic, common temporal variations are noticeable in almost all groups. The exception is $\mathbf{O}_1$, the principal lunar tide of extraordinarily large amplitude, whose degree 2 satellites have rather similar response, and the degree 3 tide is rather small, appearing to not show any systematic temporal behavior. What I need to highlight is that the amplitude of temporal variations, 0.001 in factor and 0.05 in phase, is below the limit for degree 2 tides which we get from the comparison of two sensors of the same gravimeter. Hence, we may argue if these temporal variations represent any geophysical process. Another group that has the smallest amplitude in MWA groups, $\mathbf{M}_3$*, also exhibits rather random variations but at much larger amplitudes. Notably, all tides within a group also have rather similar estimates, and satellites are significantly smaller compared to the main tide.

Distinct systematic temporal variations were previously reported by Schroth et al. (2018) and Meurers et al. (2016) in the groups $\mathbf{S}_2$, $\mathbf{L}_2$, $\mathbf{M}_2$, $\mathbf{K}_1$, $\mathbf{N}_2$, and $\boldsymbol{\mu}_2$. Groups $\mathbf{K}_1$ and $\mathbf{S}_2$ exhibit semi-annual and annual oscillations. The variation in $\mathbf{M}_2$ has a clear annual pattern, which was also noticed by Meurers et al. (2016). They point out that the modulation is caused by the inseparable contributions of α_2 and β_2. Groups $\mathbf{L}_2$, $\boldsymbol{\mu}_2$, and $\mathbf{N}_2$ contain semi-annual and precessional (8.85 years, p) periods. One could also identify a nodal (18.6 years, N') beat in the $\mathbf{N}_2$ group, which is not clearly present in the other two. Interestingly, the plots of gravimetric factor and phase of the $\mathbf{L}_2$ group resemble reflecting symmetry plots.

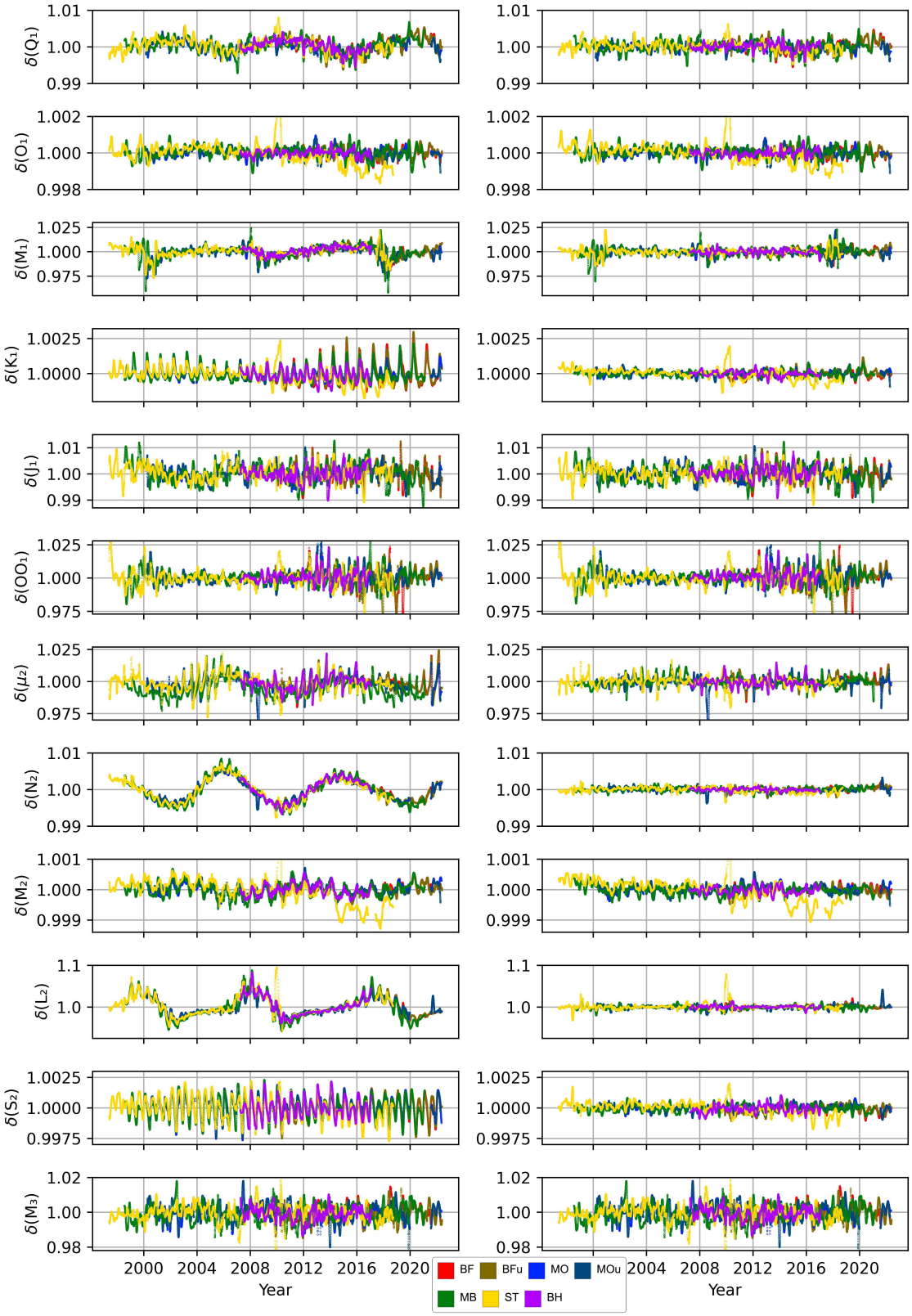

Figure 8.1.: Factor variations of European stations, results for analysis with a WDZe body response model (left) and with corresponding LRM a priori local response models (right). Values were scaled by corresponding local response models.

While we cannot spot annual or semi-annual temporal variations in $\mathbf{M}_1$, $\mathbf{Q}_1$, $\mathbf{J}_1$, and $\mathbf{OO}_1$, we may notice precessional modulation of the gravimetric factor in the $\mathbf{Q}_1$ group, and probably in the $\mathbf{J}_1$ group. Some repeating behavior of temporal variations, but rather in terms of amplitude than systematic change, is seen with nodal frequency in the $\mathbf{OO}_2$ and $\mathbf{J}_2$ groups. Also, every 8.85 years, we see a rapid, short increase in the temporal variations of $\mathbf{M}_1$. Strikingly, $\mathbf{M}_1$ exhibits a similar asymmetric "trend-like" shape in temporal variations as $\mathbf{L}_2$.

Application of a Local Response Model

After applying the corresponding local response model for each station prior to the MWA, the systematic temporal variations that were previously present in all groups and observatories have significantly decreased (Figs. 8.1 - 8.2).

The most impressive result is observed in the $\mathbf{L}_2$ group. The temporal variations, which had a normalized peak-to-peak amplitude of 0.13 (factor) and 8.5° (phase), are now difficult to spot any systematic behavior. The estimated amplitudes after applying the local model are reduced to 0.02 (factor) and 2.4° (phase). This indicates that the temporal variations in this group have decreased by a factor of 7 (factor) and 3 (phase). The absence of systematic patterns suggests that the a priori local response models explain the previous temporal variations, which were the cause of the observed beats. However, the visible increase in temporal variations from its mean in 2000, 2008, and 2017 indicates that the adjustment of the precessional satellite might need further improvement. Alternatively, it could be a non-systematic effect, such as originating from the ocean response.

The temporal variations of the $\mathbf{N}_2$ group have decreased by a factor of 4, and both the precessional and semi-annual frequencies are not visible. The semi-annual temporal variations in the $\mathbf{K}_1$, $\mathbf{S}_2$, and $\boldsymbol{\mu}_1$ groups have decreased by at least a factor of two. The annual variations in the $\mathbf{K}_1$ and $\mathbf{S}_2$ groups are not visible, and the overall character of modulation has changed. The groups $\mathbf{M}_1$, $\boldsymbol{\mu}_1$, and $\mathbf{Q}_1$ do not exhibit the long-period, precessional frequency of the beat. However, larger temporal variations are observed every 8.8 years in the $\mathbf{M}_1$ group, indicating that the local model might require further adjustment. A significant portion of the annual, semi-annual, and nodal modulation in the $\mathbf{M}_2$ group has been captured by the local model, leading to a reduction in amplitude by a factor of 2 and a decrease in coherence.

The character of temporal variations in groups $\mathbf{O}_1$, $\mathbf{J}_1$, $\mathbf{OO}_1$, and $\mathbf{M}_3$* has not clearly changed after applying the local response model, as displayed in Fig. 8.2. This is because most of these variations are not systematic and may represent stochastic noise in the data. Additionally, due to the similar response provided by the a priori model and the amplitude ratio of harmonics within these groups, significant changes were not expected. However, a closer investigation of the differences and the resulting MWA spectra (Appendix E) reveals a decrease in low-frequency temporal variations. This improvement is attributed to the enhanced ratio

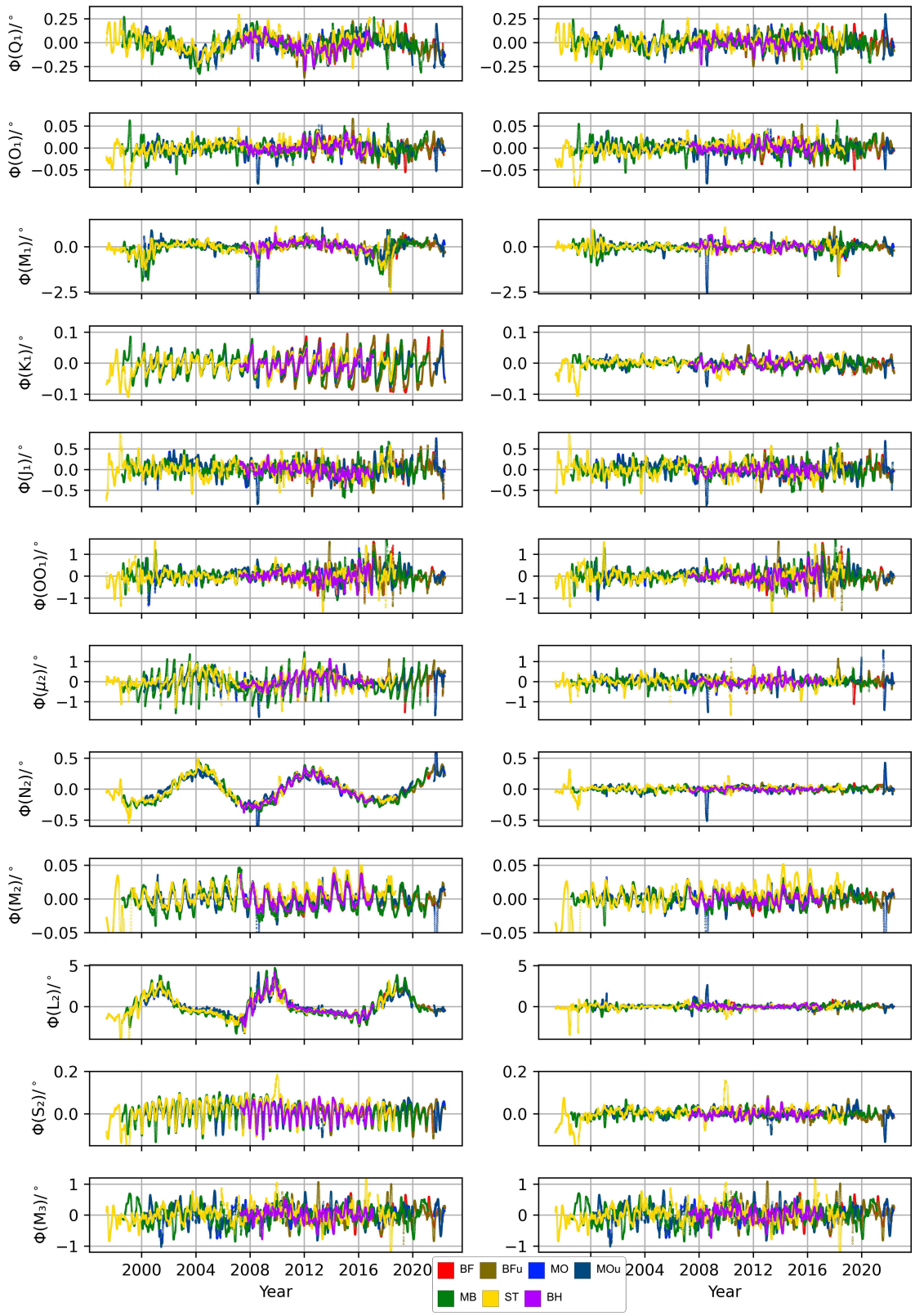

Figure 8.2.: Phase variations of European stations, results for analysis with a WDZe body response model (left) and with corresponding LRM a priori local response models (right).

between tides of degree 3 and the close satellite harmonics of major tides within each group. It is also possible that a more detailed analysis in the future, with further improved models for $\mathbf{J}_1$ and $\mathbf{OO}_1$, could explain the precessional pattern in $\mathbf{J}_1$ or the nodal period of increased temporal variations in $\mathbf{OO}_1$.

Not all systematic temporal variations of $\mathbf{M}_1$ were removed. Since some remaining modulation exhibits precessional and nodal frequencies, it is presumed that further adjustments may improve the local response model. Alternatively, these properties might change at specific times due to resonant or nonlinear ocean responses of M_1*, which the local response model cannot capture due to its non-harmonic nature. The remaining temporal variations in most observatories and groups appear to be rather stochastic. Any common trend observed at a given time would indicate a change affecting all stations, possibly due to ocean or atmospheric influences. If a station exhibits clear discrepancies compared to the others, it could suggest instrument malfunction, incorrect data pre-processing, or significant local changes. Analyzing the temporal variations of all stations, a major event in Strasbourg at the beginning of 2010 is apparent, which was not accounted for in the data pre-processing. Additionally, the estimates of gravimetric factor for major groups ($\mathbf{K}_1$, $\mathbf{O}_1$, $\mathbf{M}_2$, $\mathbf{S}_2$) show a drop around 2015, contrary to other stations that oscillate at a similar level. Both sensors at Moxa display an event in mid-2008 and at the end of 2021. The significant data gap in Moxa in 2020-2021 and the large deviations surrounding it indicate potential data handling issues or possible failure of MWA in that specific location for unknown reasons. Overall, the remaining variations across all stations remain consistent, with some periods showing surprisingly close estimates for major tides ($\mathbf{K}_1$, $\mathbf{M}_1$, $\mathbf{O}_1$, $\mathbf{S}_2$, $\mathbf{L}_2$, $\mathbf{N}_2$, $\mathbf{M}_2$). The reason for this consistency is unknown, but it could be related to the remaining ocean response or radiation tide, which was not accounted for in the local model. It is possible that these factors require better adjustments in the a priori model, or they may exhibit incoherent frequency, amplitude, and phase characteristics or time variation, making them difficult to express accurately with the local model. In such cases, the variations would be similar across all stations. Notably, the station with the largest deviations from the rest is Membach, which is located closest to the North Sea. Some larger peaks in early 2006 and 2009 are also noticeable in its temporal variations.

8.4. Global Station Analysis

Initial Temporal Variations

I display the MWA results for 6 stations that are outside Europe (Chapter 4), namely: Kamioka (Asia/Japan), Djougou (Central Africa), Sutherland (South Africa), Tigo-Conception (South America), and Canberra (Australia). For display reasons, results for the Northern Hemisphere (including Djougou) and the Southern Hemisphere are shown at different diagrams. The first

investigation uses the WDZe a priori analysis model only, but the estimates are "normalized" (eq. 3.46) by the corresponding local response model (see Chapter 7). Some of the variations of Cantley are outside the plots, and I also display results for Moxa for comparison. Part of variations seen at Cantley coincides with results for Kamioka (e.g. $\mathbf{N}_2$, $\mathbf{K}_1$).

I have selected stations with the longest available records in each region, but all of them are situated near the oceans. There is actually no truly 'continental' station in this comparison. The only somehow continental station is Djougou, located relatively far from the ocean (about 400 km) but positioned in the savanna close to the Sahara, experiencing a significant influence from the radiation tide. Djougou is also the only station in this comparison that is not located in middle latitudes but close to the equator. As a result, its diurnal tides are much weaker than the semidiurnal tides. Sutherland is located in the mountains, and it is to some extent also in proximity to the oceans. Both, Tigo-Concepcion and Kamioka are very close to the coast, practically surrounded by the oceans. Kamioka, Cantley, and Djougou are in the Northern Hemisphere (Fig. 8.3 - 8.4), while the others are in the Southern Hemisphere (Fig. 8.5 - 8.6).

While we observe systematic temporal variations for each station in almost all groups, we notice significantly different patterns (Fig. 8.3 - 8.6). Some variations have much larger amplitudes compared to what we observed in Europe. This disparity can be attributed to diverse influences from oceans and atmospheric effects. Therefore, the combined plots lack consistency across different locations.

In groups $\mathbf{J}_1$, $\mathbf{Q}_1$, $\mathbf{O}_1$, $\mathbf{M}_3$*, and $\mathbf{OO}_1$, we do not observe any systematic variations. In most stations, the variations of $\mathbf{O}_1$ and $\mathbf{M}_3$* are below the level of 0.001 (factor), which can be attributed to noise. However, the group $\mathbf{OO}_1$ shows an increase in amplitude in 2014. The temporal variations of $\mathbf{M}_1$ exhibit a clear pattern with an 8.8-year cycle from 2004 to 2012. In the case of the group $\mathbf{K}_1$, we observe large temporal variations with two patterns that are shifted in time by half a year between the two hemispheres. This observation is not surprising since the main cause of the beating is S_1, the radiation tide, which is dependent on the season. This can also be visualized in the phase plot. As expected, we do not observe significant temporal variations for the semidiurnal tides in Djougou, except for the group $\mathbf{S}_2$, which appears consistent across all stations. The groups $\mathbf{N}_2$ and $\mathbf{L}_2$ exhibit similar large variations in Canberra and Sutherland, but with a few years shift. This can be attributed to different ocean responses originating from different oceans, as confirmed by the local models. The long-period trends (p and N') are a result of the ratio to degree 3 tides. Kamioka and Cantley exhibit similar patterns. Interestingly, the variations of $\mathbf{N}_2$ and $\boldsymbol{\mu}_2$ at Tigo are similar to those in Canberra but are almost absent in $\mathbf{L}_2$. Lastly, the tide $\mathbf{M}_2$, which is of great interest, exhibits strong annual modulation in these stations but of different nature. We observe that the "peaks" for Sutherland and Cantley occur at the same time but are opposite to Tigo and Canberra. The

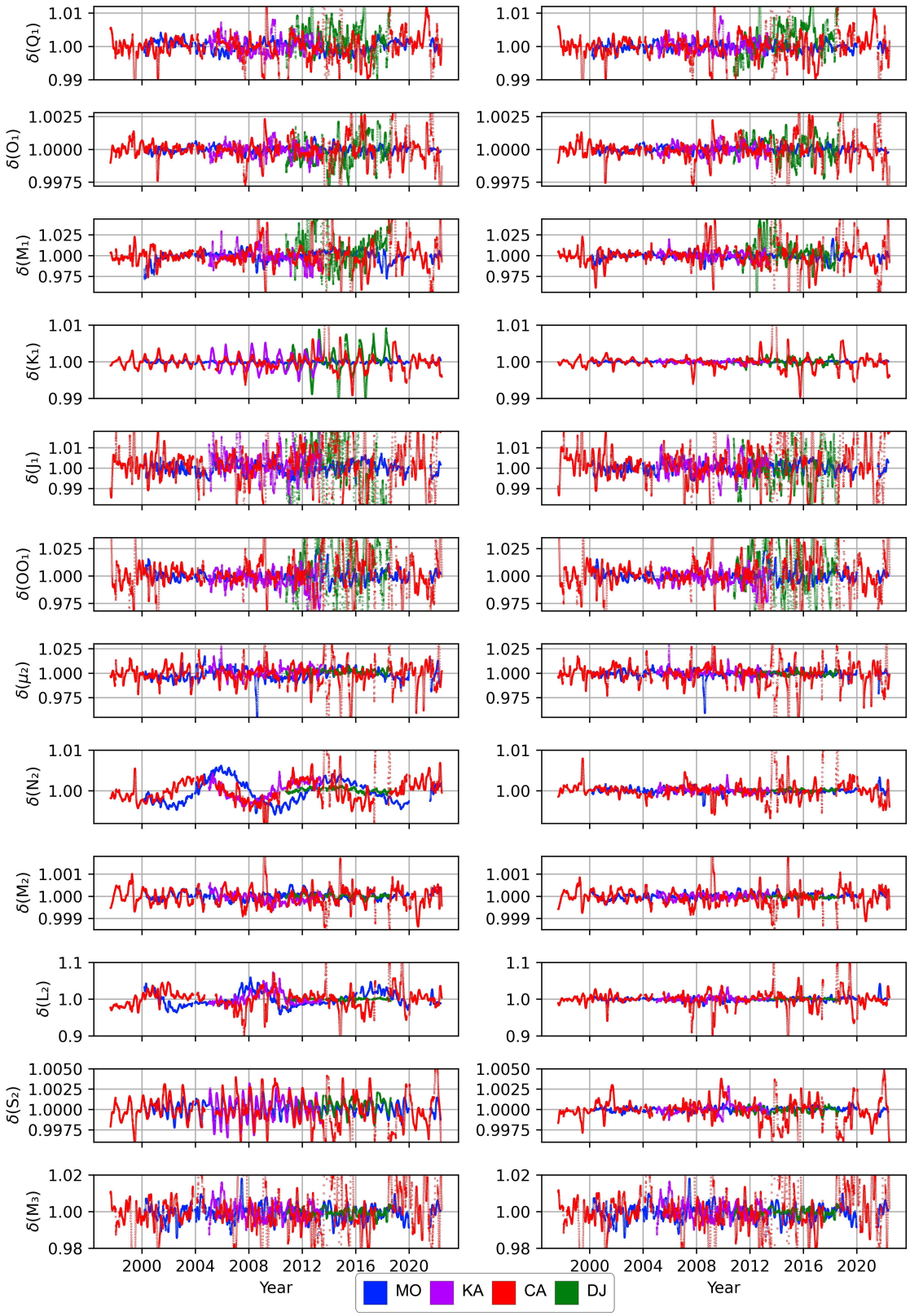

Figure 8.3.: Factor variations of stations in the Northern Hemisphere, results for analysis with a WDZe body response model (left) and with corresponding LRM a priori local response models (right). Values were scaled by corresponding local response models.

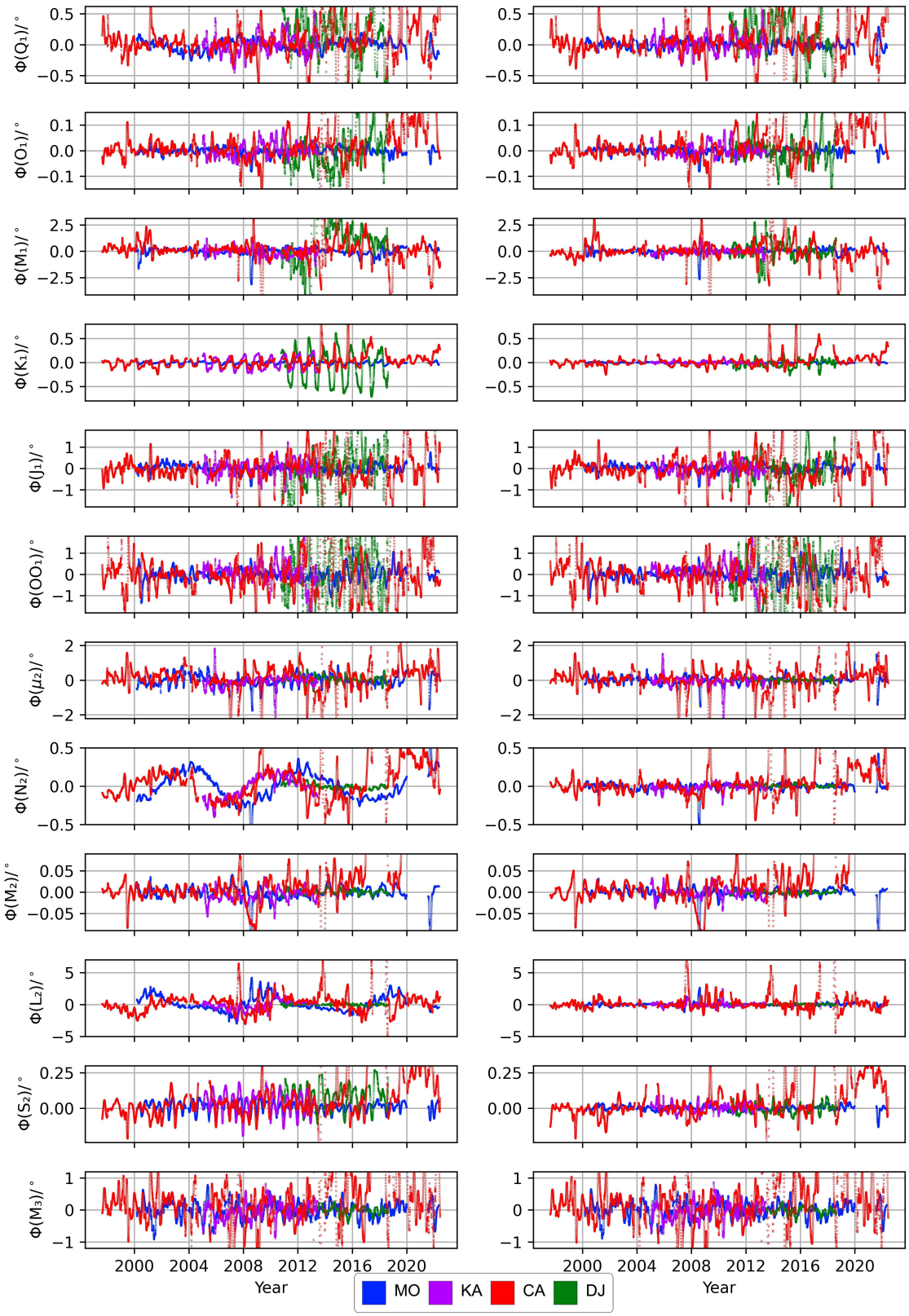

Figure 8.4.: Phase variations of stations in the Northern Hemisphere, results for analysis with a WDZe body response model (left) and with corresponding LRM a priori local response models (right).

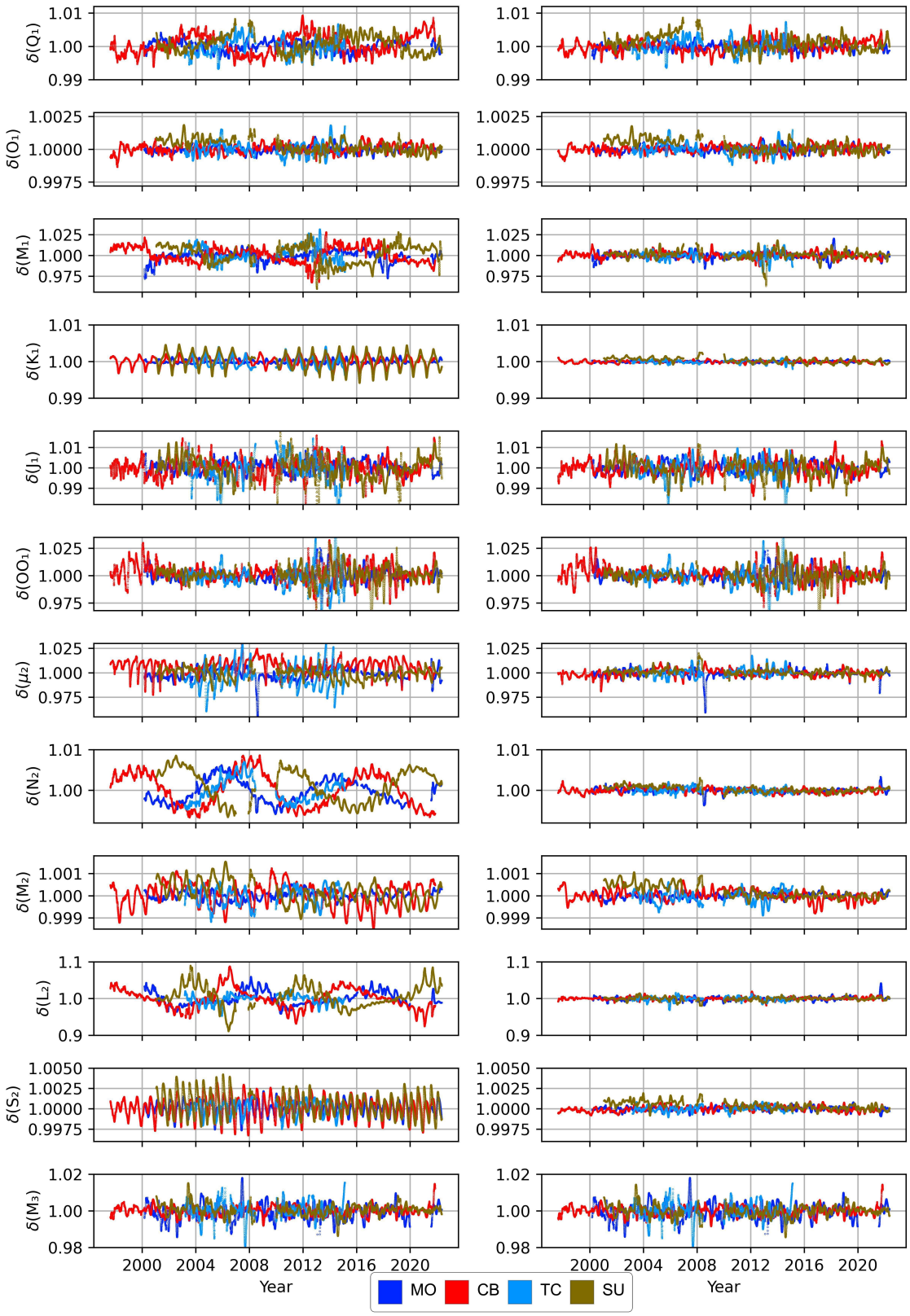

Figure 8.5.: Factor variations of stations in the Southern Hemisphere, results for analysis with a WDZe body response model (left) and with corresponding LRM a priori local response models (right). Values were scaled by corresponding local response models.

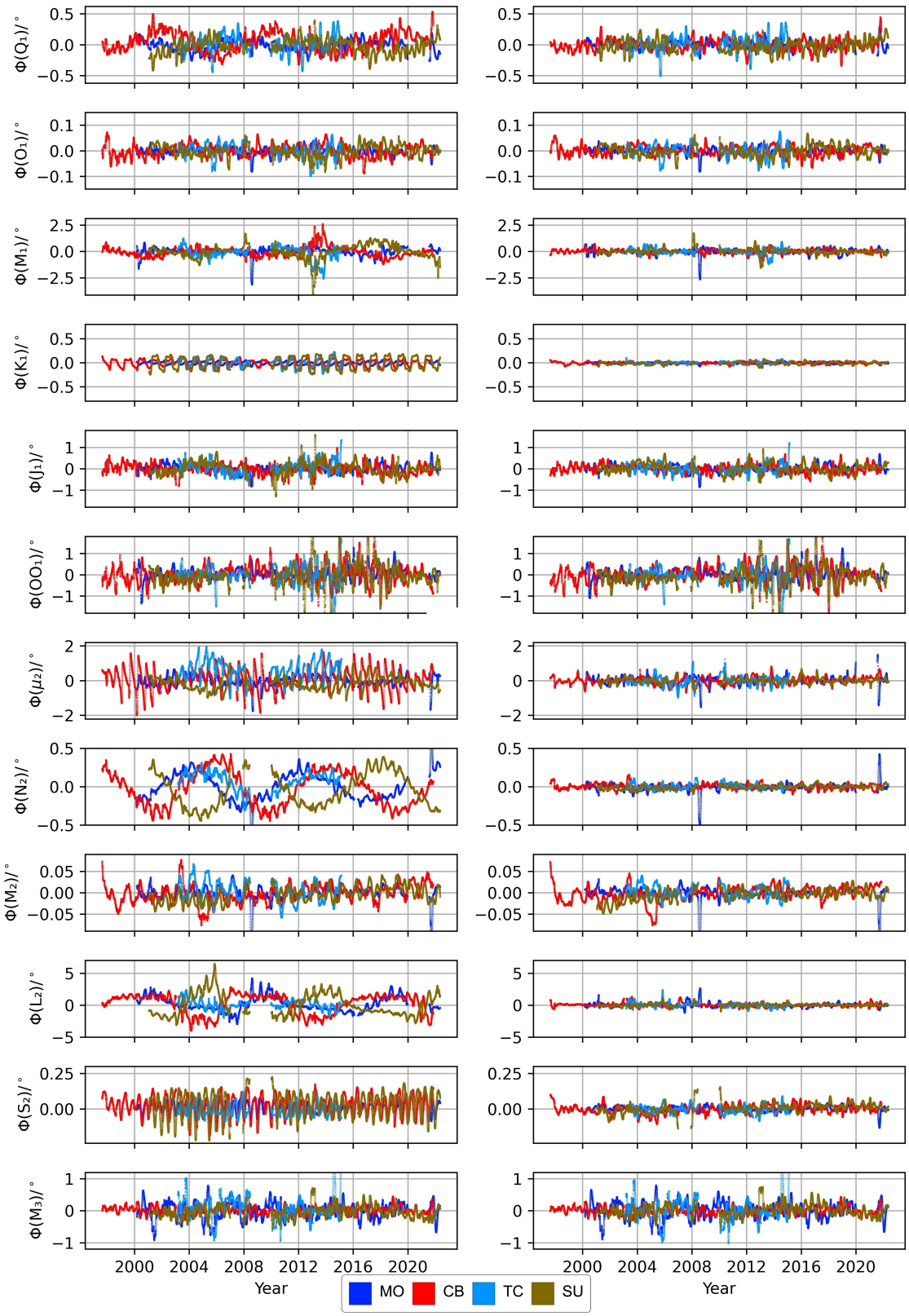

Figure 8.6.: Phase variations of stations in the Southern Hemisphere, results for analysis with a WDZe body response model (left) and with corresponding LRM a priori local response models (right).

variation in Kamioka is relatively small. Although I do not have a hypothesis to explain these observations, I can attribute them to the local response model.

In summary, despite differences in amplitudes, timing, and polarity, the overall frequencies of systematic temporal variations are similar to what we observe in European stations.

Application of a Local Response Model

After applying the local response model for each station prior to the MWA, the systematic temporal variations become less evident (Figs. 8.3 - 8.6). Previously, when using the WDZe body tide model for analysis, these patterns were clearly visible despite their differences. In the compilation of all the stations, it is no longer apparent that the temporal variations correspond to beating frequencies or modulations. Only groups $\mathbf{M}_2$ and $\boldsymbol{\mu}_2$ exhibit some remaining semi-annual variation. Even the group $\mathbf{K}_1$ does not show a clear semi-annual pattern of variation. I will discuss Cantley separately from the other stations.

The group $\mathbf{L}_2$ remains the most remarkable in terms of temporal variations. After applying the local response model, the normalised peak-to-peak amplitudes decrease from 0.18 (factor) and 10.0° (phase) to 0.03 (factor) and 1.8° (phase) respectively. This represents a decrease in temporal variations by a factor of almost 9 (factor) and 5 (phase). No long-period variations are evident, indicating that further adjustments may not be necessary.

Temporal variations in group $\mathbf{N}_2$ decrease by up to a factor of 8, making precessional and semi-annual frequencies less visible. The semi-annual variations in groups $\mathbf{K}_1$, $\mathbf{S}_2$, and $\boldsymbol{\mu}_1$ are not systematic after applying the local response model. Similarly, the annual variations in $\mathbf{K}_1$ and $\mathbf{S}_2$ are not clearly visible. These results differ from what was observed in Europe. The groups $\mathbf{M}_1$, $\boldsymbol{\mu}_1$, and $\mathbf{Q}_1$ do not exhibit long-period precessional oscillations. Unlike in Europe, there is no clear increase in temporal variations every 8.8 years in group $\mathbf{M}_1$. The local response model reasonably captures a large part of the modulation, and the remaining signals are incoherent. Notably, there is a lack of harmonic modulation in groups $\mathbf{L}_2$, $\mathbf{N}_2$, and $\boldsymbol{\mu}_2$. Stations like Djougou and Kamioka do not show any remaining annual modulation caused by $\mathbf{S}_1$ and $\mathbf{R}_2$ radiation tides, unlike what was observed in Europe. The corresponding variations in other stations for these groups are also smaller compared to Europe. The improved ratio for closely-spaced main harmonic in local response models is the main reason of that. Temporal variations in group $\mathbf{M}_2$ decrease in some cases, and the overall systematic annual modulation is not visible.

The character of temporal variations in groups $\mathbf{O}_1$, $\mathbf{J}_1$, $\mathbf{OO}_1$, and $\mathbf{M}_3$* has not significantly changed. However, a detailed analysis of each station, as seen in Appendix C, reveals that high-frequency trends (above 1 cpm) and some small long-period trends (0.1 and 2 cpy) have decreased. Although these tides have small amplitudes and high noise levels, an improved model within $\mathbf{J}_1$ and $\mathbf{OO}_1$ in future analyses may explain their precessional patterns ($\mathbf{J}_1$) or nodal periods of increased temporal variations ($\mathbf{OO}_1$).

The station Cantley exhibits less systematic temporal variations compared to other stations, but the amplitude of the variation appears rather large. It shows jumps in estimates during the second half of the analyzed period. To investigate this further, two different local models were tried: one using the full time series for estimation and the other using only the data until the end of 2012. The results show significantly smaller variations for the earlier time period in groups $\mathbf{L}_2$, $\mathbf{N}_2$, and $\mathbf{S}_2$. However, there are indications of noise leading to instability, as evidenced by the overall large amplitudes of the variations and random "peaks" or "glitches". Although some significant reduction of temporal variations is seen, the large variations still persist. The remaining oscillations appear to be non-systematic. Considering the success of the method for other stations regardless of the location or proximity to oceans, it is concluded that the noise level at the Cantley station is high or there may have been instrumental or data-processing issues. Therefore, the results from this station need to be considered with caution and may require further inspection.

Upon investigating the plots of major tides, potential problems with data for various stations were identified. A calibration offset is observed in Sutherland, where the gain for 2001-2007 is larger compared to the records from 2009-2022 (see detailed plot in Appendix C). Certain events in 2004/2005, 2005/2006, and late 2015 are noticeable in Canberra and to some extent in Sutherland. These events are most visible in groups $\mathbf{M}_1$ and $\mathbf{M}_2$. Additional events occur in Kamioka in 2010 and 2011. The remaining variations appear reasonable, with the amplitude of non-systematic oscillations at a similar level. It is speculated that some of the temporal variations observed in group $\mathbf{M}_2$ could be explained by ocean models, as presented by Schroth (2020). In Djougou, significant events are observed in 2014, late 2015, and mid-2016. Similar events can be seen in Kamioka in 2006, late 2005, late 2009, and mid-2010. Peaks are observed in Sutherland in mid-2014 and early 2017.

8.5. Subpolar: Ny-Ålesund, Syowa

The temporal variations of these two subpolar stations also differ considerably from each other (Figs. 8.7 - 8.8). Diurnal and semidiurnal tides are weak at these stations, so factors such as local resonance and changing ice coverage influencing the ocean loading play a significant role in their observations. The temporal variations at Syowa station, in particular, are non-harmonic and have large amplitudes. Additionally, the recording time at these stations is relatively short. Applying the local response model does not result in a change of the variation pattern, only a subtle shift in the response. However, there are slightly less deviating estimates in the $\mathbf{M}_2$ group. Based on the character of the variations observed in the MWA and their amplitudes, it is concluded that the results from the Syowa station cannot be considered reasonable due to the limitations of the local response method.

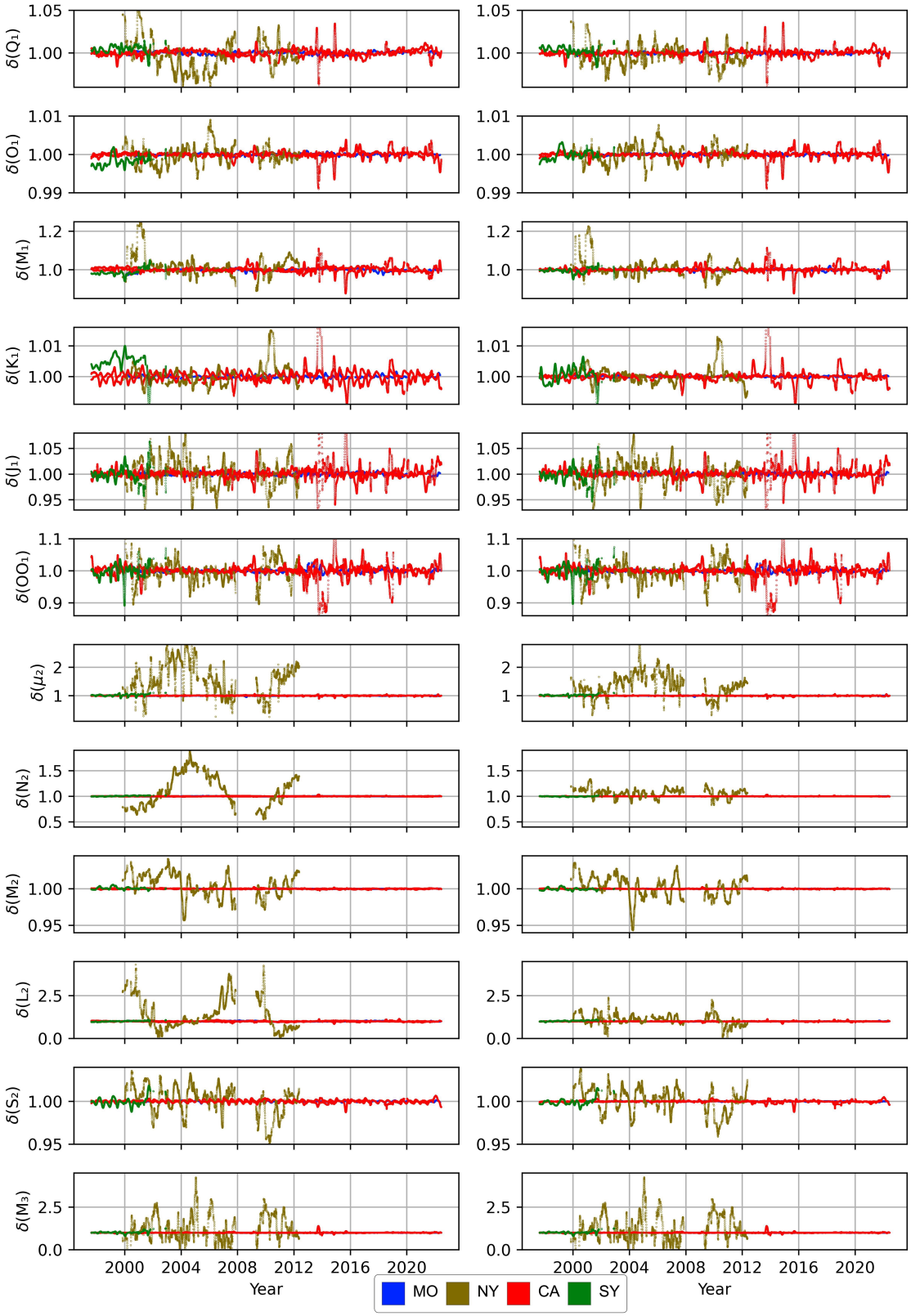

Figure 8.7.: Factor variations of Subpolar stations. Cantley and Moxa are for reference. Results for analysis with a WDZe body response model (left) and with corresponding LRM a priori local response models (right). Values were scaled by corresponding local response models.

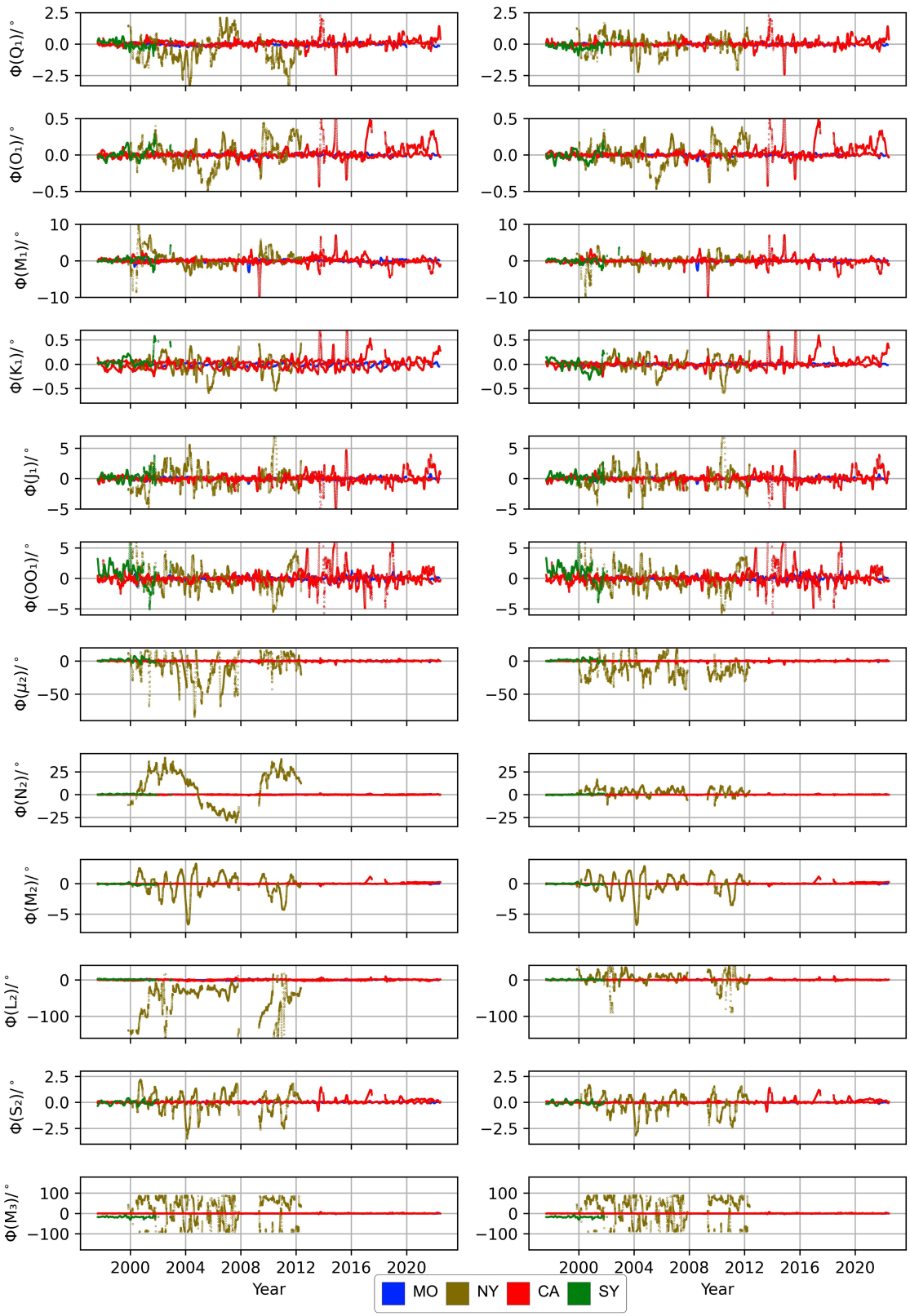

Figure 8.8.: Phase variations of Subpolar stations. Cantley and Moxa are for reference. Results for analysis with corresponding LRM a priori local response models (left).

On the contrary, the local response method explains the temporal variations of Ny-Ålesund well (Figs. 8.7 - 8.8). Although diurnal tides do not exhibit harmonic temporal variations - and at high latitudes diurnal tides are weak - the method still reduces the precessional modulation in the $\mathbf{Q}_1$ group. There is also a noticeable decrease in the temporal variations of the $\mathbf{S}_2$ group. However, the most significant improvements are observed for the semidiurnal harmonics that are strongly affected by ocean responses for degree 3 tides. These groups include $\mathbf{L}_2$, $\mathbf{N}_2$, and $\boldsymbol{\mu}_2$, with their gravimetric factor variations decreasing by up to 4 times. The phase variations of these groups, although still large, are in more reasonable levels.

For the remarkable $\mathbf{L}_2$ group, the range of variations has decreased from 180° to 50°. Similarly, the amplitude of $\mathbf{N}_2$ variations has decreased from 70° to 20°, with a reduction in strong long-period modulation. However, it should be noted that the phase variations of some groups, such as $\mathbf{M}_3$*, still exhibit extreme values. It remains uncertain whether further analysis with a more appropriate local response could further decrease the temporal variations of tides like $\mathbf{S}_2$ or $\mathbf{M}_2$, as their harmonic behavior does not appear to be systematic. In conclusion, I see the indication of the potential issues with the instrument or data in Ny-Ålesund. The beginning of 2004 and 2005, as well as in 2001, 2002, and 2010, have been identified by the MWA and need further investigation.

8.6. Summary

The successful application of the local response method in MWA demonstrates its effectiveness and rather independence from the length of the time series and station location. In some cases, the reduction of temporal variations yields remarkably good results, particularly for stations with large changes in factors and phases between frequencies that deviate significantly from the theoretical a priori WDZe model. Djougou, Kamioka, and Ny-Ålesund are excellent examples of this. Therefore, it is crucial to consider the local response for accurately assessing the ratio between harmonics in any validation method, especially when a priori grouping is involved. This separation of bias from actual temporal variations enables further investigations and analyses. Moreover, removing large systematic variations from the results of the analysis allows for the proper identification and addressing of potential data issues in stations. And eventually, after correction with good ocean models, the corrected admittances would be closer to the real Earth.

The display method that makes use of the specific local response models as in eq. (3.46) is a practical technique to visually investigate the common character of temporal variations for distinct places. While the diagrams do not reflect true physical values of gravimetric factor and phase, the relative deviations are visualised. Similar character of variations might be observed, which can be easily missed otherwise.

However, there are two stations for which the method does not significantly alter the temporal variations: Syowa and, to some extent, Cantley. The lack of significant changes in temporal variations for Syowa is expected, as the local model did not appear reasonable and the residual noise exhibited relatively large amplitude. Therefore, I can conclude that the noise level at this station is too high and data quality too low for meaningful results. The interesting case is Cantley, where a visible decrease by a factor of 2 is observed in $\mathbf{N}_2$, $\mathbf{L}_2$, and $\mathbf{S}_2$ temporal variations. However, the temporal variations of $\mathbf{K}_1$, $\mathbf{M}_1$, and $\mathbf{M}_2$ only exhibit a small decrease. It is worth noting that while most stations at similar latitudes display systematic temporal variations for $\mathbf{K}_1$, this behavior is not clearly observed after the data gap in 2004 at Cantley. Additionally, unusual large events are seen in other groups in 2007 and 2009. These observations suggest that the instrument at Cantley may have become unstable after 2004, or there were issues with data preprocessing, leading to incorrect and noise-influenced estimates for the local model.

9. Conclusions and Outlook

Conclusions

This thesis covered two important aspects of analysis of Earth tides. The first problem I revised was the resolution in the tidal analysis. The known analysis methods applied grouping as a parametrization for stable and relevant results. Based on a presumption on possible resolution, it was verified with spectral analysis of residuals - which, however, has limited resolution power next to the closely spaced, large-amplitude harmonics. The second question is the cause of temporal variations of tidal parameters. While the moving window analysis should be a good technique for investigation of instrument stability (Calvo, 2015) and admittance changes, the large systematic temporal variations as reported by Meurers et al. (2016) and Schroth et al. (2018) were unexpected. The reasons for them were unclear and they needed the clear explanation. In the study I used the data from the GGP as provided by IGETS. The original data were 1-minute sampled, pre-processed by Jean-Paul Boy, but further processing, including decimation I performed myself, after careful tests for the procedure.

For investigation of these two problems I developed the new method, `RATA`, which does not need a priori grouping. The ill-conditioning is parameterized by additional constraint in the objective function. Even though programs `Eterna 3.40`, its update `ETERNA34-ANA-V4.0`, `Baytap-G` and `VAV/2000` use different methods for grouping and its verification, none of them allows a user to investigate each contribution separately. The grouping is applied to the reference model only, not to the parameters in the linear regression. Hence, this is a qualitatively different approach, and the only available tidal analysis method for Earth tides for which each harmonic in principle can have a different set of estimates. No other software allows for investigation of the significance of harmonics or groups and the correctness of the parameters in inversion.

The solution is found by updating the reference model, where the parameters for harmonics deviate from the reference for specific harmonics. Different adjustments are applied only where results of the linear regression problem indicate that harmonics significantly require different parameters to reduce the data misfit. Hence, the grouping and the resolution is data driven. I did not follow the guidance of Rayleigh criterion. The trade-off curve (Fig. 3.2), which uses the misfit for untapered data, effectively helps to avoid over-fitting. Not being limited by frequency distance, I explored the super-resolution of tides, as suggested by Munk and Hasselmann (1964). We learned that there is a link between the actual resolution and the tide amplitude, which varies significantly depending on the location. We can handle tides of different degrees separately

(only `ETERNA34-ANA-V4.0` does it). By finding some contributions non-significant, we avoid over-fitting, trying to search only for tides necessary for a solution with the smallest possible set of parameters ("Occam's razor"). The method was first applied to the data from the Black Forest Observatory, Schiltach. After initial success of the method and recognizing its benefits, I performed the analysis for stations in Europe for validation. We learned that we can achieve high resolution, and significant, well constraint parameters for various time series length. Further, we demonstrate that the constrained approach allows us to identify variations of tidal parameters in rather narrow frequency bands, which would be lost in a priori grouping schemes. From the double-sphere instruments we found that the minimum discussed error should be 0.005 (or 0.001 for large amplitude harmonics) for δ and 0.1° (0.02° for large harmonics) in phase. While the local response models in Europe are very similar, what we expect, there are some striking differences. Most of them are possibly caused by oceans and radiation, some by instrumental problems and data. The deficiency of the `RATA` method might be also a cause. I confirmed that the resolution depends on the amplitude of the tides, hence very different grouping schemes were used for stations at different latitudes despite the same length of time series, and very similar grouping schemes for all analysed stations at the same latitudes, despite the time series length. I analysed the data for the station on each continent achieving high-resolution models that are rather smooth in the frequency response. Hence, they appear reasonable. I found that the local response models are significantly different at each place. This emphasises the influence of the ocean and atmosphere and need for verification with the corresponding models. I obtained very detailed models with fine structure. Tides of different degrees obtain separate parameters. I also identified small inconsistencies and simplifications that are present in the `Eterna 3.40` tidal analysis software.

The hypothesis regarding the significance of the improper ratio of tides forming a group in the MWA procedure has been tested. While the body tidal model, WDZe, makes an assumption about tidal response based on seismology, it is far from the reality due to the strong influence of the atmosphere and oceans. Synthetic test of harmonics in $\mathbf{K}_1$ group presented by Schroth (2020) demonstrated this problem. Therefore, I used the local response models, that describe the apparent ratio between all tides, as an adjustment to the priori body tide model in the tidal analysis. Apart from that, all other aspects of the setup were the same as in other studies, including window length and definition of wave groups. I compared the results for MWA in which standard WDZe a priori body tide was used to the one with the local response LRM model adjustment. The first results were consistent with the previous studies (Schroth et al., 2018). We used the local model adjustment to correct for different average values of the tide at given station, hence the same pattern of temporal variations is clear for Europe. This was missed in previous studies (Meurers et al., 2016). The temporal variations for other stations around the world reveal some similarities, but due to various effects they are altered. Such effects are:

different hemisphere, particular ocean loading response or specific response to radiation tides. The application of the local response practically removes systematic variation for almost all tides. In some stations it also decreases variations in tides which modulation was indiscernible from the chaotic variations, such as $\mathbf{O}_1$, $\mathbf{Q}_1$ and $\mathbf{J}_1$. The most impressive results are obtained for group $\mathbf{L}_2$, where the gravimetric factor oscillations decreased on average by 7 times, and the phase by 4 times. $\mathbf{N}_2$ variations decreased by a factor of 4. The proper ratio in K group, influenced by radiation tide S_1 strongly deviating from the theoretical ratio, in some cases even completely describes the apparent temporal variations (Djougou, Kamioka). For $\mathbf{K}_1$ it is essential not only to keep the radiation tides (S_1) separate, but also to allow for a small adjustment of the frequency dependence within the NDFW resonance. Most likely the latter is not due to the FCN model used in the a-priori body tide model being wrong, but due to loading effects taking place in this frequency band. All of the considerations lead to the final, strong conclusion that the fixed assumed ratio in a priori analysis model, since it does not explain the apparent response, was the main cause for temporal variations observed by Calvo et al. (2014); Meurers et al. (2016); Schroth et al. (2018). In the search for time-variant components of the Earth's admittance, a detailed local model must be used as a basis to which adjustments are subsequently applied. The most detailed model of the local response is achieved with regularization and data-driven grouping. Approaches based on a priori grouping schemes, like based on the Rayleigh criterion, likely miss essential properties of the admittance function. The remaining variation of the parameters for $\mathbf{M}_2$ may be understood as being caused by time varying ocean loading, as discussed by Schroth (2020). Some of the constituents (like α_2, β_2, or S_1), which are responsible for the temporal variation of larger groups, turn out to be not constant themselves. In the BF21-model they do not exactly capture the time-invariant tidal response of the Earth, but rather the specific response (in case of α_2 and β_2) or a specific non-tidal signal contribution (in case of S_1) in the analyzed time window.

Outlook

Due to the novelty of the `RATA` analysis method, it has not undergone extensive testing and verification like other results obtained over the last three decades with programs that use wave grouping. Therefore, more validation tests with real and synthetic data are expected to asses the limits and robustness of the method. There is still an open question about the estimation of uncertainties. I did not investigate the properties of model resolution and data resolution matrices, which are also means of studying the problem. In the method, I implemented the easiest constraint, the zeroth-order Tikhonov regularisation. The model constraint causes a general tendency (or bias) towards the reference model, which is to some extend unfavorable. The code can be further updated with the second-order Tikhonov regularisation that expresses the preference for the 'smooth' model. This might render the need for iterations unnecessary,

however, the possibility to test particular tides with the reference model for their significance is still an essential advance of the method compared to other available approaches.

The potential of high-resolution tidal models for relatively short time series (e.g. 1 year) might be tested. The possibility of achieving high-resolution, reasonable and high-accuracy models from short time series has applications in scenarios where gravimeters are not placed permanently but for short campaigns, or for early analysis of recently deployed stations, like these on Zugspitze or in Helgoland. Nevertheless, there are plenty of other stations in GGP that already have a reasonable data length for analysis which should be investigated with `RATA`. Just naming few interesting places, they are Boulder, Matsushiro, La Plata. In Europe I could propose Onsala, Metsähovi, Yebes or Medicina. The joint inversion for stations that had different instruments over the time, like Strasbourg, or the same instrument but that was relocated to a different station, like Vienna/Conrad is also possible, and provides enormously lengthy gravity data. All the possible stations suitable for applying the method are visible on the map, Fig. 4.1b-4.1a. A useful follow-up question, once the local response models for stations at various global locations have been determined, is to determine the body tide model by removing the ocean and atmospheric influence with the recent models (Sulzbach et al., 2022). Hence, the meaningful information about the Earth properties might be inferred or validated. Ducarme (2012); Baker and Bos (2003) compare different Earth models derived from seismology with the result of tidal analysis. Lau et al. (2017) uses tides for Earth's tomography. Amoruso and Crescentini (2020) studied NDFW parameters from strain data and Rosat et al. (2009); Ducarme et al. (2007); Calvo (2015) verify NDFW parameters from the gravity.

In the end, I tested the method only for gravity data from superconducting gravimeters (SG). One may try to apply the method to other types of data, such as tilt, strain, or spring gravimeter. With respect to the MWA, further improvement of estimates of some parameters might explain the systematic temporal variations better. Moreover, application of the ocean and atmosphere models, as Schroth (2020) presented, could further explain the remaining temporal variations in some groups. After all, up to now, the MWA is performed on wave groups. Once the local response model is established, the wave group concept can be abandoned in this procedure too. By adjusting the body tide with by the local response model a priori, and using it also as the reference model constraint, the single harmonics contributing to temporal variations might be identified by regularized MWA. This step, however, requires an optimization of the code, because currently such procedure requires relatively long computing time (weeks) and large storage.

Finally, I would like to emphasise a need for one, consistent and uniform convention for naming the tides (including different degrees). The recent developments in tidal analysis, improved accuracy and resolution driven by SGs, ocean models and long time series highlight the importance of adopting such a convention.

10. Acknowledgments

While this thesis represents a substantial amount of work, it would have been impossible for me to accomplish it all on my own. In this section, I would like to express my deepest gratitude to all who have helped, supported, and accompanied me throughout this long journey.

First and foremost, I would like to extend my special thanks to **Thomas Forbriger** for supervising this project and providing extensive support throughout my time at KIT. I am particularly grateful for his exceptional ability to provide detailed and descriptive answers, whether it was in response to scientific inquiries or feedback on my work.

I am also immensely grateful to **Walter Zürn** for the insightful discussions and for generously sharing his vast knowledge and experience in the field of Earth tides. I would like to express my sincere appreciation for his thorough feedback, comments, and review of my PhD thesis. Additionally, I would like to acknowledge **Andreas Rietbrock** for his supervision and support during my doctoral project, as well as for sharing his expertise in Inverse Problems.

I would like to express my gratitude to ***ICET*** and the ***GFZ-ISDC (IGETS)*** data centres for providing the SG time-series data and to **Jean-Paul Boy** for his invaluable work with data preprocessing. The contribution of **Daniel Hollarek** and **Konstantin Drach** in the development of the `RATA` code was truly invaluable, and I am grateful for our collaborative efforts and the enriching experience it provided.

I extend my thanks to **Kerstin Dick**, **Claudia Payne** and **Rainer Plokarz** for their assistance with administrative challenges. I would also like to acknowledge the help of **Petra Knopf**, **Thomas Hertweck**, **Thomas Nadolny**, and **Michael Fritsch** in my work with software and hardware at GPI.

I am grateful to **Jeremy Rekier** and **Angela Hibbert** for their assistance during my stays in Brussels and Liverpool. I would also like to express my appreciation to the numerous remarkable individuals I had the pleasure of meeting at ***ROB*** and ***NOC*** during those visits, who ensured that I had an enjoyable experience. I would like to extend my thanks to **Duncan Agnew**, **Philip Woodworth**, **Véronique Dehant**, and **Tim van Hoolst** for the fruitful discussions and the opportunity to share my results. A special note of gratitude goes to **Duncan Agnew** for his valuable comments on the manuscript. I am thankful for the helpful discussions and the chance to present my findings to the participants of the ***Arbeitskreis Geophysik Geodäsie***.

I would like to convey my deepest gratitude to my ***family*** for their unwavering support in my pursuit of a scientific-PhD career. They not only encouraged me but also fostered an academic environment that cultivated my interests in astronomy, nature, mathematics, and engineering.

A special thanks goes to all my friends who supported and accompanied me throughout this journey, always ready to lend an ear to my complaints and share in my joys. I am grateful to **Agnieszka**, who sent me an email with the advertisement for this project, believing it was a perfect fit for me. I am also grateful to my friends in ***Amsterdam*** (the ***India group***, all the ***Mutri***, former ***office-mates***, and beyond) who provided immense support during a challenging time when my initial PhD project didn't work out. To my GPI office-mates, **Mike** and **Sergio**, thank you for the camaraderie during our PhD journeys. Our casual conversations and practical jokes played a vital role in keeping our spirits high.

To my Polish friends, I extend my heartfelt thanks, particularly to **Daria**, who closely accompanied me for most of my PhD time in Karlsruhe, offering strong support. I thank **Magda & Krzysiek G.** for keeping in touch, and for reviewing part of the thesis. I acknowledge the discussions and great time spent with **Krzysiek B., Julia, Miras, Mieszko**, **Drożdżu** with ***Kraina Grzybów***, and many, many others.

I would like to express my appreciation to the members of the ***Schützengesellschaft Karlsruhe 1721 e.V.*** for the amazing times I spent there.

Lastly, I would like to express my profound gratitude to all those not mentioned explicitly but who have played a part in shaping my journey and academic pursuits. Your contributions, whether big or small, have made a significant impact on this thesis and my personal growth. In conclusion, I am deeply grateful to all the individuals and institutions who have contributed to this research endeavor. Your support, guidance, and encouragement have been invaluable. Thank you for being an integral part of my journey towards completing this PhD thesis.

Funding

This work was carried out in the framework of the **Temporal variation of tidal parameters** project in joint collaboration between Geophysical Institute (GPI) and Geodetic Institute (GIK), funded by the German Research Foundation (DFG grant FO-506/2-1). Conference contributions of author in 2022 and 2023 were covered directly by Geodetic Institute.

The author was supported by the Networking Grant of the Karlsruhe House of Young Scientists (KHYS) to visit Royal Observatory of Belgium in Uccle, Brussels (**ROB**) in May 2019 and National Oceanography Centre in Liverpool (**NOC**) in October 2019.

There's a plan in everything, kid,
and I love it when a plan comes together.

"Col. John 'Hannibal' Smith",
The A-Team

11. Bibliography

D. C. Agnew. Earth Tides: An Introduction, 2005. URL http://www.unavco.org:8080/.

D. C. Agnew. Earth Tides. In G. Schubert and T. Herring, editors, *Treatise on Geophysics*, volume 3, chapter 3.06, pages 163–195. Elsevier B.V., Amsterdam, Boston, 2009.

A. Amoruso and L. Crescentini. Parameters of the Earth's Free Core Nutation from Diurnal Strain Tides. *Sci Rep*, 10, 2020. https://doi.org/10.1038/s41598-020-66426-7.

R. C. Aster, B. Borchers, and C. H. Thurber. *Parameter Estimation and Inverse Problems*. Elsevier Academic Press, Amsterdam, San Diego, 2005.

Atmacs service. Atmospheric attraction computation service, 2022. URL http://atmacs.bkg.bund.de/. Data service by Federal Agency for Cartography and Geodesy (BKG).

T. F. Baker. Tidal Deformations of the Earth. *Sci. Prog.*, 69:197–233, 1984.

T. F. Baker and M. S. Bos. Validating Earth and ocean tide models using tidal gravity measurements. *Geophys. J. Int.*, 152:468–485, 2003. https://doi.org/10.1046/j.1365-246X.2003.01863.x.

J. Bartels. Gezeitenkräfte [Tidal Forces]. In S. Flügge, editor, *Handbuch der Physik*, volume 48: Geophysik: 2, Berlin, 1957. Springer. https://doi.org/10.1017/9781316998793.

J. Bartels. Tidal Forces. In J. C. Harrison, editor, *Earth tides*, Benchmark papers in Geology, chapter 2, pages 25–63. Van Nostrand Reinhold, New York, 1985. This is an abridged translation of the original paper by Bartels (1957).

C. Beaumont and J. Berger. Earthquake prediction: modification of the Earth tide tilts and strains. *Geophys. J. R. Astron. Soc.*, 39:111–121, 1974.

J. Berger. A note on thermoelastic strains and tilts. *J. Geophys. Res.*, 80:274–277, 1975.

C. Bouzard and D. Gambis. The combined solution C04 for Earth Orientation Parameters Consistent with International Terrestrial Reference Frame 2005. In H. Drewes, editor, *Geodetic Reference Frames*, International Association of Geodesy Symposia, pages 265–270, Berlin, 2009. Springer. ISBN 978-3-642-00859-7.

J.-P. Boy. Description of the Level 2 and 3 IGETS data produced by EOST. Technical report, EOST/IPGS, Strasbourg Cedex, France, 2019. URL https://isdc.gfz-potsdam.de/igets-data-base/documentation/.

J.-P. Boy, P. Gegout, and J. Hinderer. Reduction of surface gravity data from global atmospheric pressure loading. *Geophys. J. Int.*, 149:534–545, 2002.

J.-P. Boy, L. Longuevergne, F. Boudin, T. Jacob, F. Lyard, M. Llubes, N. Florsch, and M.-F. Esnoult. Modelling atmospheric and induced non-tidal oceanic loading contributions to surface gravity and tilt measurements. *J. Geodyn.*, 48:182–188, 2009.

J.-P. Boy, J.-P. Barriot, C. Förste, C. Voigt, and H. Wziontek. Achievements of the first 4 years of the International Geodynamics and Earth Tide Service (IGETS) 2015–2019. In *International Association of Geodesy Symposia*, Berlin, Heidelberg, 2020. Springer. https://doi.org/10.1007/1345_2020_94.

E. W. Brown and H. B. Hedrick. *Tables of the Motion of the Moon.* 1920.

S. G. Brush. *Nebulous Earth. The Origin of the Solar System and the Core of The Earth from Laplace to Jeffreys.* 1996.

M. Calvo. *Analysis of long-term gravity records in Europe: Consequences for the retrieval of small amplitude and low frequency signals including the core resonance effects.* PhD thesis, Université de Strasbourg; Universidad complutense de Madrid, 10 2015. URL https://tel.archives-ouvertes.fr/tel-01222234.

M. Calvo, J. Hinderer, S. Rosat, H. Legros, J.-P. Boy, B. Ducarme, and W. Zürn. Time stability of spring and superconducting gravimeters through the analysis of very long gravity records. *J. Geodyn.*, 80:20–33, 2014. https://doi.org/10.1016/j.jog.2014.04.009.

D. E. Cartwright and A. C. Edden. Corrected tables of tidal harmonics. *Geophys. J. R. Astron. Soc.*, 33(3):253–264, 1973.

D. E. Cartwright and R. J. Tayler. New Computations of the Tide-generating Potential. *Geophys. J. R. Astron. Soc.*, 23(1):45–74, 1971. https://doi.org/10.1111/j.1365-246X.1971.tb01803.x.

S. Chapman and R. S. Lindzen. *Atmospheric Tides: Gravitational and Thermal.* 1970.

T. Chojnicki. Ein Verfahren zur Erdgezeitenanalyse in Anlehnung an das Prinzip der kleinsten Quadrate [A method for Analysis of Earth Tides based on the principle of least-squares]. *Mit. Inst. Theo. Geod. U. Bonn*, 15, 1973.

A. Ciesielski and T. Forbriger. Singular value decomposition of tidal harmonics on a rigid Earth. In *Geophysical Research Abstracts*, 2019. URL https://meetingorganizer.copernicus.org/EGU2019/EGU2019-16895.pdf.

A. Ciesielski and T. Forbriger. Resolution and significant contributions of tidal forcing in flexible harmonic grouping computed using Singular Value Decomposition. In *EGU General Assembly Conference Abstracts*, 2020. https://doi.org/10.5194/egusphere-egu2020-17758.

A. Ciesielski and T. Forbriger. Investigation of bias in traditional grouping by means of regularization. In *EGU General Assembly Conference Abstracts*, pages EGU21–14747, April 2021. https://doi.org/10.5194/egusphere-egu21-14747.

A. Ciesielski, T. Forbriger, W. Zürn, and A. Rietbrock. Reduction of apparent temporal variations of tidal parameters by a proper local response model. 2023. https://doi.org/10.21203/rs.3.rs-2539898/v1.

D. J. Crossley, O. G. Jensen, and J. Hinderer. Effective barometric admittance and gravity residuals. *Phys. Earth Planet. Inter.*, 90(3):221–241, 1995. https://doi.org/10.1016/0031-9201(95)05086-Q.

F. A. Dahlen. Effect of the Earth's ellipticity on the lunar potential. *Geophys. J. Int.*, 113: 250–251, 1993.

F. A. Dahlen and J. Tromp. *Theoretical Global Seismology*. 1998.

G. H. Darwin. The harmonic analysis of tidal observation. *Oceanic Tides and Lunar Disturbances of Gravity*, 1:463, 1907.

V. Dehant. Tidal parameters for an inelastic Earth. *Phys. Earth Planet. Inter.*, 49:97–116, 1987. https://doi.org/10.1016/0031-9201(87)90134-8.

V. Dehant, P. Defraigne, and J. M. Wahr. Tides for a convective Earth. *J. Geophys. Res.*, 104: 1035–1058, 1999. https://doi.org/10.1029/1998JB900051.

H. G. Dittfeld. Analysis of third degree waves with diurnal and semi-diurnal frequencies. *Bull. Inf. Marées Terrestres.*, 111:8053–8061, November 1991.

A. T. Doodson. The harmonic development of the tide generating potential. *Proc. Roy. Soc. London, Ser. A*, 100:305–329, 1921. https://doi.org/10.1098/rspa.1921.0088.

B. Ducarme. Determination of the main Lunar waves generated by the third degree tidal potential and validity of the corresponding body tides models. *J. Geodesy*, 86(1):65–75, 2012. https://doi.org/10.1007/s00190-011-0492-9.

B. Ducarme. The influence of pressure waves in tidal gravity records. *Geodesy and Geodynamics*, 14(1):15–25, 2023. ISSN 1674-9847. https://doi.org/10.1016/j.geog.2022.07.005. URL https://www.sciencedirect.com/science/article/pii/S1674984722000738. Contemporary research in Geodynamics and Earth Tides.

B. Ducarme and K. Schüller. Canonical wave grouping as the key to optimal tidal analysis. *Bull. Inf. Marées Terrestres.*, 150:12131–12244, September 2018.

B. Ducarme and H. P. Sun. Tidal gravity results from GGP network in connection with tidal loading and Earth response. In *Proceeding 14th International Symposium on Earth Tides, J Geod Soc Jpn*, volume 47, pages 308–315, 2001. https://doi.org/10.1007/s978-3-540-85426-5.

B. Ducarme, S. Rosat, L. Vandercoilden, J.Q. Xu, and H. P. Sun. European tidal gravity observations: comparison with Earth tides models and estimation of the free core nutation (FCN) parameters. In *Sideris MG (ed) Proceedings of the 2007 IAG General Assembly, Perugia, Italy, July 2–13, 2007. Observing our changing Earth. Springer, International Association of Geodesy Symposia*, volume 133, pages 523–532, 2007. https://doi.org/10.1007/s978-3-540-85426-5.

A. M. Dziewonski and D. L. Anderson. Preliminary reference Earth model. *Phys. Earth Planet. Inter.*, 25:297–356, 1981. https://doi.org/10.1016/0031-9201(81)90046-7.

J. Elkhoury, E. Brodsky, and D. Agnew. Seismic waves increase permeability. *Nature*, 441: 1135–1138, 2006. https://doi.org/10.1038/nature04798.

D. Emter. *Tidal triggering of earthquakes and volcanic events*, volume 66 of *Lecture Notes in Earth Sciences*, pages 293–309. Springer, Berlin, 1997. ISBN 3-540-62833-9. https://doi.org/10.1007/BFb0011468.

EOST. EOST Loading Service, 2022. URL http://loading.u-strasbg.fr/sg_atmos.php. Data service by École & observatoire des sciences de la Terre (EOST).

W. E. Farrell. Deformation of the Earth by surface load. *Rev. Geoph.*, 10(3):761–797, 1972. https://doi.org/10.1029/RG010i003p00761.

T. Forbriger and A. Heck. Frequency response of the superconducting gravimeter SG056. In *(Schw)Ehre, wem (Schw)Ehre gebührt: Festschrift zur Verabschiedung von Prof. Dr.-Ing. Dr. h.c. Bernhard Heck. Hrsg.: A. Heck*, volume 2018(1) of *Schriftenreihe des Studiengangs Geodäsie und Geoinformatik / Karlsruher Institut für Technologie, Studiengang Geodäsie und Geoinformatik*, pages 57–67. KIT Scientific Publishing, Karlsruhe, 2018. ISBN 978-3-7315-0777-2. https://doi.org/10.5445/IR/1000080212.

M. G. G. Foreman. Harmonic for Tidal Heights Analysis and Prediction. Pacific Marine Science Report 77-10, Institute of Ocean Sciences, Patricia Bay, Sidney, 2004.

M. G. G. Foreman and R. F. Henry. The harmonic analysis of tidal model time series. *Advances in Water Resources*, 12(3):109–120, 1989.

O. Francis and V. Dehant. Recomputation of the Green's functions for tidal loading estimations. *Bull. Inf. Marées Terrestres.*, 100:6962–6986, 1987.

G. Godin. The resolution of tidal constituents. *International Hydrographic Review*, 47(2):133–144, 1970.

G. Godin. *The Analysis of Tides*. University of Toronto Press, 1972.

G. Guennebaud, J. Benoît, et al. Eigen v3. http://eigen.tuxfamily.org, 2010. URL `http://eigen.tuxfamily.org`.

I. D. Haigh, M. D. Pickering, J. A. M Green, B. K. Arbic, A. Arns, S. Dangendorf, D. F. Hill, K. Horsburgh, T. Howard, D. Idier, D. A. Jay, L. Jänicke, S. B. Lee, M. Müller, M. Schindelegger, S. A. Talke, S.-B. Wilmes, and P. L. Woodworth. The Tides They Are A-Changin': A Comprehensive Review of Past and Future Nonastronomical Changes in Tides, Their Driving Mechanisms, and Future Implications. *Rev. Geophys.*, 58(1):1–39, 2020. `https://doi.org/10.1029/2018RG000636`.

S. K. Haldar. Chapter 5 - Exploration Geophysics. In *Mineral Exploration*, pages 73–93. Elsevier, Boston, 2013. ISBN 978-0-12-416005-7. `https://doi.org/10.1016/B978-0-12-416005-7.00005-2`. URL `https://www.sciencedirect.com/science/article/pii/B9780124160057000052`.

F. J. Harris. On the use of windows for harmonic analysis with the discrete Fourier transform. *Proc. IEEE*, 66(1):51–83, 1978. `https://doi.org/10.1109/PROC.1978.10837`.

T. Hartmann and H.-G. Wenzel. The HW95 tidal potential catalogue. *Geophys. Res. Lett.*, 22 (24):3553–3556, 1995. `https://doi.org/10.1029/95GL03324`.

International Geodynamics and Earth Tide Service. The IGETS data base at GFZ Potsdam, 2017. URL `http://isdc.gfz-potsdam.de/igets-data-base/`.

T. Jahr. Variation der Gezeitenparameter am Geodynamischen Observatorium Moxa aus Beobachtungen mit einem supraleitenden Gravimeter [Variations of tidal parameters at the Geodynamic Observatory Moxa from observations with a superconducting gravimeter]. *Allg. Verm. Nachr. (avn)*, 122:163–167, 2015.

H. Jeffreys. The Rigidity of the Earth's Central Core. *Geo. Sup. Mon. Notices Royal Astron. Soc.*, 1:371–383, 1926. https://doi.org/10.1111/j.1365-246X.1926.tb05385.x.

H. Jeffreys. Theoretical values of the bodily tide numbers. *Bull. Inf. Marées Terrestres.*, 3:29, 1957.

H. Jeffreys and R. O. Vincente. The theory of nutation and the variation of latitude. *Mon. Not. R. Astron. Soc.*, 117:142–161, 1957.

T. Klügel and H. Wziontek. Correcting gravimeters and tiltmeters for atmospheric mass attraction using operational weather models. *J. Geodyn.*, 48:204–210, 2009.

H. Krásná, J. Böhm, and H. Schuh. Free core nutation observed by VLBI. *Astronomy and Astrophysics*, 555:A29, 2013. https://doi.org/10.1051/0004-6361/201321585.

S. M. Kudryavtsev. Improved harmonic development of the Earth tide-generating potential. *J. Geodesy*, 77:829–838, 2004.

S. M. Kudryavtsev. Harmonic development of tide-generating potential of terrestrial planets. *Celest. Mech. Dyn. Astron*, 101:337–348, 2008.

H. C. P. Lau, J. X. Mitrovica, H.-Y. Yang J. L. Davis, J. Tromp, and D. Al-Attar. Tidal tomography constrains Earth's deep-mantle buoyancy. *Nature*, 551:321—326, 2017. https://doi.org/10.1038/nature24452.

A. E. H. Love. *Some Problems of Geodynamics.* Dover, New York, 1911.

P. M. Mathews, T. A. Herring, and B. A. Buffett. Modeling of nutation and precession: New nutation series for nonrigid Earth and insights into the Earth's interior. *J. Geophys. Res.*, 107:2068, 2002. https://doi.org/10.1029/2001JB000390.

P. M. Matthews. Love numbers and gravimetric factor for diurnal tides. In *Proceeding 14th International Symposium Earth Tides. J Geod Soc Jpn*, volume 47, pages 231–236, 2001.

P. Melchior. *The tides of the planet Earth.* Pergamon Press, Oxford, 1978.

P. Melchior, B. Ducarme, and O. Francis. The response of the Earth to tidal body forces described by second- and third-degree spherical harmonics as derived from a 12 year series of measurements with the superconducting gravimeter GWR/T3 in Brussels. *Phys. Earth Planet. Inter.*, 93(3–4):223–238, 2 1996. ISSN 0031-9201. https://doi.org/10.1016/0031-9201(95)03073-5.

J. B. Merriam. Atmospheric pressure and gravity. *Geophys. J. Int.*, 109:149–500, 1992. https://doi.org/10.1111/j.1365-246X.1992.tb00112.x.

J. B. Merriam. Non-linear tides observed with the superconducting gravimeter. *Geophys. J. Int.*, 123:529–540, 1995. https://doi.org/10.1111/j.1365-246X.1995.tb06869.x.

B. Meurers. Investigation of temporal gravity variations in SG-records. *J. Geodyn.*, 38:423–435, 2004. https://doi.org/10.1016/j.jog.2004.07.011.

B. Meurers, M. Van Camp, O. Francis, and V. Pálinkáš. Temporal variation of tidal parameters in superconducting gravimeter time-series. *Geophys. J. Int.*, 205:284–300, 2016. https://doi.org/10.1093/gji/ggw017.

M. S. Molodenskii. Elastic tides, free nutation and some problems of the Earth's structure. *Acad Sc URSS Travaux Inst Geoph*, 19:3–52, 1957.

M. S. Molodenskii. The theory of nutations and diurnal earth tides. *Communications de l' Observatoire Royal de Belgique, Series Geophysique*, 58:25–56, 1961.

A. Mukai and K. Fujimori. Elastic constants in fault zone determined using strain changes obtained at an 800 m borehole. *J. Geod. Soc. Japan*, 47:470–475, 2001.

M. Müller, J. Y. Cherniawsky, M. G. G. Foreman, and J.-S. von Storch. Seasonal variation of the M2 tide. *Ocean Dyn.*, 64:159–177, 2014. https://doi.org/10.1007/s10236-013-0679-0.

W. Munk and K. Hasselmann. Super-resolution of Tides. In K. Yoshida, editor, *Studies on Oceanography*, pages 339–344. Univ. Washington Press, 1964. URL http://hdl.handle.net/21.11116/0000-0008-73AF-2.

W. H. Munk and D. E. Cartwright. Tidal spectroscopy and prediction. *Phil. Trans. Roy. Soc. London*, 259(1105):533–581, 1966. https://doi.org/10.1098/rsta.1966.0024.

M. Omura, S. Otsuka, K. Fujimori, and T. Yamamoto. Tidal strains observed at a station crossing the Otsuki fault, Kobe, Japan, before the 1995 Hyogoken-Nanbu earthquake. *Journal of the Geodetic Society of Japan*, 47(1):441–447, 2001.

L. Pou, F. Nimmo, A. Rivoldini, A. Khan, A. Bagheri, T. Gray, H. Samuel, P. Lognonné, A. C. Plesa, T. Gudkova, and D. Giardini. Tidal constraints on the Martian interior. *Journal of Geophysical Research: Planets*, 127, 2022. https://doi.org/10.1029/2022JE007291.

W. H. Press, S. A. Teukolsky, W. T. Vetterling, and B. P. Flannery. *Numerical Recipes in C*. Cambridge University Press, Cambridge, USA, second edition, 1992.

R. D. Ray. First global observations of third-degree ocean tides. *Sci. Adv.*, 6:1–8, 2020. https://doi.org/10.1126/sciadv.abd4744.

R. D. Ray, J.-P. Boy, S. Y. Erofeeva, and G. D. Egbert. Terdiurnal Radiational Tides. *J Phys Oceanogr*, 53:1139–1150, 2023. https://doi.org/10.1175/JPO-D-22-0175.1.

Y. Rogister. On the diurnal and nearly diurnal free modes of the Earth. *Geophys. J. Int.*, 144: 459–470, 2001. https://doi.org/10.1046/j.1365-246x.2001.00359.x.

F. Roosbeek. RATGP95: a harmonic development of the tide-generating potential using an analytical method. *Geophys. J. Int.*, pages 197–204, 1996.

S. Rosat, N. Florsch, J. Hinderer, and M. Llubese. Estimation of the Free Core Nutation parameters from SG data: Sensitivity study and comparative analysis using linearized least-squares and Bayesian methods. *Journal of Geodynamics*, 48:331–339, 2009. https://doi.org/10.1016/j.jog.2009.09.027.

T. Sato, J.-P. Boy, Y. Tamura, K. Matsumoto, K. Asari, H.-P. Plag, and O. Francis. Gravity tide and seasonal gravity variation at Ny-Ålesund, Svalbard in Arctic. *J. Geodyn.*, 41:234–241, 2006.

C. H. Scholz, Y. J. Tan, and F. Albino. The mechanism of tidal triggering of earthquakes at mid-ocean ridges. *Nature Communications*, 10, 2019. https://doi.org/10.1038/s41467-019-10605-2.

E. Schroth. Analyse von Gezeitenregistrierungen des Supraleitenden Gravimeters SG-056 [Analysis of tidal recordings of the superconducting gravimeter SG-056]. Diplomarbeit, Karlsruhe Institute of Technology (KIT), 2013. URL http://nbn-resolving.org/urn:nbn:de:swb:90-466565.

E. Schroth. *Analysis of temporal variations of gravimetric tidal parameters*. PhD thesis, Karlsruhe Institute of Technology (KIT), Karlsruhe, Germany, 2020.

E. Schroth, T. Forbriger, and M. Westerhaus. A catalogue of gravimetric factor and phase variations for twelve wave groups. *KIT scientific working papers*, 101, 2018. https://doi.org/10.5445/IR/1000089609.

K. Schüller. *Ein Beitrag zur Auswertung von Erdgezeitenregistrierungen [A contribution to the evaluation of Earth Tide recordings]*. PhD thesis, Bonn, 1976.

K. Schüller. Theoretical Basis for Earth Tide Analysis with the New ETERNA34-ANA-V4.0 Program. *Bull. Inf. Marées Terrestres.*, 149:12024–12061, 2015. URL https://www.eas.slu.edu/GGP/BIM_Recent_Issues/bim149-2015/schuller_theoretical_basis_Eterna-ANA_v4_BIM149.pdf.

K. Schüller. Program System ETERNA-x et34-x-v80-* for Earth and Ocean Tides Analysis and Prediction, Documentation Manual. https://web.archive.org/web/20211023075241/http://ggp.bkg.bund.de/eterna/, 2020.

P. Schureman. Manual of harmonic analysis and prediction of tides. *U.S. Coast Geod. Surv. Spec. Publ.*, 98:314, 1924.

J. L. Simon, P. Bretagnon, J. Chapront, M. Chapront-Touzé, G. Francou, and J. Laskar. Numerical expressions for precession formulas and mean elements for the Moon and the planets. *Astronomy and Astrophysics*, 282(2):663–683, 1994. URL https://ui.adsabs.harvard.edu/link_gateway/1994A%26A...282..663S/ADS_PDF.

A. Souriau. *Deep Earth structure: The Earth's cores*, volume 1, pages 655–693. Elsevier, Amsterdam, Netherlands, 2007.

F. R. Stephenson, L. V. Morrison, and C. Y. Hohenkerk. Measurement of the Earth's rotation: 720 BC to AD 2015. *Proc. R. Soc. A*, 472, 2016.

R. Sulzbach, H. Wziontek, M. Hart-Davis, H. Dobslaw, H.-G. Scherneck, M. Van Camp, O. Omang, C. Dahl, E. D. Antokoletz, C. Voigt, D. Dettmering, and M. Thomas. Modeling Gravimetric Signatures of Third-Degree Ocean Tides and their Detection in Superconducting Gravimeter Records. *J. Geodesy*, 96:35, 2022. https://doi.org/10.1007/s00190-022-01609-w.

H. Takeuchi. On the Earth tide of the compressible Earth of variable density and elasticity. *Acad Sc URSS Travaux Inst Geoph*, 31:651–689, 1950.

Y. Tamura. A Harmonic Development of the Tide-Generating Potential. *Bull. Inf. Marées Terrestres.*, 99:6813–6855, 1987. URL http://igets.u-strasbg.fr/BIM/bim099.pdf.

Y. Tamura and D. C. Agnew. Baytap08 User's Manual, UC San Diego: Scripps Institution of Oceanography, 2008. URL https://escholarship.org/uc/item/4c27740c. software.

Y. T. Tamura, M. O. Sato, and M. Ishiguro. A Procedure for Tidal Analysis with a Bayesian Information Criterion. *Geophys. J. Int.*, 104:507–516, 1991. https://doi.org/10.1111/j.1365-246X.1991.tb05697.x.

A. N. Tikhonov and V. Y. Arsenin. *Solutions of Ill-Posed Problems*. Halsted Press, New York, 1977.

T. Van Hoolst and C. Jacobs. Mercury's tides and interior structure. *J. Geophys. Res.*, 108 (E11), 2003.

A. P. Venedikov. *Application à l'analyse harmonique des observations des marées terrestres de la méthode des moindres carrés [Application of the method of least squares to the harmonic analysis of Earth tide observations]*. PhD thesis, Bulgarian Academy of Sciences, 1961.

A. P. Venedikov, J. Arnoso, and R. Vieira. New version of the program VAV for tidal data processing. *Comput. Geosci.*, 31:667–669, 2005.

J. Vidale, D. C. Agnew, M. J. S. Johnston, and D. H. Oppenheimer. Absence of Earthquake correlation with Earth tides. *J. Geophys. Res.*, 103:24567–24572, 1998. https://doi.org/10.1029/98JB00594.

C. Voigt, C. Förste, H. Wziontek, D. Crossley, B. Meurers, V. Pálinkáš, J. Hinderer, J.-P. Boy, J.-P. Barriot, and H. Sun. Report on the Data Base of the International Geodynamics and Earth Tide Service (IGETS). Technical report, GFZ German Research Centre for Geosciences, Potsdam, Germany, 2016. Scientific Technical Report STR - Data; 16/08.

J. M. Wahr. Body tides on an elliptical, rotating, elastic and oceanless earth. *Geophys. J. R. Astron. Soc.*, 64:677–703, 1981a. https://doi.org/10.1111/j.1365-246X.1981.tb02690.x.

J. M. Wahr. The forced nutations on an elliptical, rotating, elastic and oceanless Earth. *Geophys. J. R. Astron. Soc.*, 64:705–727, 1981b.

R. Wang. Tidal Response of the Solid Earth. In H. Wilhelm, W. Zürn, and H.-G. Wenzel, editors, *Tidal phenomena*, volume 66 of *Lecture Notes in Earth Sciences*, pages 27–57, Berlin, 1997. Springer. ISBN 3-540-62833-9. https://doi.org/10.1007/BFb0011456.

R. J. Warburton and J. M. Goodkind. The influence of barometric-pressure variations on gravity. *J. Geophys. Res.*, 48:281–292, 1977. https://doi.org/10.1111/j.1365-246X.1977.tb03672.x.

C. Watson, P. Tregoning, and R. Coleman. Impact of solid Earth tide models on GPS coordinate and tropospheric time series. *Geophys. Res. Lett.*, 33, 2006. https://doi.org/10.1029/2005GL025538.

H.-G. Wenzel. The nanogal software: Earth tide data processing package ETERNA 3.30. *Bull. Inf. Marées Terrestres.*, 124:9425–9439, 1996. URL http://igets.u-strasbg.fr/BIM/bim124.pdf.

H.-G. Wenzel. Eterna 3.40 — Programs for Tidal Analysis and Prediction. *KIT scientific working papers*, 1997a. https://doi.org/10.35097/746.

H.-G. Wenzel. Tide-Generating potential for the Earth. In H. Wilhelm, W. Zürn, and H.-G. Wenzel, editors, *Tidal phenomena*, volume 66 of *Lecture notes in Earth sciences*, pages 9–26, Berlin, 1997b. Springer. ISBN 3-540-62833-9. https://doi.org/10.1007/BFb0011455.

H.-G. Wenzel. Analysis of Earth Tide Observations. In H. Wilhelm, W. Zürn, and H.-G. Wenzel, editors, *Tidal phenomena*, volume 66 of *Lecture Notes in Earth Sciences*, pages 59–75, Berlin, 1997c. Springer. ISBN 3-540-62833-9. https://doi.org/10.1007/BFb0011457.

M. Westerhaus and J. Zschau. No clear evidence for temporal variations of tidal tilt prior the 1999 Izmit and Düzce earthquakes in NW-Anatolia. *J. Geod. Soc. Japan*, 47(1):448–455, 2001.

W. S. D. Wilcock. Tidal triggering of earthquakes in the Northeast Pacific Ocean. *Geophys. J. Int.*, 179:1055–1077, 2009. https://doi.org/10.1111/j.1365-246X.2009.04319.x.

H. Wilhelm. Earth's flattening effect on the tidal forcing field. *J. Geophys.*, 52:131–135, 1995.

R. Yan, X. Chen, H. Sun, J. Xu, and J. Zhou. A review of tidal triggering of global earthquakes. *Geodesy and Geodynamics*, 14(1):35–42, 2023. ISSN 1674-9847. https://doi.org/10.1016/j.geog.2022.06.005. URL https://www.sciencedirect.com/science/article/pii/S1674984722000714. Contemporary research in Geodynamics and Earth Tides.

C. F. Yoder, A. S. Konopliv, D. N. Yuan, E. M. Standish, and W. M. Folkner. Fluid Core Size of Mars from Detection of the Solar Tide. *Science*, 300(5617):299–303, 2003. https://doi.org/10.1126/science.1079645.

J. Zschau and R. Wang. Imperfect Elasticity in the Earth's Mantle. Implications for Earth Tides and Long Period Deformations. In J. T. Kuo, editor, *Proceedings of the 10th International Symposium on Earth Tides, Madrid*, 1985.

W. Zürn. The Nearly-Diurnal Free Wobble-Resonance. In H. Wilhelm, W. Zürn, and H.-G. Wenzel, editors, *Tidal phenomena*, volume 66 of *Lecture Notes in Earth Sciences*, pages 95–109, Berlin, 1997. Springer. ISBN 3-540-62833-9. https://doi.org/10.1007/BFb0011459.

W. Zürn, C. Beaumont, and L. B. Slichter. Gravity Tides and Ocean Loading in Southern Alaska. *J. Geophys. Res.*, 81:4923–4932, 1976.

12. List of Figures

13. List of Tables

A. Glossary and Acronyms

Glossary

adjustment factors x and y (and r), regression factors applied to the a-priori model that are used to adjust the implemented complex admittance factors in a-priori model to the data;

complex admittance factors X and Y, the a priori model factors, the Earth body response that given theoretical model accounts for;

constrained inversion, least squares regression fit with regularization term, harmonics are treated as separate regressors;

data error σ, the expected value of the mean noise level (RMS);

data misfit $\Delta_{\mathbf{d}}$, a normalized residual, a term in the objective function that expresses how the estimated synthetic time series deviates from the recorded data; it refers to the tapered forward operator and data;

data misfit $\Delta_{\mathbf{d}}^{\diamond}$, a data misfit that results from applying an estimated model to the untapered time series and untapered forcing operator;

distance $\Delta_{\mathbf{m}}$ to the reference model, a term in the objective function that expresses how the estimated model deviates from the reference model;

forcing signals $C_l^{\mathbf{rig}}(t_k)$ and $S_l^{\mathbf{rig}}(t_k)$, that are elements C_{kl}^{rig} and S_{kl}^{rig} of matrices $\boldsymbol{C}^{\mathrm{rig}}$ and $\boldsymbol{S}^{\mathrm{rig}}$, theoretical rigid Earth tidal forcing assumed for Earth at particular location and time;

forcing signals $C_l^{\mathbf{ini}}(t_k)$ and $S_l^{\mathbf{ini}}(t_k)$, that are elements C_{kl}^{ini} and S_{kl}^{ini} of matrices $\boldsymbol{C}^{\mathrm{ini}}$ and $\boldsymbol{S}^{\mathrm{ini}}$, theoretical tidal forcing assumed for Earth at particular location and time, rigid Earth tide;

group merge, the reference groups that used to have different common pairs of factors has one common pair of factors applied to account for parameters that have no significance in model constraint imposed by the observed signal;

group split, the reference group that used to have one common pairs of factors is divided into two or more subgroups, to account for the conflicting constraints imposed by the observed signal;

initial model, the reference model with which the iterative procedure starts, here it is local WDZe model, derived from PREM. In principle it can be any reasonable model;

in phase and quadrature, harmonic signals that are offset in phase by one-quarter cycle ($\pi/2$), two components to which a harmonic signal with angle modulation can be decomposed into; its purpose is linearization of the problem, mapping amplitude and phase on complex plane;

local response model (time-invariant), the final solution of the iterative procedure, to which no further distance to the reference model is justified by data misfit decrease; it is expected to capture the significant features of the locally recorded signal;

misfit curve, curve that displays distance to the reference model versus (untapered) data misfit for solutions under various trade-off parameter α;

objective function E**,** here: also a loss function or cost function; expresses the terms that have to be minimized in the least-squares problem;

regularization, imposing additional constraints that bias the solution to stabilize the inversion; is essential to estimate a usable solution to an otherwise intractable ill-posed or ill-conditioned inverse problem;

reference groups, the sets of harmonics to which the common reference model factors are applied;

reference model, the reasonable model which is close to the expected solution, its difference to estimates is used as an additional penalty term in LS objective function;

rigid Earth, theoretical Earth model, rigid oceanless Earth with no atmosphere that does not undergo deformation when tidal field is applied;

taper, a window function by which signal (and regressors) are multiplied to avoid spectral leakage in time series analysis;

time-invariant properties, signal or model properties which do not change in time; e.g. FCN resonance, expected solid Earth response to tidal forcing;

time-variant properties, that may periodically repeat or are systematic, mainly refers to beat or particular phenomena in ocean tides or radiation tides; periodic time variant model properties often can be expressed by a frequency dependence of time-invariant properties;

trade-off parameter α**,** a number that defines quantitatively whether LS fit seeks more for the data misfit minimum (variance) or for an additional constraint (distance to the reference model) minimum (bias);

trade-off point, point on the misfit curve where its behavior significantly changes;

unconstrained inversion, least squares regression fit without regularization term, tidal harmonics are a-priori grouped;

(a priori) wave groups, sums of tidal signals, usually in defined frequency bands. The a priori body response is applied and hence the common factors are estimated for tidal parameters of the group; the purpose of that parametrization is to stabilize the otherwise ill-posed problem.

Abbreviations

SG superconducting gravimeter

RATA Regularized Approach to Tidal Analysis

WDZe purely elastic version of body tide Earth model by Wahr-Dehant-Zschau in which phase shift is neglected but relaxation of elastic parameters is included

BF21 The final local response tidal model for BFO SG056 lower sensor (G1), obtained with the `RATA` constraint analysis,

BF21G2 The final local response tidal model for BFO SG056 upper sensor (G2), obtained with the `RATA` constraint analysis.

BF21u The final local response tidal model for BFO SG056 lower sensor (G1), obtained with unconstrained analysis (method similar to `Eterna 3.40`).

MWA Moving Window Analysis

LS Least-squares

SVD Singular Value Decomposition

LRM Local Response Model, The final local response tidal model for any given station, obtained with the `RATA` constraint analysis.

B. Local Response Models

The local response models obtained with `RATA` are provided in tables and corresponding plots. While the actual reference grouping used for the estimation of the models may be coarse, I listed values for all the harmonics defined in the Tables 2.3-2.5. Hence, some of the estimates are highly biased, or even identical to the neighbouring harmonic of larger amplitude, since they could be in the same reference group. Some extreme values are deliberately outside the plot, mainly S_1, and some reference groups in Ny-Ålesund and Syowa. Red color represents degree 3 tides, blue - degree 2 tides. Tides degree 4 are not displayed. For each given station, the diameter of the point in the display corresponds to the amplitude scaled to the largest tide (despite the degree). Depending on the location, it is K_1 or M_2.

Schiltach, BFO (lower sensor)

Table B.1.: Diurnal degree 2 parameters for the LRM-model, station Schiltach, BFO (lower sensor).

Wave	δ^{LRM}	Φ^{LRM}	δ^{LRM}	Amplitude	Frequency	Doodson
		/°	$/\delta^{\mathrm{WDZe}}$	$/\mathrm{nm\,s^{-2}}$	/cpd	
ζ_1	1.1645	-0.7939	1.0095	0.72	0.820661	115.855
$\mathrm{SGQ_1}$	1.1645	-0.7939	1.0095	1.85	0.825518	117.655
$\mathrm{2Q_1}$	1.1530	-0.7189	0.9995	6.19	0.856952	125.755
σ_1	1.1504	-0.6463	0.9973	7.46	0.861809	127.555
$\mathrm{SGX_1}$	1.1504	-0.6463	0.9973	0.50	0.864547	128.554
$\mathrm{QW_1}$	1.1472	-0.2656	0.9946	8.88	0.893097	135.645
$\mathrm{Q_1}$	1.1472	-0.2638	0.9946	47.06	0.893244	135.655
ρ_1	1.1471	-0.1725	0.9946	8.97	0.898101	137.455
$\mathrm{ROX_1}$	1.1471	-0.1725	0.9946	0.52	0.898720	137.655
$\mathrm{OW_1}$	1.1490	0.0850	0.9963	0.87	0.926798	144.556
$\mathrm{OV_1}$	1.1489	0.0850	0.9963	47.75	0.929389	145.545
$\mathrm{O_1}$	1.1489	0.0850	0.9963	253.10	0.929536	145.555
$\mathrm{OX_1}$	1.1489	0.0850	0.9963	1.63	0.930155	145.755
$\mathrm{TW_1}$	1.1556	0.0955	1.0021	0.77	0.932273	146.554
τ_1	1.1556	0.0955	1.0021	3.32	0.935012	147.555
$\mathrm{LKW_1}$	1.1532	0.2522	1.0003	1.90	0.960970	153.655
$\mathrm{LK_1}$	1.1530	0.2522	1.0003	7.29	0.965827	155.455
$\mathrm{M_1}$	1.1519	0.2517	0.9994	20.27	0.966446	155.655
$\mathrm{MN_1}$	1.1519	0.2517	0.9994	4.07	0.966593	155.665
χ_1	1.1479	0.1874	0.9960	3.88	0.971303	157.455
π_1	1.1491	0.2737	0.9998	6.95	0.994524	162.556
$\mathrm{P_1}$	1.1500	0.1989	1.0019	118.54	0.997262	163.555
$\mathrm{S_1}$	1.1882	10.8909	1.0382	2.79	1.000000	164.556
$\mathrm{KW_1}$	1.1383	0.2537	1.0031	6.99	1.002591	165.545
$\mathrm{K_1}$	1.1370	0.2537	1.0031	352.72	1.002738	165.555
κ_1	1.1360	0.3016	1.0034	47.79	1.002885	165.565
$\mathrm{KX_1}$	1.1344	0.3016	1.0034	1.02	1.003032	165.575
ψ_1	1.2699	-0.0092	1.0012	3.08	1.005476	166.554
φ_1	1.1763	0.1658	1.0064	5.16	1.008214	167.555
ϑ_1	1.1573	0.0692	1.0016	3.76	1.034173	173.655
$\mathrm{J_1}$	1.1577	0.1386	1.0021	19.61	1.039030	175.455
ι_1	1.1577	0.1389	1.0021	3.89	1.039177	175.465
$\mathrm{SO_1}$	1.1558	0.3909	1.0011	3.22	1.070464	183.555
$\mathrm{JO_1}$	1.1545	0.1050	1.0000	1.59	1.075321	185.355
$\mathrm{OO_1}$	1.1545	0.1050	1.0000	10.61	1.075940	185.555
$\mathrm{OOZ_1}$	1.1453	0.3973	0.9922	0.52	1.106756	193.455
$\mathrm{V_1}$	1.1452	0.3973	0.9922	2.06	1.112232	195.455

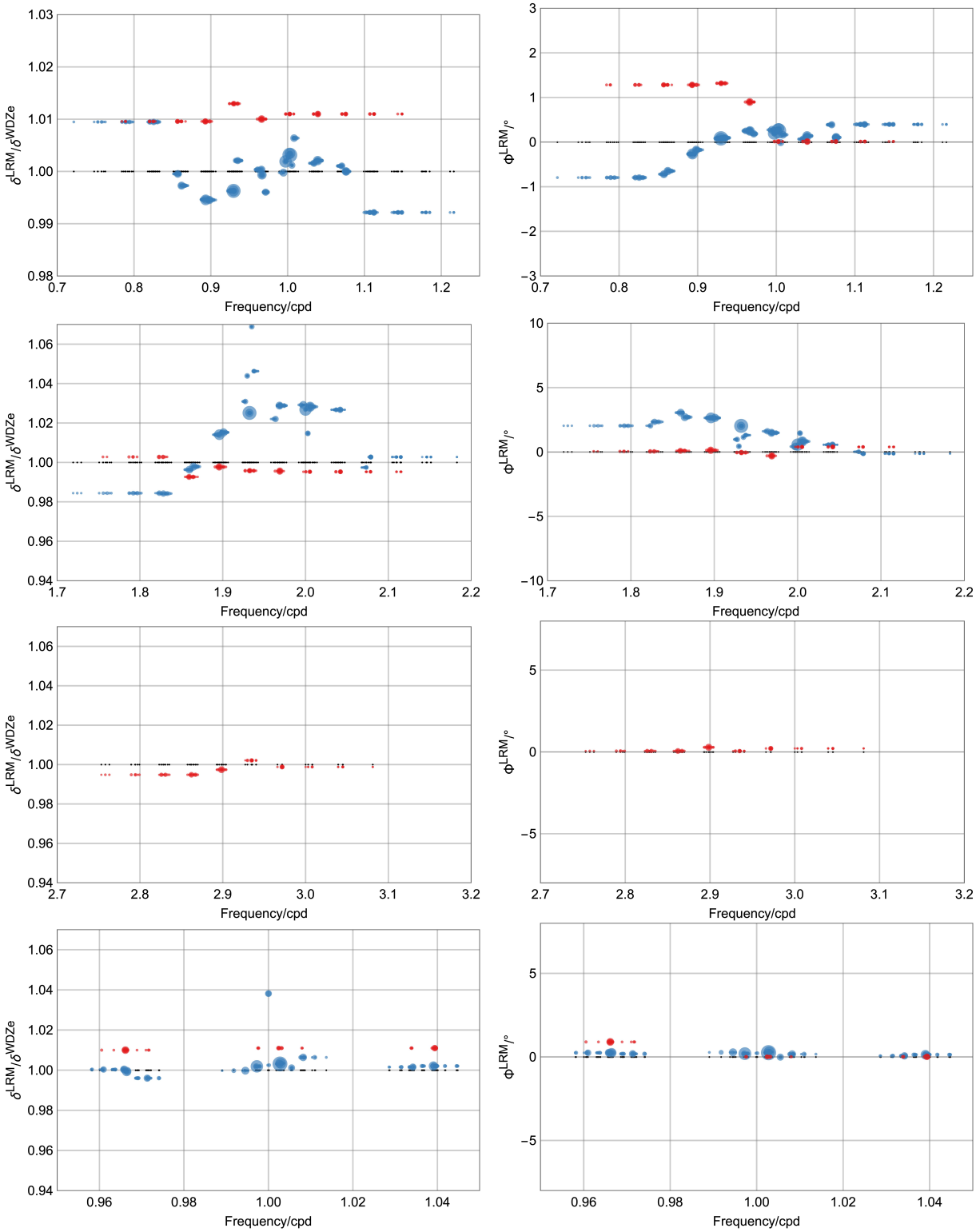

Figure B.1.: Parameters of the local response model (δ^{LRM} and Φ^{LRM}) in relation to WDZe for Schiltach, BFO (lower sensor).

Table B.2.: Semidiurnal degree 2 parameters for the LRM-model, station Schiltach, BFO (lower sensor).

Wave	δ^{LRM}	Φ^{LRM}	δ^{LRM}	Amplitude	Frequency	Doodson
		/°	$/\delta^{\mathrm{WDZe}}$	$/\mathrm{nm\,s^{-2}}$	/cpd	
$3N_2$	1.1394	2.0397	0.9844	0.77	1.823399	225.855
ϵ_2	1.1392	2.3419	0.9842	2.00	1.828256	227.655
$2N_2$	1.1533	3.0533	0.9963	6.82	1.859690	235.755
μ_2	1.1551	2.7101	0.9979	8.24	1.864547	237.555
MIX_2	1.1551	2.7101	0.9979	0.56	1.867285	238.554
NW_2	1.1738	2.6477	1.0141	0.44	1.893244	244.656
N_2	1.1738	2.6477	1.0141	51.94	1.895982	245.655
NIW_2	1.1751	2.6463	1.0152	0.49	1.898720	246.654
ν_2	1.1751	2.6463	1.0152	9.88	1.900839	247.455
NIX_2	1.1751	2.6463	1.0152	0.46	1.903577	248.454
γ_2	1.1933	0.9732	1.0309	0.82	1.927417	253.755
α_2	1.2083	0.4484	1.0439	0.94	1.929536	254.556
ω_2	1.1866	2.0296	1.0252	10.21	1.932127	255.545
M_2	1.1866	2.0301	1.0251	273.83	1.932274	255.555
β_2	1.2372	1.1532	1.0689	0.83	1.935011	256.554
δ_2	1.2111	1.3043	1.0463	0.32	1.937749	257.555
λ_2	1.1830	1.6129	1.0220	2.02	1.963708	263.655
L_2	1.1909	1.4913	1.0289	7.74	1.968565	265.455
KNO_2	1.1909	1.4913	1.0289	1.94	1.969184	265.655
LX_2	1.1909	1.4913	1.0289	0.85	1.969331	265.665
LZ_2	1.1909	1.4913	1.0289	0.37	1.974041	267.455
$2T_2$	1.1913	0.4209	1.0292	0.30	1.994524	271.557
T_2	1.1913	0.4209	1.0292	7.40	1.997262	272.556
S_2	1.1885	0.5681	1.0268	126.49	2.000000	273.555
R_2	1.1746	1.4646	1.0147	1.06	2.002738	274.554
K_2	1.1902	0.8176	1.0283	34.32	2.005476	275.555
KX_2	1.1902	0.8176	1.0283	10.23	2.005623	275.565
KY_2	1.1902	0.8176	1.0283	1.11	2.005770	275.575
KZ_2	1.1902	0.8176	1.0283	0.27	2.008214	276.554
KA_2	1.1902	0.8176	1.0283	0.23	2.010952	277.555
ζ_2	1.1884	0.5598	1.0267	0.36	2.036911	283.655
η_2	1.1884	0.5598	1.0267	1.91	2.041768	285.455
ETX_2	1.1884	0.5598	1.0267	0.83	2.041915	285.465
$2S_2$	1.1546	0.0142	0.9975	0.32	2.073202	293.555
$2K_2$	1.1607	-0.1239	1.0028	0.50	2.078678	295.555

Table B.3.: Degree 3 and 4 parameters for the LRM-model, station Schiltach, BFO (lower sensor).

Wave	δ^{LRM}	Φ^{LRM}	δ^{LRM}	Amplitude	Frequency	Doodson
		/°	$/\delta^{\mathrm{WDZe}}$	$/\mathrm{nm\,s^{-2}}$	/cpd	
$2Q_1$*	1.0831	1.2829	1.0096	0.45	0.856643	125.655
Q_1*	1.0831	1.2829	1.0096	1.66	0.892935	135.555
QX_1*	1.0831	1.2829	1.0096	0.10	0.893554	135.755
ρ_1*	1.0831	1.2829	1.0096	0.14	0.898410	137.555
O_1*	1.0867	1.3182	1.0130	0.88	0.929845	145.655
LK_1*	1.0836	0.9002	1.0100	0.81	0.965990	155.545
M_1*	1.0836	0.9002	1.0100	5.46	0.966137	155.555
χ_1*	1.0836	0.9002	1.0100	0.02	0.971613	157.555
K_1*	1.0846	0.0126	1.0110	0.29	1.002428	165.455
J_1*	1.0846	0.0126	1.0110	1.92	1.039339	175.555
$3N_2$*	1.0758	0.0475	1.0028	0.22	1.823089	225.755
ϵ_2*	1.0758	0.0475	1.0028	0.22	1.827946	227.555
$2N_2$*	1.0649	0.0888	0.9927	1.25	1.859381	235.655
μ_2*	1.0649	0.0888	0.9927	0.23	1.864238	237.455
N_2*	1.0703	0.1322	0.9977	4.57	1.895673	245.555
ν_2*	1.0703	0.1322	0.9977	0.12	1.901148	247.555
ω_2*	1.0683	-0.0438	0.9958	0.26	1.931964	255.455
M_2*	1.0683	-0.0438	0.9958	0.70	1.932583	255.655
L_2*	1.0681	-0.2997	0.9956	4.26	1.968875	265.555
KNO_2*	1.0681	-0.2997	0.9956	0.80	1.969018	265.565
K_2*	1.0677	0.3926	0.9953	0.23	2.005166	275.455
η_2*	1.0677	0.3926	0.9953	0.39	2.042077	285.555
MN_3*	1.0640	0.0621	0.9948	0.90	2.862119	345.655
M_3*	1.0667	0.2893	0.9974	3.30	2.898410	355.555
ML_3*	1.0717	0.0535	1.0021	0.19	2.934702	365.455
MK_3*	1.0682	0.2150	0.9988	0.43	2.971613	375.555
O_1+	1.0296	0.0143	0.9936	0.05	0.929536	145.555
MN_3+	1.0296	0.0143	0.9936	0.07	2.861809	345.555
M_4+	1.0283	0.0143	0.9936	0.04	3.864547	455.555

Schiltach, BFO (upper sensor)

Table B.4.: Diurnal degree 2 parameters for the LRM-model, station Schiltach, BFO (upper sensor).

Wave	δ^{LRM}	Φ^{LRM}	δ^{LRM}	Amplitude	Frequency	Doodson
		/°	$/\delta^{\mathrm{WDZe}}$	/nms^{-2}	/cpd	
ζ_1	1.1670	-0.7100	1.0116	0.72	0.820661	115.855
SGQ_1	1.1619	-0.7863	1.0072	1.85	0.825518	117.655
$2Q_1$	1.1542	-0.7078	1.0006	6.19	0.856952	125.755
σ_1	1.1509	-0.6292	0.9977	7.46	0.861809	127.555
SGX_1	1.1509	-0.6292	0.9977	0.50	0.864547	128.554
QW_1	1.1511	-0.2923	0.9980	8.88	0.893097	135.645
Q_1	1.1474	-0.2595	0.9948	47.06	0.893244	135.655
ρ_1	1.1466	-0.2030	0.9941	8.97	0.898101	137.455
ROX_1	1.1466	-0.2030	0.9941	0.52	0.898720	137.655
OW_1	1.1490	0.0854	0.9963	0.87	0.926798	144.556
OV_1	1.1490	0.0854	0.9963	47.75	0.929389	145.545
O_1	1.1490	0.0854	0.9963	253.10	0.929536	145.555
OX_1	1.1490	0.0854	0.9963	1.63	0.930155	145.755
TW_1	1.1555	0.2027	1.0020	0.77	0.932273	146.554
τ_1	1.1554	0.2027	1.0020	3.32	0.935012	147.555
LKW_1	1.1532	0.2503	1.0003	1.90	0.960970	153.655
LK_1	1.1530	0.2503	1.0003	7.29	0.965827	155.455
M_1	1.1520	0.2479	0.9994	20.27	0.966446	155.655
MN_1	1.1520	0.2479	0.9994	4.07	0.966593	155.665
χ_1	1.1472	0.3115	0.9955	3.88	0.971303	157.455
π_1	1.1497	0.2310	1.0003	6.95	0.994524	162.556
P_1	1.1500	0.2026	1.0020	118.54	0.997262	163.555
S_1	1.1984	10.0410	1.0471	2.79	1.000000	164.556
KW_1	1.1383	0.2567	1.0031	6.99	1.002591	165.545
K_1	1.1370	0.2567	1.0031	352.72	1.002738	165.555
κ_1	1.1358	0.3061	1.0032	47.79	1.002885	165.565
KX_1	1.1342	0.3061	1.0032	1.02	1.003032	165.575
ψ_1	1.2700	-0.1213	1.0013	3.08	1.005476	166.554
φ_1	1.1758	0.2689	1.0059	5.16	1.008214	167.555
ϑ_1	1.1584	0.2443	1.0025	3.76	1.034173	173.655
J_1	1.1577	0.1546	1.0021	19.61	1.039030	175.455
ι_1	1.1561	0.2127	1.0008	3.89	1.039177	175.465
SO_1	1.1551	0.3397	1.0004	3.22	1.070464	183.555
JO_1	1.1550	0.1409	1.0004	1.59	1.075321	185.355
OO_1	1.1550	0.1409	1.0004	10.61	1.075940	185.555
OOZ_1	1.1437	0.2097	0.9908	0.52	1.106756	193.455
V_1	1.1437	0.2097	0.9908	2.06	1.112232	195.455

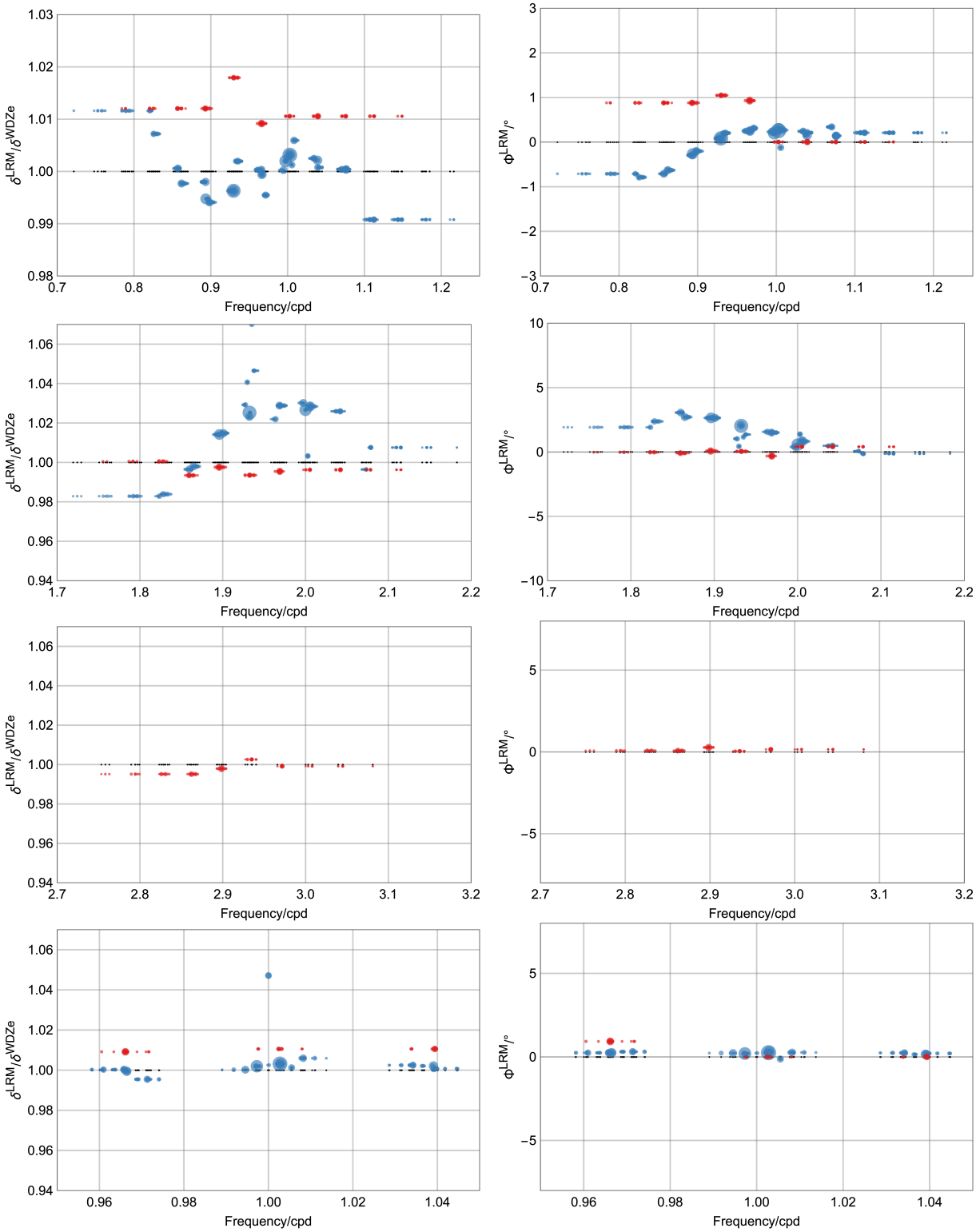

Figure B.2.: Parameters of the local response model (δ^{LRM} and Φ^{LRM}) in relation to WDZe for Schiltach, BFO (upper sensor).

Table B.5.: Semidiurnal degree 2 parameters for the LRM-model, station Schiltach, BFO (upper sensor).

Wave	δ^{LRM}	Φ^{LRM}	δ^{LRM}	Amplitude	Frequency	Doodson
		/°	$/\delta^{\mathrm{WDZe}}$	$/\mathrm{nm\,s^{-2}}$	/cpd	
$3N_2$	1.1377	1.9167	0.9829	0.77	1.823399	225.855
ϵ_2	1.1388	2.3759	0.9839	2.00	1.828256	227.655
$2N_2$	1.1535	3.0601	0.9965	6.82	1.859690	235.755
μ_2	1.1551	2.7164	0.9980	8.24	1.864547	237.555
MIX_2	1.1551	2.7164	0.9980	0.56	1.867285	238.554
NW_2	1.1739	2.6490	1.0142	0.44	1.893244	244.656
N_2	1.1739	2.6490	1.0142	51.94	1.895982	245.655
NIW_2	1.1747	2.6516	1.0148	0.49	1.898720	246.654
ν_2	1.1747	2.6516	1.0148	9.88	1.900839	247.455
NIX_2	1.1747	2.6516	1.0148	0.46	1.903577	248.454
γ_2	1.1913	1.0309	1.0292	0.82	1.927417	253.755
α_2	1.2046	0.4351	1.0407	0.94	1.929536	254.556
ω_2	1.1844	2.0817	1.0232	10.21	1.932127	255.545
M_2	1.1867	2.0327	1.0253	273.83	1.932274	255.555
β_2	1.2386	1.1677	1.0701	0.83	1.935011	256.554
δ_2	1.2114	1.3610	1.0466	0.32	1.937749	257.555
λ_2	1.1829	1.5634	1.0219	2.02	1.963708	263.655
L_2	1.1909	1.5029	1.0289	7.74	1.968565	265.455
KNO_2	1.1909	1.5029	1.0289	1.94	1.969184	265.655
LX_2	1.1909	1.5029	1.0289	0.85	1.969331	265.665
LZ_2	1.1909	1.5029	1.0289	0.37	1.974041	267.455
$2T_2$	1.1925	0.3903	1.0302	0.30	1.994524	271.557
T_2	1.1925	0.3903	1.0302	7.40	1.997262	272.556
S_2	1.1884	0.5741	1.0267	126.49	2.000000	273.555
R_2	1.1613	1.3798	1.0033	1.06	2.002738	274.554
K_2	1.1904	0.8276	1.0284	34.32	2.005476	275.555
KX_2	1.1904	0.8276	1.0284	10.23	2.005623	275.565
KY_2	1.1904	0.8276	1.0284	1.11	2.005770	275.575
KZ_2	1.1904	0.8276	1.0284	0.27	2.008214	276.554
KA_2	1.1904	0.8276	1.0284	0.23	2.010952	277.555
ζ_2	1.1876	0.4802	1.0260	0.36	2.036911	283.655
η_2	1.1876	0.4802	1.0260	1.91	2.041768	285.455
ETX_2	1.1876	0.4802	1.0260	0.83	2.041915	285.465
$2S_2$	1.1534	0.0717	0.9964	0.32	2.073202	293.555
$2K_2$	1.1663	-0.1269	1.0076	0.50	2.078678	295.555

Table B.6.: Degree 3 and 4 parameters for the LRM-model, station Schiltach, BFO (upper sensor).

Wave	δ^{LRM}	Φ^{LRM}	δ^{LRM}	Amplitude	Frequency	Doodson
		/°	$/\delta^{\mathrm{WDZe}}$	$/\mathrm{nm\,s^{-2}}$	/cpd	
$2Q_1$*	1.0857	0.8800	1.0120	0.45	0.856643	125.655
Q_1*	1.0857	0.8800	1.0120	1.66	0.892935	135.555
QX_1*	1.0857	0.8800	1.0120	0.10	0.893554	135.755
ρ_1*	1.0857	0.8800	1.0120	0.14	0.898410	137.555
O_1*	1.0921	1.0487	1.0179	0.88	0.929845	145.655
LK_1*	1.0827	0.9306	1.0092	0.81	0.965990	155.545
M_1*	1.0827	0.9306	1.0092	5.46	0.966137	155.555
χ_1*	1.0827	0.9306	1.0092	0.02	0.971613	157.555
K_1*	1.0841	0.0041	1.0106	0.29	1.002428	165.455
J_1*	1.0841	0.0041	1.0106	1.92	1.039339	175.555
$3N_2$*	1.0734	-0.0167	1.0005	0.22	1.823089	225.755
ϵ_2*	1.0734	-0.0167	1.0005	0.22	1.827946	227.555
$2N_2$*	1.0658	-0.0826	0.9935	1.25	1.859381	235.655
μ_2*	1.0658	-0.0826	0.9935	0.23	1.864238	237.455
N_2*	1.0702	0.0778	0.9976	4.57	1.895673	245.555
ν_2*	1.0702	0.0778	0.9976	0.12	1.901148	247.555
ω_2*	1.0659	0.0482	0.9936	0.26	1.931964	255.455
M_2*	1.0659	0.0482	0.9936	0.70	1.932583	255.655
L_2*	1.0679	-0.3176	0.9954	4.26	1.968875	265.555
KNO_2*	1.0679	-0.3176	0.9954	0.80	1.969018	265.565
K_2*	1.0688	0.4071	0.9963	0.23	2.005166	275.455
η_2*	1.0688	0.4071	0.9963	0.39	2.042077	285.555
MN_3*	1.0643	0.0780	0.9952	0.90	2.862119	345.655
M_3*	1.0673	0.2789	0.9980	3.30	2.898410	355.555
ML_3*	1.0723	0.0498	1.0026	0.19	2.934702	365.455
MK_3*	1.0686	0.1553	0.9992	0.43	2.971613	375.555
O_1+	1.0297	0.0126	0.9937	0.05	0.929536	145.555
MN_3+	1.0297	0.0126	0.9937	0.07	2.861809	345.555
M_4+	1.0284	0.0126	0.9937	0.04	3.864547	455.555

Moxa (lower sensor)

Table B.7.: Diurnal degree 2 parameters for the LRM-model, station Moxa (lower sensor).

Wave	δ^{LRM}	Φ^{LRM}	δ^{LRM}	Amplitude	Frequency	Doodson
		/°	$/\delta^{\mathrm{WDZe}}$	$/\mathrm{nm\,s^{-2}}$	/cpd	
ζ_1	1.1548	-0.4998	1.0013	0.71	0.820661	115.855
SGQ_1	1.1548	-0.4998	1.0013	1.83	0.825518	117.655
$2\mathrm{Q}_1$	1.1509	-0.5765	0.9979	6.11	0.856952	125.755
σ_1	1.1485	-0.5320	0.9959	7.37	0.861809	127.555
SGX_1	1.1459	-0.0657	0.9936	0.50	0.864547	128.554
QW_1	1.1474	-0.2884	0.9950	8.76	0.893097	135.645
Q_1	1.1465	-0.1757	0.9942	46.45	0.893244	135.655
ρ_1	1.1473	-0.1026	0.9950	8.85	0.898101	137.455
ROX_1	1.1369	-0.6632	0.9859	0.51	0.898720	137.655
OW_1	1.1626	-0.1205	1.0084	0.86	0.926798	144.556
OV_1	1.1490	0.1225	0.9966	47.13	0.929389	145.545
O_1	1.1490	0.1225	0.9966	249.83	0.929536	145.555
OX_1	1.1490	0.1225	0.9966	1.61	0.930155	145.755
TW_1	1.1540	0.2482	1.0009	0.76	0.932273	146.554
τ_1	1.1540	0.2482	1.0009	3.27	0.935012	147.555
LKW_1	1.1465	0.2912	0.9949	1.88	0.960970	153.655
LK_1	1.1534	0.2518	1.0009	7.19	0.965827	155.455
M_1	1.1522	0.1769	0.9999	20.00	0.966446	155.655
MN_1	1.1522	0.1769	0.9999	4.02	0.966593	155.665
χ_1	1.1504	0.1113	0.9985	3.83	0.971303	157.455
π_1	1.1508	0.1874	1.0015	6.86	0.994524	162.556
P_1	1.1495	0.1720	1.0017	117.02	0.997262	163.555
S_1	1.1660	3.5531	1.0191	2.75	1.000000	164.556
KW_1	1.1378	0.2219	1.0030	6.90	1.002591	165.545
K_1	1.1365	0.2220	1.0030	348.17	1.002738	165.555
κ_1	1.1351	0.2379	1.0029	47.17	1.002885	165.565
KX_1	1.1335	0.2379	1.0029	1.01	1.003032	165.575
ψ_1	1.2648	0.3215	0.9974	3.04	1.005476	166.554
φ_1	1.1736	0.0419	1.0043	5.09	1.008214	167.555
ϑ_1	1.1549	-0.0611	0.9998	3.71	1.034173	173.655
J_1	1.1566	0.0828	1.0014	19.35	1.039030	175.455
ι_1	1.1566	0.0828	1.0014	3.84	1.039177	175.465
SO_1	1.1524	0.4536	0.9984	3.18	1.070464	183.555
JO_1	1.1479	0.4040	0.9946	1.57	1.075321	185.355
OO_1	1.1549	0.1068	1.0006	10.47	1.075940	185.555
OOZ_1	1.1613	0.3853	1.0063	0.51	1.106756	193.455
V_1	1.1506	0.1575	0.9970	2.04	1.112232	195.455

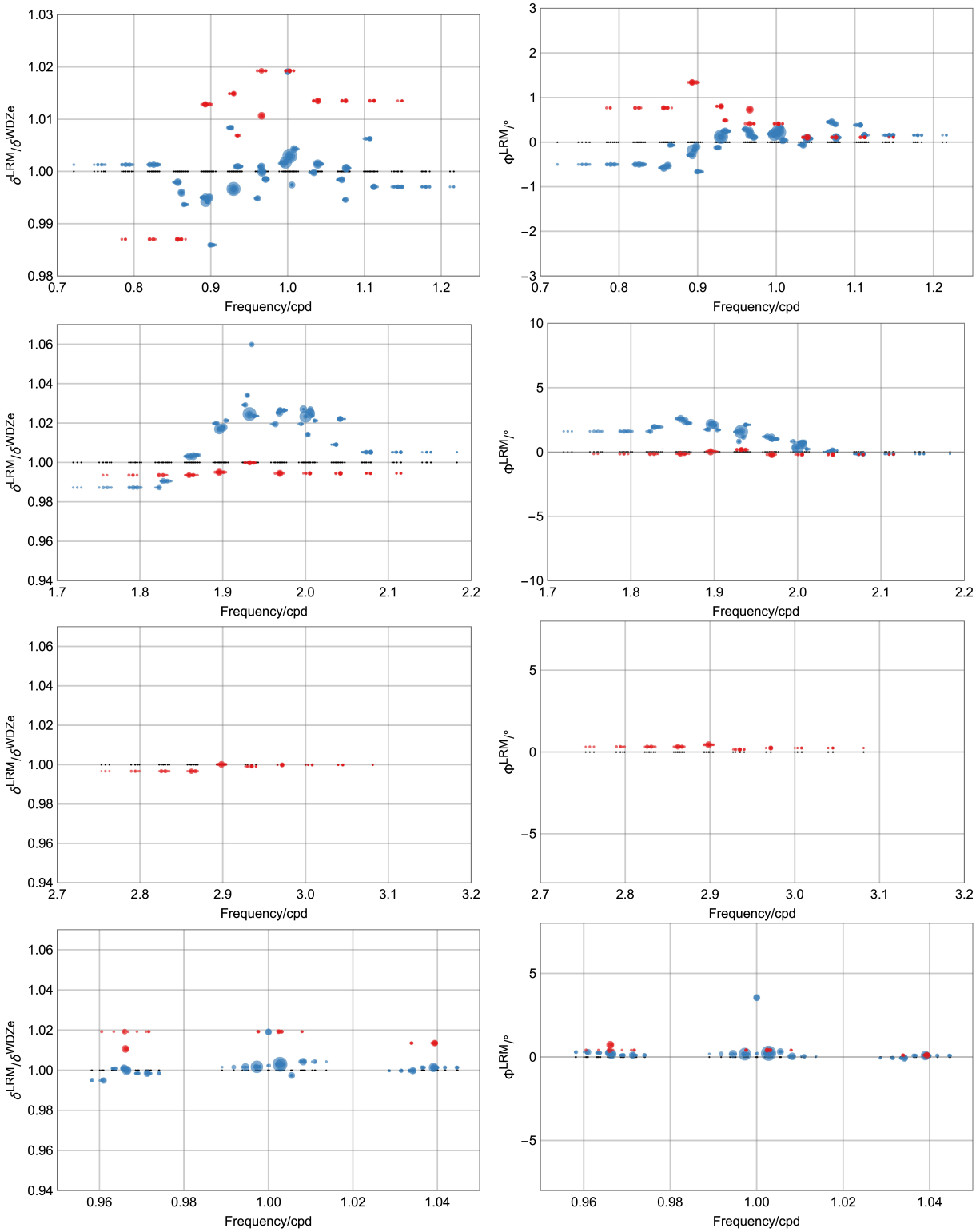

Figure B.3.: Parameters of the local response model (δ^{LRM} and Φ^{LRM}) in relation to WDZe for Moxa (lower sensor).

Table B.8.: Semidiurnal degree 2 parameters for the LRM-model, station Moxa (lower sensor).

Wave	δ^{LRM}	Φ^{LRM}	δ^{LRM}	Amplitude	Frequency	Doodson
		/°	$/\delta^{\mathrm{WDZe}}$	$/\mathrm{nm\,s^{-2}}$	/cpd	
$3N_2$	1.1425	1.6066	0.9873	0.70	1.823399	225.855
ϵ_2	1.1463	1.9461	0.9905	1.82	1.828256	227.655
$2N_2$	1.1609	2.5889	1.0031	6.21	1.859690	235.755
μ_2	1.1610	2.4279	1.0032	7.49	1.864547	237.555
MIX_2	1.1616	2.2425	1.0038	0.51	1.867285	238.554
NW_2	1.1802	1.7600	1.0198	0.40	1.893244	244.656
N_2	1.1769	2.1629	1.0170	47.24	1.895982	245.655
NIW_2	1.1769	2.2526	1.0170	0.44	1.898720	246.654
ν_2	1.1779	2.0848	1.0178	8.99	1.900839	247.455
NIX_2	1.1819	1.7255	1.0213	0.42	1.903577	248.454
γ_2	1.1911	1.5618	1.0292	0.75	1.927417	253.755
α_2	1.1967	0.8279	1.0341	0.86	1.929536	254.556
ω_2	1.1854	1.6105	1.0243	9.29	1.932127	255.545
M_2	1.1858	1.5781	1.0246	249.07	1.932274	255.555
β_2	1.2266	1.1604	1.0599	0.75	1.935011	256.554
δ_2	1.1845	2.1161	1.0235	0.29	1.937749	257.555
λ_2	1.1798	1.1976	1.0194	1.84	1.963708	263.655
L_2	1.1865	1.1279	1.0253	7.04	1.968565	265.455
KNO_2	1.1880	1.0111	1.0265	1.76	1.969184	265.655
LX_2	1.1880	1.0111	1.0265	0.78	1.969331	265.665
LZ_2	1.1880	1.0111	1.0265	0.34	1.974041	267.455
$2T_2$	1.1799	0.8341	1.0195	0.27	1.994524	271.557
T_2	1.1885	0.3461	1.0270	6.73	1.997262	272.556
S_2	1.1842	0.3407	1.0233	115.05	2.000000	273.555
R_2	1.1736	0.7159	1.0142	0.96	2.002738	274.554
K_2	1.1860	0.5803	1.0249	31.22	2.005476	275.555
KX_2	1.1871	0.6573	1.0258	9.31	2.005623	275.565
KY_2	1.1887	0.6426	1.0271	1.01	2.005770	275.575
KZ_2	1.1848	0.7984	1.0238	0.25	2.008214	276.554
KA_2	1.1819	0.2335	1.0212	0.21	2.010952	277.555
ζ_2	1.1678	0.0042	1.0091	0.33	2.036911	283.655
η_2	1.1828	0.1227	1.0221	1.73	2.041768	285.455
ETX_2	1.1828	0.1227	1.0221	0.76	2.041915	285.465
$2S_2$	1.1633	-0.1510	1.0052	0.29	2.073202	293.555
$2K_2$	1.1633	-0.1510	1.0052	0.46	2.078678	295.555

Table B.9.: Degree 3 and 4 parameters for the LRM-model, station Moxa (lower sensor).

Wave	δ^{LRM}	Φ^{LRM} /°	δ^{LRM} /δ^{WDZe}	Amplitude /nm s^{-2}	Frequency /cpd	Doodson
$2Q_1$*	1.0589	0.7702	0.9870	0.48	0.856643	125.655
Q_1*	1.0866	1.3398	1.0129	1.76	0.892935	135.555
QX_1*	1.0866	1.3398	1.0129	0.11	0.893554	135.755
ρ_1*	1.0866	1.3398	1.0129	0.15	0.898410	137.555
O_1*	1.0888	0.8057	1.0149	0.93	0.929845	145.655
LK_1*	1.0935	0.4150	1.0193	0.86	0.965990	155.545
M_1*	1.0842	0.7311	1.0107	5.79	0.966137	155.555
χ_1*	1.0935	0.4150	1.0193	0.02	0.971613	157.555
K_1*	1.0935	0.4150	1.0193	0.31	1.002428	165.455
J_1*	1.0873	0.1097	1.0135	2.04	1.039339	175.555
$3N_2$*	1.0659	-0.1367	0.9935	0.20	1.823089	225.755
ϵ_2*	1.0659	-0.1367	0.9935	0.20	1.827946	227.555
$2N_2$*	1.0659	-0.1367	0.9935	1.17	1.859381	235.655
μ_2*	1.0659	-0.1367	0.9935	0.22	1.864238	237.455
N_2*	1.0675	0.0200	0.9950	4.31	1.895673	245.555
ν_2*	1.0675	0.0200	0.9950	0.11	1.901148	247.555
ω_2*	1.0726	0.1855	0.9998	0.25	1.931964	255.455
M_2*	1.0726	0.1855	0.9998	0.66	1.932583	255.655
L_2*	1.0668	-0.1978	0.9945	4.01	1.968875	265.555
KNO_2*	1.0668	-0.1978	0.9945	0.76	1.969018	265.565
K_2*	1.0668	-0.1978	0.9945	0.22	2.005166	275.455
η_2*	1.0668	-0.1978	0.9945	0.36	2.042077	285.555
MN_3*	1.0656	0.3282	0.9967	0.78	2.862119	345.655
M_3*	1.0693	0.4453	1.0001	2.86	2.898410	355.555
ML_3*	1.0682	0.1594	0.9991	0.16	2.934702	365.455
MK_3*	1.0691	0.2464	0.9999	0.37	2.971613	375.555
O_1+	1.0361	0.0013	0.9998	0.06	0.929536	145.555
MN_3+	1.0361	0.0013	0.9998	0.06	2.861809	345.555
M_4+	1.0325	0.0286	0.9977	0.03	3.864547	455.555

Moxa (upper sensor)

Table B.10.: Diurnal degree 2 parameters for the LRM-model, station Moxa (upper sensor).

Wave	δ^{LRM}	Φ^{LRM}	δ^{LRM}	Amplitude	Frequency	Doodson
		/°	$/\delta^{\mathrm{WDZe}}$	/nm s^{-2}	/cpd	
ζ_1	1.1565	-0.4655	1.0027	0.71	0.820661	115.855
SGQ_1	1.1564	-0.4655	1.0027	1.83	0.825518	117.655
$2Q_1$	1.1508	-0.5831	0.9979	6.11	0.856952	125.755
σ_1	1.1483	-0.4952	0.9957	7.37	0.861809	127.555
SGX_1	1.1457	-0.0538	0.9935	0.50	0.864547	128.554
QW_1	1.1465	-0.2815	0.9943	8.76	0.893097	135.645
Q_1	1.1462	-0.1782	0.9940	46.45	0.893244	135.655
ρ_1	1.1471	-0.1594	0.9948	8.85	0.898101	137.455
ROX_1	1.1424	-0.8982	0.9908	0.51	0.898720	137.655
OW_1	1.1601	0.0987	1.0062	0.86	0.926798	144.556
OV_1	1.1488	0.1238	0.9965	47.14	0.929389	145.545
O_1	1.1489	0.1228	0.9965	249.84	0.929536	145.555
OX_1	1.1489	0.1228	0.9965	1.61	0.930155	145.755
TW_1	1.1518	0.1448	0.9991	0.76	0.932273	146.554
τ_1	1.1518	0.1448	0.9991	3.27	0.935012	147.555
LKW_1	1.1461	0.3780	0.9945	1.88	0.960970	153.655
LK_1	1.1541	0.2662	1.0015	7.19	0.965827	155.455
M_1	1.1520	0.1729	0.9998	20.00	0.966446	155.655
MN_1	1.1520	0.1729	0.9998	4.02	0.966593	155.665
χ_1	1.1503	0.0984	0.9984	3.83	0.971303	157.455
π_1	1.1500	0.1317	1.0008	6.86	0.994524	162.556
P_1	1.1493	0.1726	1.0016	117.03	0.997262	163.555
S_1	1.1589	3.6200	1.0129	2.75	1.000000	164.556
KW_1	1.1376	0.2203	1.0028	6.90	1.002591	165.545
K_1	1.1363	0.2203	1.0028	348.19	1.002738	165.555
κ_1	1.1349	0.2332	1.0027	47.18	1.002885	165.565
KX_1	1.1333	0.2332	1.0027	1.01	1.003032	165.575
ψ_1	1.2648	0.3354	0.9974	3.04	1.005476	166.554
φ_1	1.1731	0.0850	1.0038	5.09	1.008214	167.555
ϑ_1	1.1557	-0.0922	1.0004	3.71	1.034173	173.655
J_1	1.1564	0.0795	1.0013	19.35	1.039030	175.455
ι_1	1.1564	0.0795	1.0013	3.84	1.039177	175.465
SO_1	1.1516	0.4490	0.9977	3.18	1.070464	183.555
JO_1	1.1497	0.3599	0.9961	1.57	1.075321	185.355
OO_1	1.1545	0.1019	1.0002	10.47	1.075940	185.555
OOZ_1	1.1602	0.3815	1.0054	0.51	1.106756	193.455
V_1	1.1516	0.2063	0.9980	2.04	1.112232	195.455

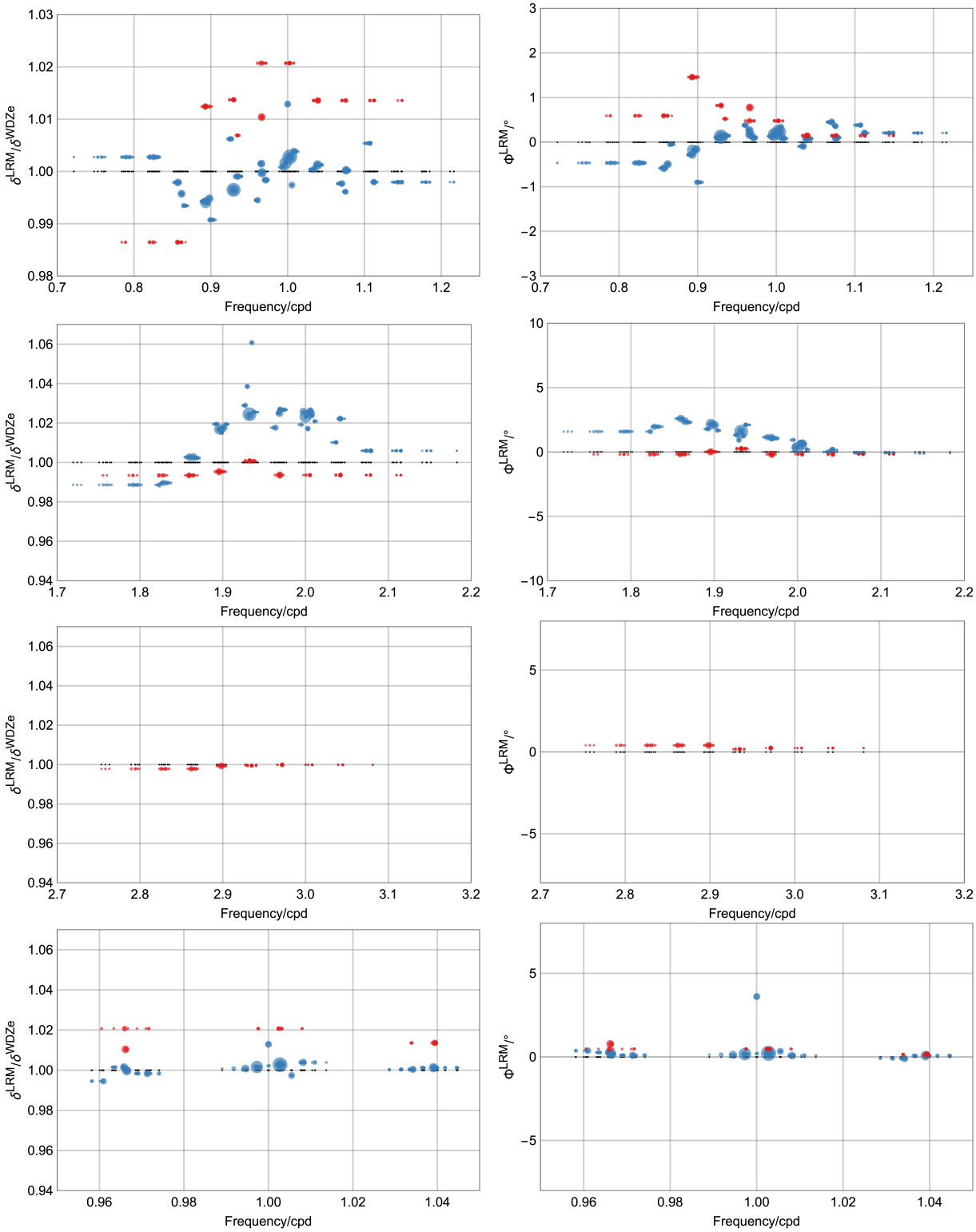

Figure B.4.: Parameters of the local response model (δ^{LRM} and Φ^{LRM}) in relation to WDZe for Moxa (upper sensor).

Table B.11.: Semidiurnal degree 2 parameters for the LRM-model, station Moxa (upper sensor).

Wave	δ^{LRM}	Φ^{LRM}	δ^{LRM}	Amplitude	Frequency	Doodson
		/°	$/\delta^{\mathrm{WDZe}}$	$/\mathrm{nm\,s^{-2}}$	/cpd	
$3N_2$	1.1441	1.5882	0.9886	0.70	1.823399	225.855
ϵ_2	1.1452	1.9665	0.9896	1.82	1.828256	227.655
$2N_2$	1.1604	2.5979	1.0027	6.21	1.859690	235.755
μ_2	1.1605	2.3996	1.0028	7.49	1.864547	237.555
MIX_2	1.1599	2.3067	1.0023	0.51	1.867285	238.554
NW_2	1.1798	1.7868	1.0195	0.40	1.893244	244.656
N_2	1.1767	2.1602	1.0168	47.24	1.895982	245.655
NIW_2	1.1749	2.2342	1.0152	0.44	1.898720	246.654
ν_2	1.1776	2.0923	1.0176	8.99	1.900839	247.455
NIX_2	1.1797	1.6735	1.0194	0.42	1.903577	248.454
γ_2	1.1908	1.3113	1.0289	0.75	1.927417	253.755
α_2	1.2019	0.9264	1.0386	0.86	1.929536	254.556
ω_2	1.1847	1.6227	1.0237	9.29	1.932127	255.545
M_2	1.1855	1.5773	1.0244	249.09	1.932274	255.555
β_2	1.2276	1.2598	1.0608	0.75	1.935011	256.554
δ_2	1.1868	2.1088	1.0255	0.29	1.937749	257.555
λ_2	1.1777	1.1530	1.0176	1.84	1.963708	263.655
L_2	1.1862	1.1163	1.0250	7.04	1.968565	265.455
KNO_2	1.1883	1.0625	1.0268	1.76	1.969184	265.655
LX_2	1.1883	1.0625	1.0268	0.78	1.969331	265.665
LZ_2	1.1883	1.0625	1.0268	0.34	1.974041	267.455
$2T_2$	1.1795	0.9361	1.0192	0.27	1.994524	271.557
T_2	1.1871	0.3690	1.0258	6.73	1.997262	272.556
S_2	1.1841	0.3354	1.0232	115.06	2.000000	273.555
R_2	1.1771	0.7292	1.0172	0.96	2.002738	274.554
K_2	1.1857	0.5742	1.0246	31.23	2.005476	275.555
KX_2	1.1870	0.6692	1.0257	9.31	2.005623	275.565
KY_2	1.1880	0.6210	1.0265	1.01	2.005770	275.575
KZ_2	1.1849	0.6660	1.0239	0.25	2.008214	276.554
KA_2	1.1814	0.2035	1.0209	0.21	2.010952	277.555
ζ_2	1.1691	0.0131	1.0102	0.33	2.036911	283.655
η_2	1.1829	0.1700	1.0222	1.73	2.041768	285.455
ETX_2	1.1829	0.1700	1.0222	0.76	2.041915	285.465
$2S_2$	1.1641	-0.0960	1.0059	0.29	2.073202	293.555
$2K_2$	1.1641	-0.0960	1.0059	0.46	2.078678	295.555

Table B.12.: Degree 3 and 4 parameters for the LRM-model, station Moxa (upper sensor).

Wave	δ^{LRM}	Φ^{LRM} /°	δ^{LRM} /δ^{WDZe}	Amplitude /nm s^{-2}	Frequency /cpd	Doodson
$2Q_1$*	1.0583	0.5924	0.9865	0.48	0.856643	125.655
Q_1*	1.0861	1.4575	1.0124	1.76	0.892935	135.555
QX_1*	1.0861	1.4575	1.0124	0.11	0.893554	135.755
ρ_1*	1.0861	1.4575	1.0124	0.15	0.898410	137.555
O_1*	1.0875	0.8226	1.0137	0.93	0.929845	145.655
LK_1*	1.0951	0.4774	1.0207	0.86	0.965990	155.545
M_1*	1.0840	0.7771	1.0104	5.79	0.966137	155.555
χ_1*	1.0951	0.4774	1.0207	0.02	0.971613	157.555
K_1*	1.0951	0.4774	1.0207	0.31	1.002428	165.455
J_1*	1.0874	0.1474	1.0136	2.04	1.039339	175.555
$3N_2$*	1.0658	-0.1855	0.9934	0.20	1.823089	225.755
ϵ_2*	1.0658	-0.1855	0.9934	0.20	1.827946	227.555
$2N_2$*	1.0658	-0.1855	0.9934	1.17	1.859381	235.655
μ_2*	1.0658	-0.1855	0.9934	0.22	1.864238	237.455
N_2*	1.0678	0.0165	0.9953	4.31	1.895673	245.555
ν_2*	1.0678	0.0165	0.9953	0.11	1.901148	247.555
ω_2*	1.0737	0.2616	1.0008	0.25	1.931964	255.455
M_2*	1.0737	0.2616	1.0008	0.66	1.932583	255.655
L_2*	1.0659	-0.1845	0.9936	4.01	1.968875	265.555
KNO_2*	1.0659	-0.1845	0.9936	0.76	1.969018	265.565
K_2*	1.0659	-0.1845	0.9936	0.22	2.005166	275.455
η_2*	1.0659	-0.1845	0.9936	0.36	2.042077	285.555
MN_3*	1.0669	0.4126	0.9979	0.78	2.862119	345.655
M_3*	1.0684	0.4107	0.9993	2.86	2.898410	355.555
ML_3*	1.0686	0.1758	0.9995	0.16	2.934702	365.455
MK_3*	1.0690	0.2436	0.9999	0.37	2.971613	375.555
O_1+	1.0365	-0.0044	1.0002	0.06	0.929536	145.555
MN_3+	1.0365	-0.0044	1.0002	0.06	2.861809	345.555
M_4+	1.0325	0.0279	0.9977	0.03	3.864547	455.555

Membach

Table B.13.: Diurnal degree 2 parameters for the LRM-model, station Membach

Wave	δ^{LRM}	Φ^{LRM} /°	$\delta^{\mathrm{LRM}}/\delta^{\mathrm{WDZe}}$	Amplitude /nm s^{-2}	Frequency /cpd	Doodson
ζ_1	1.1665	-1.1362	1.0115	0.71	0.820661	115.855
SGQ_1	1.1671	-0.9538	1.0120	1.83	0.825518	117.655
$2Q_1$	1.1528	-0.7256	0.9996	6.12	0.856952	125.755
σ_1	1.1482	-0.8225	0.9956	7.37	0.861809	127.555
SGX_1	1.1529	-0.9911	0.9997	0.50	0.864547	128.554
QW_1	1.1461	-0.2734	0.9939	8.76	0.893097	135.645
Q_1	1.1467	-0.2169	0.9944	46.46	0.893244	135.655
ρ_1	1.1479	-0.1017	0.9955	8.86	0.898101	137.455
ROX_1	1.1542	0.0590	1.0009	0.51	0.898720	137.655
OW_1	1.1531	-0.0020	1.0002	0.86	0.926798	144.556
OV_1	1.1493	0.1000	0.9968	47.14	0.929389	145.545
O_1	1.1494	0.1017	0.9969	249.90	0.929536	145.555
OX_1	1.1463	-0.0133	0.9943	1.61	0.930155	145.755
TW_1	1.1417	0.8887	0.9903	0.76	0.932273	146.554
τ_1	1.1555	0.1961	1.0023	3.27	0.935012	147.555
LKW_1	1.1548	0.4645	1.0020	1.88	0.960970	153.655
LK_1	1.1514	0.3432	0.9992	7.20	0.965827	155.455
M_1	1.1528	0.2147	1.0004	20.01	0.966446	155.655
MN_1	1.1562	0.2622	1.0033	4.02	0.966593	155.665
χ_1	1.1468	0.1906	0.9953	3.83	0.971303	157.455
π_1	1.1513	0.2017	1.0019	6.86	0.994524	162.556
P_1	1.1497	0.2211	1.0019	117.05	0.997262	163.555
S_1	1.1786	4.7962	1.0301	2.75	1.000000	164.556
KW_1	1.1408	0.4541	1.0056	6.90	1.002591	165.545
K_1	1.1372	0.2734	1.0036	348.27	1.002738	165.555
κ_1	1.1360	0.3044	1.0037	47.19	1.002885	165.565
KX_1	1.1403	0.0041	1.0089	1.01	1.003032	165.575
ψ_1	1.2653	0.1487	0.9978	3.04	1.005476	166.554
φ_1	1.1745	0.1932	1.0051	5.10	1.008214	167.555
ϑ_1	1.1566	-0.0297	1.0012	3.71	1.034173	173.655
J_1	1.1581	0.1473	1.0027	19.36	1.039030	175.455
ι_1	1.1554	0.2394	1.0004	3.84	1.039177	175.465
SO_1	1.1571	0.3930	1.0025	3.18	1.070464	183.555
JO_1	1.1546	0.0341	1.0003	1.57	1.075321	185.355
OO_1	1.1559	0.0763	1.0014	10.47	1.075940	185.555
OOZ_1	1.1526	0.4685	0.9987	0.51	1.106756	193.455
V_1	1.1534	0.1617	0.9995	2.04	1.112232	195.455

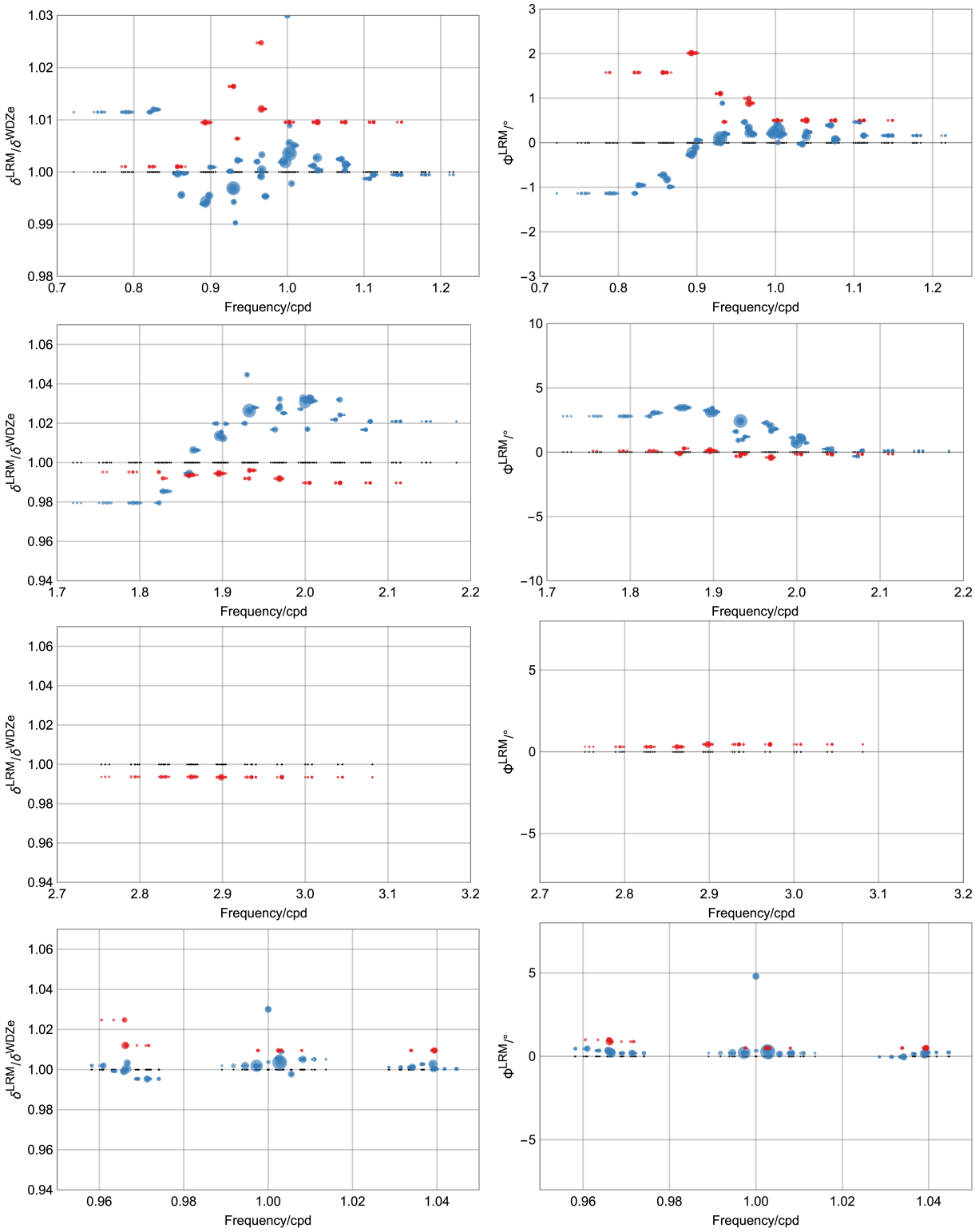

Figure B.5.: Parameters of the local response model (δ^{LRM} and Φ^{LRM}) in relation to WDZe for Membach.

Table B.14.: Semidiurnal degree 2 parameters for the LRM-model, station Membach.

Wave	δ^{LRM}	Φ^{LRM}	δ^{LRM}	Amplitude	Frequency	Doodson
		/°	$/\delta^{\mathrm{WDZe}}$	$/\mathrm{nm\,s^{-2}}$	/cpd	
$3N_2$	1.1336	2.7951	0.9795	0.70	1.823399	225.855
ϵ_2	1.1404	3.0626	0.9854	1.82	1.828256	227.655
$2N_2$	1.1510	3.4523	0.9946	6.22	1.859690	235.755
μ_2	1.1647	3.4640	1.0064	7.51	1.864547	237.555
MIX_2	1.1646	3.4710	1.0063	0.51	1.867285	238.554
NW_2	1.1803	3.2422	1.0199	0.40	1.893244	244.656
N_2	1.1730	3.1011	1.0136	47.32	1.895982	245.655
NIW_2	1.1752	3.4210	1.0155	0.44	1.898720	246.654
ν_2	1.1716	3.0687	1.0124	9.00	1.900839	247.455
NIX_2	1.1801	3.1426	1.0197	0.42	1.903577	248.454
γ_2	1.1804	1.6119	1.0200	0.75	1.927417	253.755
α_2	1.2089	0.9204	1.0447	0.86	1.929536	254.556
ω_2	1.1879	2.4046	1.0264	9.31	1.932127	255.545
M_2	1.1879	2.4266	1.0264	249.45	1.932274	255.555
β_2	1.2515	0.9842	1.0814	0.76	1.935011	256.554
δ_2	1.1896	1.1969	1.0280	0.29	1.937749	257.555
λ_2	1.1767	2.2711	1.0168	1.84	1.963708	263.655
L_2	1.1893	2.0553	1.0277	7.05	1.968565	265.455
KNO_2	1.1947	1.6575	1.0323	1.76	1.969184	265.655
LX_2	1.1909	1.6836	1.0291	0.78	1.969331	265.665
LZ_2	1.1863	1.8059	1.0251	0.34	1.974041	267.455
$2T_2$	1.1887	1.1321	1.0272	0.27	1.994524	271.557
T_2	1.1951	0.6794	1.0327	6.74	1.997262	272.556
S_2	1.1928	0.7529	1.0307	115.23	2.000000	273.555
R_2	1.1769	1.2701	1.0170	0.96	2.002738	274.554
K_2	1.1946	1.0156	1.0322	31.27	2.005476	275.555
KX_2	1.1949	1.1553	1.0326	9.32	2.005623	275.565
KY_2	1.1948	1.0463	1.0325	1.01	2.005770	275.575
KZ_2	1.1931	1.0308	1.0310	0.25	2.008214	276.554
KA_2	1.1935	0.7270	1.0313	0.21	2.010952	277.555
ζ_2	1.1826	0.2549	1.0219	0.33	2.036911	283.655
η_2	1.1942	0.2534	1.0320	1.74	2.041768	285.455
ETX_2	1.1853	0.0030	1.0242	0.76	2.041915	285.465
$2S_2$	1.1766	-0.3146	1.0167	0.29	2.073202	293.555
$2K_2$	1.1815	0.1143	1.0209	0.46	2.078678	295.555

Table B.15.: Degree 3 and 4 parameters for the LRM-model, station Membach.

Wave	δ^{LRM}	Φ^{LRM} /°	δ^{LRM} /δ^{WDZe}	Amplitude /nms^{-2}	Frequency /cpd	Doodson
$2Q_1$*	1.0739	1.5742	1.0010	0.48	0.856643	125.655
Q_1*	1.0830	2.0136	1.0095	1.76	0.892935	135.555
QX_1*	1.0830	2.0136	1.0095	0.11	0.893554	135.755
ρ_1*	1.0830	2.0136	1.0095	0.15	0.898410	137.555
O_1*	1.0904	1.1031	1.0164	0.93	0.929845	145.655
LK_1*	1.0994	0.9952	1.0248	0.86	0.965990	155.545
M_1*	1.0858	0.8870	1.0121	5.79	0.966137	155.555
χ_1*	1.0858	0.8870	1.0121	0.02	0.971613	157.555
K_1*	1.0831	0.5009	1.0096	0.31	1.002428	165.455
J_1*	1.0831	0.5009	1.0096	2.04	1.039339	175.555
$3N_2$*	1.0677	0.0980	0.9952	0.20	1.823089	225.755
ϵ_2*	1.0643	0.0893	0.9920	0.20	1.827946	227.555
$2N_2$*	1.0658	-0.0976	0.9935	1.18	1.859381	235.655
μ_2*	1.0660	0.2882	0.9937	0.22	1.864238	237.455
N_2*	1.0669	0.1198	0.9945	4.31	1.895673	245.555
ν_2*	1.0669	0.1198	0.9945	0.11	1.901148	247.555
ω_2*	1.0642	-0.3178	0.9920	0.25	1.931964	255.455
M_2*	1.0686	-0.1493	0.9961	0.66	1.932583	255.655
L_2*	1.0641	-0.4140	0.9919	4.02	1.968875	265.555
KNO_2*	1.0641	-0.4140	0.9919	0.76	1.969018	265.565
K_2*	1.0618	-0.1491	0.9897	0.22	2.005166	275.455
η_2*	1.0618	-0.1491	0.9897	0.36	2.042077	285.555
MN_3*	1.0624	0.3051	0.9937	0.78	2.862119	345.655
M_3*	1.0623	0.4543	0.9935	2.87	2.898410	355.555
ML_3*	1.0623	0.4543	0.9935	0.16	2.934702	365.455
MK_3*	1.0623	0.4543	0.9935	0.37	2.971613	375.555
O_1+	1.0361	0.0895	0.9998	0.06	0.929536	145.555
MN_3+	1.0361	0.0895	0.9998	0.06	2.861809	345.555
M_4+	1.0326	0.0773	0.9978	0.03	3.864547	455.555

Strasbourg

Table B.16.: Diurnal degree 2 parameters for the LRM-model, station Strasbourg.

Wave	δ^{LRM}	Φ^{LRM} /°	$\delta^{\mathrm{LRM}}/\delta^{\mathrm{WDZe}}$	Amplitude /nm s^{-2}	Frequency /cpd	Doodson
ζ_1	1.1553	-0.2104	1.0015	0.72	0.820661	115.855
SGQ_1	1.1570	-0.6420	1.0030	1.85	0.825518	117.655
$2Q_1$	1.1560	-0.6621	1.0022	6.19	0.856952	125.755
σ_1	1.1513	-0.5885	0.9981	7.45	0.861809	127.555
SGX_1	1.1513	-0.5882	0.9981	0.50	0.864547	128.554
QW_1	1.1481	-0.3040	0.9954	8.87	0.893097	135.645
Q_1	1.1470	-0.2854	0.9944	47.00	0.893244	135.655
ρ_1	1.1471	-0.1689	0.9945	8.96	0.898101	137.455
ROX_1	1.1470	-0.1701	0.9945	0.52	0.898720	137.655
OW_1	1.1495	0.0957	0.9968	0.87	0.926798	144.556
OV_1	1.1494	0.0957	0.9968	47.68	0.929389	145.545
O_1	1.1488	0.0795	0.9962	252.76	0.929536	145.555
OX_1	1.1489	0.0773	0.9963	1.63	0.930155	145.755
TW_1	1.1576	-0.1299	1.0038	0.77	0.932273	146.554
τ_1	1.1534	0.2008	1.0002	3.31	0.935012	147.555
LKW_1	1.1512	0.1807	0.9986	1.90	0.960970	153.655
LK_1	1.1510	0.1800	0.9986	7.28	0.965827	155.455
M_1	1.1521	0.2037	0.9996	20.24	0.966446	155.655
MN_1	1.1574	0.2413	1.0042	4.06	0.966593	155.665
χ_1	1.1511	0.2564	0.9989	3.87	0.971303	157.455
π_1	1.1485	0.2602	0.9993	6.94	0.994524	162.556
P_1	1.1495	0.2154	1.0015	118.39	0.997262	163.555
S_1	1.1771	2.2327	1.0285	2.79	1.000000	164.556
KW_1	1.1375	0.2822	1.0025	6.98	1.002591	165.545
K_1	1.1369	0.2653	1.0030	352.26	1.002738	165.555
κ_1	1.1367	0.2871	1.0041	47.73	1.002885	165.565
KX_1	1.1352	0.2862	1.0042	1.02	1.003032	165.575
ψ_1	1.2704	0.0663	1.0016	3.08	1.005476	166.554
φ_1	1.1754	0.1726	1.0056	5.15	1.008214	167.555
ϑ_1	1.1578	0.1453	1.0020	3.76	1.034173	173.655
J_1	1.1576	0.1463	1.0020	19.58	1.039030	175.455
ι_1	1.1576	0.1524	1.0021	3.88	1.039177	175.465
SO_1	1.1532	0.0595	0.9989	3.21	1.070464	183.555
JO_1	1.1561	0.1136	1.0014	1.59	1.075321	185.355
OO_1	1.1561	0.1162	1.0014	10.60	1.075940	185.555
OOZ_1	1.1558	0.4228	1.0013	0.52	1.106756	193.455
V_1	1.1558	0.4243	1.0013	2.06	1.112232	195.455

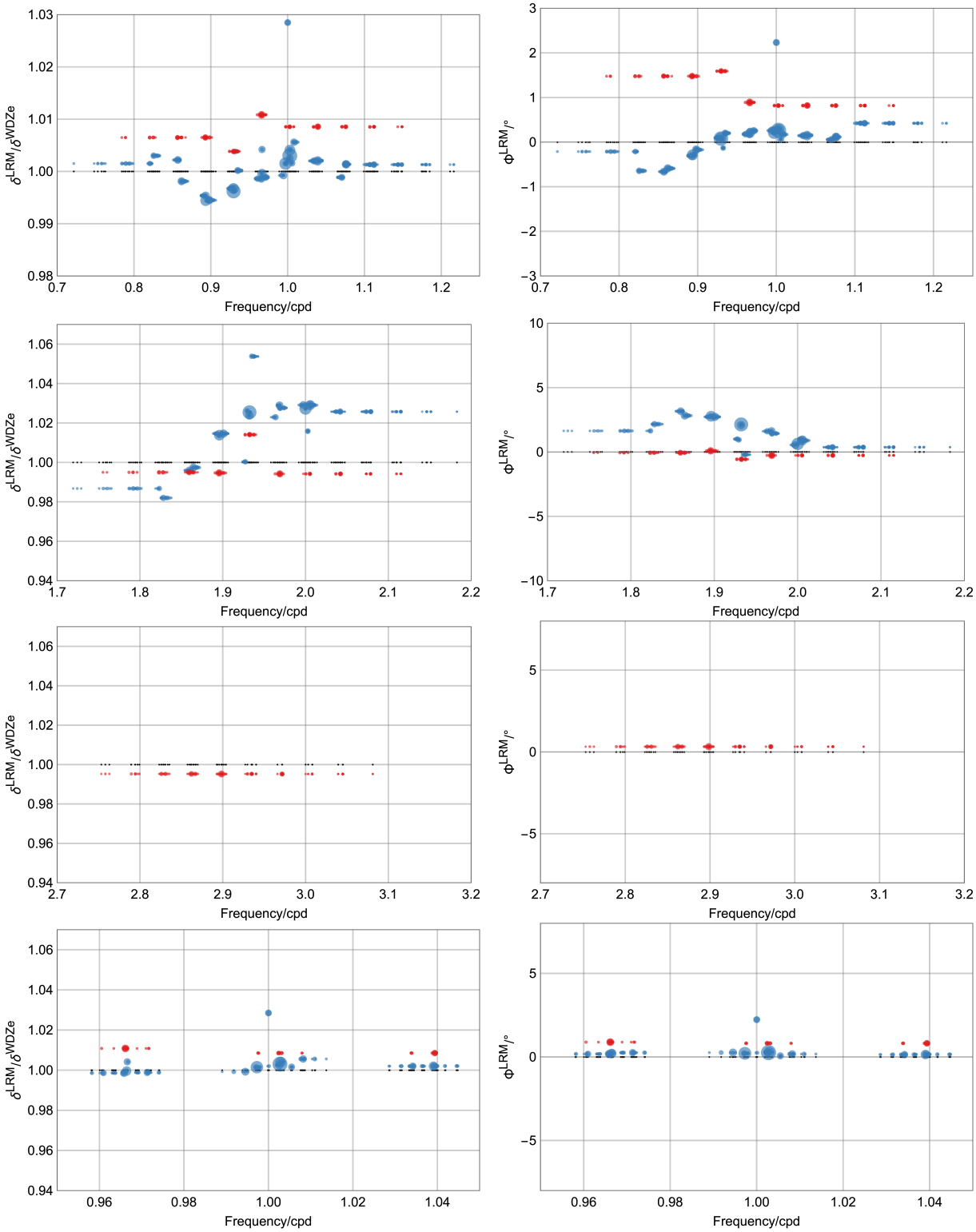

Figure B.6.: Parameters of the local response model (δ^{LRM} and Φ^{LRM}) in relation to WDZe for Strasbourg.

Table B.17.: Semidiurnal degree 2 parameters for the LRM-model, station Strasbourg.

Wave	δ^{LRM}	Φ^{LRM}	δ^{LRM}	Amplitude	Frequency	Doodson
		/°	$/\delta^{\mathrm{WDZe}}$	$/\mathrm{nm\,s^{-2}}$	/cpd	
$3N_2$	1.1422	1.6421	0.9868	0.76	1.823399	225.855
ϵ_2	1.1367	2.1662	0.9820	1.97	1.828256	227.655
$2N_2$	1.1528	3.1663	0.9960	6.75	1.859690	235.755
μ_2	1.1545	2.8293	0.9975	8.14	1.864547	237.555
MIX_2	1.1545	2.8297	0.9975	0.55	1.867285	238.554
NW_2	1.1745	2.7320	1.0147	0.43	1.893244	244.656
N_2	1.1735	2.7748	1.0139	51.34	1.895982	245.655
NIW_2	1.1745	2.7317	1.0147	0.48	1.898720	246.654
ν_2	1.1744	2.7331	1.0147	9.77	1.900839	247.455
NIX_2	1.1744	2.7319	1.0147	0.45	1.903577	248.454
γ_2	1.1579	1.0066	1.0003	0.81	1.927417	253.755
α_2	1.1878	0.9449	1.0262	0.93	1.929536	254.556
ω_2	1.1850	2.0885	1.0238	10.09	1.932127	255.545
M_2	1.1869	2.1411	1.0255	270.67	1.932274	255.555
β_2	1.2199	-0.2149	1.0539	0.82	1.935011	256.554
δ_2	1.2197	-0.2130	1.0538	0.32	1.937749	257.555
λ_2	1.1841	1.6109	1.0230	2.00	1.963708	263.655
L_2	1.1911	1.6223	1.0290	7.65	1.968565	265.455
KNO_2	1.1895	1.4418	1.0277	1.91	1.969184	265.655
LX_2	1.1895	1.4416	1.0277	0.84	1.969331	265.665
LZ_2	1.1895	1.4414	1.0277	0.37	1.974041	267.455
$2T_2$	1.1912	0.5493	1.0291	0.30	1.994524	271.557
T_2	1.1912	0.5488	1.0291	7.31	1.997262	272.556
S_2	1.1891	0.6315	1.0273	125.03	2.000000	273.555
R_2	1.1758	0.9733	1.0159	1.05	2.002738	274.554
K_2	1.1911	0.8918	1.0291	33.93	2.005476	275.555
KX_2	1.1913	0.9134	1.0292	10.11	2.005623	275.565
KY_2	1.1911	0.8940	1.0290	1.10	2.005770	275.575
KZ_2	1.1911	0.8943	1.0291	0.27	2.008214	276.554
KA_2	1.1911	0.8940	1.0291	0.23	2.010952	277.555
ζ_2	1.1873	0.3718	1.0258	0.36	2.036911	283.655
η_2	1.1874	0.3729	1.0258	1.89	2.041768	285.455
ETX_2	1.1873	0.3713	1.0258	0.82	2.041915	285.465
$2S_2$	1.1873	0.3717	1.0258	0.31	2.073202	293.555
$2K_2$	1.1873	0.3718	1.0258	0.50	2.078678	295.555

Table B.18.: Degree 3 and 4 parameters for the LRM-model, station Strasbourg.

Wave	δ^{LRM}	Φ^{LRM}	δ^{LRM}	Amplitude	Frequency	Doodson
		/°	$/\delta^{\mathrm{WDZe}}$	$/\mathrm{nm\,s^{-2}}$	/cpd	
$2Q_1$*	1.0798	1.4793	1.0065	0.46	0.856643	125.655
Q_1*	1.0798	1.4812	1.0065	1.68	0.892935	135.555
QX_1*	1.0798	1.4787	1.0065	0.10	0.893554	135.755
ρ_1*	1.0798	1.4789	1.0065	0.14	0.898410	137.555
O_1*	1.0769	1.5934	1.0038	0.88	0.929845	145.655
LK_1*	1.0844	0.8891	1.0108	0.81	0.965990	155.545
M_1*	1.0844	0.8899	1.0108	5.50	0.966137	155.555
χ_1*	1.0844	0.8893	1.0108	0.02	0.971613	157.555
K_1*	1.0820	0.8204	1.0086	0.30	1.002428	165.455
J_1*	1.0820	0.8210	1.0086	1.94	1.039339	175.555
$3N_2$*	1.0674	-0.0540	0.9950	0.21	1.823089	225.755
ϵ_2*	1.0674	-0.0537	0.9950	0.22	1.827946	227.555
$2N_2$*	1.0674	-0.0538	0.9950	1.24	1.859381	235.655
μ_2*	1.0674	-0.0539	0.9950	0.23	1.864238	237.455
N_2*	1.0671	0.0938	0.9947	4.54	1.895673	245.555
ν_2*	1.0671	0.0910	0.9947	0.12	1.901148	247.555
ω_2*	1.0879	-0.5665	1.0141	0.26	1.931964	255.455
M_2*	1.0880	-0.5676	1.0141	0.69	1.932583	255.655
L_2*	1.0666	-0.2659	0.9942	4.23	1.968875	265.555
KNO_2*	1.0666	-0.2657	0.9942	0.80	1.969018	265.565
K_2*	1.0666	-0.2656	0.9942	0.23	2.005166	275.455
η_2*	1.0666	-0.2654	0.9942	0.38	2.042077	285.555
MN_3*	1.0644	0.3269	0.9952	0.88	2.862119	345.655
M_3*	1.0644	0.3278	0.9952	3.24	2.898410	355.555
ML_3*	1.0644	0.3275	0.9952	0.18	2.934702	365.455
MK_3*	1.0644	0.3277	0.9952	0.42	2.971613	375.555
O_1+	1.0357	0.0088	0.9994	0.05	0.929536	145.555
MN_3+	1.0357	0.0088	0.9994	0.07	2.861809	345.555
M_4+	1.0319	0.0011	0.9970	0.04	3.864547	455.555

Bad Homburg

Table B.19.: Diurnal degree 2 parameters for the LRM-model, station Bad Homburg.

Wave	δ^{LRM}	Φ^{LRM} /°	δ^{LRM} /δ^{WDZe}	Amplitude /nm s^{-2}	Frequency /cpd	Doodson
ζ_1	1.1710	-0.4872	1.0153	0.71	0.820661	115.855
SGQ_1	1.1654	-0.4357	1.0105	1.83	0.825518	117.655
$2Q_1$	1.1496	-0.5381	0.9968	6.13	0.856952	125.755
σ_1	1.1494	-0.7004	0.9967	7.39	0.861809	127.555
SGX_1	1.1483	-0.7073	0.9957	0.50	0.864547	128.554
QW_1	1.1495	-0.1028	0.9968	8.79	0.893097	135.645
Q_1	1.1474	-0.2002	0.9950	46.58	0.893244	135.655
ρ_1	1.1484	-0.0805	0.9959	8.88	0.898101	137.455
ROX_1	1.1534	0.0663	1.0002	0.51	0.898720	137.655
OW_1	1.1546	-0.0798	1.0014	0.86	0.926798	144.556
OV_1	1.1500	0.1155	0.9975	47.26	0.929389	145.545
O_1	1.1501	0.1037	0.9975	250.54	0.929536	145.555
OX_1	1.1515	-0.3739	0.9987	1.62	0.930155	145.755
TW_1	1.1551	0.0516	1.0019	0.76	0.932273	146.554
τ_1	1.1551	0.0518	1.0019	3.28	0.935012	147.555
LKW_1	1.1567	0.4238	1.0036	1.88	0.960970	153.655
LK_1	1.1543	0.3851	1.0016	7.21	0.965827	155.455
M_1	1.1526	0.1877	1.0002	20.06	0.966446	155.655
MN_1	1.1535	0.1256	1.0010	4.03	0.966593	155.665
χ_1	1.1517	0.1921	0.9996	3.84	0.971303	157.455
π_1	1.1510	0.5339	1.0016	6.88	0.994524	162.556
P_1	1.1508	0.2028	1.0028	117.35	0.997262	163.555
S_1	1.1336	3.1845	0.9907	2.76	1.000000	164.556
KW_1	1.1392	0.2561	1.0042	6.92	1.002591	165.545
K_1	1.1380	0.2521	1.0042	349.17	1.002738	165.555
κ_1	1.1370	0.2968	1.0046	47.30	1.002885	165.565
KX_1	1.1353	0.3047	1.0045	1.01	1.003032	165.575
ψ_1	1.2567	0.7207	0.9910	3.05	1.005476	166.554
φ_1	1.1771	-0.1344	1.0073	5.11	1.008214	167.555
ϑ_1	1.1549	0.1154	0.9997	3.72	1.034173	173.655
J_1	1.1590	0.1110	1.0035	19.41	1.039030	175.455
ι_1	1.1585	0.4014	1.0030	3.85	1.039177	175.465
SO_1	1.1522	0.3343	0.9982	3.18	1.070464	183.555
JO_1	1.1526	0.1462	0.9985	1.57	1.075321	185.355
OO_1	1.1562	0.0671	1.0017	10.50	1.075940	185.555
OOZ_1	1.1656	0.3900	1.0100	0.51	1.106756	193.455
V_1	1.1457	0.1463	0.9928	2.04	1.112232	195.455

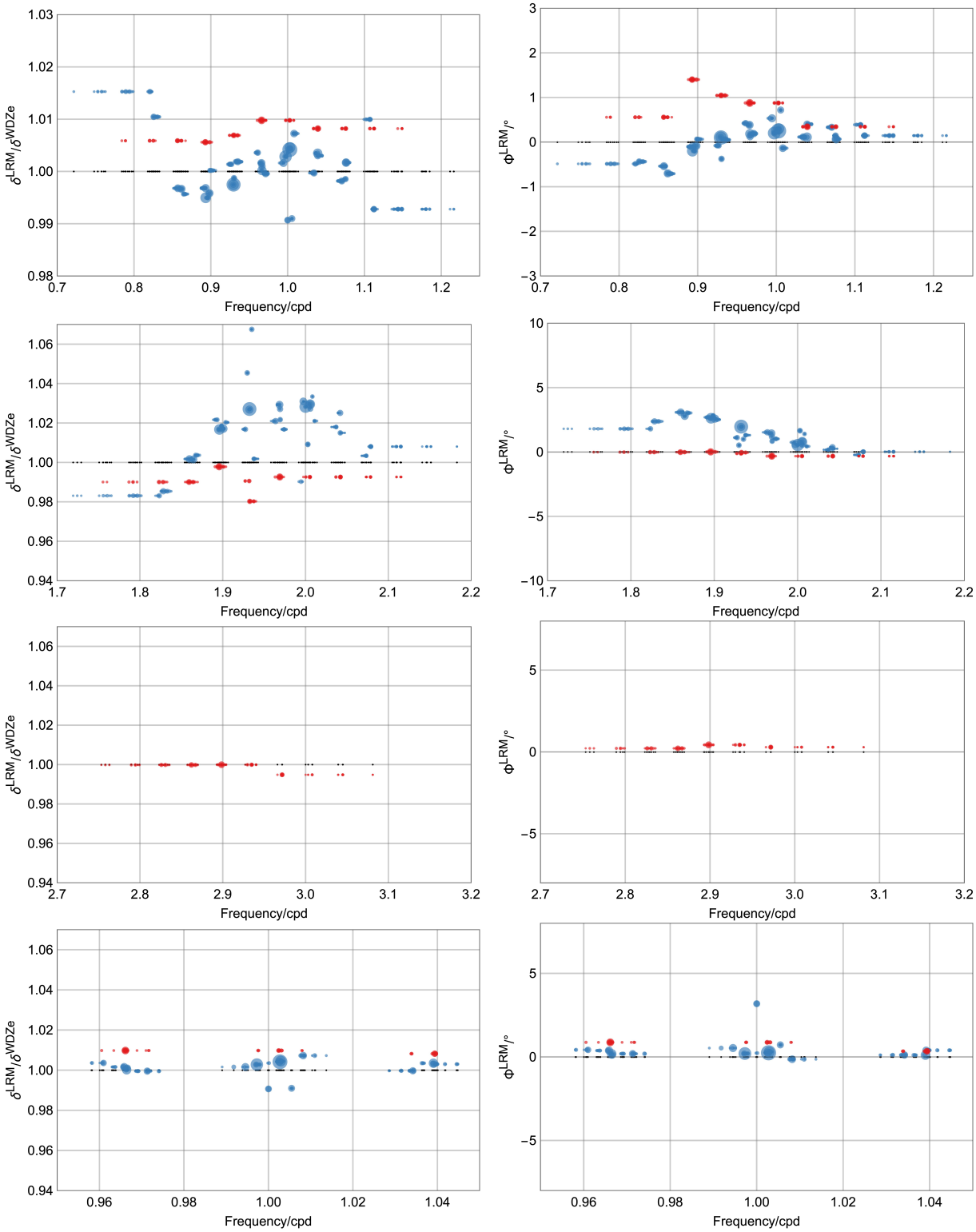

Figure B.7.: Parameters of the local response model (δ^{LRM} and Φ^{LRM}) in relation to WDZe for Bad Homburg.

Table B.20.: Semidiurnal degree 2 parameters for the LRM-model, station Bad Homburg.

Wave	δ^{LRM}	Φ^{LRM}	δ^{LRM}	Amplitude	Frequency	Doodson
		/°	$/\delta^{\mathrm{WDZe}}$	/nm s^{-2}	/cpd	
$3N_2$	1.1378	1.8045	0.9831	0.71	1.823399	225.855
ϵ_2	1.1404	2.3794	0.9854	1.85	1.828256	227.655
$2N_2$	1.1593	3.0811	1.0017	6.32	1.859690	235.755
μ_2	1.1591	2.7962	1.0015	7.63	1.864547	237.555
MIX_2	1.1616	3.0318	1.0037	0.51	1.867285	238.554
NW_2	1.1823	2.6965	1.0216	0.40	1.893244	244.656
N_2	1.1767	2.6206	1.0167	48.08	1.895982	245.655
NIW_2	1.1788	2.8263	1.0186	0.45	1.898720	246.654
ν_2	1.1771	2.5907	1.0171	9.15	1.900839	247.455
NIX_2	1.1808	2.5148	1.0203	0.42	1.903577	248.454
γ_2	1.1768	1.1139	1.0169	0.76	1.927417	253.755
α_2	1.2099	0.5273	1.0455	0.87	1.929536	254.556
ω_2	1.1884	1.9490	1.0268	9.46	1.932127	255.545
M_2	1.1887	1.9732	1.0271	253.50	1.932274	255.555
β_2	1.2355	0.9963	1.0675	0.77	1.935011	256.554
δ_2	1.1594	1.3088	1.0018	0.30	1.937749	257.555
λ_2	1.1816	1.5271	1.0210	1.87	1.963708	263.655
L_2	1.1912	1.4566	1.0293	7.17	1.968565	265.455
KNO_2	1.1887	1.1846	1.0271	1.79	1.969184	265.655
LX_2	1.1824	0.8440	1.0217	0.79	1.969331	265.665
LZ_2	1.1767	1.0185	1.0168	0.34	1.974041	267.455
$2T_2$	1.1461	0.7566	0.9903	0.28	1.994524	271.557
T_2	1.1932	0.5978	1.0310	6.85	1.997262	272.556
S_2	1.1900	0.5384	1.0283	117.10	2.000000	273.555
R_2	1.1679	1.6529	1.0092	0.98	2.002738	274.554
K_2	1.1914	0.7852	1.0295	31.78	2.005476	275.555
KX_2	1.1915	0.8074	1.0295	9.47	2.005623	275.565
KY_2	1.1888	0.5362	1.0272	1.03	2.005770	275.575
KZ_2	1.1960	1.4054	1.0334	0.25	2.008214	276.554
KA_2	1.1816	0.4353	1.0210	0.22	2.010952	277.555
ζ_2	1.1781	0.1703	1.0180	0.34	2.036911	283.655
η_2	1.1864	0.3745	1.0251	1.77	2.041768	285.455
ETX_2	1.1747	0.2518	1.0150	0.77	2.041915	285.465
$2S_2$	1.1612	-0.2243	1.0034	0.29	2.073202	293.555
$2K_2$	1.1666	0.0204	1.0081	0.46	2.078678	295.555

Table B.21.: Degree 3 and 4 parameters for the LRM-model, station Bad Homburg.

Wave	δ^{LRM}	Φ^{LRM} / °	δ^{LRM} / δ^{WDZe}	Amplitude / nm s^{-2}	Frequency / cpd	Doodson
$2Q_1$*	1.0791	0.5576	1.0059	0.48	0.856643	125.655
Q_1*	1.0788	1.4028	1.0056	1.75	0.892935	135.555
QX_1*	1.0788	1.4026	1.0056	0.11	0.893554	135.755
ρ_1*	1.0788	1.4026	1.0056	0.15	0.898410	137.555
O_1*	1.0802	1.0459	1.0069	0.92	0.929845	145.655
LK_1*	1.0833	0.8775	1.0098	0.85	0.965990	155.545
M_1*	1.0833	0.8776	1.0098	5.74	0.966137	155.555
χ_1*	1.0833	0.8775	1.0098	0.02	0.971613	157.555
K_1*	1.0833	0.8776	1.0098	0.31	1.002428	165.455
J_1*	1.0816	0.3458	1.0082	2.02	1.039339	175.555
$3N_2$*	1.0621	-0.0101	0.9901	0.21	1.823089	225.755
ϵ_2*	1.0621	-0.0101	0.9901	0.21	1.827946	227.555
$2N_2$*	1.0621	-0.0101	0.9901	1.19	1.859381	235.655
μ_2*	1.0621	-0.0101	0.9901	0.22	1.864238	237.455
N_2*	1.0705	0.0083	0.9978	4.36	1.895673	245.555
ν_2*	1.0705	0.0080	0.9978	0.11	1.901148	247.555
ω_2*	1.0627	-0.1090	0.9906	0.25	1.931964	255.455
M_2*	1.0516	-0.0409	0.9803	0.66	1.932583	255.655
L_2*	1.0649	-0.3235	0.9926	4.06	1.968875	265.555
KNO_2*	1.0649	-0.3235	0.9926	0.76	1.969018	265.565
K_2*	1.0649	-0.3234	0.9926	0.22	2.005166	275.455
η_2*	1.0649	-0.3235	0.9926	0.37	2.042077	285.555
MN_3*	1.0691	0.2256	0.9998	0.80	2.862119	345.655
M_3*	1.0692	0.4332	0.9999	2.94	2.898410	355.555
ML_3*	1.0692	0.4332	0.9999	0.17	2.934702	365.455
MK_3*	1.0637	0.2944	0.9948	0.38	2.971613	375.555
O_1+	1.0359	0.0285	0.9997	0.06	0.929536	145.555
MN_3+	1.0359	0.0285	0.9997	0.07	2.861809	345.555
M_4+	1.0310	0.0214	0.9963	0.03	3.864547	455.555

Djougou

Table B.22.: Diurnal degree 2 parameters for the LRM-model, station Djougou.

Wave	δ^{LRM}	Φ^{LRM} /°	δ^{LRM} /δ^{WDZe}	Amplitude /nms^{-2}	Frequency /cpd	Doodson
ζ_1	1.1788	1.8145	1.0183	0.24	0.820661	115.855
SGQ_1	1.1788	1.8145	1.0183	0.62	0.825518	117.655
$2Q_1$	1.1788	1.8145	1.0183	2.08	0.856952	125.755
σ_1	1.1844	0.5770	1.0232	2.51	0.861809	127.555
SGX_1	1.1844	0.5770	1.0232	0.17	0.864547	128.554
QW_1	1.1768	-0.0744	1.0167	2.99	0.893097	135.645
Q_1	1.1768	-0.0744	1.0167	15.83	0.893244	135.655
ρ_1	1.1768	-0.0744	1.0167	3.02	0.898101	137.455
ROX_1	1.1768	-0.0744	1.0167	0.17	0.898720	137.655
OW_1	1.1586	-0.8117	1.0012	0.29	0.926798	144.556
OV_1	1.1586	-0.8117	1.0012	16.06	0.929389	145.545
O_1	1.1556	-0.7414	0.9986	85.13	0.929536	145.555
OX_1	1.1556	-0.7414	0.9986	0.55	0.930155	145.755
TW_1	1.1168	-1.2371	0.9651	0.26	0.932273	146.554
τ_1	1.1168	-1.2371	0.9651	1.12	0.935012	147.555
LKW_1	1.1173	-1.0985	0.9658	0.64	0.960970	153.655
LK_1	1.1237	-1.0081	0.9715	2.45	0.965827	155.455
M_1	1.1374	-1.0343	0.9833	6.82	0.966446	155.655
MN_1	1.1497	-0.0769	0.9939	1.37	0.966593	155.665
χ_1	1.1229	-0.6609	0.9709	1.30	0.971303	157.455
π_1	1.1276	-2.6788	0.9776	2.34	0.994524	162.556
P_1	1.1122	-0.4967	0.9655	39.88	0.997262	163.555
S_1	2.3183	47.9263	2.0185	0.94	1.000000	164.556
KW_1	1.0660	-1.1026	0.9361	2.35	1.002591	165.545
K_1	1.0950	-0.2674	0.9626	118.66	1.002738	165.555
κ_1	1.0962	-0.0210	0.9648	16.08	1.002885	165.565
KX_1	1.0946	-0.0210	0.9648	0.34	1.003032	165.575
ψ_1	1.1335	-2.2768	0.8908	1.04	1.005476	166.554
φ_1	1.1168	1.2973	0.9521	1.74	1.008214	167.555
ϑ_1	1.1155	1.2485	0.9620	1.27	1.034173	173.655
J_1	1.1150	0.8579	0.9618	6.60	1.039030	175.455
ι_1	1.1705	1.1884	1.0097	1.31	1.039177	175.465
SO_1	1.1240	2.6806	0.9701	1.08	1.070464	183.555
JO_1	1.1240	2.6806	0.9701	0.53	1.075321	185.355
OO_1	1.1240	2.6806	0.9701	3.57	1.075940	185.555
OOZ_1	1.1238	2.6806	0.9701	0.17	1.106756	193.455
V_1	1.1238	2.6806	0.9701	0.69	1.112232	195.455

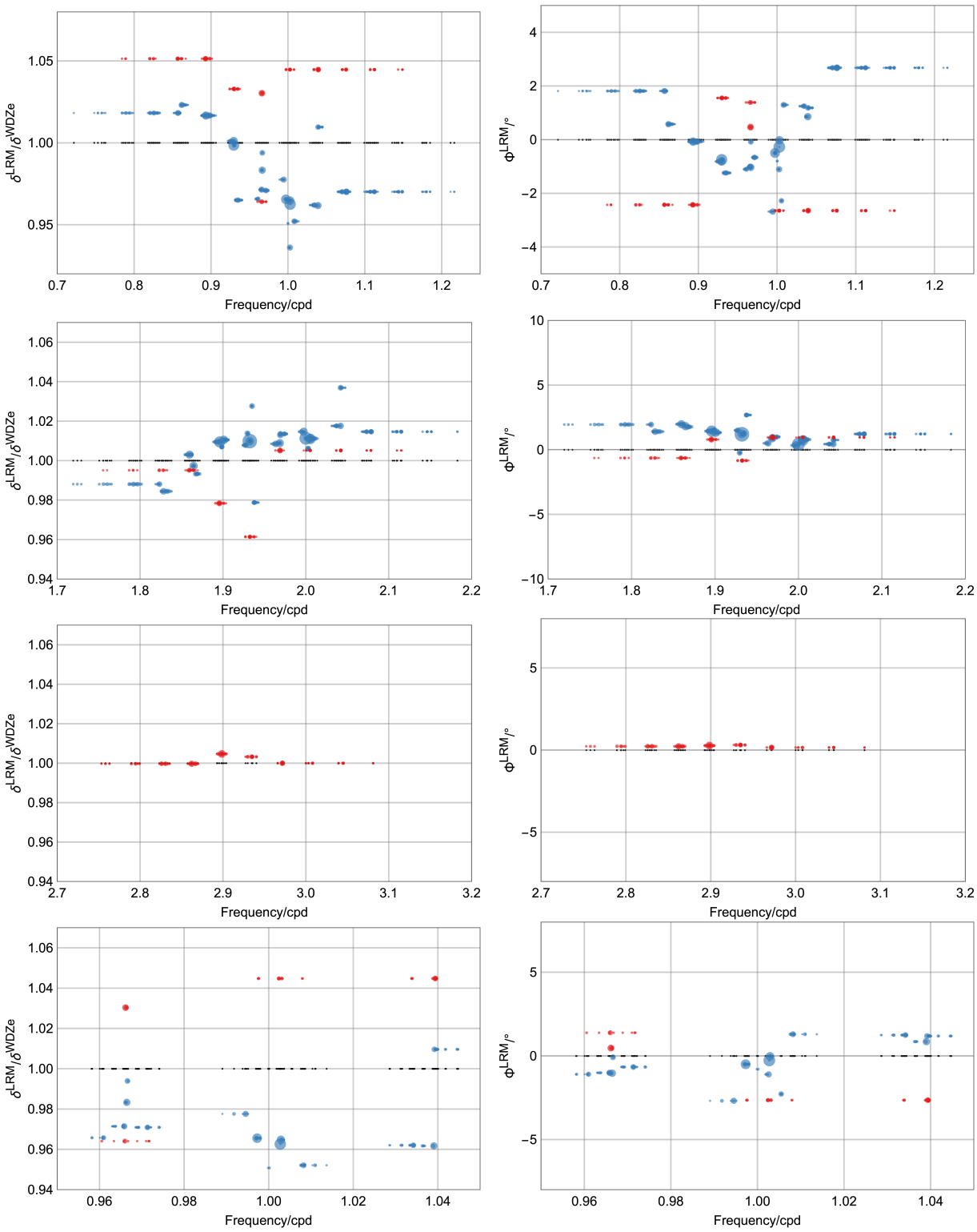

Figure B.8.: Parameters of the local response model (δ^{LRM} and Φ^{LRM}) in relation to WDZe for Djougou.

Table B.23.: Semidiurnal degree 2 parameters for the LRM-model, station Djougou.

Wave	δ^{LRM}	Φ^{LRM}	δ^{LRM}	Amplitude	Frequency	Doodson
		/°	$/\delta^{\mathrm{WDZe}}$	/nm s^{-2}	/cpd	
$3N_2$	1.1469	1.9459	0.9881	1.70	1.823399	225.855
ϵ_2	1.1427	1.4027	0.9845	4.39	1.828256	227.655
$2N_2$	1.1642	1.9765	1.0030	15.00	1.859690	235.755
μ_2	1.1575	1.8200	0.9973	18.12	1.864547	237.555
MIX_2	1.1529	1.7705	0.9933	1.22	1.867285	238.554
NW_2	1.1717	1.4436	1.0095	0.96	1.893244	244.656
N_2	1.1717	1.4436	1.0095	114.25	1.895982	245.655
NIW_2	1.1688	1.5176	1.0070	1.07	1.898720	246.654
ν_2	1.1729	1.3288	1.0105	21.73	1.900839	247.455
NIX_2	1.1729	1.3288	1.0105	1.00	1.903577	248.454
γ_2	1.1698	1.5011	1.0078	1.81	1.927417	253.755
α_2	1.1767	-0.2349	1.0138	2.07	1.929536	254.556
ω_2	1.1721	1.2290	1.0099	22.46	1.932127	255.545
M_2	1.1721	1.1939	1.0099	602.28	1.932274	255.555
β_2	1.1928	1.2529	1.0276	1.82	1.935011	256.554
δ_2	1.1361	2.6881	0.9788	0.71	1.937749	257.555
λ_2	1.1705	0.5064	1.0085	4.45	1.963708	263.655
L_2	1.1710	0.8905	1.0089	17.02	1.968565	265.455
KNO_2	1.1758	0.9162	1.0130	4.26	1.969184	265.655
LX_2	1.1764	0.9913	1.0135	1.88	1.969331	265.665
LZ_2	1.1764	0.9913	1.0135	0.81	1.974041	267.455
$2T_2$	1.1777	0.3386	1.0147	0.66	1.994524	271.557
T_2	1.1777	0.3386	1.0147	16.27	1.997262	272.556
S_2	1.1739	0.4361	1.0114	278.21	2.000000	273.555
R_2	1.1677	0.6628	1.0061	2.33	2.002738	274.554
K_2	1.1735	0.7162	1.0110	75.51	2.005476	275.555
KX_2	1.1737	0.7883	1.0112	22.51	2.005623	275.565
KY_2	1.1737	0.7883	1.0112	2.44	2.005770	275.575
KZ_2	1.1737	0.7883	1.0112	0.59	2.008214	276.554
KA_2	1.1737	0.7883	1.0112	0.51	2.010952	277.555
ζ_2	1.1811	0.4400	1.0176	0.80	2.036911	283.655
η_2	1.1811	0.4400	1.0176	4.19	2.041768	285.455
ETX_2	1.2036	0.7578	1.0370	1.83	2.041915	285.465
$2S_2$	1.1777	1.2166	1.0147	0.70	2.073202	293.555
$2K_2$	1.1777	1.2166	1.0147	1.10	2.078678	295.555

Table B.24.: Degree 3 and 4 parameters for the LRM-model, station Djougou.

Wave	δ^{LRM}	Φ^{LRM}	δ^{LRM}	Amplitude	Frequency	Doodson
		/°	$/\delta^{\mathrm{WDZe}}$	$/\mathrm{nm\,s^{-2}}$	/cpd	
$2Q_1$*	1.1280	-2.4249	1.0514	0.33	0.856643	125.655
Q_1*	1.1280	-2.4249	1.0514	1.19	0.892935	135.555
QX_1*	1.1280	-2.4249	1.0514	0.07	0.893554	135.755
ρ_1*	1.1280	-2.4249	1.0514	0.10	0.898410	137.555
O_1*	1.1082	1.5536	1.0330	0.63	0.929845	145.655
LK_1*	1.0343	1.3888	0.9641	0.58	0.965990	155.545
M_1*	1.1054	0.4677	1.0303	3.91	0.966137	155.555
χ_1*	1.0343	1.3888	0.9641	0.02	0.971613	157.555
K_1*	1.1208	-2.6427	1.0448	0.21	1.002428	165.455
J_1*	1.1208	-2.6427	1.0448	1.38	1.039339	175.555
$3N_2$*	1.0676	-0.6415	0.9951	0.11	1.823089	225.755
ϵ_2*	1.0676	-0.6415	0.9951	0.11	1.827946	227.555
$2N_2$*	1.0676	-0.6415	0.9951	0.62	1.859381	235.655
μ_2*	1.0676	-0.6415	0.9951	0.12	1.864238	237.455
N_2*	1.0496	0.7890	0.9784	2.27	1.895673	245.555
ν_2*	1.0496	0.7890	0.9784	0.06	1.901148	247.555
ω_2*	1.0314	-0.8385	0.9614	0.13	1.931964	255.455
M_2*	1.0314	-0.8385	0.9614	0.35	1.932583	255.655
L_2*	1.0783	0.9549	1.0052	2.11	1.968875	265.555
KNO_2*	1.0783	0.9549	1.0052	0.40	1.969018	265.565
K_2*	1.0783	0.9549	1.0052	0.11	2.005166	275.455
η_2*	1.0783	0.9549	1.0052	0.19	2.042077	285.555
MN_3*	1.0731	0.2298	0.9997	2.93	2.862119	345.655
M_3*	1.0785	0.2767	1.0047	10.74	2.898410	355.555
ML_3*	1.0769	0.3157	1.0032	0.61	2.934702	365.455
MK_3*	1.0734	0.1584	1.0000	1.39	2.971613	375.555
O_1+	1.0369	-0.3969	1.0006	0.05	0.929536	145.555
MN_3+	1.0369	-0.3969	1.0006	0.05	2.861809	345.555
M_4+	0.8649	-9.6482	0.8345	0.19	3.864547	455.555

Kamioka

Table B.25.: Diurnal degree 2 parameters for the LRM-model, station Kamioka.

Wave	δ^{LRM}	Φ^{LRM}	δ^{LRM}	Amplitude	Frequency	Doodson
		/°	$/\delta^{\mathrm{WDZe}}$	$/\mathrm{nm\,s^{-2}}$	/cpd	
ζ_1	1.2216	2.8518	1.0575	0.69	0.820661	115.855
SGQ_1	1.2231	2.2345	1.0588	1.78	0.825518	117.655
$2Q_1$	1.2108	1.3600	1.0482	5.96	0.856952	125.755
σ_1	1.2170	1.3798	1.0536	7.18	0.861809	127.555
SGX_1	1.2225	1.5573	1.0584	0.48	0.864547	128.554
QW_1	1.2072	0.8606	1.0452	8.54	0.893097	135.645
Q_1	1.2034	1.0186	1.0419	45.30	0.893244	135.655
ρ_1	1.2007	0.9549	1.0395	8.63	0.898101	137.455
ROX_1	1.1992	0.9861	1.0383	0.50	0.898720	137.655
OW_1	1.2124	-0.3081	1.0498	0.84	0.926798	144.556
OV_1	1.2006	0.5432	1.0397	45.96	0.929389	145.545
O_1	1.2011	0.5644	1.0401	243.66	0.929536	145.555
OX_1	1.2010	0.0872	1.0400	1.57	0.930155	145.755
TW_1	1.2200	2.7912	1.0565	0.74	0.932273	146.554
τ_1	1.2160	0.9197	1.0530	3.19	0.935012	147.555
LKW_1	1.1968	-0.2927	1.0368	1.83	0.960970	153.655
LK_1	1.1987	0.0960	1.0385	7.01	0.965827	155.455
M_1	1.2011	0.2504	1.0406	19.51	0.966446	155.655
MN_1	1.1865	-0.0253	1.0280	3.92	0.966593	155.665
χ_1	1.1935	0.2378	1.0342	3.73	0.971303	157.455
π_1	1.2111	-0.2887	1.0522	6.69	0.994524	162.556
P_1	1.1922	-0.1505	1.0373	114.10	0.997262	163.555
S_1	1.4813	33.6532	1.2925	2.69	1.000000	164.556
KW_1	1.1745	0.4723	1.0337	6.73	1.002591	165.545
K_1	1.1807	-0.1329	1.0402	339.53	1.002738	165.555
κ_1	1.1783	-0.1998	1.0394	46.00	1.002885	165.565
KX_1	1.1811	0.2765	1.0432	0.99	1.003032	165.575
ψ_1	1.2930	-3.2851	1.0181	2.97	1.005476	166.554
φ_1	1.2145	-0.1926	1.0376	4.97	1.008214	167.555
ϑ_1	1.2001	-0.4036	1.0372	3.62	1.034173	173.655
J_1	1.1918	-0.8588	1.0302	18.87	1.039030	175.455
ι_1	1.2024	-1.1220	1.0394	3.74	1.039177	175.465
SO_1	1.1733	-2.0935	1.0148	3.10	1.070464	183.555
JO_1	1.1872	-1.0337	1.0269	1.53	1.075321	185.355
OO_1	1.1824	-1.3917	1.0228	10.21	1.075940	185.555
OOZ_1	1.1585	-0.2578	1.0022	0.50	1.106756	193.455
V_1	1.1650	-0.8719	1.0079	1.98	1.112232	195.455

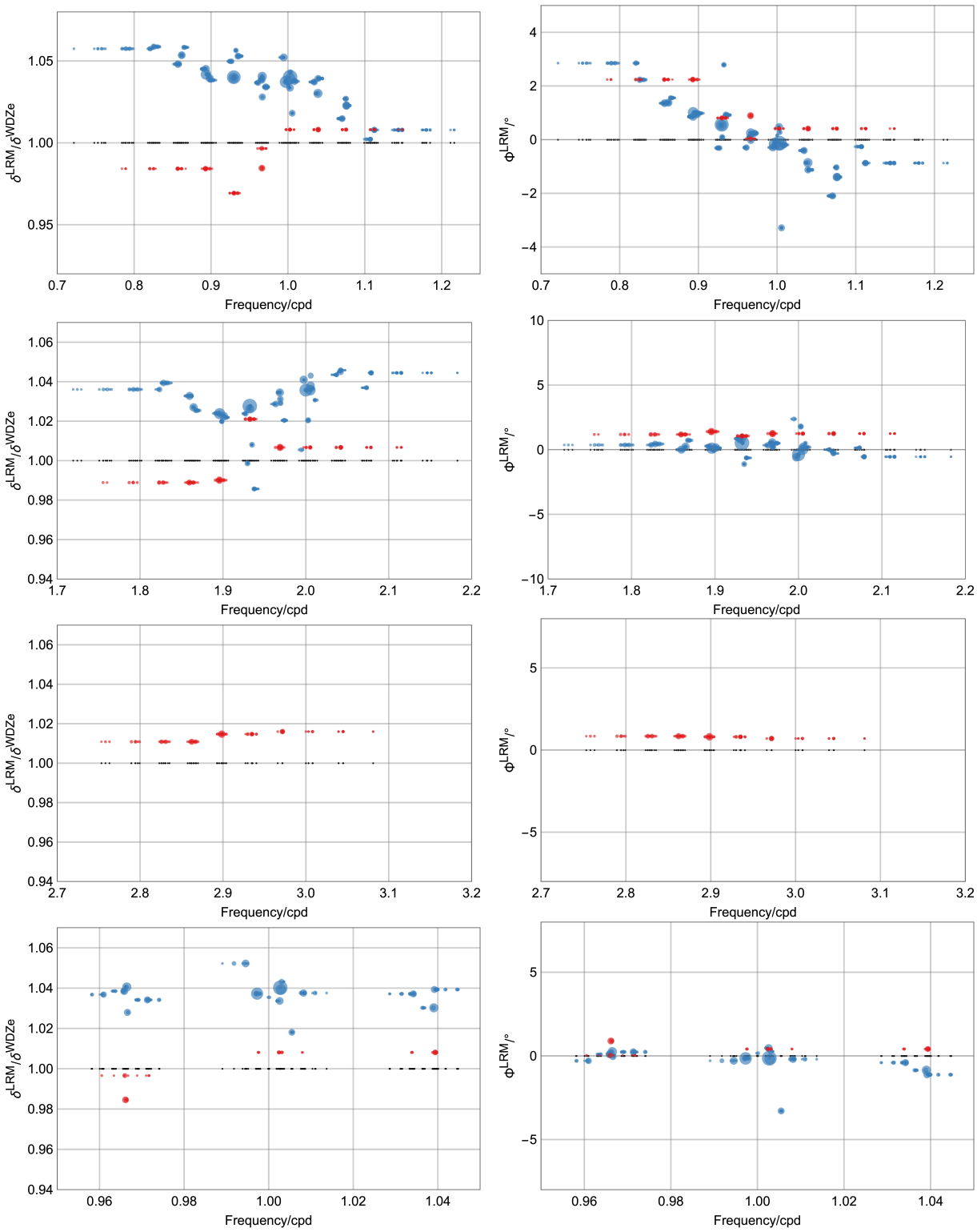

Figure B.9.: Parameters of the local response model (δ^{LRM} and Φ^{LRM}) in relation to WDZe for Kamioka.

Table B.26.: Semidiurnal degree 2 parameters for the LRM-model, station Kamioka.

Wave	δ^{LRM}	Φ^{LRM}	δ^{LRM}	Amplitude	Frequency	Doodson
		/°	$/\delta^{\mathrm{WDZe}}$	/nm s^{-2}	/cpd	
$3N_2$	1.2006	0.3724	1.0361	1.13	1.823399	225.855
ϵ_2	1.2043	0.4482	1.0393	2.92	1.828256	227.655
$2N_2$	1.1968	0.0111	1.0328	10.0	1.859690	235.755
μ_2	1.1901	0.2218	1.0270	12.07	1.864547	237.555
MIX_2	1.1882	0.7215	1.0254	0.81	1.867285	238.554
NW_2	1.1865	0.2803	1.0240	0.64	1.893244	244.656
N_2	1.1863	0.1178	1.0238	76.10	1.895982	245.655
NIW_2	1.1818	-0.0386	1.0199	0.71	1.898720	246.654
ν_2	1.1849	0.1631	1.0226	14.47	1.900839	247.455
NIX_2	1.1841	0.1322	1.0219	0.67	1.903577	248.454
γ_2	1.1863	0.8608	1.0238	1.20	1.927417	253.755
α_2	1.1572	0.7227	0.9986	1.38	1.929536	254.556
ω_2	1.1893	0.8580	1.0264	14.96	1.932127	255.545
M_2	1.1908	0.5223	1.0276	401.20	1.932274	255.555
β_2	1.1681	-1.1144	1.0081	1.21	1.935011	256.554
δ_2	1.1421	-0.6342	0.9857	0.47	1.937749	257.555
λ_2	1.1920	0.3503	1.0287	2.96	1.963708	263.655
L_2	1.1988	0.5692	1.0345	11.34	1.968565	265.455
KNO_2	1.1949	0.2420	1.0312	2.84	1.969184	265.655
LX_2	1.1925	0.2362	1.0291	1.25	1.969331	265.665
LZ_2	1.1824	0.5052	1.0204	0.54	1.974041	267.455
$2T_2$	1.1651	2.3772	1.0055	0.44	1.994524	271.557
T_2	1.2063	-0.5887	1.0410	10.84	1.997262	272.556
S_2	1.2002	-0.3845	1.0358	185.33	2.000000	273.555
R_2	1.1825	1.7922	1.0205	1.55	2.002738	274.554
K_2	1.2002	0.0175	1.0358	50.30	2.005476	275.555
KX_2	1.2028	0.2149	1.0380	14.99	2.005623	275.565
KY_2	1.2087	0.1678	1.0431	1.63	2.005770	275.575
KZ_2	1.2010	0.5043	1.0365	0.40	2.008214	276.554
KA_2	1.1943	0.2017	1.0307	0.34	2.010952	277.555
ζ_2	1.2092	0.0088	1.0435	0.53	2.036911	283.655
η_2	1.2109	-0.1650	1.0450	2.79	2.041768	285.455
ETX_2	1.2118	-0.2951	1.0458	1.22	2.041915	285.465
$2S_2$	1.2016	0.1508	1.0370	0.47	2.073202	293.555
$2K_2$	1.2103	-0.5400	1.0445	0.73	2.078678	295.555

Table B.27.: Degree 3 and 4 parameters for the LRM-model, station Kamioka.

Wave	δ^{LRM}	Φ^{LRM}	δ^{LRM}	Amplitude	Frequency	Doodson
		/°	$/\delta^{\mathrm{WDZe}}$	$/\mathrm{nm\,s^{-2}}$	/cpd	
$2Q_1$*	1.0559	2.2398	0.9842	0.23	0.856643	125.655
Q_1*	1.0559	2.2398	0.9842	0.85	0.892935	135.555
QX_1*	1.0559	2.2398	0.9842	0.05	0.893554	135.755
ρ_1*	1.0559	2.2398	0.9842	0.07	0.898410	137.555
O_1*	1.0399	0.8128	0.9693	0.45	0.929845	145.655
LK_1*	1.0691	0.0329	0.9966	0.41	0.965990	155.545
M_1*	1.0563	0.8934	0.9846	2.80	0.966137	155.555
χ_1*	1.0691	0.0329	0.9966	0.01	0.971613	157.555
K_1*	1.0815	0.4121	1.0081	0.15	1.002428	165.455
J_1*	1.0815	0.4121	1.0081	0.98	1.039339	175.555
$3N_2$*	1.0609	1.1789	0.9889	0.25	1.823089	225.755
ϵ_2*	1.0609	1.1789	0.9889	0.25	1.827946	227.555
$2N_2$*	1.0609	1.1789	0.9889	1.45	1.859381	235.655
μ_2*	1.0609	1.1789	0.9889	0.27	1.864238	237.455
N_2*	1.0622	1.4014	0.9901	5.32	1.895673	245.555
ν_2*	1.0622	1.4014	0.9901	0.13	1.901148	247.555
ω_2*	1.0954	1.0615	1.0210	0.30	1.931964	255.455
M_2*	1.0954	1.0615	1.0210	0.81	1.932583	255.655
L_2*	1.0800	1.2496	1.0067	4.95	1.968875	265.555
KNO_2*	1.0800	1.2496	1.0067	0.93	1.969018	265.565
K_2*	1.0800	1.2496	1.0067	0.27	2.005166	275.455
η_2*	1.0800	1.2496	1.0067	0.45	2.042077	285.555
MN_3*	1.0826	0.8492	1.0109	1.60	2.862119	345.655
M_3*	1.0868	0.8097	1.0147	5.85	2.898410	355.555
ML_3*	1.0868	0.8097	1.0147	0.33	2.934702	365.455
MK_3*	1.0882	0.7085	1.0160	0.76	2.971613	375.555
O_1+	1.0350	-0.5086	0.9987	0.03	0.929536	145.555
MN_3+	1.0350	-0.5086	0.9987	0.10	2.861809	345.555
M_4+	1.0257	1.0845	0.9904	0.08	3.864547	455.555

Canberra

Table B.28.: Diurnal degree 2 parameters for the LRM-model, station Canberra.

Wave	δ^{LRM}	Φ^{LRM}	δ^{LRM}	Amplitude	Frequency	Doodson
		$/^\circ$	$/\delta^{\mathrm{WDZe}}$	$/\mathrm{nm\,s^{-2}}$	/cpd	
ζ_1	1.2142	1.6339	1.0510	0.68	0.820661	115.855
$\mathrm{SGQ_1}$	1.2174	1.4931	1.0537	1.76	0.825518	117.655
$\mathrm{2Q_1}$	1.2102	0.3585	1.0475	5.89	0.856952	125.755
σ_1	1.2062	0.2059	1.0441	7.10	0.861809	127.555
$\mathrm{SGX_1}$	1.2071	0.3846	1.0449	0.48	0.864547	128.554
$\mathrm{QW_1}$	1.1879	-0.7304	1.0284	8.44	0.893097	135.645
$\mathrm{Q_1}$	1.1858	-0.6599	1.0265	44.73	0.893244	135.655
ρ_1	1.1808	-0.7290	1.0222	8.53	0.898101	137.455
$\mathrm{ROX_1}$	1.1794	-0.7374	1.0210	0.49	0.898720	137.655
$\mathrm{OW_1}$	1.1629	-1.0348	1.0069	0.83	0.926798	144.556
$\mathrm{OV_1}$	1.1690	-0.7426	1.0121	45.39	0.929389	145.545
$\mathrm{O_1}$	1.1693	-0.7493	1.0125	240.60	0.929536	145.555
$\mathrm{OX_1}$	1.1739	-0.5748	1.0164	1.55	0.930155	145.755
$\mathrm{TW_1}$	1.1739	1.1344	1.0164	0.73	0.932273	146.554
τ_1	1.1871	-0.0356	1.0279	3.15	0.935012	147.555
$\mathrm{LKW_1}$	1.1543	-0.7647	0.9998	1.81	0.960970	153.655
$\mathrm{LK_1}$	1.1587	-0.7996	1.0037	6.93	0.965827	155.455
$\mathrm{M_1}$	1.1600	-0.7212	1.0049	19.27	0.966446	155.655
$\mathrm{MN_1}$	1.1637	-0.7635	1.0081	3.87	0.966593	155.665
χ_1	1.1574	-0.8209	1.0028	3.69	0.971303	157.455
π_1	1.1383	-0.7249	0.9889	6.61	0.994524	162.556
$\mathrm{P_1}$	1.1477	-0.8620	0.9984	112.69	0.997262	163.555
$\mathrm{S_1}$	1.2766	-17.5644	1.1138	2.65	1.000000	164.556
$\mathrm{KW_1}$	1.1306	-0.7450	0.9949	6.65	1.002591	165.545
$\mathrm{K_1}$	1.1316	-0.8377	0.9968	335.32	1.002738	165.555
κ_1	1.1309	-0.8435	0.9974	45.43	1.002885	165.565
$\mathrm{KX_1}$	1.1239	-0.7986	0.9927	0.97	1.003032	165.575
ψ_1	1.2412	0.1590	0.9772	2.93	1.005476	166.554
φ_1	1.1612	-0.7571	0.9920	4.91	1.008214	167.555
ϑ_1	1.1456	-0.8747	0.9900	3.58	1.034173	173.655
$\mathrm{J_1}$	1.1400	-0.7834	0.9853	18.64	1.039030	175.455
ι_1	1.1386	-0.7644	0.9842	3.70	1.039177	175.465
$\mathrm{SO_1}$	1.1306	-0.9535	0.9778	3.06	1.070464	183.555
$\mathrm{JO_1}$	1.1273	0.1242	0.9750	1.51	1.075321	185.355
$\mathrm{OO_1}$	1.1259	-0.0675	0.9738	10.08	1.075940	185.555
$\mathrm{OOZ_1}$	1.1300	1.2383	0.9774	0.49	1.106756	193.455
$\mathrm{V_1}$	1.1317	1.3124	0.9790	1.96	1.112232	195.455

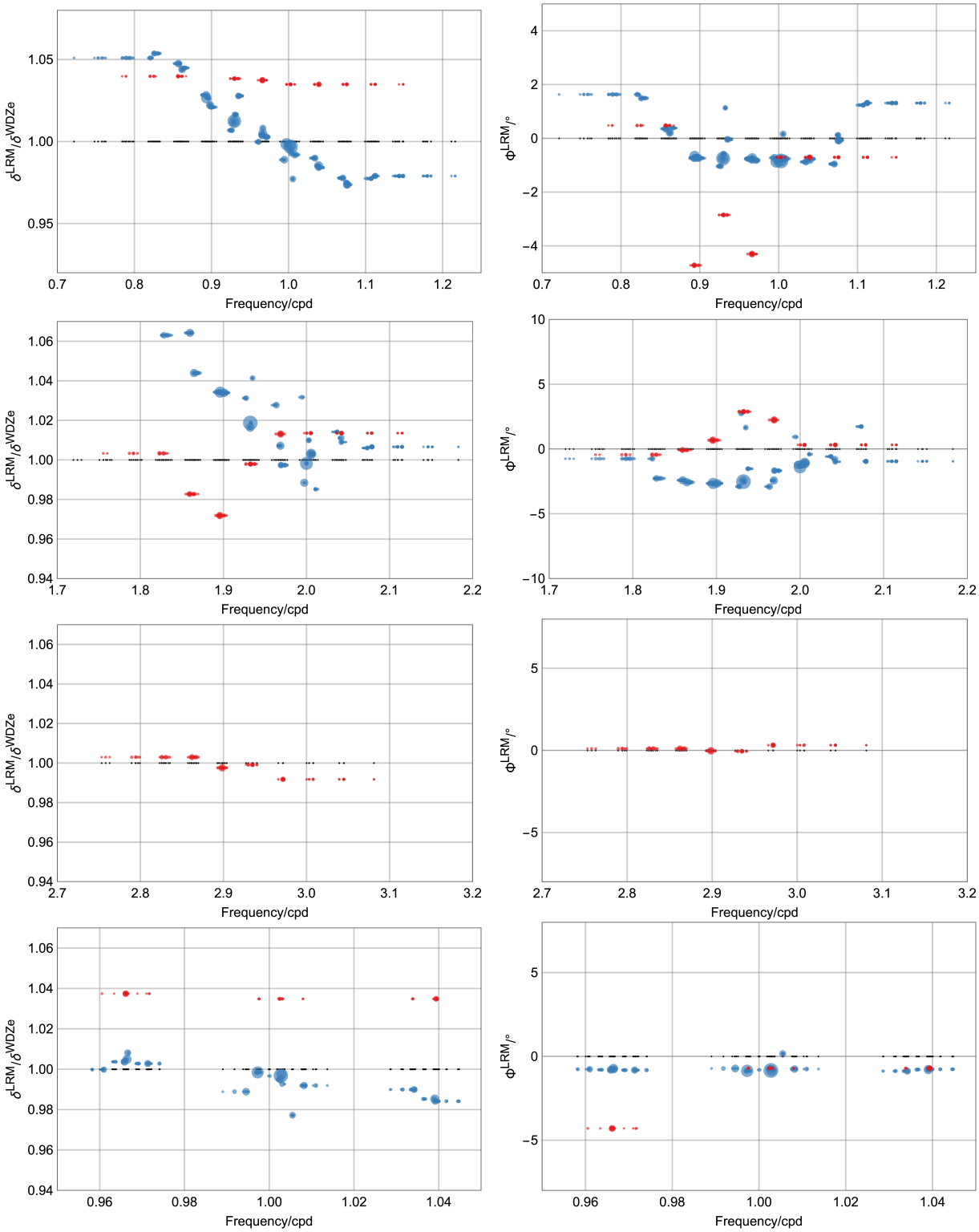

Figure B.10.: Parameters of the local response model (δ^{LRM} and Φ^{LRM}) in relation to WDZe for Canberra.

Table B.29.: Semidiurnal degree 2 parameters for the LRM-model, station Canberra.

Wave	δ^{LRM}	Φ^{LRM}	δ^{LRM}	Amplitude	Frequency	Doodson
		$/^\circ$	$/\delta^{\mathrm{WDZe}}$	$/\mathrm{nm\,s^{-2}}$	/cpd	
$3N_2$	1.2436	-0.7517	1.0731	1.16	1.823399	225.855
ϵ_2	1.2319	-2.2686	1.0630	3.01	1.828256	227.655
$2N_2$	1.2333	-2.4097	1.0642	10.28	1.859690	235.755
μ_2	1.2098	-2.5600	1.0440	12.41	1.864547	237.555
MIX_2	1.2098	-2.5600	1.0440	0.84	1.867285	238.554
NW_2	1.1986	-2.6623	1.0343	0.66	1.893244	244.656
N_2	1.1986	-2.6623	1.0343	78.26	1.895982	245.655
NIW_2	1.1982	-2.6507	1.0340	0.73	1.898720	246.654
ν_2	1.1982	-2.6507	1.0340	14.88	1.900839	247.455
NIX_2	1.1982	-2.6507	1.0340	0.69	1.903577	248.454
γ_2	1.1951	-2.8981	1.0313	1.24	1.927417	253.755
α_2	1.2432	2.7626	1.0727	1.42	1.929536	254.556
ω_2	1.1779	-2.4390	1.0164	15.39	1.932127	255.545
M_2	1.1805	-2.5190	1.0187	412.60	1.932274	255.555
β_2	1.2068	1.6554	1.0414	1.25	1.935011	256.554
δ_2	1.0728	-1.5263	0.9258	0.48	1.937749	257.555
λ_2	1.1910	-2.9040	1.0278	3.05	1.963708	263.655
L_2	1.1672	-2.4326	1.0072	11.66	1.968565	265.455
KNO_2	1.1559	-1.6715	0.9974	2.92	1.969184	265.655
LX_2	1.1559	-1.6715	0.9974	1.29	1.969331	265.665
LZ_2	1.1559	-1.6715	0.9974	0.56	1.974041	267.455
$2T_2$	1.1957	0.9279	1.0318	0.45	1.994524	271.557
T_2	1.1455	-1.2187	0.9885	11.14	1.997262	272.556
S_2	1.1568	-1.3766	0.9983	190.60	2.000000	273.555
R_2	1.1704	-1.2700	1.0100	1.59	2.002738	274.554
K_2	1.1624	-1.0828	1.0030	51.72	2.005476	275.555
KX_2	1.1624	-1.0828	1.0030	15.42	2.005623	275.565
KY_2	1.1624	-1.0828	1.0030	1.67	2.005770	275.575
KZ_2	1.1624	-1.0828	1.0030	0.41	2.008214	276.554
KA_2	1.1417	-0.4051	0.9852	0.35	2.010952	277.555
ζ_2	1.1753	-0.5826	1.0142	0.55	2.036911	283.655
η_2	1.1717	-0.7840	1.0111	2.87	2.041768	285.455
ETX_2	1.1693	-0.9823	1.0090	1.25	2.041915	285.465
$2S_2$	1.1658	1.7330	1.0060	0.48	2.073202	293.555
$2K_2$	1.1665	-0.9498	1.0066	0.76	2.078678	295.555

Table B.30.: Degree 3 and 4 parameters for the LRM-model, station Canberra.

Wave	δ^{LRM}	Φ^{LRM} /°	δ^{LRM} /δ^{WDZe}	Amplitude /nm s^{-2}	Frequency /cpd	Doodson
$2Q_1$*	1.1155	0.4806	1.0398	0.21	0.856643	125.655
Q_1*	1.2333	-4.7201	1.1496	0.76	0.892935	135.555
QX_1*	1.2333	-4.7201	1.1496	0.05	0.893554	135.755
ρ_1*	1.2333	-4.7201	1.1496	0.07	0.898410	137.555
O_1*	1.1139	-2.8498	1.0384	0.40	0.929845	145.655
LK_1*	1.1129	-4.3021	1.0374	0.37	0.965990	155.545
M_1*	1.1129	-4.3021	1.0374	2.49	0.966137	155.555
χ_1*	1.1129	-4.3021	1.0374	0.01	0.971613	157.555
K_1*	1.1102	-0.7040	1.0349	0.13	1.002428	165.455
J_1*	1.1102	-0.7040	1.0349	0.88	1.039339	175.555
$3N_2$*	1.0764	-0.4366	1.0033	0.25	1.823089	225.755
ϵ_2*	1.0764	-0.4366	1.0033	0.25	1.827946	227.555
$2N_2$*	1.0543	-0.0804	0.9827	1.45	1.859381	235.655
μ_2*	1.0543	-0.0804	0.9827	0.27	1.864238	237.455
N_2*	1.0426	0.6795	0.9719	5.33	1.895673	245.555
ν_2*	1.0426	0.6795	0.9719	0.13	1.901148	247.555
ω_2*	1.0706	2.8885	0.9979	0.30	1.931964	255.455
M_2*	1.0706	2.8885	0.9979	0.81	1.932583	255.655
L_2*	1.0869	2.2460	1.0131	4.96	1.968875	265.555
KNO_2*	1.0869	2.2460	1.0131	0.93	1.969018	265.565
K_2*	1.0873	0.3231	1.0136	0.27	2.005166	275.455
η_2*	1.0873	0.3231	1.0136	0.45	2.042077	285.555
MN_3*	1.0744	0.1106	1.0030	1.66	2.862119	345.655
M_3*	1.0686	-0.0237	0.9976	6.10	2.898410	355.555
ML_3*	1.0702	-0.0483	0.9991	0.35	2.934702	365.455
MK_3*	1.0624	0.3209	0.9918	0.79	2.971613	375.555
O_1+	1.0339	-0.1000	0.9977	0.04	0.929536	145.555
MN_3+	1.0339	-0.1000	0.9977	0.10	2.861809	345.555
M_4+	1.0460	1.0673	1.0100	0.09	3.864547	455.555

Tigo-Concepcion

Table B.31.: Diurnal degree 2 parameters for the LRM-model, station Tigo-Concepcion.

Wave	δ^{LRM}	Φ^{LRM} /°	$\delta^{\mathrm{LRM}}/\delta^{\mathrm{WDZe}}$	Amplitude /nms^{-2}	Frequency /cpd	Doodson
ζ_1	1.1723	2.1416	1.0148	0.69	0.820661	115.855
SGQ_1	1.1751	2.1632	1.0173	1.79	0.825518	117.655
$2Q_1$	1.1712	2.2268	1.0139	5.99	0.856952	125.755
σ_1	1.1799	2.3484	1.0215	7.22	0.861809	127.555
SGX_1	1.1781	2.3631	1.0199	0.49	0.864547	128.554
QW_1	1.1856	2.3980	1.0265	8.58	0.893097	135.645
Q_1	1.1834	2.3253	1.0247	45.50	0.893244	135.655
ρ_1	1.1812	2.3028	1.0227	8.67	0.898101	137.455
ROX_1	1.1822	2.2835	1.0236	0.50	0.898720	137.655
OW_1	1.1940	1.7165	1.0339	0.84	0.926798	144.556
OV_1	1.1936	1.8463	1.0336	46.16	0.929389	145.545
O_1	1.1937	1.8251	1.0338	244.70	0.929536	145.555
OX_1	1.1924	1.6969	1.0326	1.58	0.930155	145.755
TW_1	1.2143	1.0929	1.0516	0.74	0.932273	146.554
τ_1	1.2122	1.1120	1.0498	3.21	0.935012	147.555
LKW_1	1.2021	1.6308	1.0414	1.84	0.960970	153.655
LK_1	1.1978	1.7394	1.0378	7.05	0.965827	155.455
M_1	1.1978	1.1439	1.0378	19.60	0.966446	155.655
MN_1	1.1966	1.0458	1.0367	3.93	0.966593	155.665
χ_1	1.1999	1.0816	1.0398	3.75	0.971303	157.455
π_1	1.1970	0.7160	1.0400	6.72	0.994524	162.556
P_1	1.1966	0.8241	1.0412	114.61	0.997262	163.555
S_1	1.0187	-17.4666	0.8889	2.70	1.000000	164.556
KW_1	1.1824	0.9199	1.0406	6.76	1.002591	165.545
K_1	1.1865	0.8335	1.0454	341.01	1.002738	165.555
κ_1	1.1833	0.8593	1.0438	46.20	1.002885	165.565
KX_1	1.1819	0.8154	1.0440	0.99	1.003032	165.575
ψ_1	1.2978	1.0799	1.0219	2.98	1.005476	166.554
φ_1	1.2220	0.3013	1.0441	4.99	1.008214	167.555
ϑ_1	1.2087	0.3271	1.0447	3.64	1.034173	173.655
J_1	1.2026	-0.2098	1.0396	18.96	1.039030	175.455
ι_1	1.2063	-0.4268	1.0428	3.76	1.039177	175.465
SO_1	1.1803	-0.7307	1.0209	3.11	1.070464	183.555
JO_1	1.1907	-1.3188	1.0300	1.54	1.075321	185.355
OO_1	1.1906	-1.3137	1.0299	10.26	1.075940	185.555
OOZ_1	1.1574	-1.3373	1.0014	0.50	1.106756	193.455
V_1	1.1578	-1.3629	1.0017	1.99	1.112232	195.455

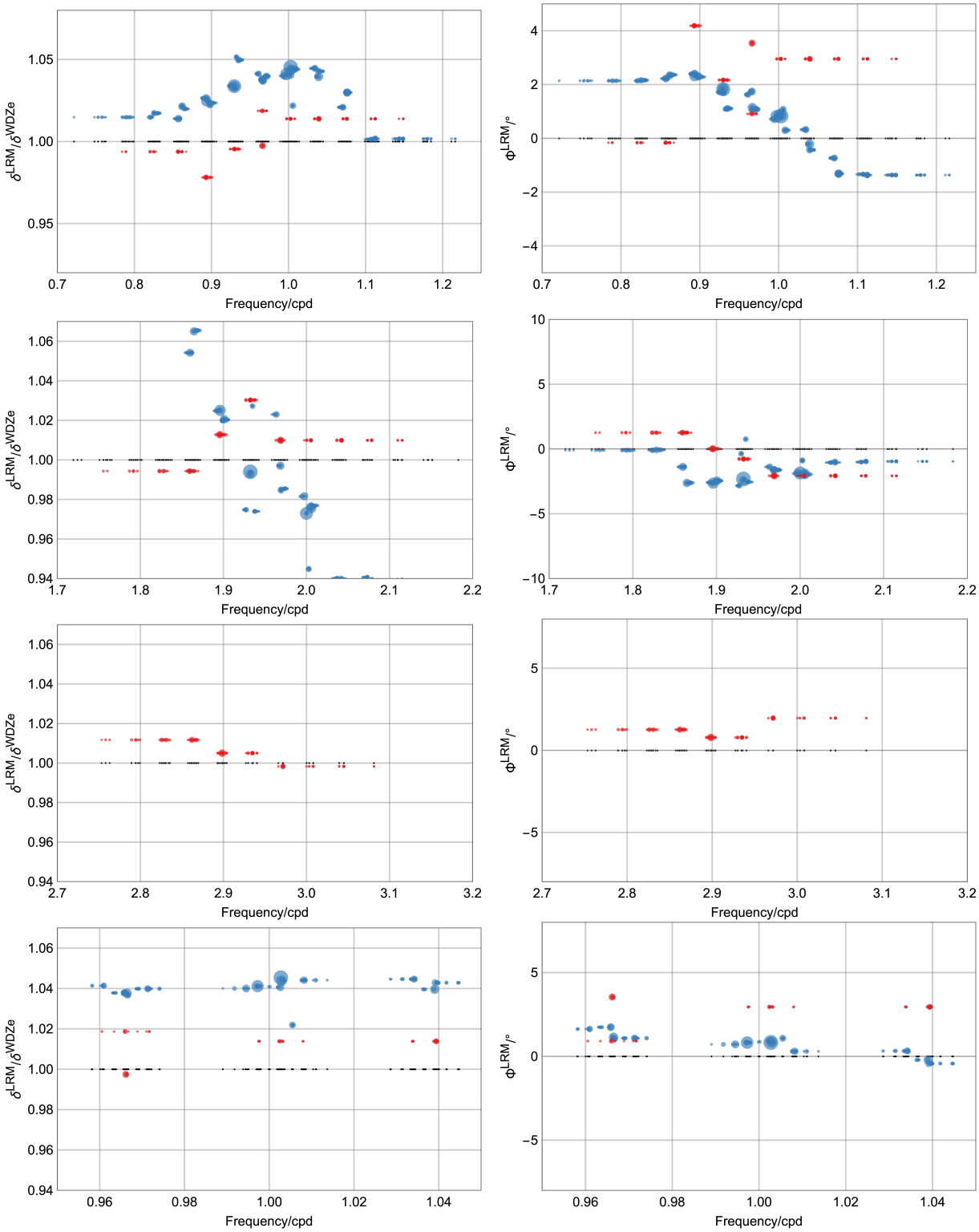

Figure B.11.: Parameters of the local response model (δ^{LRM} and Φ^{LRM}) in relation to WDZe for Tigo-Concepcion.

Table B.32.: Semidiurnal degree 2 parameters for the LRM-model, station Tigo-Concepcion.

Wave	δ^{LRM}	Φ^{LRM}	δ^{LRM}	Amplitude	Frequency	Doodson
		/°	$/\delta^{\mathrm{WDZe}}$	$/\mathrm{nm\,s^{-2}}$	/cpd	
$3N_2$	1.2581	-0.0990	1.0858	1.12	1.823399	225.855
ϵ_2	1.2614	-0.0618	1.0886	2.89	1.828256	227.655
$2N_2$	1.2216	-1.3826	1.0542	9.89	1.859690	235.755
μ_2	1.2341	-2.6234	1.0650	11.94	1.864547	237.555
MIX_2	1.2346	-2.6070	1.0655	0.81	1.867285	238.554
NW_2	1.1875	-2.5880	1.0249	0.63	1.893244	244.656
N_2	1.1878	-2.6280	1.0251	75.28	1.895982	245.655
NIW_2	1.1817	-2.4358	1.0199	0.70	1.898720	246.654
ν_2	1.1826	-2.4555	1.0206	14.32	1.900839	247.455
NIX_2	1.1822	-2.4562	1.0203	0.66	1.903577	248.454
γ_2	1.1295	-2.8308	0.9748	1.19	1.927417	253.755
α_2	1.2587	-0.3601	1.0863	1.36	1.929536	254.556
ω_2	1.1505	-2.4233	0.9929	14.80	1.932127	255.545
M_2	1.1518	-2.3142	0.9940	396.86	1.932274	255.555
β_2	1.1903	0.7644	1.0273	1.20	1.935011	256.554
δ_2	1.1286	-2.5518	0.9740	0.47	1.937749	257.555
λ_2	1.1854	-1.3772	1.0230	2.93	1.963708	263.655
L_2	1.1553	-1.6236	0.9970	11.22	1.968565	265.455
KNO_2	1.1408	-1.5977	0.9846	2.81	1.969184	265.655
LX_2	1.1414	-1.5500	0.9851	1.24	1.969331	265.665
LZ_2	1.1419	-1.6111	0.9855	0.54	1.974041	267.455
$2T_2$	1.1373	-1.8867	0.9816	0.44	1.994524	271.557
T_2	1.1374	-1.8652	0.9816	10.72	1.997262	272.556
S_2	1.1274	-1.8493	0.9730	183.34	2.000000	273.555
R_2	1.0948	-0.8833	0.9449	1.53	2.002738	274.554
K_2	1.1305	-1.9255	0.9756	49.75	2.005476	275.555
KX_2	1.1312	-1.9485	0.9763	14.83	2.005623	275.565
KY_2	1.1322	-1.9265	0.9771	1.61	2.005770	275.575
KZ_2	1.1316	-1.9607	0.9766	0.39	2.008214	276.554
KA_2	1.1320	-1.9605	0.9769	0.34	2.010952	277.555
ζ_2	1.0894	-1.0429	0.9402	0.53	2.036911	283.655
η_2	1.0886	-0.9910	0.9395	2.76	2.041768	285.455
ETX_2	1.0892	-1.0421	0.9400	1.20	2.041915	285.465
$2S_2$	1.0900	-1.0047	0.9407	0.46	2.073202	293.555
$2K_2$	1.0886	-0.9577	0.9395	0.73	2.078678	295.555

Table B.33.: Degree 3 and 4 parameters for the LRM-model, station Tigo-Concepcion.

Wave	δ^{LRM}	Φ^{LRM}	δ^{LRM}	Amplitude	Frequency	Doodson
		/°	$/\delta^{\mathrm{WDZe}}$	$/\mathrm{nm\,s^{-2}}$	/cpd	
$2Q_1$*	1.0662	-0.1617	0.9938	0.24	0.856643	125.655
Q_1*	1.0494	4.1871	0.9782	0.89	0.892935	135.555
QX_1*	1.0494	4.1871	0.9782	0.05	0.893554	135.755
ρ_1*	1.0494	4.1871	0.9782	0.08	0.898410	137.555
O_1*	1.0679	2.1691	0.9955	0.47	0.929845	145.655
LK_1*	1.0929	0.9108	1.0187	0.43	0.965990	155.545
M_1*	1.0701	3.5395	0.9975	2.91	0.966137	155.555
χ_1*	1.0929	0.9108	1.0187	0.01	0.971613	157.555
K_1*	1.0877	2.9554	1.0139	0.16	1.002428	165.455
J_1*	1.0877	2.9554	1.0139	1.03	1.039339	175.555
$3N_2$*	1.0667	1.2652	0.9944	0.25	1.823089	225.755
ϵ_2*	1.0667	1.2652	0.9944	0.25	1.827946	227.555
$2N_2$*	1.0667	1.2652	0.9944	1.45	1.859381	235.655
μ_2*	1.0667	1.2652	0.9944	0.27	1.864238	237.455
N_2*	1.0865	0.0194	1.0128	5.31	1.895673	245.555
ν_2*	1.0865	0.0194	1.0128	0.13	1.901148	247.555
ω_2*	1.1053	-0.7691	1.0303	0.30	1.931964	255.455
M_2*	1.1053	-0.7691	1.0303	0.81	1.932583	255.655
L_2*	1.0834	-2.0729	1.0099	4.95	1.968875	265.555
KNO_2*	1.0834	-2.0729	1.0099	0.93	1.969018	265.565
K_2*	1.0834	-2.0729	1.0099	0.27	2.005166	275.455
η_2*	1.0834	-2.0729	1.0099	0.45	2.042077	285.555
MN_3*	1.0835	1.2684	1.0117	1.57	2.862119	345.655
M_3*	1.0764	0.7911	1.0050	5.75	2.898410	355.555
ML_3*	1.0764	0.7911	1.0050	0.33	2.934702	365.455
MK_3*	1.0692	1.9663	0.9984	0.74	2.971613	375.555
O_1+	1.0369	0.0699	1.0006	0.03	0.929536	145.555
MN_3+	1.0369	0.0699	1.0006	0.10	2.861809	345.555
M_4+	1.0316	1.1364	0.9961	0.08	3.864547	455.555

Sutherland

Table B.34.: Diurnal degree 2 parameters for the LRM-model, station Sutherland.

Wave	δ^{LRM}	Φ^{LRM}	δ^{LRM}	Amplitude	Frequency	Doodson
		/°	$/\delta^{\mathrm{WDZe}}$	$/\mathrm{nm\,s^{-2}}$	/cpd	
ζ_1	1.1450	0.7974	0.9908	0.65	0.820661	115.855
SGQ_1	1.1450	0.7974	0.9908	1.69	0.825518	117.655
$2\mathrm{Q}_1$	1.1518	0.9948	0.9967	5.65	0.856952	125.755
σ_1	1.1530	0.7432	0.9977	6.80	0.861809	127.555
SGX_1	1.1530	0.7432	0.9977	0.46	0.864547	128.554
QW_1	1.1492	0.7015	0.9945	8.09	0.893097	135.645
Q_1	1.1606	0.6186	1.0044	42.90	0.893244	135.655
ρ_1	1.1628	0.5473	1.0064	8.18	0.898101	137.455
ROX_1	1.1628	0.5473	1.0064	0.47	0.898720	137.655
OW_1	1.1627	0.1301	1.0064	0.79	0.926798	144.556
OV_1	1.1627	0.1301	1.0064	43.53	0.929389	145.545
O_1	1.1626	0.1130	1.0063	230.75	0.929536	145.555
OX_1	1.1565	-0.1383	1.0010	1.49	0.930155	145.755
TW_1	1.1659	-0.5680	1.0091	0.70	0.932273	146.554
τ_1	1.1658	-0.5680	1.0091	3.02	0.935012	147.555
LKW_1	1.1655	0.2145	1.0092	1.73	0.960970	153.655
LK_1	1.1593	-0.1006	1.0040	6.64	0.965827	155.455
M_1	1.1579	-0.3144	1.0027	18.48	0.966446	155.655
MN_1	1.1543	-0.3913	0.9997	3.71	0.966593	155.665
χ_1	1.1565	-0.2739	1.0017	3.53	0.971303	157.455
π_1	1.1495	-0.4605	0.9983	6.34	0.994524	162.556
P_1	1.1499	-0.5313	1.0001	108.08	0.997262	163.555
S_1	1.1388	-30.0939	0.9932	2.54	1.000000	164.556
KW_1	1.1292	-0.5634	0.9933	6.37	1.002591	165.545
K_1	1.1343	-0.5002	0.9989	321.59	1.002738	165.555
κ_1	1.1327	-0.4763	0.9987	43.57	1.002885	165.565
KX_1	1.1311	-0.4763	0.9987	0.93	1.003032	165.575
ψ_1	1.2309	0.2707	0.9688	2.81	1.005476	166.554
φ_1	1.1610	-0.6354	0.9915	4.70	1.008214	167.555
ϑ_1	1.1440	-0.6893	0.9883	3.43	1.034173	173.655
J_1	1.1455	-0.4992	0.9898	17.87	1.039030	175.455
ι_1	1.1495	-0.6395	0.9933	3.54	1.039177	175.465
SO_1	1.1442	0.5202	0.9893	2.93	1.070464	183.555
JO_1	1.1413	0.0212	0.9867	1.45	1.075321	185.355
OO_1	1.1325	0.1006	0.9792	9.68	1.075940	185.555
OOZ_1	1.1470	0.4872	0.9919	0.47	1.106756	193.455
V_1	1.1470	0.4872	0.9919	1.88	1.112232	195.455

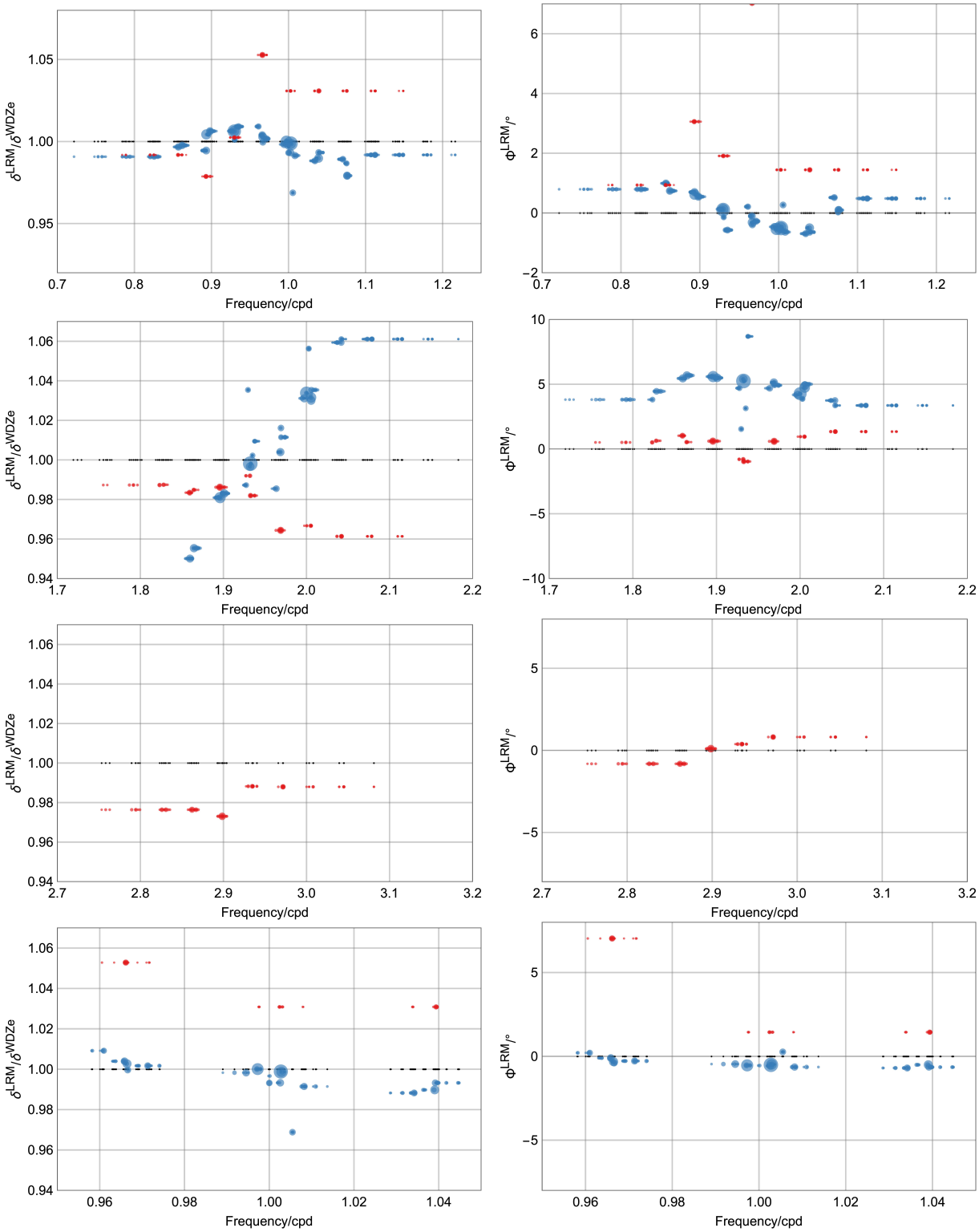

Figure B.12.: Parameters of the local response model (δ^{LRM} and Φ^{LRM}) in relation to WDZe for Sutherland.

Table B.35.: Semidiurnal degree 2 parameters for the LRM-model, station Sutherland.

Wave	δ^{LRM}	Φ^{LRM} /°	δ^{LRM} /δ^{WDZe}	Amplitude /nms^{-2}	Frequency /cpd	Doodson
$3N_2$	1.0782	3.8125	0.9302	1.24	1.823399	225.855
ϵ_2	1.0798	4.4528	0.9316	3.22	1.828256	227.655
$2N_2$	1.1013	5.4473	0.9501	11.01	1.859690	235.755
μ_2	1.1074	5.6828	0.9554	13.30	1.864547	237.555
MIX_2	1.1074	5.6828	0.9554	0.90	1.867285	238.554
NW_2	1.1371	5.5933	0.9810	0.70	1.893244	244.656
N_2	1.1371	5.5933	0.9810	83.86	1.895982	245.655
NIW_2	1.1395	5.4955	0.9831	0.78	1.898720	246.654
ν_2	1.1395	5.4955	0.9831	15.95	1.900839	247.455
NIX_2	1.1395	5.4955	0.9831	0.74	1.903577	248.454
γ_2	1.1444	4.6983	0.9872	1.33	1.927417	253.755
α_2	1.2002	1.5469	1.0354	1.52	1.929536	254.556
ω_2	1.1553	5.3975	0.9967	16.49	1.932127	255.545
M_2	1.1570	5.2548	0.9981	442.13	1.932274	255.555
β_2	1.1618	3.1452	1.0023	1.34	1.935011	256.554
δ_2	1.1701	8.6953	1.0094	0.52	1.937749	257.555
λ_2	1.1423	4.6948	0.9855	3.26	1.963708	263.655
L_2	1.1637	5.1323	1.0039	12.49	1.968565	265.455
KNO_2	1.1779	5.0528	1.0161	3.12	1.969184	265.655
LX_2	1.1724	4.9227	1.0115	1.38	1.969331	265.665
LZ_2	1.1724	4.9227	1.0115	0.60	1.974041	267.455
$2T_2$	1.1953	4.1841	1.0312	0.48	1.994524	271.557
T_2	1.1953	4.1841	1.0312	11.94	1.997262	272.556
S_2	1.1984	4.2694	1.0339	204.24	2.000000	273.555
R_2	1.2244	3.8700	1.0563	1.71	2.002738	274.554
K_2	1.1958	4.7450	1.0316	55.42	2.005476	275.555
KX_2	1.1940	4.8969	1.0301	16.52	2.005623	275.565
KY_2	1.2002	5.0101	1.0354	1.79	2.005770	275.575
KZ_2	1.2002	5.0101	1.0354	0.44	2.008214	276.554
KA_2	1.2002	5.0101	1.0354	0.38	2.010952	277.555
ζ_2	1.2280	3.7459	1.0594	0.59	2.036911	283.655
η_2	1.2280	3.7459	1.0594	3.08	2.041768	285.455
ETX_2	1.2300	3.3629	1.0611	1.34	2.041915	285.465
$2S_2$	1.2300	3.3629	1.0611	0.51	2.073202	293.555
$2K_2$	1.2300	3.3629	1.0611	0.81	2.078678	295.555

Table B.36.: Degree 3 and 4 parameters for the LRM-model, station Sutherland.

Wave	δ^{LRM}	Φ^{LRM}	δ^{LRM}	Amplitude	Frequency	Doodson
		/°	$/\delta^{\mathrm{WDZe}}$	$/\mathrm{nm\,s^{-2}}$	/cpd	
$2Q_1$*	1.0641	0.9376	0.9919	0.14	0.856643	125.655
Q_1*	1.0500	3.0598	0.9787	0.50	0.892935	135.555
QX_1*	1.0500	3.0598	0.9787	0.03	0.893554	135.755
ρ_1*	1.0500	3.0598	0.9787	0.04	0.898410	137.555
O_1*	1.0755	1.9128	1.0025	0.27	0.929845	145.655
LK_1*	1.1295	7.0364	1.0528	0.25	0.965990	155.545
M_1*	1.1295	7.0364	1.0528	1.66	0.966137	155.555
χ_1*	1.1295	7.0364	1.0528	0.01	0.971613	157.555
K_1*	1.1059	1.4450	1.0309	0.09	1.002428	165.455
J_1*	1.1059	1.4450	1.0309	0.58	1.039339	175.555
$3N_2$*	1.0592	0.5125	0.9873	0.25	1.823089	225.755
ϵ_2*	1.0593	0.6341	0.9874	0.25	1.827946	227.555
$2N_2$*	1.0550	1.0298	0.9834	1.44	1.859381	235.655
μ_2*	1.0566	0.5328	0.9849	0.27	1.864238	237.455
N_2*	1.0580	0.6066	0.9862	5.28	1.895673	245.555
ν_2*	1.0580	0.6066	0.9862	0.13	1.901148	247.555
ω_2*	1.0642	-0.7963	0.9920	0.30	1.931964	255.455
M_2*	1.0535	-0.9605	0.9820	0.80	1.932583	255.655
L_2*	1.0346	0.5888	0.9644	4.92	1.968875	265.555
KNO_2*	1.0346	0.5888	0.9644	0.93	1.969018	265.565
K_2*	1.0371	0.9550	0.9667	0.27	2.005166	275.455
η_2*	1.0314	1.3474	0.9614	0.45	2.042077	285.555
MN_3*	1.0462	-0.8165	0.9764	1.85	2.862119	345.655
M_3*	1.0426	0.1095	0.9731	6.76	2.898410	355.555
ML_3*	1.0589	0.3840	0.9883	0.38	2.934702	365.455
MK_3*	1.0586	0.8133	0.9880	0.88	2.971613	375.555
O_1+	1.0255	0.1814	0.9896	0.05	0.929536	145.555
MN_3+	1.0255	0.1814	0.9896	0.11	2.861809	345.555
M_4+	1.0915	0.7513	1.0538	0.10	3.864547	455.555

Ny-Ålesund

Table B.37.: Diurnal degree 2 parameters for the LRM-model, station Ny-Ålesund.

Wave	δ^{LRM}	Φ^{LRM} /°	$\delta^{\mathrm{LRM}}/\delta^{\mathrm{WDZe}}$	Amplitude /nm s^{-2}	Frequency /cpd	Doodson
ζ_1	1.0340	-7.2531	0.8987	0.27	0.820661	115.855
SGQ_1	1.0340	-7.2531	0.8987	0.70	0.825518	117.655
$2Q_1$	1.0339	-7.2531	0.8987	2.35	0.856952	125.755
σ_1	1.0705	-2.9763	0.9306	2.83	0.861809	127.555
SGX_1	1.0705	-2.9763	0.9306	0.19	0.864547	128.554
QW_1	1.0817	1.4667	0.9404	3.36	0.893097	135.645
Q_1	1.0850	1.2509	0.9433	17.82	0.893244	135.655
ρ_1	1.0812	1.4276	0.9399	3.40	0.898101	137.455
ROX_1	1.0812	1.4276	0.9399	0.20	0.898720	137.655
OW_1	1.1477	1.2265	0.9979	0.33	0.926798	144.556
OV_1	1.1477	1.2265	0.9979	18.09	0.929389	145.545
O_1	1.1509	1.2360	1.0007	95.89	0.929536	145.555
OX_1	1.1509	1.2360	1.0007	0.62	0.930155	145.755
TW_1	1.1192	-1.9595	0.9732	0.29	0.932273	146.554
τ_1	1.1192	-1.9595	0.9732	1.26	0.935012	147.555
LKW_1	1.2747	5.9227	1.1088	0.72	0.960970	153.655
LK_1	1.1964	0.5685	1.0408	2.76	0.965827	155.455
M_1	1.1694	-0.5864	1.0174	7.68	0.966446	155.655
MN_1	1.1220	-1.6051	0.9761	1.54	0.966593	155.665
χ_1	1.1139	-1.3545	0.9692	1.47	0.971303	157.455
π_1	1.1950	-1.3830	1.0425	2.63	0.994524	162.556
P_1	1.1645	-1.7126	1.0174	44.90	0.997262	163.555
S_1	0.6931	-8.5738	0.6073	1.06	1.000000	164.556
KW_1	1.1516	-1.8222	1.0177	2.65	1.002591	165.545
K_1	1.1504	-1.8222	1.0177	133.61	1.002738	165.555
κ_1	1.1447	-2.3568	1.0139	18.10	1.002885	165.565
KX_1	1.1431	-2.3568	1.0139	0.39	1.003032	165.575
ψ_1	1.3786	-3.2327	1.0896	1.17	1.005476	166.554
φ_1	1.3452	-0.7881	1.1540	1.96	1.008214	167.555
ϑ_1	1.1518	-1.6590	0.9995	1.43	1.034173	173.655
J_1	1.1516	-1.6590	0.9995	7.43	1.039030	175.455
ι_1	1.1516	-1.6590	0.9995	1.47	1.039177	175.465
SO_1	1.1282	0.0048	0.9798	1.22	1.070464	183.555
JO_1	1.1282	0.0048	0.9798	0.60	1.075321	185.355
OO_1	1.1282	0.0048	0.9798	4.02	1.075940	185.555
OOZ_1	1.1280	0.0048	0.9798	0.20	1.106756	193.455
V_1	1.1279	0.0048	0.9798	0.78	1.112232	195.455

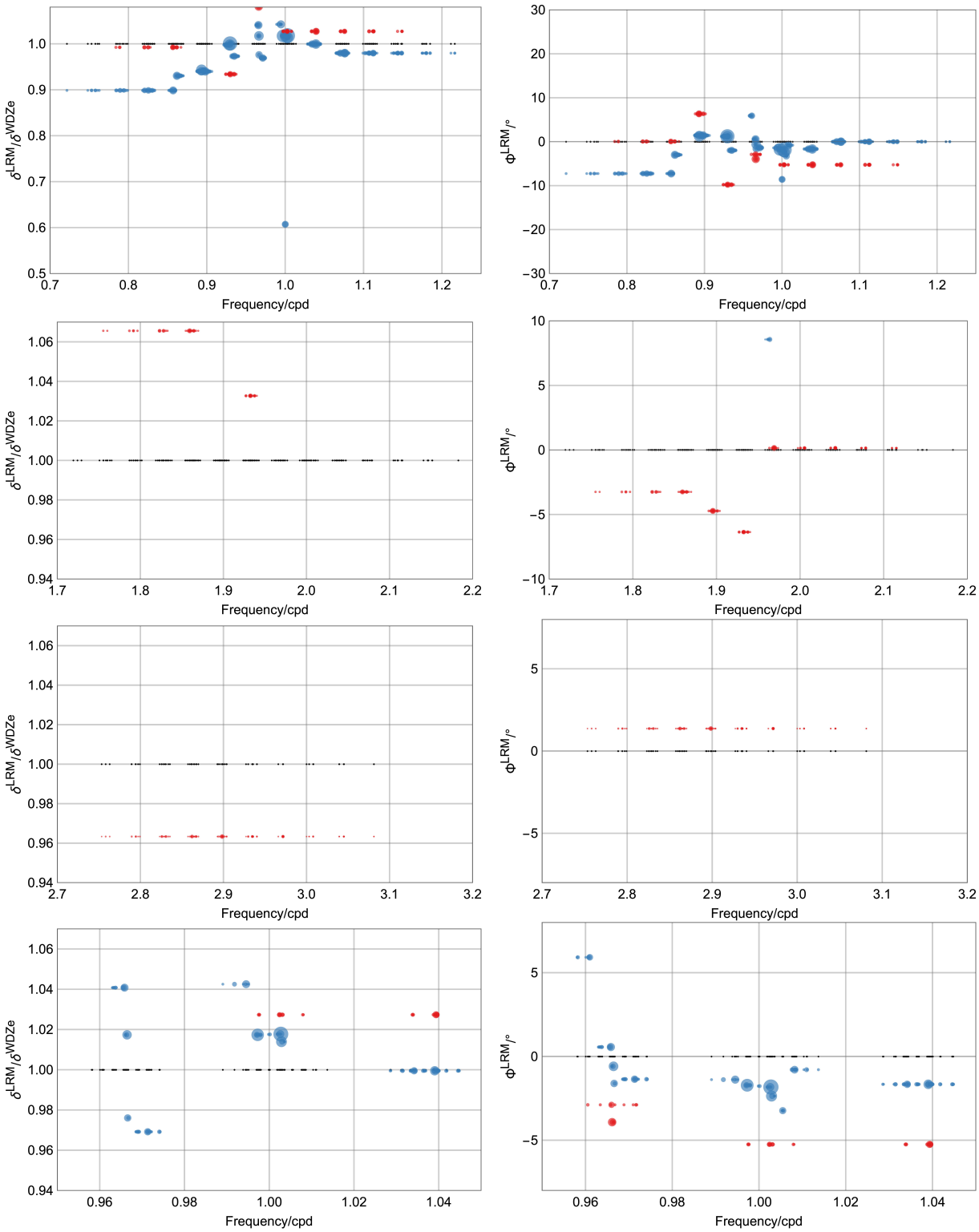

Figure B.13.: Parameters of the local response model (δ^{LRM} and Φ^{LRM}) in relation to WDZe for Ny-Ålesund.

Table B.38.: Semidiurnal degree 2 parameters for the LRM-model, station Ny-Ålesund.

Wave	δ^{LRM}	Φ^{LRM} /°	δ^{LRM} /δ^{WDZe}	Amplitude /nm s^{-2}	Frequency /cpd	Doodson
$3N_2$	0.4936	81.4213	0.4274	0.06	1.823399	225.855
ϵ_2	0.4936	81.4213	0.4274	0.17	1.828256	227.655
$2N_2$	0.5030	78.3528	0.4354	0.57	1.859690	235.755
μ_2	0.4409	73.7361	0.3817	0.69	1.864547	237.555
MIX_2	0.4409	73.7361	0.3817	0.05	1.867285	238.554
NW_2	0.4644	-13.9071	0.4020	0.04	1.893244	244.656
N_2	0.4644	-13.9071	0.4020	4.33	1.895982	245.655
NIW_2	0.4083	-33.8185	0.3535	0.04	1.898720	246.654
ν_2	0.4083	-33.8185	0.3535	0.82	1.900839	247.455
NIX_2	0.4083	-33.8185	0.3535	0.04	1.903577	248.454
γ_2	0.5124	38.1867	0.4436	0.07	1.927417	253.755
α_2	0.4472	33.8919	0.3872	0.08	1.929536	254.556
ω_2	0.6962	-70.8421	0.6027	0.85	1.932127	255.545
M_2	0.7753	-71.7212	0.6712	22.81	1.932274	255.555
β_2	0.6769	-81.6443	0.5861	0.07	1.935011	256.554
δ_2	0.7692	-72.4974	0.6659	0.03	1.937749	257.555
λ_2	0.9073	8.5659	0.7855	0.17	1.963708	263.655
L_2	0.9862	72.9396	0.8538	0.65	1.968565	265.455
KNO_2	0.9764	71.6478	0.8454	0.16	1.969184	265.655
LX_2	0.9764	71.6478	0.8454	0.07	1.969331	265.665
LZ_2	0.9764	71.6478	0.8454	0.03	1.974041	267.455
$2T_2$	1.4171	52.0426	1.2269	0.03	1.994524	271.557
T_2	1.4171	52.0426	1.2269	0.62	1.997262	272.556
S_2	1.3908	58.4734	1.2041	10.54	2.000000	273.555
R_2	1.4743	57.8180	1.2764	0.09	2.002738	274.554
K_2	1.4021	60.3637	1.2139	2.86	2.005476	275.555
KX_2	1.4021	60.3637	1.2139	0.85	2.005623	275.565
KY_2	1.4021	60.3637	1.2139	0.09	2.005770	275.575
KZ_2	1.4021	60.3637	1.2139	0.02	2.008214	276.554
KA_2	1.4021	60.3637	1.2139	0.02	2.010952	277.555
ζ_2	1.4021	60.3637	1.2139	0.03	2.036911	283.655
η_2	1.4021	60.3637	1.2139	0.16	2.041768	285.455
ETX_2	1.4021	60.3637	1.2139	0.07	2.041915	285.465
$2S_2$	1.4021	60.3637	1.2139	0.03	2.073202	293.555
$2K_2$	1.4021	60.3637	1.2139	0.04	2.078678	295.555

Table B.39.: Degree 3 and 4 parameters for the LRM-model, station Ny-Ålesund.

Wave	δ^{LRM}	Φ^{LRM}	δ^{LRM}	Amplitude	Frequency	Doodson
		/°	$/\delta^{\mathrm{WDZe}}$	$/\mathrm{nm\,s^{-2}}$	/cpd	
$2Q_1$*	1.0649	0.0689	0.9926	0.28	0.856643	125.655
Q_1*	1.3117	6.3406	1.2226	1.03	0.892935	135.555
QX_1*	1.3117	6.3406	1.2226	0.06	0.893554	135.755
ρ_1*	1.3117	6.3406	1.2226	0.09	0.898410	137.555
O_1*	1.0020	-9.7740	0.9340	0.54	0.929845	145.655
LK_1*	1.1714	-2.8860	1.0919	0.50	0.965990	155.545
M_1*	1.1599	-3.9216	1.0812	3.38	0.966137	155.555
χ_1*	1.1714	-2.8860	1.0919	0.01	0.971613	157.555
K_1*	1.1022	-5.2444	1.0274	0.18	1.002428	165.455
J_1*	1.1022	-5.2444	1.0274	1.19	1.039339	175.555
$3N_2$*	1.1432	-3.2485	1.0656	0.02	1.823089	225.755
ϵ_2*	1.1432	-3.2485	1.0656	0.02	1.827946	227.555
$2N_2$*	1.1432	-3.2485	1.0656	0.14	1.859381	235.655
μ_2*	1.1432	-3.2485	1.0656	0.03	1.864238	237.455
N_2*	1.1550	-4.7260	1.0766	0.50	1.895673	245.555
ν_2*	1.1550	-4.7260	1.0766	0.01	1.901148	247.555
ω_2*	1.1079	-6.3628	1.0327	0.03	1.931964	255.455
M_2*	1.1079	-6.3628	1.0327	0.08	1.932583	255.655
L_2*	1.2332	0.1475	1.1495	0.47	1.968875	265.555
KNO_2*	1.2332	0.1475	1.1495	0.09	1.969018	265.565
K_2*	1.2332	0.1475	1.1495	0.03	2.005166	275.455
η_2*	1.2332	0.1475	1.1495	0.04	2.042077	285.555
MN_3*	1.0274	1.3717	0.9634	0.02	2.862119	345.655
M_3*	1.0274	1.3717	0.9634	0.08	2.898410	355.555
ML_3*	1.0274	1.3717	0.9634	0.00	2.934702	365.455
MK_3*	1.0274	1.3717	0.9634	0.01	2.971613	375.555
O_1+	1.0349	0.1289	0.9986	0.08	0.929536	145.555
MN_3+	1.0349	0.1289	0.9986	0.00	2.861809	345.555
M_4+	1.0339	0.0156	1.0000	0.00	3.864547	455.555

Cantley

Table B.40.: Diurnal degree 2 parameters for the LRM-model, station Cantley.

Wave	δ^{LRM}	Φ^{LRM} /°	$\delta^{\mathrm{LRM}}/\delta^{\mathrm{WDZe}}$	Amplitude /nm s^{-2}	Frequency /cpd	Doodson
ζ_1	1.1717	1.0285	1.0154	0.72	0.820661	115.855
SGQ_1	1.1717	1.0285	1.0154	1.86	0.825518	117.655
$2Q_1$	1.1560	0.7414	1.0018	6.24	0.856952	125.755
σ_1	1.1641	0.3198	1.0089	7.51	0.861809	127.555
SGX_1	1.1641	0.3198	1.0089	0.51	0.864547	128.554
QW_1	1.1686	0.3856	1.0128	8.94	0.893097	135.645
Q_1	1.1648	0.5403	1.0095	47.37	0.893244	135.655
ρ_1	1.1655	0.6555	1.0102	9.03	0.898101	137.455
ROX_1	1.1655	0.6555	1.0102	0.52	0.898720	137.655
OW_1	1.1660	0.5315	1.0107	0.87	0.926798	144.556
OV_1	1.1660	0.5315	1.0107	48.06	0.929389	145.545
O_1	1.1654	0.5509	1.0102	254.82	0.929536	145.555
OX_1	1.1654	0.5509	1.0102	1.64	0.930155	145.755
TW_1	1.1535	0.6733	0.9999	0.77	0.932273	146.554
τ_1	1.1535	0.6733	0.9999	3.34	0.935012	147.555
LKW_1	1.1855	0.7608	1.0281	1.91	0.960970	153.655
LK_1	1.1585	1.0397	1.0047	7.34	0.965827	155.455
M_1	1.1649	0.3869	1.0104	20.40	0.966446	155.655
MN_1	1.1483	0.1720	0.9959	4.10	0.966593	155.665
χ_1	1.1764	1.1788	1.0204	3.90	0.971303	157.455
π_1	1.1568	0.6705	1.0062	7.00	0.994524	162.556
P_1	1.1604	0.4981	1.0107	119.35	0.997262	163.555
S_1	1.2312	5.9555	1.0754	2.81	1.000000	164.556
KW_1	1.1612	0.5912	1.0230	7.04	1.002591	165.545
K_1	1.1473	0.5978	1.0118	355.10	1.002738	165.555
κ_1	1.1461	0.5664	1.0121	48.11	1.002885	165.565
KX_1	1.1445	0.5665	1.0121	1.03	1.003032	165.575
ψ_1	1.2871	0.8699	1.0144	3.10	1.005476	166.554
φ_1	1.1890	0.4427	1.0169	5.20	1.008214	167.555
ϑ_1	1.1770	0.5108	1.0183	3.79	1.034173	173.655
J_1	1.1670	0.6356	1.0098	19.74	1.039030	175.455
ι_1	1.1723	0.3657	1.0144	3.91	1.039177	175.465
SO_1	1.1720	0.0958	1.0147	3.24	1.070464	183.555
JO_1	1.1749	-0.1150	1.0173	1.60	1.075321	185.355
OO_1	1.1702	0.5205	1.0133	10.68	1.075940	185.555
OOZ_1	1.1654	-0.1162	1.0093	0.52	1.106756	193.455
V_1	1.1654	-0.1162	1.0093	2.08	1.112232	195.455

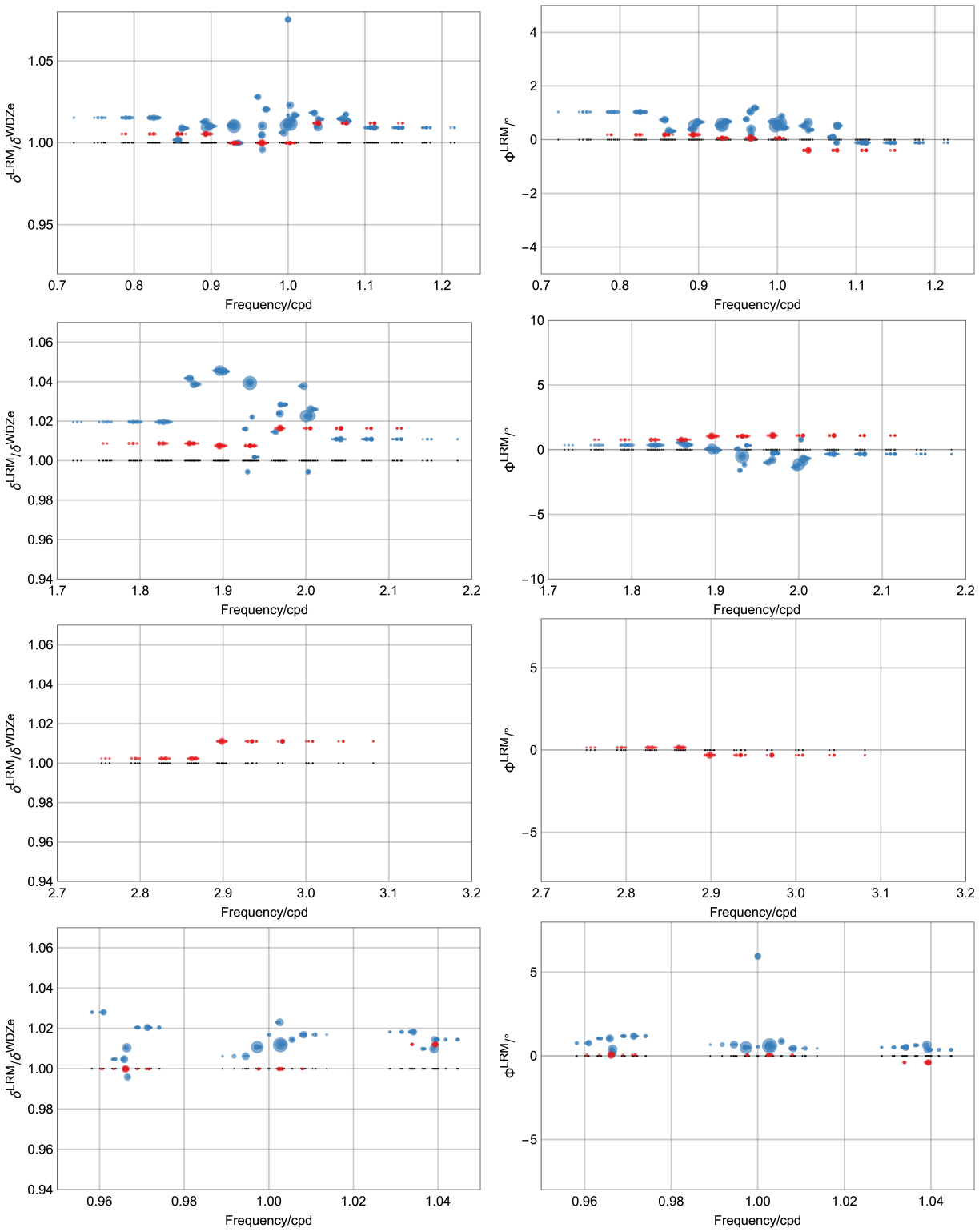

Figure B.14.: Parameters of the local response model (δ^{LRM} and Φ^{LRM}) in relation to WDZe for Cantley.

Table B.41.: Semidiurnal degree 2 parameters for the LRM-model, station Cantley.

Wave	δ^{LRM}	Φ^{LRM}	δ^{LRM}	Amplitude	Frequency	Doodson
		/°	$/\delta^{\mathrm{WDZe}}$	$/\mathrm{nm\,s^{-2}}$	/cpd	
$3N_2$	1.1804	0.3498	1.0196	0.85	1.823399	225.855
ϵ_2	1.1804	0.3498	1.0196	2.21	1.828256	227.655
$2N_2$	1.2060	0.5399	1.0417	7.56	1.859690	235.755
μ_2	1.2026	0.3729	1.0387	9.13	1.864547	237.555
MIX_2	1.2026	0.3729	1.0387	0.62	1.867285	238.554
NW_2	1.2106	0.0519	1.0456	0.48	1.893244	244.656
N_2	1.2106	0.0519	1.0456	57.55	1.895982	245.655
NIW_2	1.2101	-0.0378	1.0452	0.54	1.898720	246.654
ν_2	1.2101	-0.0378	1.0452	10.94	1.900839	247.455
NIX_2	1.2101	-0.0378	1.0452	0.51	1.903577	248.454
γ_2	1.1763	0.0595	1.0160	0.91	1.927417	253.755
α_2	1.1512	-1.5886	0.9943	1.04	1.929536	254.556
ω_2	1.2035	-0.5288	1.0395	11.32	1.932127	255.545
M_2	1.2033	-0.5099	1.0393	303.44	1.932274	255.555
β_2	1.1833	-1.1473	1.0220	0.92	1.935011	256.554
δ_2	1.1599	0.3257	1.0018	0.36	1.937749	257.555
λ_2	1.1746	-0.9885	1.0145	2.24	1.963708	263.655
L_2	1.1854	-0.7953	1.0238	8.58	1.968565	265.455
KNO_2	1.1906	-0.2703	1.0283	2.15	1.969184	265.655
LX_2	1.1906	-0.2703	1.0283	0.95	1.969331	265.665
LZ_2	1.1906	-0.2703	1.0283	0.41	1.974041	267.455
$2T_2$	1.2015	-1.3536	1.0378	0.33	1.994524	271.557
T_2	1.2015	-1.3536	1.0378	8.20	1.997262	272.556
S_2	1.1839	-1.1340	1.0226	140.17	2.000000	273.555
R_2	1.1513	0.7776	0.9944	1.17	2.002738	274.554
K_2	1.1840	-0.8751	1.0227	38.04	2.005476	275.555
KX_2	1.1879	-0.6817	1.0260	11.34	2.005623	275.565
KY_2	1.1879	-0.6817	1.0260	1.23	2.005770	275.575
KZ_2	1.1879	-0.6817	1.0260	0.30	2.008214	276.554
KA_2	1.1879	-0.6817	1.0260	0.26	2.010952	277.555
ζ_2	1.1704	-0.3395	1.0109	0.40	2.036911	283.655
η_2	1.1704	-0.3395	1.0109	2.11	2.041768	285.455
ETX_2	1.1704	-0.3395	1.0109	0.92	2.041915	285.465
$2S_2$	1.1704	-0.3395	1.0109	0.35	2.073202	293.555
$2K_2$	1.1704	-0.3395	1.0109	0.56	2.078678	295.555

Table B.42.: Degree 3 and 4 parameters for the LRM-model, station Cantley.

Wave	δ^{LRM}	Φ^{LRM} /°	$\delta^{\mathrm{LRM}}/\delta^{\mathrm{WDZe}}$	Amplitude /nm s^{-2}	Frequency /cpd	Doodson
$2Q_1$*	1.0786	0.1846	1.0054	0.41	0.856643	125.655
Q_1*	1.0786	0.1846	1.0054	1.51	0.892935	135.555
QX_1*	1.0786	0.1846	1.0054	0.09	0.893554	135.755
ρ_1*	1.0786	0.1846	1.0054	0.13	0.898410	137.555
O_1*	1.0727	0.0548	0.9999	0.80	0.929845	145.655
LK_1*	1.0727	0.0548	0.9999	0.74	0.965990	155.545
M_1*	1.0727	0.0548	0.9999	4.97	0.966137	155.555
χ_1*	1.0727	0.0548	0.9999	0.02	0.971613	157.555
K_1*	1.0727	0.0548	0.9999	0.27	1.002428	165.455
J_1*	1.0858	-0.3971	1.0121	1.75	1.039339	175.555
$3N_2$*	1.0821	0.7693	1.0087	0.23	1.823089	225.755
ϵ_2*	1.0821	0.7693	1.0087	0.23	1.827946	227.555
$2N_2$*	1.0821	0.7693	1.0087	1.32	1.859381	235.655
μ_2*	1.0821	0.7693	1.0087	0.25	1.864238	237.455
N_2*	1.0808	1.0406	1.0075	4.85	1.895673	245.555
ν_2*	1.0808	1.0406	1.0075	0.12	1.901148	247.555
ω_2*	1.0808	1.0406	1.0075	0.28	1.931964	255.455
M_2*	1.0808	1.0406	1.0075	0.74	1.932583	255.655
L_2*	1.0904	1.0963	1.0164	4.51	1.968875	265.555
KNO_2*	1.0904	1.0963	1.0164	0.85	1.969018	265.565
K_2*	1.0904	1.0963	1.0164	0.24	2.005166	275.455
η_2*	1.0904	1.0963	1.0164	0.41	2.042077	285.555
MN_3*	1.0724	0.1505	1.0024	1.05	2.862119	345.655
M_3*	1.0816	-0.3145	1.0110	3.85	2.898410	355.555
ML_3*	1.0816	-0.3145	1.0110	0.22	2.934702	365.455
MK_3*	1.0816	-0.3145	1.0110	0.50	2.971613	375.555
O_1+	1.0356	0.0340	0.9993	0.03	0.929536	145.555
MN_3+	1.0356	0.0340	0.9993	0.08	2.861809	345.555
M_4+	1.0347	-0.0190	0.9996	0.05	3.864547	455.555

Syowa

Table B.43.: Diurnal degree 2 parameters for the LRM-model, station Syowa.

Wave	δ^{LRM}	Φ^{LRM}	δ^{LRM}	Amplitude	Frequency	Doodson
		/°	$/\delta^{\mathrm{WDZe}}$	$/\mathrm{nm\,s^{-2}}$	/cpd	
ζ_1	1.2063	0.6348	1.0479	0.48	0.820661	115.855
$\mathrm{SGQ_1}$	1.2550	0.7008	1.0902	1.25	0.825518	117.655
$\mathrm{2Q_1}$	1.2605	4.4267	1.0950	4.17	0.856952	125.755
σ_1	1.2789	3.7359	1.1110	5.02	0.861809	127.555
$\mathrm{SGX_1}$	1.2789	3.7360	1.1110	0.34	0.864547	128.554
$\mathrm{QW_1}$	1.2970	2.1618	1.1269	5.97	0.893097	135.645
$\mathrm{Q_1}$	1.2972	2.1514	1.1271	31.66	0.893244	135.655
ρ_1	1.2999	2.1987	1.1294	6.03	0.898101	137.455
$\mathrm{ROX_1}$	1.2999	2.1991	1.1294	0.35	0.898720	137.655
$\mathrm{OW_1}$	1.2799	1.1793	1.1121	0.58	0.926798	144.556
$\mathrm{OV_1}$	1.2798	1.1800	1.1121	32.12	0.929389	145.545
$\mathrm{O_1}$	1.2730	0.8656	1.1062	170.28	0.929536	145.555
$\mathrm{OX_1}$	1.2729	0.8691	1.1061	1.10	0.930155	145.755
$\mathrm{TW_1}$	1.2205	-0.7809	1.0606	0.52	0.932273	146.554
τ_1	1.2204	-0.7809	1.0606	2.23	0.935012	147.555
$\mathrm{LKW_1}$	1.2374	-0.9976	1.0757	1.28	0.960970	153.655
$\mathrm{LK_1}$	1.2373	-0.9985	1.0757	4.90	0.965827	155.455
$\mathrm{M_1}$	1.2518	0.1245	1.0883	13.63	0.966446	155.655
$\mathrm{MN_1}$	1.2519	0.1249	1.0884	2.74	0.966593	155.665
χ_1	1.2021	-1.1165	1.0453	2.61	0.971303	157.455
π_1	1.2349	-1.8895	1.0767	4.68	0.994524	162.556
$\mathrm{P_1}$	1.2201	0.0952	1.0653	79.76	0.997262	163.555
$\mathrm{S_1}$	1.2823	5.8315	1.1228	1.88	1.000000	164.556
$\mathrm{KW_1}$	1.1950	0.1733	1.0554	4.70	1.002591	165.545
$\mathrm{K_1}$	1.1947	0.1617	1.0563	237.31	1.002738	165.555
κ_1	1.1582	1.3479	1.0253	32.14	1.002885	165.565
$\mathrm{KX_1}$	1.1567	1.3452	1.0253	0.69	1.003032	165.575
ψ_1	1.2568	-6.8203	0.9927	2.07	1.005476	166.554
φ_1	1.1375	1.9144	0.9752	3.47	1.008214	167.555
ϑ_1	1.2097	0.8425	1.0492	2.53	1.034173	173.655
$\mathrm{J_1}$	1.2009	0.5794	1.0417	13.19	1.039030	175.455
ι_1	1.2010	0.5782	1.0418	2.62	1.039177	175.465
$\mathrm{SO_1}$	1.2261	0.5574	1.0641	2.16	1.070464	183.555
$\mathrm{JO_1}$	1.1611	0.3630	1.0078	1.07	1.075321	185.355
$\mathrm{OO_1}$	1.2047	0.7958	1.0457	7.14	1.075940	185.555
$\mathrm{OOZ_1}$	1.1883	-0.7279	1.0316	0.35	1.106756	193.455
$\mathrm{V_1}$	1.1883	-0.7279	1.0317	1.39	1.112232	195.455

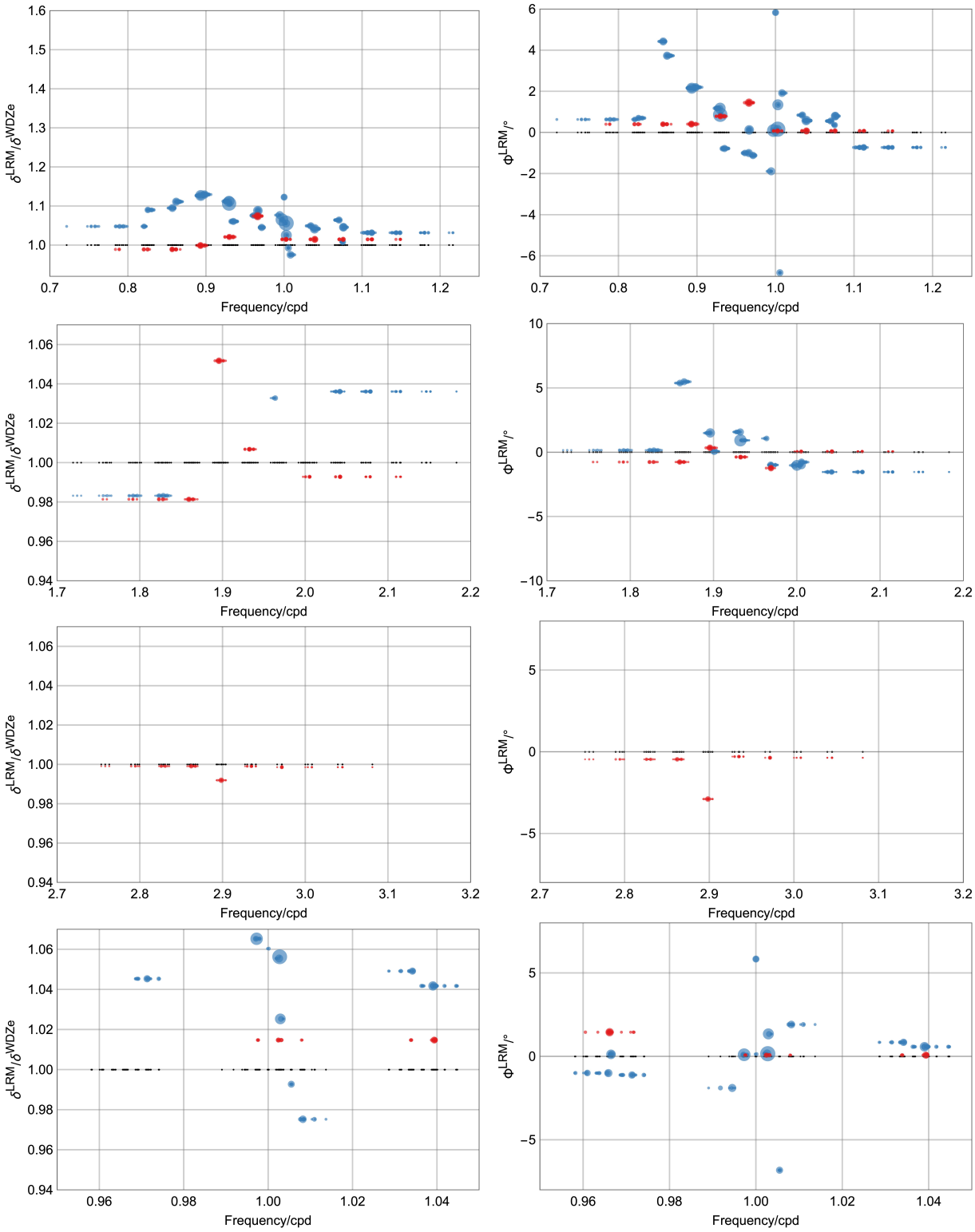

Figure B.15.: Parameters of the local response model (δ^{LRM} and Φ^{LRM}) in relation to WDZe for Syowa.

Table B.44.: Semidiurnal degree 2 parameters for the LRM-model, station Syowa.

Wave	δ^{LRM}	Φ^{LRM}	δ^{LRM}	Amplitude	Frequency	Doodson
		/°	$/\delta^{\mathrm{WDZe}}$	$/\mathrm{nm\,s^{-2}}$	/cpd	
$3N_2$	1.1362	0.1581	0.9832	0.22	1.823399	225.855
ϵ_2	1.1362	0.1581	0.9832	0.58	1.828256	227.655
$2N_2$	1.2756	5.3757	1.1038	1.98	1.859690	235.755
μ_2	1.2440	5.4772	1.0765	2.39	1.864547	237.555
MIX_2	1.2440	5.4769	1.0765	0.16	1.867285	238.554
NW_2	1.4201	1.4938	1.2289	0.13	1.893244	244.656
N_2	1.4201	1.4959	1.2289	15.07	1.895982	245.655
NIW_2	1.4076	0.0641	1.2181	0.14	1.898720	246.654
ν_2	1.4076	0.0642	1.2181	2.87	1.900839	247.455
NIX_2	1.4076	0.0641	1.2181	0.13	1.903577	248.454
γ_2	1.4366	1.5734	1.2432	0.24	1.927417	253.755
α_2	1.4366	1.5732	1.2432	0.27	1.929536	254.556
ω_2	1.4366	1.5734	1.2432	2.96	1.932127	255.545
M_2	1.4001	0.9217	1.2116	79.45	1.932274	255.555
β_2	1.4001	0.9214	1.2116	0.24	1.935011	256.554
δ_2	1.4001	0.9215	1.2116	0.09	1.937749	257.555
λ_2	1.1935	1.0707	1.0328	0.59	1.963708	263.655
L_2	1.3687	-0.9954	1.1844	2.25	1.968565	265.455
KNO_2	1.3686	-0.9956	1.1844	0.56	1.969184	265.655
LX_2	1.3686	-0.9956	1.1844	0.25	1.969331	265.665
LZ_2	1.3686	-0.9956	1.1844	0.11	1.974041	267.455
$2T_2$	1.5020	-1.0188	1.2997	0.09	1.994524	271.557
T_2	1.5020	-1.0183	1.2997	2.15	1.997262	272.556
S_2	1.5020	-1.0189	1.2997	36.70	2.000000	273.555
R_2	1.5020	-1.0189	1.2997	0.31	2.002738	274.554
K_2	1.5146	-0.9883	1.3107	9.96	2.005476	275.555
KX_2	1.4497	-0.7738	1.2545	2.97	2.005623	275.565
KY_2	1.4497	-0.7739	1.2545	0.32	2.005770	275.575
KZ_2	1.4497	-0.7739	1.2545	0.08	2.008214	276.554
KA_2	1.4497	-0.7739	1.2545	0.07	2.010952	277.555
ζ_2	1.1973	-1.5354	1.0361	0.11	2.036911	283.655
η_2	1.1973	-1.5355	1.0361	0.55	2.041768	285.455
ETX_2	1.1973	-1.5353	1.0361	0.24	2.041915	285.465
$2S_2$	1.1973	-1.5354	1.0361	0.09	2.073202	293.555
$2K_2$	1.1973	-1.5354	1.0361	0.15	2.078678	295.555

Table B.45.: Degree 3 and 4 parameters for the LRM-model, station Syowa.

Wave	δ^{LRM}	Φ^{LRM}	δ^{LRM}	Amplitude	Frequency	Doodson
		/°	$/\delta^{\mathrm{WDZe}}$	$/\mathrm{nm\,s^{-2}}$	/cpd	
$2Q_1$*	1.0611	0.4046	0.9891	0.46	0.856643	125.655
Q_1*	1.0718	0.4059	0.9990	1.69	0.892935	135.555
QX_1*	1.0718	0.4051	0.9990	0.10	0.893554	135.755
ρ_1*	1.0718	0.4052	0.9990	0.15	0.898410	137.555
O_1*	1.0952	0.7897	1.0208	0.89	0.929845	145.655
LK_1*	1.1525	1.4482	1.0743	0.82	0.965990	155.545
M_1*	1.1525	1.4488	1.0743	5.54	0.966137	155.555
χ_1*	1.1525	1.4482	1.0743	0.02	0.971613	157.555
K_1*	1.0886	0.0716	1.0147	0.30	1.002428	165.455
J_1*	1.0886	0.0717	1.0147	1.95	1.039339	175.555
$3N_2$*	1.0528	-0.7634	0.9814	0.08	1.823089	225.755
ϵ_2*	1.0528	-0.7634	0.9814	0.08	1.827946	227.555
$2N_2$*	1.0528	-0.7634	0.9814	0.45	1.859381	235.655
μ_2*	1.0528	-0.7634	0.9814	0.08	1.864238	237.455
N_2*	1.1283	0.3422	1.0518	1.66	1.895673	245.555
ν_2*	1.1283	0.3426	1.0518	0.04	1.901148	247.555
ω_2*	1.0801	-0.3773	1.0068	0.10	1.931964	255.455
M_2*	1.0801	-0.3773	1.0068	0.25	1.932583	255.655
L_2*	1.2053	-1.2380	1.1235	1.55	1.968875	265.555
KNO_2*	1.2053	-1.2380	1.1235	0.29	1.969018	265.565
K_2*	1.0651	0.0520	0.9928	0.08	2.005166	275.455
η_2*	1.0651	0.0520	0.9928	0.14	2.042077	285.555
MN_3*	1.0662	-0.4630	0.9991	0.14	2.862119	345.655
M_3*	1.0585	-2.8904	0.9919	0.52	2.898410	355.555
ML_3*	1.0661	-0.2958	0.9990	0.03	2.934702	365.455
MK_3*	1.0656	-0.3614	0.9986	0.07	2.971613	375.555
O_1+	1.0363	0.0117	1.0000	0.12	0.929536	145.555
MN_3+	1.0363	0.0117	1.0000	0.01	2.861809	345.555
M_4+	1.0343	0.0223	1.0002	0.00	3.864547	455.555

C. Moving Window Analyses

Compilation of MWA diagrams of investigated observatories. Green color corresponds to WDZe a priori model used in the analysis. Orange color corresponds to the LRM response model for a given station. Contrary to Chapter 8, the results are displayed with their physical meaning, i.e. gravimetric factor and phase. This is consistent with the method used for display in Chapter 6. The lower and upper curves of the same color are the MWA results shifted by the standard deviation estimates. Dashed lines represent the estimate of the main harmonic in the group resulting from the analysis by `RATA` method (Chapter 7 and Appendix B).

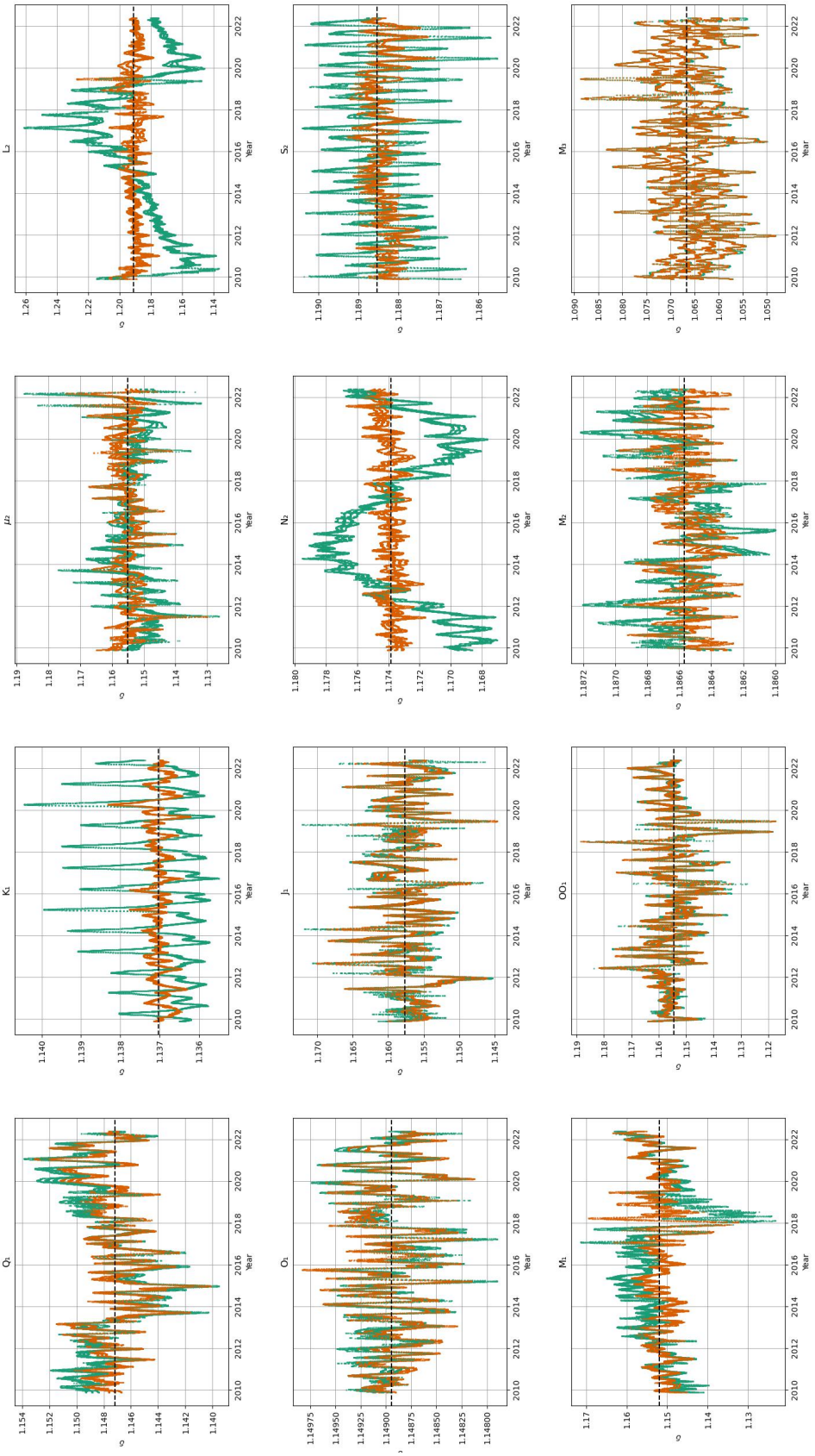

Figure C.1.: Diagrams with MWA estimates for gravimetric factors in Black Forest Observatory (lower sensor).

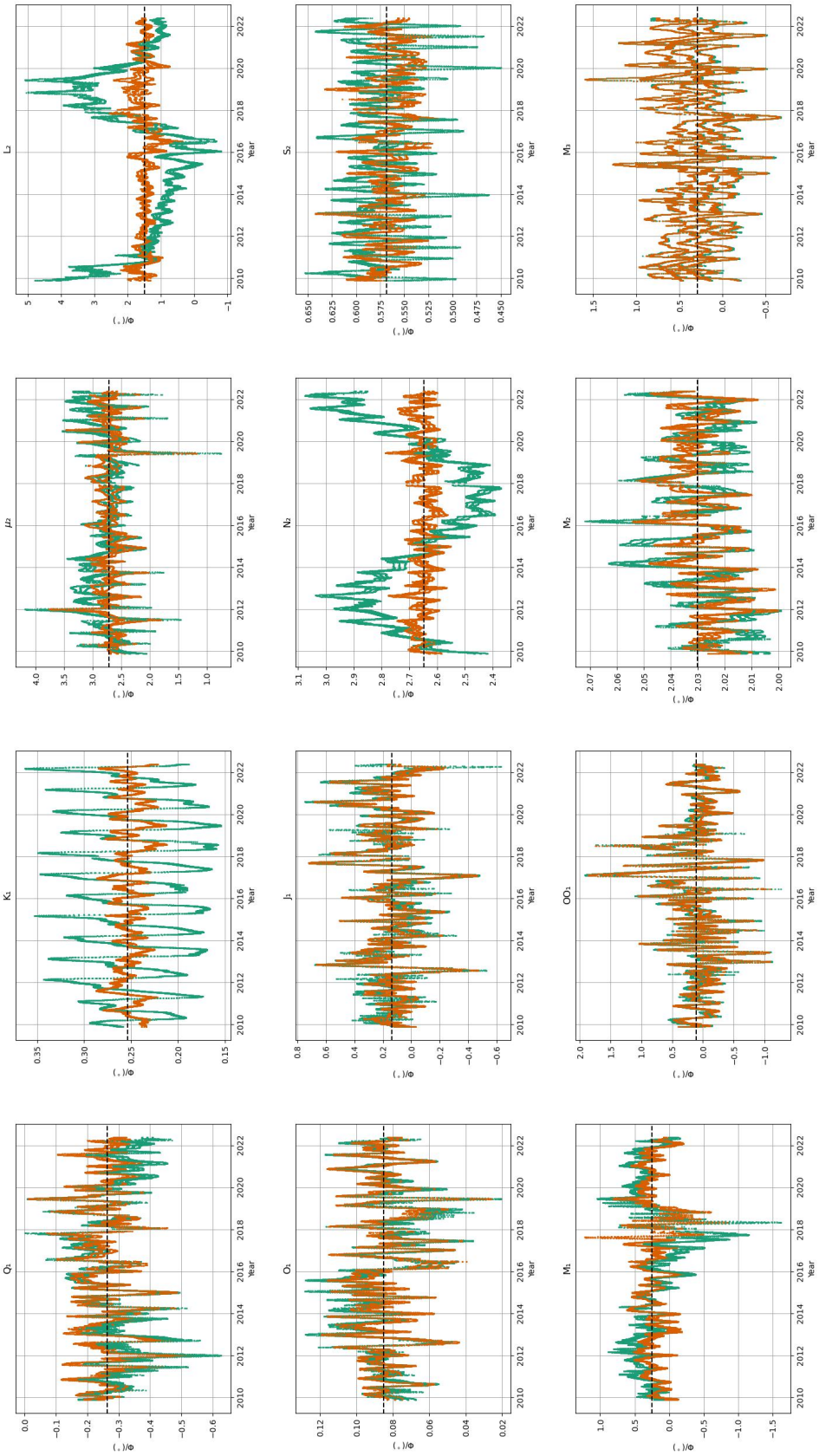

Figure C.2.: Diagrams with MWA estimates for gravimetric phases in Black Forest Observatory (lower sensor).

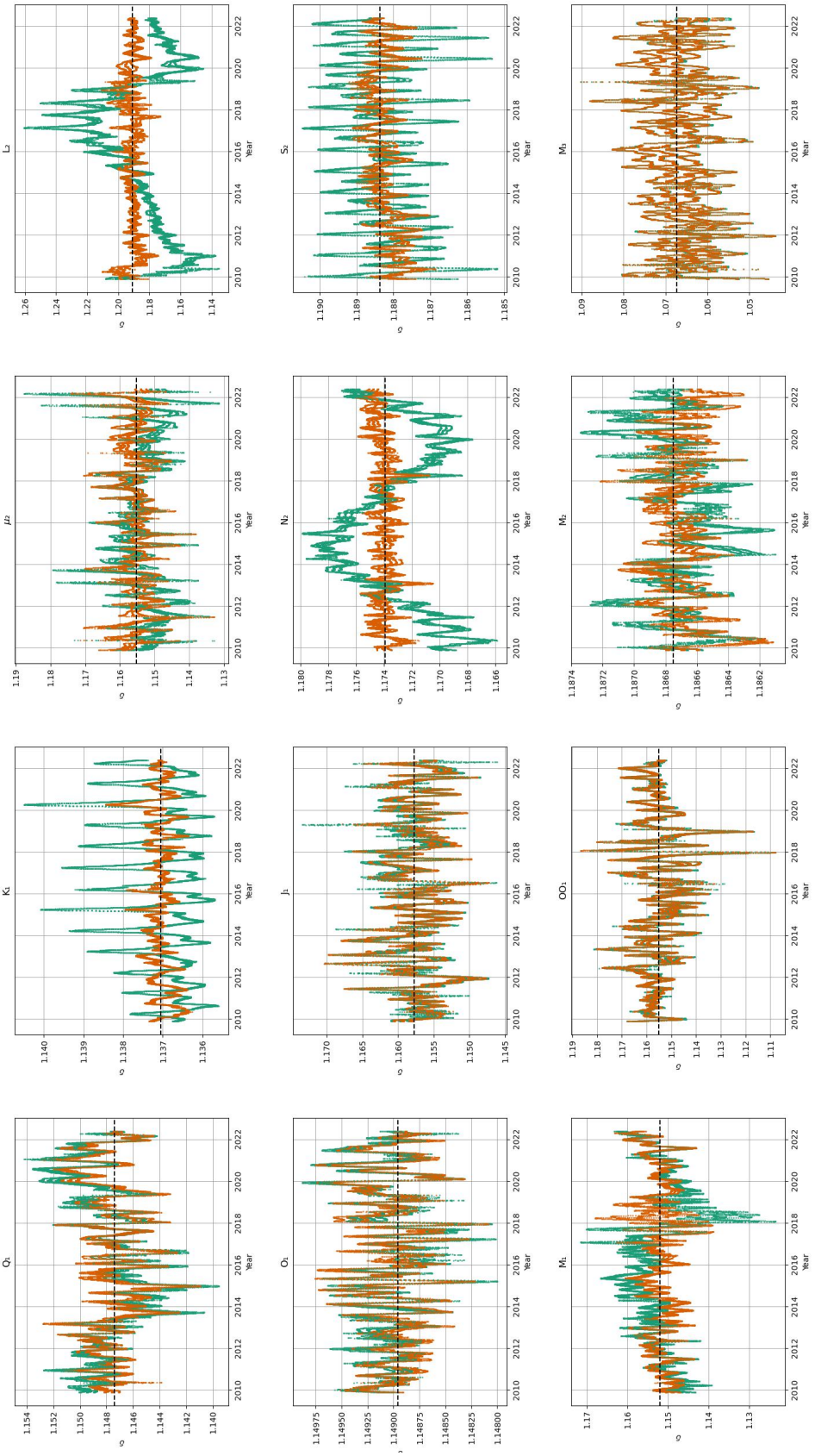

Figure C.3.: Diagrams with MWA estimates for gravimetric factors in Black Forest Observatory (upper sensor).

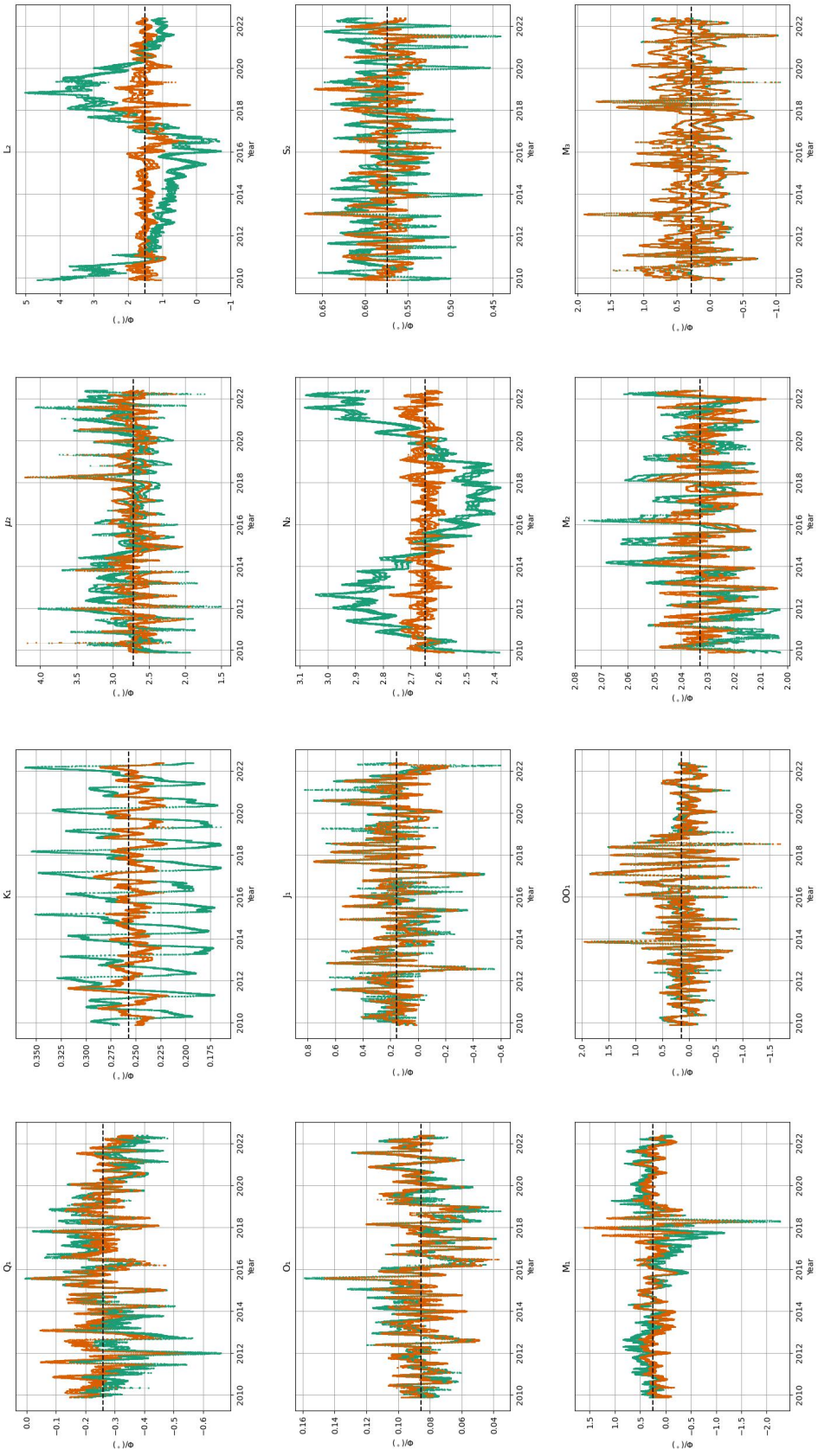

Figure C.4.: Diagrams with MWA estimates for gravimetric phases in Black Forest Observatory (upper sensor).

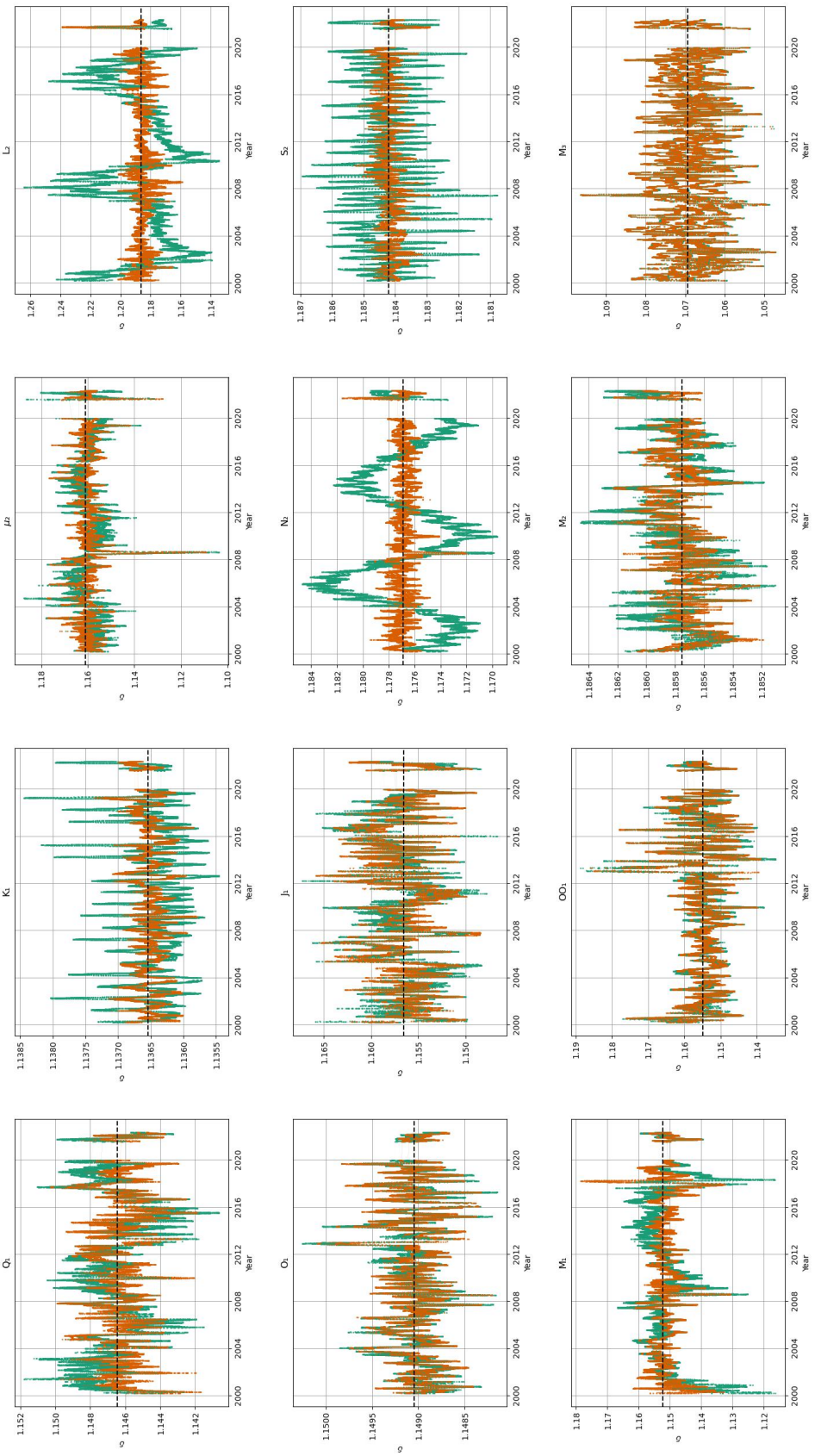

Figure C.5.: Diagrams with MWA estimates for gravimetric factors in Moxa (lower sensor).

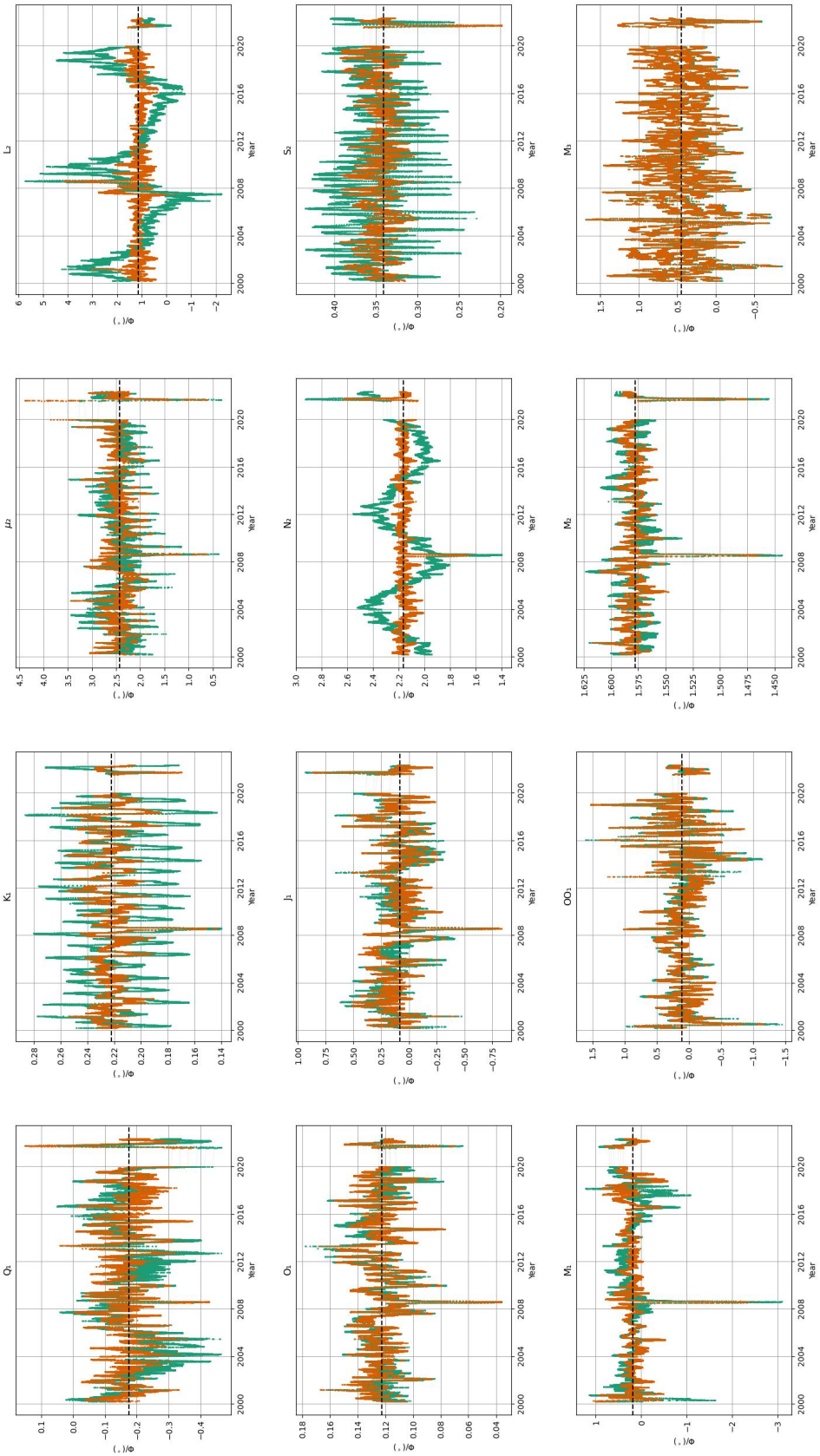

Figure C.6.: Diagrams with MWA estimates for gravimetric phases in Moxa (lower sensor).

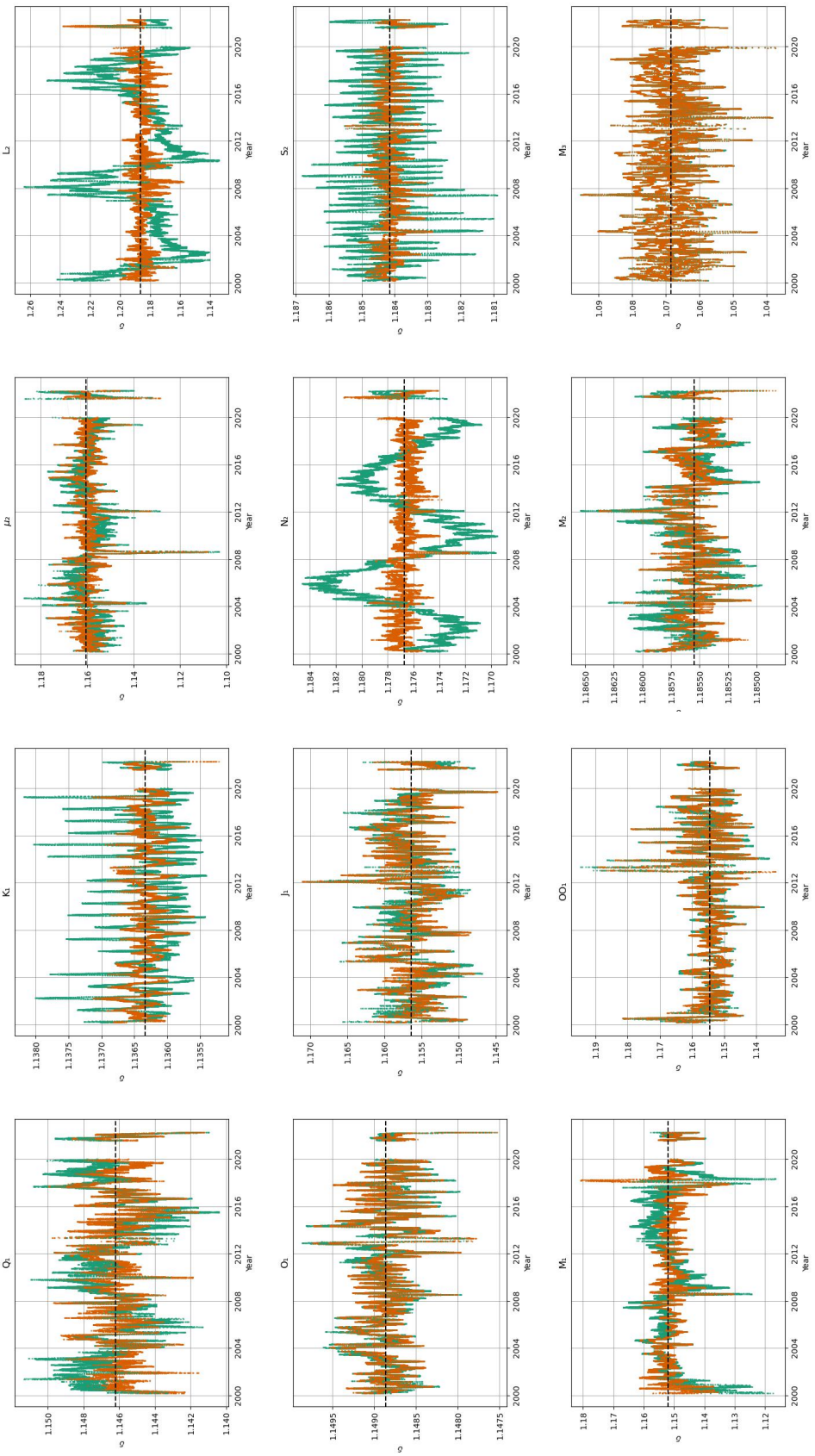

Figure C.7.: Diagrams with MWA estimates for gravimetric factors in Moxa (upper sensor).

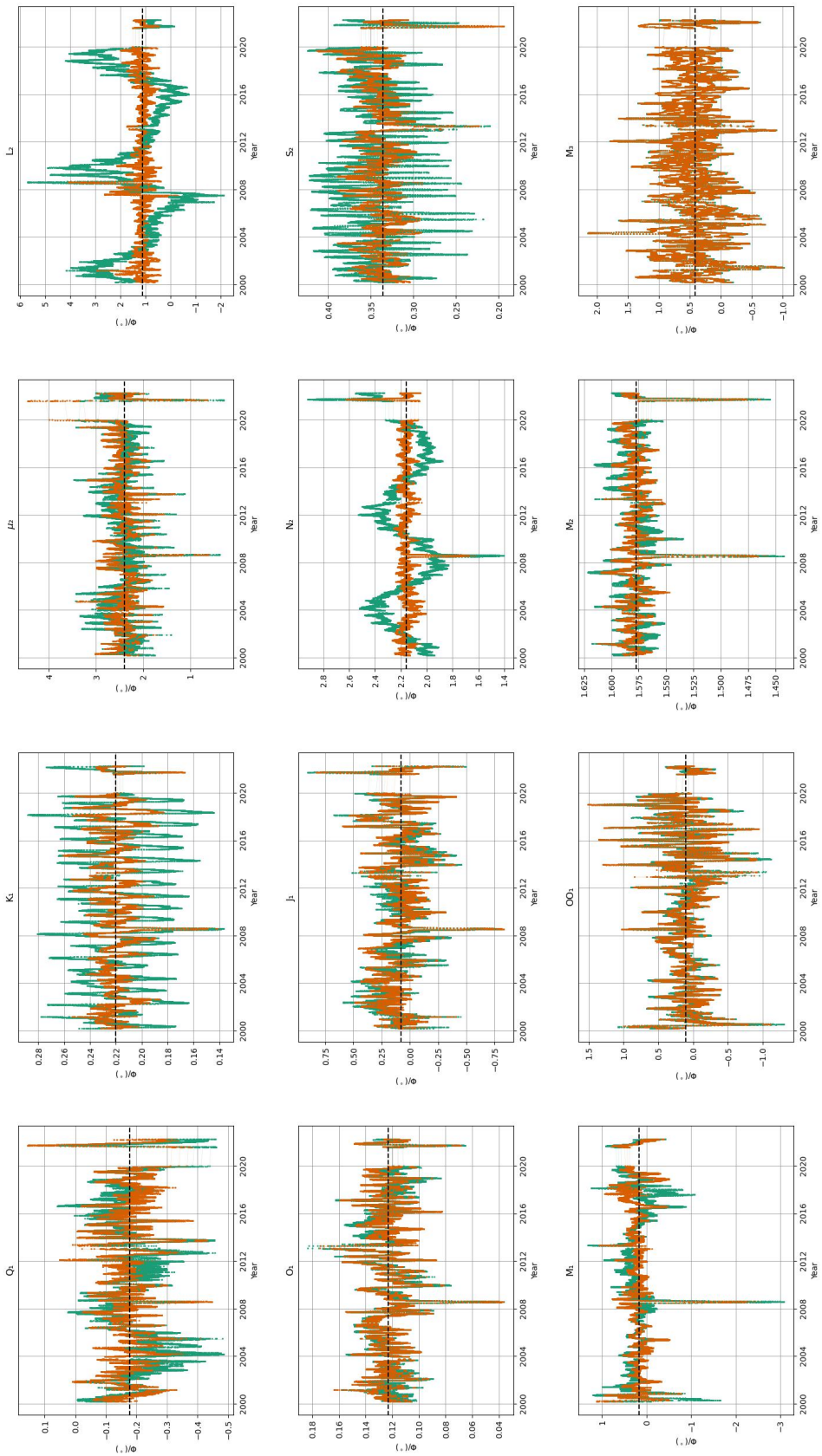

Figure C.8.: Diagrams with MWA estimates for gravimetric phases in Moxa (upper sensor).

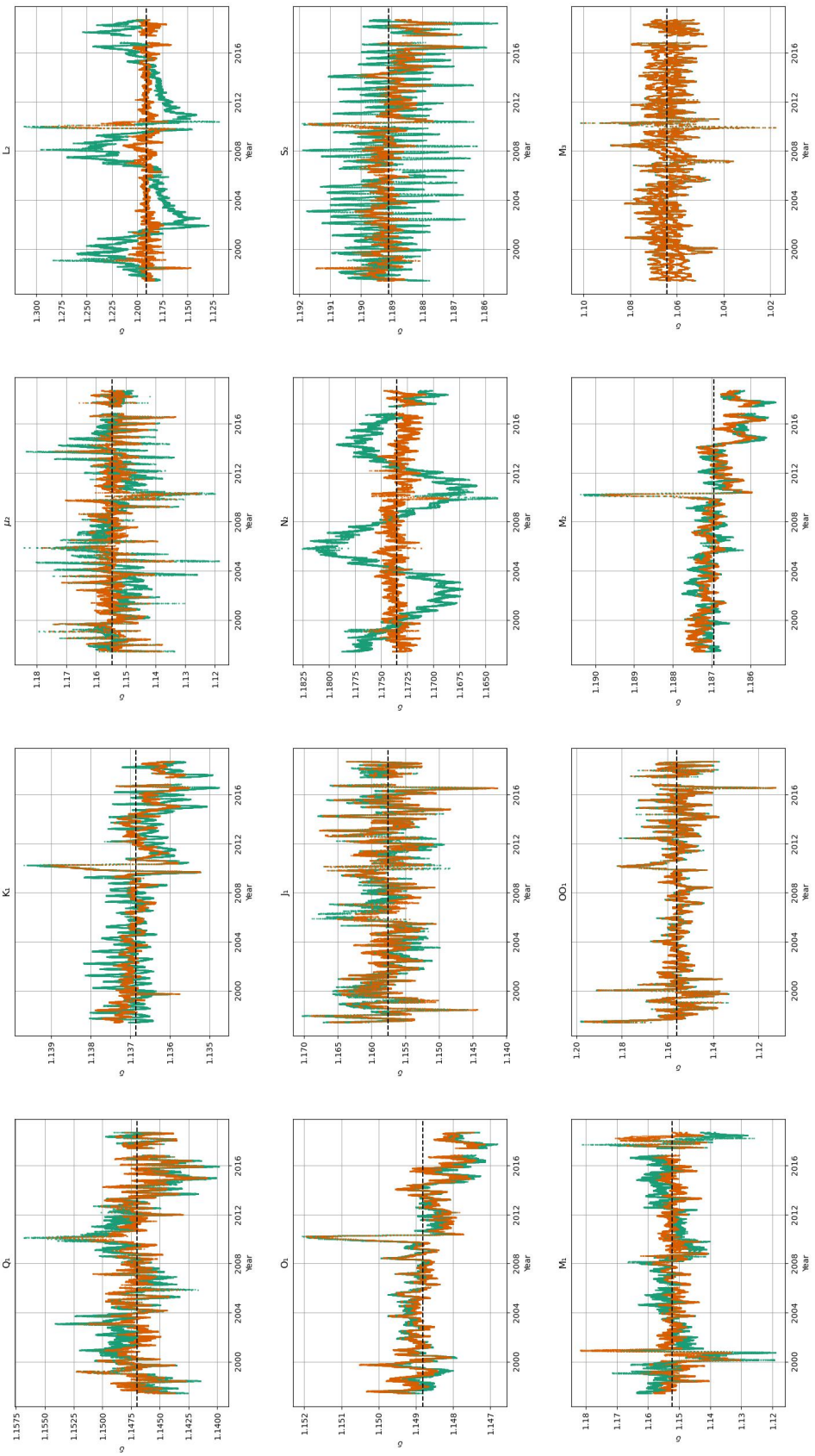

Figure C.9.: Diagrams with MWA estimates for gravimetric factors in Strasbourg.

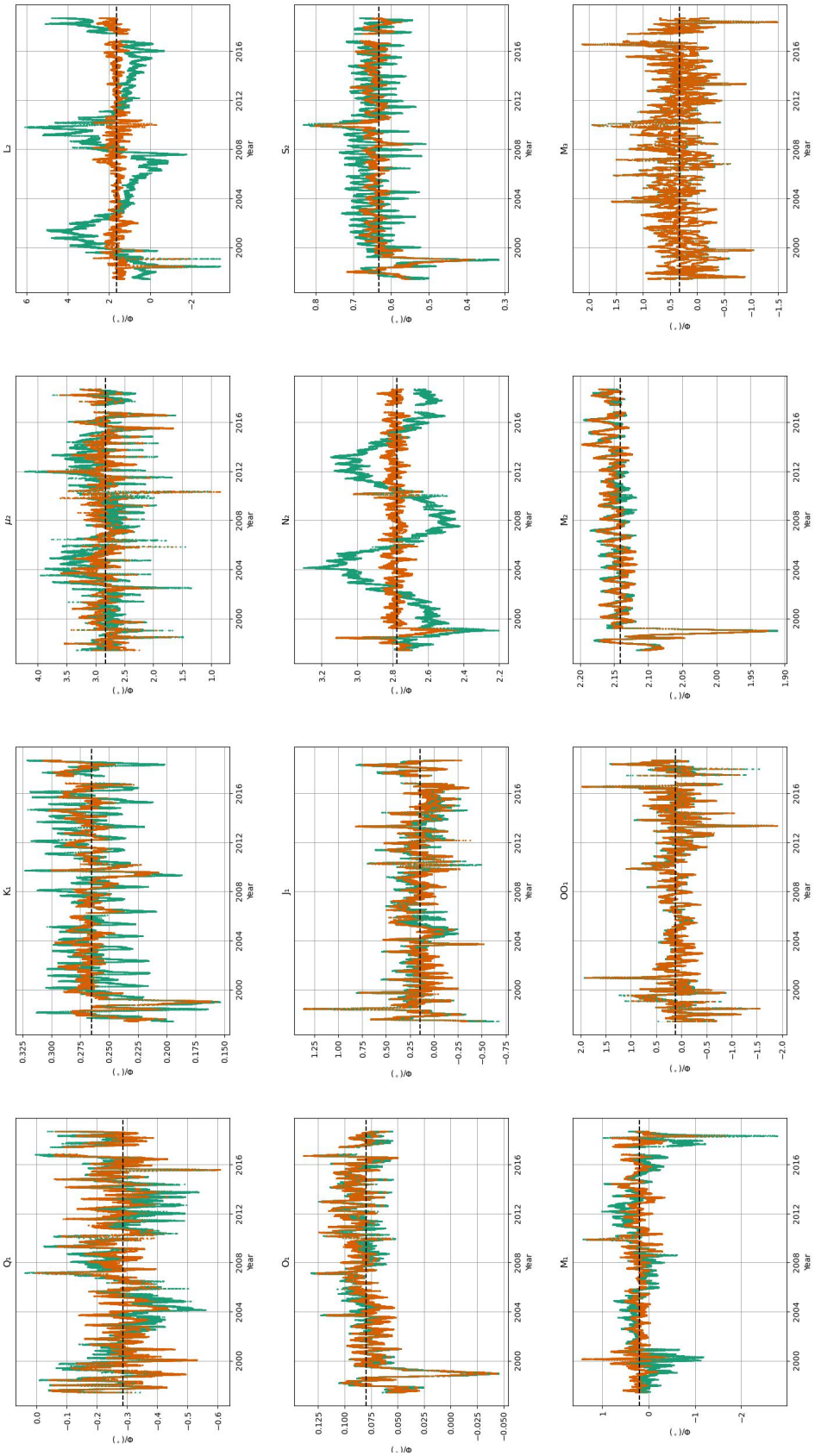

Figure C.10.: Diagrams with MWA estimates for gravimetric phases in Strasbourg.

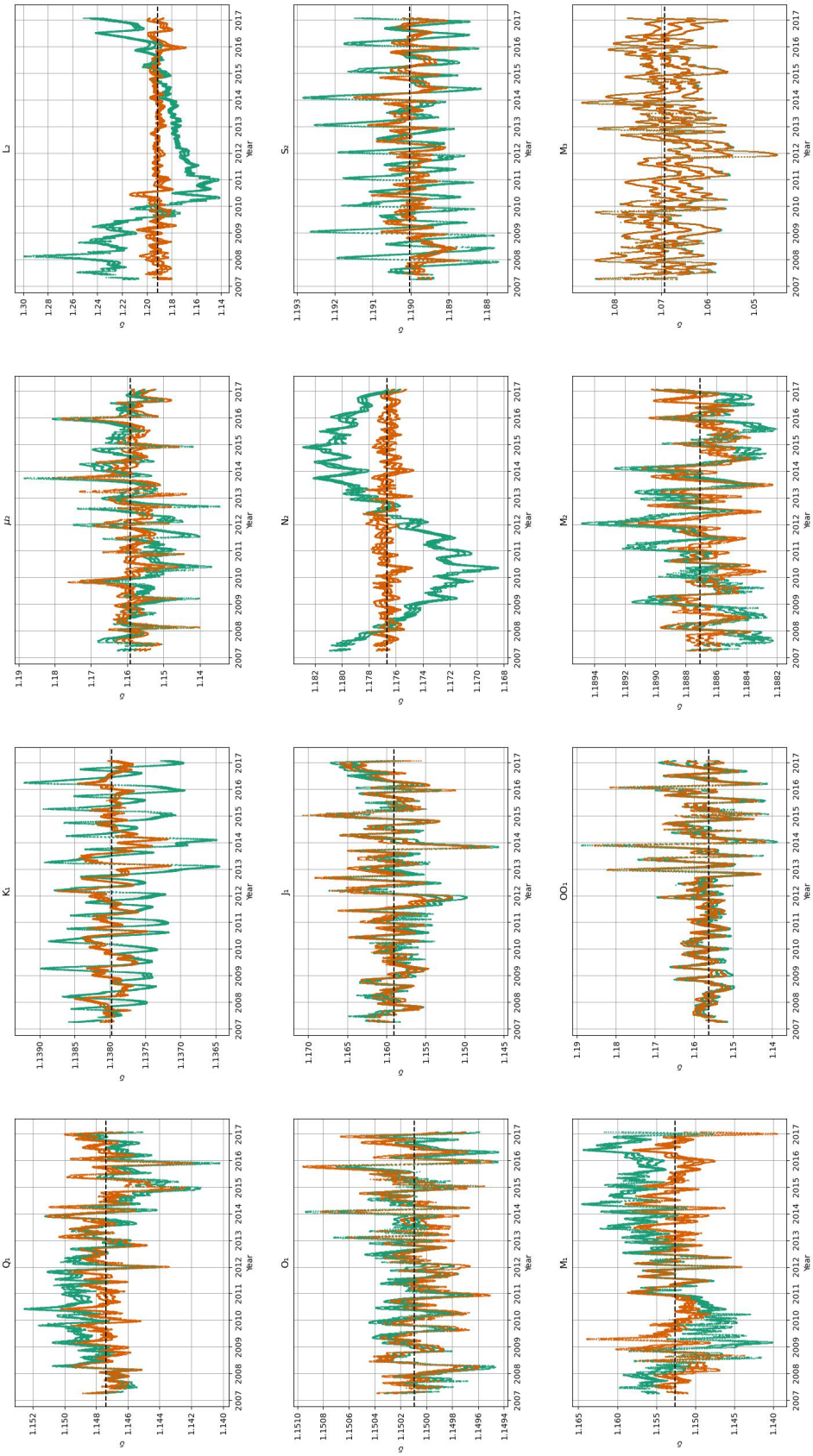

Figure C.11.: Diagrams with MWA estimates for gravimetric factors in Bad Homburg.

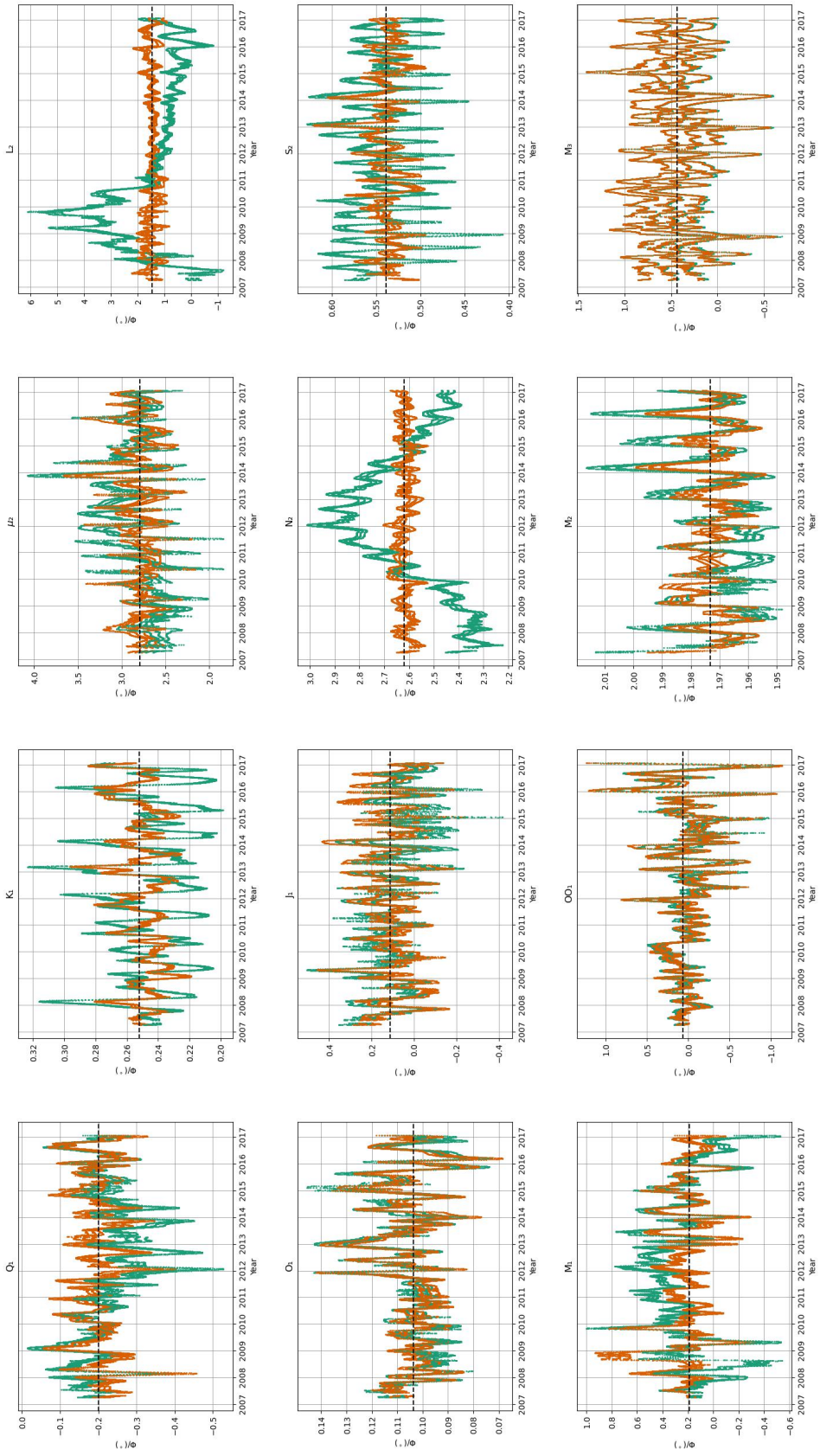

Figure C.12.: Diagrams with MWA estimates for gravimetric phases in Bad Homburg.

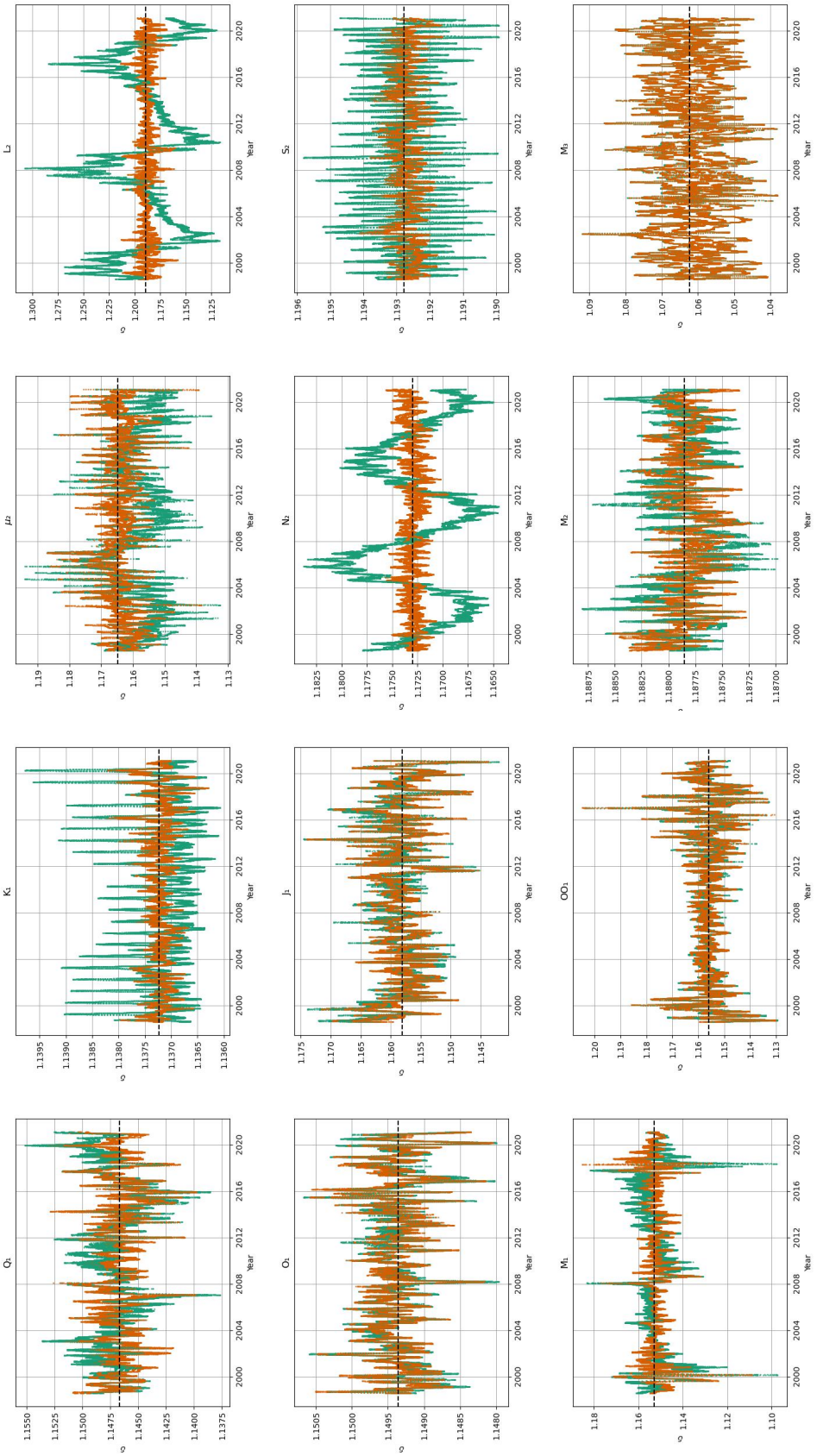

Figure C.13.: Diagrams with MWA estimates for gravimetric factors in Membach.

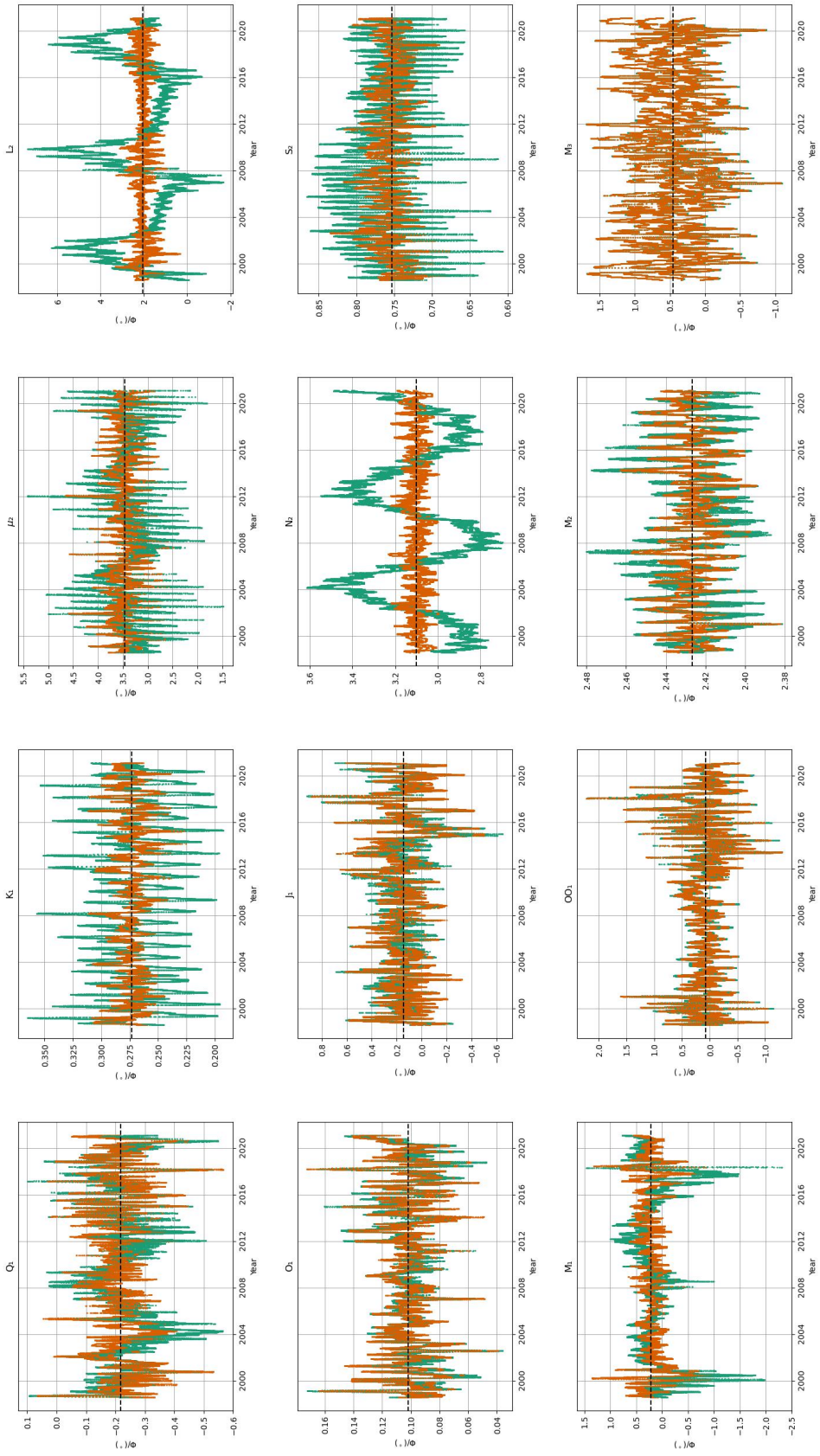

Figure C.14.: Diagrams with MWA estimates for gravimetric phases in Membach.

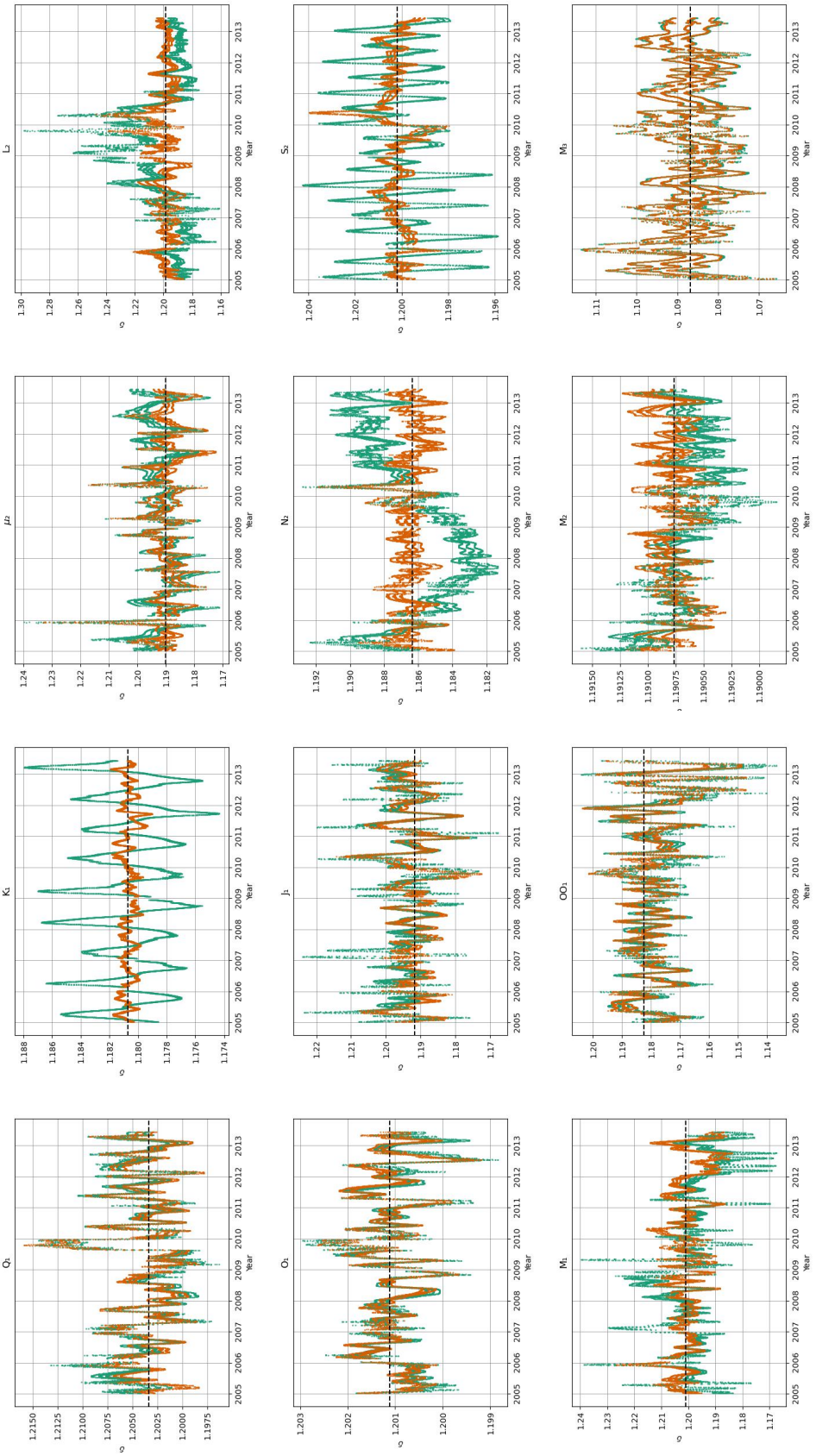

Figure C.15.: Diagrams with MWA estimates for gravimetric factors in Kamioka.

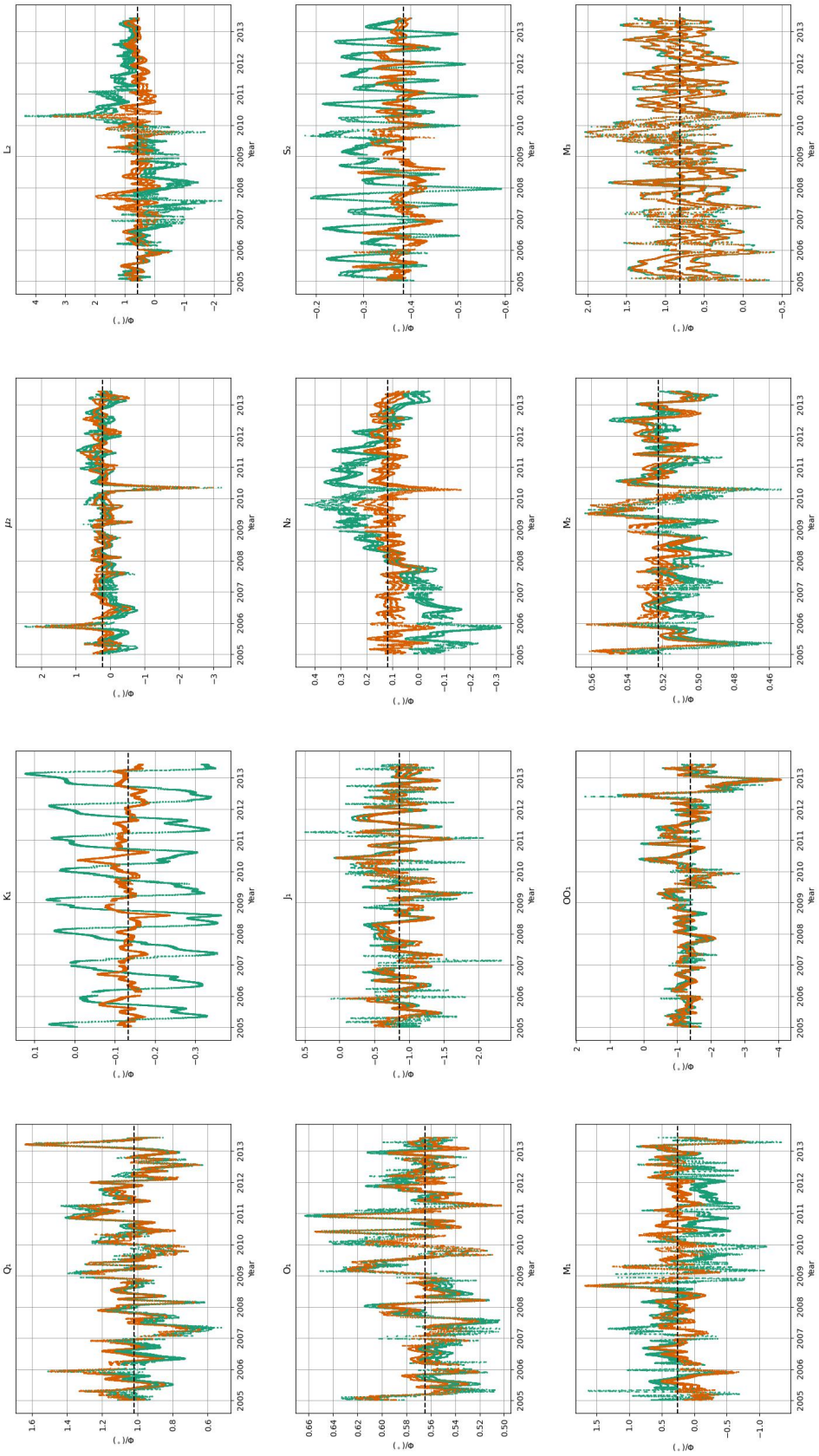

Figure C.16.: Diagrams with MWA estimates for gravimetric phases in Kamioka.

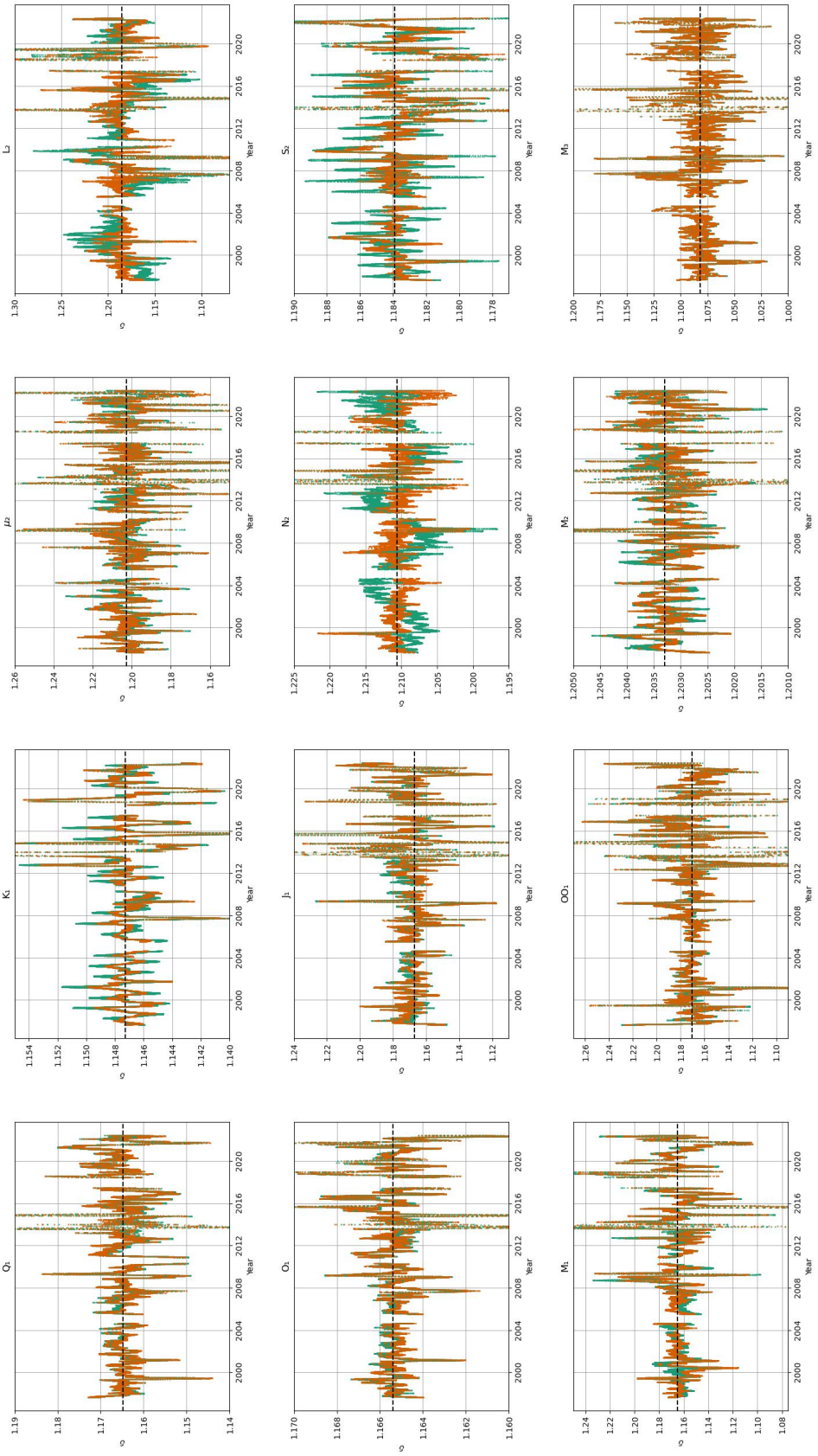

Figure C.17.: Diagrams with MWA estimates for gravimetric factors in Cantley.

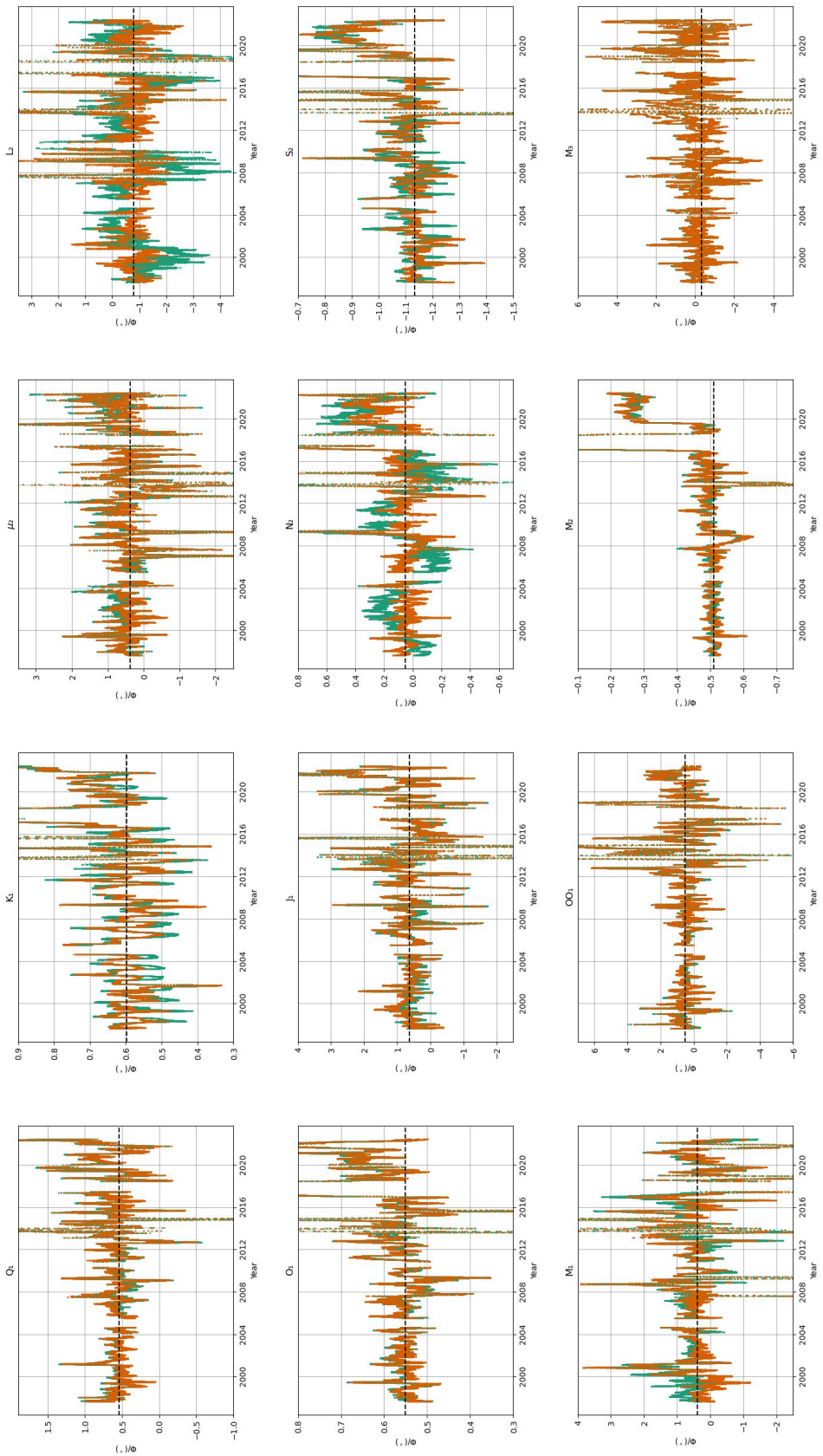

Figure C.18.: Diagrams with MWA estimates for gravimetric phases in Cantley.

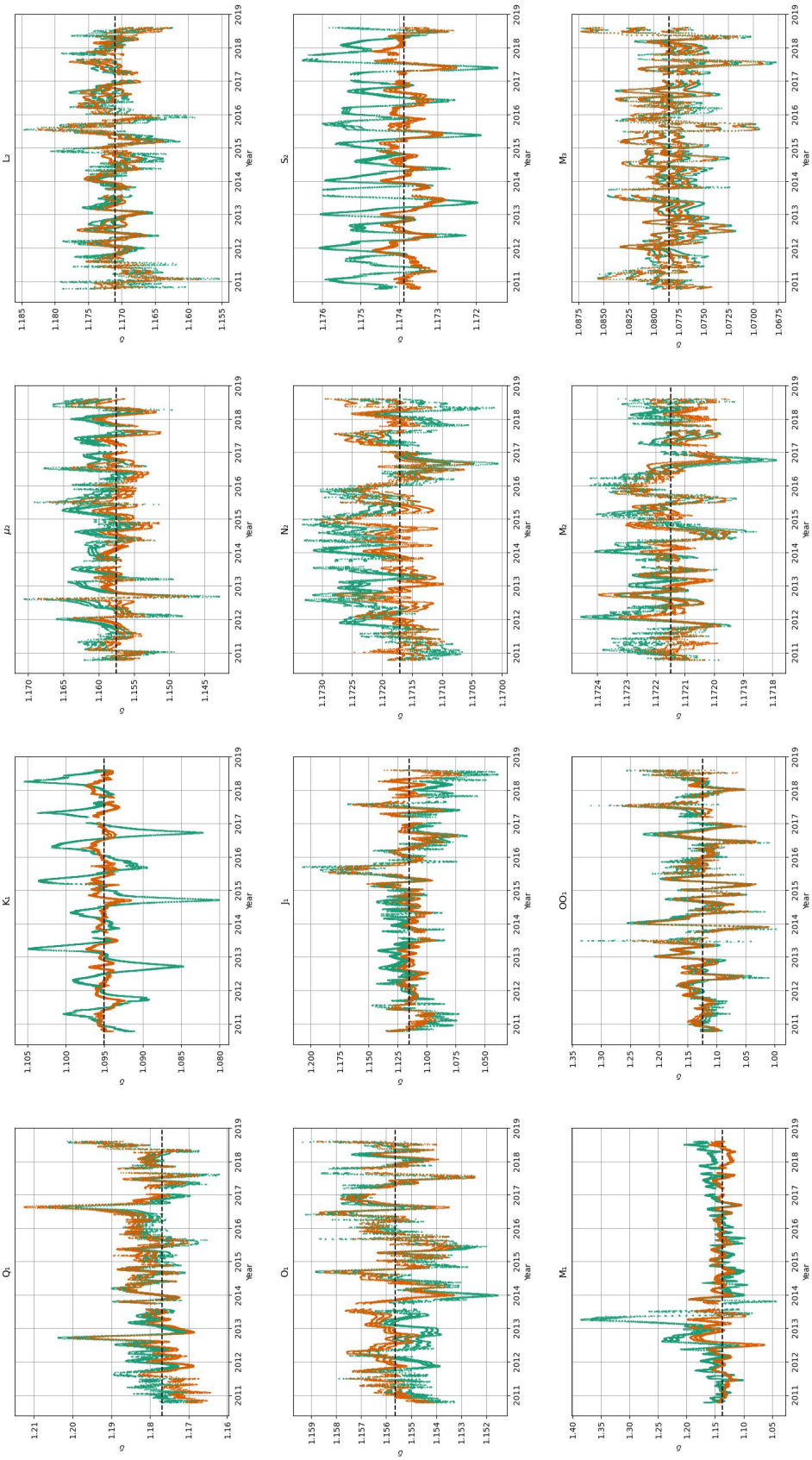

Figure C.19.: Diagrams with MWA estimates for gravimetric factors in Djougou.

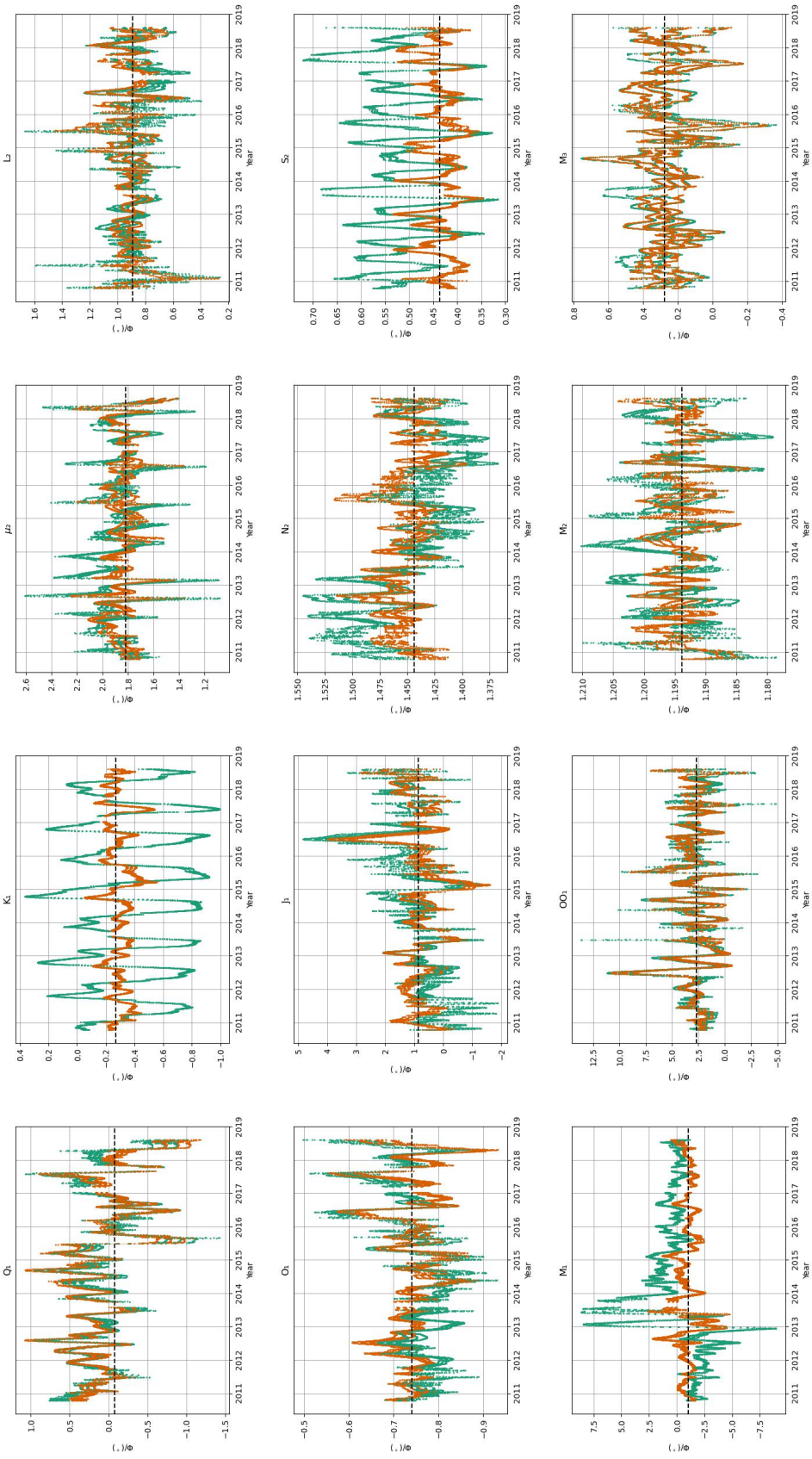

Figure C.20.: Diagrams with MWA estimates for gravimetric phases in Djougou.

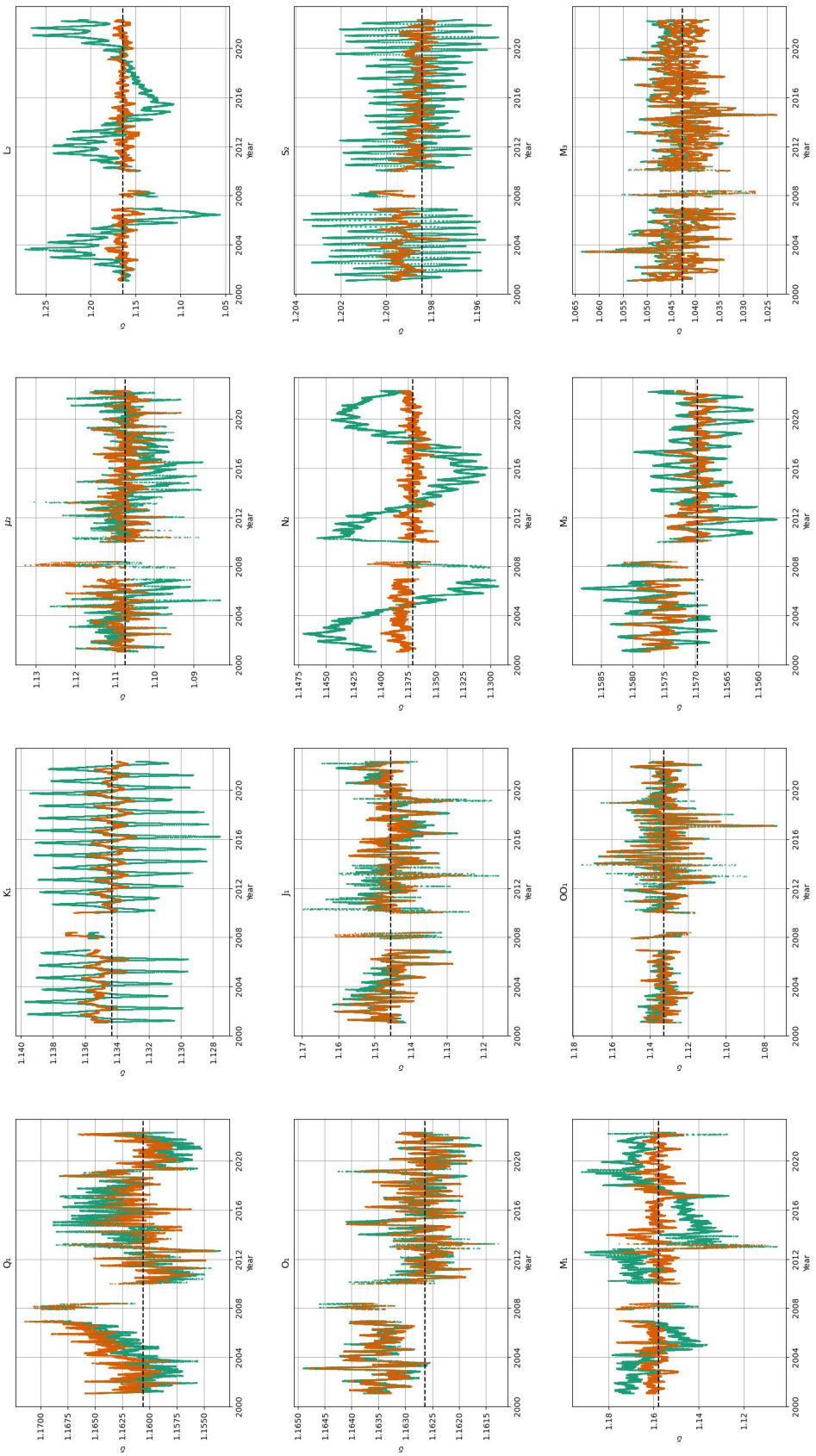

Figure C.21.: Diagrams with MWA estimates for gravimetric factors in Sutherland (lower sensor).

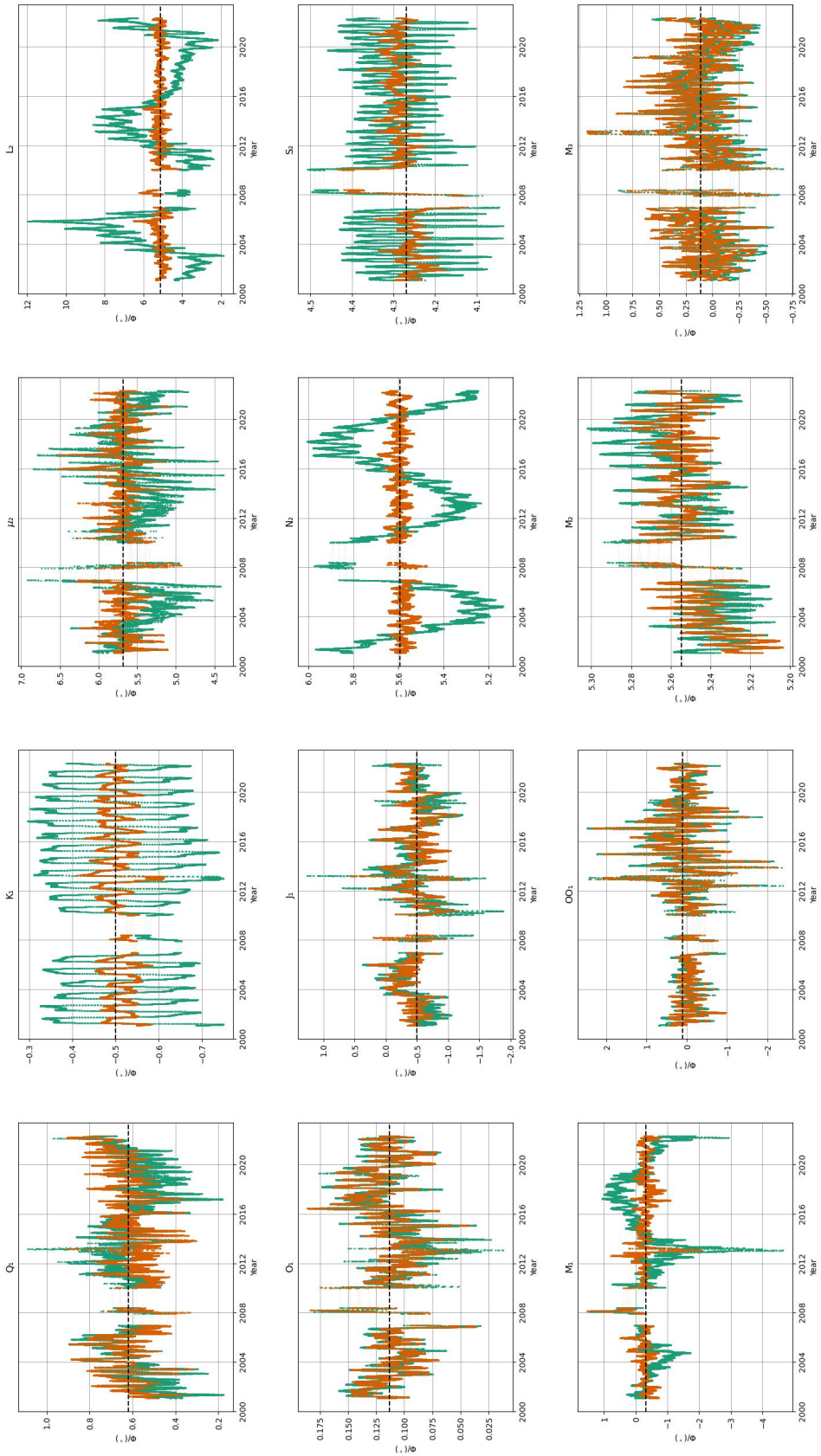

Figure C.22.: Diagrams with MWA estimates for gravimetric phases in Sutherland (lower sensor).

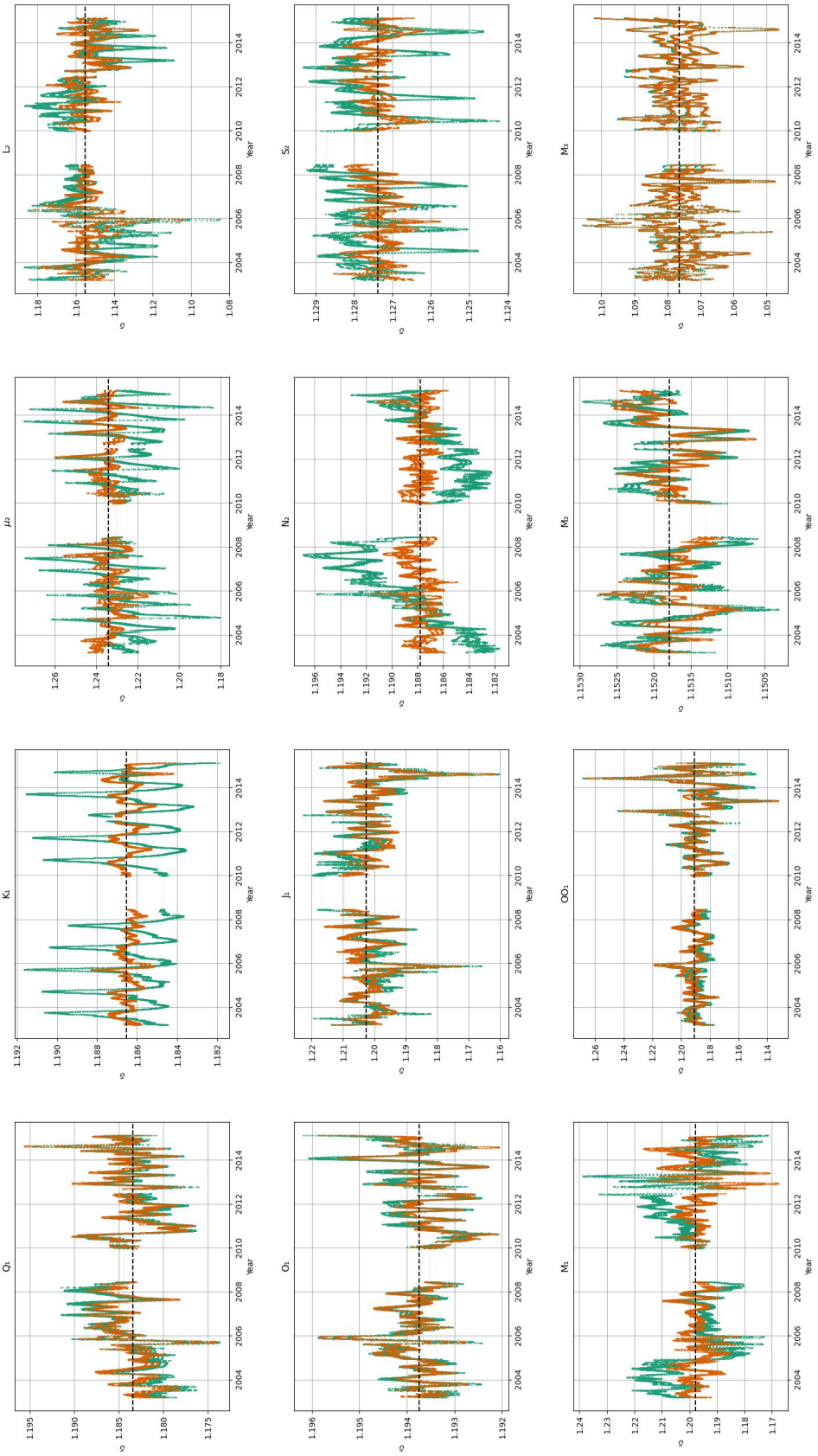

Figure C.23.: Diagrams with MWA estimates for gravimetric factors in Tigo-Concepcion.

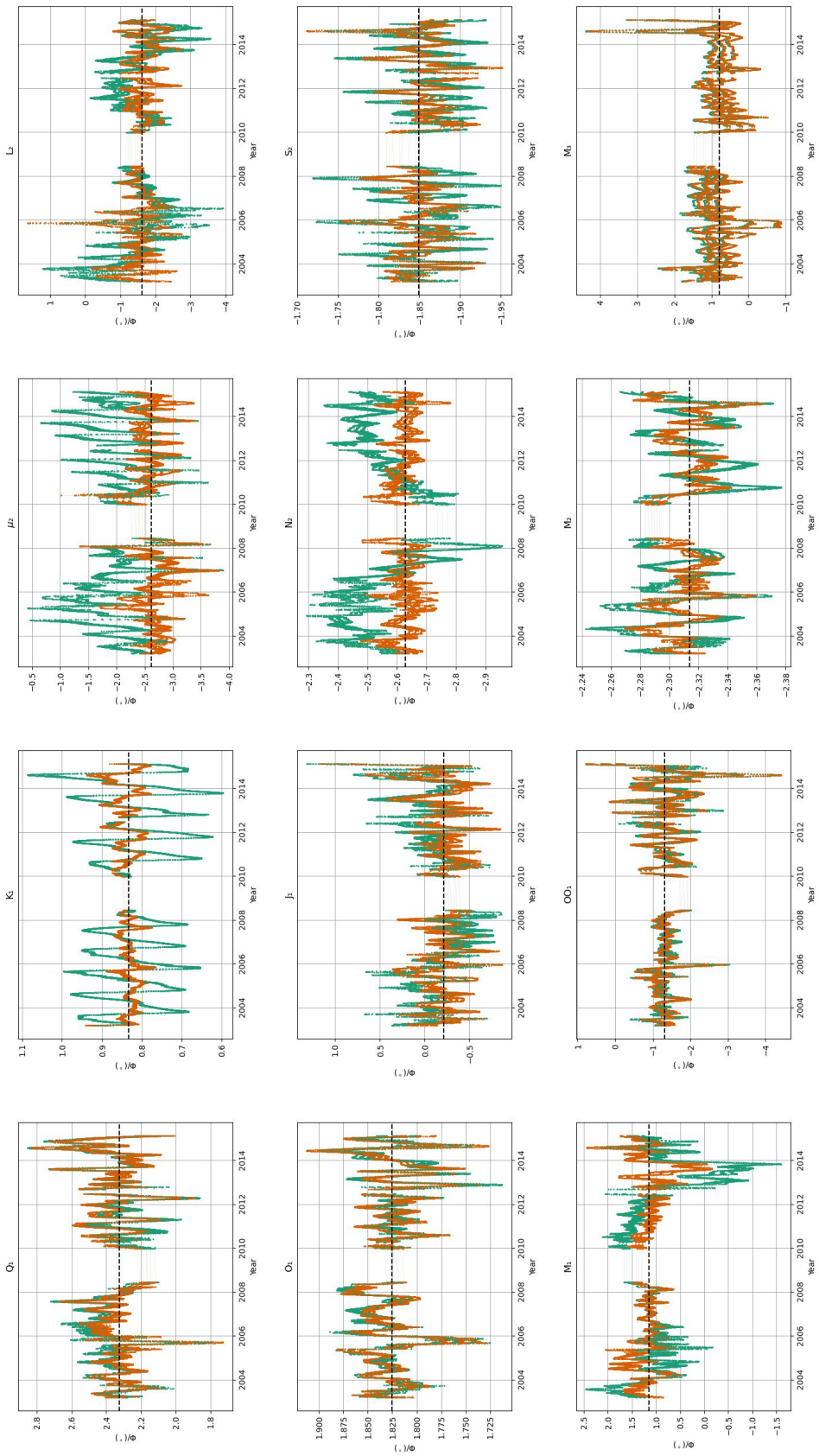

Figure C.24.: Diagrams with MWA estimates for gravimetric phases in Tigo-Concepcion.

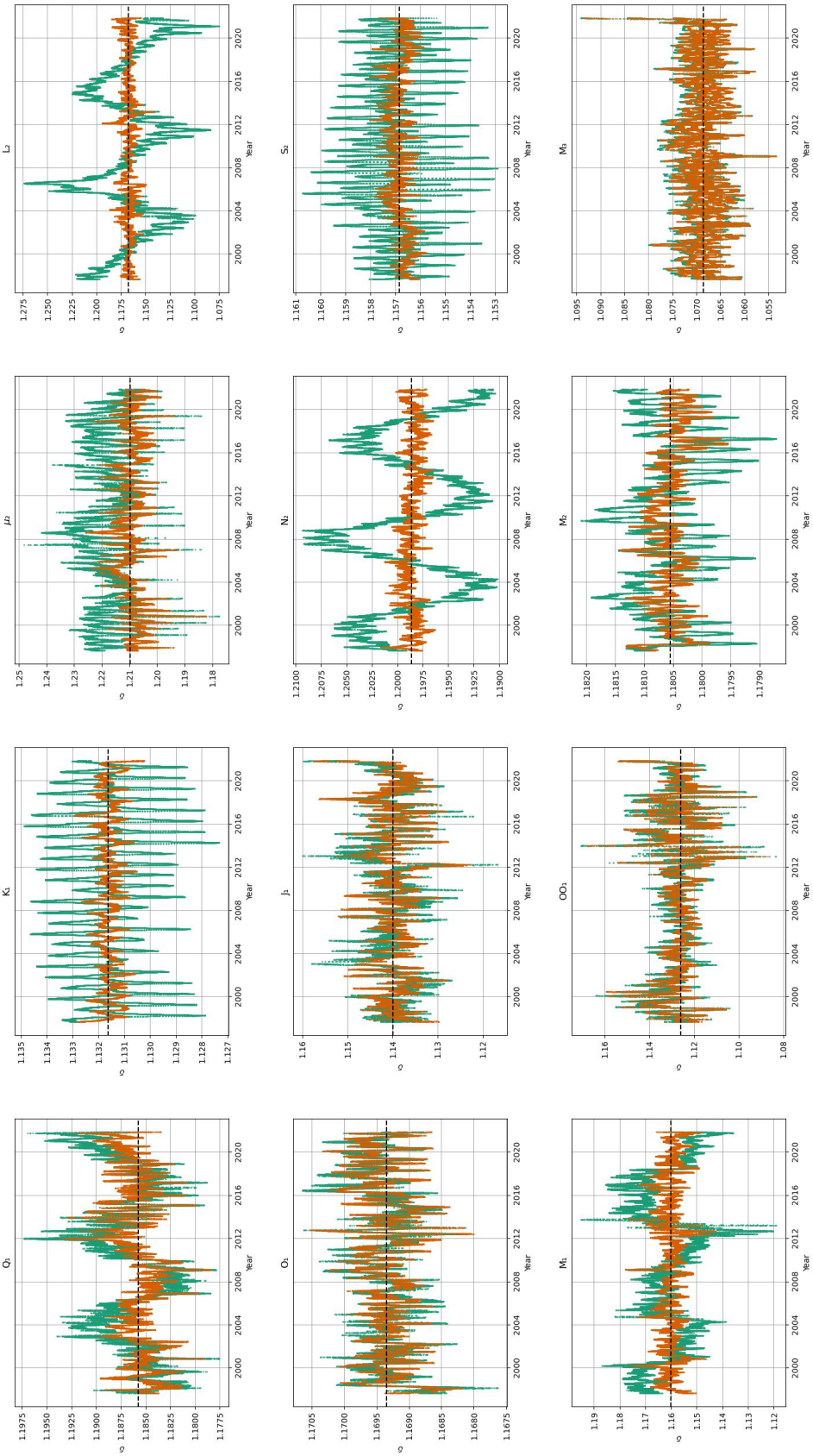

Figure C.25.: Diagrams with MWA estimates for gravimetric factors in Canberra.

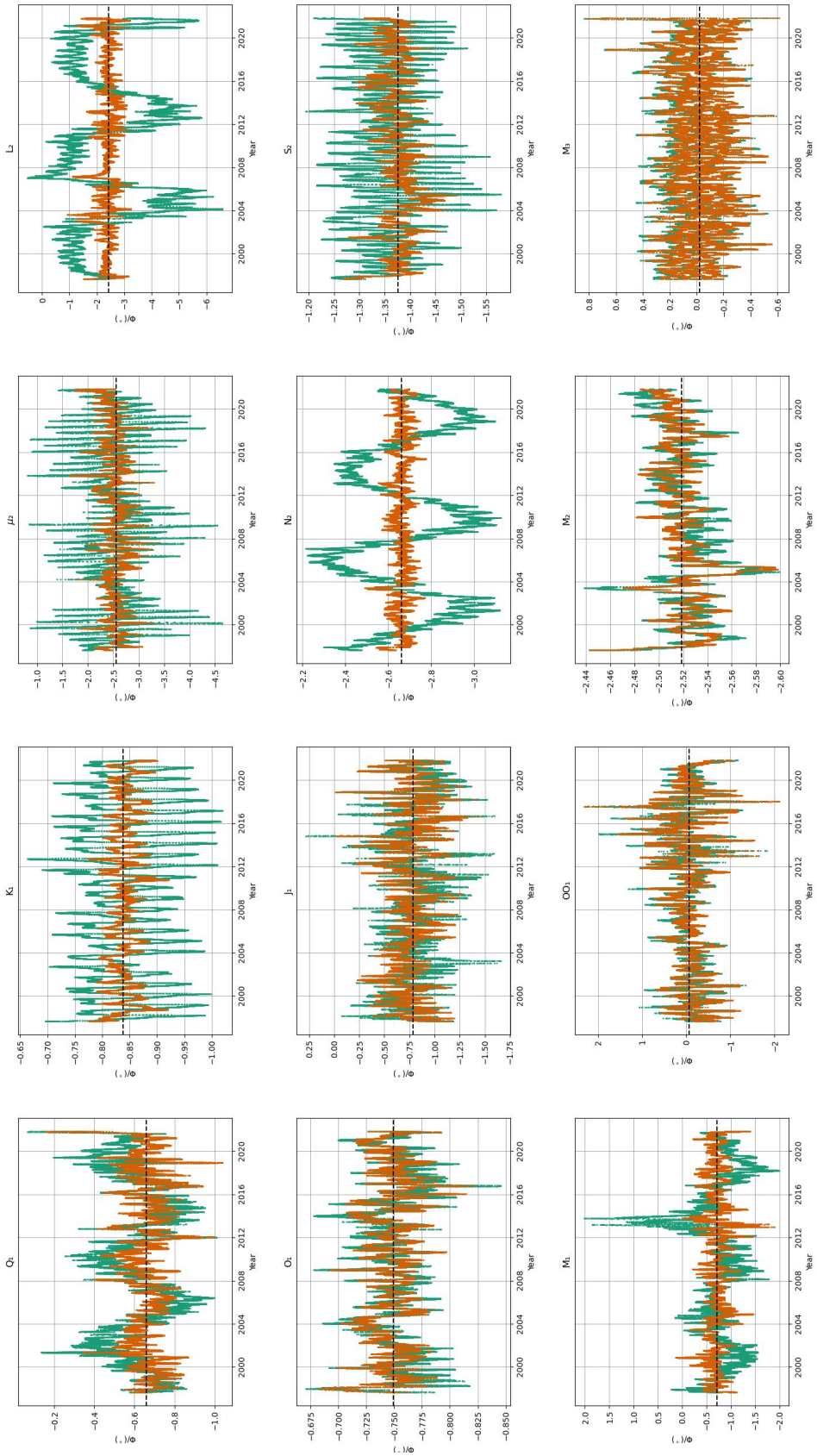

Figure C.26.: Diagrams with MWA estimates for gravimetric phases in Canberra.

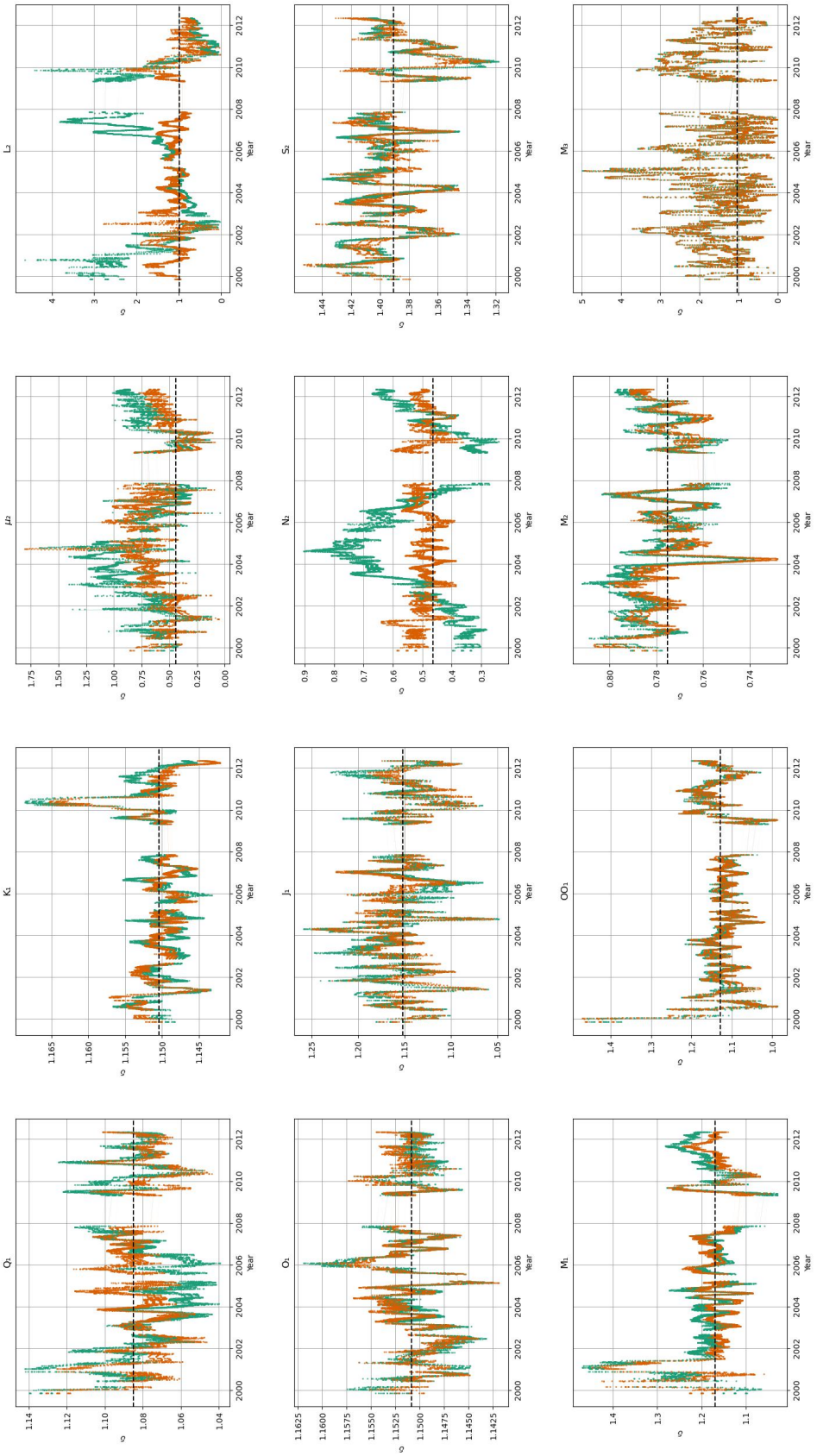

Figure C.27.: Diagrams with MWA estimates for gravimetric factors in Ny-Ålesund.

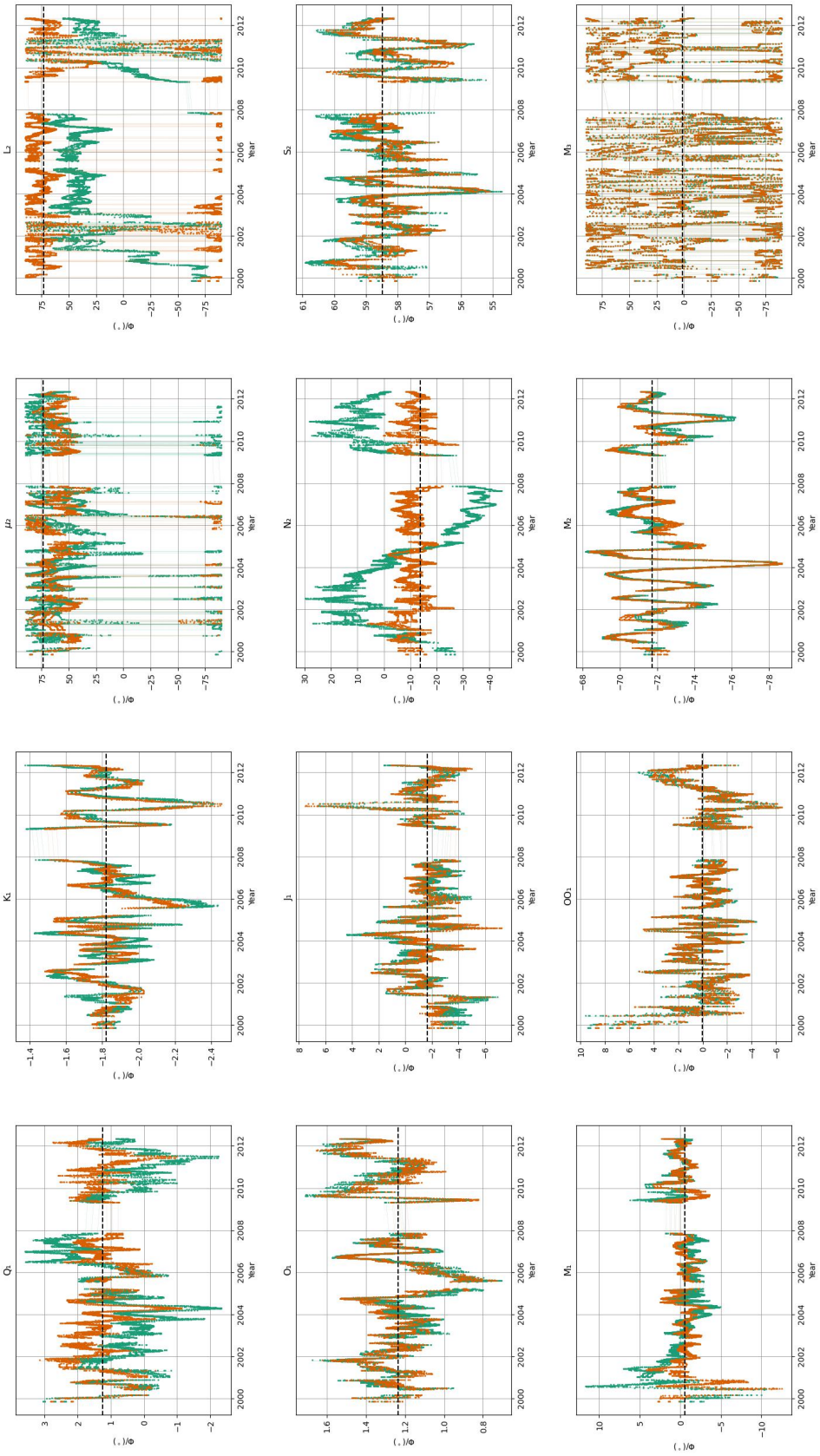

Figure C.28.: Diagrams with MWA estimates for gravimetric phases in Ny-Ålesund.

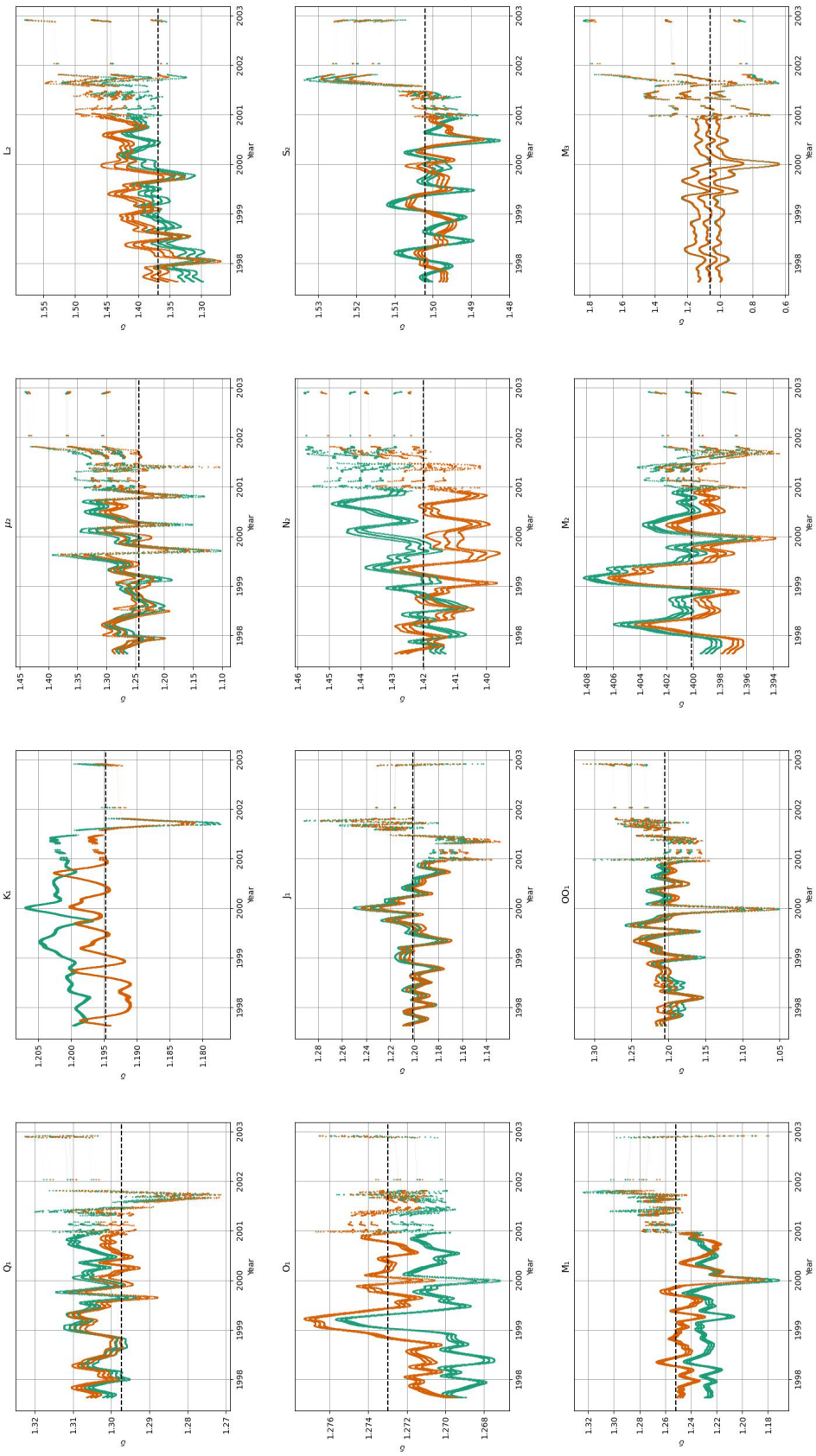

Figure C.29.: Diagrams with MWA estimates for gravimetric factors in Syowa.

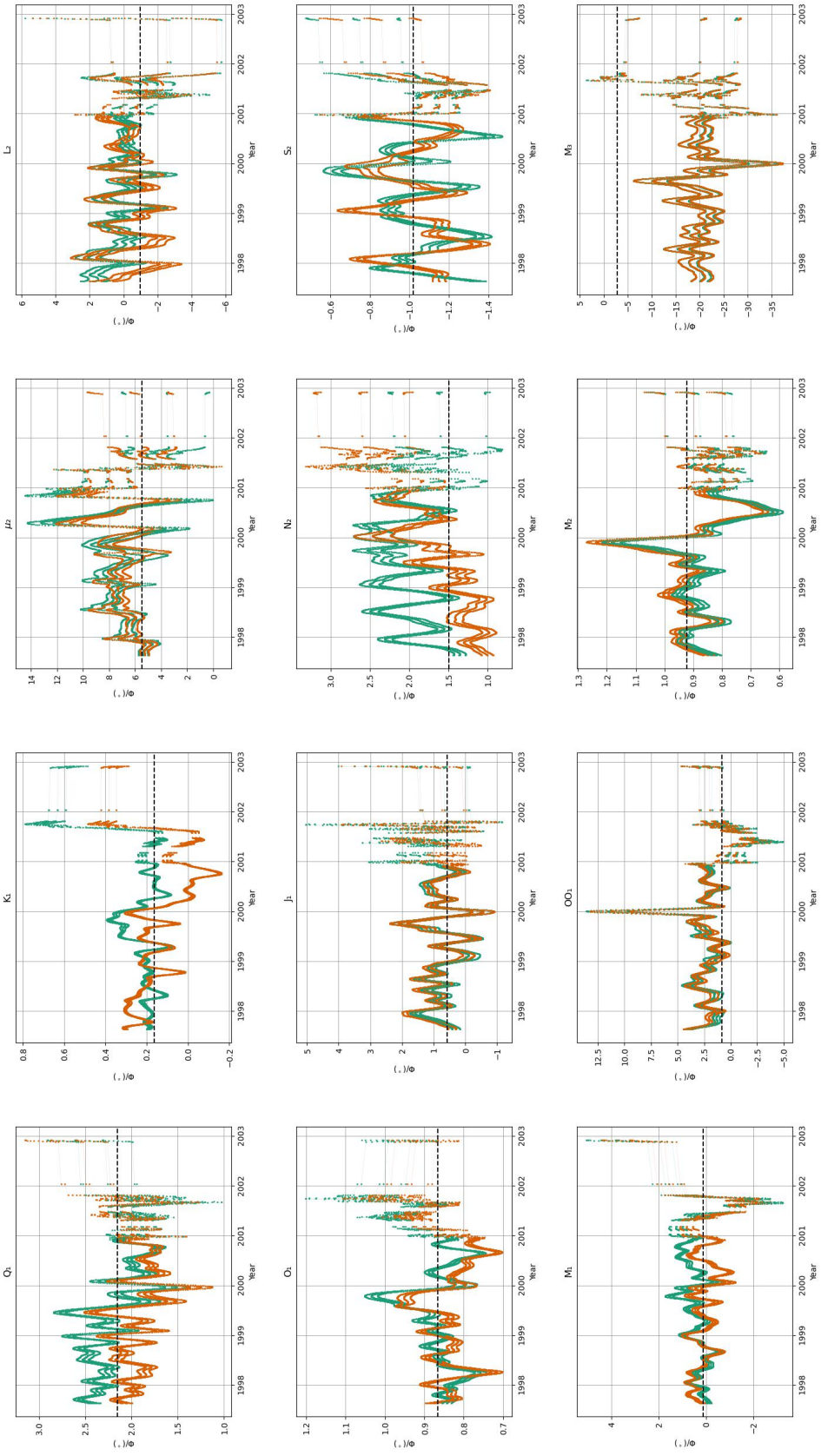

Figure C.30.: Diagrams with MWA estimates for gravimetric phases in Syowa.

D. Histograms

Compilation of histograms of MWA diagrams of investigated observatories. Green color corresponds to WDZe a priori model used in the analysis. Orange color corresponds to the LRM response model for a given station. The results are displayed with their physical meaning, i.e. gravimetric factor and phase.

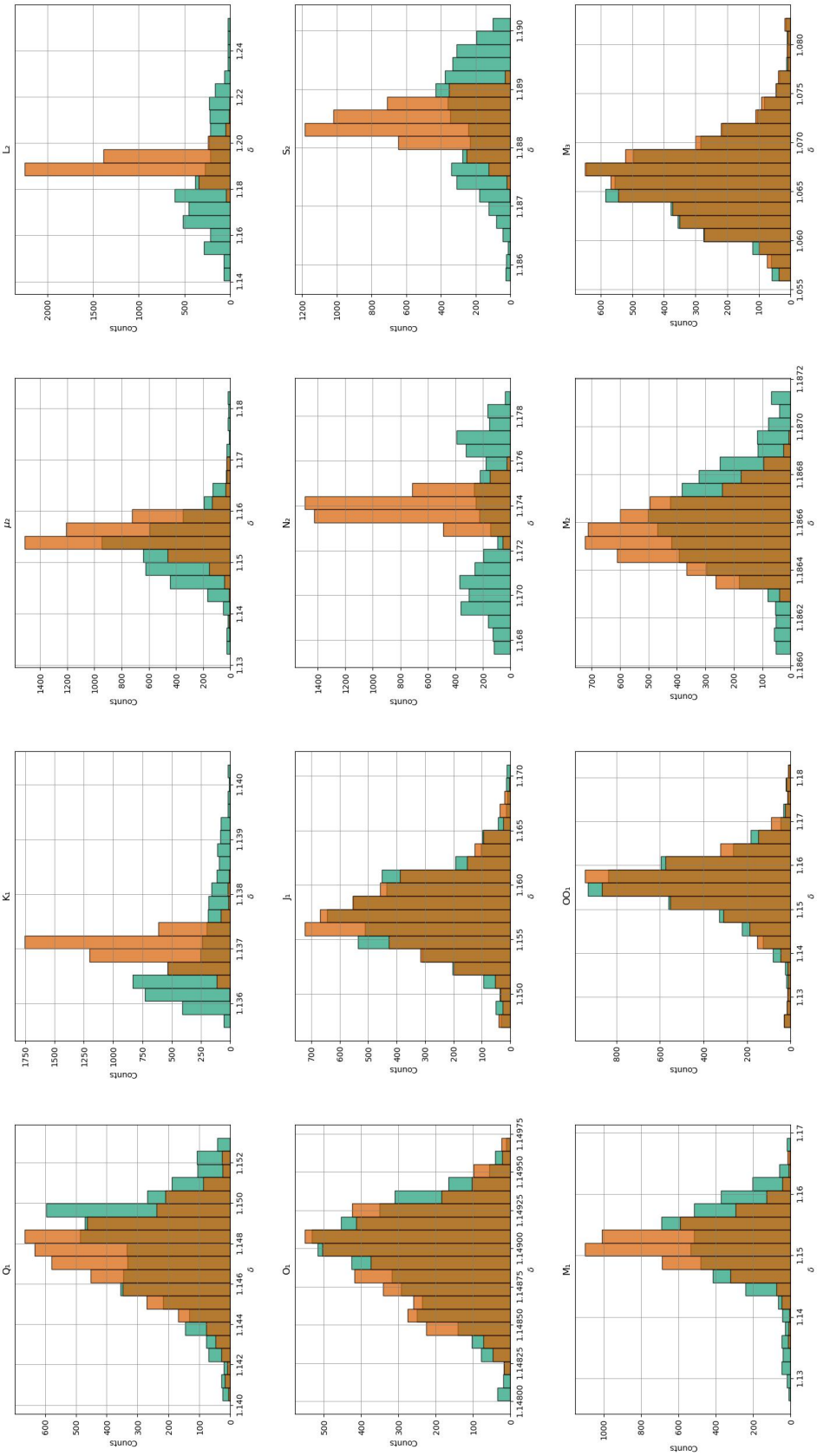

Figure D.1.: Histograms of MWA estimates for gravimetric factors in Black Forest Observatory (lower sensor).

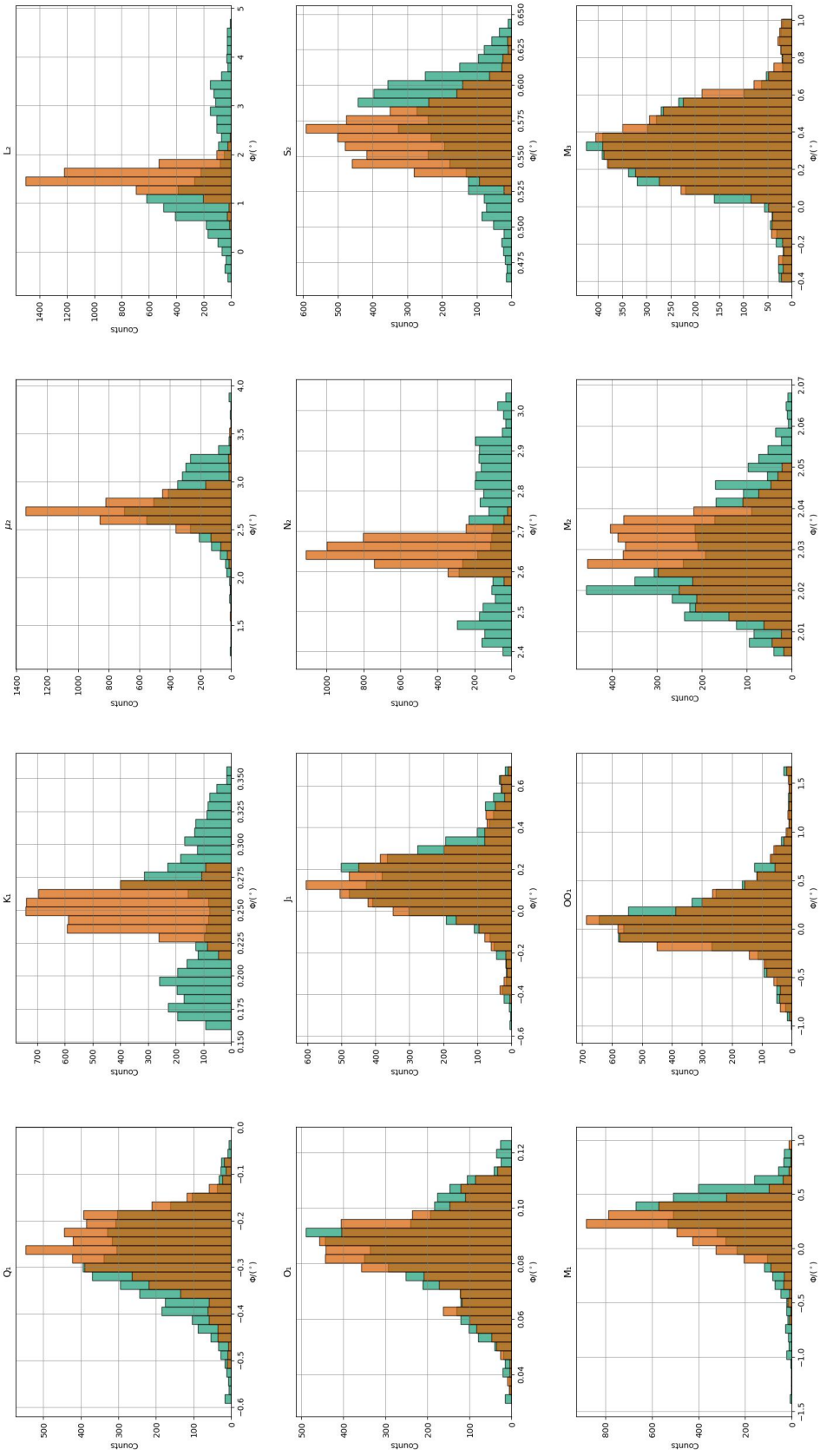

Figure D.2.: Histograms of MWA estimates for gravimetric phases in Black Forest Observatory (lower sensor).

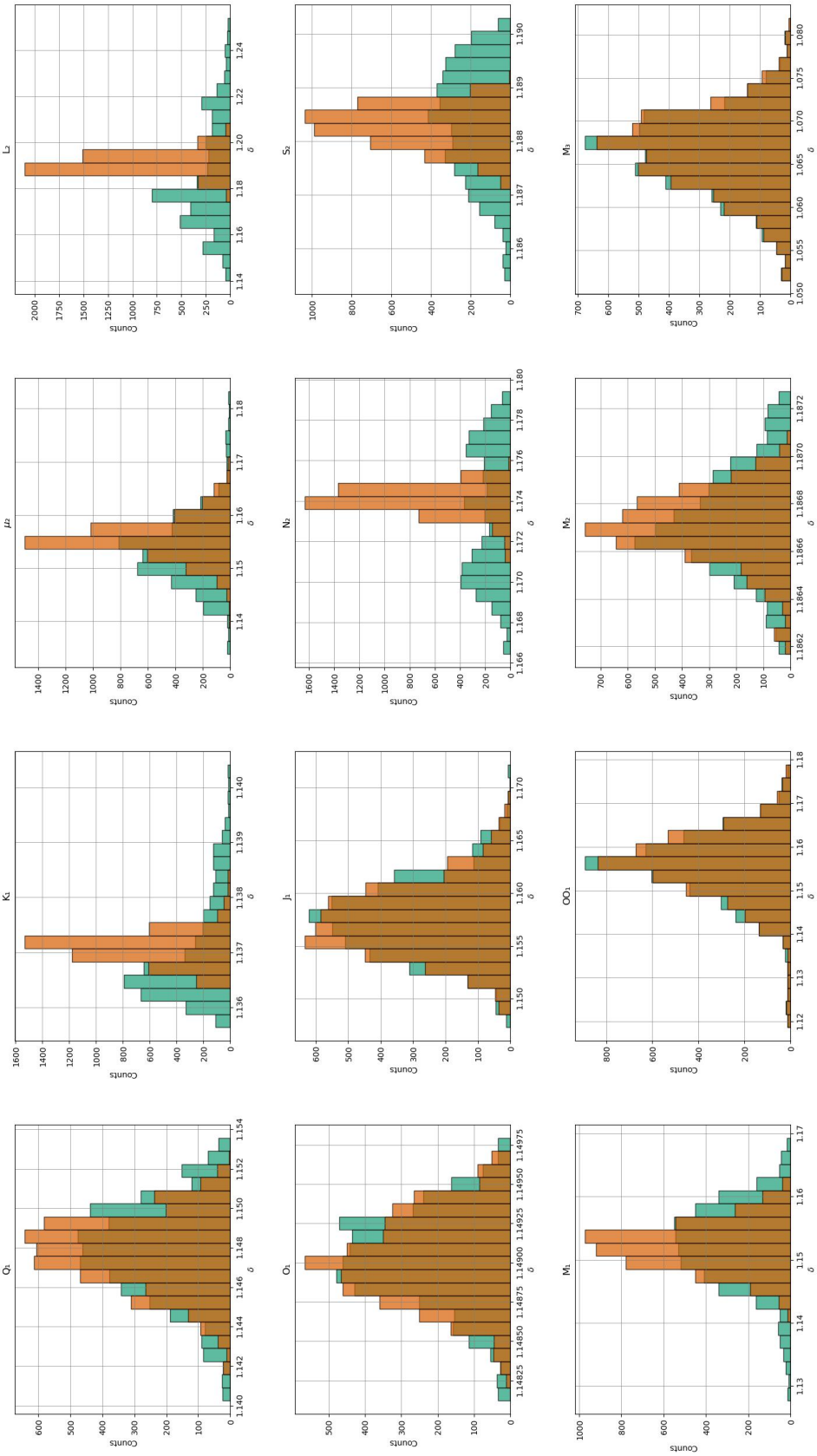

Figure D.3.: Histograms of MWA estimates for gravimetric factors in Black Forest Observatory (upper sensor).

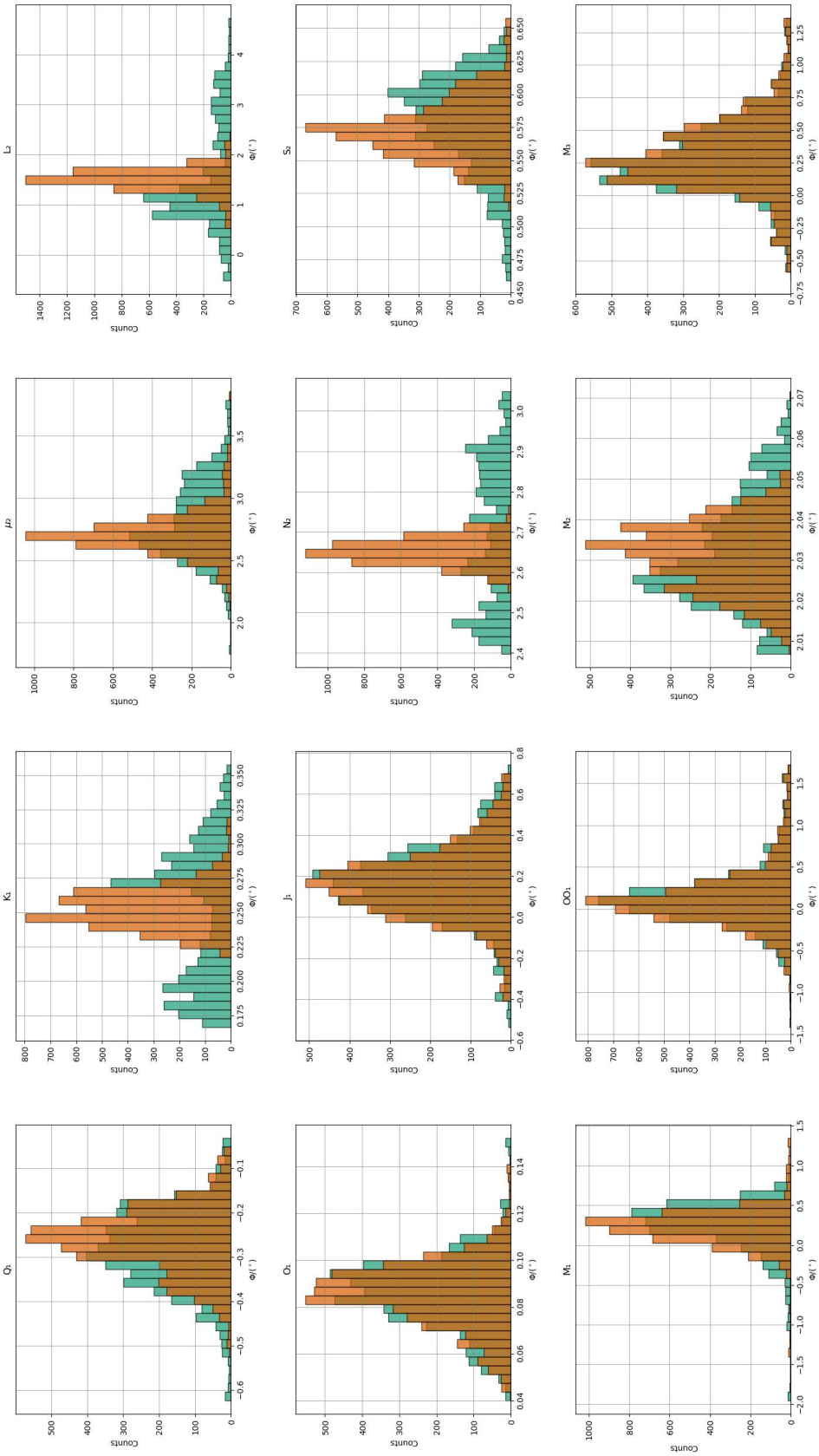

Figure D.4.: Histograms of MWA estimates for gravimetric phases in Black Forest Observatory (upper sensor).

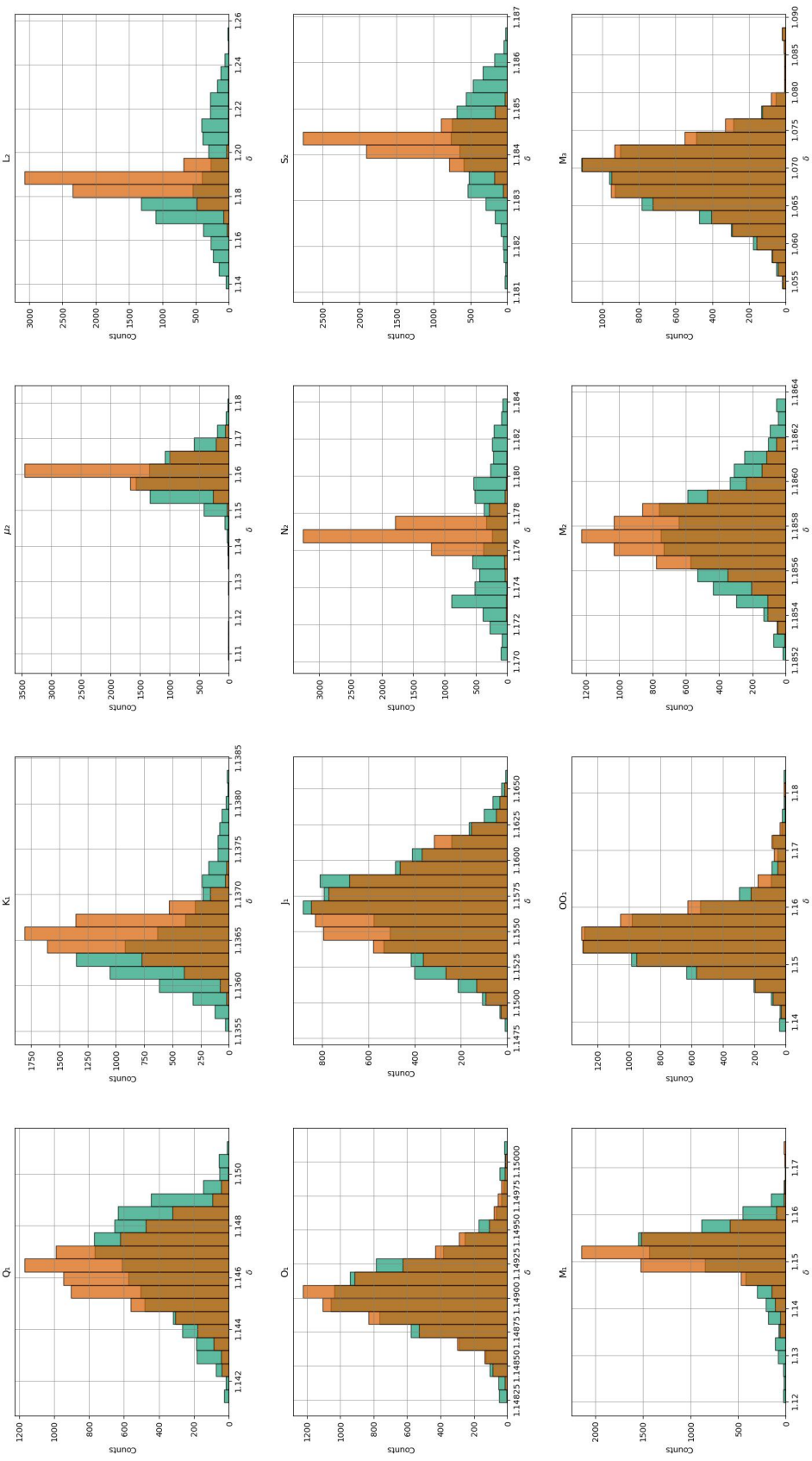

Figure D.5.: Histograms of MWA estimates for gravimetric factors in Moxa (lower sensor).

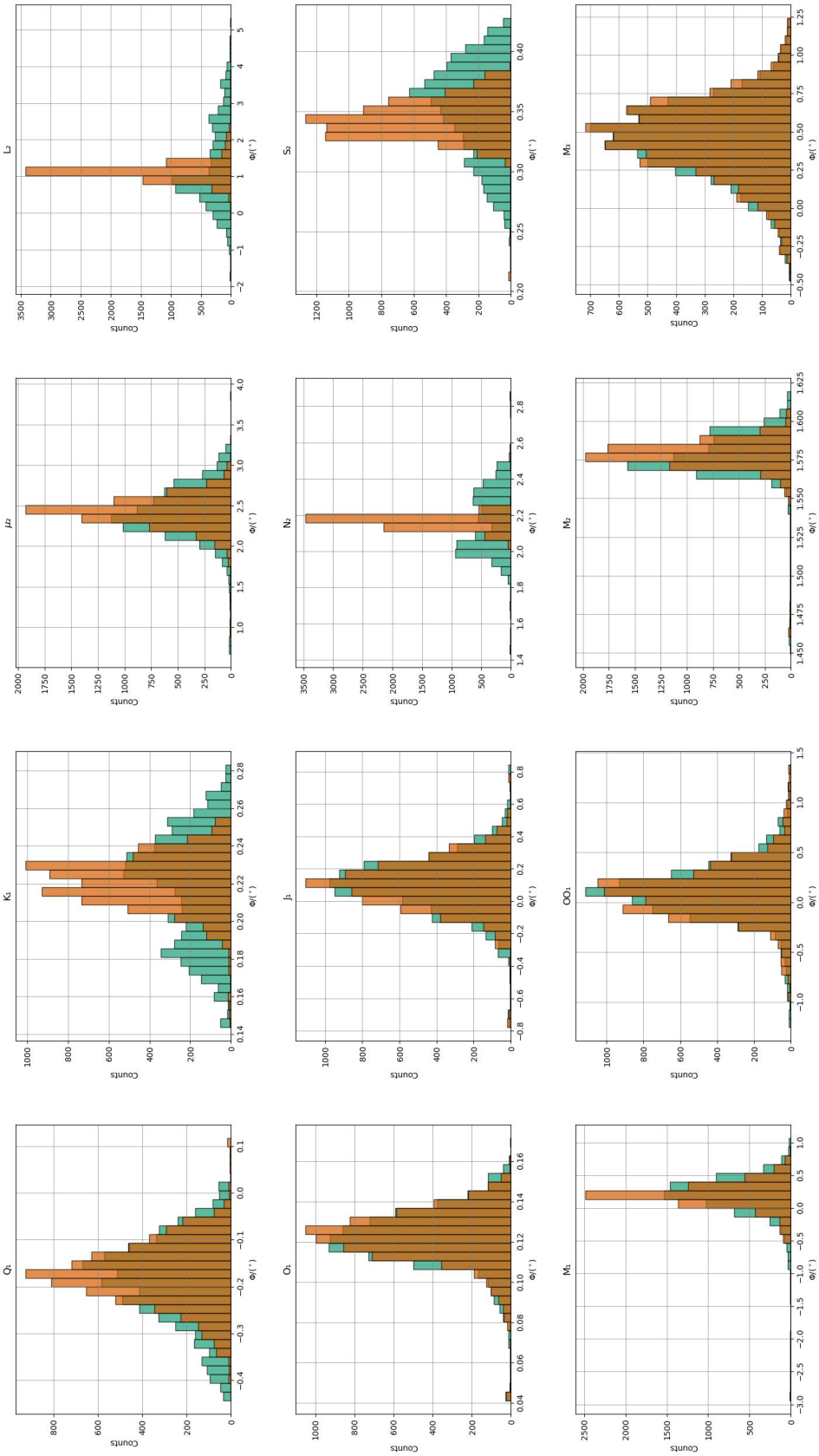

Figure D.6.: Histograms of MWA estimates for gravimetric phases in Moxa (lower sensor).

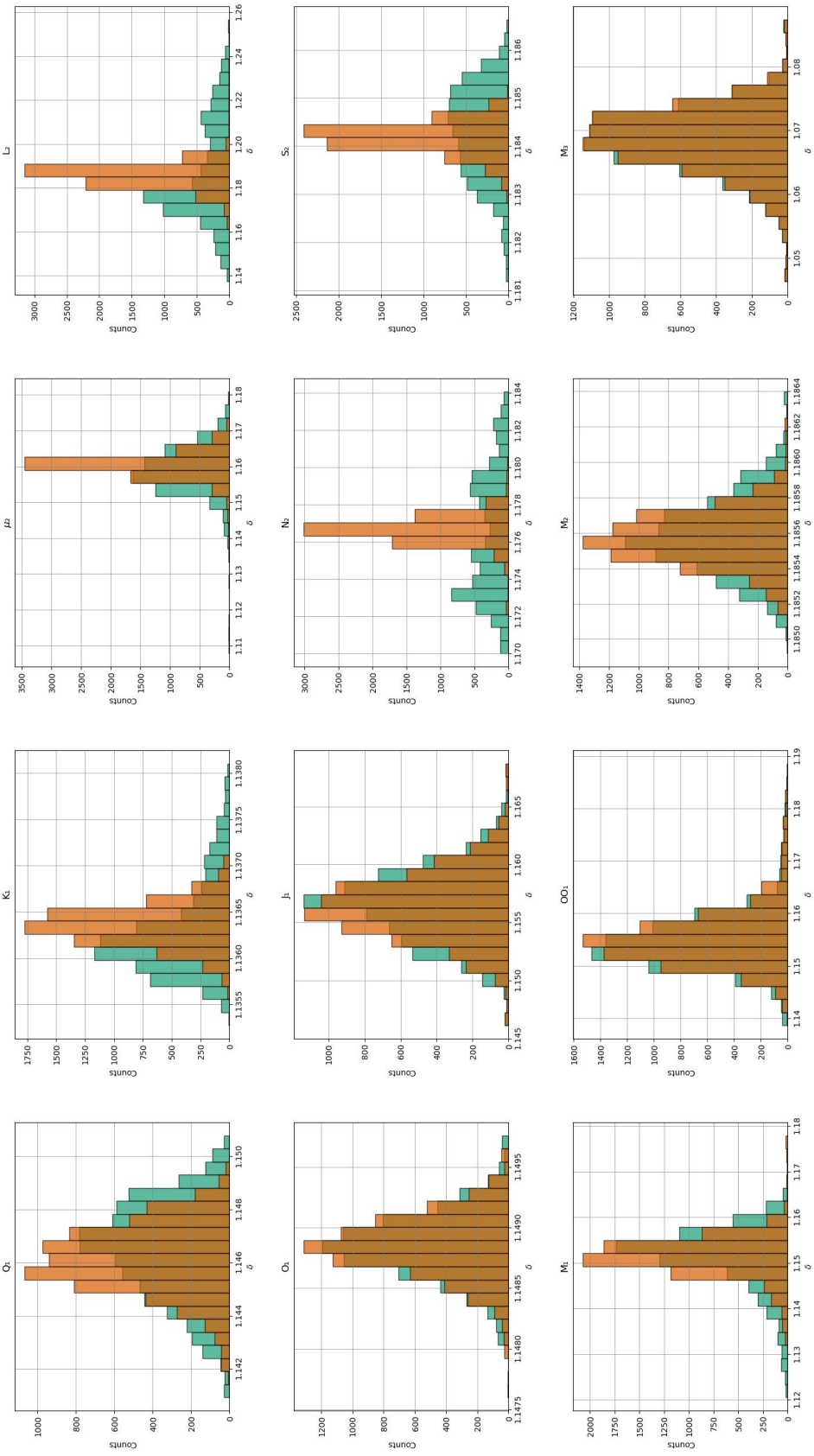

Figure D.7.: Histograms of MWA estimates for gravimetric factors in Moxa (upper sensor).

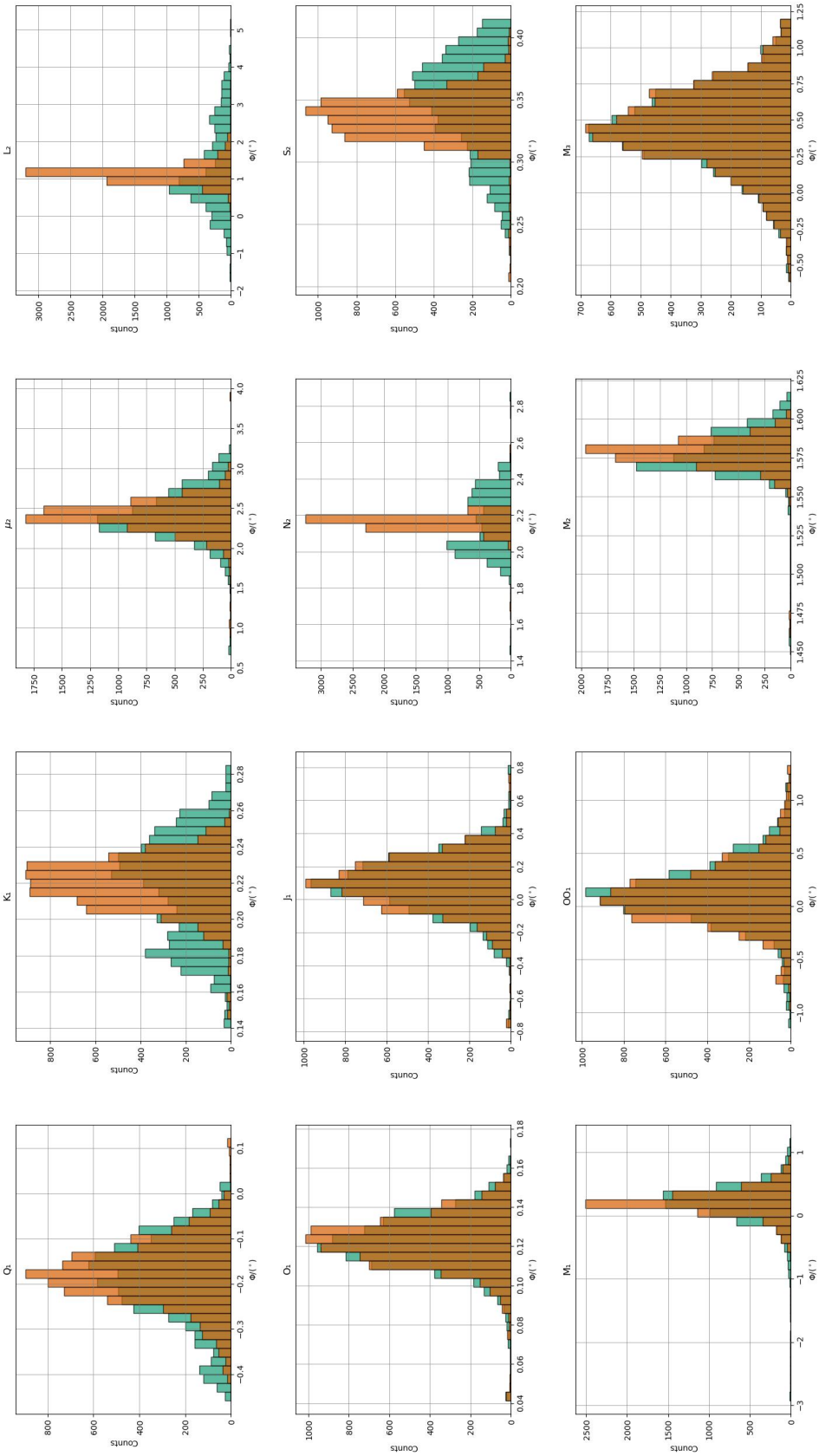

Figure D.8.: Histograms of MWA estimates for gravimetric phases in Moxa (upper sensor).

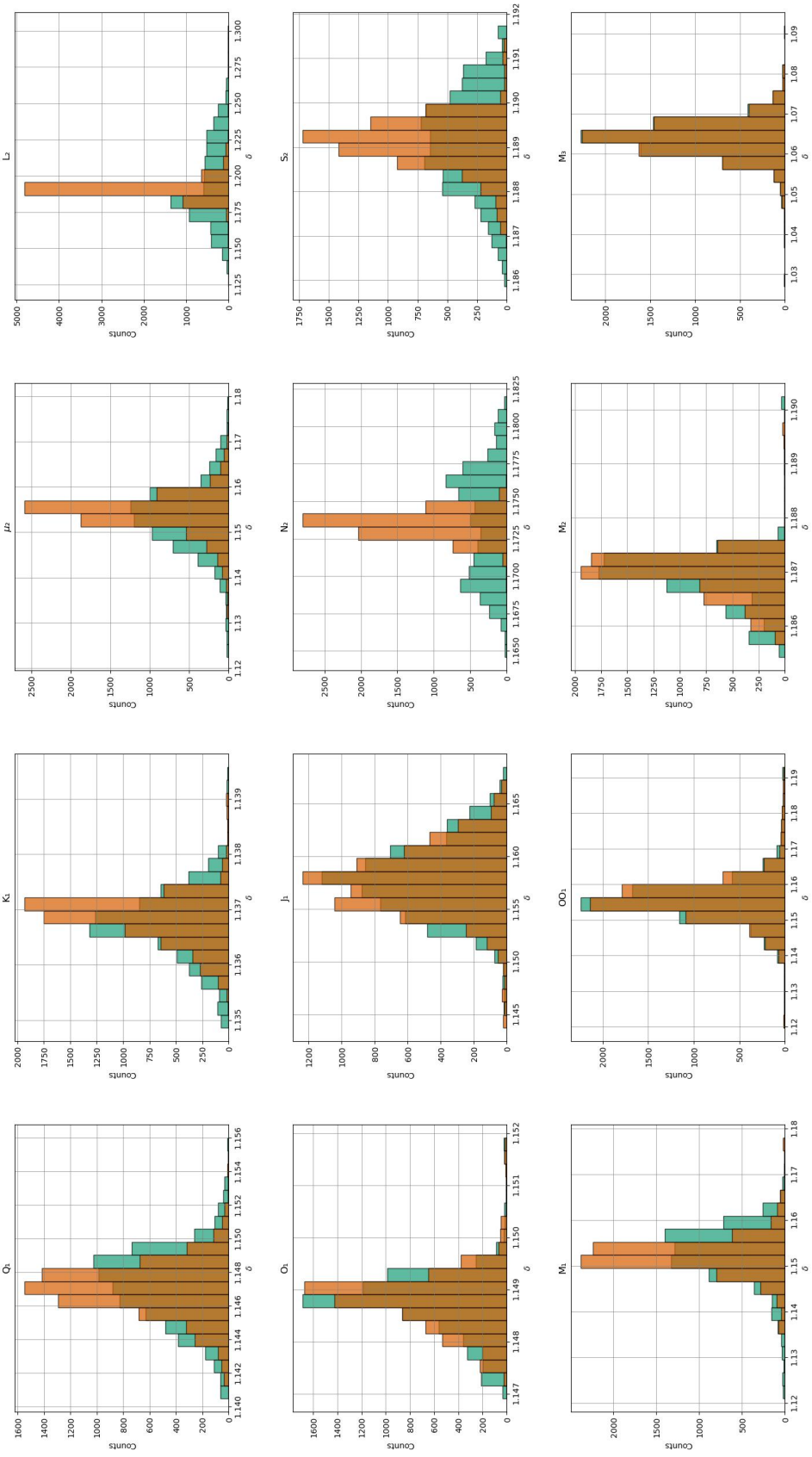

Figure D.9.: Histograms of MWA estimates for gravimetric factors in Strasbourg.

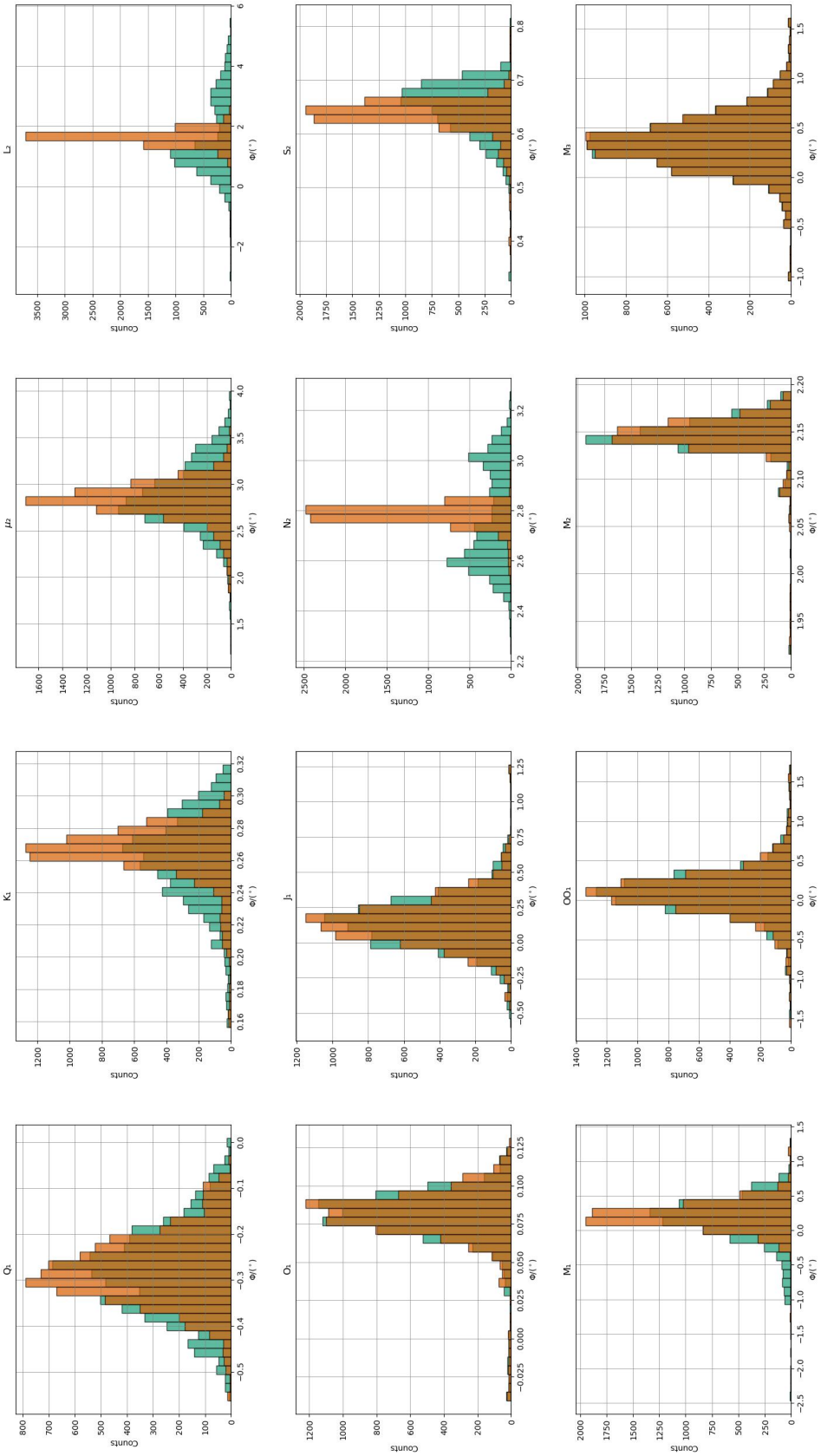

Figure D.10.: Histograms of MWA estimates for gravimetric phases in Strasbourg.

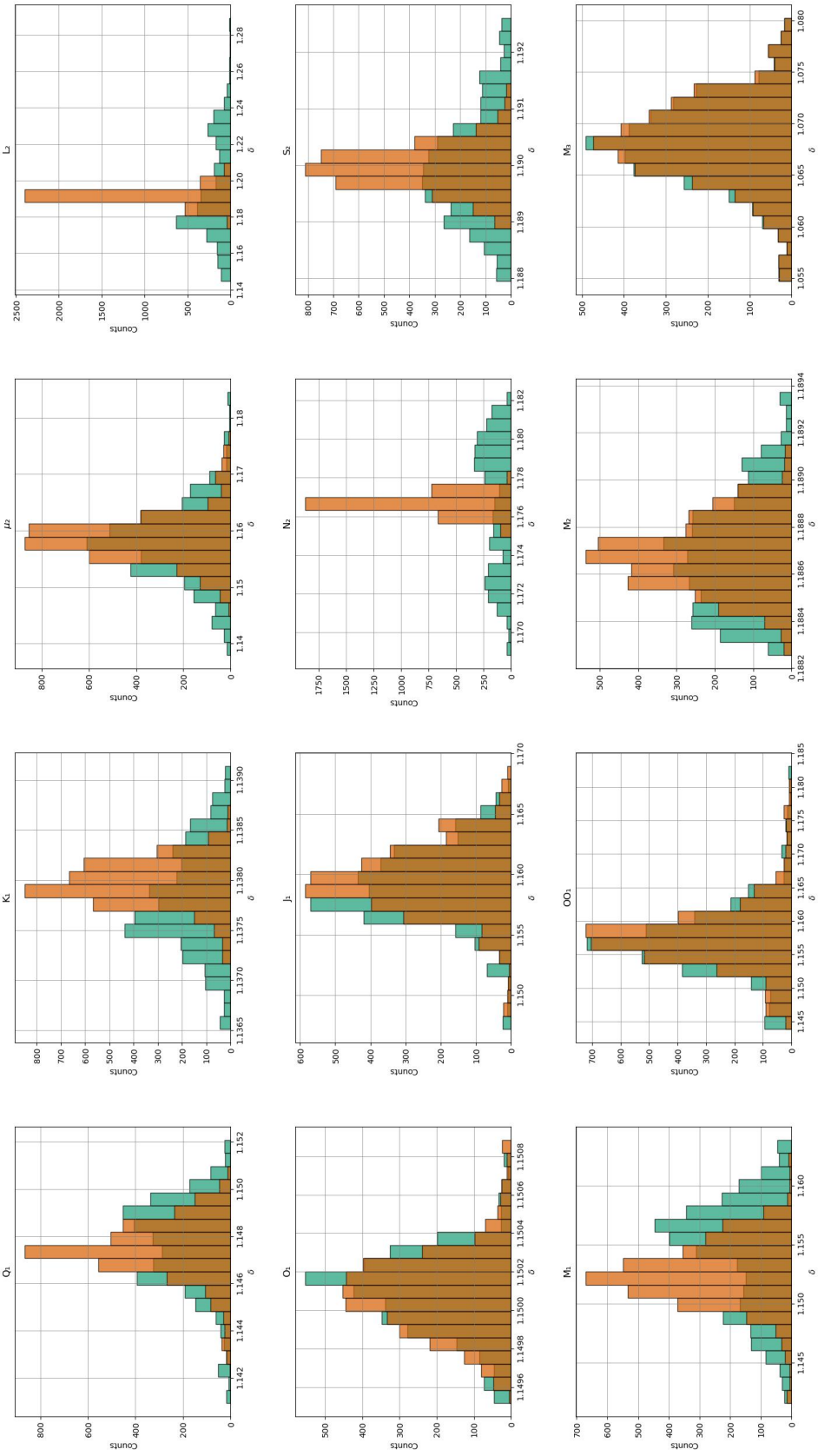

Figure D.11.: Histograms of MWA estimates for gravimetric factors in Bad Homburg.

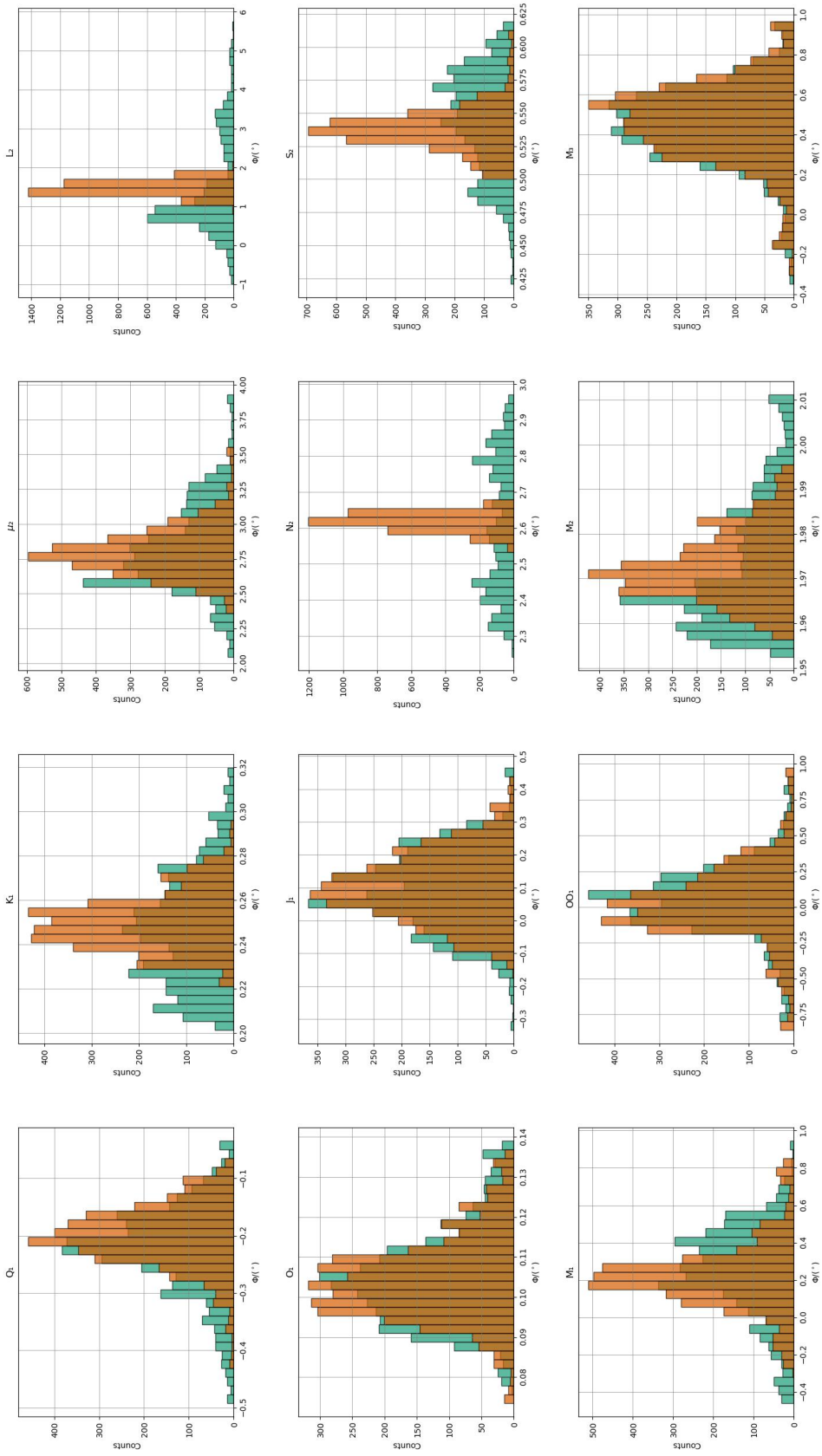

Figure D.12.: Histograms of MWA estimates for gravimetric phases in Bad Homburg.

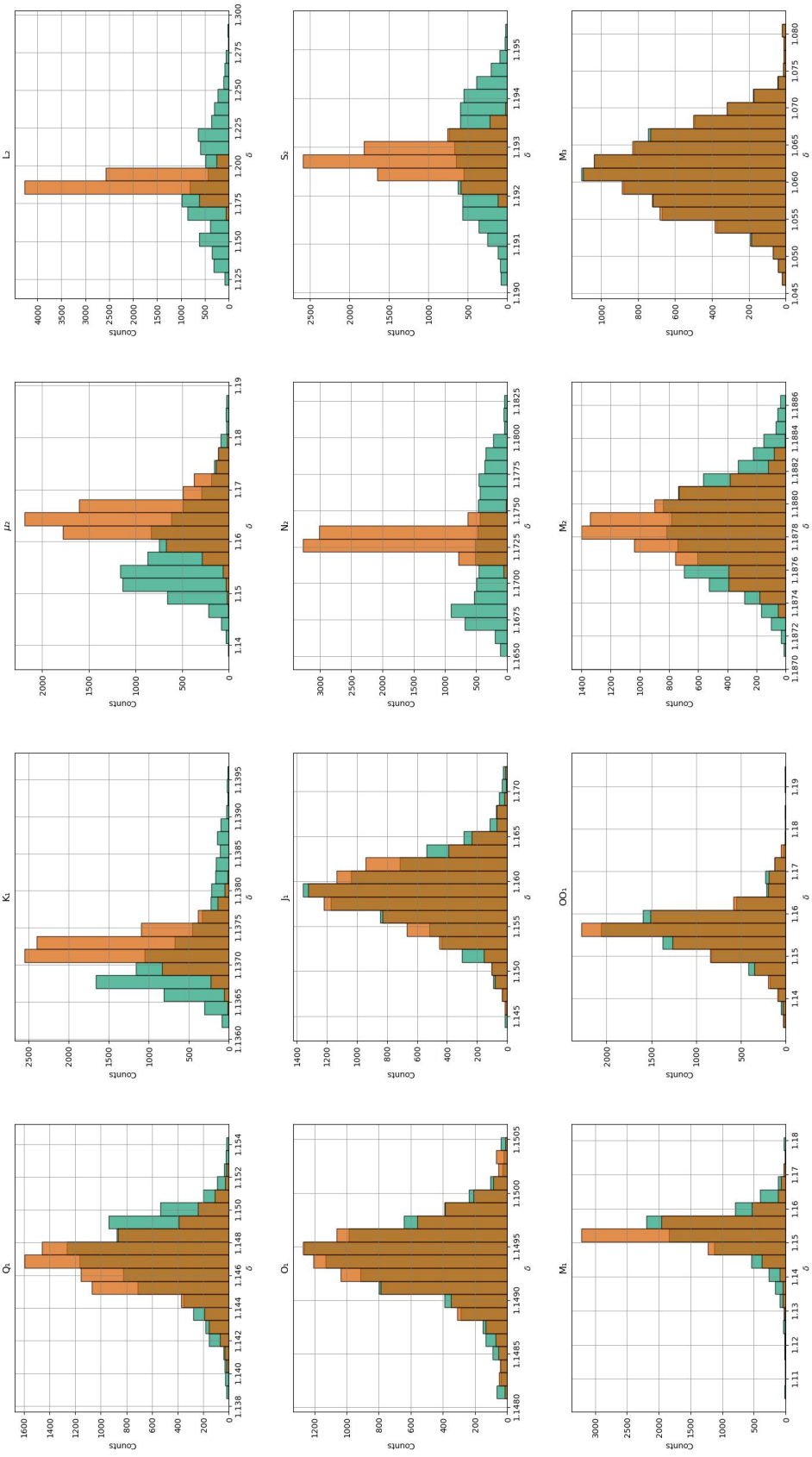

Figure D.13.: Histograms of MWA estimates for gravimetric factors in Membach.

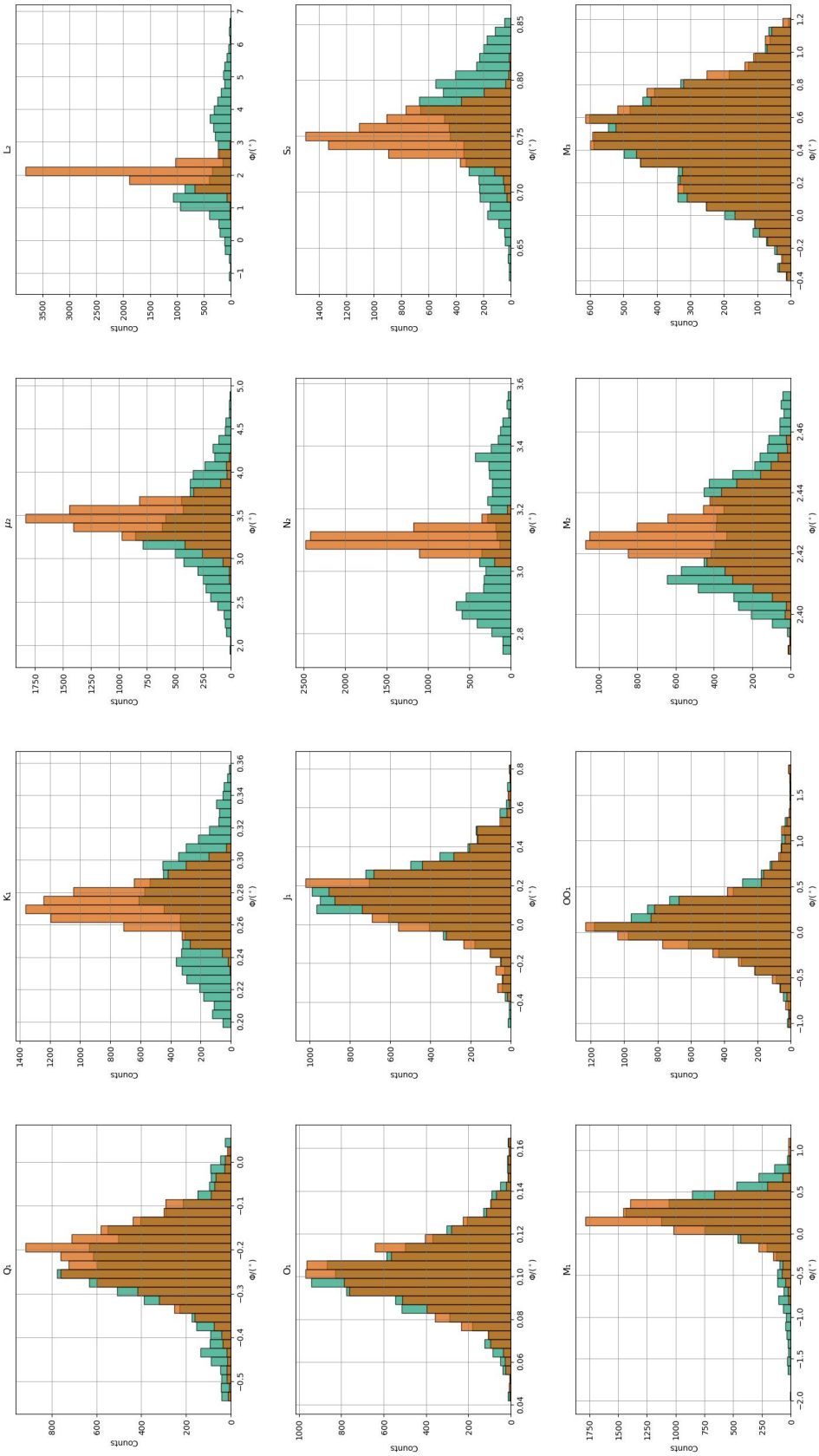

Figure D.14.: Histograms of MWA estimates for gravimetric phases in Membach.

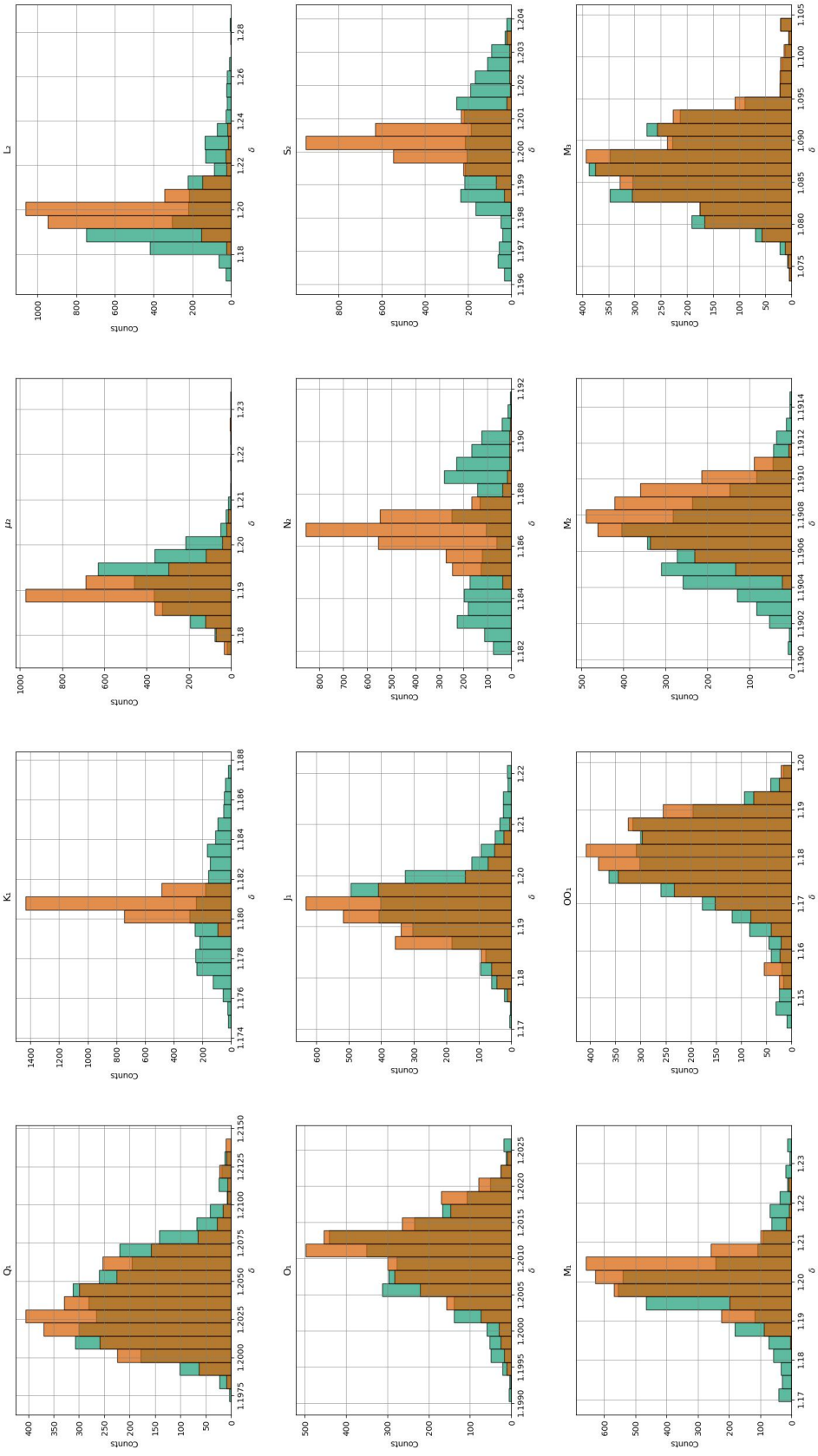

Figure D.15.: Histograms of MWA estimates for gravimetric factors in Kamioka.

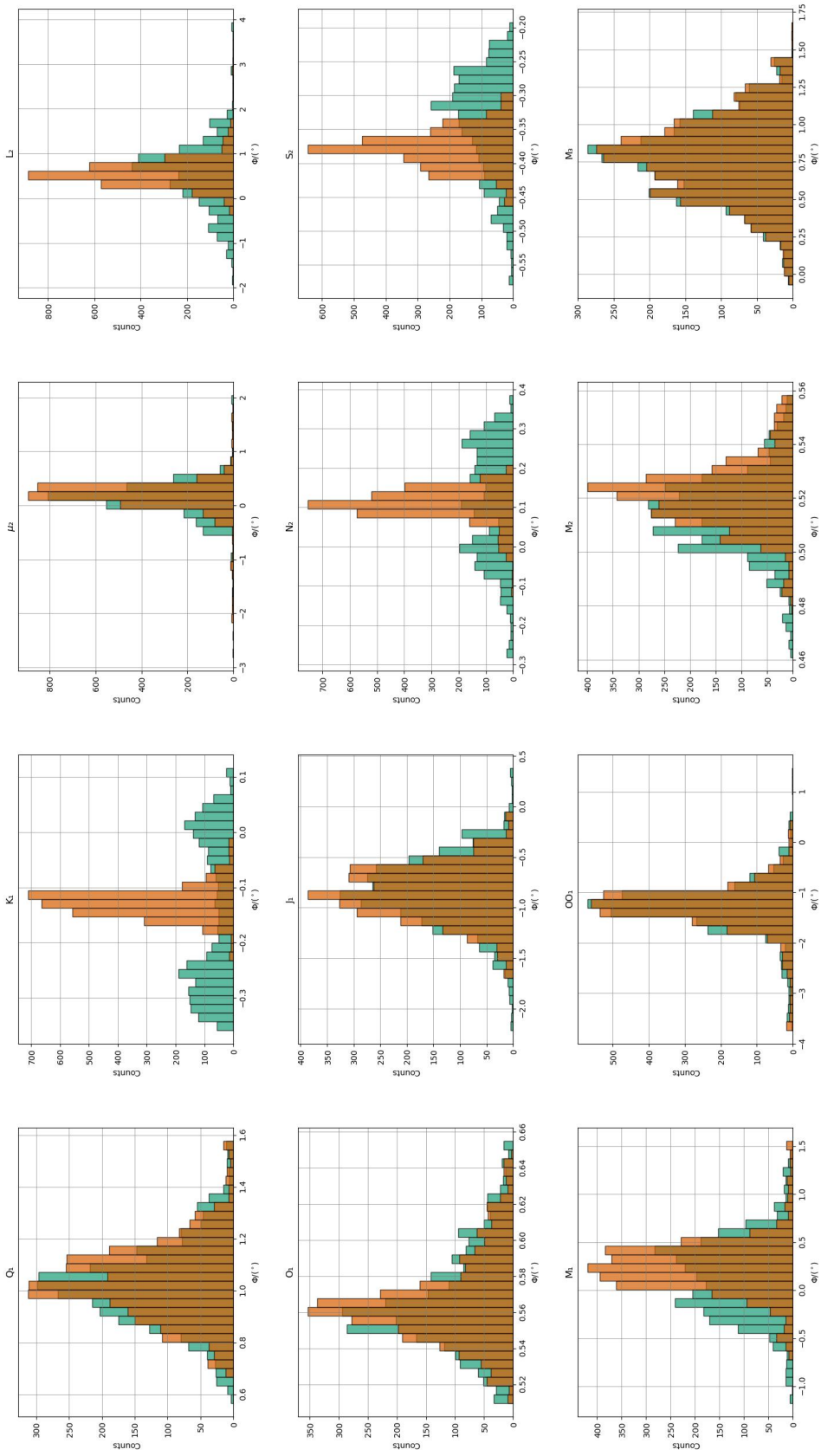

Figure D.16.: Histograms of MWA estimates for gravimetric phases in Kamioka.

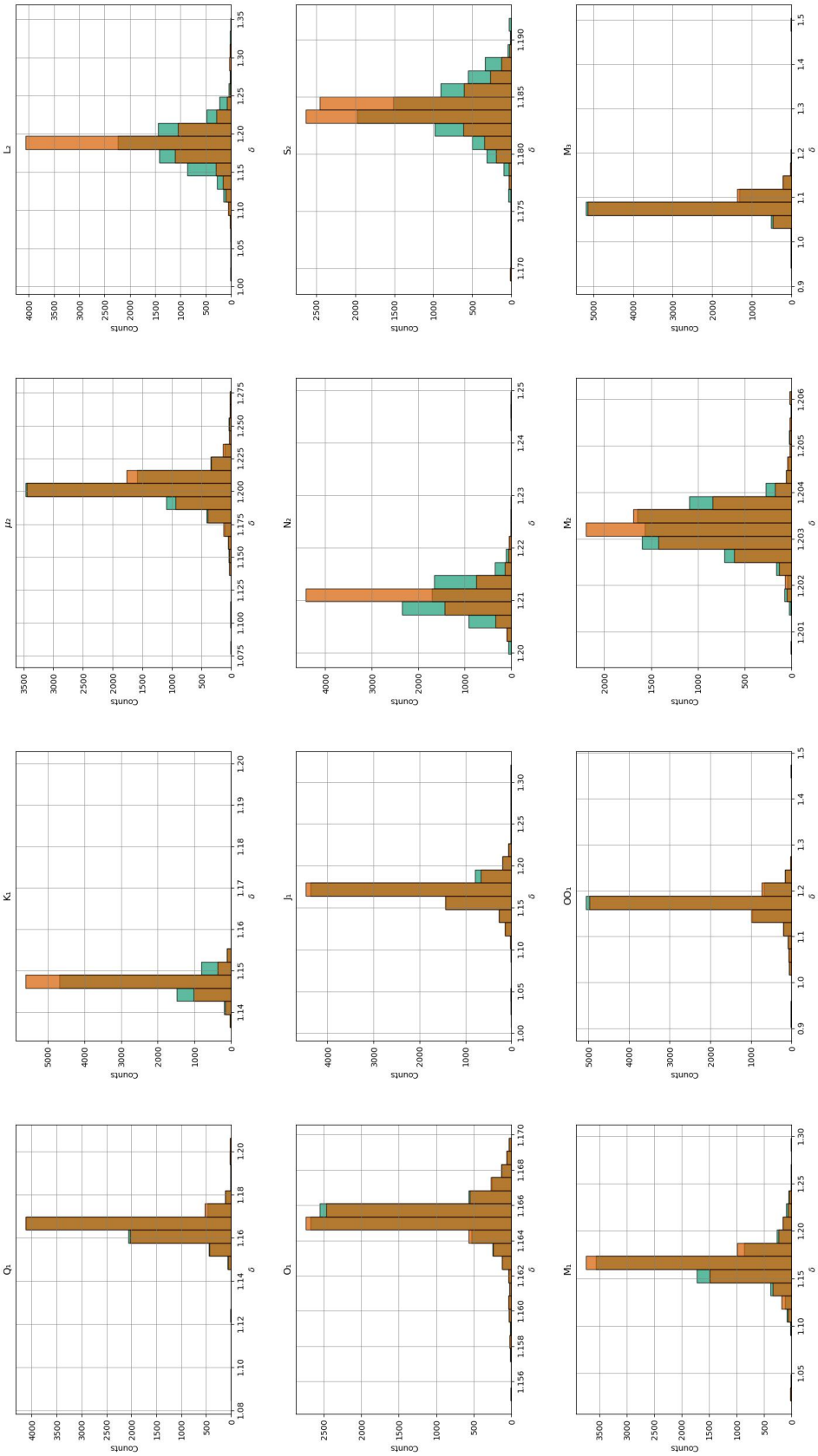

Figure D.17.: Histograms of MWA estimates for gravimetric factors in Cantley.

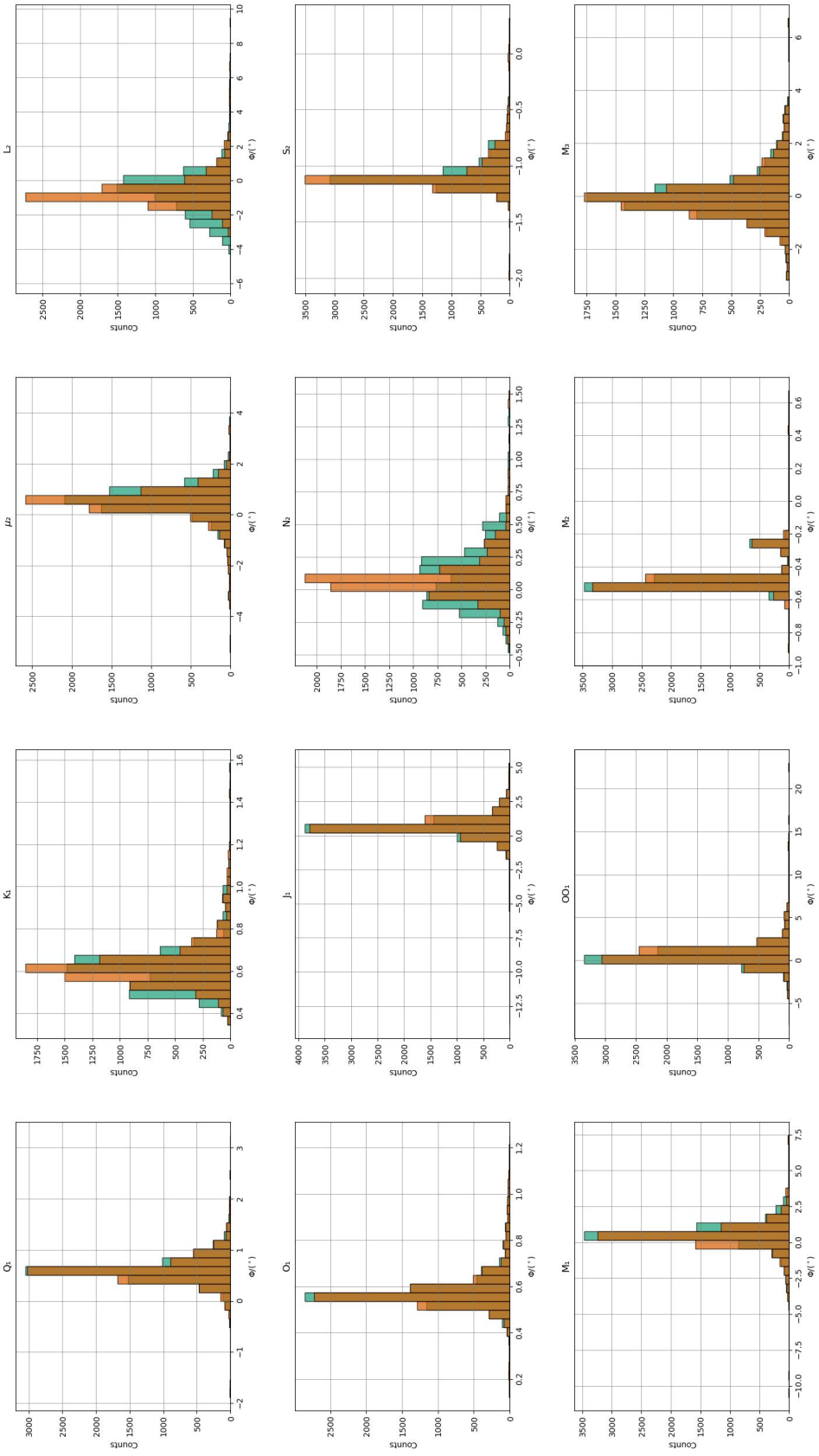

Figure D.18.: Histograms of MWA estimates for gravimetric phases in Cantley.

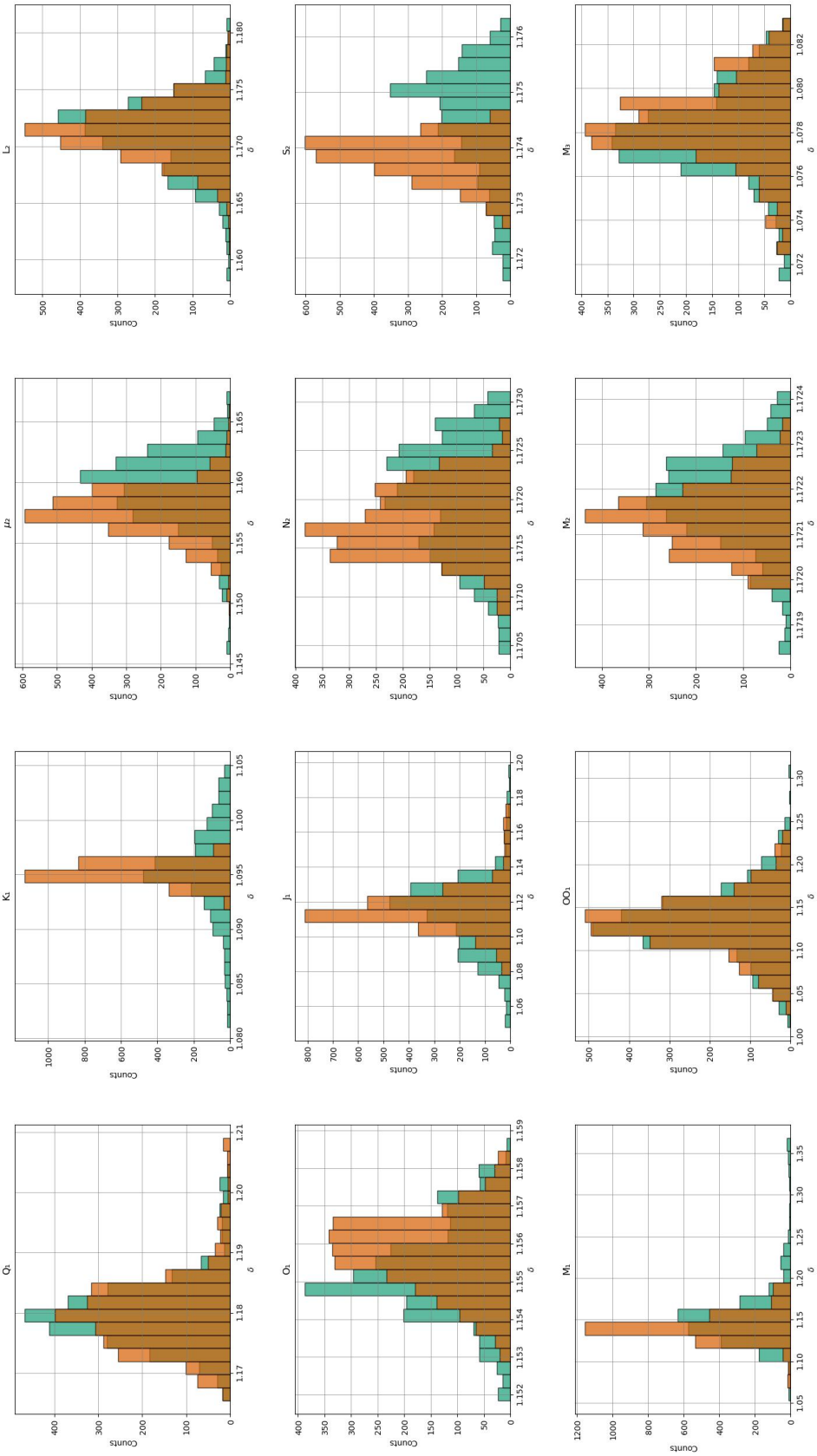

Figure D.19.: Histograms of MWA estimates for gravimetric factors in Djougou.

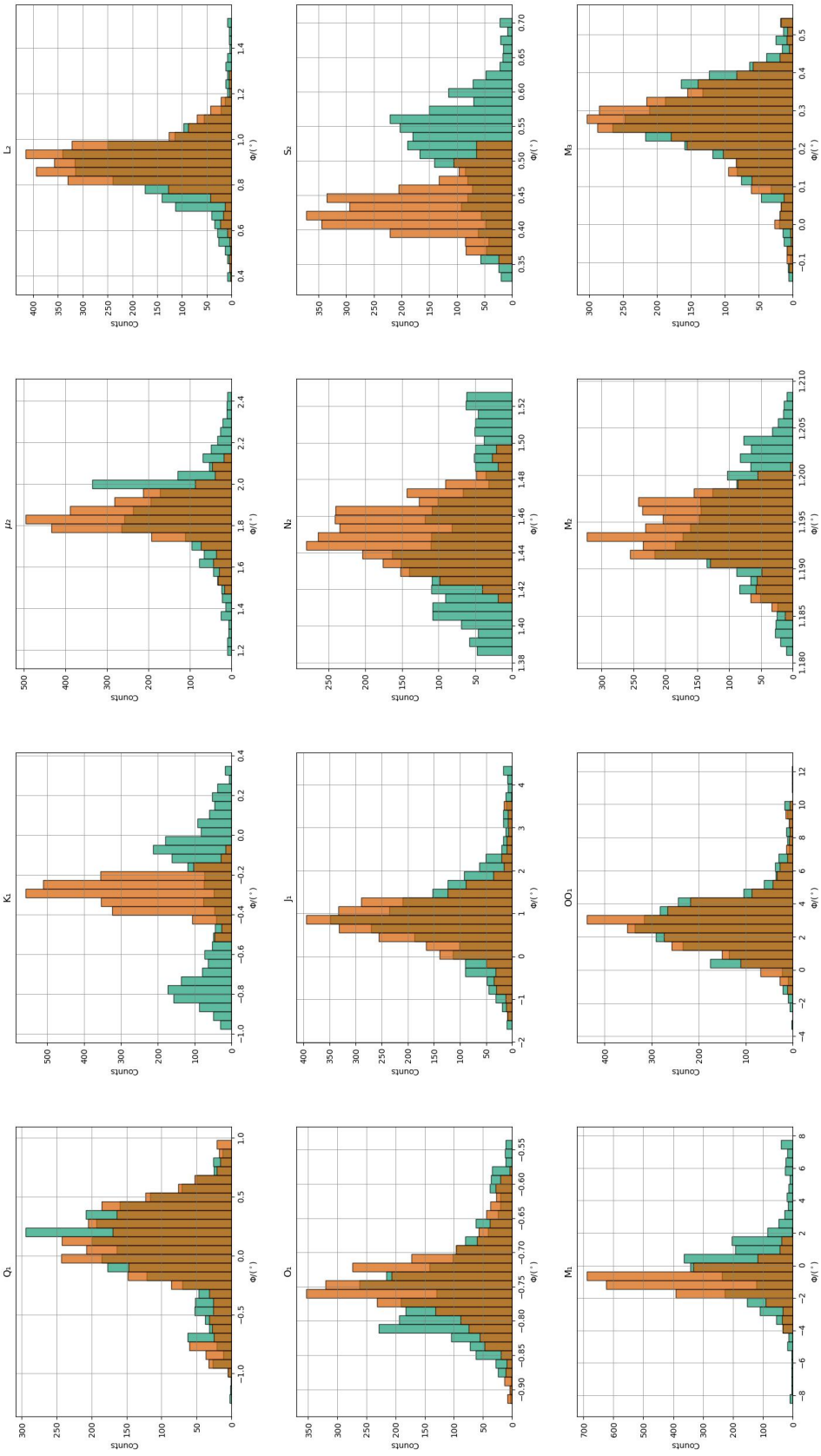

Figure D.20.: Histograms of MWA estimates for gravimetric phases in Djougou.

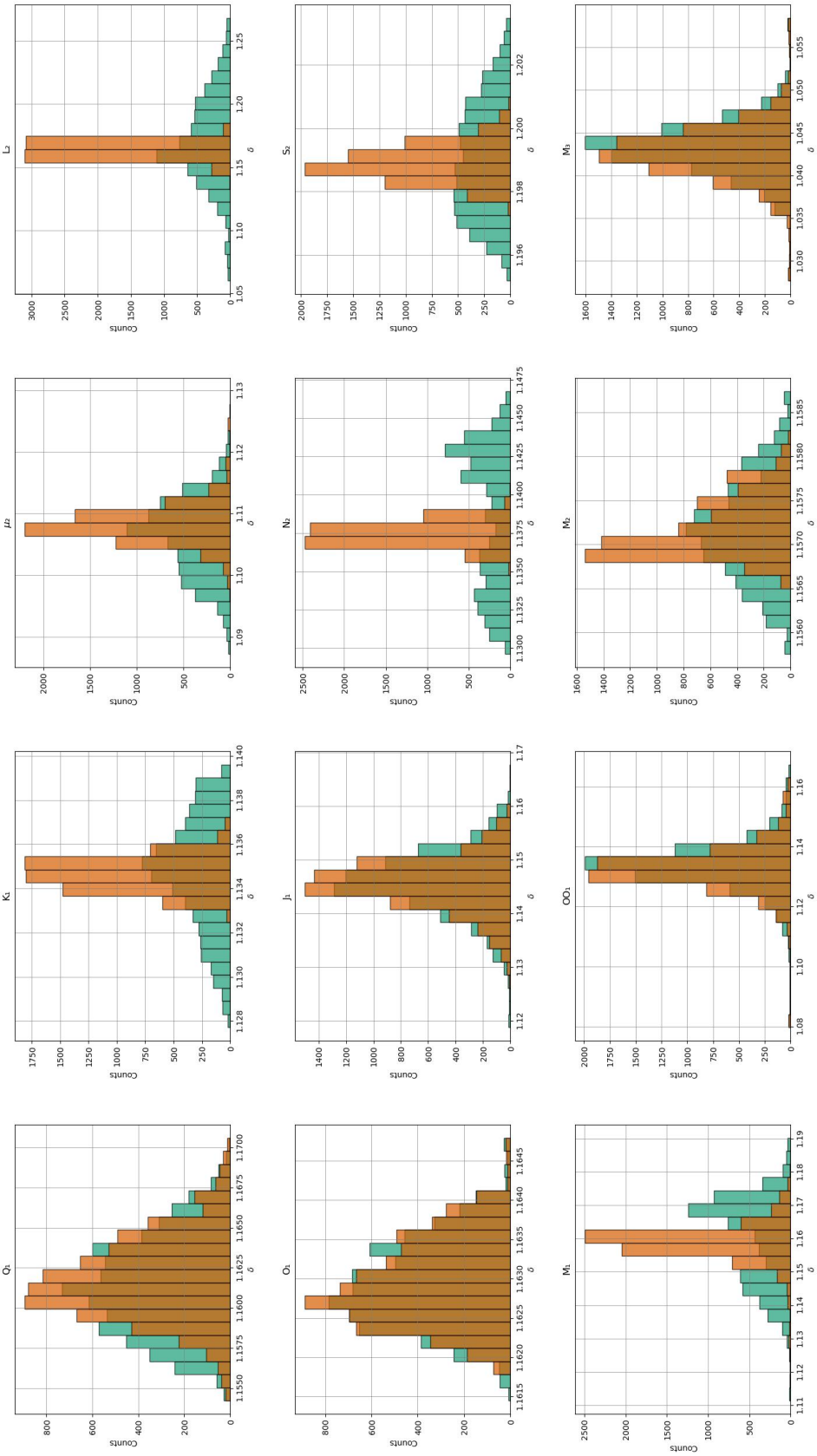

Figure D.21.: Histograms of MWA estimates for gravimetric factors in Sutherland (lower sensor).

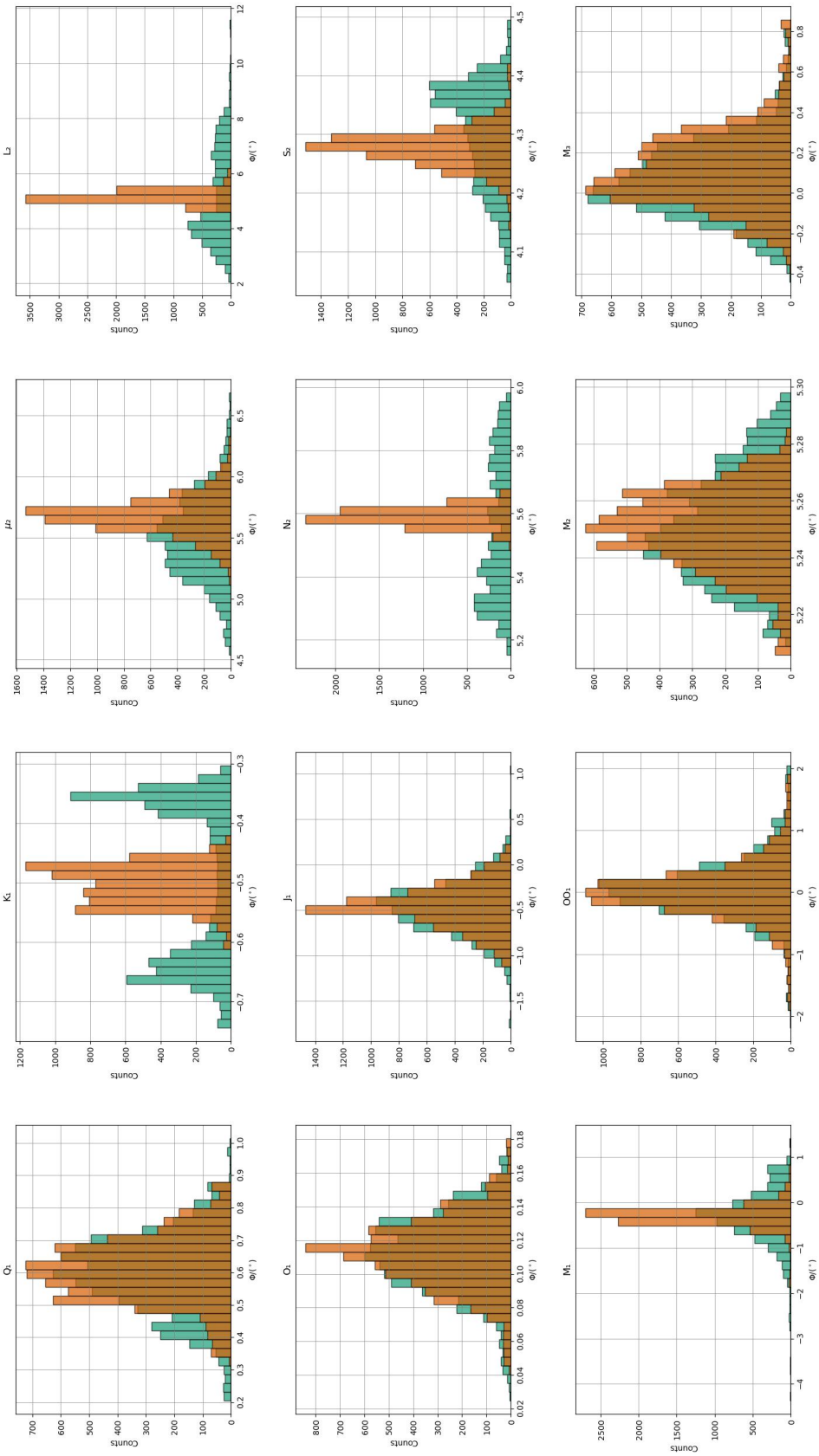

Figure D.22.: Histograms of MWA estimates for gravimetric phases in Sutherland (lower sensor).

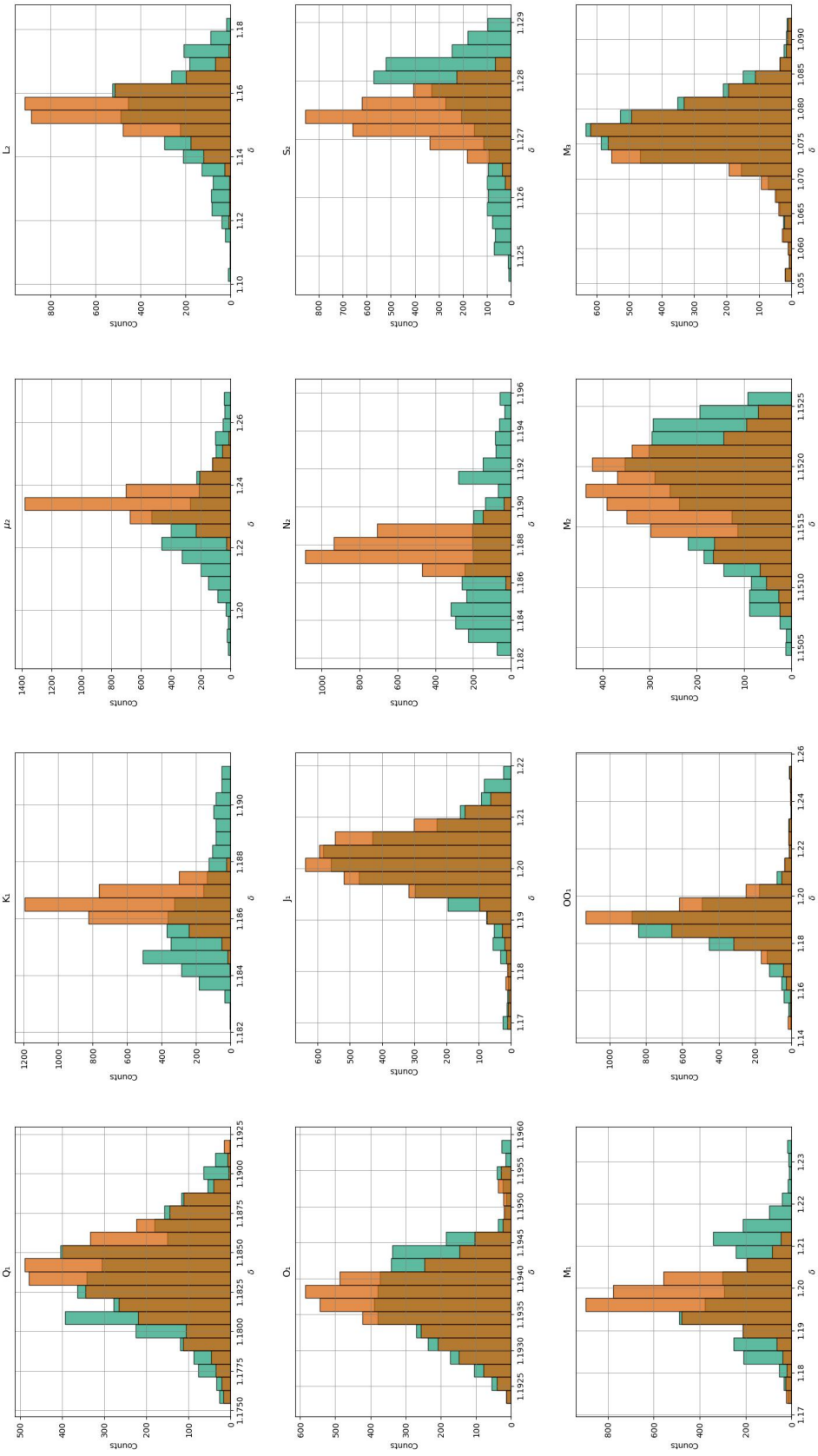

Figure D.23.: Histograms of MWA estimates for gravimetric factors in Tigo-Concepcion.

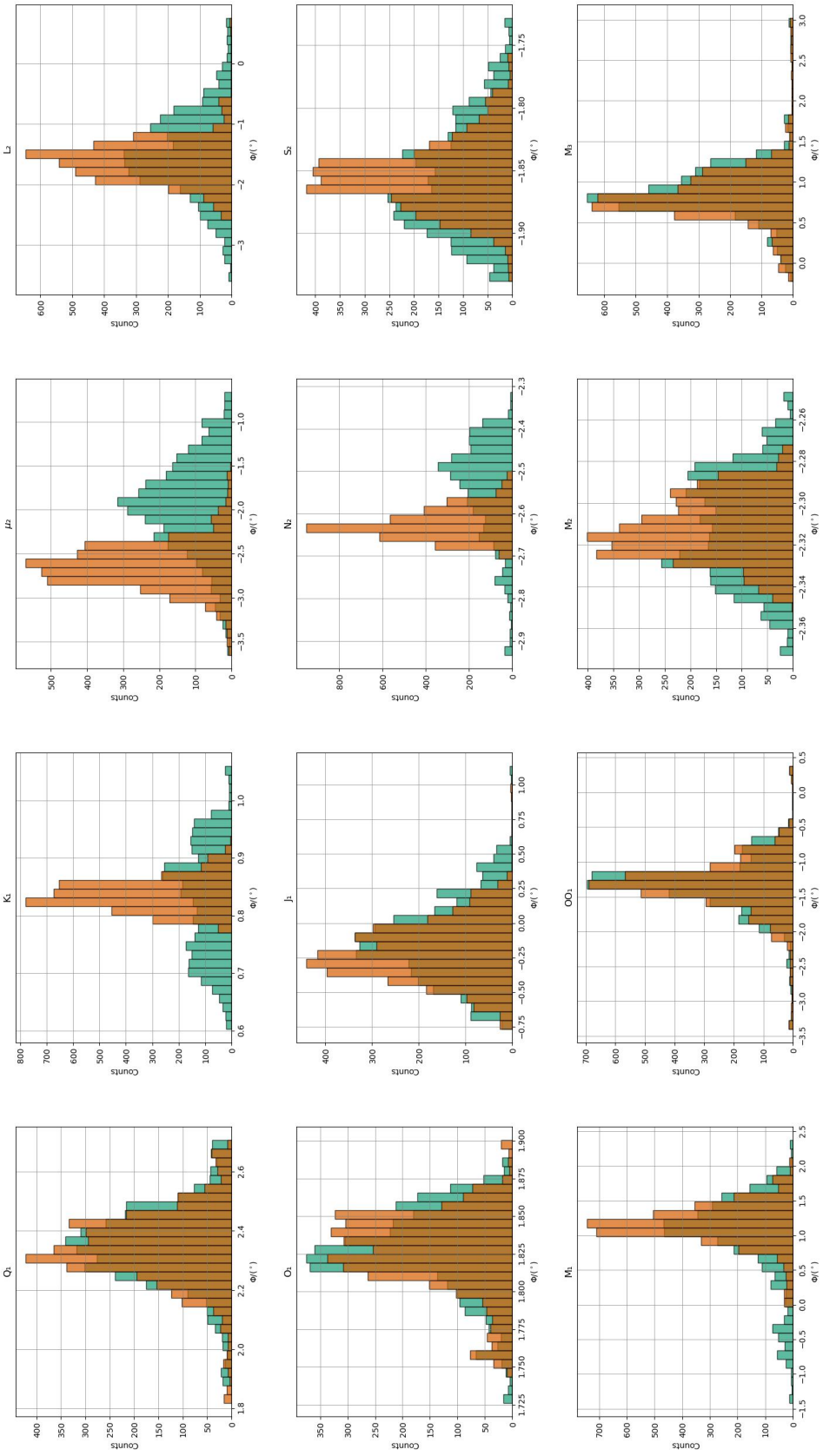

Figure D.24.: Histograms of MWA estimates for gravimetric phases in Tigo-Concepcion.

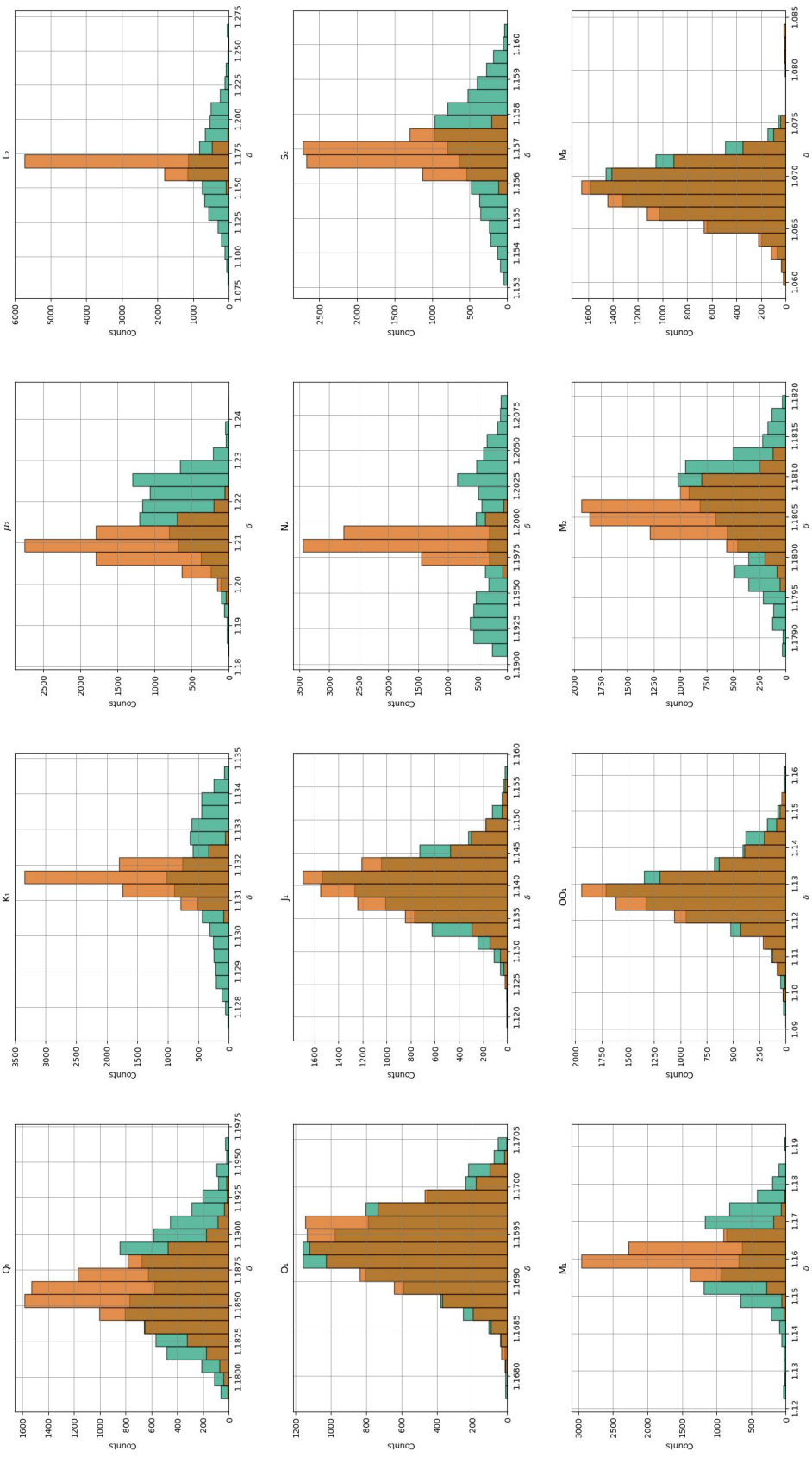

Figure D.25.: Histograms of MWA estimates for gravimetric factors in Canberra.

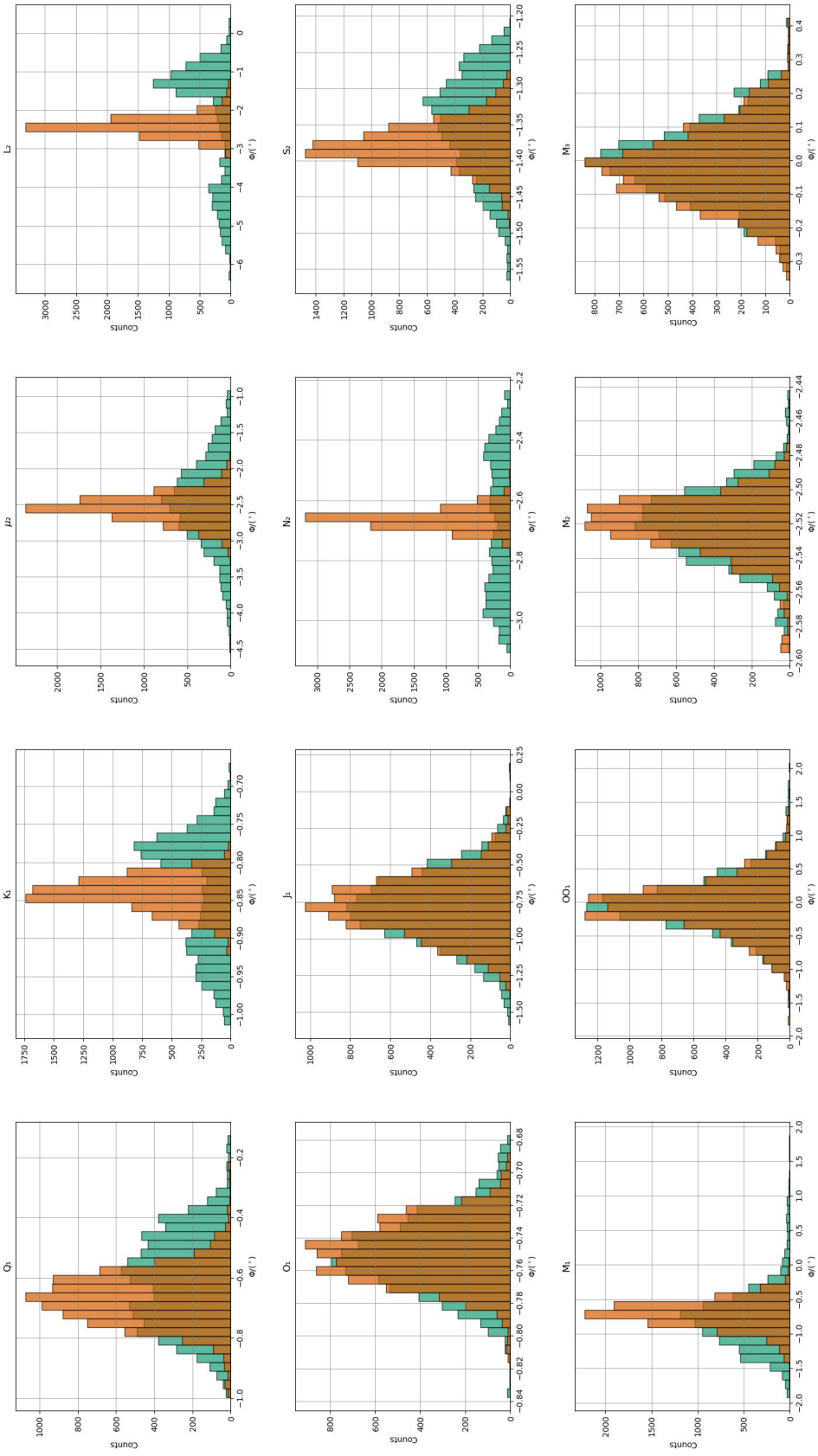

Figure D.26.: Histograms of MWA estimates for gravimetric phases in Canberra.

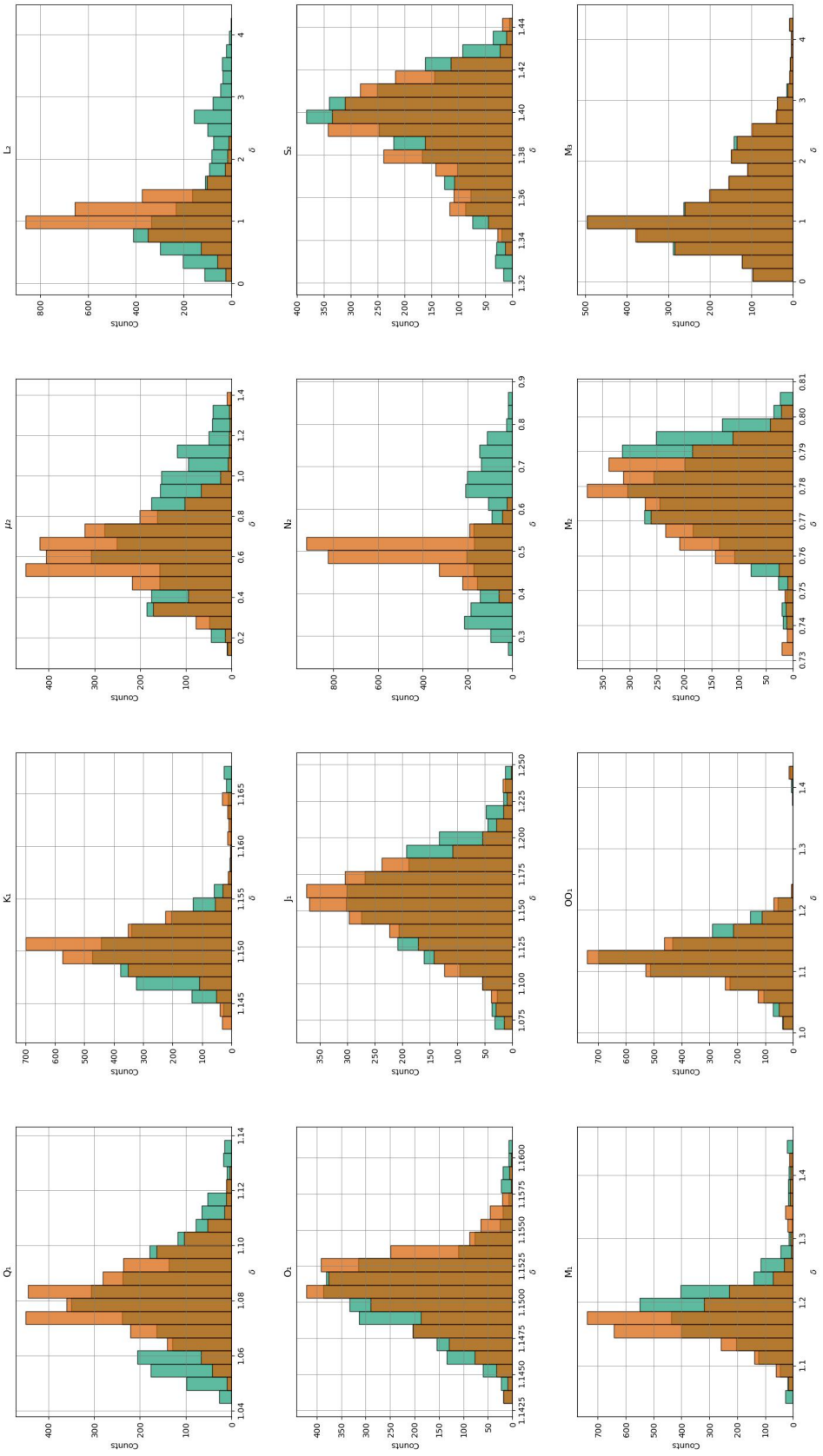

Figure D.27.: Histograms of MWA estimates for gravimetric factors in Ny-Ålesund.

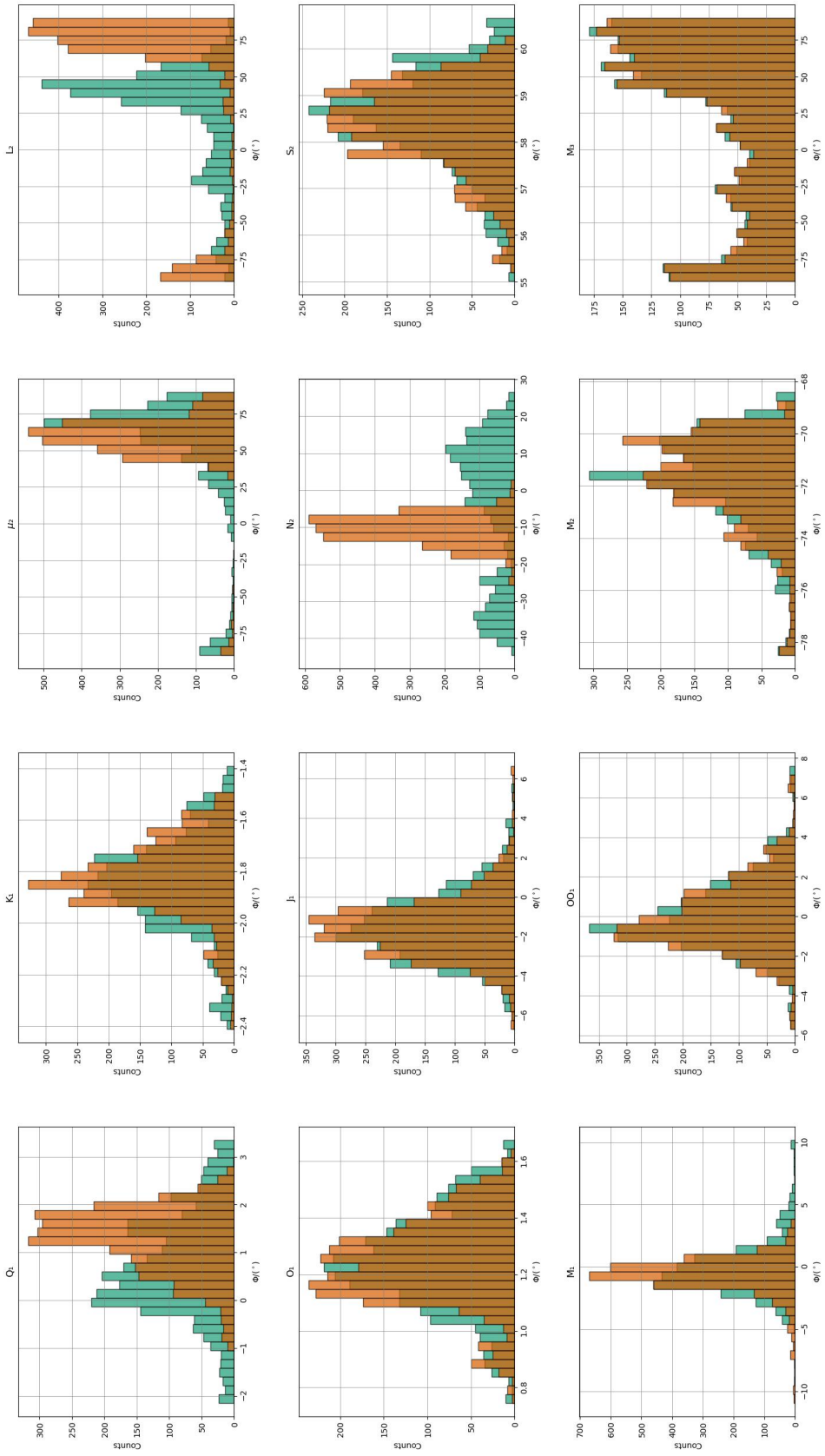

Figure D.28.: Histograms of MWA estimates for gravimetric phases in Ny-Ålesund.

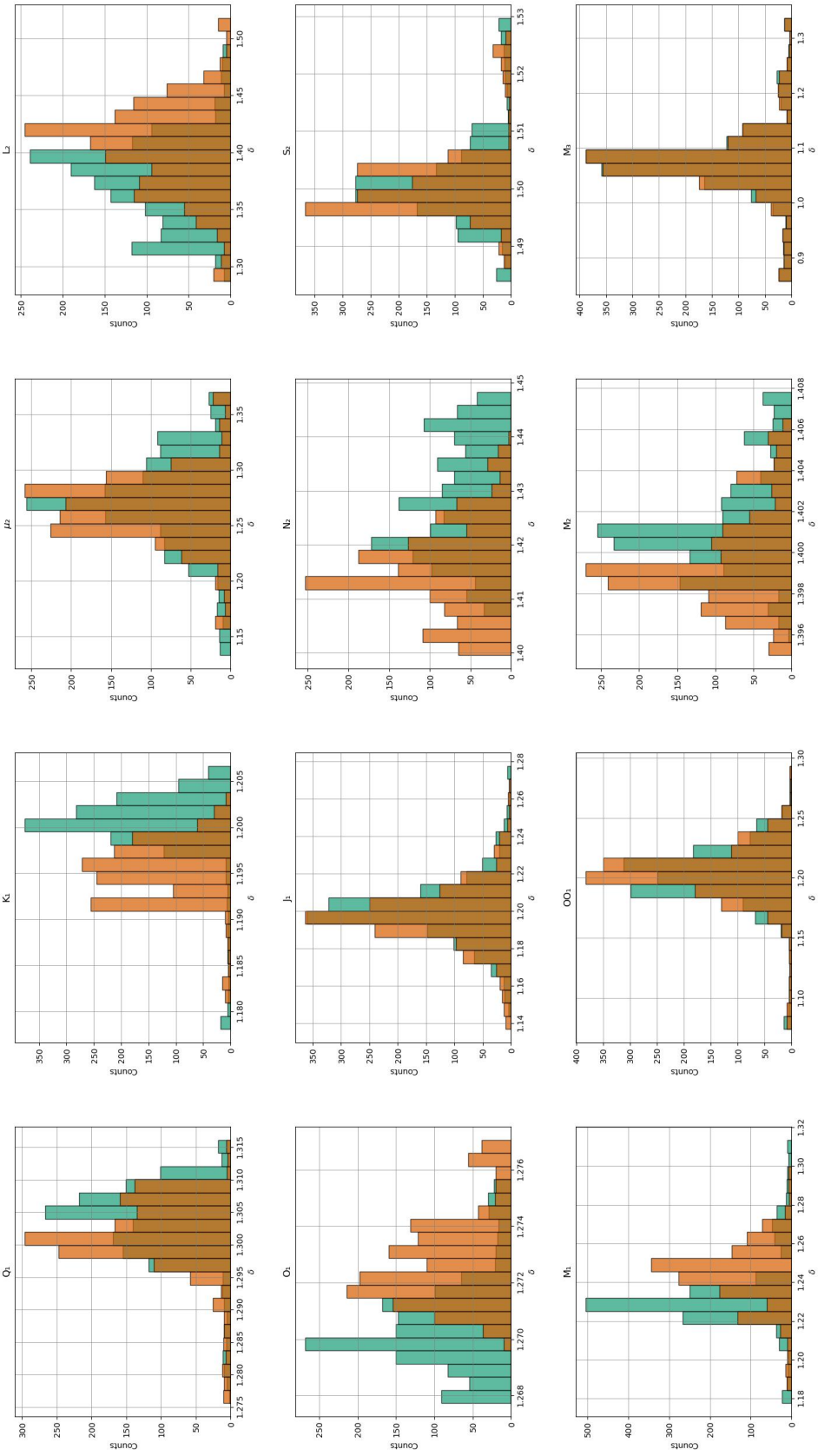

Figure D.29.: Histograms of MWA estimates for gravimetric factors in Syowa.

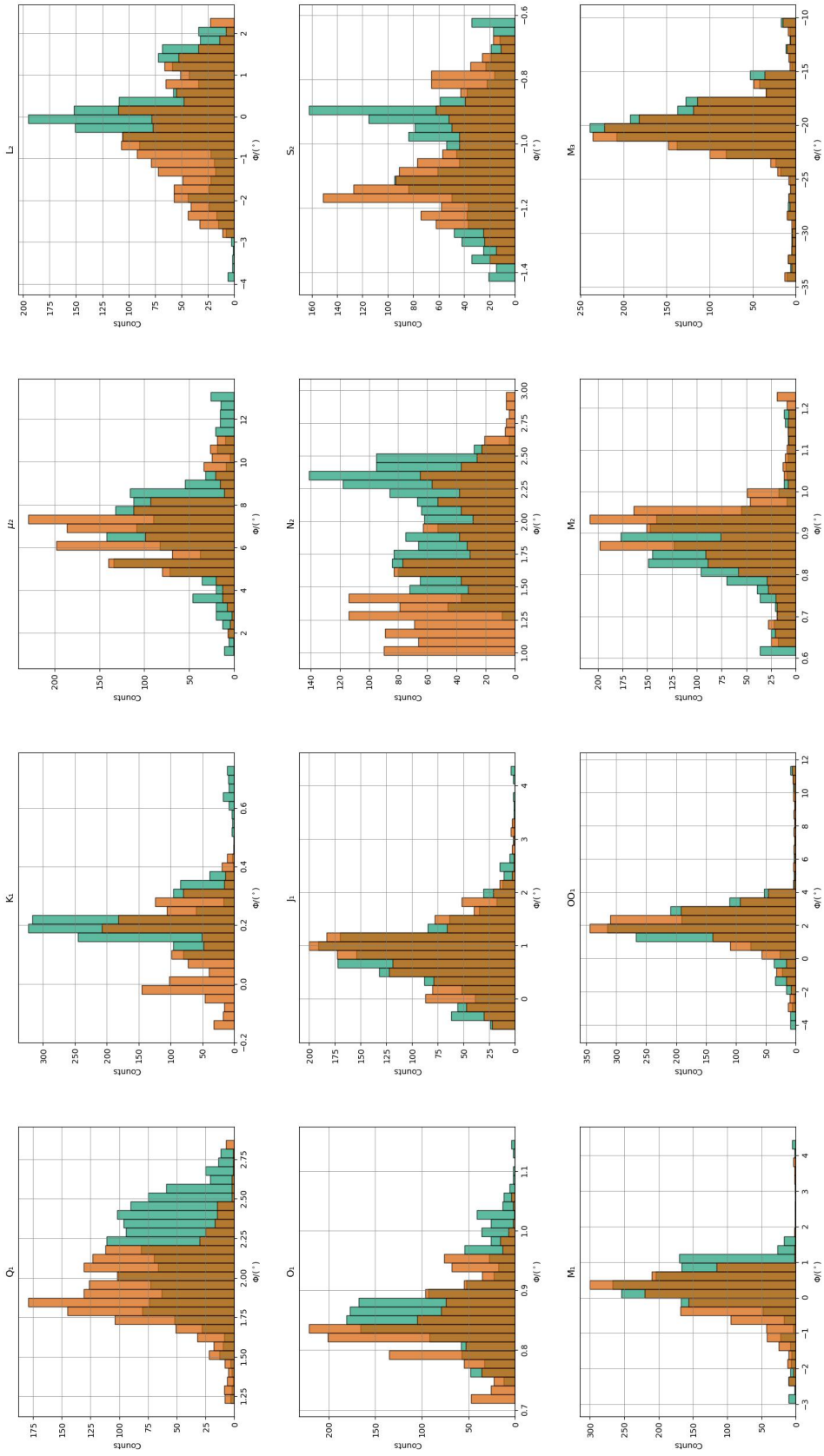

Figure D.30.: Histograms of MWA estimates for gravimetric phases in Syowa.

E. Spectra of MWA

Compilation of spectra of MWA diagrams of investigated observatories. Green color corresponds to WDZe a priori model used in the analysis. Orange color corresponds to the LRM response model for a given station. Prior to the FFT, the linear trend was removed and the MWA time series was tapered using Hann window. The plot ranges are consistent between groups and stations, except phases in semidiurnal groups for Syowa and Ny-Ålesund.

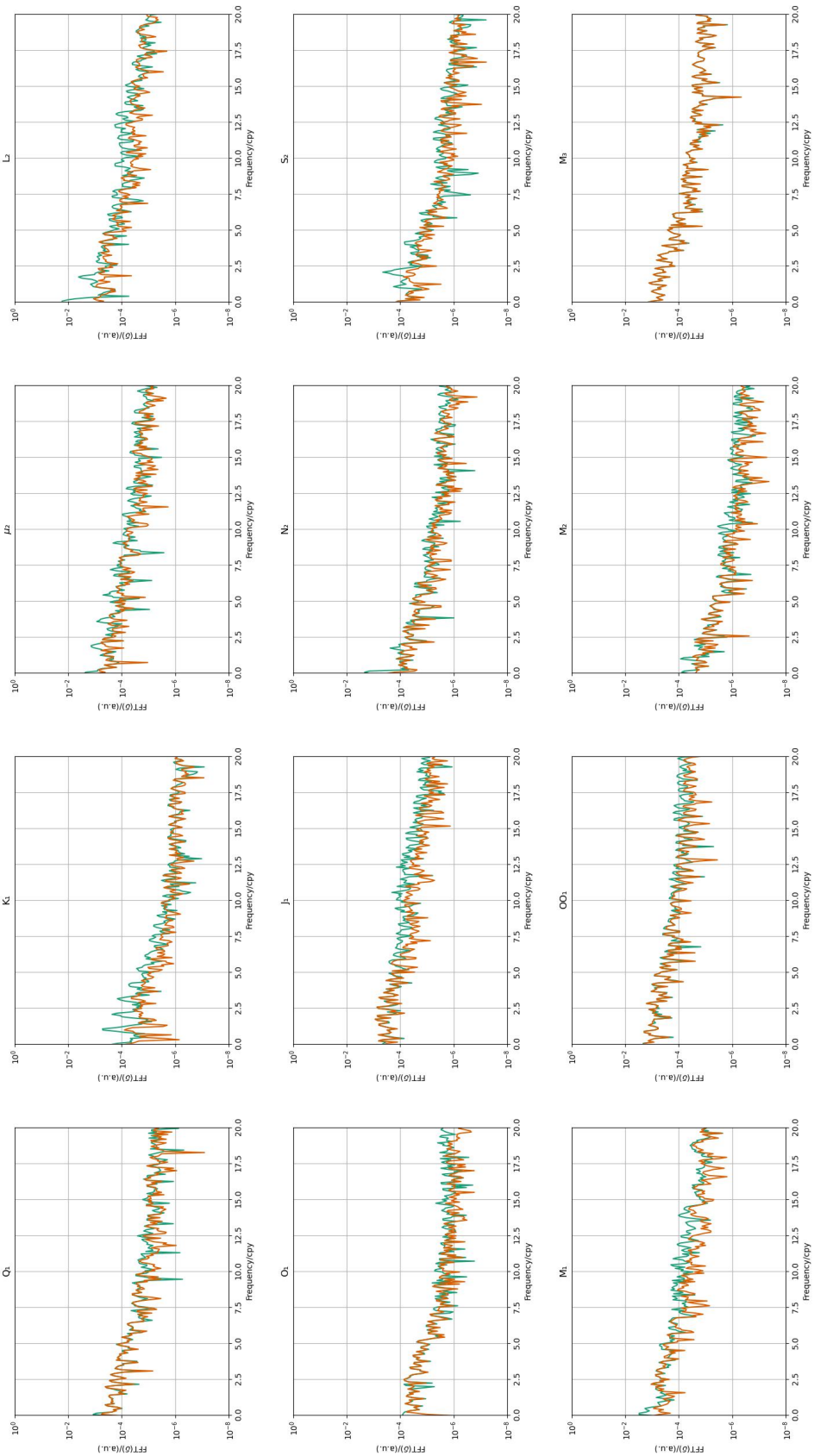

Figure E.1.: Spectral analysis (FFT) of MWA estimates for gravimetric factors in Black Forest Observatory (lower sensor).

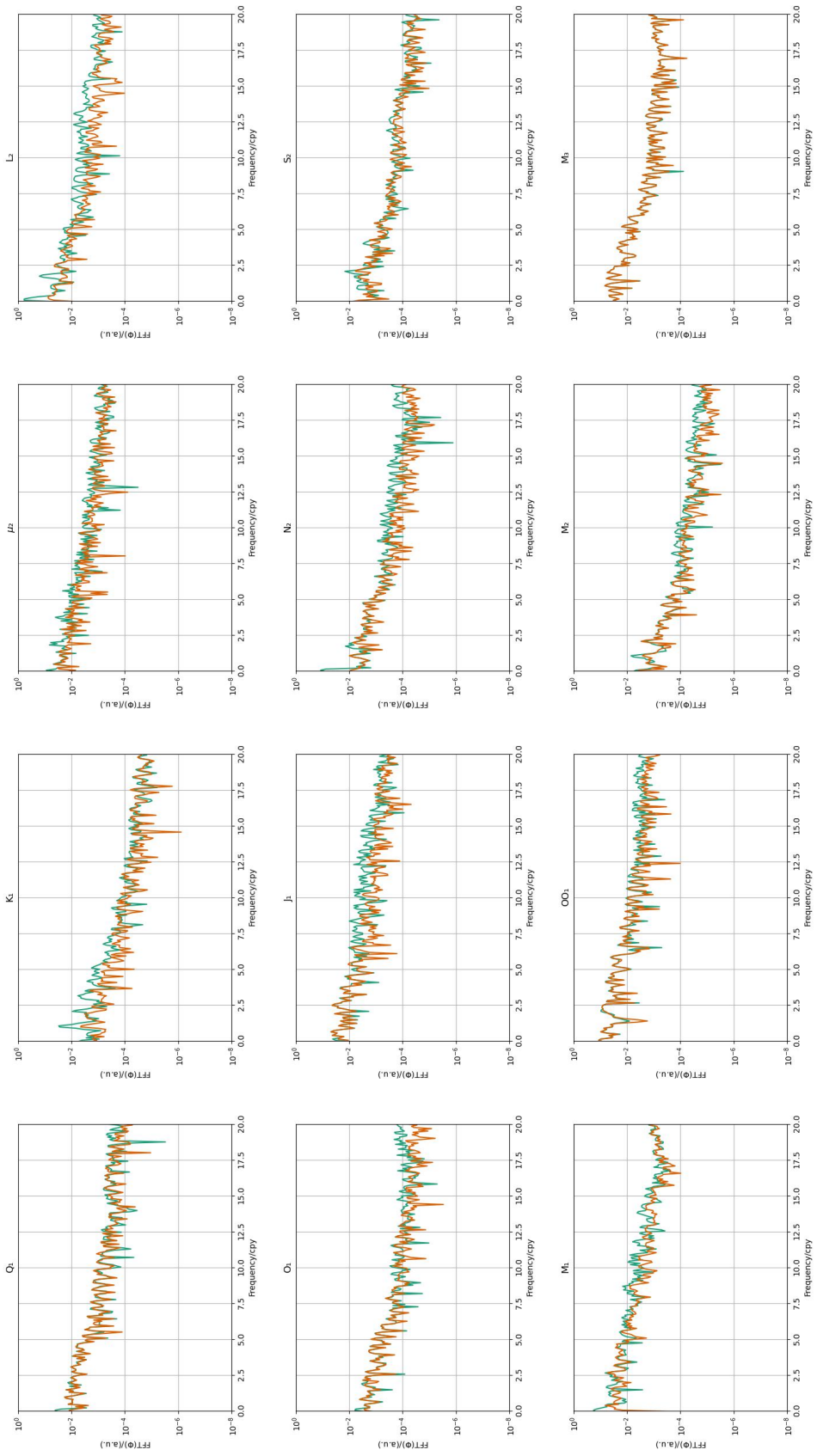

Figure E.2.: Spectral analysis (FFT) of MWA estimates for gravimetric phases in Black Forest Observatory (lower sensor).

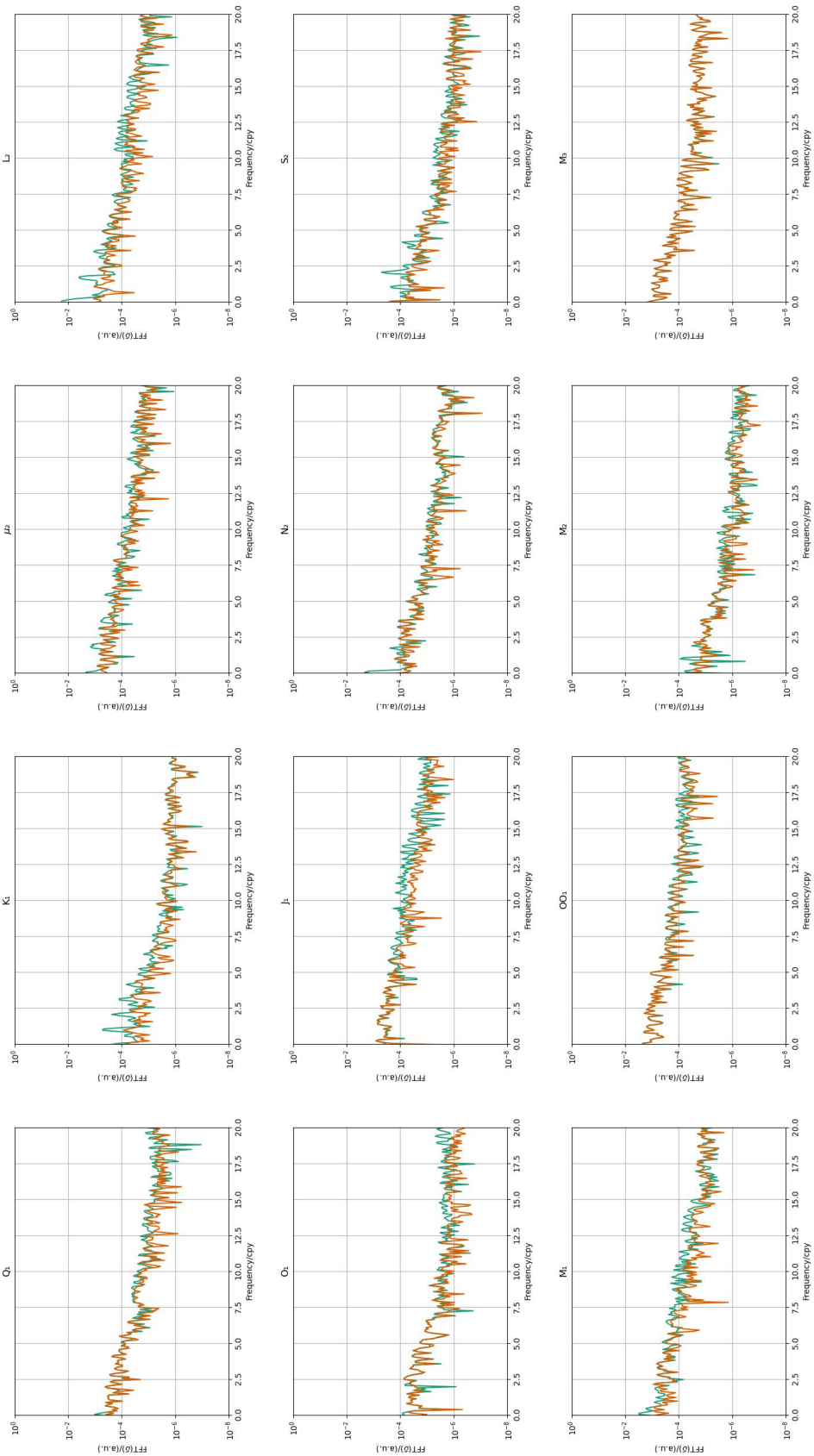

Figure E.3.: Spectral analysis (FFT) of MWA estimates for gravimetric factors in Black Forest Observatory (upper sensor).

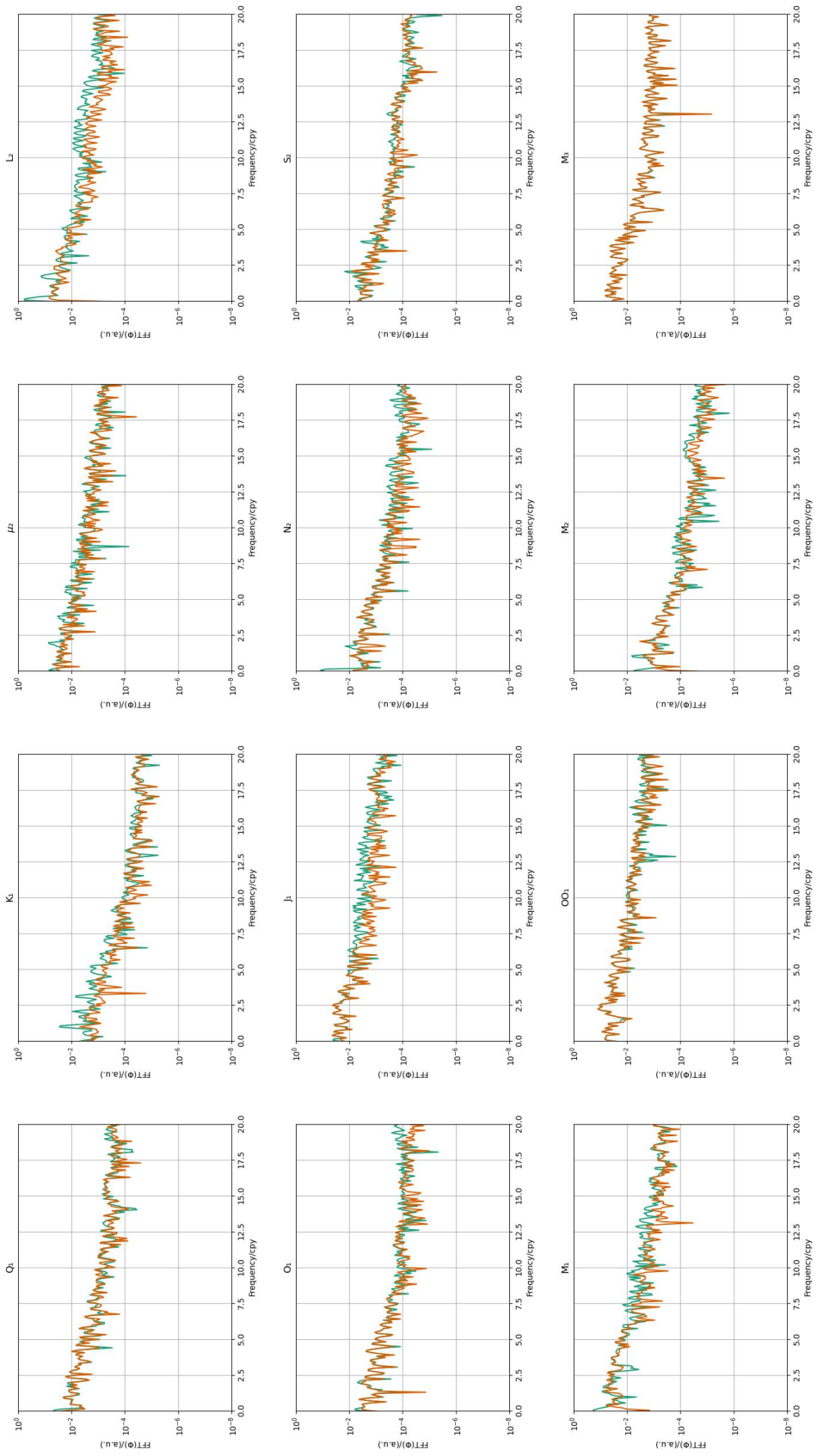

Figure E.4.: Spectral analysis (FFT) of MWA estimates for gravimetric phases in Black Forest Observatory (upper sensor).

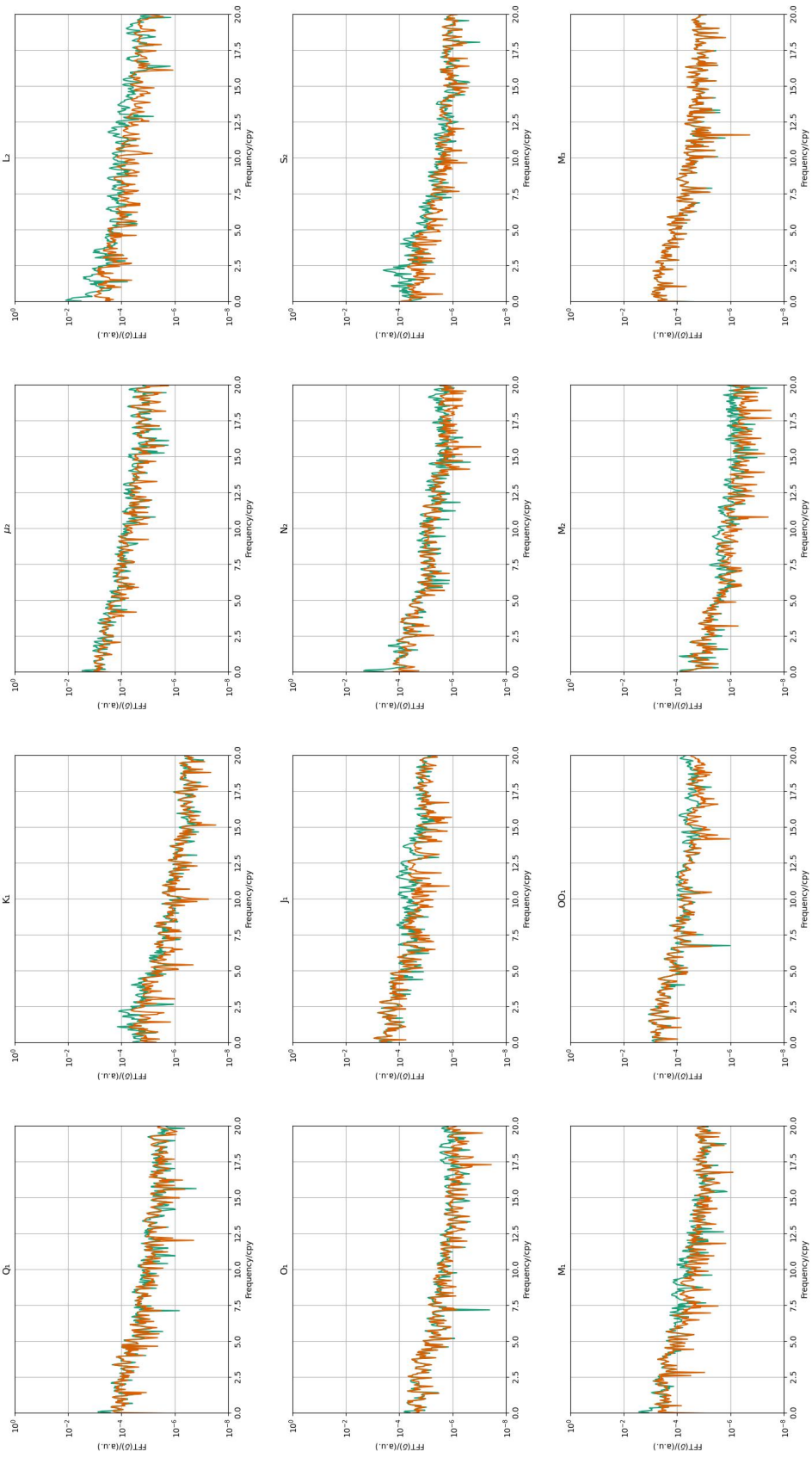

Figure E.5.: Spectral analysis (FFT) of MWA estimates for gravimetric factors in Moxa (lower sensor).

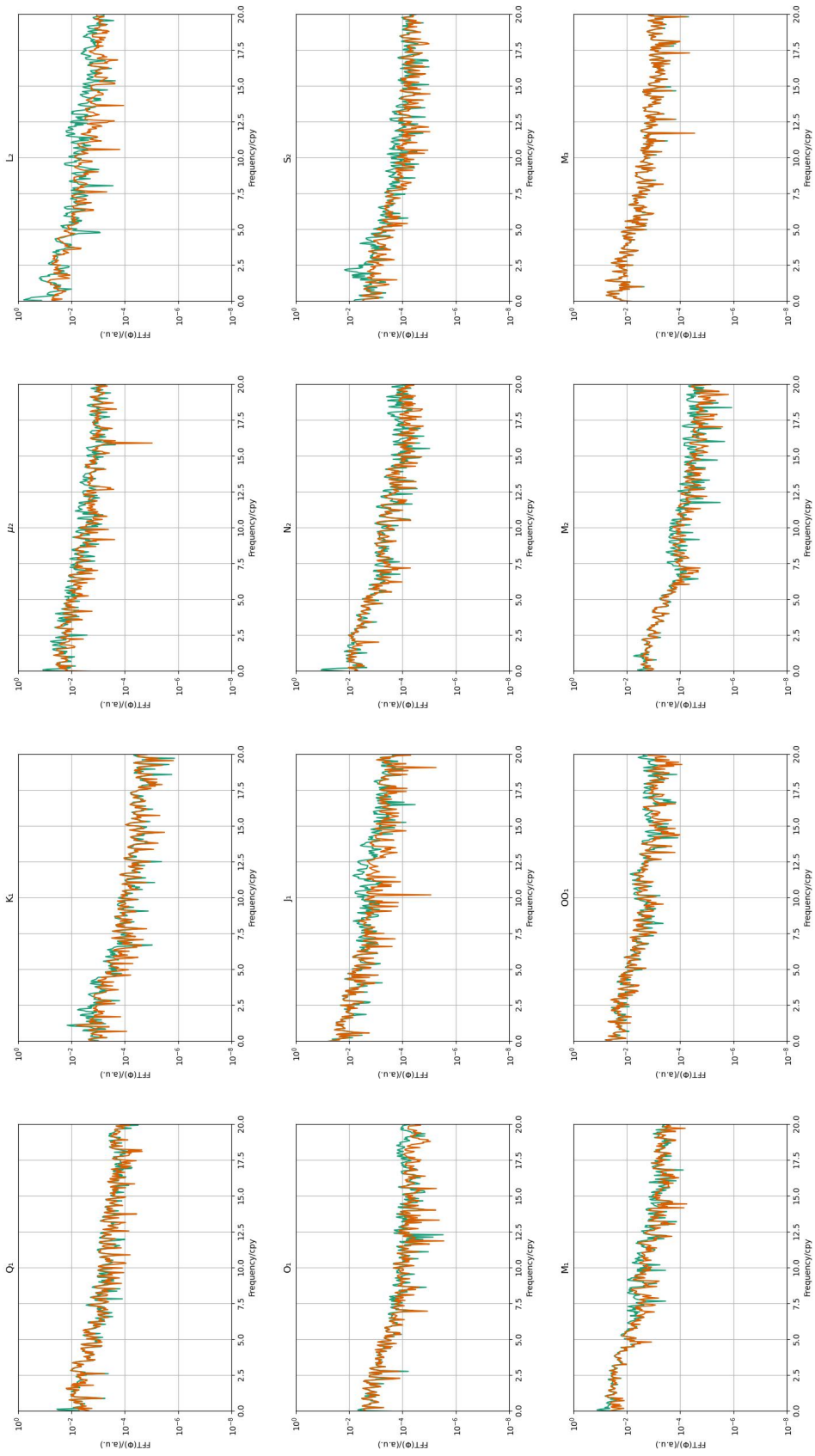

Figure E.6.: Spectral analysis (FFT) of MWA estimates for gravimetric phases in Moxa (lower sensor).

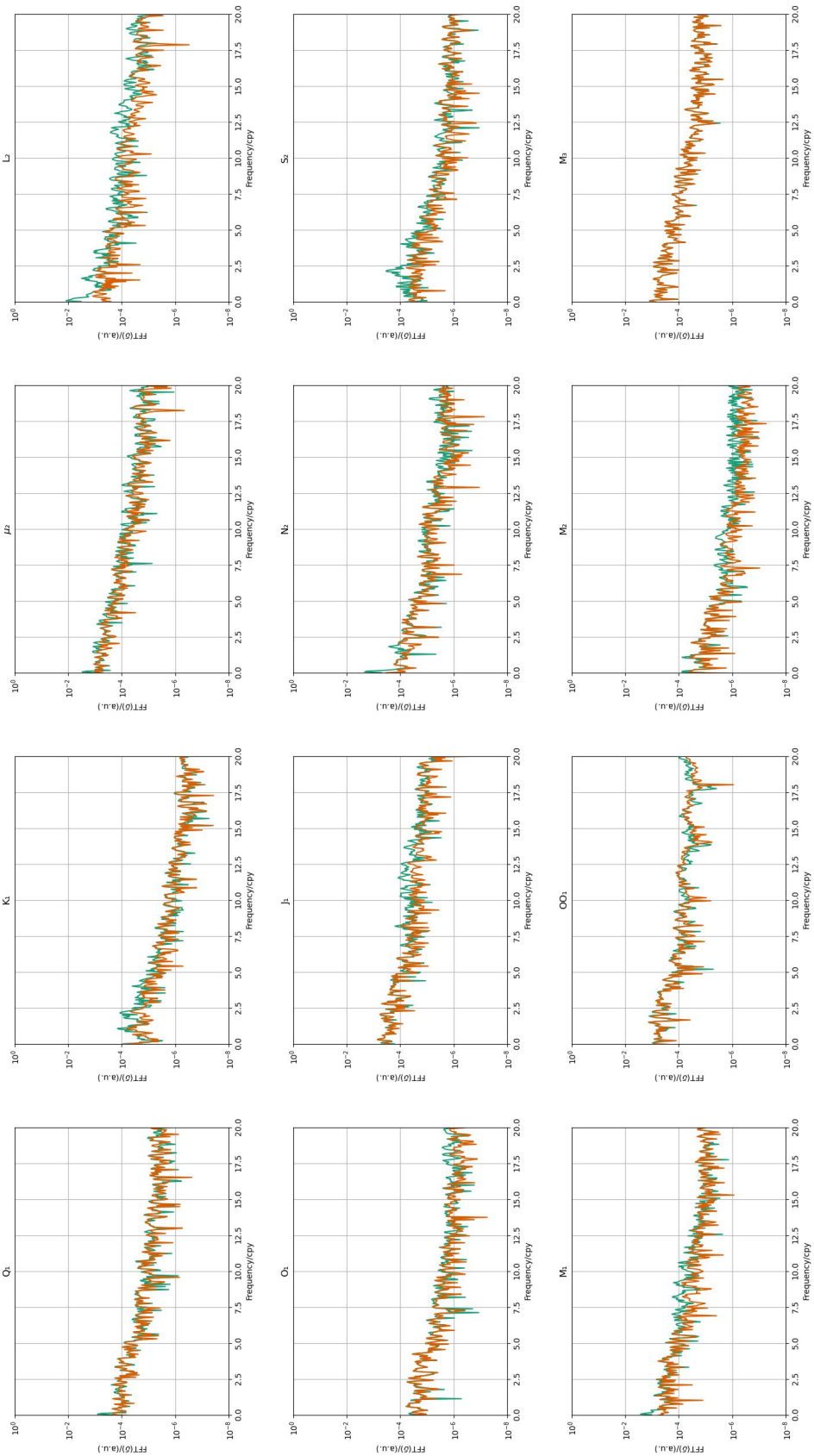

Figure E.7.: Spectral analysis (FFT) of MWA estimates for gravimetric factors in Moxa (upper sensor).

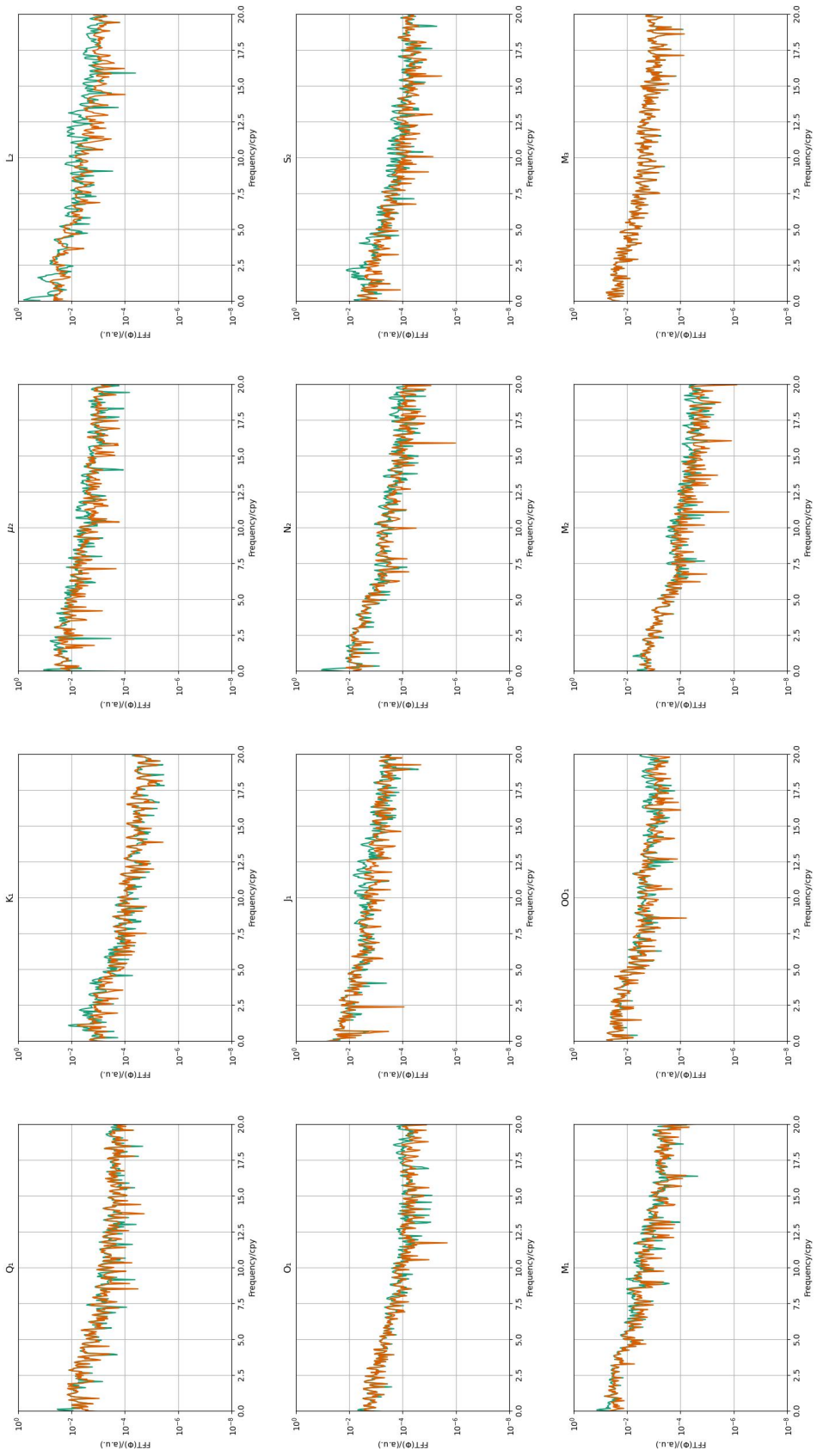

Figure E.8.: Spectral analysis (FFT) of MWA estimates for gravimetric phases in Moxa (upper sensor).

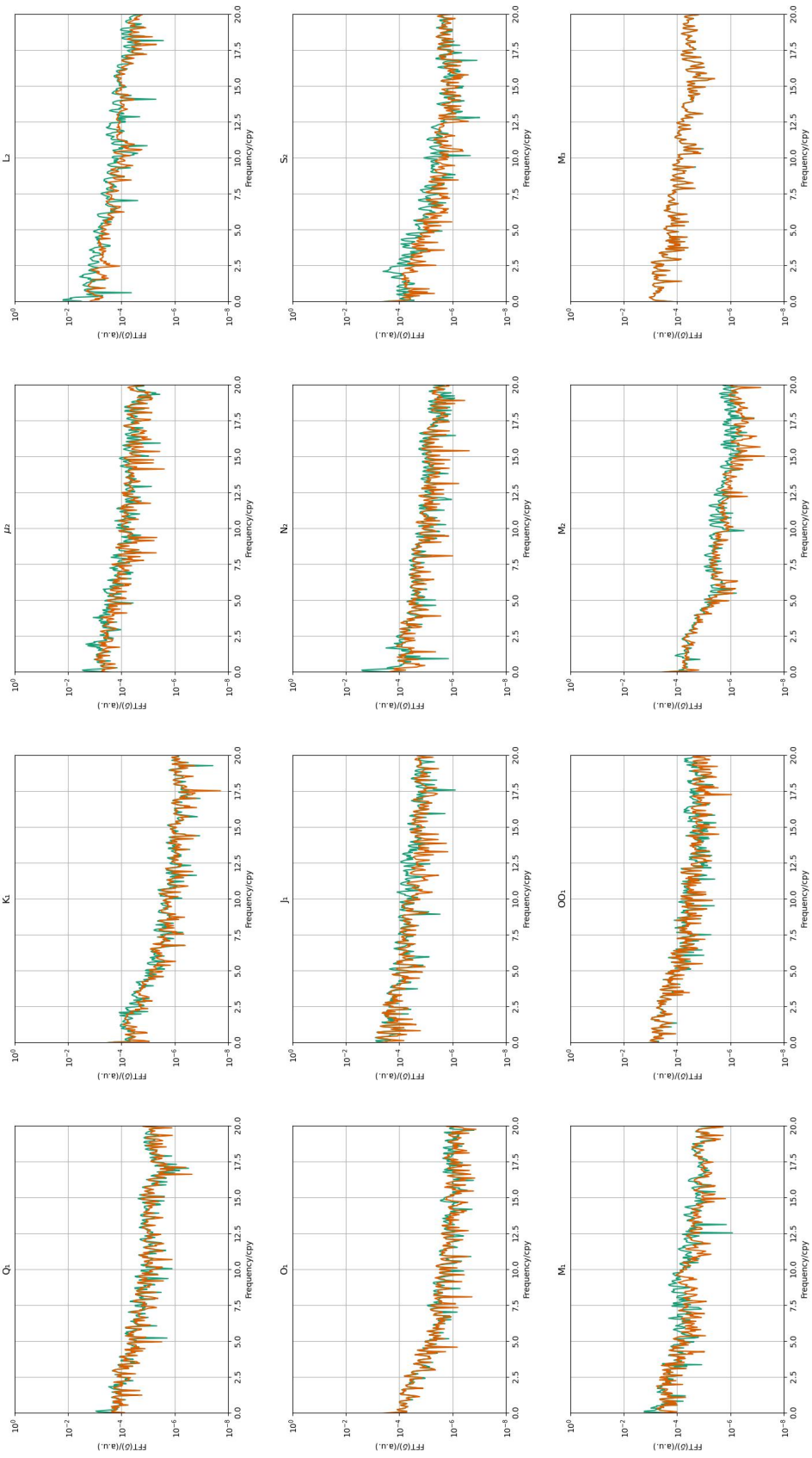

Figure E.9.: Spectral analysis (FFT) of MWA estimates for gravimetric factors in Strasbourg.

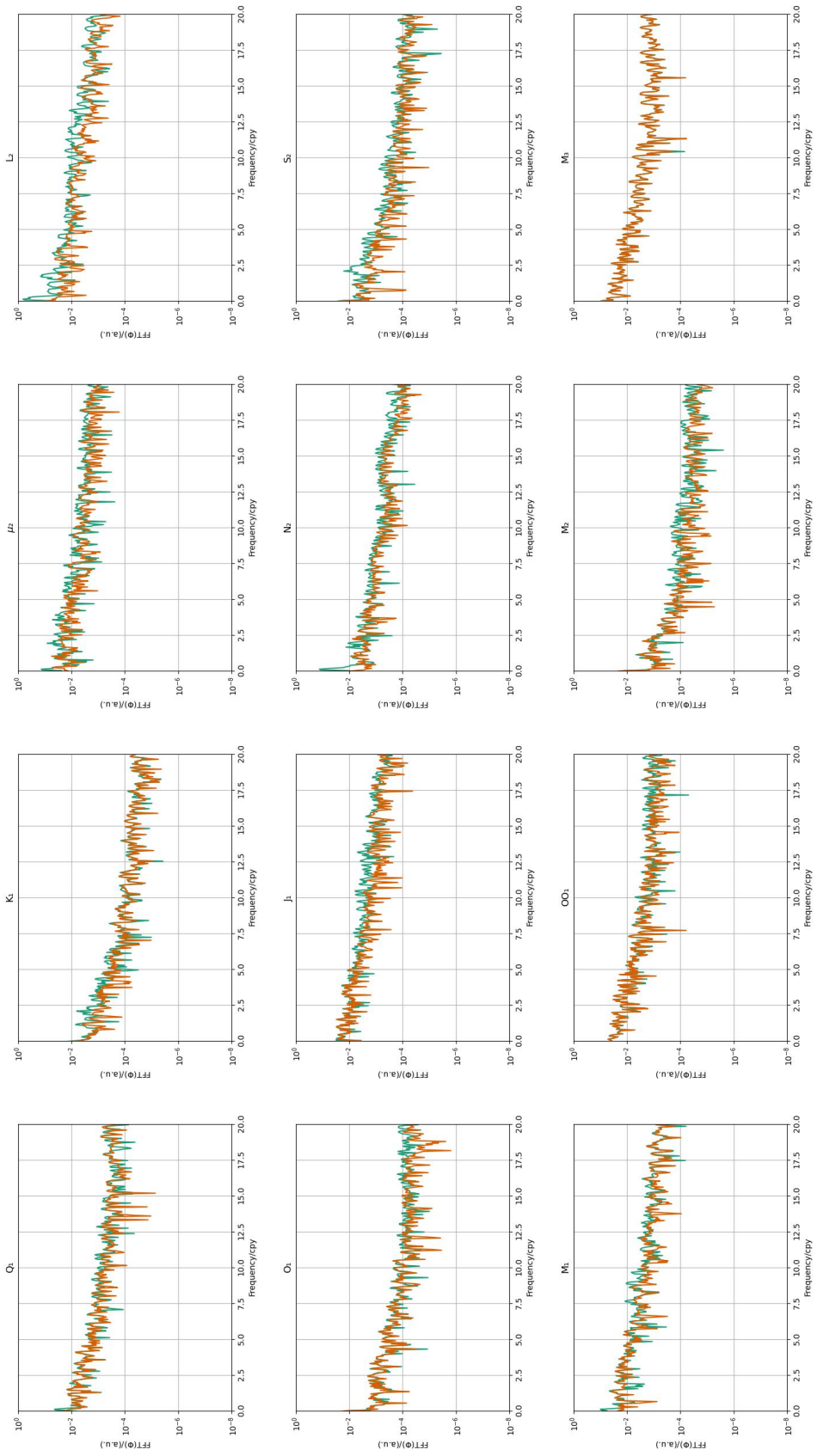

Figure E.10.: Spectral analysis (FFT) of MWA estimates for gravimetric phases in Strasbourg.

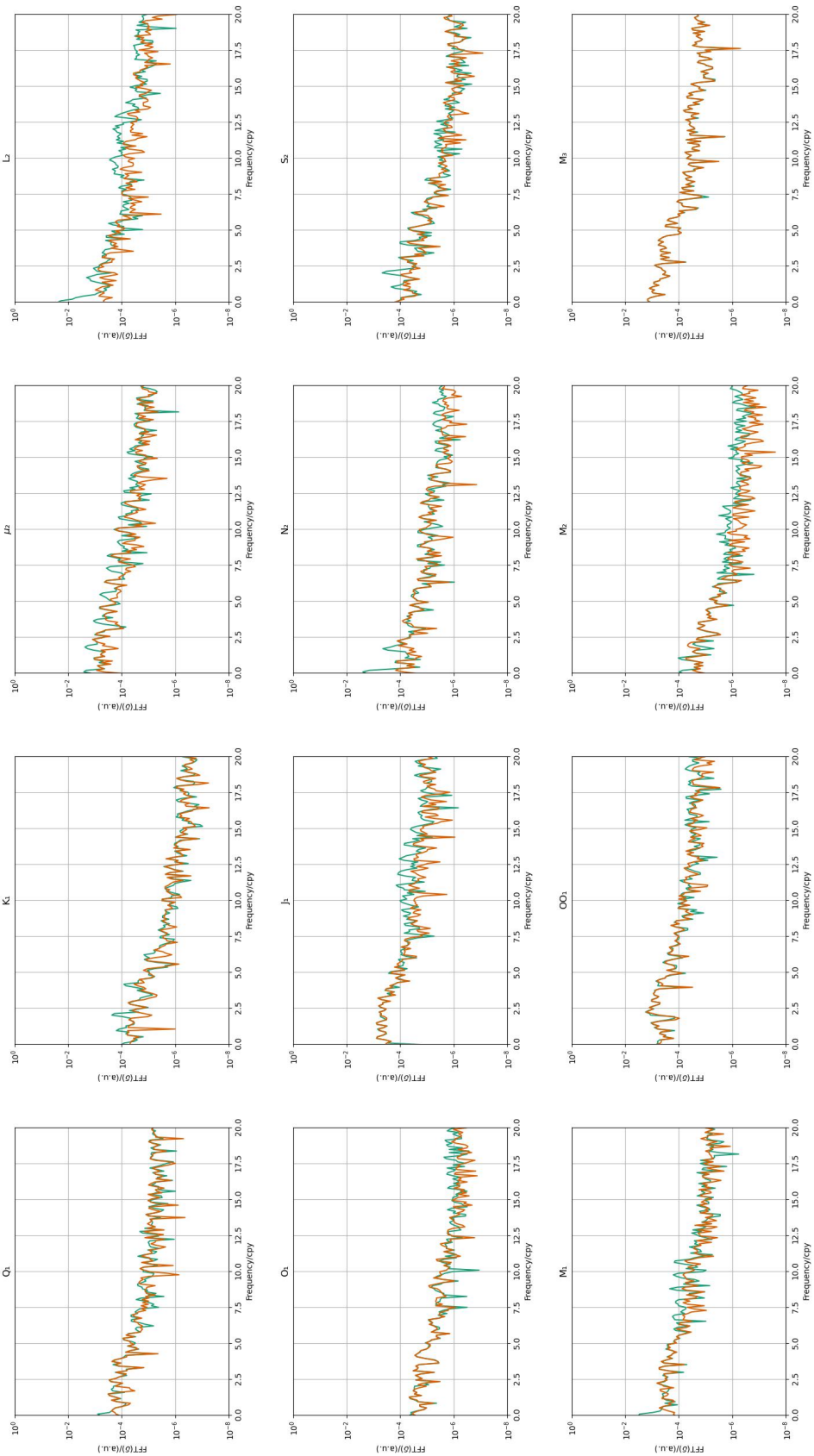

Figure E.11.: Spectral analysis (FFT) of MWA estimates for gravimetric factors in Bad Homburg.

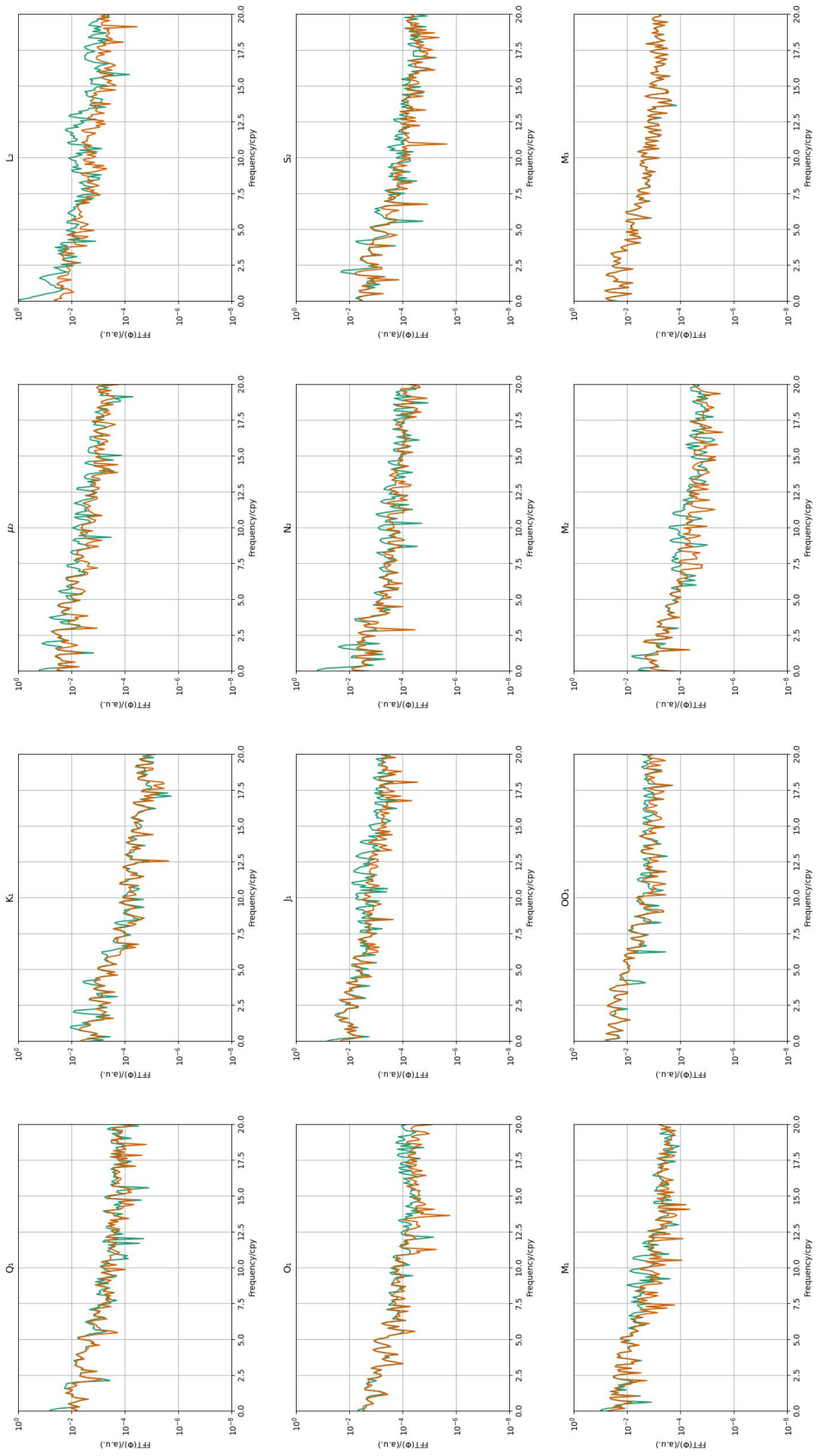

Figure E.12.: Spectral analysis (FFT) of MWA estimates for gravimetric phases in Bad Homburg.

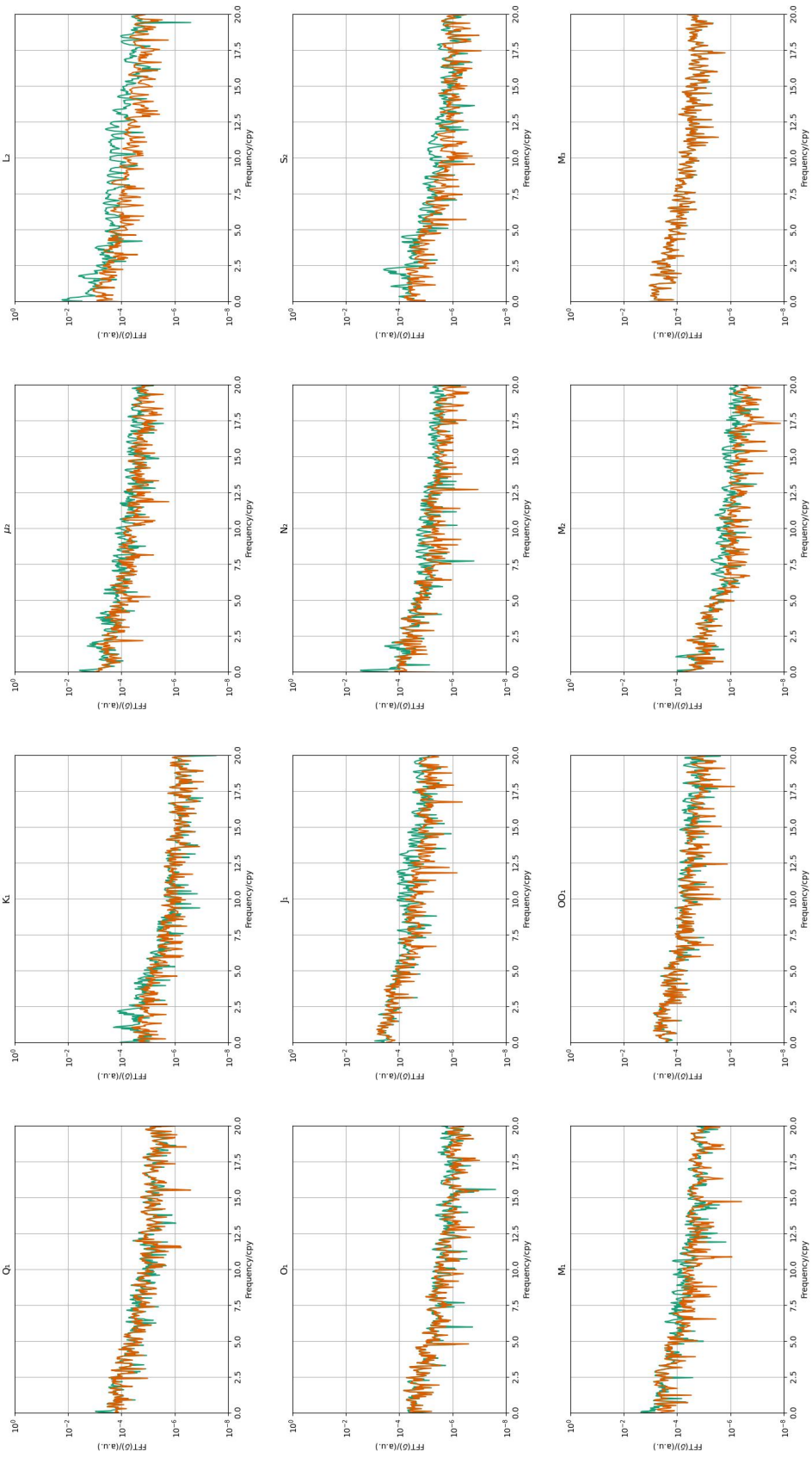

Figure E.13.: Spectral analysis (FFT) of MWA estimates for gravimetric factors in Membach.

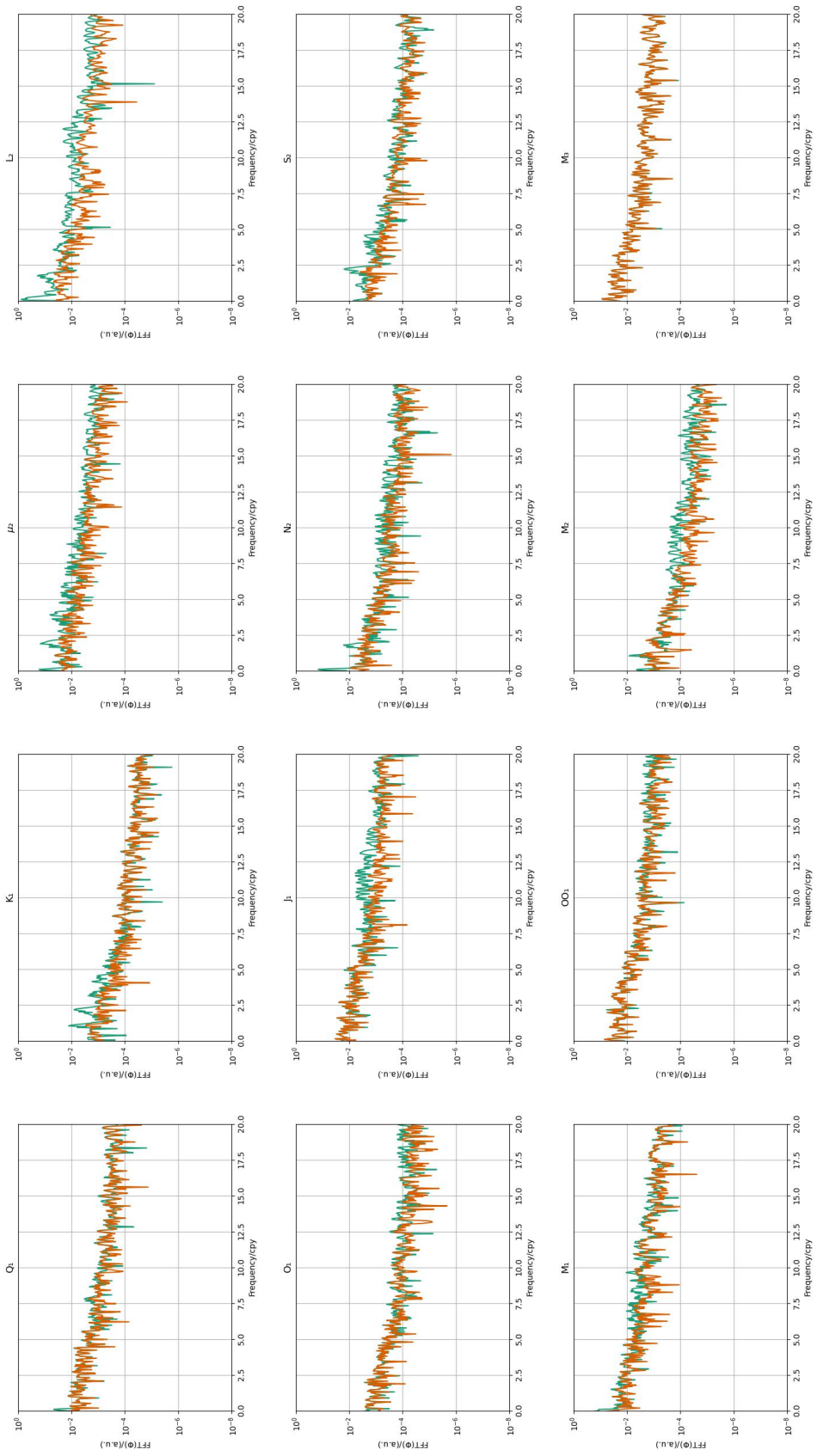

Figure E.14.: Spectral analysis (FFT) of MWA estimates for gravimetric phases in Membach.

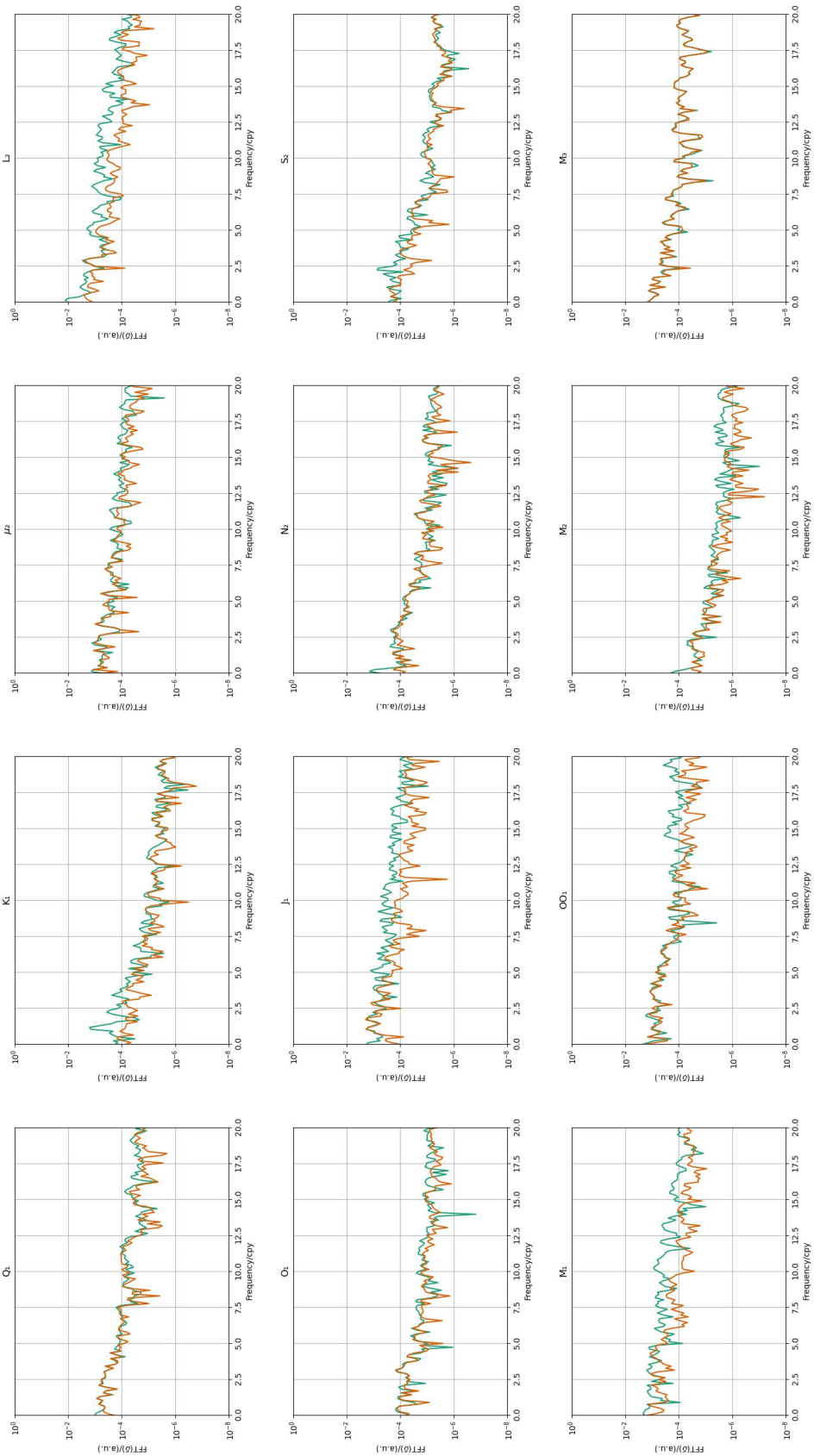

Figure E.15.: Spectral analysis (FFT) of MWA estimates for gravimetric factors in Kamioka.

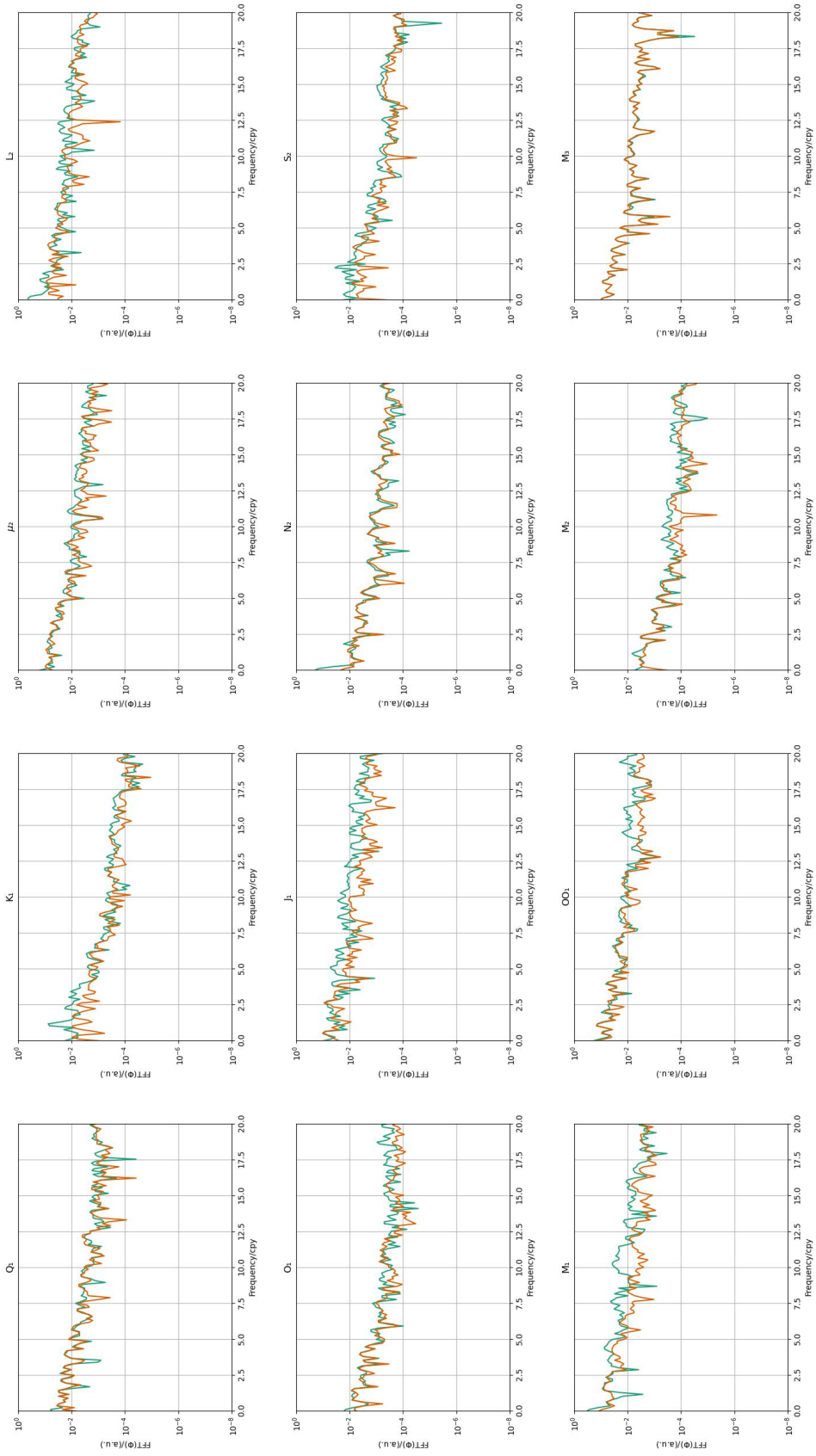

Figure E.16.: Spectral analysis (FFT) of MWA estimates for gravimetric phases in Kamioka.

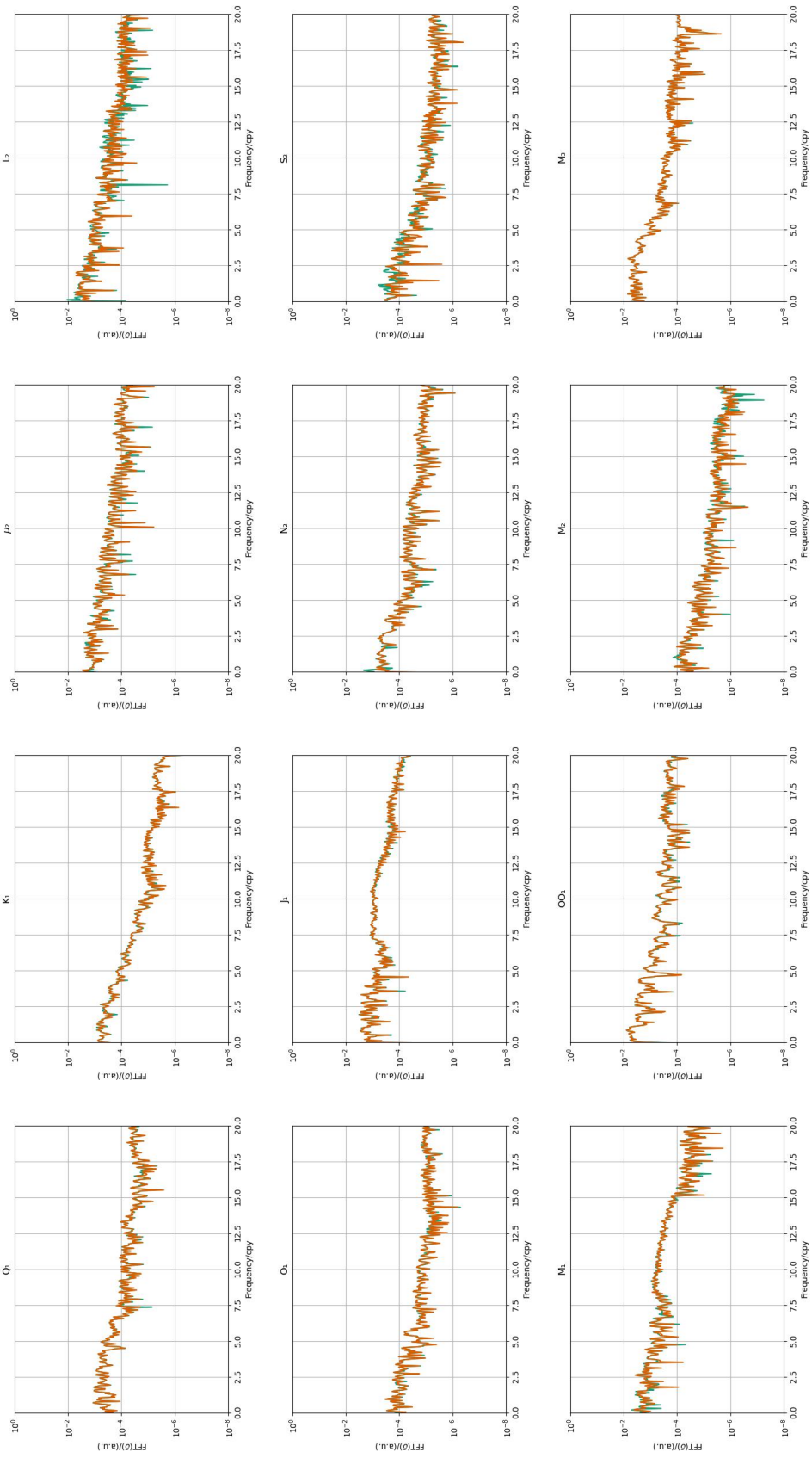

Figure E.17.: Spectral analysis (FFT) of MWA estimates for gravimetric factors in Cantley.

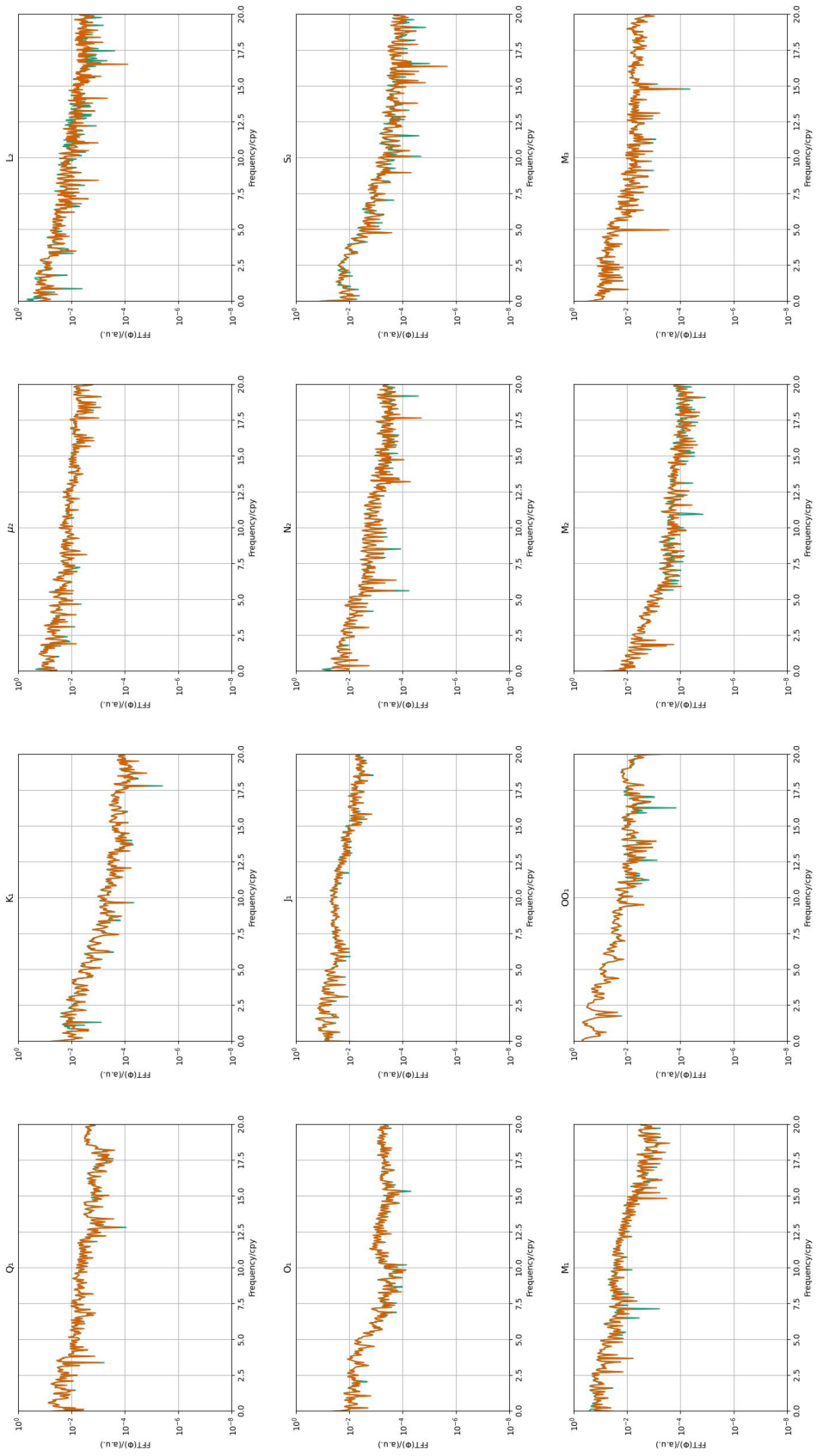

Figure E.18.: Spectral analysis (FFT) of MWA estimates for gravimetric phases in Cantley.

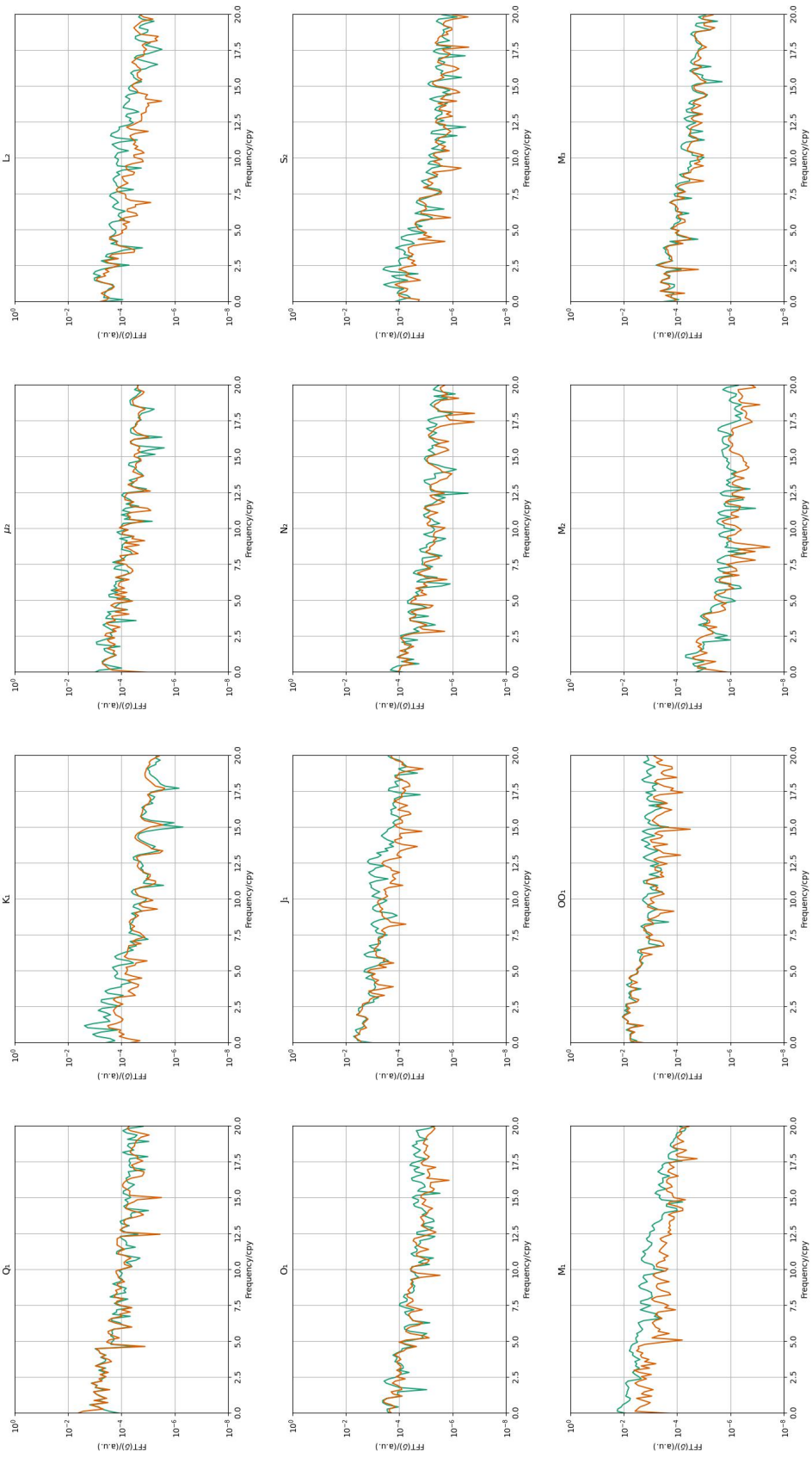

Figure E.19.: Spectral analysis (FFT) of MWA estimates for gravimetric factors in Djougou.

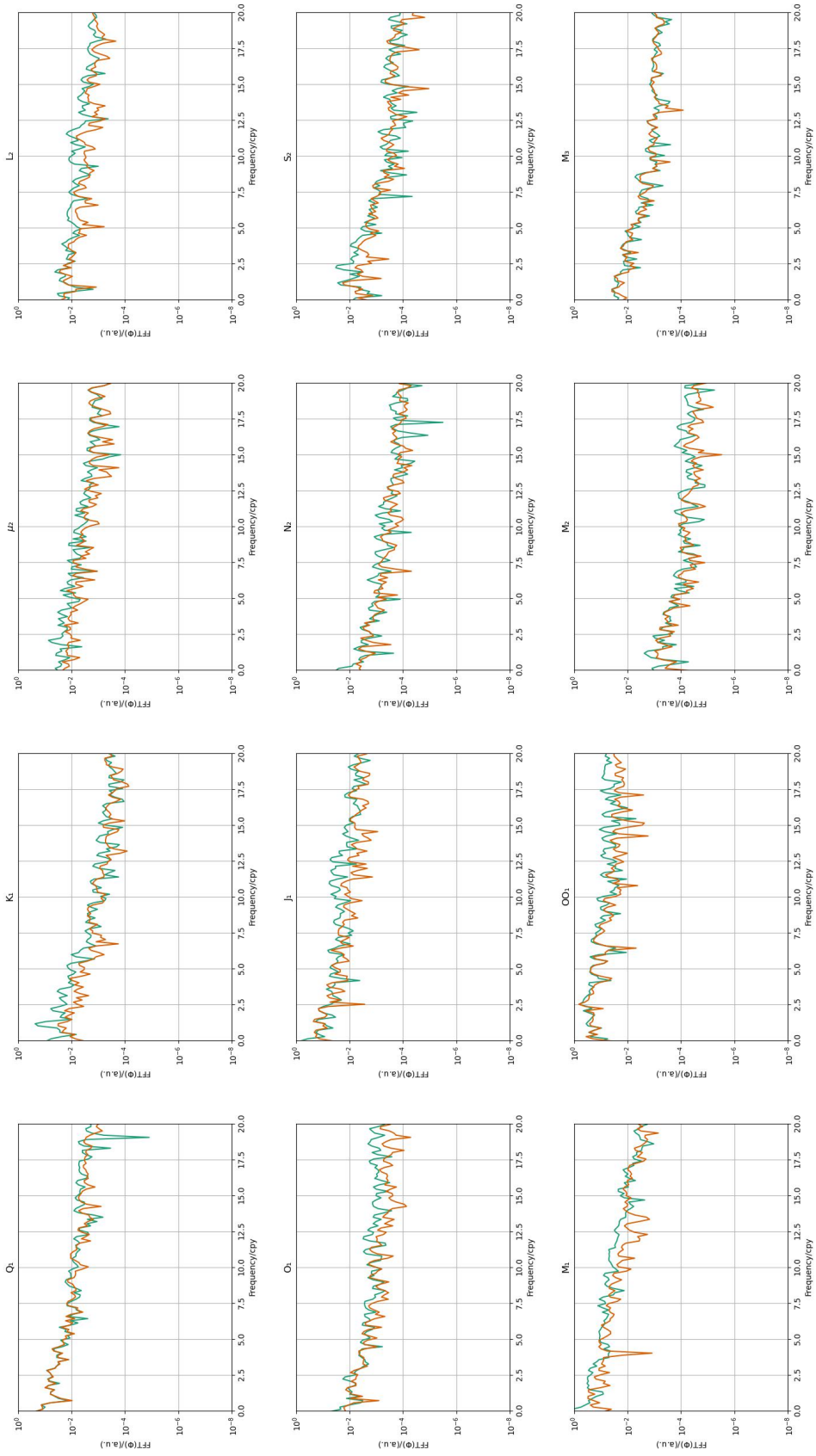

Figure E.20.: Spectral analysis (FFT) of MWA estimates for gravimetric phases in Djougou.

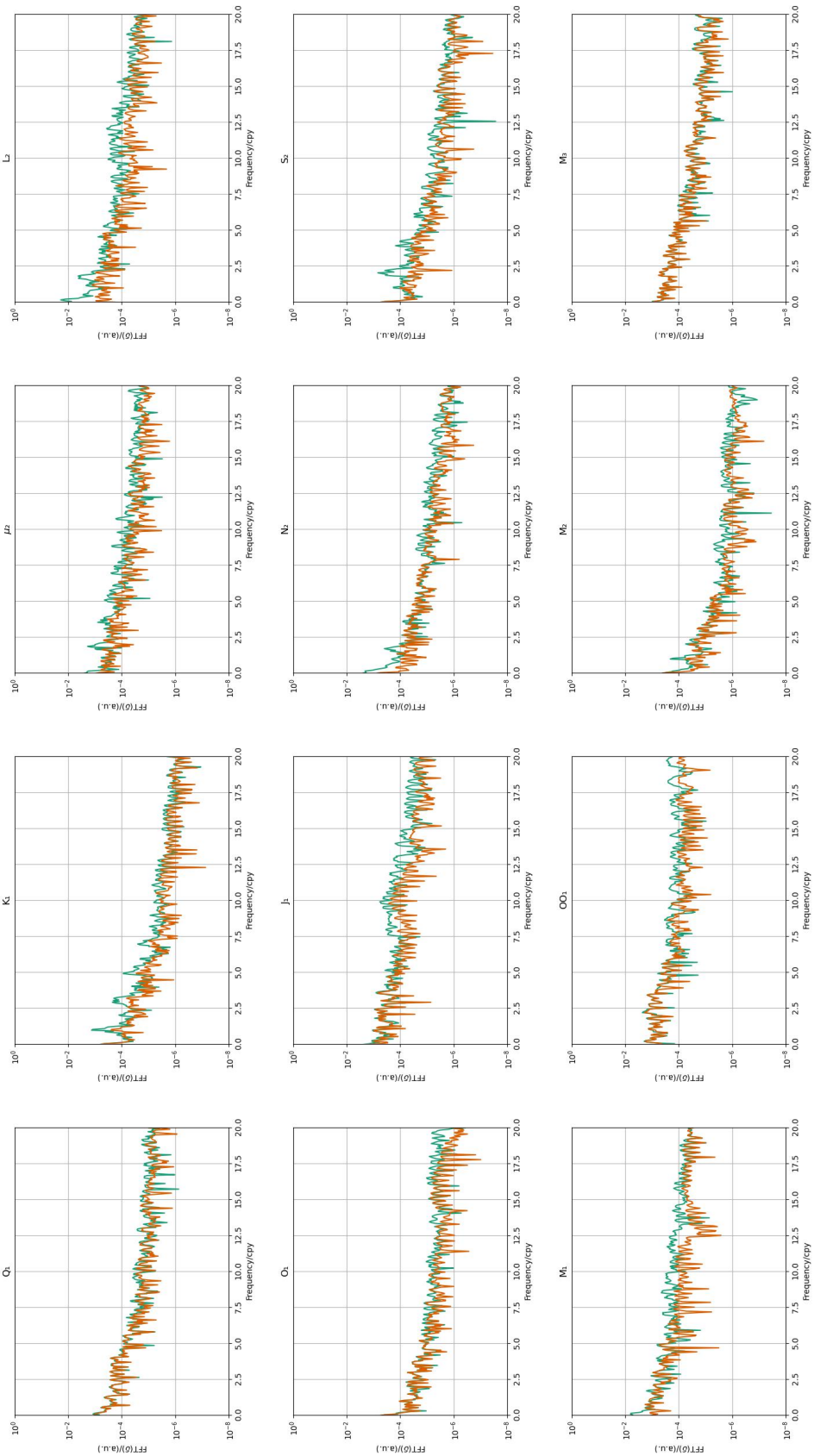

Figure E.21.: Spectral analysis (FFT) of MWA estimates for gravimetric factors in Sutherland (lower sensor).

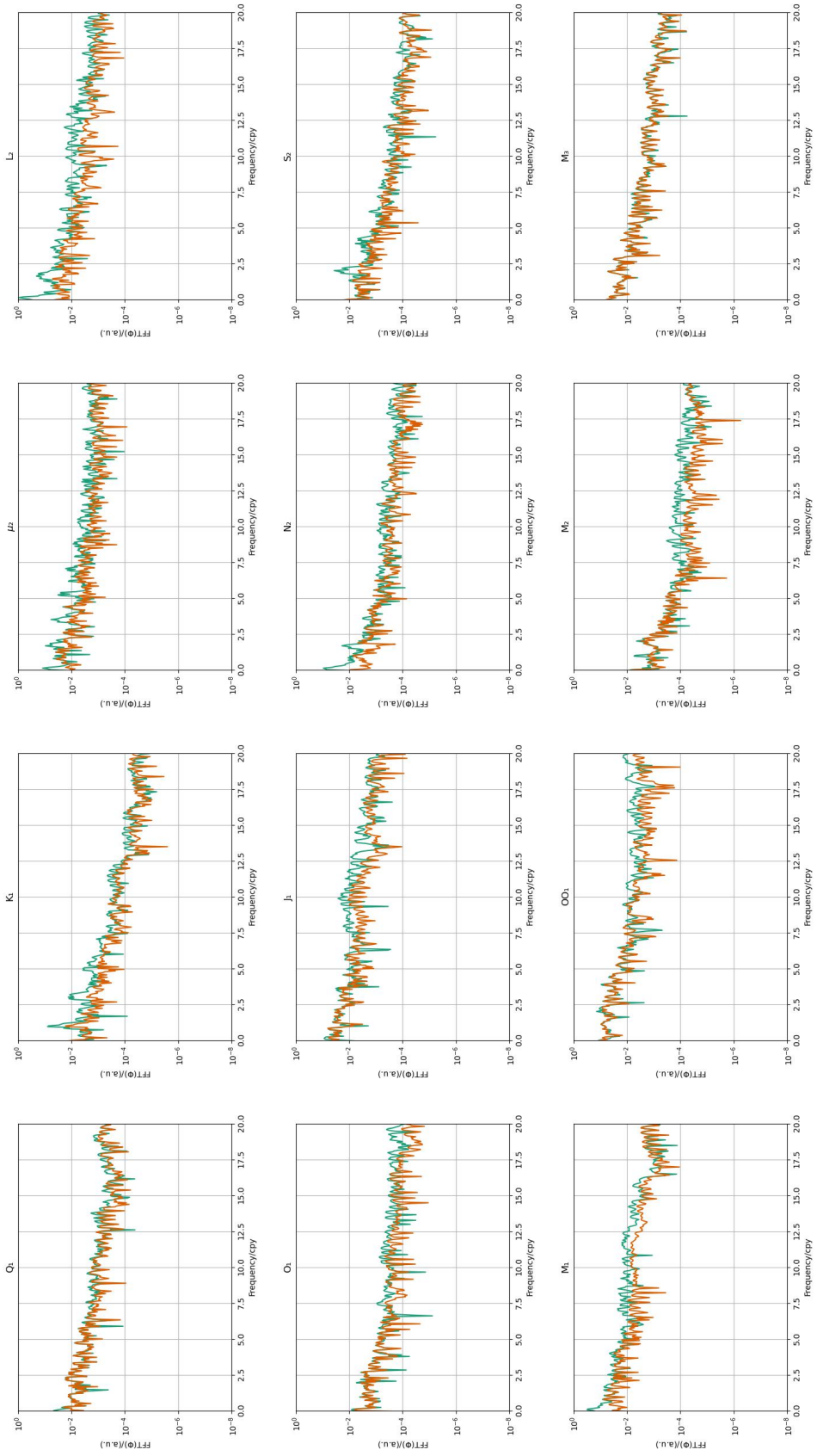

Figure E.22.: Spectral analysis (FFT) of MWA estimates for gravimetric phases in Sutherland (lower sensor).

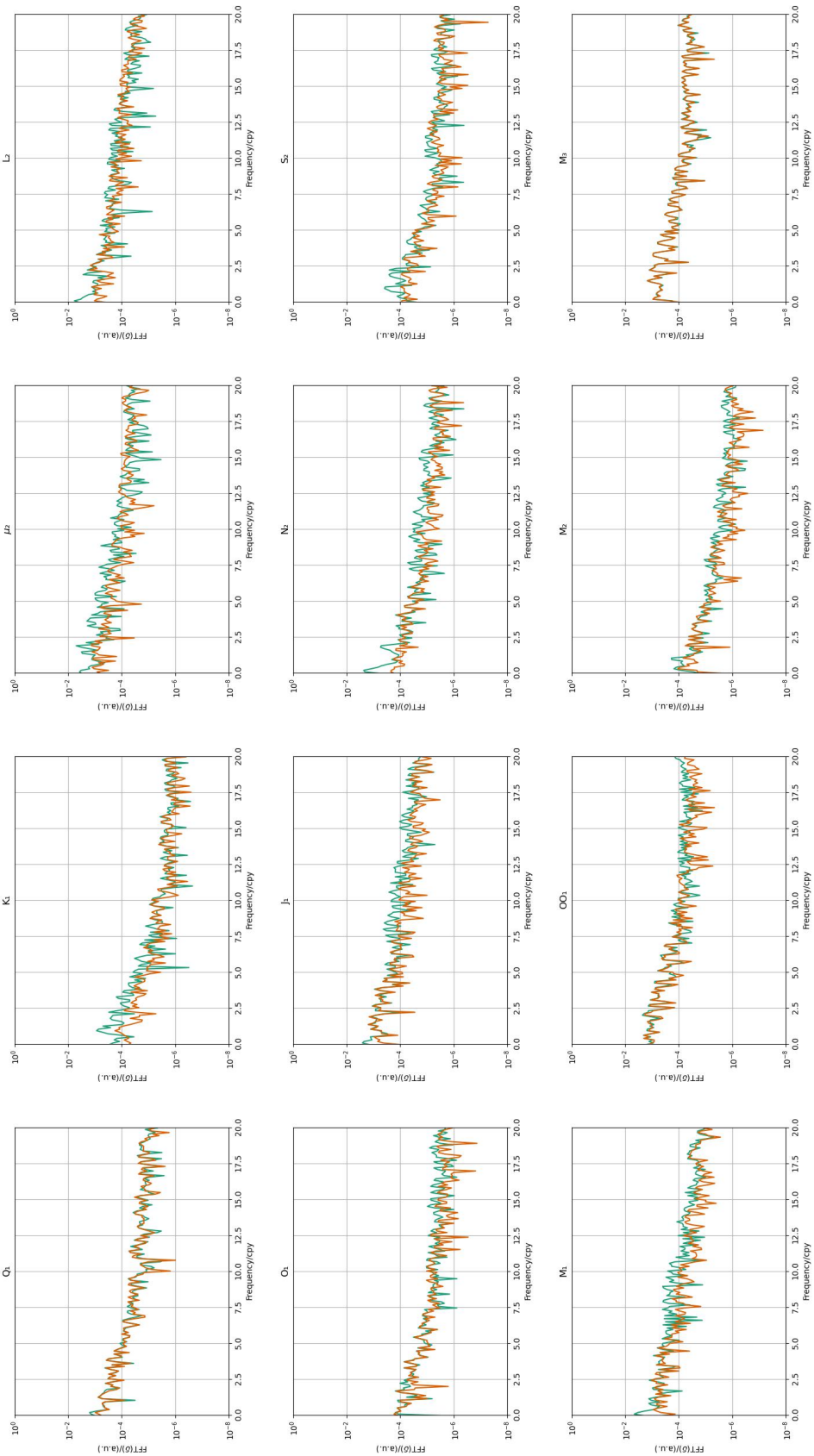

Figure E.23.: Spectral analysis (FFT) of MWA estimates for gravimetric factors in Tigo-Concepcion.

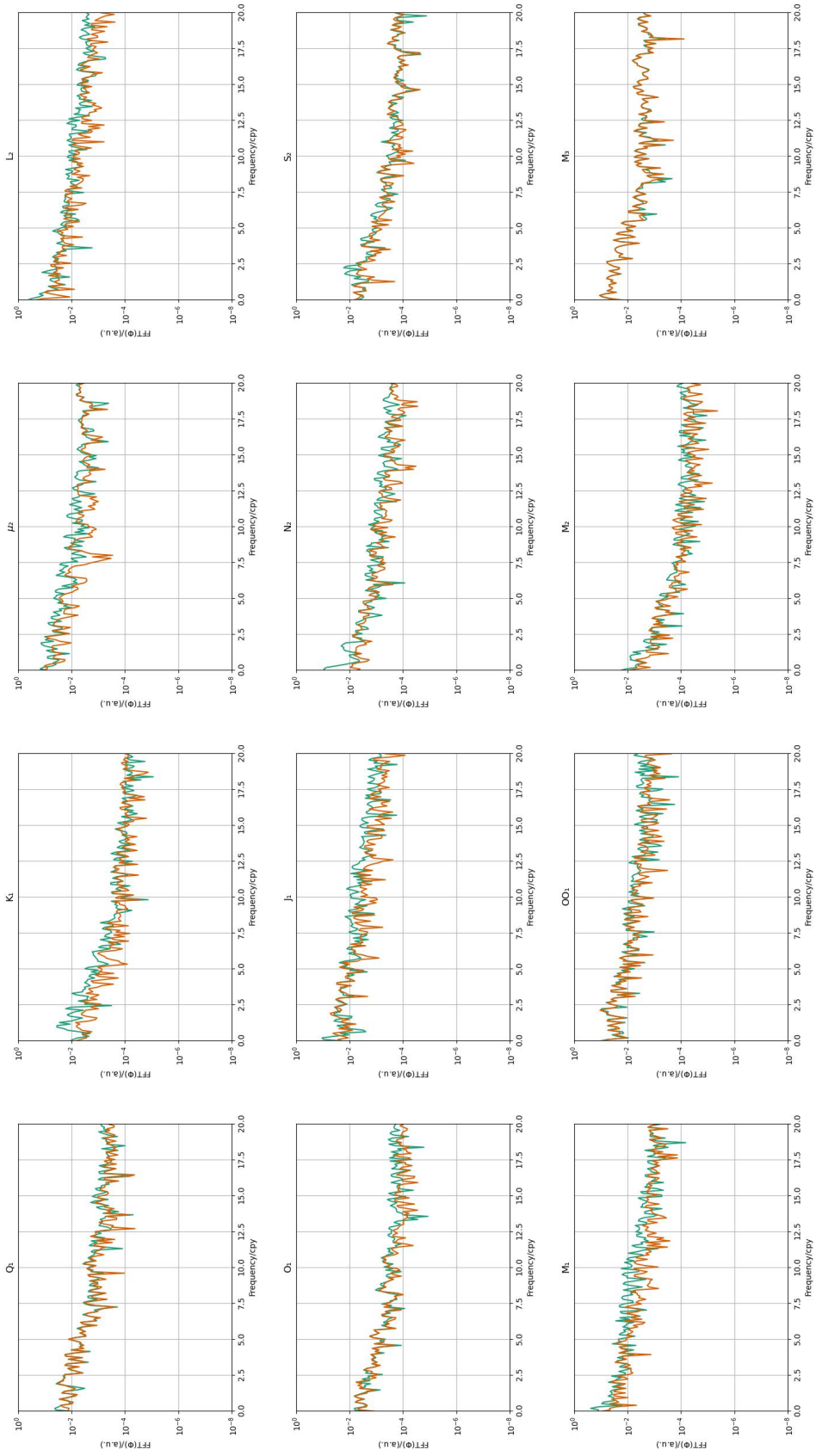

Figure E.24.: Spectral analysis (FFT) of MWA estimates for gravimetric phases in Tigo-Concepcion.

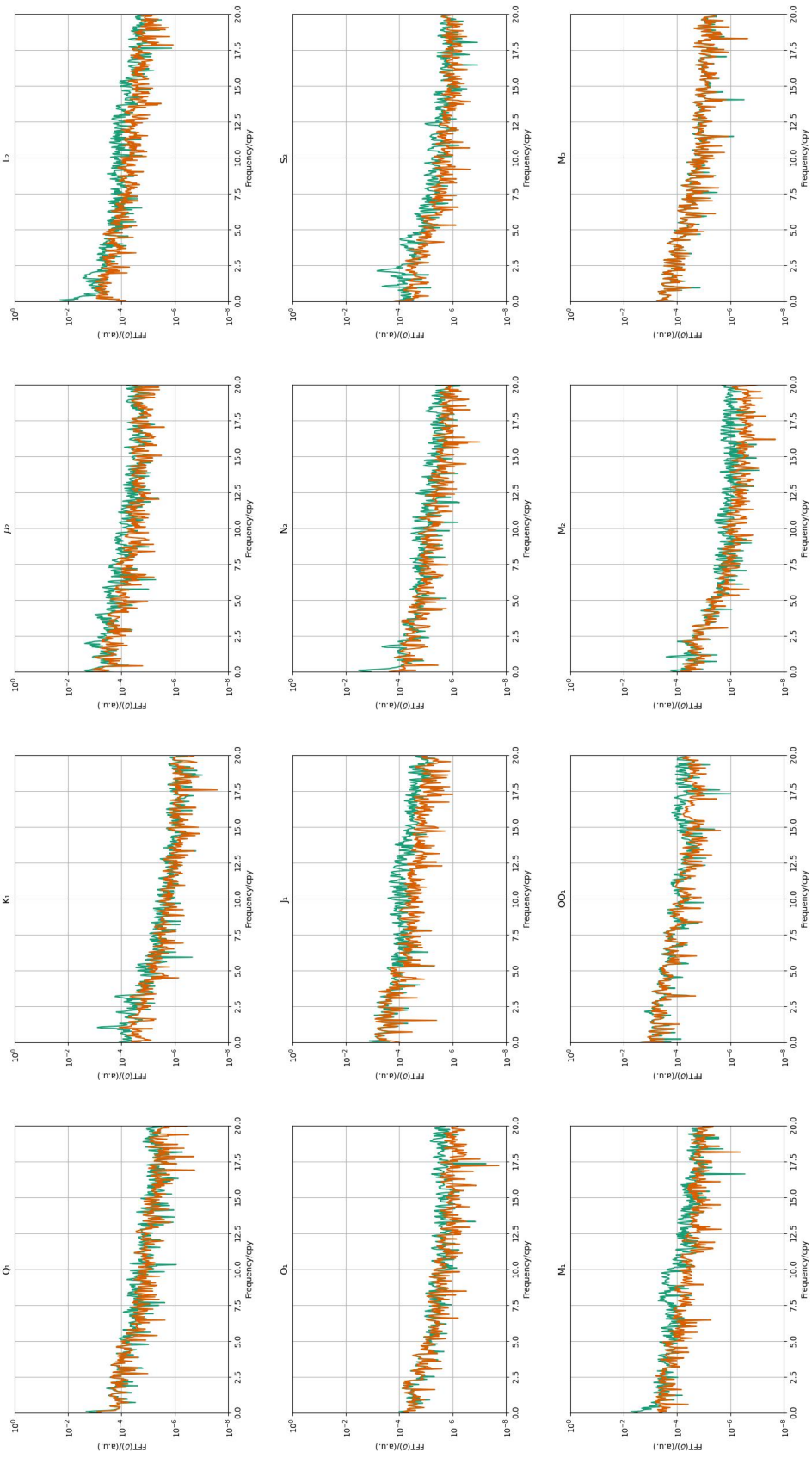

Figure E.25.: Spectral analysis (FFT) of MWA estimates for gravimetric factors in Canberra.

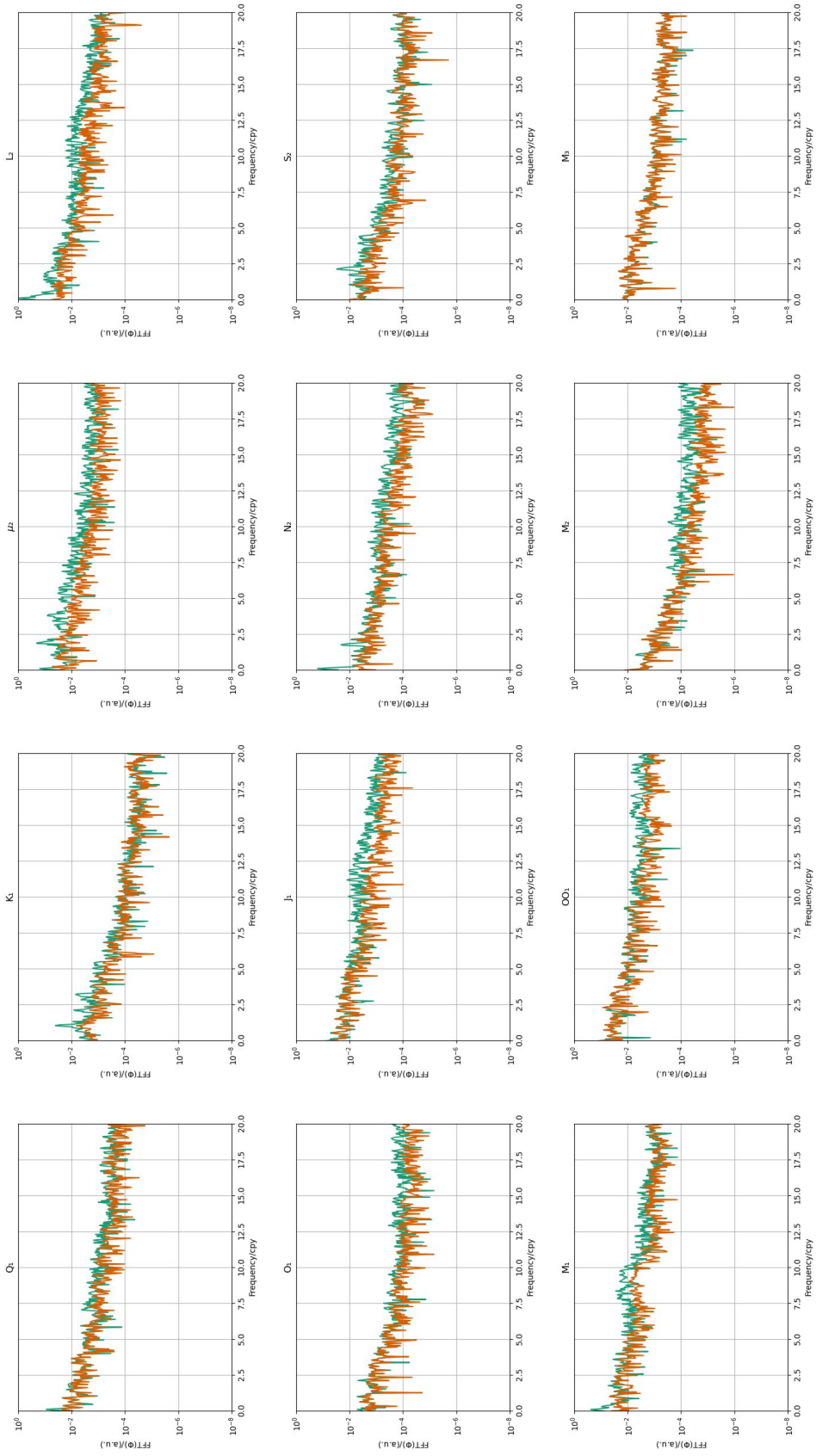

Figure E.26.: Spectral analysis (FFT) of MWA estimates for gravimetric phases in Canberra.

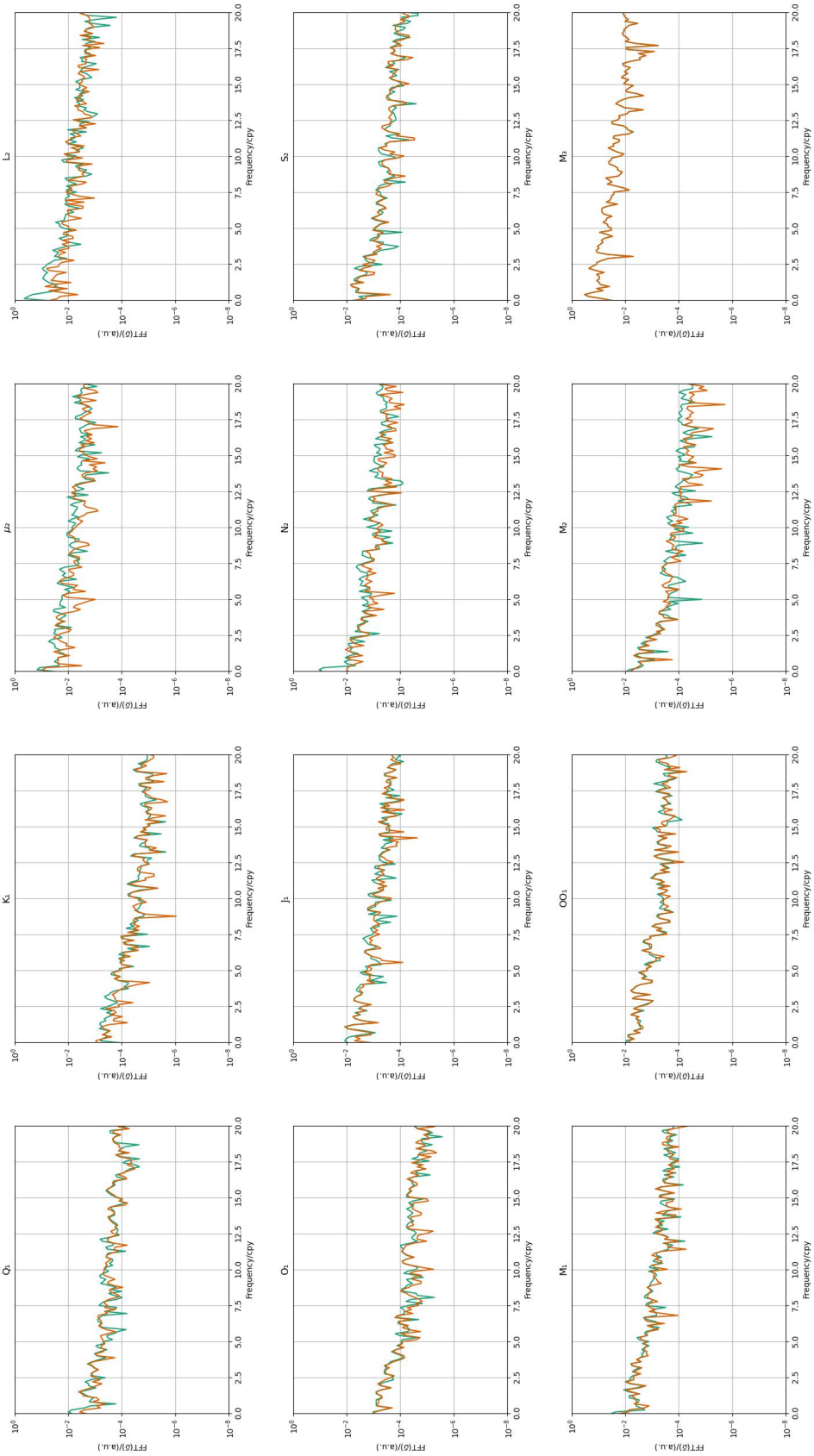

Figure E.27.: Spectral analysis (FFT) of MWA estimates for gravimetric factors in Ny-Ålesund.

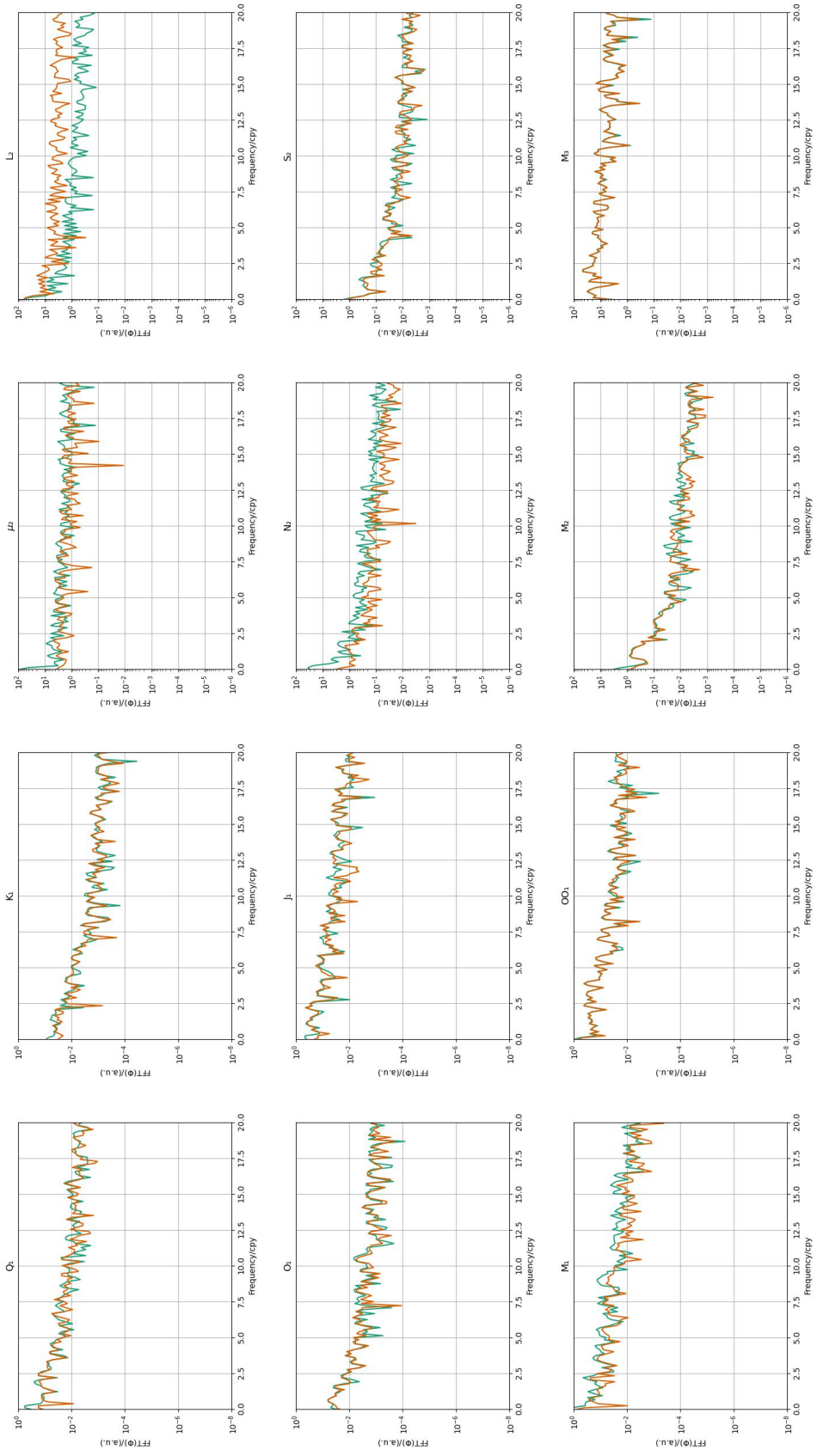

Figure E.28.: Spectral analysis (FFT) of MWA estimates for gravimetric phases in Ny-Ålesund.

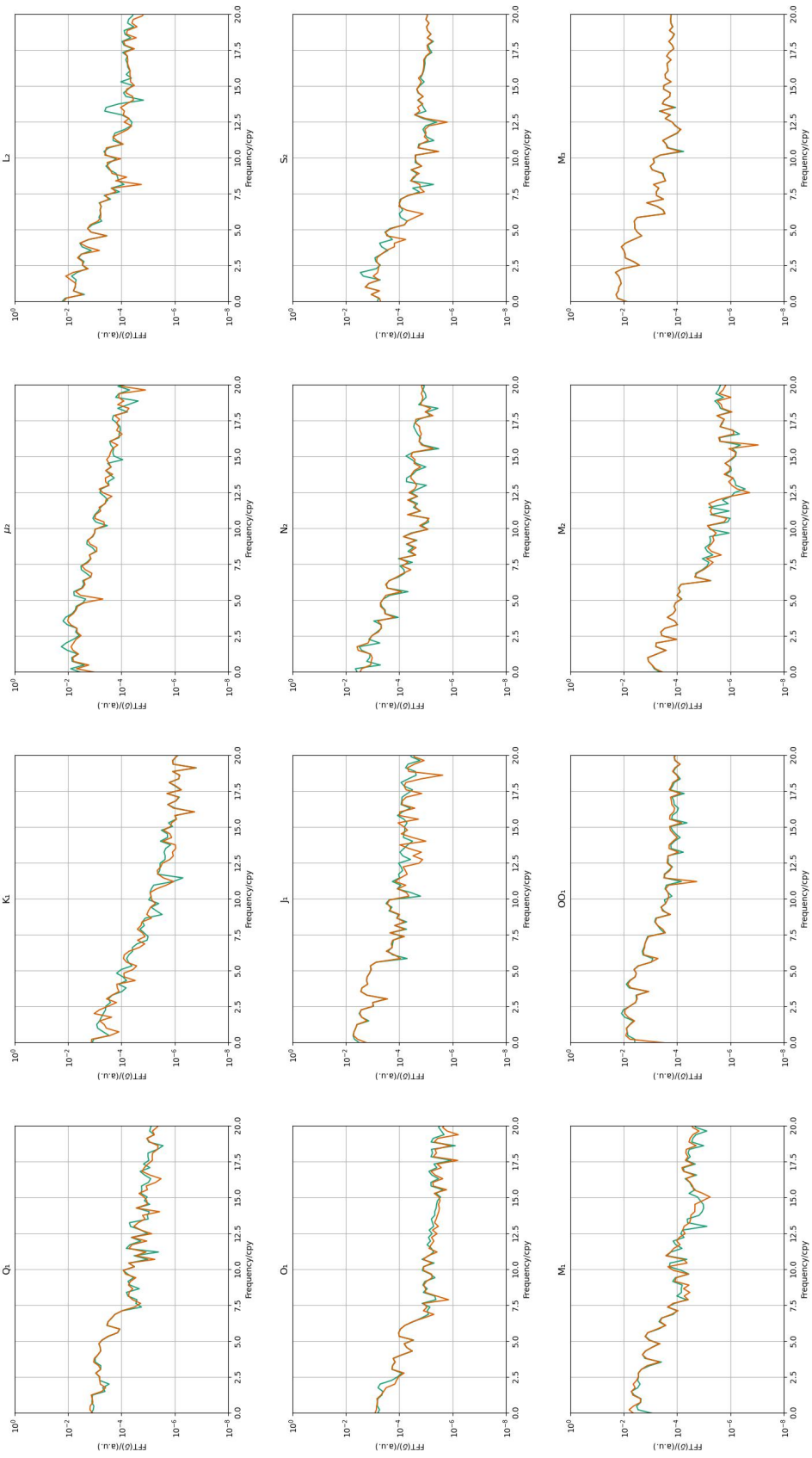

Figure E.29.: Spectral analysis (FFT) of MWA estimates for gravimetric factors in Syowa.

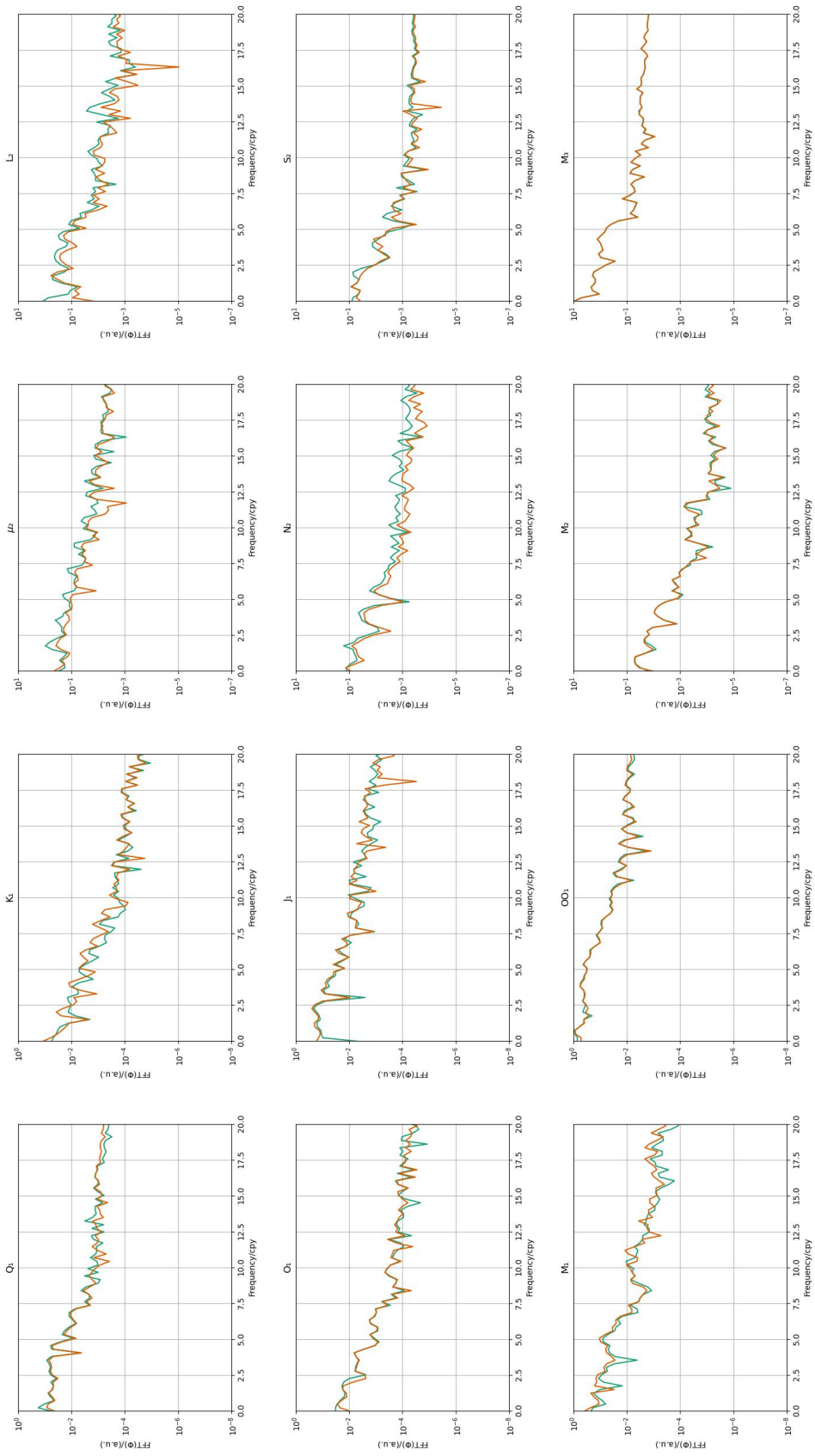

Figure E.30.: Spectral analysis (FFT) of MWA estimates for gravimetric phases in Syowa.

F. Air Pressure and Data Misfit

Compilation of diagrams of MWA of air pressure correction factor and gravity residual signal in each window for analysed observatories. Corresponding histograms and spectra of MWA are also presented. Green color corresponds to WDZe a priori model used in the analysis. Orange color corresponds to the LRM response model for a given station. Prior to the FFT, the linear trend was removed and the MWA time series was tapered using Hann window.

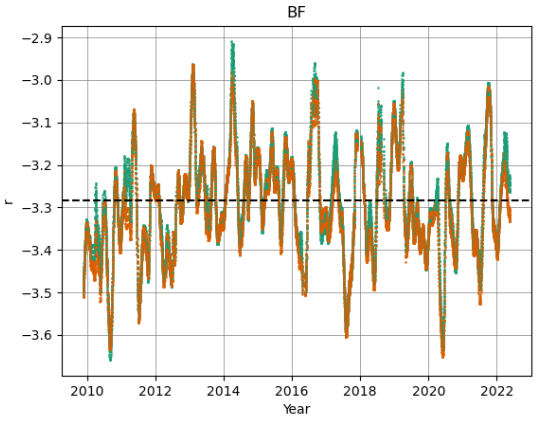

(a) Regression factor of air pressure.

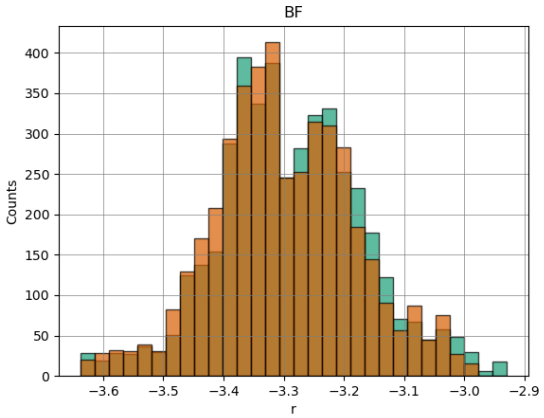

(b) Distribution of regression factor of air pressure.

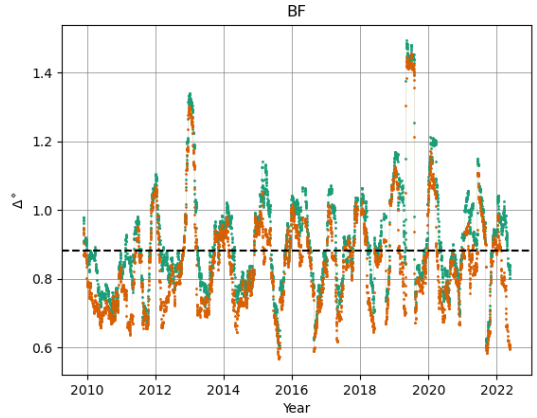

(c) Data misfit of untapered signals.

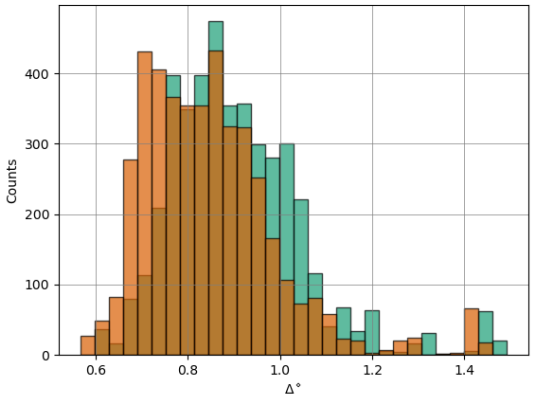

(d) Distribution of data misfit of untapered signals.

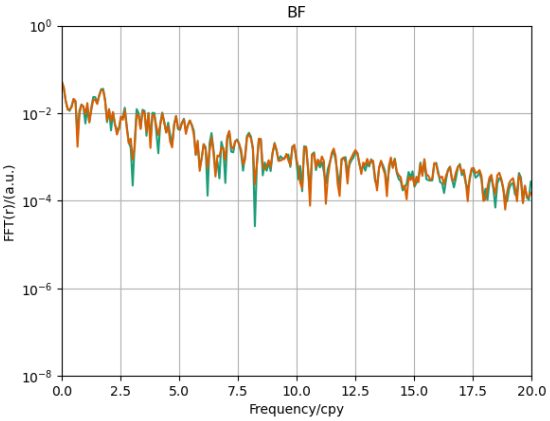

(e) Spectra of the coefficient for air pressure regression factor.

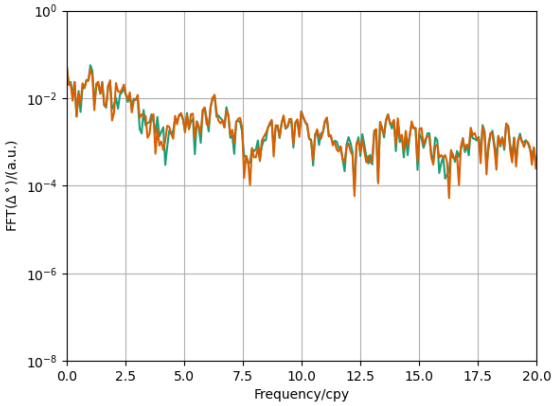

(f) Spectra of the data misfit of untapered signals.

Figure F.1.: The moving window analysis: air pressure regression factor, data misfit (untapered), their spectra and distribution. Station: Schiltach, BFO (lower sensor).

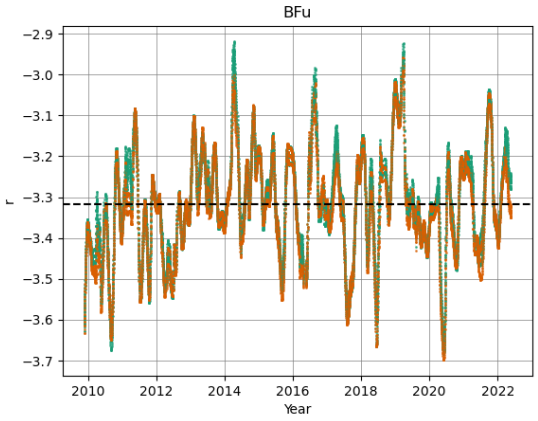

(a) Regression factor of air pressure.

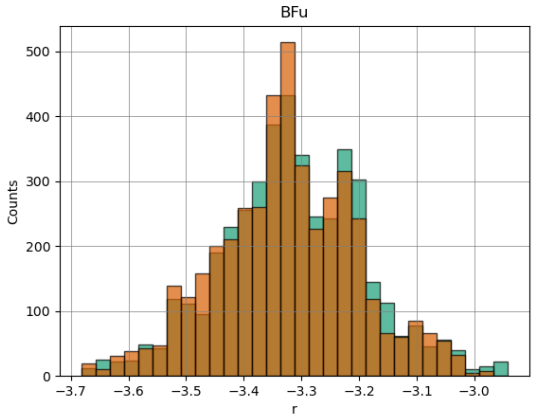

(b) Distribution of regression factor of air pressure.

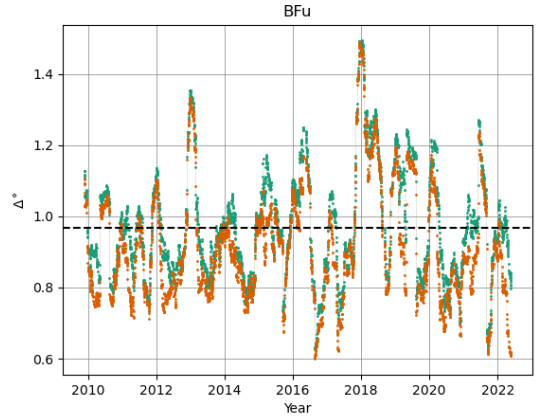

(c) Data misfit of untapered signals.

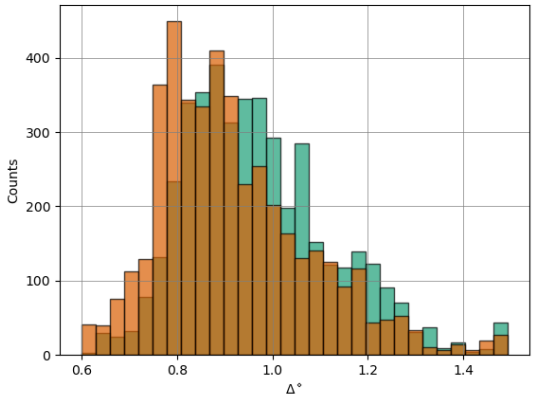

(d) Distribution of data misfit of untapered signals.

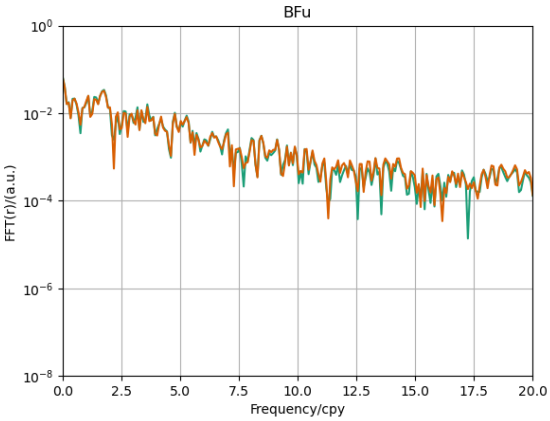

(e) Spectra of the coefficient for air pressure regression factor.

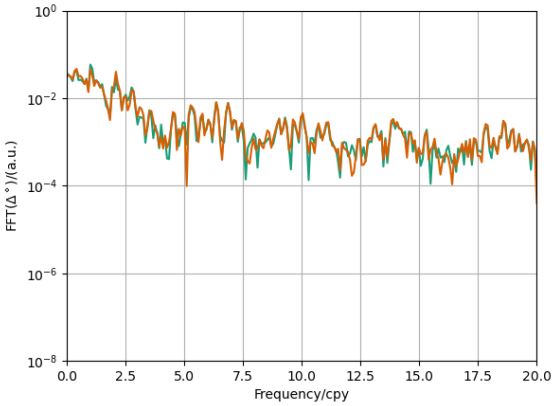

(f) Spectra of the data misfit of untapered signals.

Figure F.2.: The moving window analysis: air pressure regression factor, data misfit (untapered), their spectra and distribution. Station: Schiltach, BFO (upper sensor).

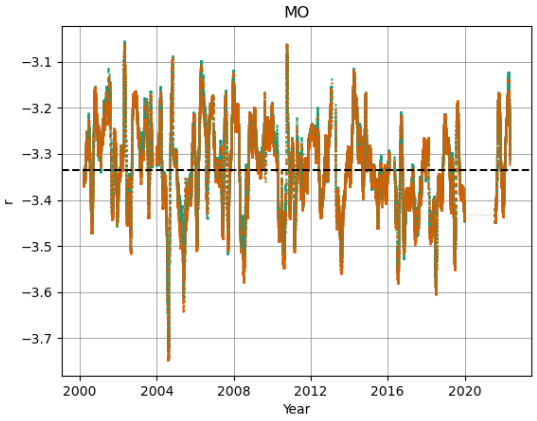

(a) Regression factor of air pressure.

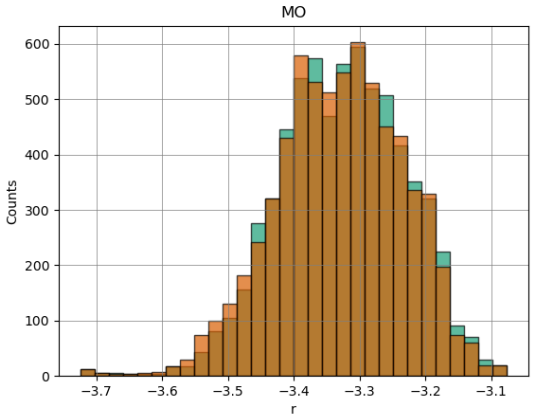

(b) Distribution of regression factor of air pressure.

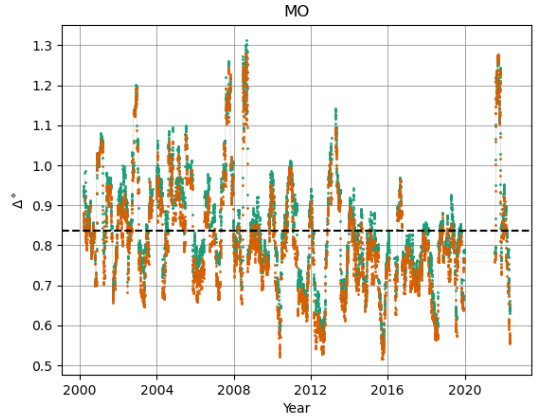

(c) Data misfit of untapered signals.

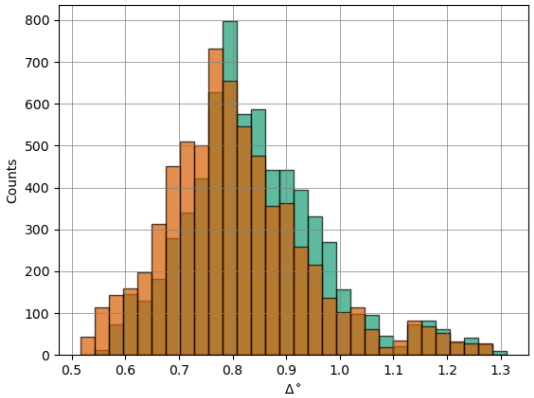

(d) Distribution of data misfit of untapered signals.

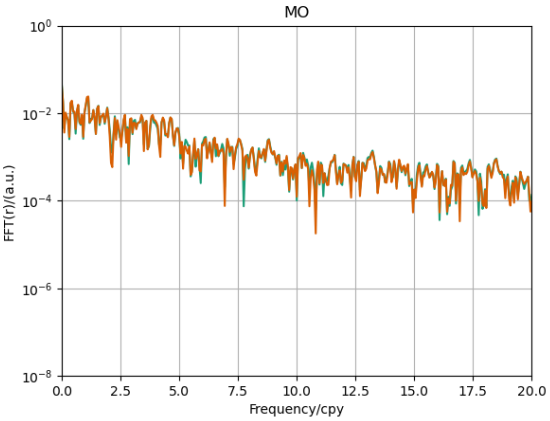

(e) Spectra of the coefficient for air pressure regression factor.

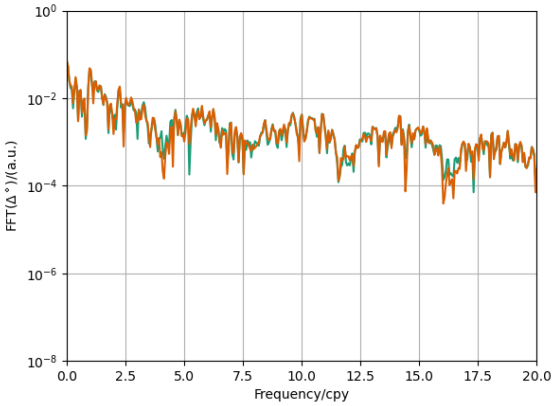

(f) Spectra of the data misfit of untapered signals.

Figure F.3.: The moving window analysis: air pressure regression factor, data misfit (untapered), their spectra and distribution. Station: Moxa (lower sensor).

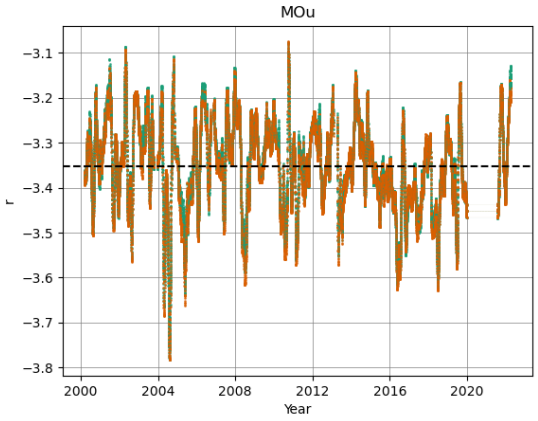

(a) Regression factor of air pressure.

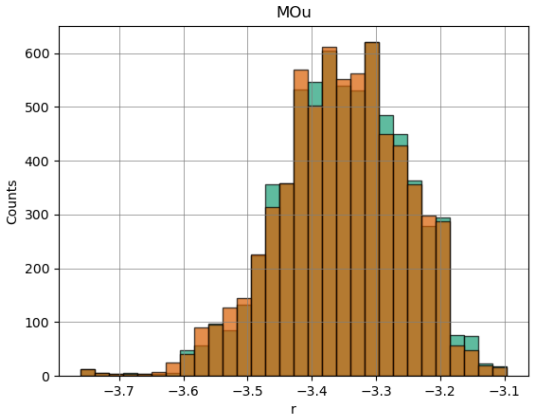

(b) Distribution of regression factor of air pressure.

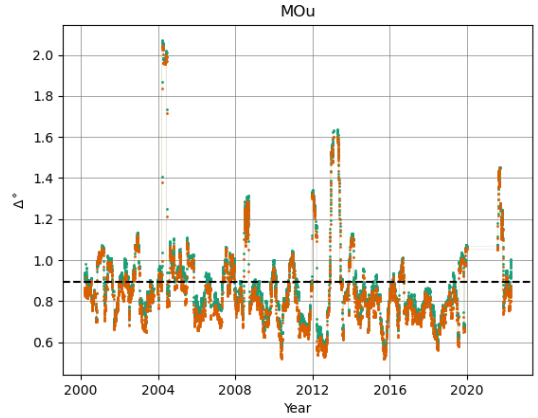

(c) Data misfit of untapered signals.

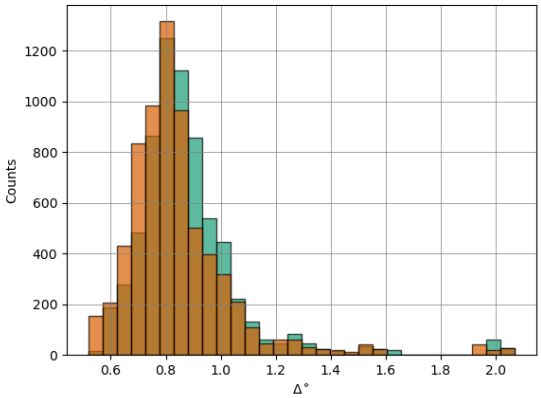

(d) Distribution of data misfit of untapered signals.

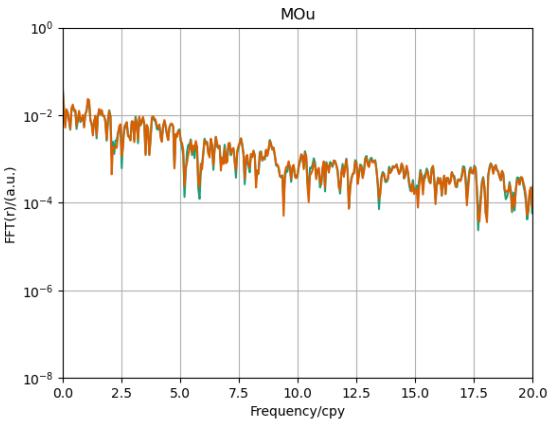

(e) Spectra of the coefficient for air pressure regression factor.

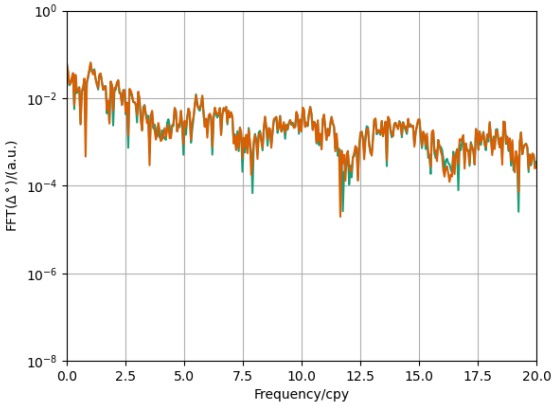

(f) Spectra of the data misfit of untapered signals.

Figure F.4.: The moving window analysis: air pressure regression factor, data misfit (untapered), their spectra and distribution. Station: Moxa (upper sensor).

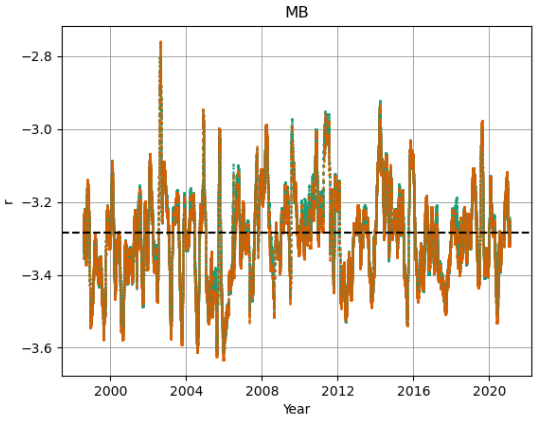

(a) Regression factor of air pressure.

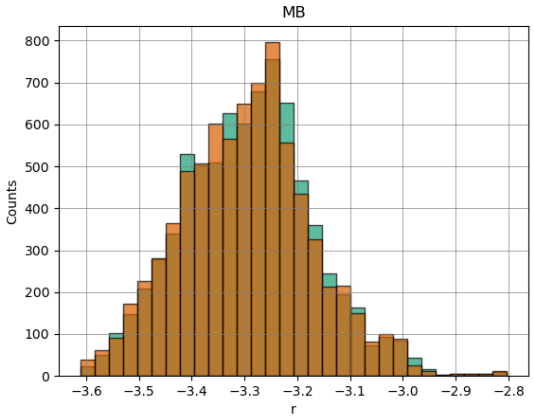

(b) Distribution of regression factor of air pressure.

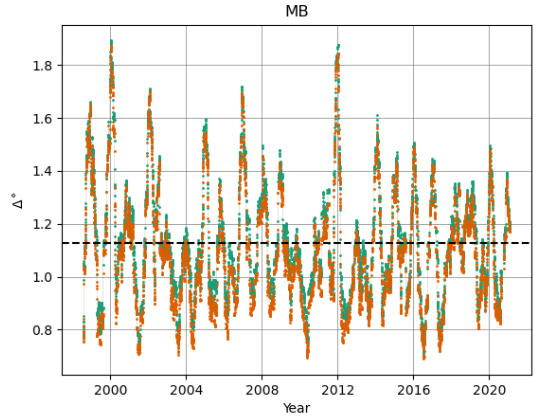

(c) Data misfit of untapered signals.

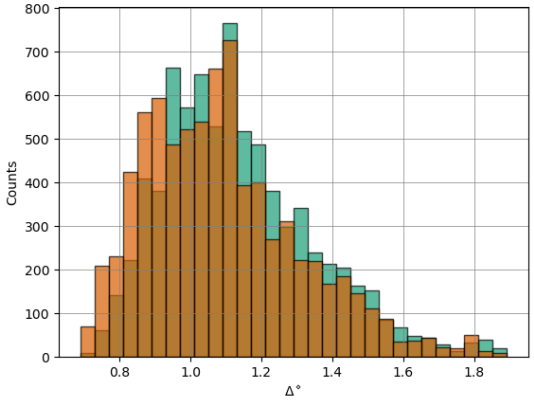

(d) Distribution of data misfit of untapered signals.

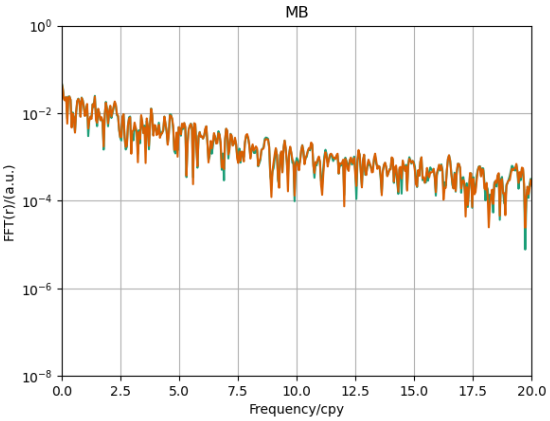

(e) Spectra of the coefficient for air pressure regression factor.

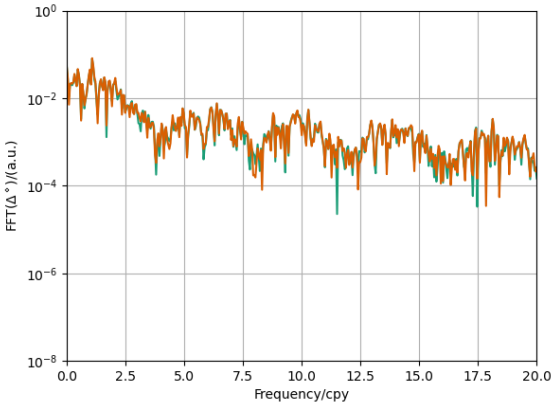

(f) Spectra of the data misfit of untapered signals.

Figure F.5.: The moving window analysis: air pressure regression factor, data misfit (untapered), their spectra and distribution. Station: Membach.

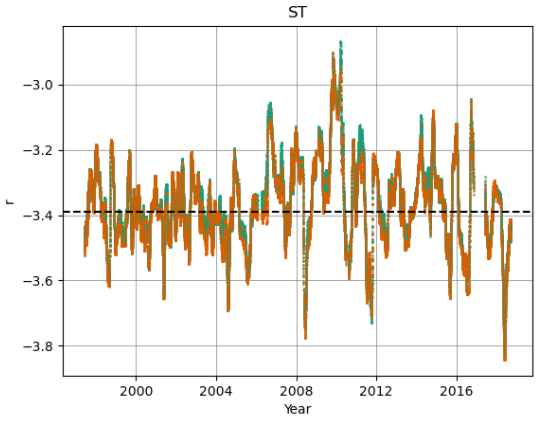

(a) Regression factor of air pressure.

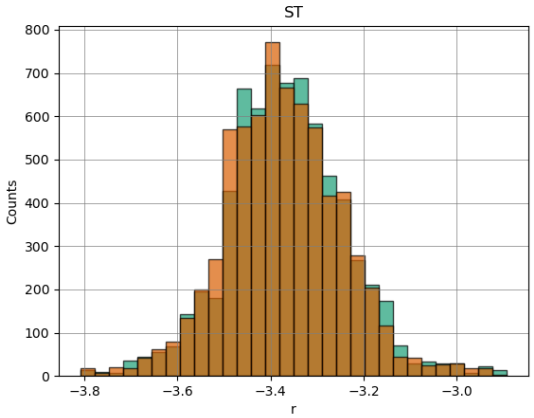

(b) Distribution of regression factor of air pressure.

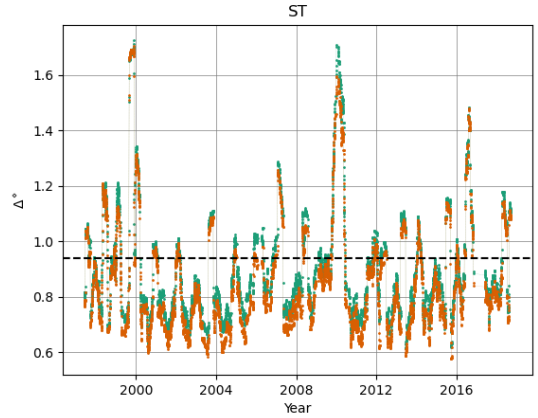

(c) Data misfit of untapered signals.

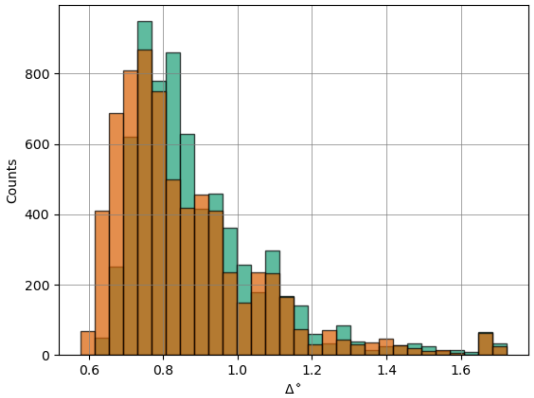

(d) Distribution of data misfit of untapered signals.

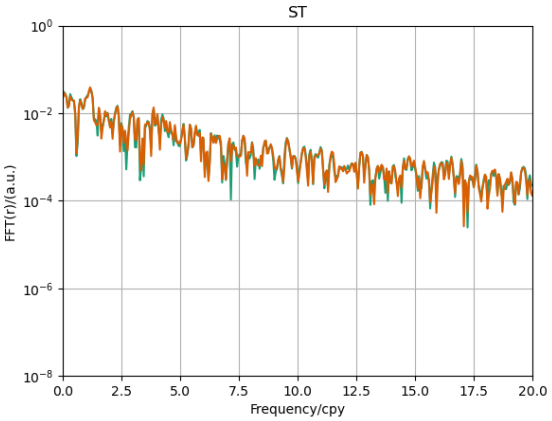

(e) Spectra of the coefficient for air pressure regression factor.

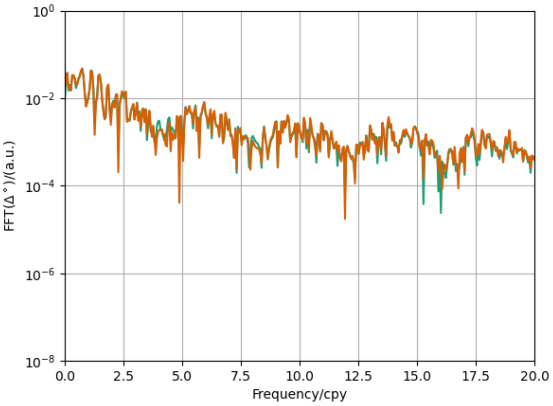

(f) Spectra of the data misfit of untapered signals.

Figure F.6.: The moving window analysis: air pressure regression factor, data misfit (untapered), their spectra and distribution. Station: Strasbourg.

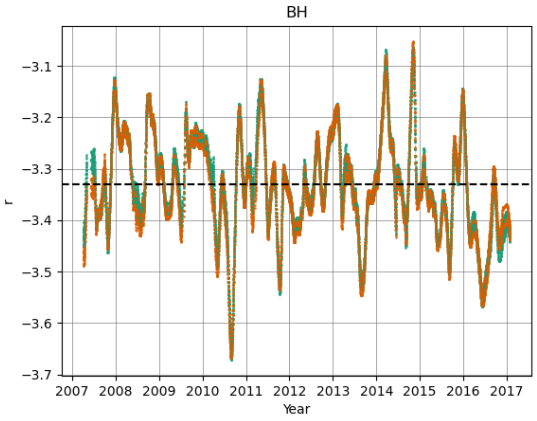

(a) Regression factor of air pressure.

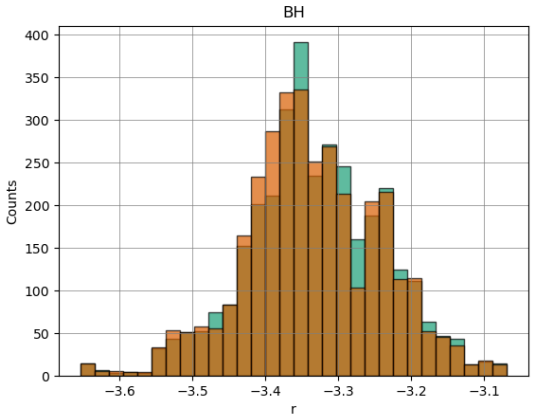

(b) Distribution of regression factor of air pressure.

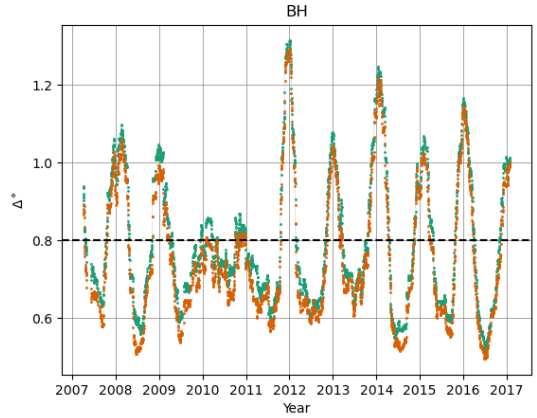

(c) Data misfit of untapered signals.

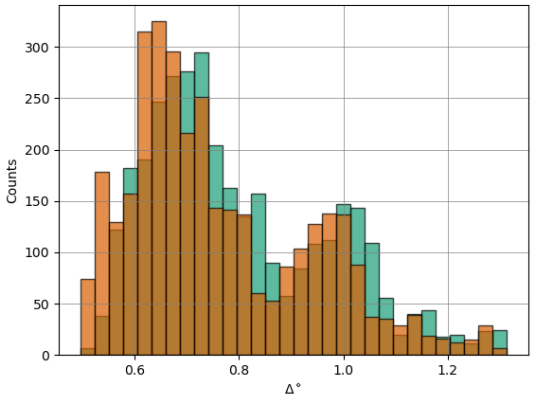

(d) Distribution of data misfit of untapered signals.

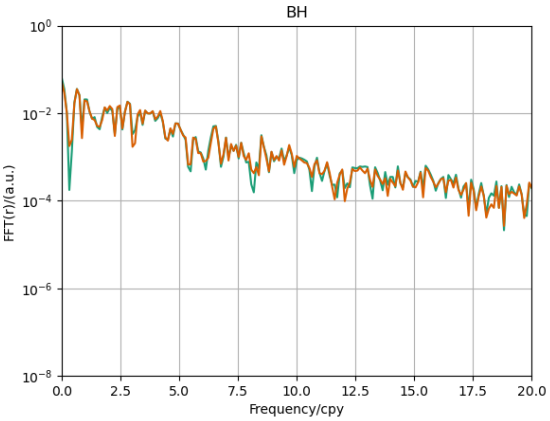

(e) Spectra of the coefficient for air pressure regression factor.

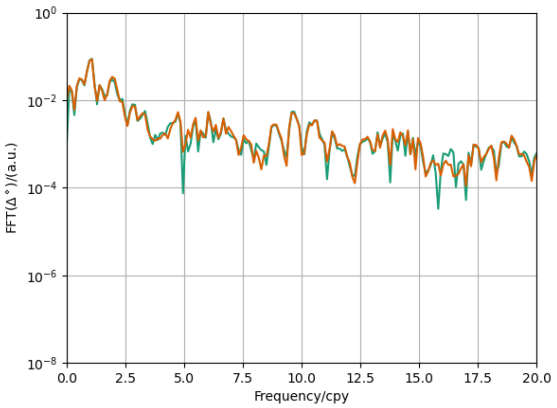

(f) Spectra of the data misfit of untapered signals.

Figure F.7.: The moving window analysis: air pressure regression factor, data misfit (untapered), their spectra and distribution. Station: Bad Homburg.

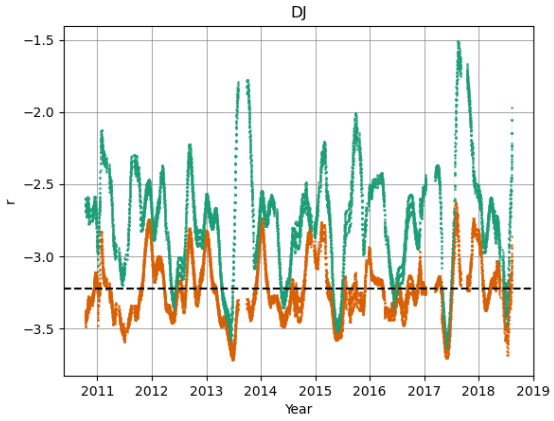

(a) Regression factor of air pressure.

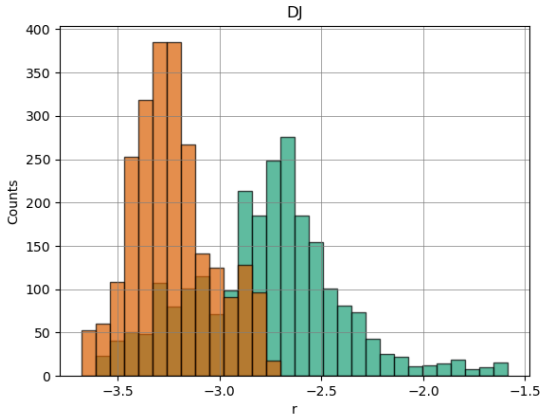

(b) Distribution of regression factor of air pressure.

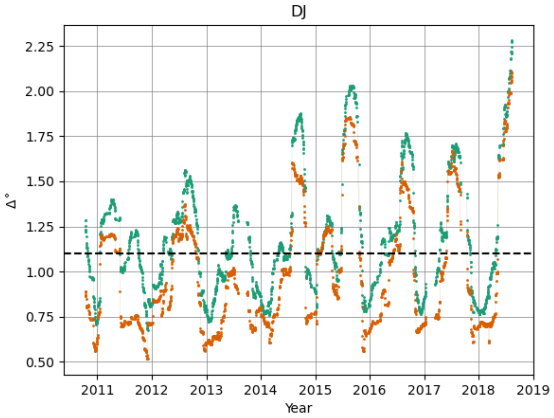

(c) Data misfit of untapered signals.

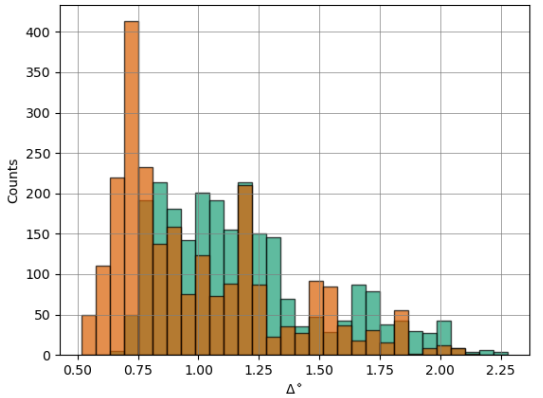

(d) Distribution of data misfit of untapered signals.

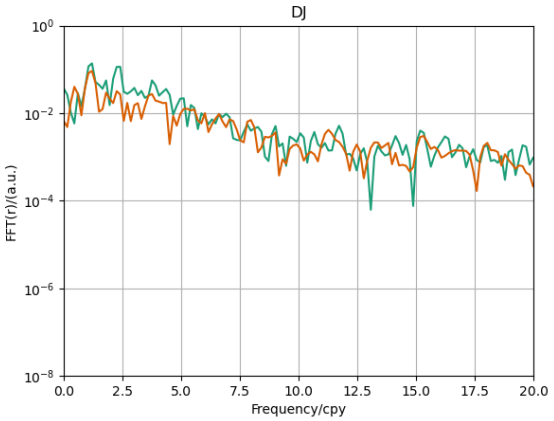

(e) Spectra of the coefficient for air pressure regression factor.

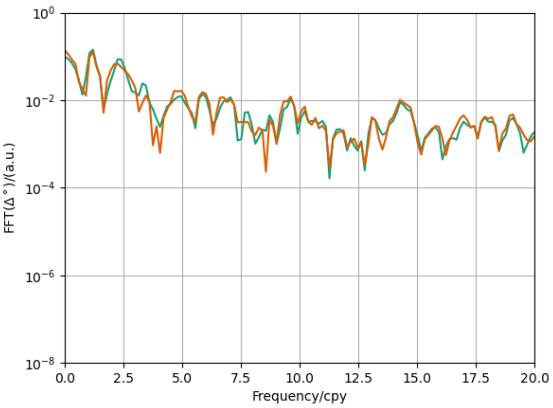

(f) Spectra of the data misfit of untapered signals.

Figure F.8.: The moving window analysis: air pressure regression factor, data misfit (untapered), their spectra and distribution. Station: Djougou.

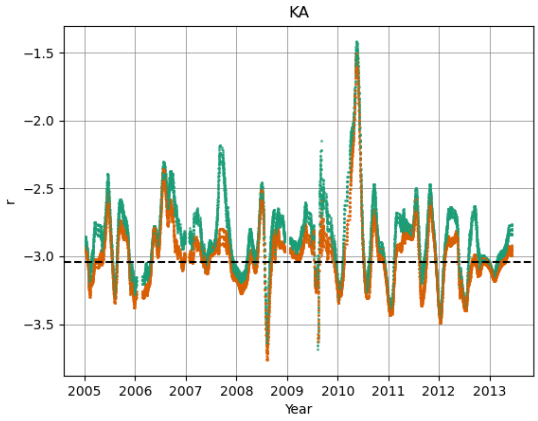

(a) Regression factor of air pressure.

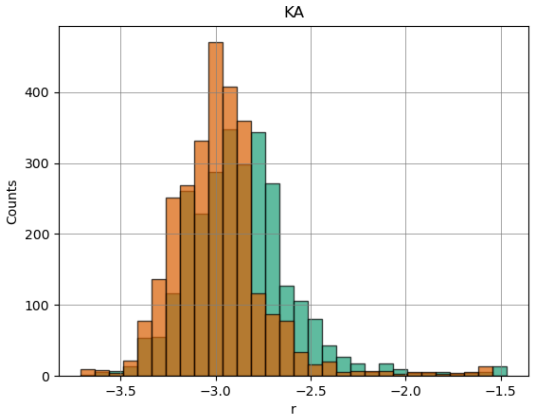

(b) Distribution of regression factor of air pressure.

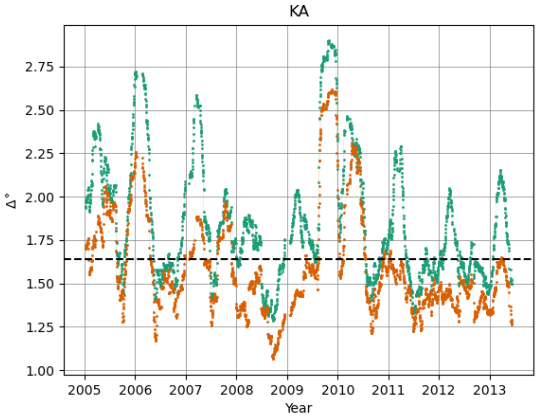

(c) Data misfit of untapered signals.

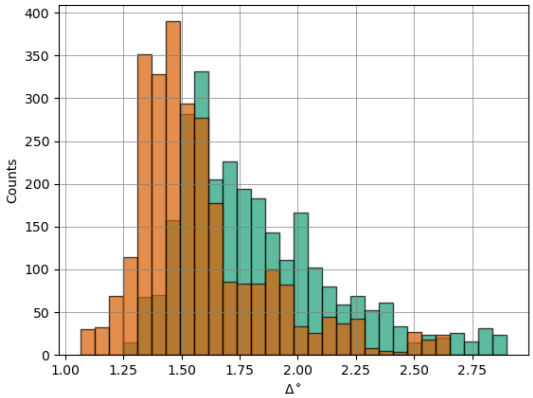

(d) Distribution of data misfit of untapered signals.

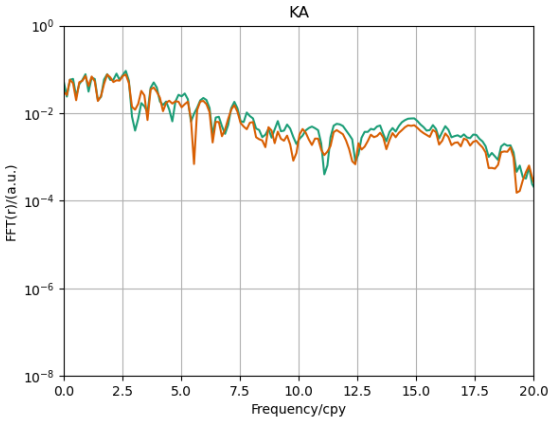

(e) Spectra of the coefficient for air pressure regression factor.

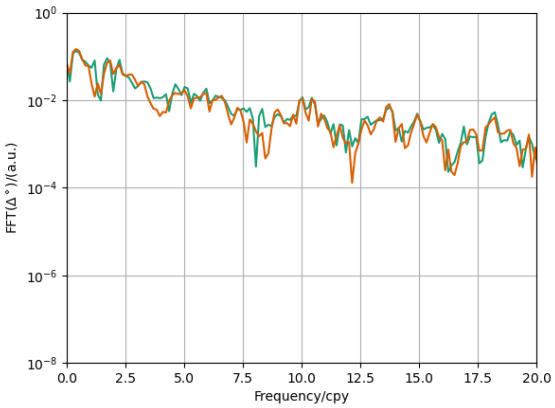

(f) Spectra of the data misfit of untapered signals.

Figure F.9.: The moving window analysis: air pressure regression factor, data misfit (untapered), their spectra and distribution. Station: Kamioka.

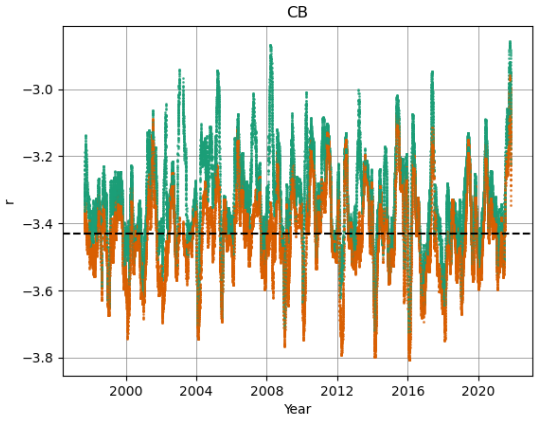

(a) Regression factor of air pressure.

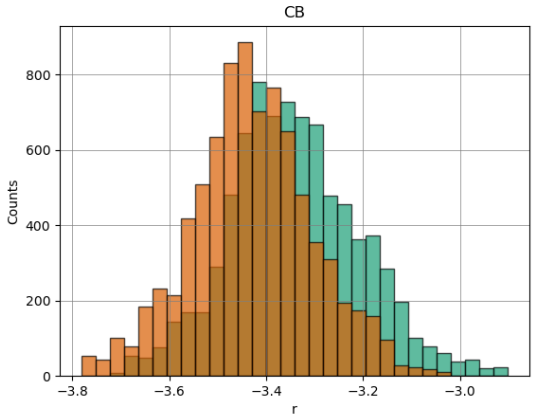

(b) Distribution of regression factor of air pressure.

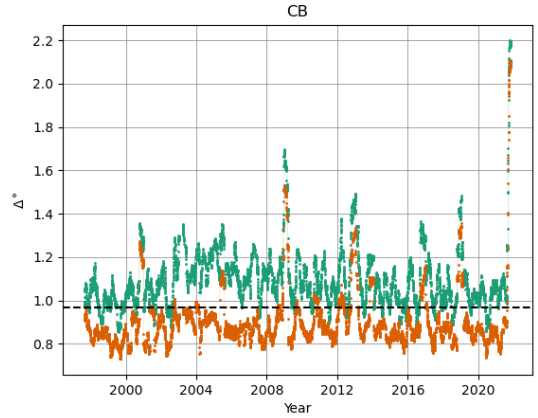

(c) Data misfit of untapered signals.

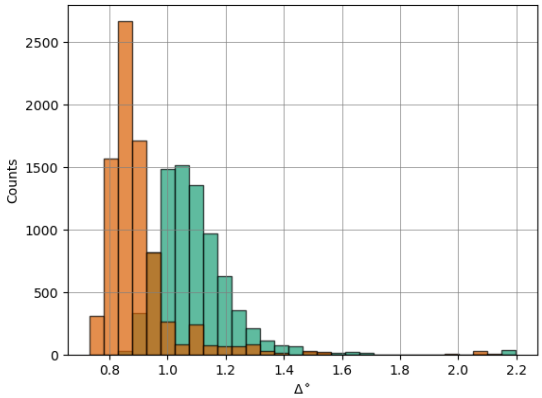

(d) Distribution of data misfit of untapered signals.

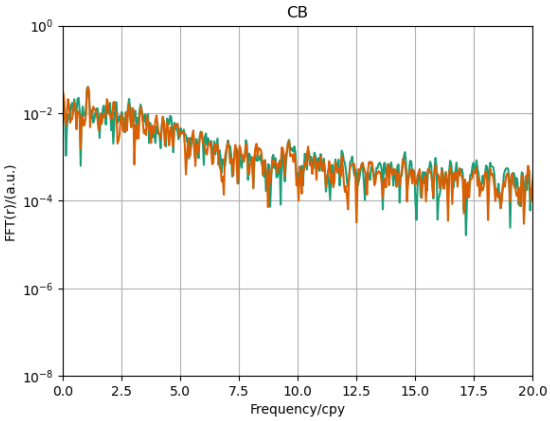

(e) Spectra of the coefficient for air pressure regression factor.

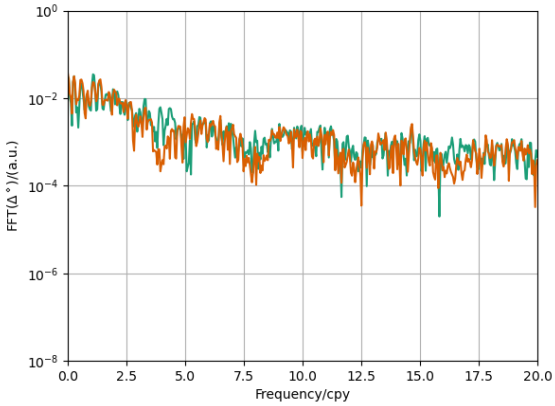

(f) Spectra of the data misfit of untapered signals.

Figure F.10.: The moving window analysis: air pressure regression factor, data misfit (untapered), their spectra and distribution. Station: Canberra.

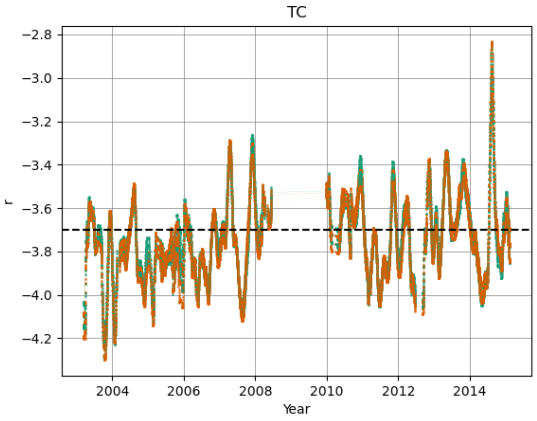

(a) Regression factor of air pressure.

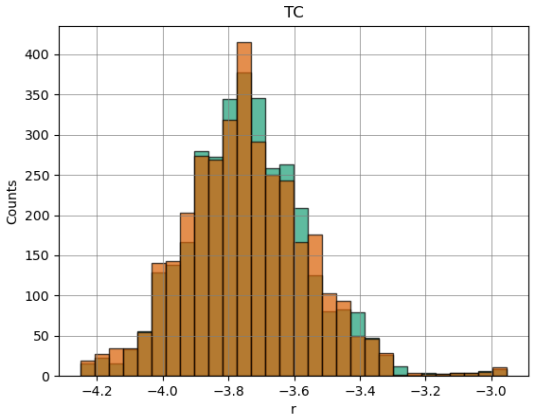

(b) Distribution of regression factor of air pressure.

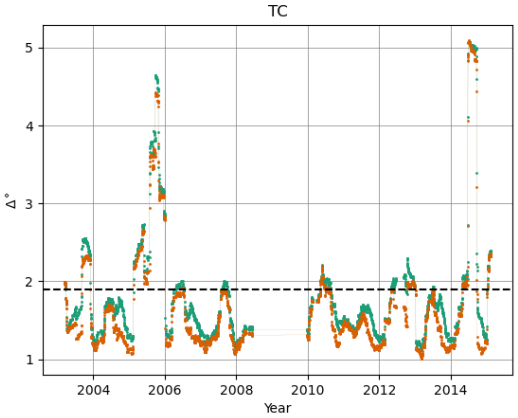

(c) Data misfit of untapered signals.

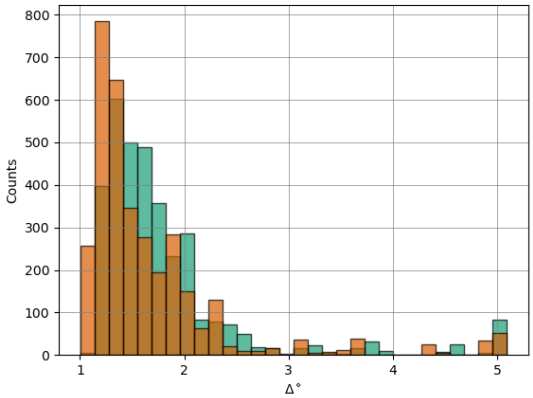

(d) Distribution of data misfit of untapered signals.

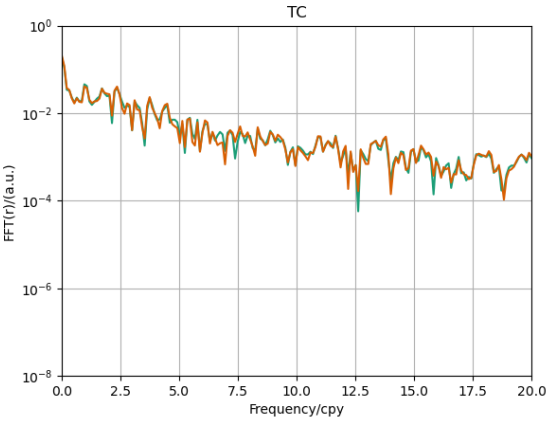

(e) Spectra of the coefficient for air pressure regression factor.

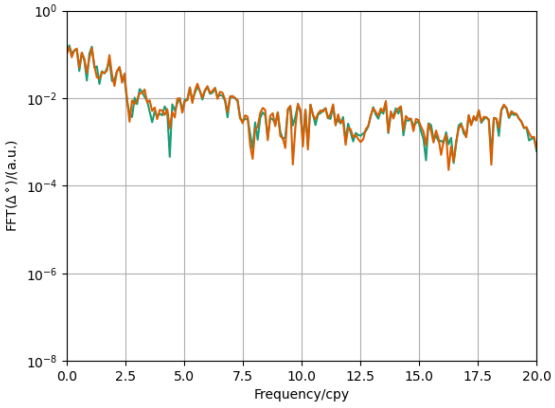

(f) Spectra of the data misfit of untapered signals.

Figure F.11.: The moving window analysis: air pressure regression factor, data misfit (untapered), their spectra and distribution. Station: Tigo-Concepcion.

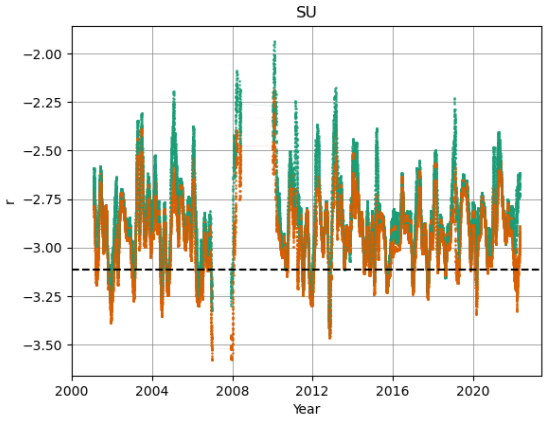

(a) Regression factor of air pressure.

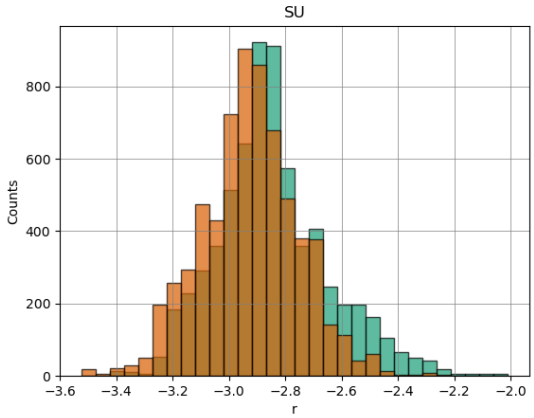

(b) Distribution of regression factor of air pressure.

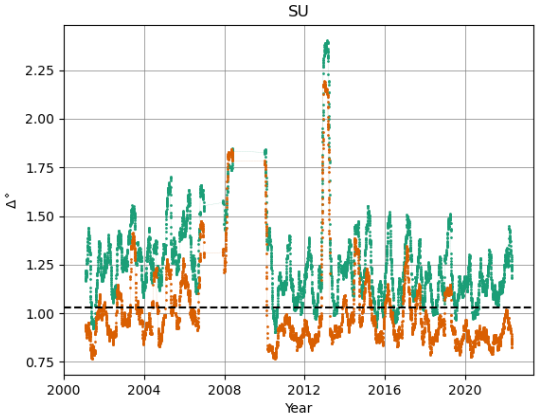

(c) Data misfit of untapered signals.

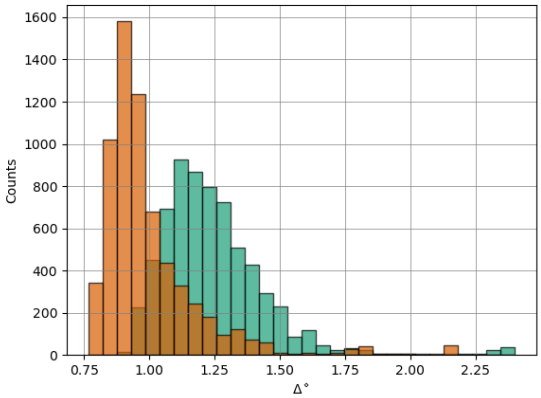

(d) Distribution of data misfit of untapered signals.

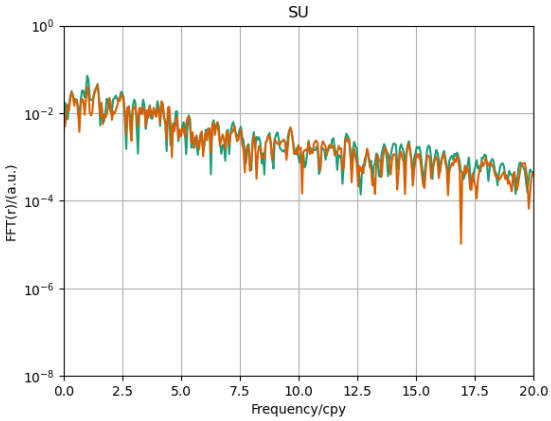

(e) Spectra of the coefficient for air pressure regression factor.

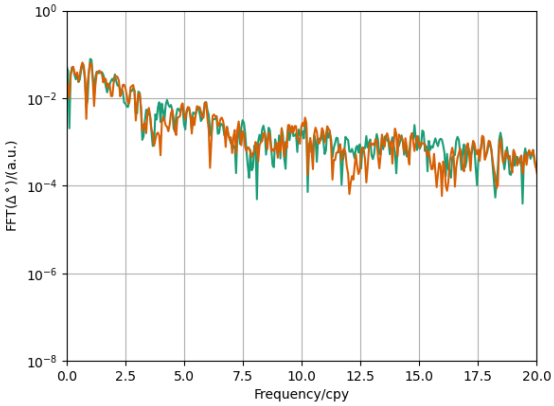

(f) Spectra of the data misfit of untapered signals.

Figure F.12.: The moving window analysis: air pressure regression factor, data misfit (untapered), their spectra and distribution. Station: Sutherland.

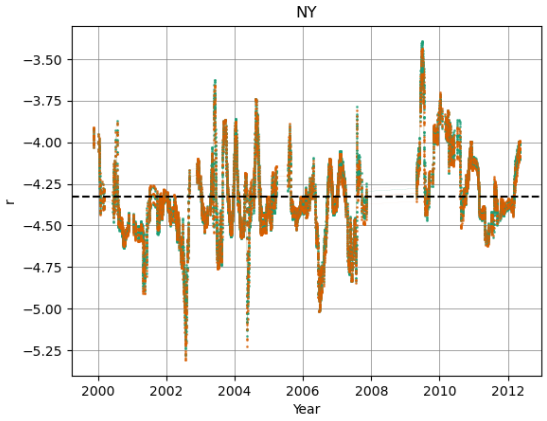

(a) Regression factor of air pressure.

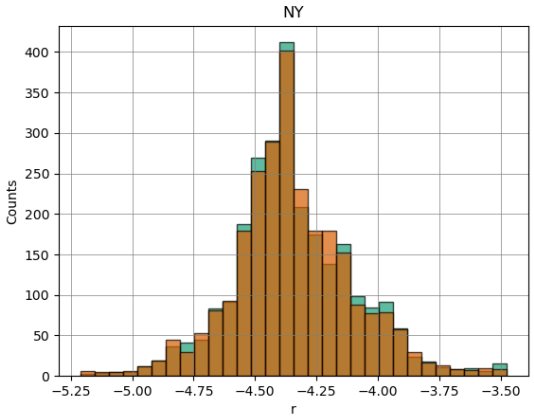

(b) Distribution of regression factor of air pressure.

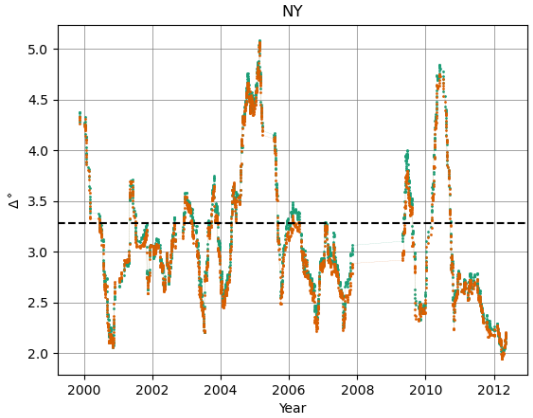

(c) Data misfit of untapered signals.

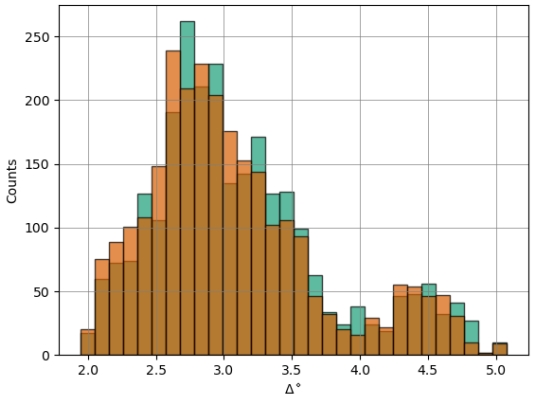

(d) Distribution of data misfit of untapered signals.

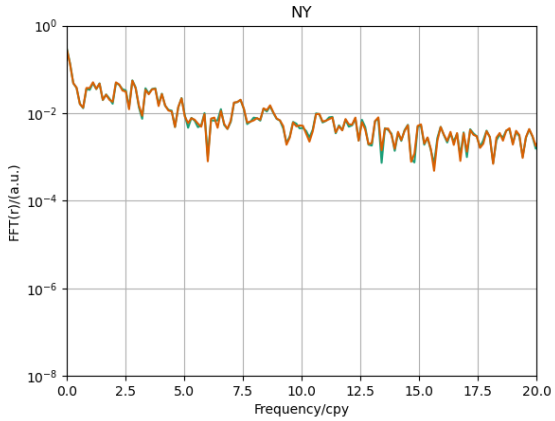

(e) Spectra of the coefficient for air pressure regression factor.

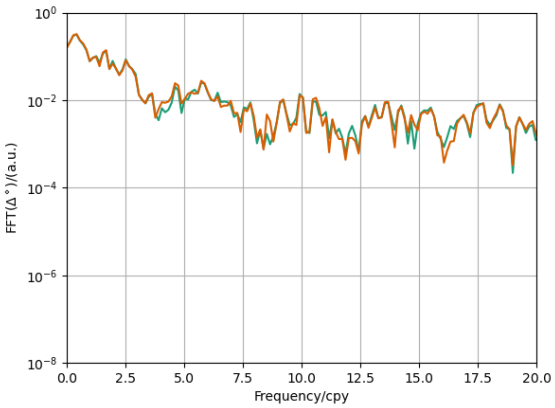

(f) Spectra of the data misfit of untapered signals.

Figure F.13.: The moving window analysis: air pressure regression factor, data misfit (untapered), their spectra and distribution. Station: Ny-Ålesund.

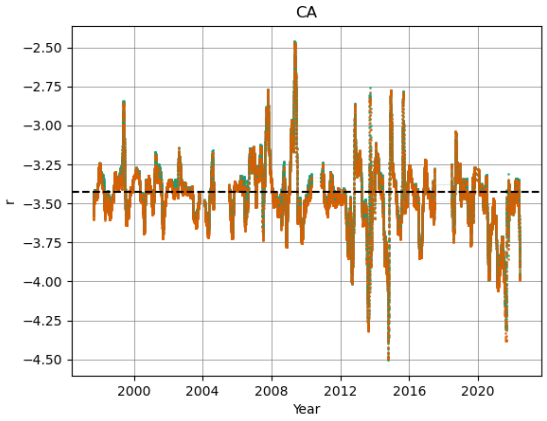

(a) Regression factor of air pressure.

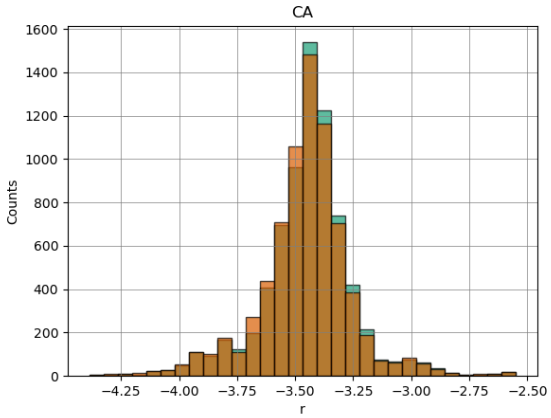

(b) Distribution of regression factor of air pressure.

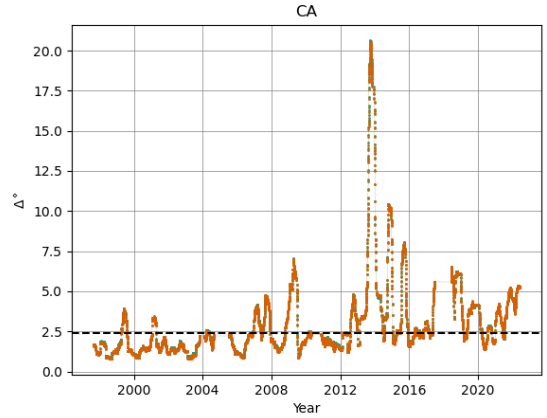

(c) Data misfit of untapered signals.

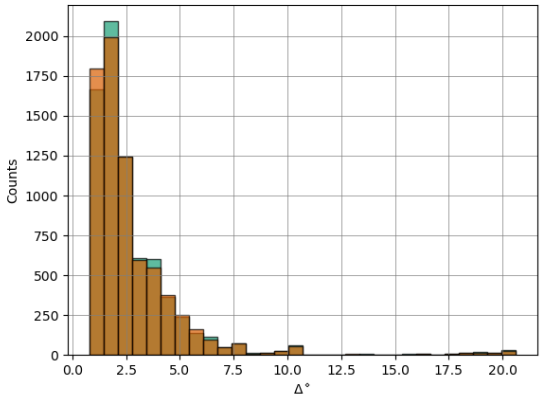

(d) Distribution of data misfit of untapered signals.

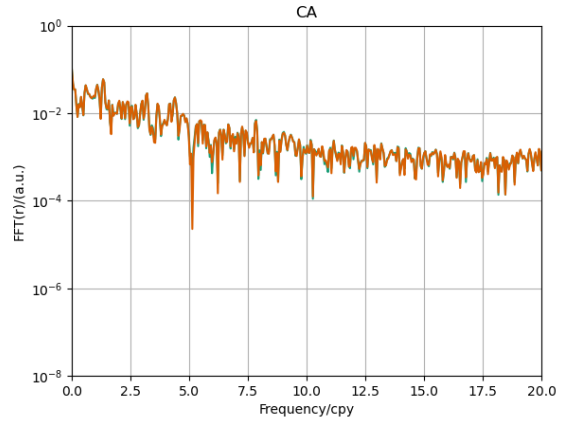

(e) Spectra of the coefficient for air pressure regression factor.

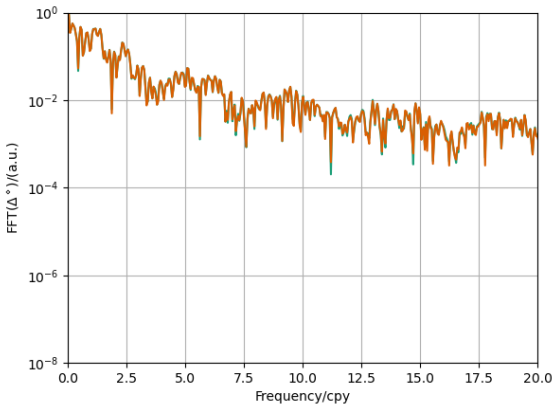

(f) Spectra of the data misfit of untapered signals.

Figure F.14.: The moving window analysis: air pressure regression factor, data misfit (untapered), their spectra and distribution. Station: Cantley.

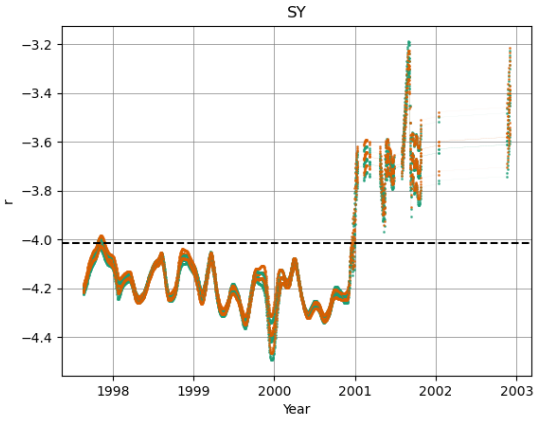

(a) Regression factor of air pressure.

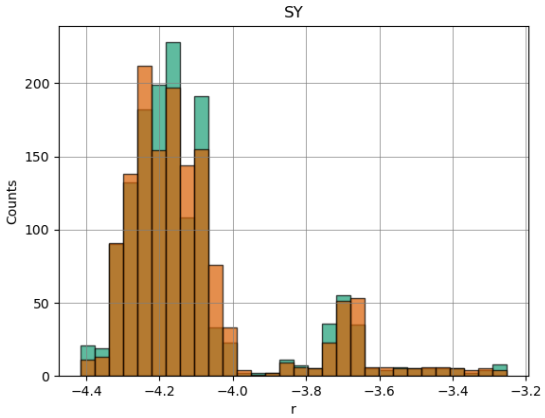

(b) Distribution of regression factor of air pressure.

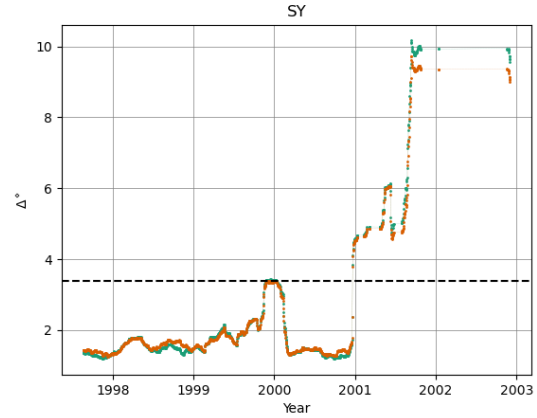

(c) Data misfit of untapered signals.

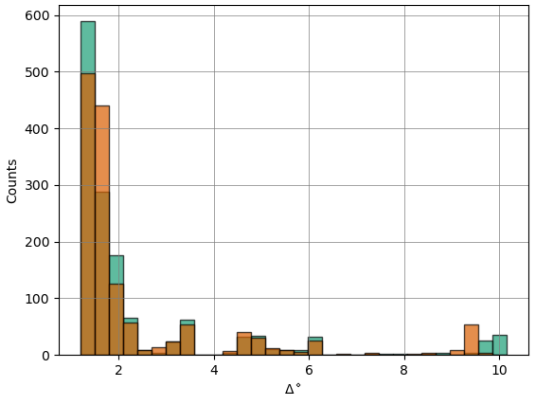

(d) Distribution of data misfit of untapered signals.

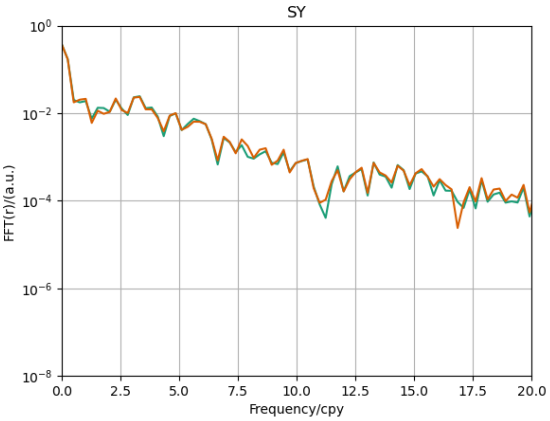

(e) Spectra of the coefficient for air pressure regression factor.

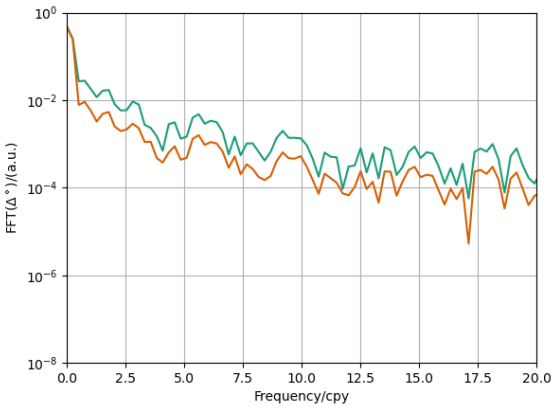

(f) Spectra of the data misfit of untapered signals.

Figure F.15.: The moving window analysis: air pressure regression factor, data misfit (untapered), their spectra and distribution. Station: Syowa.